Ministero dell'Istruzione, dell'Università e della Ricerca

UNIVERSIDADE DE COIMBRA

DEPARTMENT OF CIVIL ENGINEERING

PhD course in Risk and Sustainability in Civil, Architecture and Environmental Engineering Systems

XXXI CYCLE - N.S. (2015-2018)

University of Salerno

DEPARTMENT OF CIVIL ENGINEERING

PhD course in Steel and Composite Construction

University of Coimbra

PSEUDO DYNAMIC TESTS AND NUMERICAL ANALYSIS OF FREE FROM DAMAGE MULTISTOREY STEEL BUILDINGS WITH INNOVATIVE CONNECTIONS

a.a. 2018/2019

Giovanni Ferrante Cavallaro

Tutor
Prof. Gianvittorio Rizzano
Co-tutor
Prof. Vincenzo Piluso

President of the Doctoral College
Prof. Fernando Fraternali

Tutor
Prof. Aldina Santiago
Co-tutor
Prof. Luís Simões da Silva

President of the Doctoral College
Prof. Luís Simões da Silva

“E se per caso non doveste vederci più,

sarete certi, che come ogni altra cosa al mondo,

ci rivedremo un giorno tra le stelle.”

Claudio Santoriello

Contents

List of figures

List of tables

ABSTRACT

One of the most widespread structural systems is represented by Moment Resisting Frames (MRFs). This structural system is made up of frames capable of resisting seismic actions through predominantly flexural tension states. The stiffness and lateral resistance of the system depend on the flexural strength of the members and the type of connection, while the development of the plastic hinges guarantee the dissipation of the seismic input energy. The location of the dissipative zones varies according to the design approach adopted, typically they develop in beams, columns and connections. The most widespread design philosophy is to have strong columns, weak beams and full-strength rigid connections with complete resistance restoration, in this way all the seismic energy tends to be dissipated by the plastic hinges at the ends of the beams and at the base of the columns of the first level.

In order to overcome the traditional design approach, the present research work introduces a new type of beam-column connection capable of exhibiting a remarkable rigidity in service conditions (SLE) and able to exhibit a remarkable dissipative capacity when a rare seismic event occurs. The codes currently in force provide that for seismic events characterized by a period of return comparable with the useful life of the construction (frequent or occasional events) the structures remain in the elastic field ensuring that the seismic energy is completely dissipated through viscous damping. Vice versa, the seismic energy must be dissipated through plastic engagement of parts of the

structure, with wide and stable hysteresis cycles, for rare and very rare seismic events with a return period of about 500 years. The development of the hysteresis involves structural damage that have to be such as not to lead to the collapse of the structure in order to guarantee the protection of the life of those who occupy the building. The prediction of the behaviour of the structure in non-linear field for rare seismic events represents an aspect that only experimental research can describe in depth by developing new analytical models and innovative design philosophies. The execution of quasi-static tests can provide useful information in order to investigate the nonlinear behaviour of the members and the assemblages even if the forces or the displacement histories applied during the tests do not correspond exactly to the actions that occur during a real seismic event. The information obtained through these test procedures is however useful for calibrating analytical models and comparing the behaviour of structural components. The execution of tests on real scale structures is the best way to investigate the global behaviour of a structural system. For a more complete knowledge about the response in the dynamic field, the pseudo-dynamic tests represent a test protocol able to provide information of the structural response of a component or of a structure in a dynamic field through a static test.

The main purpose of this work, developed within the FREEDAM research project financed by the European Community, is to develop an innovative beam-column connection. These innovative connections are equipped with an additional damper able to dissipate the energy deriving from destructive seismic events.

The FREEDAM beam-column connection, through an appropriate design of the various components, is able to withstand frequent earthquakes and rare events without causing damage to the structural elements.

The thesis is divided into six chapters.

The ***Chapter 1*** reports a brief introduction to the traditional beam-column connections, specifying the characteristics of the different types of connections and their influence on the behaviour of the Moment Resisting Frames. In the last part of the chapter the FREEDAM dissipative connection is presented, specifying its peculiarities and the benefits that its introduction into the structural system brings. The ***Chapter 2*** is devoted to the description of the results obtained from an extensive experimental campaign developed at the STRENGTH laboratory of the University of Salerno, for the choice of the material for the friction dampers used in the FREEDAM connections by carrying out a statistical characterization of the static and dynamic friction coefficients. The ***Chapter 3*** collects the results of a further experimental campaign carried out at the University of Salerno laboratory and aimed at studying the tightening losses for pre-loading bolt systems equipped with different washers. In ***Chapter 4*** a design procedure has been define for the FREEDAM beam-column connections, then this procedure has been applied in order to design two different types of connections that have been experimentally tested at the University of Coimbra Laboratory (PT). In the same chapter, the test layouts and the results obtained from the cyclic tests carried out on the nodes equipped with FREEDAM friction dampers have been described, finally developing models to the finite elements and

comparing the experimental results with the computerized models. Finally, the ***Chapter 5*** shows the results of the pseudo-dynamic tests carried out on a full-scale steel Moment Resistant Frame equipped in a first case with traditional full strength beam-column connections (dogbone) and in a second case equipped with the innovative connections proposed. These results have been compared to each other and with the results obtained from finite element models.

CHAPTER 1

1.1. Traditional Moment – Resisting Frames (MRFs)

The Moment Resisting Frames represent one of the most diffused structural solution. On one hand, this structural system is able to exploit the flexural resistance of the members that compose it to resist lateral loads. On the other hand, the dissipation of the seismic input energy is guarantee by the development of dissipative zones. The location of the dissipative zones strongly depends from the adopted design approach, commonly they are located in correspondence of the beam ends, or in columns and joints (Fig. 1.1).

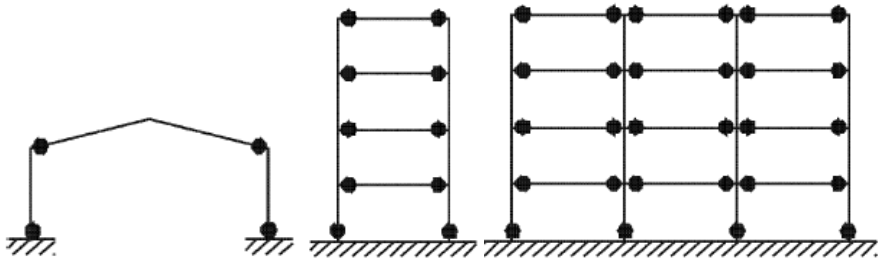

Fig. 1.1 – Structural typologies of moment resistant frames

From the application of the capacity design criterion to the design of a MRF usually it derives that the beams correspond to the weak element and the columns to the strong one, while the connections are rigid. This classical approach involves that the structure is able to fully exploit its ductility and its dissipation capacity by means of the development of plastic hinges in correspondence of the beam ends and the columns of

the first storey. Alternative approaches are possible, one of the most important consist into the plastic engagement of the joints, removing the assumption of full strength joints, in this way the joint components provide a contribution to the energy dissipation.

The use of the Moment Resisting Frames is affected by a series of disadvantages, above all the structural behaviour is strongly affected by the second order effects that provoke an increase of the lateral drifts, making more difficult to comply with the code requirements for checks both at the ULS and at the SLS.

The traditional MRFs can be classified into three different categories based on the arrangement of the seismic-resistant frames: space frames, perimeter frames and few distributed MRFs.

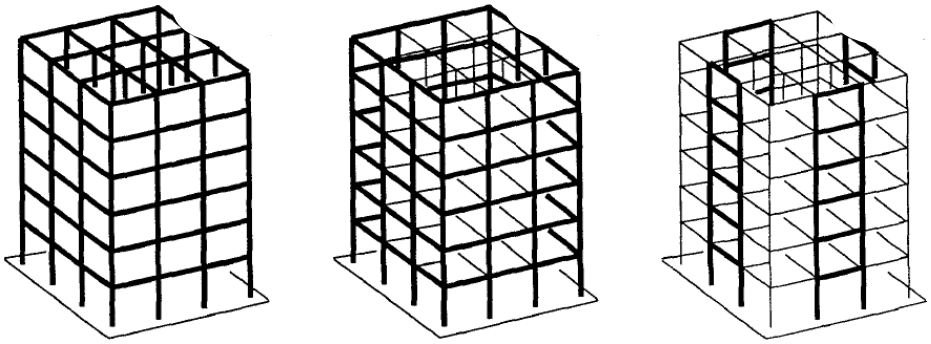

a) b) c)

Fig. 1.2 – Spatial distribution: a) space frames; b) perimeter frames; c) MRFs in only a few rigid bays – Source: Astaneh-Asl [1]

A three directional structural system (Fig. 1.2a) is composed by columns, beams and connections, and it is able to resist to the applied loads exploiting the flexural stiffness, the strength and the ductility of each member sometimes with the help of horizontal diaphragms or floor Bracing systems.

The perimeter MRF (Fig. 1.2b) is characterized by the presence of the moment resisting frames only in correspondence of the perimeter of the structures, in such a way to resist to the lateral loads like a box. The members that belong to the frames placed in the central part of the building are designed to resist only to gravitational loads. In any case the members designed to the resist only to gravity loads, the floor diaphragms and the other non-structural elements, also provide a contribution in terms of stiffness, strength and damping to the lateral load resistance of the structure. The main advantage of this solution is represented by the reduction of the number of rigid moment connections with respect to a comparable space frame, consequently reducing the cost of the structure.

The structures belonging to the last category (Fig. 1.2c) present rigid connections in only few bays of the entire planar frame. For this reason, the columns that are not part of the moment-resisting frame have to resist only to gravity loads, while the connections are simple shear connections, and the contribution of these members to resistance to the lateral loads of the structure is neglected.

1.1.1. Joints classification

The dynamic response and the post-elastic behaviour of the MRFs is strongly related to the typology of connections adopted. Furthermore, the evaluation of the internal actions in the structure, both in Serviceability Limit States (SLSs) and Ultimate Limit States (ULSs), strongly depends on the elastic and plastic response of the connecting system, that can range from rigid to flexible.

There are two main different typologies of beam-to-column joint: the first one does not allow relative rotation between the connected members, in other words all the elements converging in the joint present the same rotation, the second one permits the relative rotations. In the first case the frames are continuous, in the second one are pinned. When an elastic design procedure is adopted, the connection is mainly characterized by the rotational stiffness, leading to classify the connections into three categories:

- Nominally pinned connections, that are able to rotate without develop bending moment actions and for this reason influencing negatively the column resisting capacity. This type of connection is able to transfer shear and axial forces from the beam to the column.
- Rigid connections, that are able to transmit all the reactions without develop significant deformations and without altering the moment distribution.
- Semi-rigid connections, whose behaviour is related to the moment-rotation curve of the joint.

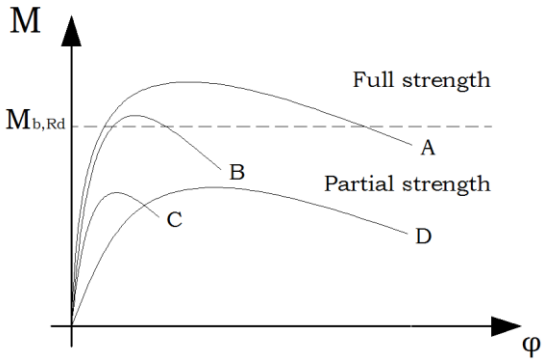

Fig. 1.3 – Beam-to-column joints classification according to their flexural resistance

In case of a rigid-plastic design, according to Eurocode 3 [2], the connections are classified based on the joint flexural resistance as following:

- Full strength joints with a design resistance equal or greater than the resistance of the connected members. Obviously, the development of plastic hinges takes place in correspondence of the member ends. The plastic rotation capacity of the joint is related to the ratio between the width and the thickness of the plates that constitute the member sections (Case A). When the strain-hardening of the material is not enough to prevent the yielding of the connection, the rotational capacity of the beam sections is not completely exploited and the additional plastic rotation of the joint plays an important rule (Case B).
- Partial strength connections, that are characterized by a design resistance lower than the connected members, and this means that a sufficient rotational capacity of the joint is needed (Case D). In case C the rotational capacity of the connection could be exceeded.
- Nominally pinned connections, that present a design resistance lower than the connected members.

The last classification criterion, based on the plastic rotation supply, divides the joints into two categories:

- Full ductility connections, that can develop a rotation in plastic field greater than the one that connected member can exhibit.
- Partial ductility connections, that cannot develop a plastic rotation greater than the one exhibits by the connected member.

The different classification for the joints are summarized in Table 1.1.

Table 1.1 – Joint classification

Method of global analysis	***Classification of the joint***		
elastic	*nominally pinned*	*rigid*	*semi-rigid*
			Semi-rigid and partial-strength
elastic - plastic	*nominally pinned*	*rigid and full-strength*	*Semi-rigid and full-strength*
			rigid and partial-strength
rigid - plastic	*nominally pinned*	*full-strength*	*partial-strength*
Type of joint model	***Simple***	***Continuous***	***Semi-continuous***

1.1.2. Frame classification

The frames classification depends on the joints classification. In fact, the relationship between the bending moment and the joint rotation, that is related to the joints strength, stiffness and rotational capacity, influences the distribution of actions on the structures and also the structure ductility.

The fames, as provided by Eurocode 3 [2], can be classified as sway and non-sway, according to their susceptibility to second order effects. In particular, a frame is non-sway if the internal actions due to the lateral deformation of the frame are negligible, conversely, a fame is sway when the deformed shape of the frame increase the internal actions and modify the structural behaviour.

Another classification divides the frames in braced and unbraced. The braced frames are characterized by the presence of stiffeners that

reduce the lateral displacement of at least the 80%, in all the other cases the frames are defined unbraced.

Depending on the joint characteristics, the Eurocode 3 [2] provides a further classification. In particular, the frame can be divided in:

- simple: when the joints are not able to transmit the bending moment to the columns and they allow the free rotation of the connected beams, in other words the structural system can be consider pendular;
- Continuous: when the joints resistance is greater than the one of the connected beams and the joints can be considered rigid;
- semi-continuous: when the joints assume an intermediate behaviour and it is necessary to define a proper model to take into account the real moment-rotation curve of the joints.

A further classification of the MRFs is referred to the ductility of the structure (Table 1.2). It is possible to define two different parameters in order to describe the ductility properties of a structure: the global ductility, that is defined as the ratio between the ultimate sway displacement and the elastic sway displacement evaluated in correspondence of the top of the structure; and the local ductility, that concerns the rotational capacities of the plastic hinges located at the beam ends and/or in the joints.

Table 1.2 - Classification of structures with reference to their ductility supply

EUROCODE 8
Ductility Class LOW (DCL)
Ductility Class MEDIUM (DCM)
Ductility Class HIGH (DCH)

Actually, the codes provide some requirements regarding the ductility of the structures, in particular the formation of the plastic hinges is not permitted in the columns, while they require to locate the dissipative zones at the beam ends or in other zones. In Table 1.3 the required rotation capacity for the plastic hinges are shown.

Table 1.3 – Connection required ductility

EUROCODE 8	
Ductility Class	***Rotational Capacity [mrad]***
Ductility Class LOW (DCL)	*35*
Ductility Class MEDIUM (DCM)	*25*
Ductility Class HIGH (DCH)	*-*

1.1.3. Seismic design of MRFs

In order to the increase the energy dissipation capacities of the structures when a seismic event occurs, a great number of the plastic hinges have to be developed in the structural elements. The Eurocodes, in line with others international codes, suggest to use the hierarchy criteria in such a way to assure that the plastic engagement to dissipate seismic energy. The plastic engagement has to be concentrated in the so-called "dissipative zones" (typically the beam ends), that are characterized by wide and stable hysteresis loops, while the "non-dissipative zones" have to resist to the maximum actions that dissipative zones can transfer, remaining in the elastic field to avoid a

brittle failure mode and/or storey mechanism. In other words, it is needed to avoid the yielding of the columns and at the same time assure a global dissipative collapse mechanism.
In order to satisfy the code provisions, the beam-to-column joints play a very important rule, because the actions are transmitted from the beams to the columns by means of the joints. For this reason, many research efforts are devoted to investigate the behaviour of the joints within the framework of the seismic design of MRFs.
Whatever the design solution adopted in the field of traditional design strategies, the damage of the structural elements is required to dissipate the seismic input energy.

1.2. Recent research developments and proposal for an innovative solution

Nowadays many efforts of the scientific community are devoted to the development of new structural seismic systems able to avoid the damage of the structural elements or to very easily repair them after a strong earthquake. Many researchers focused their attention on the dissipation of seismic input energy by the introduction of supplemental damping devices reducing the seismic engage of the structural elements. The adoption of supplemental damping devices requires specific structural details, in particular a detailed beam-to-column joint is required. In order to achieve this objective, the Double Split Tee Connection represents the most appropriated partial strength joint typology, characterized by easy replaceable connecting elements. The structural response of this type of connection depends on the T-stubs

behaviour. Several research groups investigated the behaviour of simple T-stub under cyclic loads, in order to correctly predict the response of the upper and lower Tee of the connection [1]. The scientific literature shows that pinching is one of the main aspects that characterizes the behaviour of T-stubs subject to axial load, mainly due to the plastic deformation of the bolts and contact phenomena. Taking into account the results of monotonic and cyclic tests on T-stubs [1,3-4], the researchers focused their efforts on how to increase energy dissipation [5], identifying two different approaches. In both cases supplemental dampers are added to the structures, in first case yielding type dampers, applying the same concepts adopted for ADAS devices, while in second case friction dampers, taking advantage of the friction properties of materials. In last decades, new design strategies have been developed, the concept of performance levels have been introduced into seismic codes, dealing to these design procedures the structures have to remain in elastic range in case of frequent seismic events (Serviceability Limit States), while the damage can occur in case of rare seismic events (Ultimate Limit States). The satisfaction of the performance level related to the Ultimate Limit State require to govern the structural ductility at local and global level exploiting the capacity design criteria and in this way controlling the failure mode of the structure. In other word, the capacity of the structures to satisfy the inelastic demand depend on the capacity to develop damage in specific zones engaged in plastic range. The Eurocode 8 [6], in case of steel Moment Resisting Frames (MRFs), suggests two different solutions: in the first case the plastic zones are located at the beam ends, adopting full-strength joints and over-strength columns (continuous frames), in the second case the structural damage is concentrated in connections, which are partial-

strength joints [7,8], verifying that their rotational capacity is able to overcome the seismic demand (semi-continuous frames). This topic is object of discussion in scientific community, with several research groups currently engaged in the investigation of the criteria to guarantee the correct ductility supply to the connections [9-14].

However, regardless of the approach adopted and despite the fact that in the last decades both solutions have been validated by numerous and authoritative researchers, the main drawback of traditional design strategies consist in the development of structural damage [15-21] Even if structural damage is useful to preserve human life avoiding the total collapse of the structures, on the other hand it represents also the main source of direct and indirect losses when a rare seismic event occurs. Starting from 90s, aiming to solve this issue, several strategies have been proposed, in particular supplemental energy dissipation systems have been widely investigated, developing different typologies of dissipaters to be insert in particular zones of the structure. The dissipaters, located where the structure exhibit high relative displacement or velocity under destructive earthquake, work like a fuse with the aim to dissipate input energy, exploiting different dissipative mechanism such as dry friction, viscosity of fluids and yielding material [22,24]. The introduction of supplementary energy dissipation design strategies certainly brings an advantage in controlling the failure mode of the structure, but it is not able to avoid damage of the structural elements because sway displacement of the structure is necessary in order to activate the seismic dissipaters.

As part of the additional energy dissipation, the FREEDAM connection represents a type of innovative connection that is the object of a research project funded by the European Community. The new

proposed strategy, whose name derive from “FREE from DAMage”, is based on the use of friction dampers conceived in such a way to substitute the traditional dissipative zoned of MRFs, i.e. the beam ends. The friction dampers, located at the bottom flange level, have to be design to assure the transmission of the beam bending moment required to fulfil serviceability limit state requirements and to withstand without slippage to the gravity loads. In addition, they have to be designed in order to assure the dissipation of the earthquake input energy corresponding to the ULS without any damage.

1.3. Objective of the thesis

Starting from the results obtained by the research groups in the past decades, this work aims to investigate and validate an innovative connection for steel structures able to dissipate by means of friction the input seismic energy avoiding the damage of the structural members. The introduction of the supplemental damping device allows to overcome the main drawbacks of the traditional connection both in serviceability and ultimate conditions. In particular, in case of rare seismic event the beam-to-column connection equipped with the damping device permits the relative rotation between the members assuring at the same time no damage of the structure. This new design strategy is the subject of a RFCS project named “FREEDAM” (FREE from DAMage), granted by European Community.

The structure of the thesis follows the different phases of the FREEDAM research project. In detail, chapter 2 is devoted to the introduction of the innovative connection, reporting the results of the tests for the choice and the characterization of the friction material, analysing the

influence of different parameters like the bolts' preload, the variability of the friction coefficient for the friction material of the FREEDAM connection, the type of washers adopted. At the end of the chapter the design procedure for the FREEDAM connection has been proposed. Chapter 3 provides a focus on the tightening procedure for pre-loadable bolts and the loss of pre-load, consisting of several tests performed at the STRENGHT laboratory (STRuctural ENGinering Testing Hall) of the University of Salerno. The results of these tests have been used to define the tightening method to apply the preload for the bolts of a FREEDAM connection and the loss of preload expected during lifetime of the friction device. Chapter 4 shows the results of the experimental investigation of the behaviour of an internal beam-to-column joint equipped with the innovative connections in two different configurations performed at the ISISE (Institute for Sustainability and Innovation in Structure Engineering) laboratory of the University of Coimbra. In detail the chapter contains the description of the design procedure for both configurations, the results of the cyclic tests and the FE models. The last chapter regards the execution of two pseudo-dynamic tests on a real scale frame performed at the STRENGHT laboratory of the University of Salerno. The first pseudo-dynamic test has been performed on a structure equipped with a traditional beam-to-column joint, while the second test has been performed on a structure equipped with the innovative connections in order to demonstrate the benefit on the seismic response of the structure deriving by the introduction of the FREEDAM device. Finally, a brief conclusion containing a summary of the activities developed during the research projects is presented.

1.4. References

1. A. Astaneh-Asl: *"Seismic Design of Bolted Steel Moment-Resisting Frames*". July, 1995.
2. CEN: "*Eurocode 3: Design of Steel Structures – Part 1-1: General rules and rules for buildings*", EN 1993-1-1, 2005.
3. C. Faella, V. Piluso and G. Rizzano: *"Structural Steel Semirigid Connections"*, CRC Press, Boca Raton, Ann Arbor, London, Tokyo. ISBN 0-8493-7433-2, 1999.
4. V. Giouncu and F. Mazzolani: *"Seismic Resistant Steel Structures".* New York: CISM Courses and Lectures No 420, 2000.
5. CEN: "*Eurocode 3: Design of Steel Structures – Part 1-8: Design of Joints*", EN 1993-1-8, 2005.
6. CEN, EN 1998-1-1: "*Eurocode 8: Design of structures for earthquake resistance - Part 1: General rules, seismic actions and rules for buildings",* European committee for standardization, 2005.
7. American Institute of Steel Construction, ANSI/AISC 341-10, AISC, 2010.
8. FEMA-358: "*Prequalified Connections for Special and Intermediate Steel Moment Frames for Seismic Applications*", American Institute of steel construction, 2010, incl. Supplement No. 1.
9. ECCS-CECM-EKS: *"European Recommendation for Steel Structures in Seismic Zones, Technical Working Group 1.3: Seismic Design"*, n. 54, 1988.
10. K.S. Moore, J.O. Malley and M.D. Engelhardt: *"Design of reduced Beam Section (RBS) Moment Frame Connections"*, AISC Structural Steel Educational Council, Moraga, CA., 1999.

11. C.J. Carter and N. Iwankiw: *"Improved Ductility in Seismic Steel Moment Frames with Dogbone Connections"*, Journal of Constructional Steel Research, Vol. 46, No. 1-3, Paper No. 253.

12. C. Joh and W.F. Chen: "*Fracture Strength of Welded Flange-Bolted Web Connections"*, Journal of Structural Engineering, ASCE, Vol. 125, No. 5, pp. 565-571, 1999.

13. S.J. Chen, J.M. Chu and Z.L. Chou: *"Dynamic Behaviour of Steel Frames with Beam Flanges Shaved Around Connection*", Journal of Constructional Steel Research, Vol. 42, No. 1, pp. 49-70, 1997.

14. R. Richard, J.E. Partridge, J. Allen and S. Radau: *"Finite Element Analysis and Tests of Beam-to-Column Connections"*, Modern Steel Construction, AISC, Vol. 35, No. 10, pp. 44-47, 1995.

15. D. Grecea, F. Dinu and D. Dubina: *"Performance criteria for MR steel frames in seismic zones"*, Journal of Constructional Steel Research, Vol. 60, pp. 739-749, 2004.

16. FEMA 351. "*Recommended Seismic Evaluation and Upgrade Criteria for Existing Welded Steel Moment-Frame Buildings",* Federal Emergency Management Agency, Washington, 2000.

17. SAC: *"Recommended Design Criteria for New Steel Moment Resisting Frames Buildings"*, California, 2000.

18. R. Montuori, E. Nastri and V. Piluso: *"Advances on the theory of Plastic Mechanism Control: Close Form solution for MR Frames"*, Earthquake Engineering & Structural Engineering, vol. 4, pp. 1035-1054, 2014.

19. C. Faella, R. Montuori, V. Piluso and G. Rizzano: *"Failure Mode Control: Economy of Semi-Rigid Frames",* Proc. of the XI European Conference on Earthquake Engineering, Paris, 6-13 September, 1998.

20. J.M. Aribert and D. Grecea: *"Numerical investigation of the q-factor for steel frames with semi-rigid and partial-strength joints",* Proc. of the Third International Conference STESSA 2000, Montreal, August 21-24, 2000.

21. A. Astaneh-Asl and N. Nader: *"Proposed code provision for seismic design of steel semi-rigid and rigid frames",* Proc. of the 5th U.S. National Conference of Earthquake Engineering, EERI, Chicago, 1994.

22. ID Aiken, PW Clark and J.M. Kelly: *"Design and Ultimate-Level Earthquake Tests of a ½.5 Scale Base-Isolated Reinforced-Concrete Building".* Proceedings of ATC-17-1 Seminar on seismic Isolation, Passive Energy Dissipation and Active Control. San Francisco. California, 1993.

23. M.C. Constantinou, T.T Soong and G.F. Dargush: *"Passive Energy Dissipation Systems for Structural Design and Retrofit".* Multidisciplinary Center for Earthquake Engineering Re-search, University at Buffalo, State of New York, 1998.

24. J.M. Castro, A.Y Elghazouli and B.A. Izzudin: *"Modelling of the panel zone in steel and composite moment frames".* Engineering Structures.27:129-144, 2005.

CHAPTER 2

2.1 The FREEDAM connection

The FREEDAM (FREE from DAMage) design strategy consists in a new typology of beam-to-column connection able to dissipate input seismic energy by meaning the introduction of friction damping devices and, at the same time, differently from the traditional strategies, avoiding the damage of structural parts both at SLS and ULS. The philosophy behind this kind of approach is very simple: on one side is possible design rigid frames with fully rigid connections (as in case of full-strength design, continuous frames) whose resistance is very close to the beam resistance (as in case of partial – or equal – strength design) and, on the other side, the damping devices dissipate input energy (as in case of supplementary energy dissipation strategies) and in addition they avoid the structural damage.

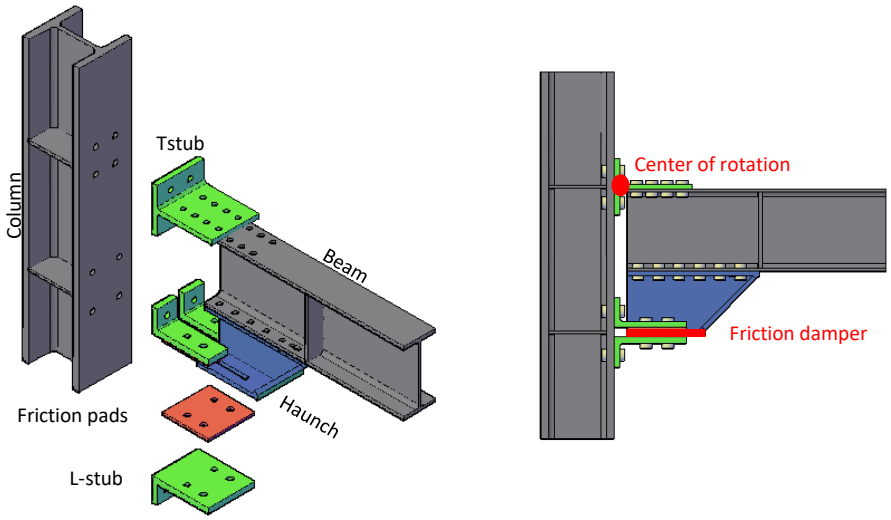

Fig. 2.1 – FREEDAM connection

The FREEDAM design strategy aims to define a configuration of the structure able to dissipate seismic energy and such as not to suffer damage to the connections and members during a seismic event, through the addition of friction devices located in correspondence of the joints. In practice, the FREEDAM connections are innovative beam-to-column connections equipped with a friction device at level of the lower beam flange realized using steel plates and friction pads pre-stressed by means of high strength bolts. The typical configuration of FREEDAM derive from the classical detail of a Double Split Tee Joints (DST), where instead of the bottom Tee element there is a symmetrical friction connection [1-4], constituted by a slotted haunch which slips on friction shims preliminarily stressed with high stress bolts.

The behaviour of this type of connection is quite simple, in fact, when a seismic event occurs there is an increase of the bending actions, and the joint start to rotate around a rotation center, that in this case is located in correspondence of the upper T-stub web while the energy dissipation is guarantee by the alternate slippage of the haunch on friction pads. In practice, the design procedure of a FREEDAM connection is extremely simple and it can be divided in few steps:

- design of the friction dampers. The actions to be considered in this steps derive from the ULS load combinations, and the design of the dampers can follow two different approaches. The first approach considers the connected beam more resistant of the damper (partial-strength), while the second one consider the same resistance for both (equal strength) [5-6];
- design of non-dissipative parts of the connection. In this step it is necessary to properly taking into account the over-strength

due to random variability of the property of the material chosen for friction pads. It is important to underline that the strain-hardening is not computed in the over-strength factor because the response of the friction dampers is rigid-plastic. The design of the element constituting the joint can be developed in order to achieve a fully rigidity, that represents an advantage for the SLS checks respect to the classical semi-continuous design. This is possible because the slip resistance of the friction damper is uncoupled from the stiffness of connection;

- design of columns. This step can be performed by referring to the procedures provided by Eurocode 8 [7] or other more advanced procedures, such as the Theory of Plastic Mechanism Control [8], that guarantee a global type failure mechanism.

The main parameters that influence the resistance of the FREEDAM connections are the preload force in the bolts and the friction coefficient, for this reason it is important on one hand control the pre-loading force applied and on the other hand characterize accurately the value of the friction coefficient. The EN1090-2 [9] suggests different methods to control the pre-loading force applied by means high strength bolts: torque method, combined method, DTI washers. The application of pre-load to the bolts using one of the methods suggested by EN1090-2 [9] guarantee the minimum 95% reliability on the tightening required by EN1090-2 [9]. Regarding the definition of the value of the friction coefficient, it depends from several factors and for this reason it has to be estimate experimentally. The friction coefficient strongly depends on the material employed to realize the friction interface and on the

tribological properties, i.e. the superficial finishing, micro and macro hardness, shear resistance and roughness [10,11].

2.2 Choice of friction material

The main goal of the experimental campaign performed at the STRENGHT laboratory (STRuctural ENGineering Testing Hall) of the University of Salerno is to evaluate the behaviour of different materials, in particular define, with a sufficient level of accuracy, the values of static and dynamic friction coefficients, and consequently choose the best material for FREEDAM connection. This task within the FREEDAM research project represents the starting point without which all the subsequent steps could not develop correctly, lacking fundamental parameters to design the parts that make up the friction connection. The experimental program consists of 63 specimens, designed according to the guidelines provided by EN 1090-2 [9] and EN 15129 [12], that have been tested into two phases. During the first phase 13 tests have been performed in order to investigate the behaviour (in terms of static and kinetic friction, and in terms of degradation) of the friction interfaces realized combined stainless steel plates with eight different materials. The second phase is devoted to a more in-depth characterization of the response of the three materials that showed the best results during the first phase. For this purpose, the influence of the bolts pre-load level and the typology of the adopted washers is analysed. Regarding the influence of bolts pre-load, several tests are performed at different value of the pressure applied to the interfaces, varying the values of the pre-loading between 40% and 100% of the standard pre-loading value, while the influence of the washers is

investigated performing tests with two typologies of washers: standard flat washers and Belleville disc springs, the latter arranged in different configurations of washers in series or in parallel. The comparison between the results of the tests on specimens equipped with standard flat washers and the ones equipped with Belleville disc springs is useful to assess the effectiveness of the Belleville washers in the reduction of bolt's loosening during cyclic test.

In order to provide corrosion resistance fundamental for the durability of the damper, the internal surface of the damper is made of stainless steel, while the materials for the friction pads have been applied to the support by means of thermal spray process. Taking into consideration the indications deriving from the analysis of the technical literature, for the first phase of tests, eight materials have been chosen with values of the superficial hardness much higher or much lower than stainless steel, in fact, as hypothesized by Bowden and Tabor in [13], the fiction coefficient (μ) of a metal interface is related to the ratio between of the shear resistance of the weakest material (s_0) and the superficial hardness of the softest material (σ_0) constituting the interface:

$$\mu = \frac{s_0}{\sigma_0} \tag{2.1}$$

Therefore, to achieve a high value of the friction coefficient, it is necessary to have a high value of the shear resistance of the weakest material and/or a very low value of the superficial hardness of the softest material. Considering that the stainless steel adopted for the FREEDAM connections is AISI 304 type, characterized by a superficial hardness of 130 HV, then the materials to be coupled have been selected, among those commercially available, with much higher or

much lower values of the superficial hardness. Of the eight chosen materials, five are soft materials composed by non-ferrous pure metals or metal alloys with Vickers Hardness lower than 30 and labelled with the ID tags M1-M5, conversely, the other three are "hard" materials, two produced as powder blend and one with Electroless Nickel process from 3M Deutschland GmbH, and labelled with labels from M6 to M8, present a superficial hardness higher than 550 HV, that in case of friction shim produced using Electroless Nickel process is between 600 and 900 HV. The response of the interfaces is strongly influenced by the material coupled to the stainless steel, in fact, when it is coupled with soft materials the wear is concentrated in correspondence of the friction shims, conversely, when it is combined with hard materials, the consumption of the stainless steel is promoted. In both cases the friction coefficient essentially depends to the ratio between shear resistance and superficial hardness.

2.2.1 Friction shims coating process

The coating of the friction pads with the eight chosen materials took place using processes belonging to two macro categories: thermal spray and Electroless Nickel Plating. In turn, the processes included in thermal spraying category can be subdivided into further sub-categories according to the technology adopted, in this case only two of them have been used: Electric Arc Wire and Atmospheric Plasma Spray Solutions. In detail, the specimens marked with the codes M1 to M5 have been produced using the Electric Arc Wire process (soft materials); while the first two hard materials (carbide M6 and M7) have been produced exploiting the Atmospheric Plasma Spray Solution; and finally the

specimens marked with the M8 code have been produced using Electroless Nickel Plating technology.

Thermal spray processes

Thermal spray is an industrial procedure to apply coatings by means of special devices/systems through which melted or molten metals are propelled at high speed on cleaned and prepared component surfaces. In this procedure the coating material is melted by a heat source and then it is propelled by means of gases on a base material, where it solidifies forming a solid layer. Because the adhesion of the coating to the substrate predominantly consists of mechanical bonding, a careful cleaning and pre-treatment of the surfaces to be coated is extremely important. To this scope, after the removal of surface impurities by means of chemical or mechanical methods, the surface is usually roughened using mechanical-blasting and grinding. Grinding usually is performed by means of grit blasting with dry corundum. Depending on the thermal spray process the coating material can be in wire or powder form and there are several different processes that can be used to apply a thermal sprayed coating.

Electric Arc Wire Spray

In this procedure, an arc is formed by the contact of two oppositely charged metallic wires, usually of the same composition. This leads to melting at the tip of the wire material and compressed air is used to atomize the melted spray material on the substrate.
The electric arc wire process requires a heat source to melt the coating feedstock, but it does not employ gases to generate the heat source like in the other processes. The electric arc wire spray process is in some

way very similar to gas metal arc welding and uses two metallic wires, usually of the same composition, as the coating feedstock. The two wires are electrically charged with opposed polarities (+/-) and they are fed into the arc gun at a precise, controlled speed. When the wires are brought together at the contact point, the opposing charges on the wires create an arc that continuously melts the tips of the wires. Compressed air is used to atomize the molten material in order to shot it on a properly prepared work piece surface. The procedure of application of these coatings has been followed directly in the shop in order to control the quality of the application and to document the industrial procedure. In particular, the total number of plates coated with arc wire spray was 48 employing the 5 different soft materials (M1 to M5).

Before coating the plates with the selected materials, some preliminary treatments were carried out. The first treatment (Fig. 2.2) has consisted in a mechanical blasting at low pressure with metal grit and corundum mesh (particle diameter less than 1,41 mm).

Fig. 2.2 – Preliminary treatment: a) plates before treatment; b) mechanical blasting; c) grinding.

Fig. 2.3 – Electric arc wire spray: a) plates before spray; b) machine for electric arc wire spray; c) spray coating.

Then the plates have been grinded using an angle grinder with discs of zirconium oxide and corundum. Subsequently, before spraying the coatings, on all the plates an adhesion layer has been applied. The expected coating thickness was 300μm, with a further 100μm of adhesion layer, for a total of 400μm. The main setting parameters of the machine employed to apply the coatings are the amperage, voltage and pressure of the air, which have been changed for the various materials according to the melting temperature of the materials applied. In Fig. 2.3 the different phases of electric arc wire spray process are shown, while Fig. 2.4 shows the plates at the end of the process.

Fig. 2.4 – Plates at the end of the process.

During the spray application, in order to verify the correct application of the coating layers on each plate, a series of measurements with an electronic feeler gauge have been performed. From the results of these measures it derives that the thickness of the coating layer also on the same face of the plate can have a significant variation. This is due to the fact that the arc-wire spray process is a completely manual procedure and, obviously, leads to significant approximations in the value of the thickness of the coating layer. Nevertheless, on the other hand, such a big variation of the thickness leads also to a superficial roughness much higher compared to the roughness that it is possible to obtain with other spraying procedures.

Atmospheric Plasma Spray Solutions (APS)

In this type of treatment, a high frequency arc is ignited between an anode and a tungsten cathode. The gas flowing through the electrodes is ionized such that a plasma plume develops. The spray material is injected as a powder outside of the gun nozzle into the plasma plume, where it is melted and hurled by the gas onto the substrate surface. There are two different variants of the process, in the first one the plasma is sprayed in a controlled low pressure atmosphere (APS), instead in second one the melted particles are sprayed in a vacuum environment, obtaining coatings of considerably higher quality.

The flexibility of the plasma spray process comes from its ability to develop easily the energy required to melt almost any coating feedstock material in powder form. The plasma gun uses a chamber with one or more cathodes (electrodes) and an anode (nozzle). With this process gasses flowing through the chamber, direct current power is applied to the cathode, which arcs to the anode. The powerful arc strips the gas

molecules of their electrons to form a plasma plume. As the unstable plasma ions recombine back to the gaseous state, a tremendous level of thermal energy is released. The feedstock material is injected into the hot gas plume, where it is melted and propelled towards the target substrate to form the coating. The process gases typically used are argon, hydrogen, nitrogen and helium, either individually on in mixtures of two or even three gases. The gas flows and the applied current can be accurately regulated. In addition, the shape and bare size of the nozzle, the point and angle that the material is injected into the plume, as well as the distance of the gun to the target surface are also controlled.

The M6 and M7 materials have been applied using this procedure. In particular, the powder was applied on the surface with the APS procedure, by means of computer numerical control machine that, in fourteen subsequent passes applied the 300μm of coating layer. Also in this case, before spraying the carbide powder, a preliminary treatment was realized in order to clean the plate surfaces. In addition, as adhesion layer was preliminarily applied. Even in this case, in order to verify the correct application of the coating layer, a series of measurements with an electronic feeler gauge were carried out on each pads. these measurements the homogeneous distribution of the coating material on the plate surfaces is evident because the values of the thickness measured in different points on the same plate are practically constant.

Electroless Nickel Plating

Electroless nickel plating is a process for depositing a nickel alloy from aqueous solutions onto a substrate without the use of electric current.

It differs, therefore, from electroplating which depends on an external source of direct current to reduce nickel ions in the electrolyte to nickel metal on the substrate. Electroless nickel plating is a chemical process which reduces nickel ions in solution to nickel metal by chemical reduction. The most common reducing agent used is sodium hypophosphite. Alternatives are sodium borohydride and dimethylamine borane, but they are used much less frequently. It is estimated that sodium hypophosphite is used in more than 99% of all electroless nickel plating. Some of the unique properties of electroless nickel, such as thickness uniformity, hardness, corrosion resistance and magnetic response have resulted in its use in many different industries. The application of the Electroless Nickel Plating to the friction shims of FREEDAM dampers has provided a very uniform coating with a constant thickness of 20μm on both sides of the plates.

2.2.2 Experimental layout

The specimens' layout is inspired to the provision for slip tests suggested by EN1090-2 [9]. The specimen is constituted by a system of steel plates obtained assembling stainless steel plates and friction shims in order to have a uniaxial slippage of the friction interfaces. In detail, the stainless steel plate realized in AISI 304 steel, is constituted by a slotted steel plate, while another steel plate with normal holes is used to connect the specimen to the testing machine, finally, there are the external steel plates and the friction shims. All the plates are pre-stressed with M20 class 10.9 HV bolts [14] (Fig. 2.5)

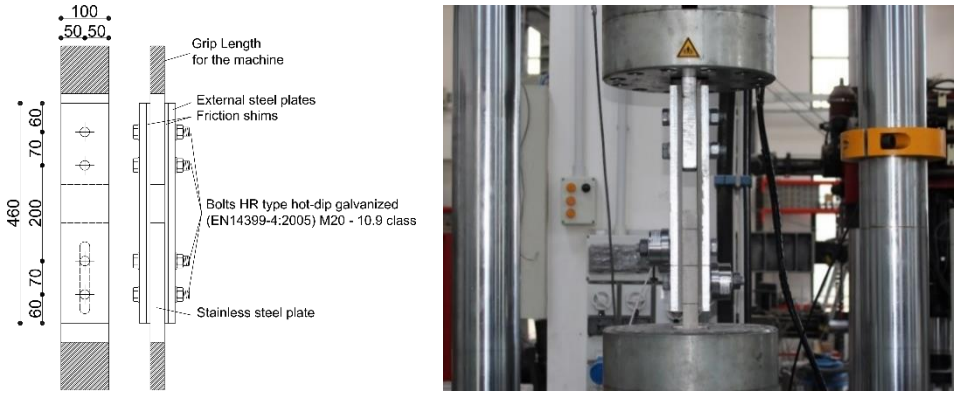

Fig. 2.5 – a) Typical layout of a specimen; b) Specimen in the testing machine

The aim of the test is to determine the initial slippage force and its degradation, for this purpose the cyclic load have been applied to the specimens according to the loading protocol given by EN 15129 (2009) [12], the reference code for testing of dissipative devices. In order to the device under actual working conditions, the code requires to tests under cyclic load the specimens, applying to the damper cycles with three different amplitudes, respectably the 25%, 50% and 100% of the maximum design displacement, equal to ±25mm. The maximum amplitude has been derived considering a prevision of the displacement demand in correspondence of the friction damper in real applications. In detail, considering the typical configuration of the FREEDAM connection, the value of the lever arm (distance between the upper T-stub and the mid-center of the friction damper) is equal to 600mm, while the maximum rotation expected is 40mrad (greater than 35mrad, maximum value suggested by Eurocode 8 [7]), so in conclusion the displacement demand at level of the damper has been evaluated as 0.04 · 600 = 24mm, then it has been rounded to 25 mm. The number of cycles to perform vary for each amplitude, the code suggests at least 5

cycles for the intermediate amplitudes and 10 cycles for the maximum. For this reasons, following the provision of EN 15129 (2009) [12], the adopted loading protocol is constituted by 5 cycles at the amplitude of 6.25mm, 5 cycles at the amplitude of 12.5mm and 40 cycles at the maximum amplitude of 25mm. The tests are performed in a quasi-static range, for this reason the test speed increases following the increase in amplitude of the cycles varying from 1mm/s for first 10 cycles to 5mm/s for the cycles at maximum amplitude, according to the capabilities of the testing machine. It is important to underline that the speed with which the displacement is applied to the specimen can influence the friction coefficient, in this regard specific tests have been foreseen within the FREEDAM research project carried out in the industrial FIP laboratories at a speed of 200mm/s. As said previously, the pre-load force represents an important parameter for the frictional behaviour of the connection, for this reason both upper and lower M20 high strength bolts have been tightened by a means a calibrated torque wrench, and the pre-load has been monitored using annular load cells installed in correspondence of the lower bolts, where the friction shims are located and there is the displacement. In the detail, considering that the admissible maximum level of pre-load for M20 HV 10.9 class bolts is equal to $0.7 \cdot A_{bolt} \cdot f_{ub} = 0.7 \cdot 245 \cdot 1000 = 171500$N, the upper bolts are pre-loaded with the maximum force, conversely for the lower bolts the preloading force varying from 40% to 100% depending on the tested specimen.

The universal testing machine (model Schenck Hydopuls S56) employed to perform the test is constituted by a hydraulic piston with loading capacity equal to ±630kN and maximum stroke equal to ±125mm located within a self-balanced frame. This machine is provided of an

internal displacement transducer and a load cell by means of which the displacement of the specimen and the slippage force respectively have been monitored. During the tests other transducers have been applied on the specimens in order to record data about the tests. The application of the pre-loading force to the high strength bolts, through a torque wrench, has been monitored by means a torque sensor Futek TAT430 with maximum capacity equal to 680Nm. Furthermore, the variation of the pre-load applied to the high strength bolts before and during the tests has been monitored using donut load cells Futek LTH500 with maximum capacity of 222kN. The geometrical configuration of this special typology of load cell is characterize by the application of the load on an internal cylinder in the middle of the load cell that is transferred to an external cylinder through a shear panel. In order to not alter the distribution of tensions on the plates, a custom washer with a diameter equal to the external diameter of the load cell coupled with a normal washer have been interposed between the load cell and the external plates of the specimen. Finally, according to the observations of the first results, during the second phase of tests two thermocouple have been introduced on the lower bolts and external plates of the specimens, to monitor the increase of temperature due to the friction.

The tightening procedure adopted to apply the pre-load to the bolts has been the subject of an in-depth study that will be illustrated in details in the next chapter, but it is useful to introduce some aspects in this part of the work. The EN 1090-2 [9] establishes that the force (the maximum admissible level of pre-load) to be applied to the bolts by means of a hand torque wrench has to be multiplied for an amplification factor equal to 1.1. The aim of this amplification is to

provide to the pre-load the meaning of a mean value. Considering for the adopted bolts an average value of the k-factor equal to 0.13, the tightening torque applied to the bolts, for the maximum level of pre-load, is equal to 0.13·171.5·20=446Nm.

For the sole purpose of giving an idea of the tightening procedure adopted for apply pre-load on the lower bolts, that will be analysed in the next chapter, the force versus time diagram is shown (Fig. 2.6).

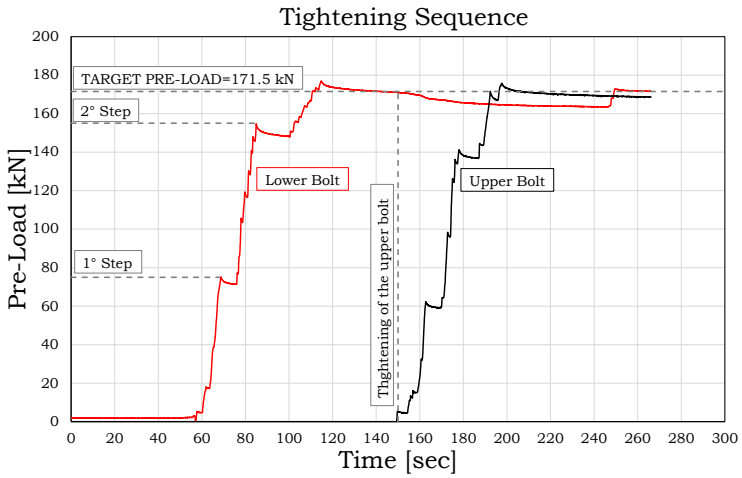

Fig. 2.6 – Tightening sequence

Observing Fig. 2.6 it is simple to notice that pre-load is applied in two different steps, in the first one the 75% of the admissible maximum pre-load is applied, while in the second step the admissible maximum pre-load amplified for a 1.1 factor is applied, according to the provision for torque method suggested by EN 1090-2 [9].

Others important issues that is possible to put in evidence are: an instantaneous loosening of pre-load of 5-10% due to several phenomena

and a group effect due to the fact that the tightening of the second bolt reduce the pre-load force applied on the first bolt.

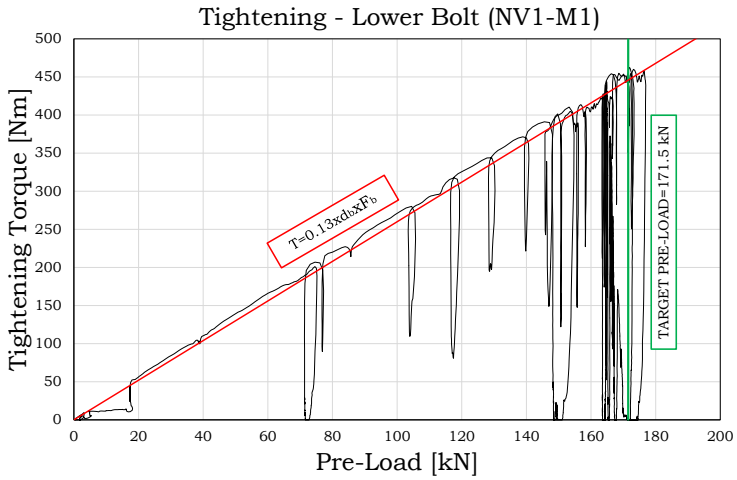

Fig. 2.7 – Typical Torque vs Pre-load diagram

The diagram in Fig. 2.7 shows the relationship between pre-load and tightening torque from which is simple to observe a linear behaviour where the slope of the straight line is equal to the k-factor of the bolt.

2.2.3 Experimental tests – Results 1st phase

The experimental program consists of two identical tests for each one of the eight materials to test. A summary of the tests performed is reported in Table 2.1.

Table 2.1 - Summary of the tests – 1st phase

Specimen code	***Material code***	***Test performed***
NV - 1	*M1*	*x*
NV - 2		*x*
NV - 3	*M2*	*x*
NV - 4		
NV - 5	*M3*	*x*
NV - 6		
NV - 7	*M4*	*x*
NV - 8		*x*
NV - 9	*M5*	*x*
NV - 10		
NV - 11	*M6*	*x*
NV - 12		*x*
NV - 13	*M7*	*x*
NV - 14		*x*
NV - 15	*M8*	*x*
NV - 16		*x*

As mentioned before, several parameters have been monitored during the tests: the slippage force read using the load cell of the testing machine, the displacement of the specimen with the internal transducer of the testing machine, the bolt forces measured with the donut load cells. In particular, the main interest is in the estimation and comparison of the friction coefficient of the tested materials. The data acquired during the test permit two different evaluation of the friction coefficient with two different meanings: the "effective" value and the "actual" value. The first one ($\mu_{effective}$) is defined by the ratio between the slippage force and the sum of the nominal pre-stress forces applied through the tightening of the bolts. In other word the effective friction coefficient takes into account both the degradation due to the wear of the friction interfaces and the degradation due to the loss of pre-load of the bolts. The main advantage is that the value of friction coefficient can be directly used for the seismic design of the FREEDAM connection.

Conversely, the second coefficient (μ_{actual}) is determined by the ratio between the slippage force and the sum of the instantaneous values of the preload of the bolts read thought the load cells during the test. In practice the actual friction coefficient provides a real measure of friction purified from the effect due to the loss of pre-load of the bolts and depending only by the degradation of the friction interfaces. The main experimental results and a comparison between the behaviours of the different materials is reported in the following.

Experimental behaviour of the "Soft" Materials (M1-M5)

The results of the tests on these materials are shown into two groups. In fact, three of the them, namely M2, M3 and M5, belong to a first group characterized by a similar response with alternate starts and stops of the motion. This behaviour is known as stick and slip and it is characterized by sudden releases of energy and strong vibrations. According to the technical literature, this behaviour is related to the difference between static and kinetic value of the friction coefficient. As a consequence, after the initial slippage there is a jump of velocity and a deceleration until stop, then a higher value of force is necessary to restart the movement to overcome the static friction but when the specimen restarts to move, the phenomenon repeats itself again and the continuous jumps are evident from the observation of the force-displacement diagram. The detailed study of the stick and slip phenomenon is not one of the objectives of the present research work, but the important result lies in having understood that no doubt these materials cannot be used for the friction pads of the FREEDAM connections.

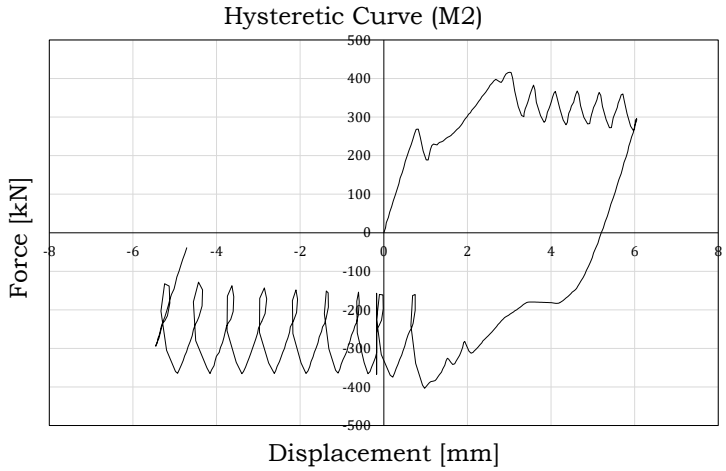

Fig. 2.8 – Hysteretic behaviour of soft materials: M2

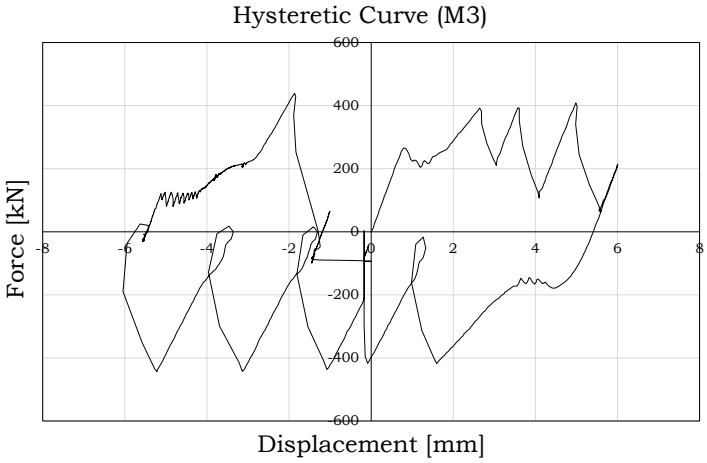

Fig. 2.9 – Hysteretic behaviour of soft materials: M3

In detail, for M2 and M3 materials, as reported in Fig. 2.8 and Fig. 2.9, the initial slippage force is about 200kN, afterwards there is a relevant increase of the slippage resistance until 400kN, that corresponds to a friction coefficient equal to about 0.58. The remaining part of the

diagrams is characterized by alternative jumps of the force due to the stick and slip phenomenon. The cyclic behaviour of these materials is not appropriate for seismic application where a more stable behaviour is required, but probably, taking into account the high value of the friction coefficient, they can find an application in friction connections designed for static loads.

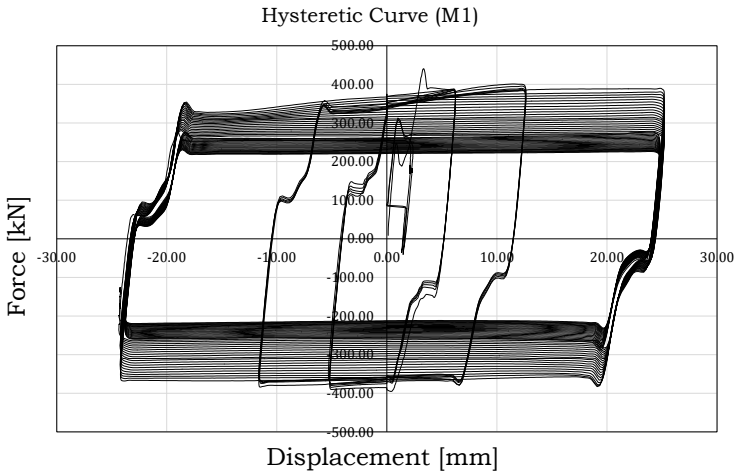

Fig. 2.10 – Hysteretic behaviour of soft materials: M1

The remaining two materials, M1 and M4, exhibited a quite similar behaviour (Fig. 2.10 and Fig. 2.11). In both cases there is a significant degradation of slippage force during the tests, mainly due to the loss of pre-load in the bolts and the damage of the friction pads.

Another important issue is represented by the fact that performing two identical tests on the same material the results are significantly different. This random variability can be better understood by comparing the results of the two tests executed on M4 material in terms of friction coefficient and bolt forces.

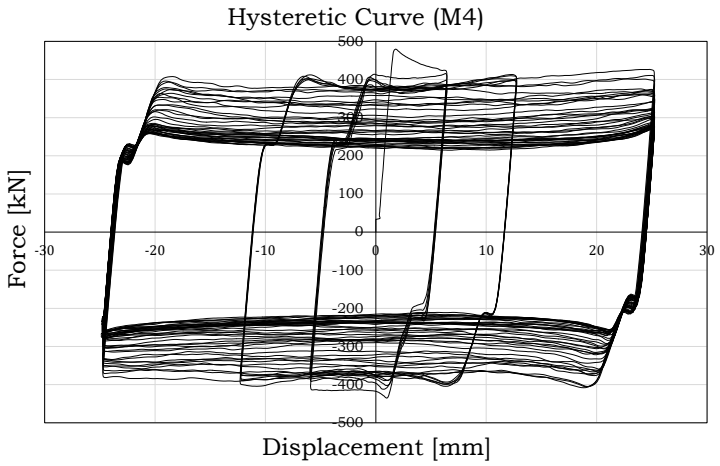

Fig. 2.11 – Hysteretic behaviour of soft materials: M4

In Fig. 2.12 is evident that the values of the actual friction do not vary in the two tests, this means that the bolts are the main cause of the different response of the whole hysteretic behaviour.

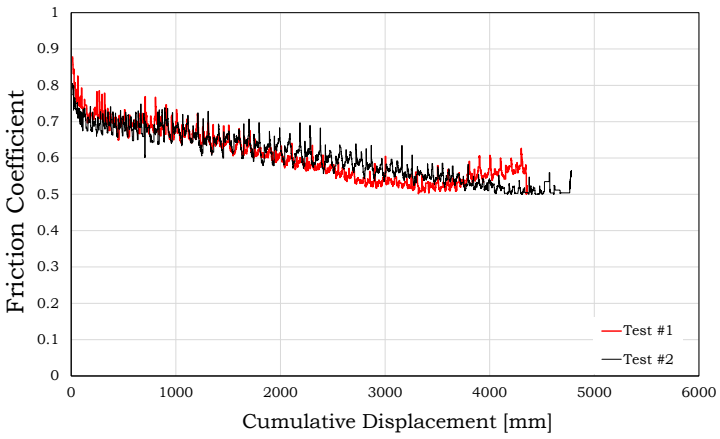

Fig. 2.12 – Actual friction coefficient – M4

In fact, observing the diagram of the bolt forces versus cumulating

travel done by the damper in Fig. 2.13, one of the two tests exhibits at the beginning of the test sudden loss of pre-load in the bolts of about the 15%, with a subsequent proportional loss of the sliding force.

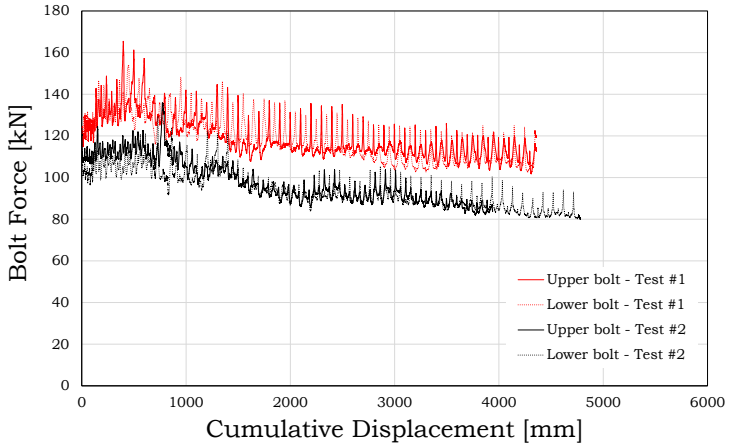

Fig. 2.13 – Bolt forces – M4

It is important to underline that the production process of the coating material in case of soft coating is completely manual and for this reason the thickness is non-uniform on the friction pads, thus influencing the response of the specimens. Anyway, both materials are characterized by high values of the initial friction coefficient, equal to 0.55/0.65 and 0.7/.09 for M1 and M4 respectively, but showing a significant degradation of the initial slip force, that is equal to about 45% for M1 material and 50% for M4 at the end of the test.

Opening the specimens after the tests (Fig. 2.14), in order to see the damage of the interfaces, it is possible to note that the friction pads are heavily worn while stainless steel plates are practically undamaged, as expected.


a)

b)

Fig. 2.14 – Damage of the interfaces: a) M1; b) M4

As anticipated above, during the tests a considerable increase of the temperature of all the elements has been observed. In order to investigate the influence of the temperature on the friction coefficient and to develop a thermo-mechanical model of the specimen, in the second phase of the experimental campaign, two thermocouples have been placed on the specimen. The thermocouples have been placed one in correspondence of the lower part of external plate surface and another on the bolt head to monitor the thermal variation and the non-uniform propagation of heat in the specimen during the tests.

Experimental behaviour of the "Hard" Materials (Carbide M6-M7, 3M friction shim M8)

The results of the tests performed on the specimens equipped with friction pads coated with "hard" materials, are reported in Figs. 2.15-2.17 in terms of hysteretic curves. Even if two tests have been performed for each material, for sake of simplicity and for clarity of representation, the result of only one test for each one is reported. These materials are characterized by a very regular and stable behaviour with a very low variability of the friction coefficient in all the cases.

In detail, the M6 coating material developed an initial value of the slip force equal to about 350kN, value that progressively degrades of about 20% until the end of the test. This material, as it is possible to note from Fig. 2.15, is affected by stick and slip phenomenon with alternate jumps of the force and sudden releases of energy during the first cycle. Probably, during the first phase of the test the adhesive component of friction is prevalent, so the energy is spent to break the interatomic bonds between the contact surfaces, after that, the slippage occurs regularly, without jumps and sudden energy releases.

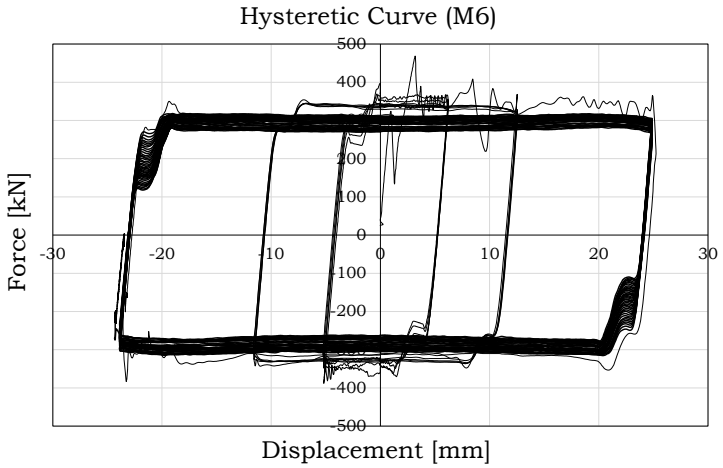

Fig. 2.15 – Hysteretic behaviour of hard materials: Carbide M6

In case of specimen with M7 coating, the response is very similar to the one with M6. The initial slip force in this case is equal to about 250kN, but after the firsts cycles the value increases until the stable value of about 300kN. It is important to underline that also in this case there is a significant stick and slip behaviour, with strong vibration due to the sudden energy releases. Cause to the so strong vibration, in order to

avoid damages to the equipment, the testing speed has been reduced up to 0,01mm/s corresponding to the complete disappearance of the stick and slip phenomenon.

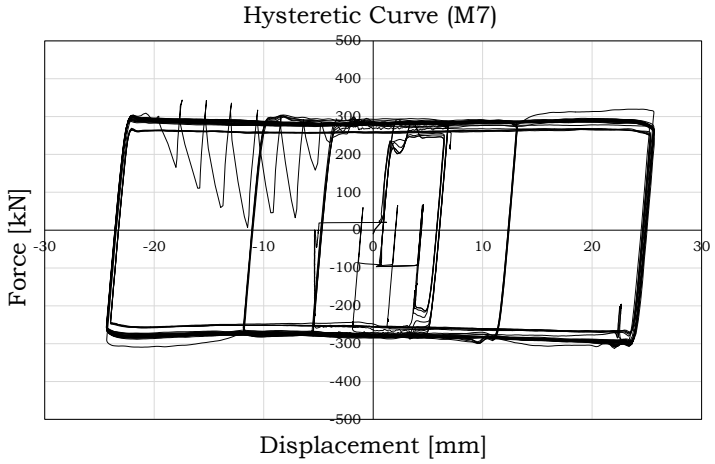

Fig. 2.16 – Hysteretic behaviour of hard materials: Carbide M7

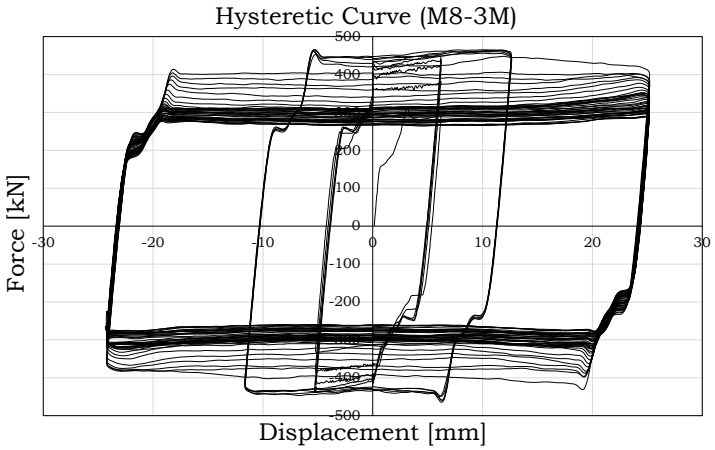

Fig. 2.17 – Hysteretic behaviour of hard materials: 3M friction shims

The last material is identified as M8 and its response is very similar to the one exhibited by brass or some types of phenolic rubbers [15]. The response is characterized by two different phases: in the first one there is an increase of the slippage resistance of about 60% (a typical strain hardening behaviour); instead during the second phase the interfaces exhibit a reduction of the slippage force which reaches the starting value at the end of the test. For this material the value of the slippage force does not present jumps, in fact no stick and slip response has been observed. The initial value of the slippage force is equal to about 400kN. Also for hard materials the specimens have been disassembled and the damage of the interfaces has been observed.

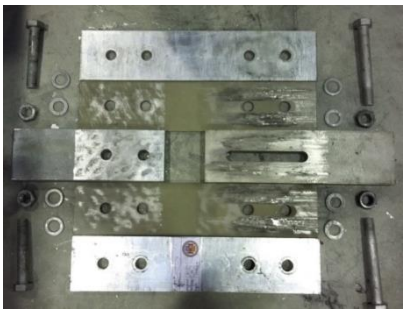

a)

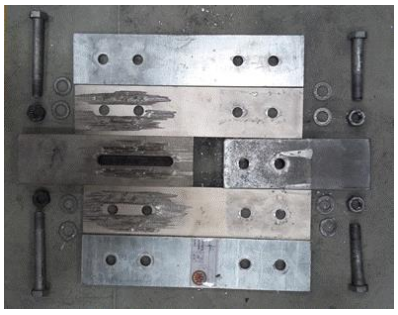

b)

Fig. 2.18 – Damage of the interfaces: a) M6; b) 3M friction shims

Observing the Fig. 2.18a and Fig. 2.18b, it is possible to see like the damage is concentrated on the stainless steel plates of specimens rather than on friction pads in M6 and M8 material respectively. This is not surprising because the hard materials are characterized by a hardness greater than the stainless steel. Another effect that is possible to note is that the damage is greater in correspondence of the bolts. In Fig. 2.19, that represents the diagram of the bolt forces versus the cumulative travel done by the damper, it is possible to note that the bolts are

initially tightened to reach the proof load equal to 171.5kN, but after the first cycle a loss of pre-load of about 7% is recorded, that increase progressively up to 20% at the end of the test. The initial loss, that occurs when the damper starts to slip, has to be accounted for in the design of the damper.

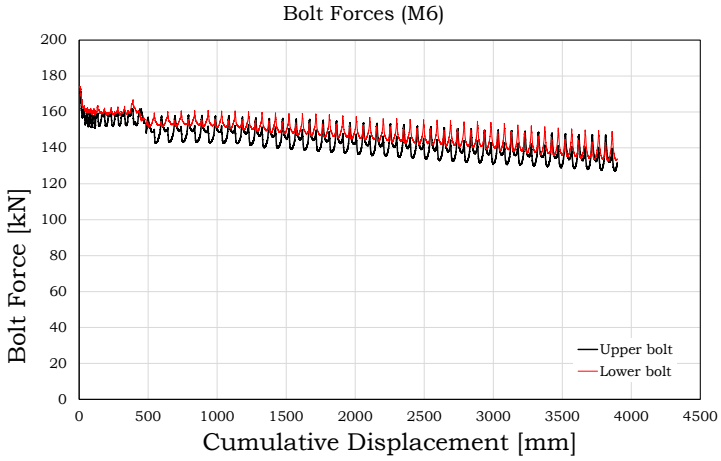

Fig. 2.19 – Typical diagrams of the bolt forces

The comparison between Fig. 2.15, Fig. 2.19 and Fig. 2.20 allows us to understand that the degradation of the sliding force during the test is due quite exclusively to the reduction of pre-load in the bolts. In fact, in Fig 2.20 the value of the "actual" friction coefficient remains practically constant for all the duration of the test.

The detailed results of each test performed on hard materials are not reported only for the sake of simplicity, even because the results in more cases are analogous to the results showed above both in terms of bolts' loosening and in terms of degradation of the sliding force.

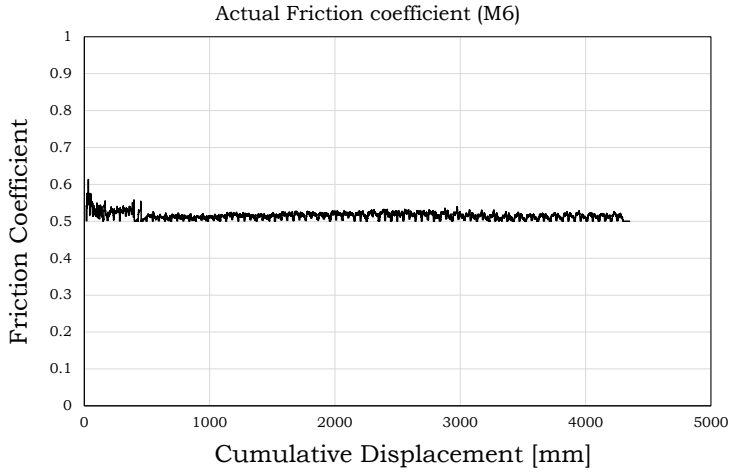

Fig. 2.20 – "Actual" friction coefficient vs cumulative travel: M6

At this point it is possible to take stock of the tests results, in particular by comparing the behaviour of the materials that have completed the entire test protocol. A first comparison can be carry out plotting on two diagrams the responses of the tested materials in terms of actual and effective values of the friction coefficients (Fig. 2.21 and Fig. 2.22).

In general, soft materials (M1 and M4) provide a higher value of the initial friction coefficient respect to hard materials (M6 and 3M). Even if soft materials exhibit a very high friction coefficient, this value is not stable during all the test and the response can change significantly from one specimen to another, probably due to the fact that the coating is not uniform because it is applied on friction pads through a manual procedure. In practice the prediction of the friction coefficient for soft materials may result more difficult with a lower accuracy.

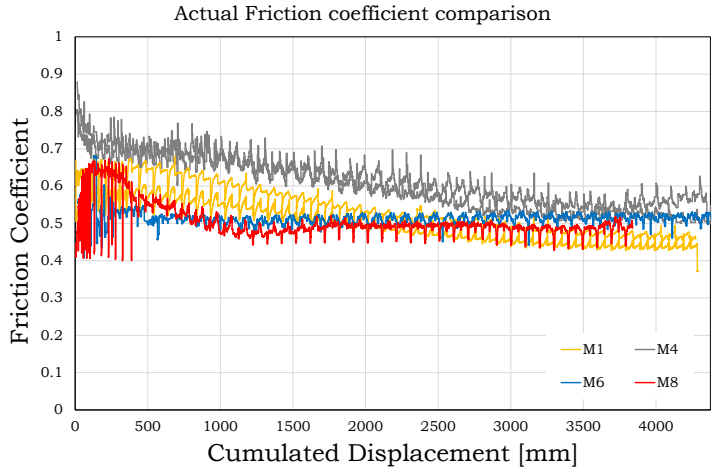

Fig. 2.21 – Comparisons: "Actual" friction coefficient vs cumulated displacement

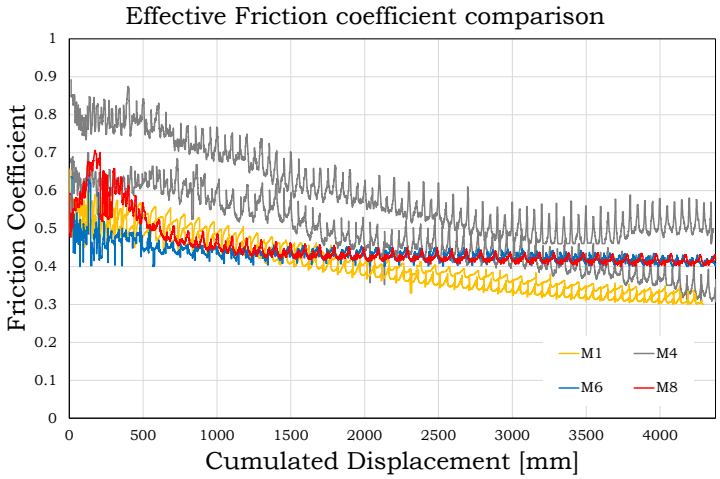

Fig. 2.22 – Comparisons: "Effective" friction coefficient vs cumulated displacement

On the other hand, the hard materials present in general a lower value of friction coefficient and a more stable behaviour due to the production

process completely industrialized. As an example the M6 presents a very limited degradation and so the possibility to predict the value of the friction coefficient with high accuracy. Conversely, the 3M material presents a disadvantage due to an increase of the friction coefficient at the beginning of the test that decrease and stabilize in the second part of the test, with a clear difficulty to determine a univocal value of the friction coefficient to be used in design. The adoption of 3M material for the friction pads would require, in seismic design, a significant oversize of non-dissipative parts of the connection and of the frame in order to take into account the overstrength of this coating with respect to the initial slippage value and to allow the complete development of the dissipative mechanism in the FREEDAM connections.

A further confirmation of the considerations made so far comes from the analysis of the results reported in terms of energy dissipation and energy degradation vs cumulated displacements in Fig. 2.23 and Fig. 2.24 respectively. In Fig. 2.23 it is simple to note as the energy dissipation capacity, in particular in case of soft materials, varies during the test according to the degradation of the friction coefficient. In fact, the soft materials dissipate a highest amount of energy respect to hard materials until a value of the cumulative displacement approximately equal to about 1800mm, conversely for higher value of the cumulative displacement, the hard materials exhibit a greater energy dissipation with respect to the soft materials. In other words, for the lower values of the cumulative displacement the soft materials are able to dissipate more energy because the friction coefficient is higher than hard materials, conversely for higher value of the cumulative displacement there is a decrease of value of the dissipated energy for soft materials due to the degradation of coating of the surfaces, while

for the hard materials the value of the dissipated energy is more stable due to a limited degradation of the value of the friction coefficient.

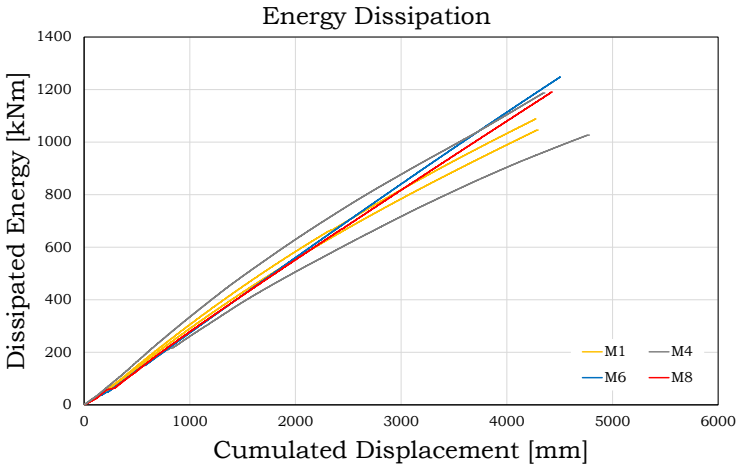

Fig. 2.23 – Energy dissipation capacity

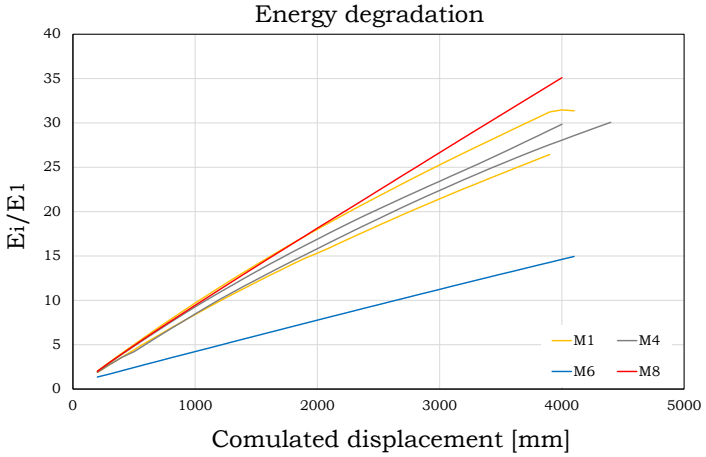

Fig. 2.24 – Energy degradation

In order to establish the maximum cumulative displacement expected during a real earthquake, a wide set of incremental analysis on the reference building will be carried out in subsequent phase of the FREEDAM research project.
Finally, taking into account the results of the tests performed during the first phase of the experimental campaign, only three coating materials have been chosen for the execution of the next experimental phase: M1 and M4 between the soft materials and M6 between the hard materials.

2.2.4 Experimental tests – Results 2nd phase

This 2nd phase of tests is devoted to investigate several aspects: the influence of the bolts' pre-load and the disc springs configuration over the friction coefficient, the degradation of the bolts preload, the effective damping deterioration, the random variability of the friction coefficient. In detail 21 tests have been performed in order to analyse the effects of preload, of the configuration of the washers, of the effective damping degradation, of the loss of preload; while further 30 tests (10 for each coating material) have been performed to investigate the random variability of the friction coefficient. The data acquired during the tests by means of the sensors applied on the specimens as detailed in the previous paragraphs, will be represented in the continuous.

Influence of the preload of the bolts

In order to evaluate the influence of the bolts' preload on the friction coefficient the force-displacement curves of the tests performed varying the preload of the bolts have been represented from Fig. 2.25 to Fig. 2.27 for each coating material.

The most evident result is that, in all the tests carried out, the static friction coefficient is higher than the dynamic one obtained in the first stabilized cycle. In fact, all cases are characterized by a very high initial stiffness until the peak that corresponds to the achievement of the slippage force

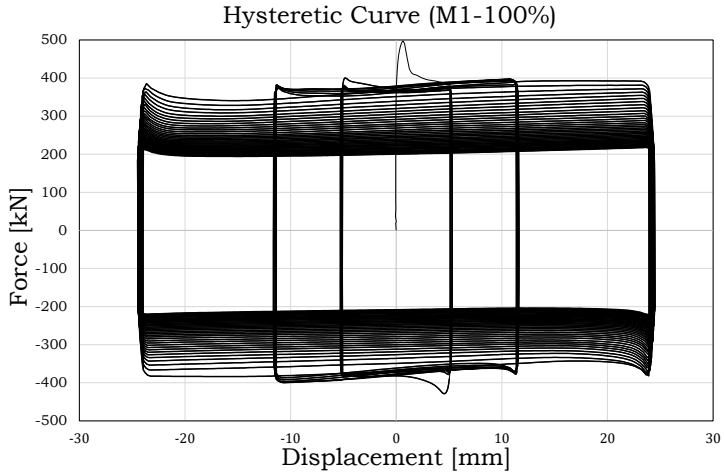

a)

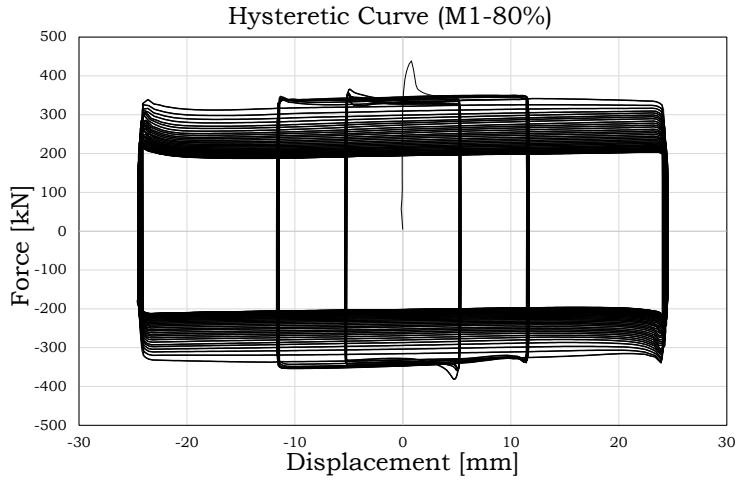

b)

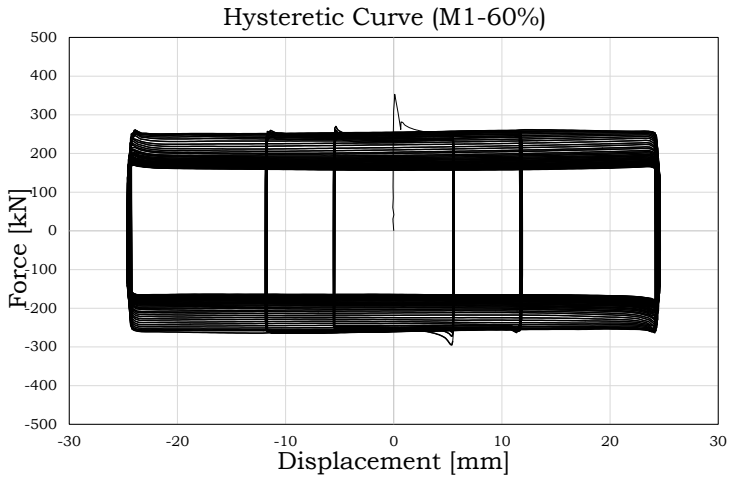

c)

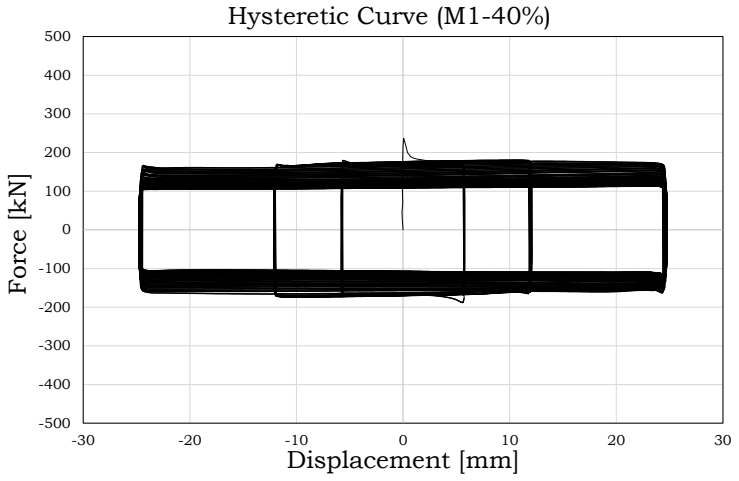

d)

Fig. 2.25 – Influence of the bolts' pre-load over the force-displacement hysteretic response (M1)

.

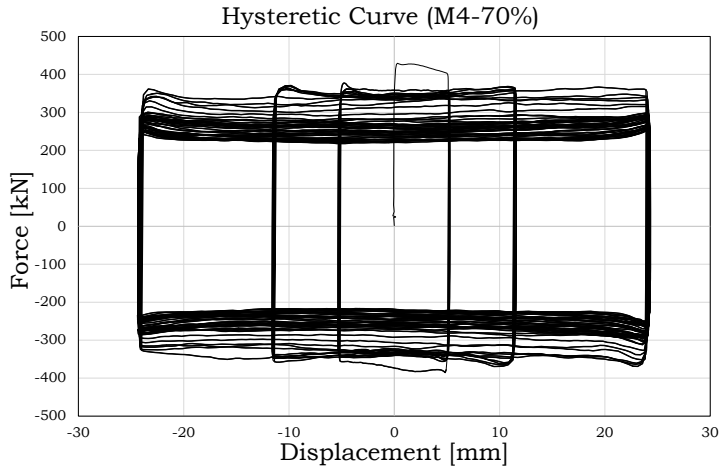
Hysteretic Curve (M4-70%)
Force [kN]
Displacement [mm]
500
400
300
200
100
0
-100
-200
-300
-400
-500
-30
-20
-10
0
10
20
30

a)

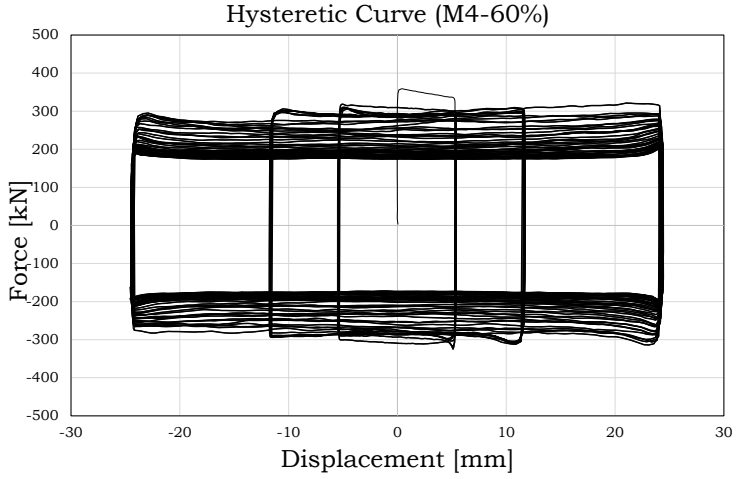
Hysteretic Curve (M4-60%)
Force [kN]
Displacement [mm]
500
400
300
200
100
0
-100
-200
-300
-400
-500
-30
-20
-10
0
10
20
30

b)

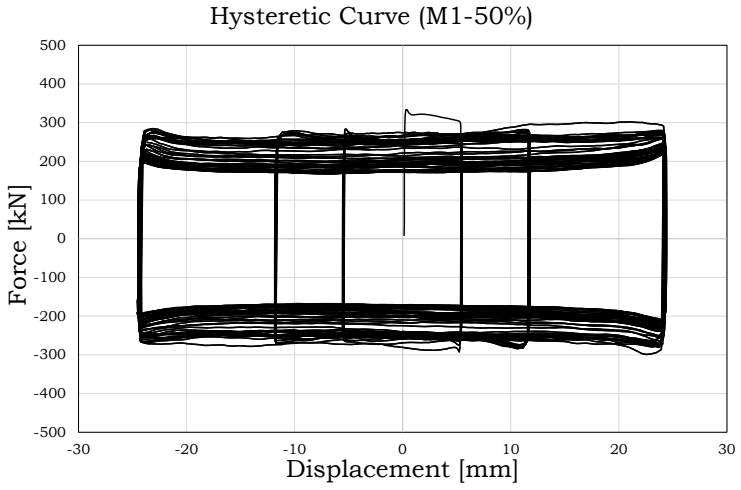

c)

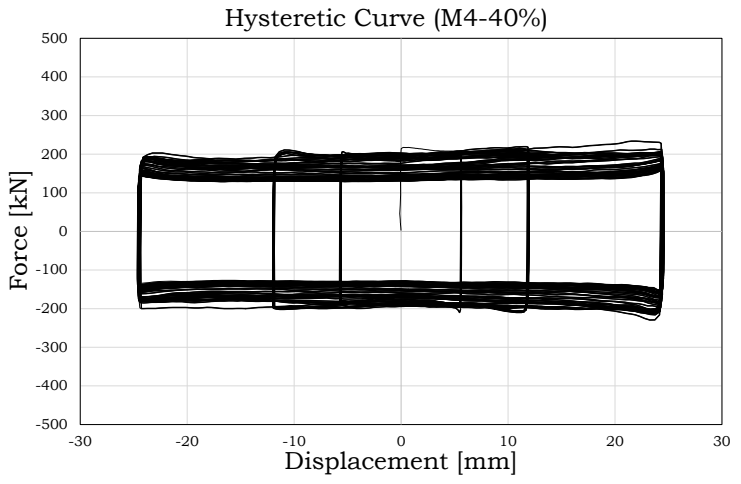

d)

Fig. 2.26 – Influence of the bolts' pre-load over the force-displacement hysteretic response (M4)

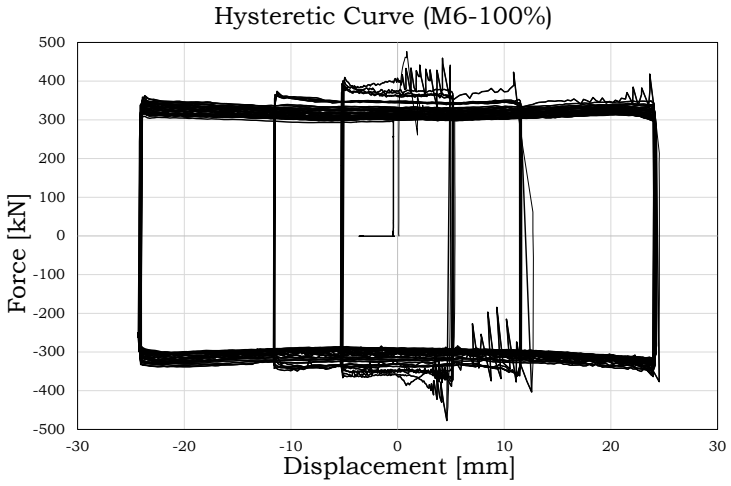
Hysteretic Curve (M6-100%)
Force [kN]
Displacement [mm]
500
400
300
200
100
0
-100
-200
-300
-400
-500
-30
-20
-10
0
10
20
30

a)

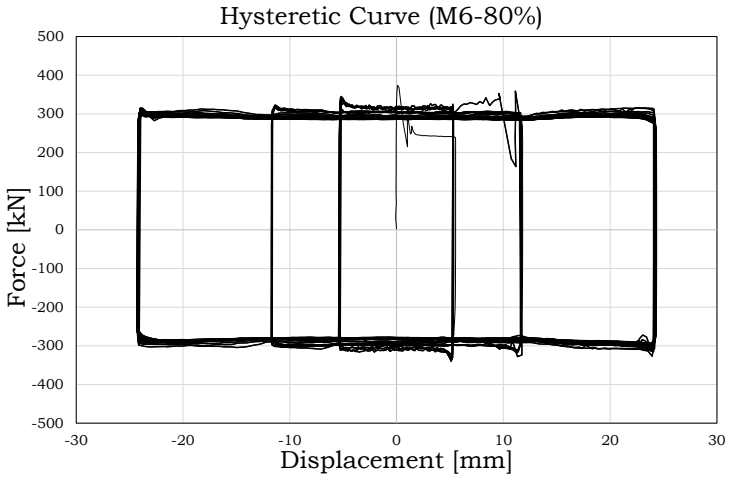
Hysteretic Curve (M6-80%)
Force [kN]
Displacement [mm]
500
400
300
200
100
0
-100
-200
-300
-400
-500
-30
-20
-10
0
10
20
30

b)

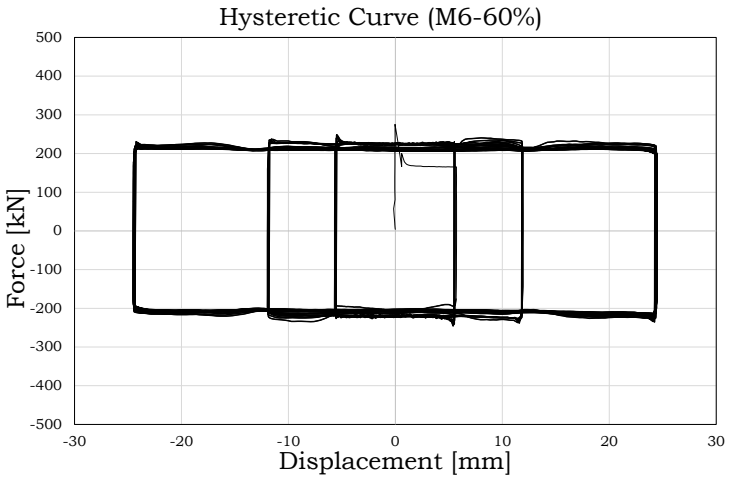

c)

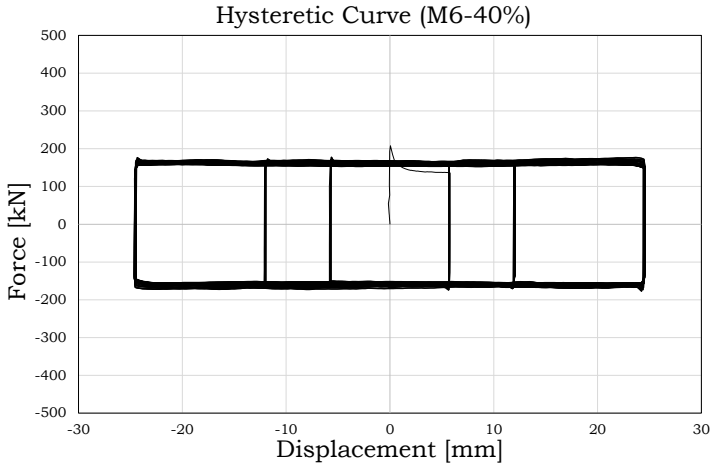

d)

Fig. 2.27 – Influence of the bolts' pre-load over the force-displacement hysteretic response (M6)

Another important aspect that is possible to put in evidence is the shape of the hysteresis loops in terms of force-displacement response,

that is very regular, substantially rectangular, for all the materials tested. Regarding the behaviour of the specimen equipped with friction pads coated using M6 material, it is important to put in evidence, observing Fig. 2.27, like the stick and slip phenomenon reduce according to the reduction of the tightening of the bolts, revealing that this phenomenon strongly depends on the contact pressure generated on the sliding surface.

The results in terms of friction coefficient for the three materials shows that for M1 material the initial value of the friction coefficient is included in the interval between 0.67 and 0.75, while for M4 between 0.71 and 0.94 and finally for M6 between 0.62 and 0.65. For all three materials there is no significant variation of the friction coefficient whose values remain within the normal range observed during the execution of the tests aimed at the evaluation of the random variability of the coefficient and equal to 0.62-0.81 for M1 material, 0.69-0.84 for material M4 and 0.52-0.68 for M6 material.

Considering the results represented in Fig. 2.28, these results did not reveal a clear relationship between the friction coefficient and the bolt's force. Conversely, normalizing the bolt's force with respect to the initial preload and representing it versus the cumulative travel, and also representing the effective damping degradation versus the number of cycles for the maximum amplitude cycles, it is possible to note that a reduction of the preloading force corresponds to a lower energy degradation.

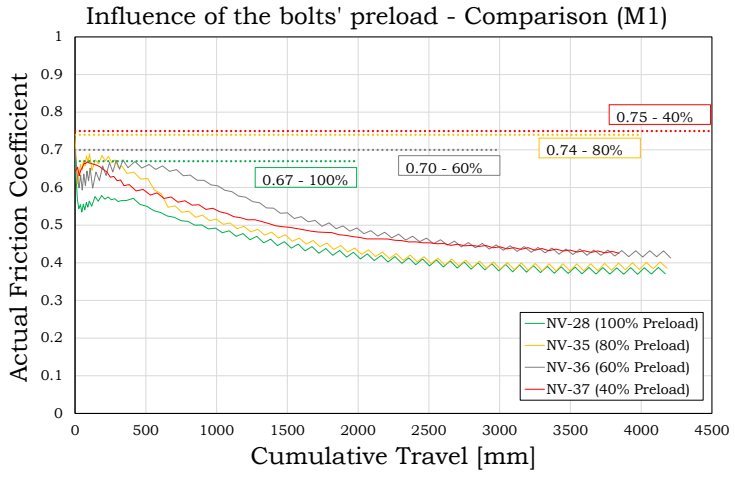
Influence of the bolts' preload - Comparison (M1)
Actual Friction Coefficient
Cumulative Travel [mm]
0.75 - 40%
0.74 - 80%
0.70 - 60%
0.67 - 100%
NV-28 (100% Preload)
NV-35 (80% Preload)
NV-36 (60% Preload)
NV-37 (40% Preload)

a)

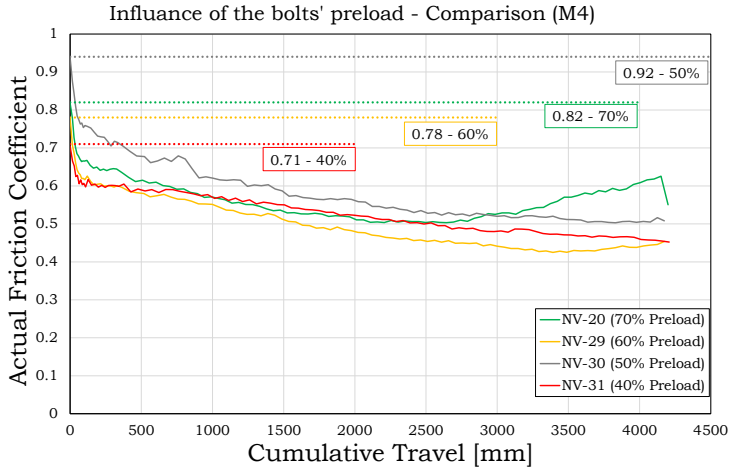
Influance of the bolts' preload - Comparison (M4)
Actual Friction Coefficient
Cumulative Travel [mm]
0.92 - 50%
0.82 - 70%
0.78 - 60%
0.71 - 40%
NV-20 (70% Preload)
NV-29 (60% Preload)
NV-30 (50% Preload)
NV-31 (40% Preload)

b)

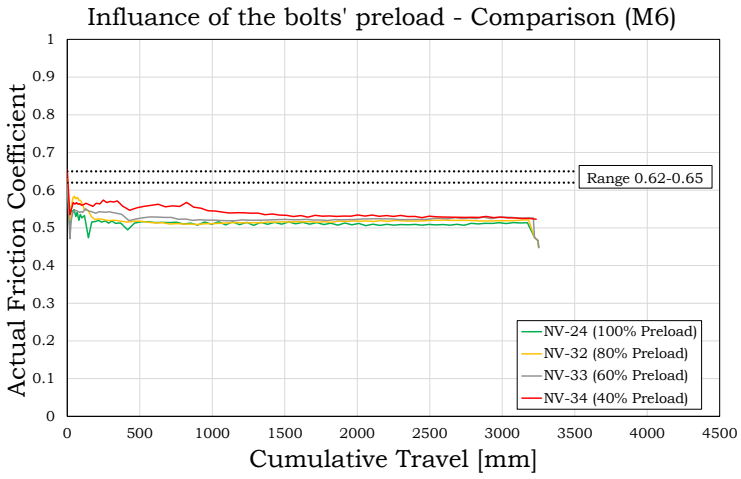

c)

Fig. 2.28 – Influence of the bolts' pre-load over the actual friction coefficient

According to the provision of the EN15129 [12] code, the effective damping degradation at the 10th cycle must be lower than the 10%. The results of the tests showed that for M1 and M4 materials (Fig. 2.29 and Fig. 2.30) the code provisions are satisfied only if the load pressure is limited to the 60% of the proof load, while for M6 material (Fig. 2.31) the effective damping degradation is always lower than the 10%.

In conclusion, in order to avoid on one hand, the stick and slip phenomena for the hard material (M6) and on the other hand a high damping degradation for the soft materials (M1 and M4), the maximum value of preload, for all interfaces, has to be equal to the 60% of the proof load codified in Eurocode 3 part 1.8 [16].

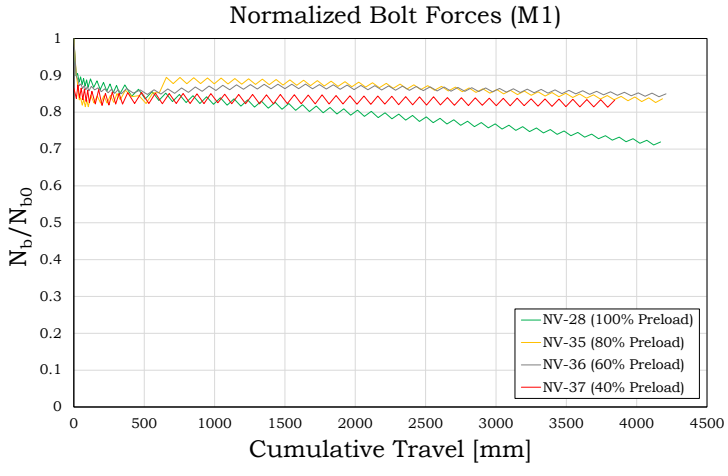

a)

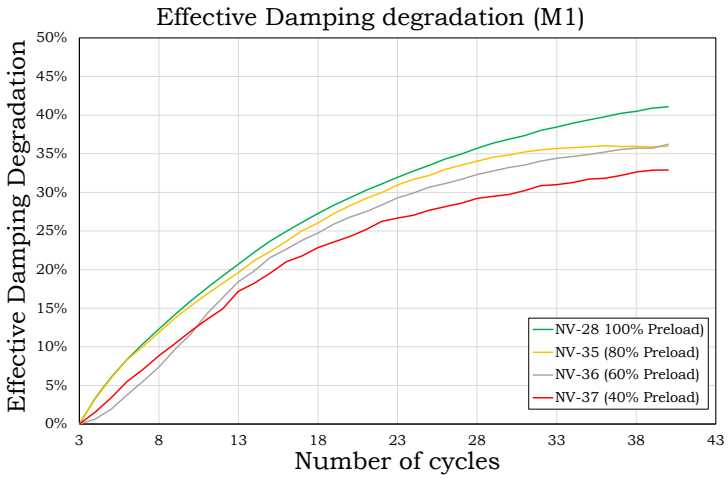

b)

Fig. 2.29 – Bolts' preloading and effective damping for material M1

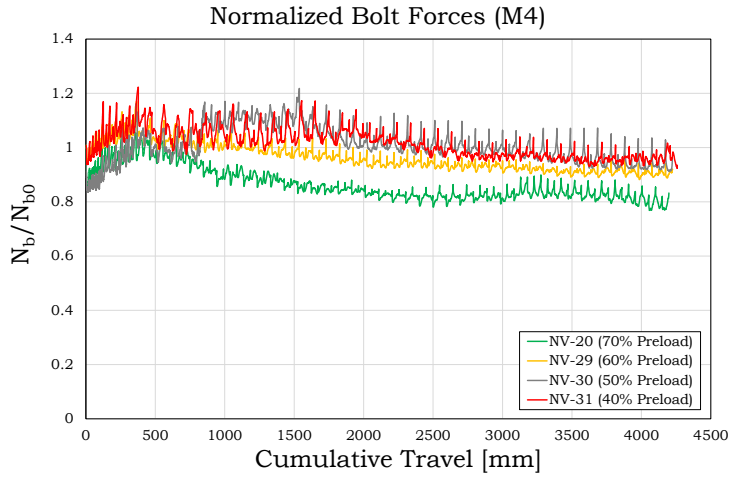

Fig. 2.30 – Bolts' preloading and effective damping for material M4

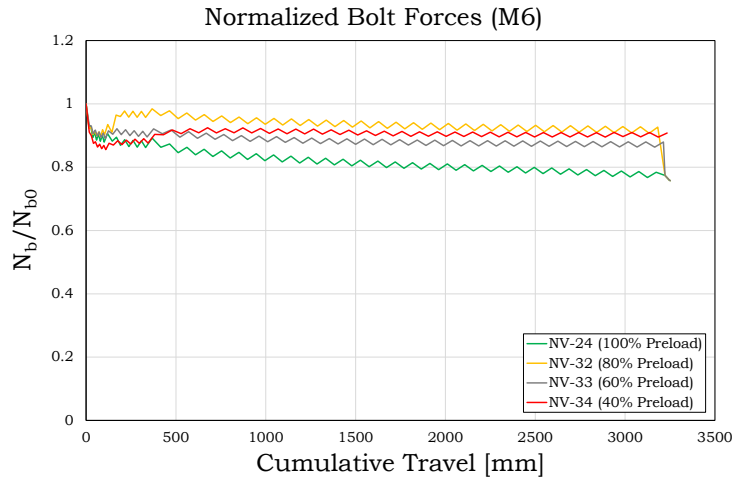

a)

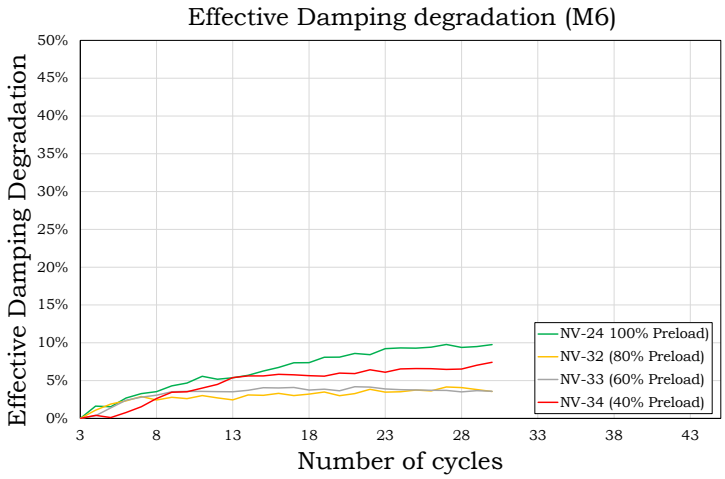

b)

Fig. 2.31 – Bolts' preloading and effective damping for material M6

Influence of disc spring' configuration

One of the most common way to maintain constant the pre-load applied in bolts over the life-time, in particular when they are subjected to vibrations, creep or elastic interactions, is represented by the adoption of particular type of washers called disc spring washers, also often referred as Belleville. These type of washers are characterized by a truncated cone shape and by a significant stiffness when they are subject to elastic compression until complete flattening. Their shape allows two different configurations: series stack or parallel stack. In the first case the washers are arranged one over the other, while in the second one they are arranged face to face, in order to double the resistance or the deformability respectively. The Fig. 2.32 shows a comparison between the behaviour of an assembly equipped with traditional washers and one equipped with Belleville washers, from which it is simple to understand as the elongation of the bolt shank is compensated by the compression of the Belleville washers.

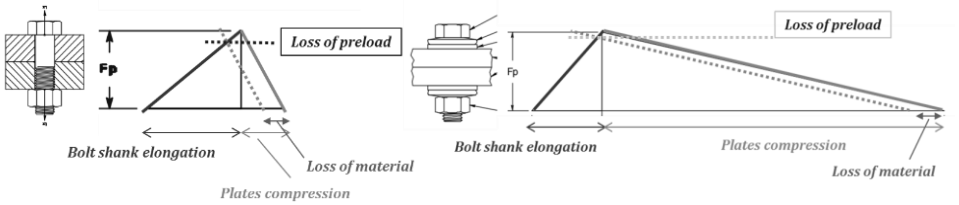

Fig. 2.32 – Effect of disc springs

The results of the tests performed not varying significantly changing the materials of the friction pads, for this reason the considerations are substantially the same both for soft and hard materials.

Observing the results of the tests (Fig. 2.33 to Fig. 2.35), the configuration of the disc springs not seems to influence the hysteretic

response, the only aspect that can be highlighted is a slightly worse behaviour as the number of disc springs increases. This behaviour can be explained through the analysis of the bolts' force trend and damping degradation during the tests.

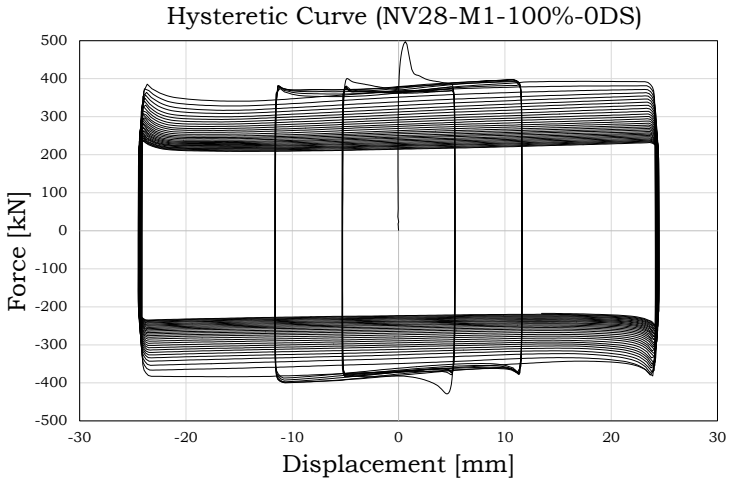

a)

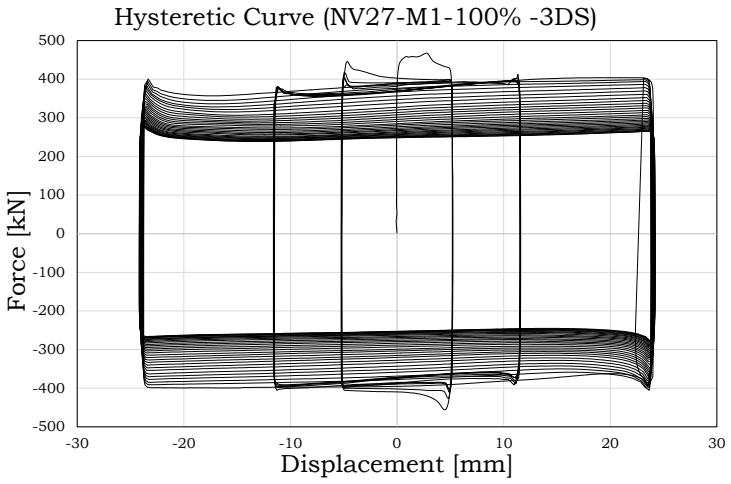

b)

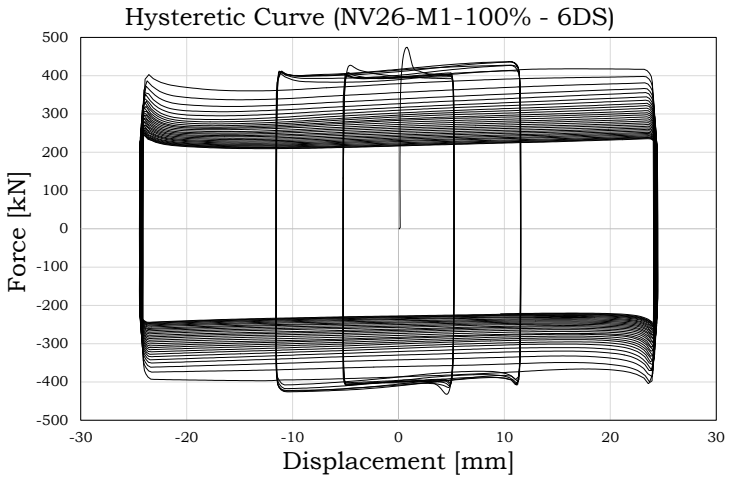

c)

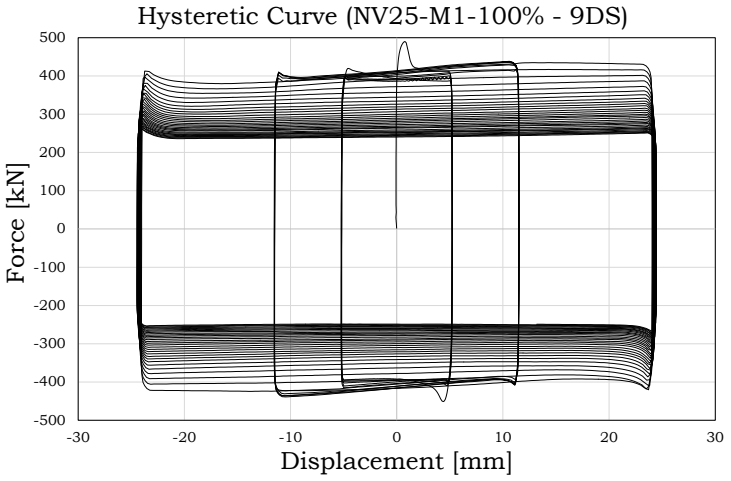

d)

Fig. 2.33 – Influence of the disc spring configuration over the hysteretic response (M1)

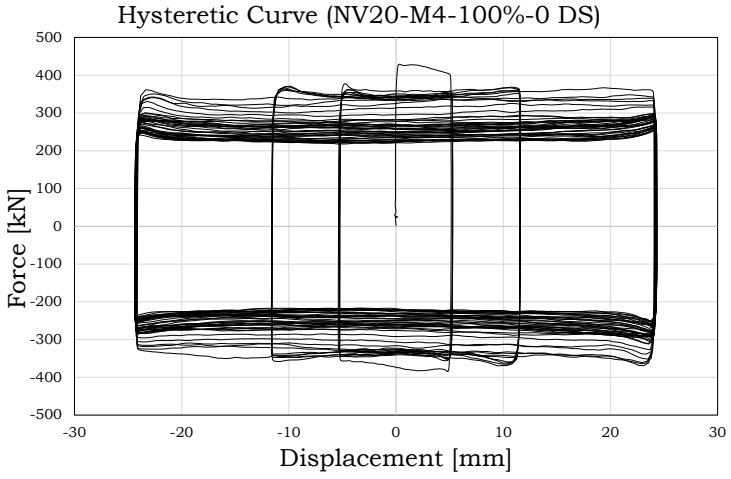
Hysteretic Curve (NV20-M4-100%-0 DS)
Force [kN]
Displacement [mm]
500
400
300
200
100
0
-100
-200
-300
-400
-500
-30
-20
-10
0
10
20
30

a)

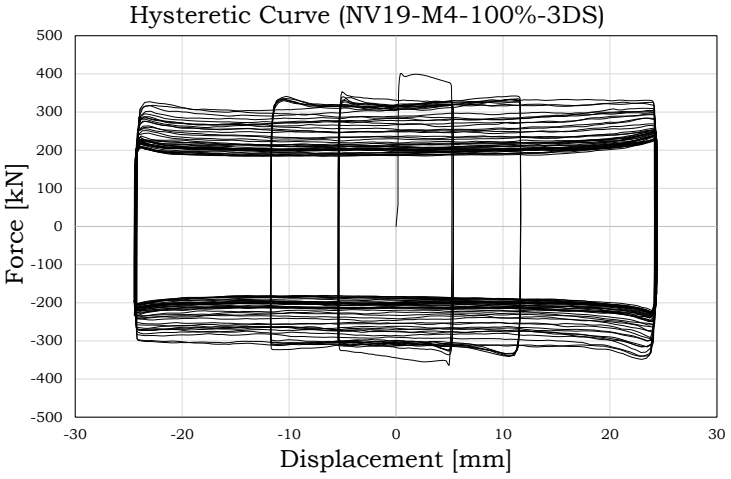
Hysteretic Curve (NV19-M4-100%-3DS)
Force [kN]
Displacement [mm]
500
400
300
200
100
0
-100
-200
-300
-400
-500
-30
-20
-10
0
10
20
30

b)

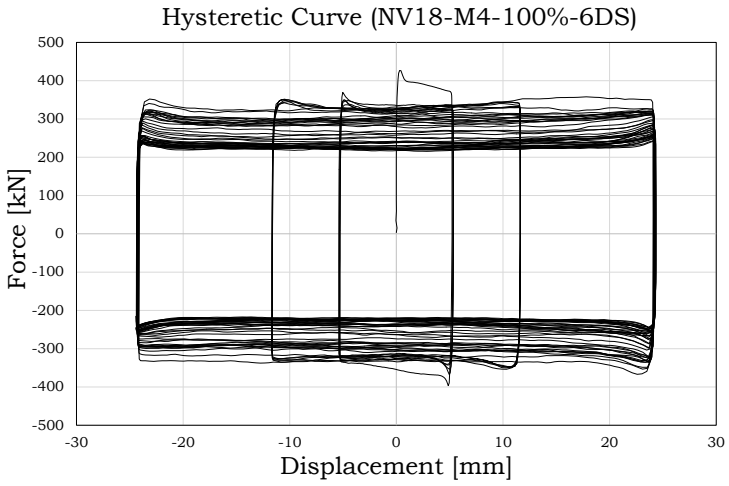

c)

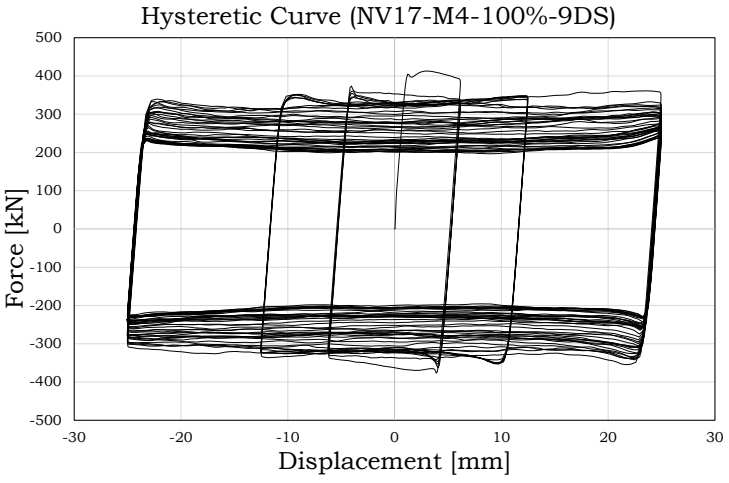

d)

Fig. 2.34 – Influence of the disc spring configuration over the hysteretic response (M4)

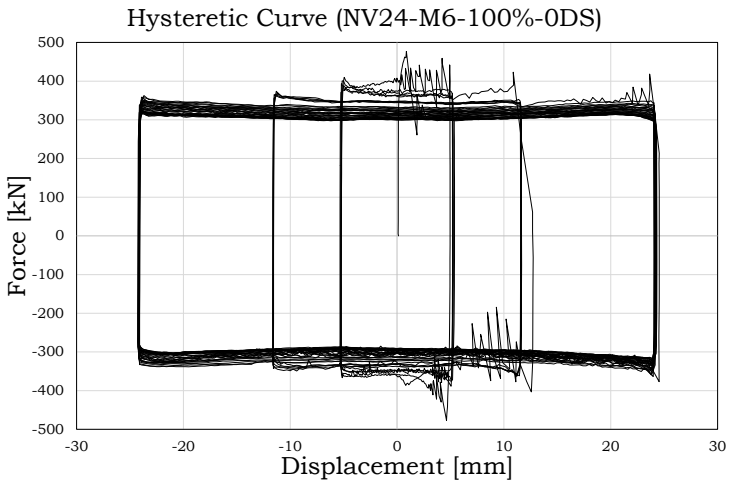
Hysteretic Curve (NV24-M6-100%-0DS)
Force [kN]
Displacement [mm]
500
400
300
200
100
0
-100
-200
-300
-400
-500
-30
-20
-10
0
10
20
30

a)

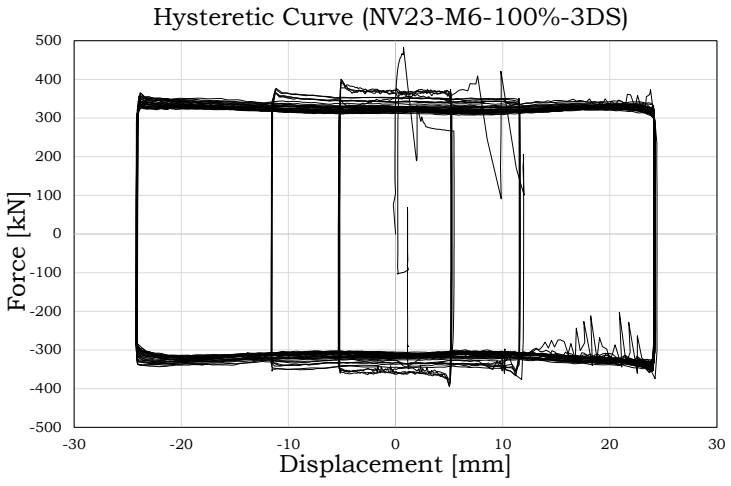
Hysteretic Curve (NV23-M6-100%-3DS)
Force [kN]
Displacement [mm]
500
400
300
200
100
0
-100
-200
-300
-400
-500
-30
-20
-10
0
10
20
30

b)

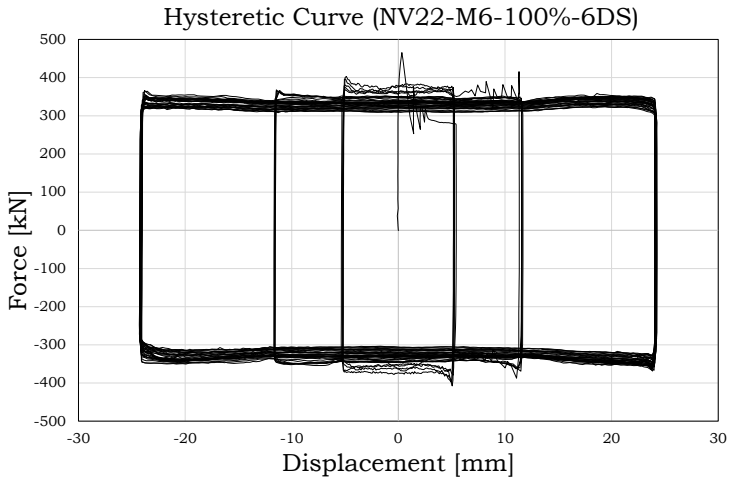

c)

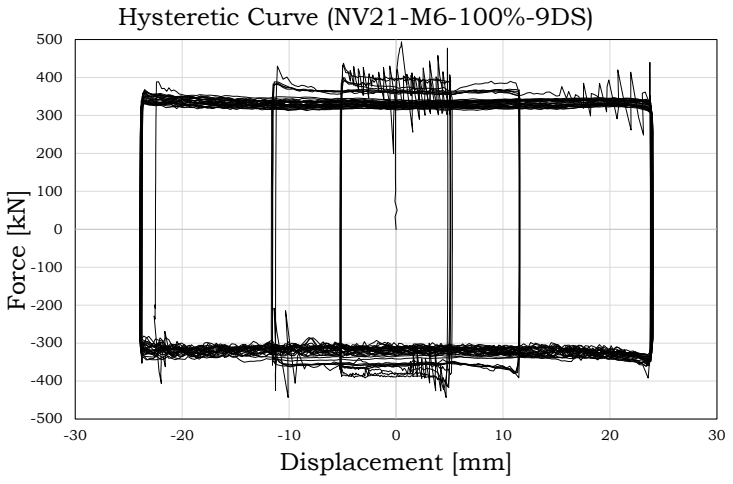

d)

Fig. 2.35 – Influence of the disc spring configuration over the hysteretic response (M6)

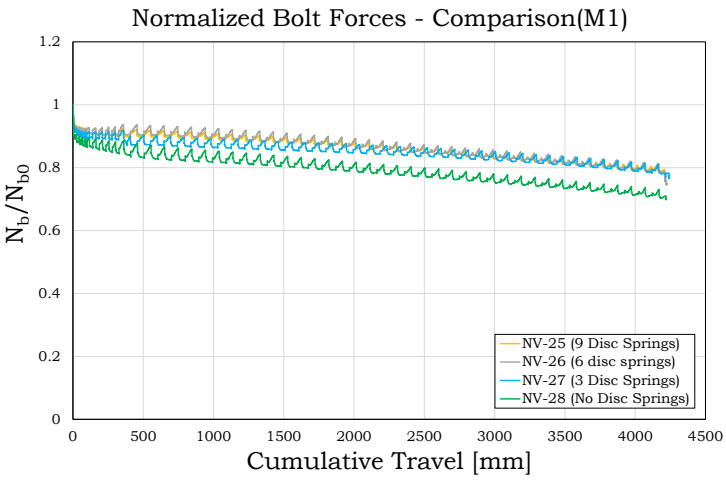

a)

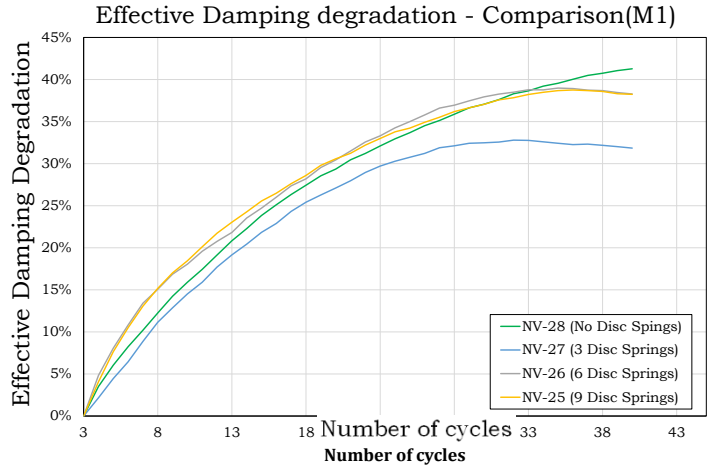

b)

Fig. 2.36 – Bolts' preloading and effective damping for material M1

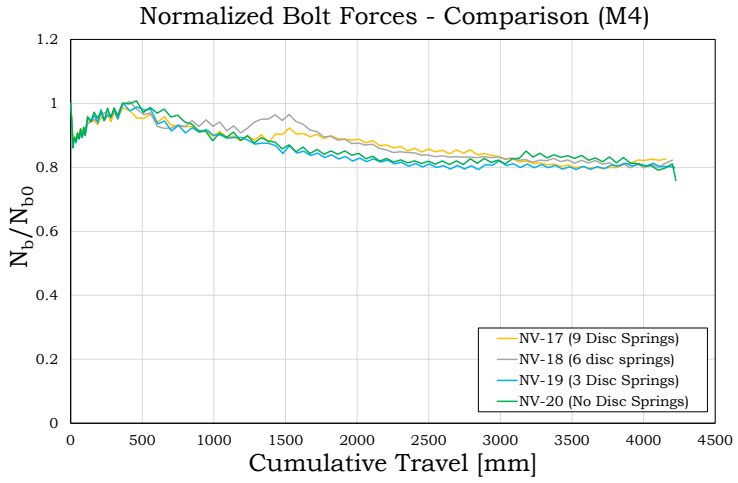

a)

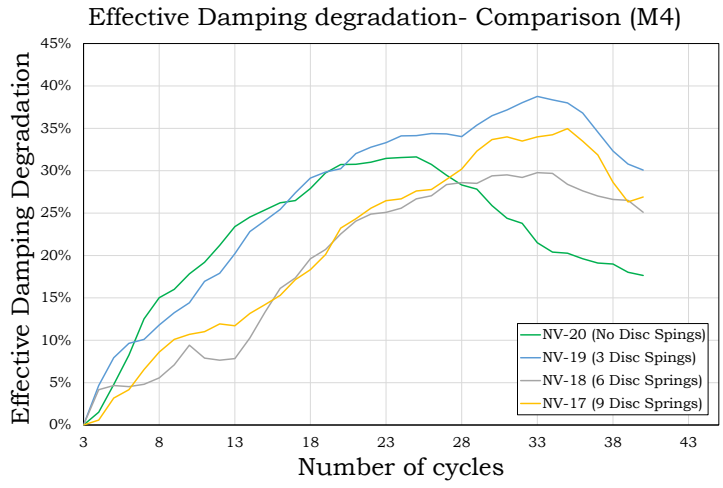

b)

Fig. 2.37 – Bolts' preloading and effective damping for material M4

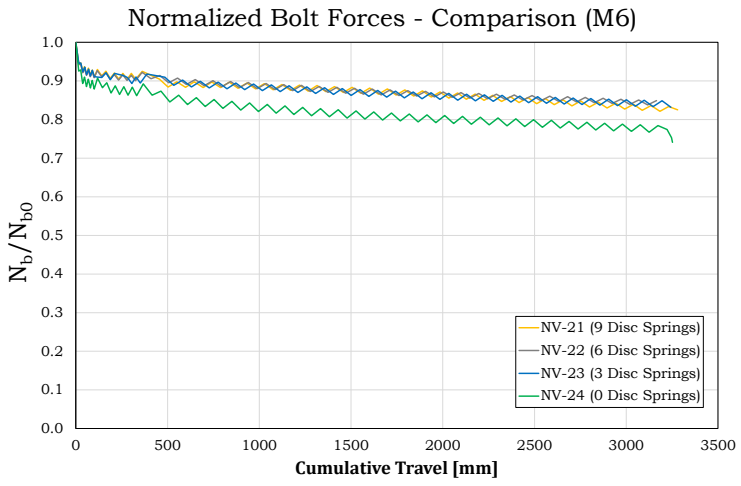

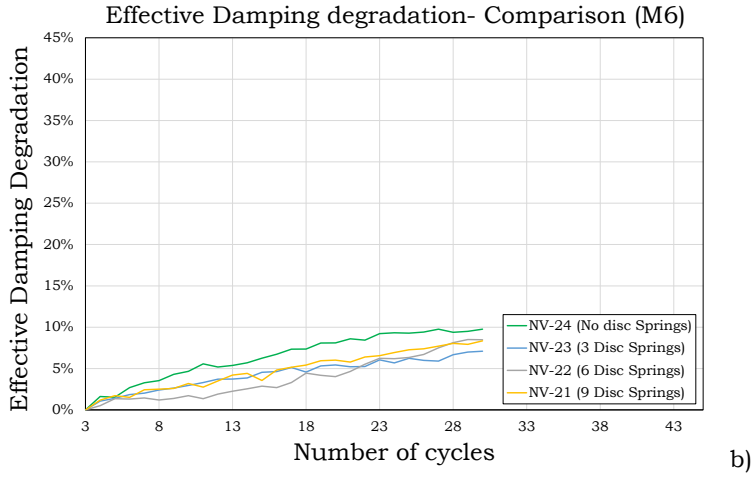

Fig. 2.38 – Bolts' preloading and effective damping for material M6

The diagrams from Fig. 2.36 to Fig. 2.38 are useful to put in evidence like the introduction of the disc springs reduce the loss of preload in the bolts during the tests. Conversely, as a consequence of the higher level

of preload in the bolts during the tests, a higher wearing of the coating material and a higher damping degradation have been recorded for the specimens equipped with Belleville washers. In this way the benefit of a more constant level of pressure over the interfaces is thwarted by the wear and tear of the friction pads, not improving, if not worsening, the cyclic response of materials.
In conclusion the effectiveness of the introduction of the disc springs in terms of improvement of the cyclic response seems negligible, while they could play a more relevant role in order to limit loss of preload of the bolts due to vibrations or thermal effects.

Influence of randomness over the friction coefficient

The aim of the last session of this experimental campaign is to determine a statistical range of variation of the cyclic response of the three materials, in particular the statistical characterization of the value of the friction coefficient, that is fundamental to correctly project the FREEDAM device. In fact, the randomness of the design parameters must be taken into account for the SLS and ULS checks, in detail, for the SLS check the characteristic value of the static friction coefficient has to be determine, while for the ULS check it is necessary to split the issue into two steps.
On one hand, the characteristic value of the dynamic friction coefficient is needed in order to properly design the dissipative components, on the other hand, in the framework of capacity design, the design of non-dissipative zones (some parts of the connection and columns), requires to determine the upper bound of the static friction equal to the 95% fractile.

In order to estimate the maximum force that the damper can transfer to the structure before the activation of the sliding motion, corresponding to the 95% fractile of the value of the friction coefficient, a series of ten experimental tests for each material has been performed, applying the 60% of the maximum preload, as shown in the previous tests, and adopting a configuration of two sets of 3 disc springs in parallel of disc spring arranged in series.

Table 2.2 - Summary of the tests – 2nd phase (The round brackets represent the disc springs configuration, n° of parallel or series)

	Specimen code	***Material code***	***Preload kN***	***% of PL/1.1***	***Spring configuration***
Different DS Configuration	NV - 17	M4	134.75	70%	3X3)))((()))
	NV - 18				3X3)))(((
	NV – 19				3X3)))
	NV - 20				NONE
	NV - 21	M6	188.65	100%	3X3)))((()))
	NV - 22				3X3)))(((
	NV – 23				3X3)))
	NV - 24				NONE
	NV - 25	M1	188.65	100%	3X3)))((()))
	NV - 26				3X3)))(((
	NV – 27				3X3)))
	NV - 28				NONE
Variable Pre-load	NV - 29	M4	113.19	60%	NONE
	NV - 30		94.33	50%	
	NV – 31		75.46	40%	
	NV - 32	M6	150.92	80%	NONE
	NV - 33		113.19	60%	
	NV - 34		75.46	40%	
	NV - 35	M1	150.92	80%	NONE
	NV - 36		113.19	60%	
	NV - 37		75.46	40%	

Random variation Friction Coefficient	NV - 38	M4	113.19	60%	2+3))(())
	NV - 39				
	NV - 40				
	NV - 41				
	NV - 42				
	NV - 43				
	NV - 44				
	NV - 45				
	NV - 46				
	NV - 47				
Random variation Friction Coefficient	NV - 49	M6	113.19	60%	2+3))(())
	NV - 50				
	NV - 51				
	NV - 52				
	NV - 53				
	NV - 54				
	NV - 55				
	NV - 56				
	NV - 57				
	NV - 58				
Random variation Friction Coefficient	NV - 60	M1	113.19	60%	2+3))(())
	NV - 61				
	NV - 62				
	NV - 63				
	NV - 64				
	NV - 65				
	NV - 66				
	NV - 67				
	NV - 68				
	NV - 69				

The results of all the performed tests have been collected in diagrams similar to those seen previously. From the point of view of the designer of the friction damper, the most important design parameter is

obviously the friction coefficient, for this reason the effective friction coefficient has been represented in function of the cumulative travel.

It is useful to reminder that the effective friction coefficient is defined as the ratio between the sliding force measured during the tests and the sum of the initial pre-loading forces multiplied for the number of interfaces (two in the current case).

In Fig. 2.39 each diagram collects the result of a series of tests on the same material. In this way it had been simple to trace the curves of the mean value of the effective friction coefficient (continuous line) and curves referred to the 5% and 95% fractiles (lower and upper dashed lines) evaluated for the three different materials tested. The 5% and 95% fractile curves have been evaluated for each value of the cumulative travel starting from the mean value and subtracting or adding respectively k times the coefficient of variation, where the value of k has been determined according to the procedure provided by Eurocode 0 [17] in section D7.2, in this case equal to 1.92 (normal distribution).

In general, the response of the tested material is very regular in case of the M6 material (the hard coating), conversely for M1 and M4 materials (the soft coatings) the answer is characterized by a higher dispersion, even if such dispersion is less relevant at the beginning of the test, in correspondence of the initial peak value defined as the static slippage force.

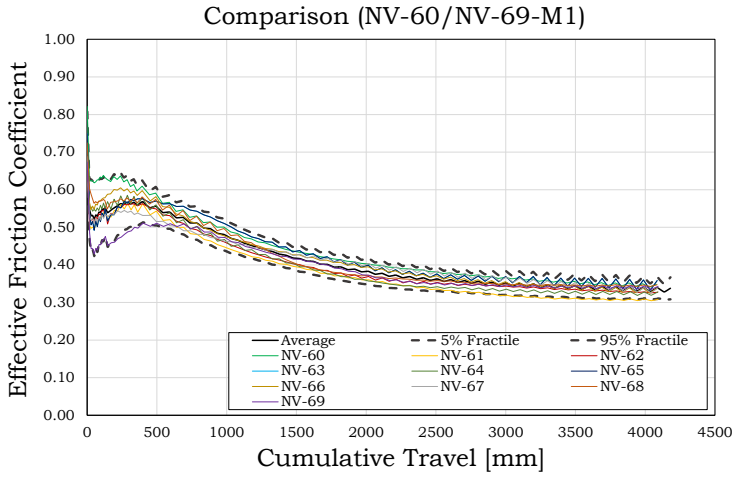
Comparison (NV-60/NV-69-M1)
Effective Friction Coefficient
1.00
0.90
0.80
0.70
0.60
0.50
0.40
0.30
0.20
0.10
0.00
0
500
1000
1500
2000
2500
3000
3500
4000
4500
Cumulative Travel [mm]
Average
5% Fractile
95% Fractile
NV-60
NV-61
NV-62
NV-63
NV-64
NV-65
NV-66
NV-67
NV-68
NV-69

a)

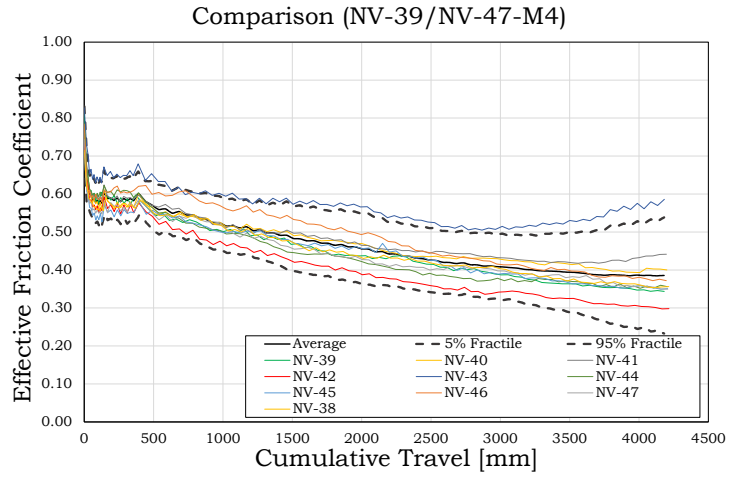
Comparison (NV-39/NV-47-M4)
Effective Friction Coefficient
1.00
0.90
0.80
0.70
0.60
0.50
0.40
0.30
0.20
0.10
0.00
0
500
1000
1500
2000
2500
3000
3500
4000
4500
Cumulative Travel [mm]
Average
5% Fractile
95% Fractile
NV-39
NV-40
NV-41
NV-42
NV-43
NV-44
NV-45
NV-46
NV-47
NV-38

b)

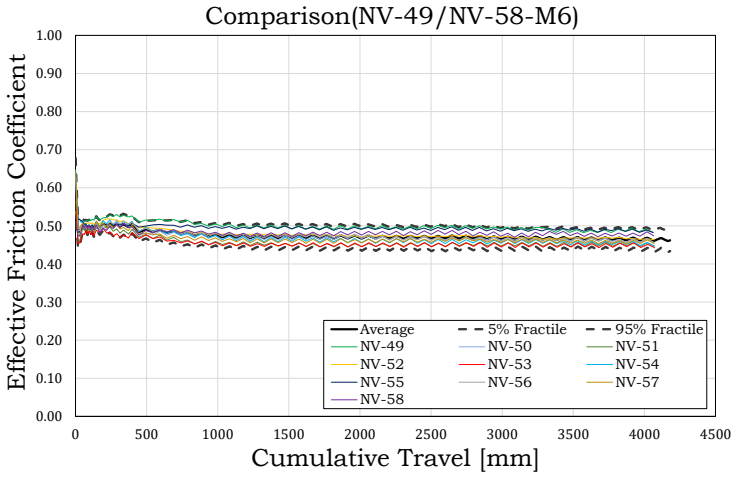

c)

Fig. 2.39 – Influence of the disc spring configuration over the preload and effective friction coefficient

2.3. Conclusions

In conclusion, considering the results obtained from the experimental tests only three materials appear adequate to the use in friction damper: M1, M4 and M6. Comparing the two soft materials, M1 and M4, the behaviour is quite similar with a comparable value of the static friction coefficient, but on the other hand, the M4 demonstrated a higher value of the dynamic friction coefficient. Regarding the M6 material, the friction coefficients both static and dynamic, are lower than M4 material, conversely, the degradation of the hard material is substantially less than soft materials.

In order to obtain the best compromise between mechanical properties and economic cost, the material chosen for the FREEDAM friction damper is M4. Even if the M4 presents a higher degradation, the effects

of the wear of the friction surfaces seems not affect the value of the friction coefficient in range of cumulative travel of the device corresponding to destructive seismic event.

2.4. References

1. H. Khoo, G. Clifton, G. Macrae and S. Ramhormozian: "*Proposed design models for the asymmetric friction connection*". Earthquake Engineering & Structural Dynamics. Vol. 44(8):1309-132, 2014.
2. H. Khoo, C. Clifton C, J. Butterworth, G. MacRae, S. Gledhill and G. Sidwell: "*Development of the self-centering Sliding Hinge Joint with friction ring springs*". Journal of Constructional Steel Research, 78:201-211, 2012.
3. H. Khoo, C. Clifton C, J. Butterworth and G. MacRae: "*Experimental Study of Full-Scale Self-Centering Sliding Hinge Joint Connections with Friction Ring Springs*". Journal of Earthquake Engineering. September (17):972-997, 2013.
4. J. Borzouie, G. Macrae and J. Chase: "*Cyclic Performance of Asymmetric Friction Connections*". The Bridge and Structural Engineer. March;45(1), 2015.
5. M. Latour M and G. Rizzano: *"Full Strength Design of Column Base Connections accounting for Random Material Variability*". Engineering Structures.48:458-471, 2013.
6. F.M. Mazzolani and V. Piluso: "*Theory and Design of Seismic Resistant Steel Frames*". London: E & FN Spon, an Imprint of Chapman & Hall; 1996.
7. CEN, 2005c. "*Eurocode 8: Design of structures for earthquake resistance - Part 1: General rules, seismic actions and rules for buildings*". s.l.:s.n.

8. R. Montuori, E. Nastri and V. Piluso: *"Advances on the theory of Plastic Mechanism Control: Close Form solution for MR Frames"*, Earthquake Engineering & Structural Engineering, vol. 4, pp. 1035-1054, 2014
9. EN 1090-2: "*Execution of steel structure and aluminium structure: Technical requirements for steel structures. Annex G: Test to determine slip factor*". 2008.
10. M. Latour, V. Piluso and G. Rizzano: "*Experimental Analysis of Friction Materials for supplemental damping devices*". Construction and Building Materials, 2014.
11. G. Ferrante Cavallaro, A.B. Francavilla, M. Latour, V. Piluso and G. Rizzano: "*Experimental behaviour of innovative thermal spray coating materials for FREEDAM joints*". Composites Part B Engineering, 2016.
12. EN 15129, (2009): "*Anti-seismic devices*".
13. F. Bowden and D. Tabor: "*The Friction and Lubrication of Solids: part I*". Oxford: Oxford University Press, 1950.
14. M. Latour, V. Piluso and G. Rizzano: "*Free from damage beam-to-column joints: Testing and design of DST connections with friction pads*". Engineering Structures.85:219-233, 2015.
15. J.P. Jaspart, 2002: "*Design of Structural Joints in Building Frames. Progress in Structural Engineering and Materials*", Vol.4(18-34), 2002.
16. CEN, 2005b. "Eurocode 3: *Design of steel structures - Part 1-8: Design of joints*". s.l.:s.n.
17. CEN, 2005. "*Eurocode 0: Basis of Structural Design*".

CHAPTER 3

3.1 Bolts pre-load

In the previous chapter, one of the most important parameters that govern the friction response of the FREEDAM device have been investigated: the friction coefficient of the materials employed to realize the dissipative interface. As said previously, the friction coefficient – static (to be used in serviceability limit state design) or dynamic (to be used in ultimate limit state design) – depends on the tribological properties of the shims (micro and macro hardness, shear resistance, roughness, superficial finishing, etc.) used in the damper and the values of the friction coefficient have been characterized statistically for several possible materials, defining upper and lower bound regression models able to provide the friction coefficient as a variable dependent on the cumulative travel [1,2].

The main purpose of this chapter is to investigate another important parameter which can significantly influence the behaviour of the damper: the bolt preloading force. In fact, as also noted during the execution of the tests for the characterization of the friction coefficient for the different materials, after the installation and during the life-time of the connection, aside from the procedure applied to tighten, the preload force is progressively reduced. This reduction depends on many complex phenomena involving: i) embedment relaxation, ii) bolt creep, iii) vibrations, iv) elastic interactions, and v) differential thermal expansions [3-9]. These effects affect the maintenance of the initial preload level in an unpredictable way using a deterministic approach therefore, to be quantified, need to rely on experimental investigation. Some of the aspects that most others involve a reduction in the preload

are: the velocity of application of the pre-load with the torque wrench, the tightening procedure, the crushing of micro-spots of the steel plates under the bolt head or nut and the creep of the coating materials. Regarding the tightening procedures, EN 1090-2 [10] currently provides four different methods for the installation of High Strength bolts (both of HR or HV type) in friction bearing connections: torque method, combined method, HRC, DTI. All these methods have been calibrated and checked only for traditional friction connection. An experimental campaign has been conducted in order to extend the validity of these methods also to AFC or SFC dampers. In fact, in case of friction joints such as those herein described, the bolts are used to pre-stress particular types of friction shims, while the classical friction connections are realised with steel plates uncoated or coated with paintings or zinc, for this reason there could be significant differences in terms of initial or long-term response.

The tests executed within this experimental campaign aim primarily to assess the accuracy of some of the European standardised tightening procedures on sub-assemblies of symmetrical friction dampers and subsequently to assess the possible influence of time-related effects on the initial bolt tension, with specific tests carried out for periods of time, extending up to one month. One month represent a duration sufficient to determine the tangent of the displacement-log time curve and to consequently derive the data adopting a procedure similar to that suggested by EN 1090-2 [10] for creep tests. A further purpose of the performed tests is represented by the evaluation of the efficiency of the European standardised type of Belleville spring washer (which complies to DIN 6796 [11]) in maintaining the preloading of the bolt assemblies constant during the life-time.

The experimental campaign consists of 84 tightening tests on specimens of friction damper. The force applied to the bolts has been monitored for all the performed tests by means of annular load cells, in order to evaluate the initial achievement of the target preload adopting one of the tightening procedures provided by EN 1090-2 [10]. Furthermore, in 26 cases the loss of preload has been monitored for a period of time from 18h up to a month it is important to underline that the preload losses due to the alternate sliding of the connection in case of a rare earthquake have not been taken into account. In the final part of the chapter the test results are discussed critically, proposing a statistical characterization and a regression study for the loss of preload, thus providing a useful tool for the design.

3.1.1. Tightening procedures according to EN 1090-2

The different types of bolts for steel structures are identify in EN 14399 [12], EN 898-1 [13] and EN 15048 [14] codes, where their geometrical and mechanical features are specified. The European codes divide bolts into two macro-categories depending on the type of assembly: pre-loadable assemblies of HV, HR, and HRC type, and standard assemblies (SB) for normal connections. The research activity focuses the attention on the first category of bolts, for which the EN 1090-2 [10] introduces four different methods to tighten bolts: torque, combined, HRC, and DTI.

One of the tightening method investigated is the torque method, that is basically a force control (torque control) procedure. The application of the preload is divided into two steps: the 75% of the torque reference value (i.e. $T_r=0.7A_bf_{ub}k_d$, where A_b is the bolt's net area, f_{ub} is the

ultimate stress of the bolt's material, d is the bolt's nominal diameter and k is a constant depending on the bolt's assembly) is applied during the first step, while the 110% of the torque reference value is applied during the second step. Respect to the nominal value of the tightening torque there is an increment of the 10% in the second step due to the fact that it is necessary to assure that the target mean preload value is equal to $(1+1.65V_k) \cdot 0.7A_bf_{ub}$, being V_k the coefficient of variation, assumed by the code as equal to 0.06 (see clause 8.5.3 of [10]). In other words, the increment of the 10% takes into account the random variation of the bolts tightening ensuring contemporarily that the 5% fractile of the pre-load (lower bound value) is higher than the nominal preload ($0.7A_bf_{ub}$), and that the 95% fractile (upper bound value) is lower than the bolt's nominal tensile strength ($0.9A_bf_{ub}$) (Fig.3.1a). The first condition assures that the preload force applied to the bolts is higher than the design value, the second one assures that the applied tightening torque does not exceed the bolt yield strength. In this regard it should be noted that Barenbak [15] demonstrated that the torque method, as currently codified is not able to assure the minimum 95% reliability required by Eurocode 0 [16]. In fact, the coefficient of variation adopted for the bolt assemblies is equal to 0.06 [15], but it does not guarantee the required level of reliability, essentially due to the influence of other random effects that should be taken into account during the design process. The other random parameters that influence the estimate of k are: the accuracy of the bolt measuring device used in the k-test (± 0.02) and its repeatability (± 0.01), the accuracy of the bolt torque measurer used in the k-test (± 0.01) and its repeatability and finally the accuracy of the torque wrench used to apply the preload which, as required by the EN 1090-2 [10], for the torque method, must

be at most equal to the ±4%. The combination of all these factors together with the maximum coefficient of variation allowed for bolt assemblies (0.06) could lead to an overall coefficient of variation equal to 0.77. Due to this, it could be verified with simple calculations that when a target mean value of $1.1 \cdot 0.7 A_b f_{ub}$ is assumed, the reliability with respect to the upper bound value is guaranteed (98.6%), but it does not guarantee the reliability for the nominal preload which is only equal to the 88.2% (Fig.3.1a).

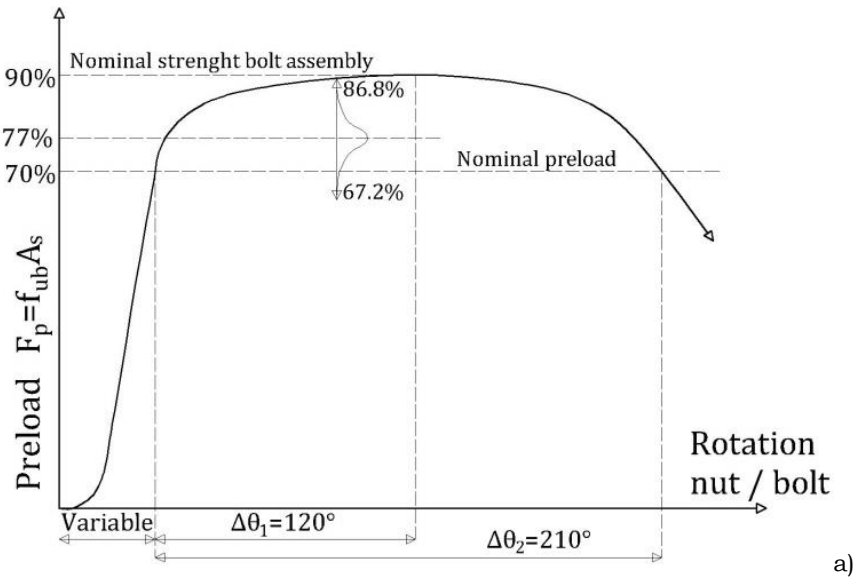

a)

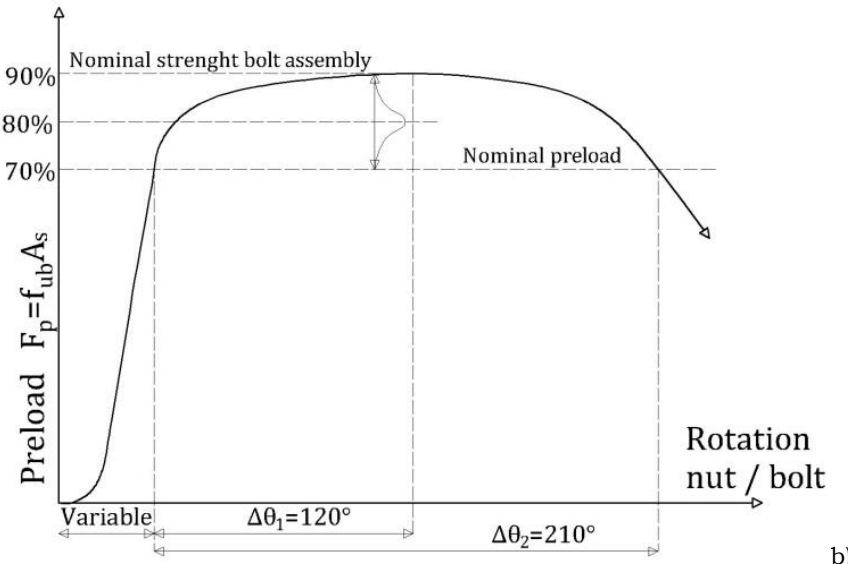

b)

Fig. 3.1 – Torque method. a) Current procedure with V_k=0.06 and mean value equal to $0.77f_{ub}A_b$; b) Improved procedure with mean value equal to $0.80f_{ub}A_b$

It is worth noting that, in order to respect the minimum reliability of the 95% for both bound pre-load values, the torque procedure could be easily corrected, imposing a target mean value equal to $0.8A_bf_{ub}$ [15] (Fig.3.1b). Additionally, it must be underlined that the torque method, relying on a pre-qualification of the bolts based on the so-called k-test (the test used to determine the correlation factor between torque and pretension), needs to be applied only on bolts which are exactly in the same conditions of the tested bolts. Therefore, they must have no rust or dust in the threads, and they must be in the same lubrication state. This requirement can be practically considered satisfied only if the installed bolts are delivered and taken from closed boxes and if, before installation, it is possible to verify that the nut is able to turn freely through performing a free-nut turn check.

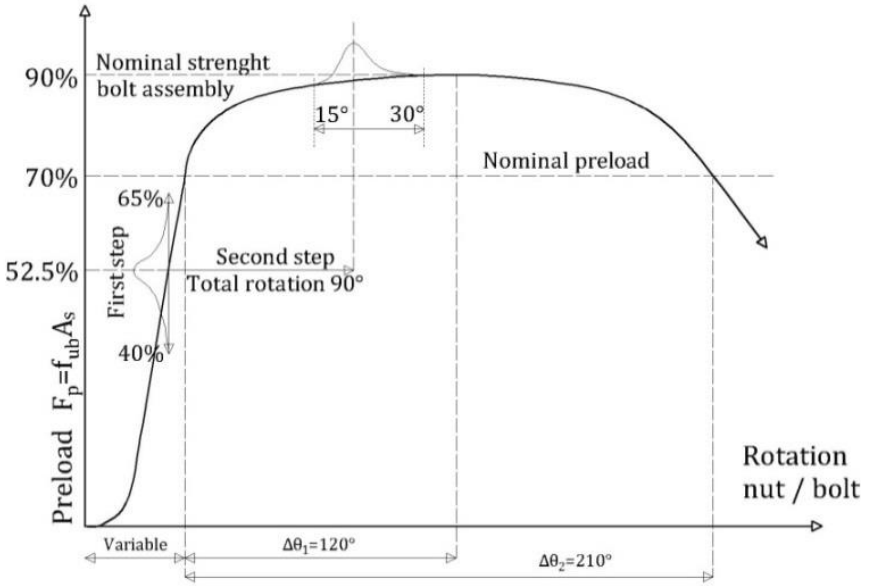

Fig. 3.2 – Combined method, distribution preload according to EN 1090-2 [10]

Conversely, the combined method is substantially a displacement-control (turn-of-the-nut control) procedure, divided into two phases: a first one equal to the first step of the torque method, and a second consisting in a controlled part-turn rotation of the nut determined as a function of the thickness of the assembly. This procedure, as opposed to the previous one, is able to provide a 100% reliability with respect to the minimum tightening force required, because the displacement control phase is meant to assure that the preloading force achieves the plastic branch of the pre-load/elongation curve. Nevertheless, as shown hereinafter, this procedure does not allow a clear control of the upper bound value of the preloading force and, in fact, can lead in many cases

to the development of pre-loads higher than the nominal bolt's resistance (Fig.3.2).

The HRC system is very different from the other methods because it requires a particular assembly and the employment of a special wrench equipped with two co-axial sockets that react against each other to tighten the bolt. In this case, it is not necessary to calibrate the wrench because the maximum torque is determined by the strength of the splined end. In any case, the accuracy of this method also depends on the quality of the threads which must be checked prior to installation. Finally, the Direct Tension Indicator (DTI) method comprises the use of special washers with compressible nibs on one face that deform to indicate when the maximum preload has been reached. The tightening process is divided into two steps: during the first step, the bolt assembly is tightened until the nibs just begin to deform, while during the second step the bolt assembly is tightened until reaching the full compression of the protrusion.

This investigation seeks to evaluate the possibility to extend the two easiest procedures to symmetric friction dampers, namely the torque, and combined methods. These tightening methods can be applied using only HV or HR bolts. The HV and HR assemblies are very similar, and they can both be used for friction bearing connections. Their main difference is the shape of the threads and the height of the nut, which lead to a different failure mechanism under tension: in the HR system, the failure occurs in the bolt's shank, while in the HV system the failure occurs in the threads of the nut. This failure mode of the HV system is not typical in other countries but, nevertheless, represents the most common type of pre-loadable bolt assembly in Europe. Further discussions on this topic are reported in [17].

From the point of view of the qualification procedures for bolts belonging to preloaded assemblies, the relevant European standards, EN 14399-3/4 [18,19], and EN 1090-2 [10], divide the bolts into three classes: k_0 class (no requirements for the k-factor); k_1 class (minimum 5 tests on bolts and $0.10 \le k_t \le 0.16$); and K_2 class (minimum 5 tests on bolts and $0.10 \le k_m \le 0.23$ with $V_k \le 0.10$). The k_2 bolts can be used for both, the combined and the torque method, assuming $k=k_m$ (declared by manufacturer), while k_1 bolts can be used only for the combined method. However, in this case, the value of the k coefficient is assumed equal to 0.13 for the first tightening step (the mean value between 0.10 and 0.16), if not differently specified. It is worth noting that currently, the minimum requirements for the k-classes are poorly defined. In fact, as explained before, the torque method for a consistent application needs a maximum value of the coefficient of variation to be equal to 0.06 as required by EN 1090-2 [10], while EN 14399 [18,19] allows the use of the torque method for bolts having a coefficient of variation up to 0.10. Hence, in order to fulfil both the requirements of EN 1090-2 [10] and EN 14399-3/4 [18,19], bolts which are contemporarily complying with the requirements for k_1 and k_2 classes with $0.10 \le k_t \le 0.16$, $0.10 \le k_m \le 0.16$, with a coefficient of variation lower than 0.06 are currently available on the market. In the tests reported subsequently, bolt assemblies of this type have been used and their use is suggested, in general, for the application of the torque method.

3.2. Tightening tests and short-term relaxation tests on SFC sub-assemblies

3.2.1 Experimental layout

In order to evaluate the accuracy of the EN 1090-2 [10] tightening procedures and the possible short- and mid-term loss of the initial tension of bolts installed in friction dampers, 58 tightening tests on simple bolt assemblies and 26 relaxation tests were performed at the laboratory STRENGTH (STRuctural ENGineering Testing Hall) of the University of Salerno. The typical specimen adopted to evaluate the accuracy of the tightening procedures is a simple modification of the specimen suggested by EN 1090-2 [10] for slip tests adapted to the case of a SFC connection. It is constituted by 8 mm friction shims, realised with steel plates coated with three different coating materials, a couple of 15 mm hot-dip galvanised external steel plates and a couple of plates, one realised with S275JR steel and normal holes (upper part of the specimen, Fig.3.3) and the other realised with stainless steel and a slotted hole (steel equivalent to the AISI 304 [20], lower part of the specimen, Fig.3.3). The specimen is designed to be similar to the typical configuration of an SFC employed in SHJs recently tested and similar to the SFC reported in [21,22] In fact, the stainless-steel plate simulates the internal plate of the haunch located under the bottom flange of the beam, while the external plates simulate the angles used to fasten the friction pads to the column. In the upper and lower part of the specimen two bolts and one bolt M20 10.9 HV have been used, respectively, to

tighten the specimen. The bolts used in the experimental analysis are produced by SBE-Varvit S.p.A (Italy).

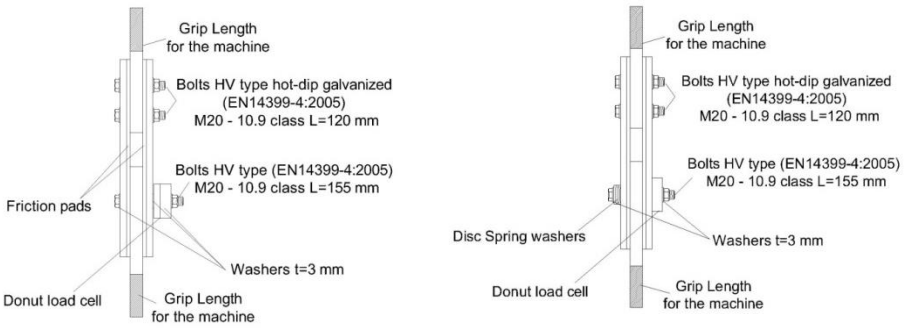

Fig. 3.3 – Configurations adopted for the tightening tests. a) HV washers; b) HV + Disc Spring washers.

The tests were performed measuring the preload applied, the tightening torque and the rotation of the nut using specific devices. The tightening torque, applied through a hand torque wrench calibrated according to EN 1090-2 [10] in order to reach the accuracy of ± 4%, was also monitored, using a torque sensor FUTEK TAT430 with a maximum capacity equal to 680Nm. Conversely, the preload applied to the bolts was measured through a donut load cell, FUTEK LTH500, with maximum capacity of 222kN located on the side of the bolt's nut. Finally, to measure the rotation of the nut, a digital angle meter, USAG 831A, with a tolerance of ±2% was used.

The tested bolts are 10.9 class HV with size M20x155 mm with the following characteristics certified by the manufacturer: k_m=0.119 and V_k<0.06, so that they can be classified both as K2 or K1 class according to EN 14399-2 [23] and they can be tightened using the torque method or the combined method, indifferently (EN 1090-2 [10]). Two different configurations have been tested: one with standard flat washers (EN

14399-6 [24]) (Fig.3.3a) and another one with flat and disc springs washers (DIN 6796 [25]) (Fig.3.3b). The normal flat washers have been used also in the second case to comply with the value of the k-factor provided by the bolt's manufacturer. The disc spring washers, also called Belleville, are conical washers made of high strength steel (usually C60 grade), able to compress elastically until reaching a threshold value beyond which they show a significant increase of stiffness until complete flattening (Fig.3.4).

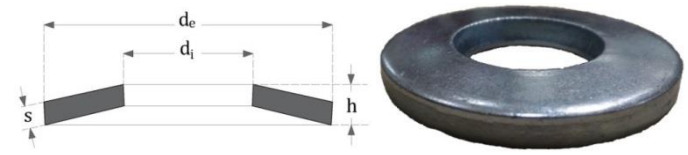

a)

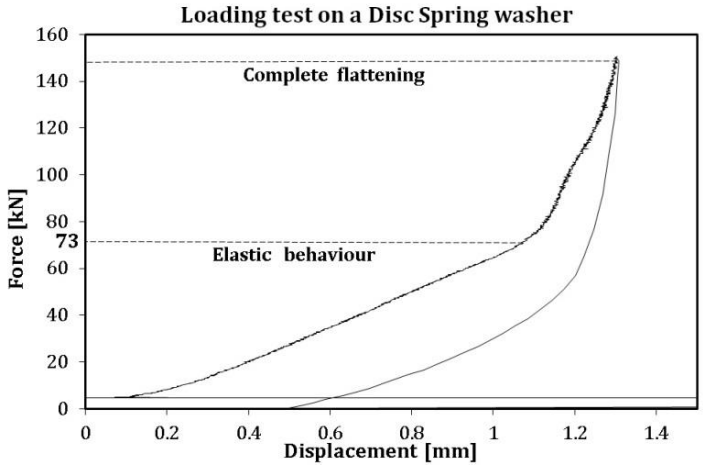

b)

Fig. 3.4 – Disc Spring washers. a) Geometric features of a Disc Spring washer; b) Experimental behaviour of a disc spring washer

The aim of the introduction of these washers in SFC is to increase the axial deformability of the bolt assembly in order to limit the loss of preload due to long-term relaxation, vibration, and thermal effects [3-9,

26-28]. In fact, during the life-time of a friction connection, when the bolts relax or the coatings of the friction shims creep, the disc washers act as springs, pushing the bolt and restoring the preload force initially applied. The Belleville springs can be assembled in different ways to create a system of desired stiffness. Usually, it is possible to stack them one over the other, obtaining an increase of stiffness and resistance proportional to the number of disc springs (parallel configuration); face-to-face, obtaining an increase of the deformability proportional to the number of disc springs (series configuration), or in groups of series and parallels. Preliminarily, in order to determine the load-bearing capacity of the disc springs, a compression test has been performed highlighting that the standardised European disc springs for M20 bolts are able to resist to a force of about 73kN elastically, value beyond which they exhibit an increase of stiffness until complete flattening (Fig.3.4b). Considering that the single disc spring can resist to 73kN, three disc springs in parallel have been necessary to withstand the upper bound value of the tightening force which, as explained before, may be at most equal to the bolt's yielding resistance (for M20 bolts, class 10.9, *245x900=220.5kN*). Therefore, in order to understand the influence of the disc springs over the tightening procedure and the short- or mid-term relaxation, as an alternative to the configuration with normal washers, a simple configuration composed of three disc springs arranged in parallel has been considered. Obviously, this configuration is selected only to provide a first comparison of the behaviour of normal flat washers and standardised Belleville washers. Further experimental efforts should be, eventually, devoted to understanding the influence of the configurations or of other disc springs typologies on the short-term or long-term behaviour of the bolt assembly.

3.2.2. Tightening tests

The accuracy of the EN1090-2 [10] tightening methods applied to SFC dampers has been verified carrying out 36 tightening tests on bolt assemblies employing normal flat washers and 22 tightening tests on bolt assemblies employing also disc springs. The typology and number of tests performed are summarised in Table 3.1.

Table 3.1. Tightening tests' list

Flat washers	Torque method	15 tightening tests
	Combined Method	21 tightening tests
Disc Springs	Torque method	11 tightening tests
	Combined Method	11 tightening tests

The torque method has been applied adopting the procedure previously described, namely: during the first step, the target preload has been fixed equal to $0.75F_p=128.6kN$, while during the second one, the target preload force has been assumed equal to $1.10F_p=188.7kN$.

Conversely, the combined method has been executed applying to the specimens initially a tightening control phase analogous to the one performed with the torque method and, afterwards, a controlled part-turn rotation of the nut. In the case under study in this paper, as far as the total thickness of the specimens was equal to 84mm, the rotation of the nut was assumed equal to 90° according to the EN 1090-2 [10] provisions.

In Fig.3.5 the results of the application of the two different procedures are delivered, representing in terms of torque vs preload and preload vs time a typical tightening session, both for the torque and for the combined method. In both cases, it is possible to note that the

relationship between the torque and the preload is linear, with a slope corresponding approximately to the k-factor. Additionally, in the preload vs time curves, the two loading steps previously mentioned are easily recognisable, showing the approximate achievement of the target values. All the specimens have been tightened following these methodologies, and the results are herein critically discussed.

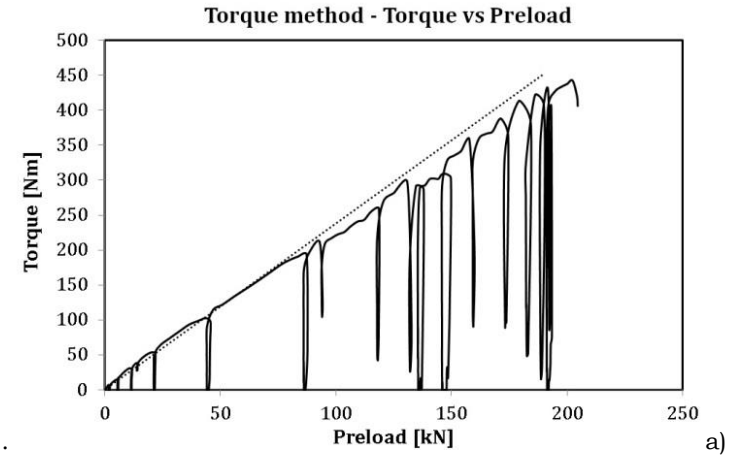

a)

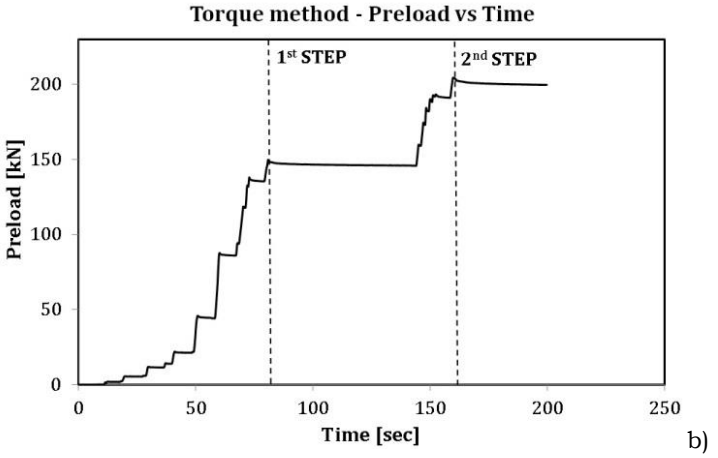

b)

Fig. 3.5 – Examples of tightening sessions

In order to assess the results, they have been collected into four charts delivered in Fig.3.6, while in Table 3.2 the main statistical parameters obtained for each group of tightening tests have been summarised. From the diagrams, it is possible to note some significant differences between the two tightening methods individuating some criticisms, especially with respect to the possible application to SFC dampers. First, a preliminary useful observation is that, the two procedures could assure, in all the tightening tests, a value of the pre-load higher than the minimum characteristic value used in design equal to 171.5kN. Therefore, they seemed to perform adequately from this point of view. Despite this, the results obtained with the torque and the combined method were significantly different (Fig.3.6). These differences, according to the authors, are essentially due to the different goals that the two methods want to achieve. In fact, as previously mentioned, the torque method (even though it has the criticisms previously evidenced) is executed basically under force control and is calibrated to assure that, in the same time, the characteristic value of the preload is higher than the nominal value used in design and that the 95% fractile of the preload is lower than the nominal resistance of the bolt. Conversely, the combined method is a displacement control procedure, able to guarantee that the nominal value of the bolt preload is attained. However, even though it is very effective in achieving this objective, it does not provide a clear control on the applied upper bound value of the pre-load, which is based only on an empirical relationship between the part-turn rotation of the nut and the thickness of the bolted assembly.
The varied accuracy of the two methods is very clear from the results represented in Fig.3.6.

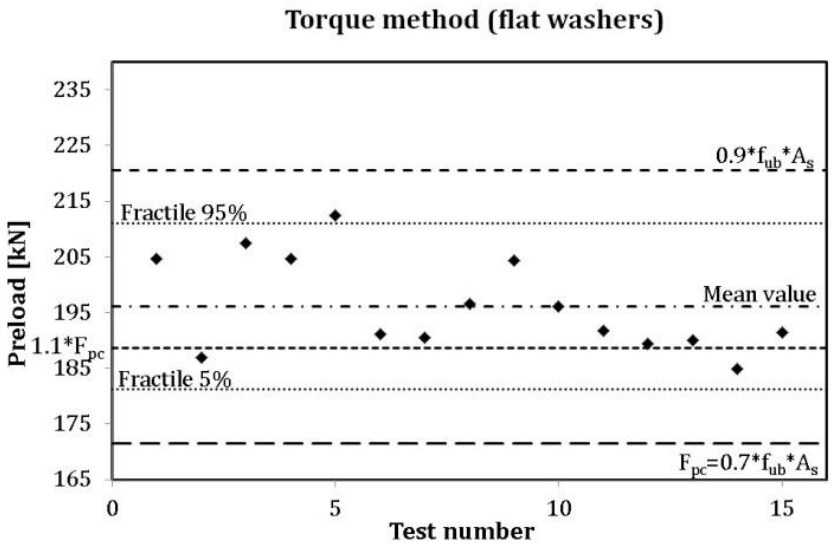
Torque method (flat washers)
Preload [kN]
Test number
0.9*f_ub*A_s
Fractile 95%
Mean value
1.1*F_pc
Fractile 5%
F_pc=0.7*f_ub*A_s
235
225
215
205
195
185
175
165
0
5
10
15

a)

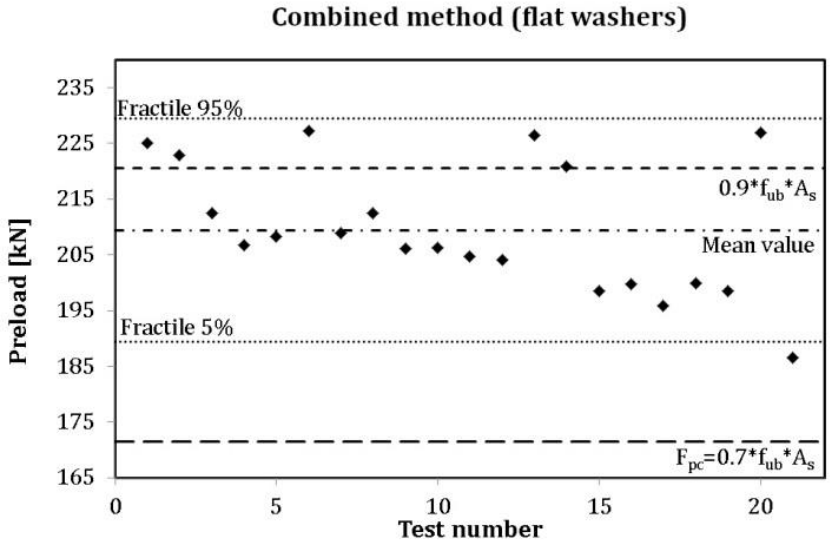
Combined method (flat washers)
Preload [kN]
Test number
Fractile 95%
0.9*f_ub*A_s
Mean value
Fractile 5%
F_pc=0.7*f_ub*A_s
235
225
215
205
195
185
175
165
0
5
10
15
20

b)

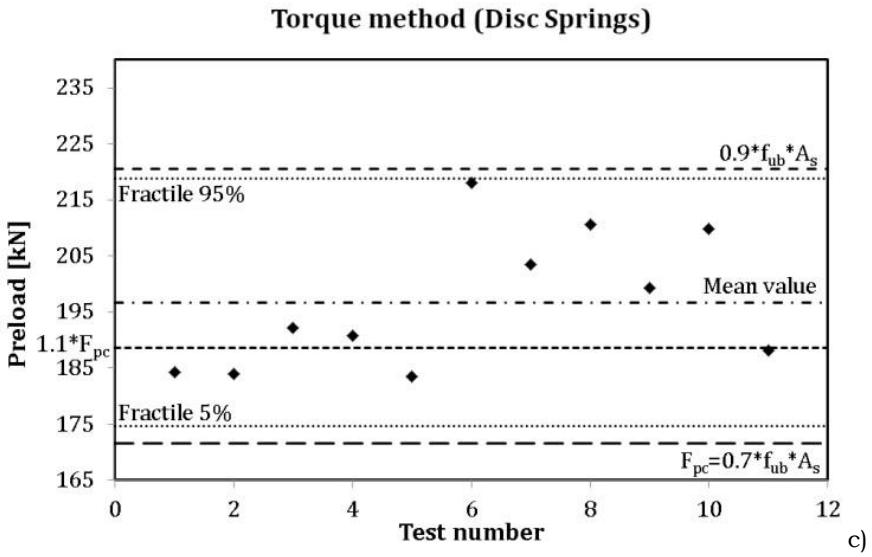

c)

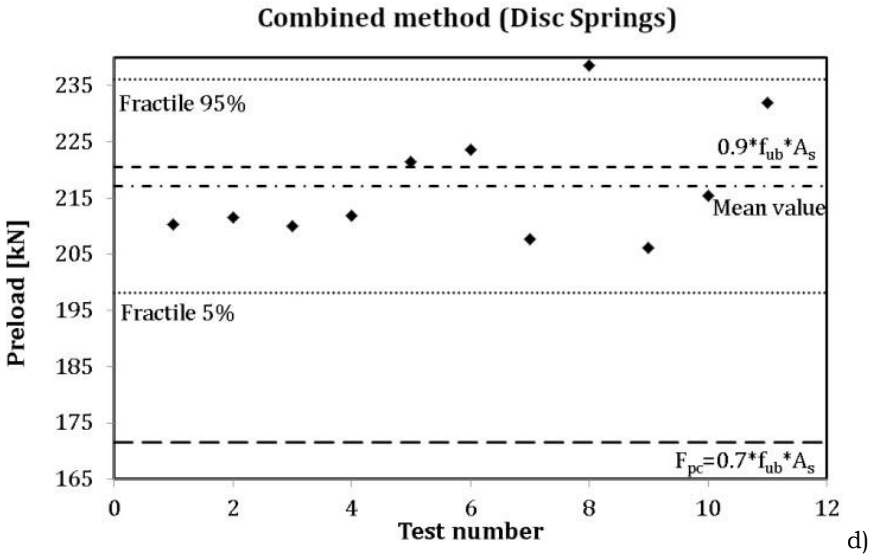

d)

Fig. 3.6 – Summary of the tightening tests

In fact, for the torque method, under the assumption of a normal distribution, it resulted in the lower and upper bound fractiles of the preloads being always contained in between the bound values represented by the bolt's yield strength and nominal resistance. This happened both, for assemblies employing flat washers, and for those equipped with disc springs. Conversely, for the combined method, it is easy to note from Fig.3.6 that while, on the one hand, the minimum preload was always achieved, on the other hand, in many cases the obtained pre-load was greater than the nominal resistance of the bolt, with the consequent risk to over-load the bolts.

In terms of statistical parameters, both methods provided low values for the coefficient of variation (lower than 0.06), complying with the minimum requirements of EN 1090-2 [10], but the tightening forces applied with the combined method were characterised by an upward shift of the mean value (very close to the bolt's nominal resistance) and of the upper and lower bound fractiles. Particularly with the combined method, in both cases (with or without disc springs), the upper bound fractile exceeded the minimum bolt yielding resistance. Additionally, in the case of the torque method, the presence of the disc springs did not seem influent on the response of the assembly, while for the combined method the presence of the disc springs provided a further upward shift of the mean value. This is probably because the procedure suggested by EN1090-2 [10] has been extended straightforwardly to assemblies with disc springs, adopting the same angle of rotation of the nut (90°). Supposedly, with disc springs, due to the difference in the stiffness of the assembly, a recalibration of the part-turn of the nut should be performed. This should be investigated in greater detail in further analyses. Furthermore, this result may be also related to the fact that

these disc springs are usually sold without "pre-setting" as, instead, suggested by [29] in application to AFC of SHJs.

Table 3.2. Tightening tests – Summary of statistical results

	Flat washers		***Disc springs***	
	Torque Method	***Combined Method***	***Torque Method***	***Combined Method***
μ [kN]	*196.14*	*209.44*	*196.73*	*217.15*
σ [kN]	*8.19*	*11.35*	*10.53*	*10.03*
CV	*0.04*	*0.05*	*0.05*	*0.05*
Fractile 5% [kN]	*181.24*	*189.41*	*172.96*	*198.16*
Fractile 95% [kN]	*211.04*	*229.47*	*214.25*	*236.15*
F_p [kN]	*171.5*	*171.5*	*171.5*	*171.5*
1,1F_p [kN]	*188.65*	-	*188.65*	-

As a conclusion, from the developed analyses, it seems that the torque method provided reliable results, fully complying with the EN 1090-2 [10] requirements, both in case of traditional HV assemblies and in case of HV assemblies with disc springs. Nevertheless, it must be underlined that, as already specified before, a good threads quality is a fundamental feature for the consistent application of this methodology. Conversely, the combined method, even though on the one hand provided a reliable response in terms of achievement of the minimum preload, on the other hand showed to be more empirical, leading, in some cases, to values of the tightening force being very close to or exceeding the bolt's yielding resistance. Additionally, it was evident from the experimental data that the part-turn rotations currently indicated in EN1090-2 [10] should not be extended straightforwardly to assemblies with disc springs. In fact, when disc springs are employed, due to the

different stiffness of the assembly, a recalibration of the part-turns should be previously performed.

3.2.3. Short-term and mid-term relaxation tests

In order to investigate the possible short- and medium-term relaxation effects of bolted assemblies, specific tests have been conducted on specimens, in some cases employing disc springs and HV washers, in other cases only with standard HV washers. The tests were performed similarly to the tightening tests. Therefore, the specimens were tightened and the preload was monitored for a period of time. No tensile force was applied to the specimens. Some tests were performed by tightening according to the torque method and others using the combined method. In 24 cases, the preload has been monitored for a period of at least 18 hours (short-term tests) and in 4 cases, the bolts' force has been recorded for a minimum of 30 days (mid-term tests).

Table 3.3. Short term relaxation tests list

Flat Washers	*Torque method*	*6 tightening tests*
	Combined Method	*6 tightening tests*
Disc Springs	*Torque Method*	*6 tightening tests*
	Combined Method	*6 tightening tests*

In Table 3.3, the typology of short-term tests performed are reported. The results, which are not reported here in extensive detail for reasons of brevity, demonstrate that there is no significant correlation between the tightening method and the bolts' loss of tension, while it was possible to observe a very strong difference comparing the behaviour of the assemblies with or without disc springs. In particular, as shown afterwards, when disc springs were included in the assembly, the loss of

preload was significantly higher, even though the experimental data were characterised by a lower dispersion.

In Table 3.4, the results of the tests performed on specimens with HV flat washers are summarised. For the sake of simplicity, even though the loss of tension was monitored continuously during the tests, they are reported in this table in correspondence of precise instants, namely at 1h, 6h, 12h and 18h. For each time instant, the losses are reported summarising the results of the twelve tightening tests in terms of statistical parameters. It is evident from Table 3.4 that in each time instant the coefficient of variation is very high, underlining the strong aleatory nature of the phenomena, while the average loss varies from about 4% to 5.3% at 1h and 18h from the initial tightening, respectively. In the last column of the table, the expected loss at 50 years (reference life-time of the structure) is estimated through extrapolation of the data (according to EN 1090-2 [10]), considering the possibility to define, starting from the test data, an equation providing the loss over the time. To this scope, four regression curves are proposed, normalising the loss with respect to the loss of initial bolt tension that occurred at different time instants (1h, 6h, 12h, and 18h) (Fig.3.7). These regressions can be used as rapid tools to evaluate the bolts' loss of initial tension over time. Additionally, they can also be interpreted from a statistical standpoint, assuming as a random variable the loss at 1h, 6h, 12h, and 18h, with the mean values and coefficients of variations reported in Table 3.4. Therefore, the regressions can be expressed in the following way:

$$\frac{p_{\%}(t)}{p_{\%,\#h}} = c_1 \ln(t) + c_2 \tag{3.1}$$

where $p_{\%}$ (t) is the loss of preload at time t (in hours), c_1 and c_2 are two constants calibrated on the experimental data by means of least square regression, and $p_{\%,\#h}$ is the loss of preload at time #, with # equal to 1h, 6h, 12h, or 18h. Based on the obtained data, according to the procedure provided by Eurocode 0 [16], $p_{\%,\#h}$ is a variable that can be assumed normally distributed with mean value equal to the mean value (reported in the second column of Table 3.4) and coefficient of variation estimated from the sample (reported in the fourth column of Table 3.4). In this way, the mean, lower bound and upper bound fractiles of the loss used to normalise the regression can be determined as follows:

$$p_{\%\#h,5\%fractile} = p_{\%\#h,mean}(1 - \gamma \times CV) \tag{3.2}$$

$$p_{\%\#h,95\%fractile} = p_{\%\#h,mean}(1 + \gamma \times CV) \tag{3.3}$$

where γ accounts for the narrowness of the sample and can be expressed as:

$$\gamma = \left(1 + \frac{1}{n}\right)^{0.50} t_{\alpha,n} \tag{3.4}$$

where n is the numerosity of the sample, and $t_{\alpha,n}$ is the quantile of the t-student's distribution with *a=0.05*.

The results of the regression curves are summarised in Table 3.4 with the correlation coefficients reported directly in Fig.3.7. In general, the results of the tests demonstrate that for bolt assemblies with normal washers, the loss occurring in 50 years, on average, is approximately equal to 10%, and that half of the total loss occurring during the life-time of the bolted assemblies occurs in the first 12h.

Table 3.4. Short term relaxation tests result (Flat washers)

	μ [%]	σ [%]	CV	Fractile 5% [%]	Fractile 95% [%]	Expected loss at 50 years (Regression curve)			c_1	c_2
						5%	Mean	95%		
1h	4.03	1.0	25.1	2.22	5.83	5.3	9.72	14.0	0.107	1.013
6h	4.79	1.3	28.2	2.38	7.20	4.7	9.60	14.4	0.089	0.842
12h	5.09	1.5	30.7	2.30	7.87	4.3	9.55	14.7	0.083	0.789
18h	5.26	1.7	32.3	2.23	8.30	4.0	9.53	15.0	0.080	0.760

For the specimens equipped with disc spring, the same number of tests and the same analysis of the data have been carried out. The results are reported in Table 3.5 and Fig.3.8. In this case, it is easy to note from Table 3.5 that in the assemblies with disc springs the observed loss of tension was always greater but, as stated, was also characterised by a lower variability. In fact, the coefficient of variation evaluated at different time instants was, in this case, equal to about 8%. As before, in order to have a fast tool to estimate the bolts' loss of tension over time, regression analyses of the data have been carried out, normalising the regression curves with the loss occurring at 1h, 6h, 12h, and 18h. The loss of tension occurred at different time instants with the mean values and coefficients of variations reported in Table 3.5.

The analysis of the data points out that in assemblies with disc springs, the loss of preload estimated at 50 years is, on average, of about 27% and that half of this loss occurs in the first 12h.

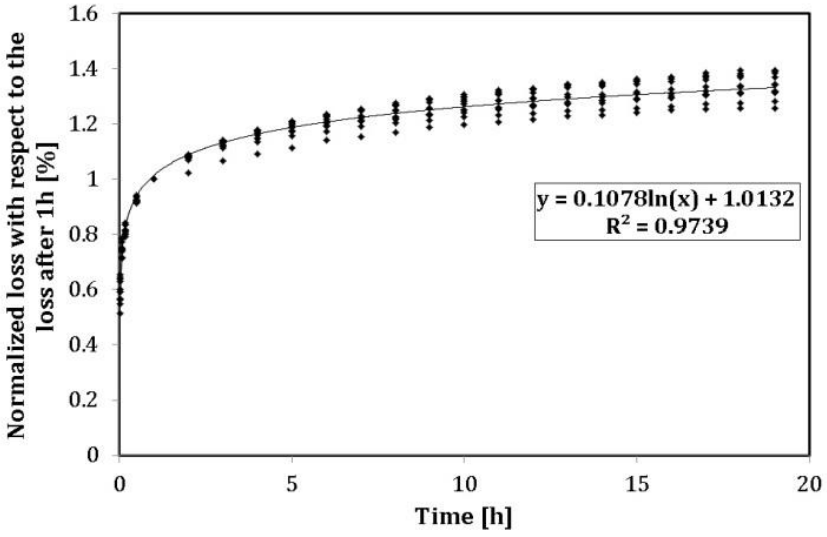
Normalized loss with respect to the loss after 1h [%]
Time [h]
y = 0.1078ln(x) + 1.0132
R² = 0.9739
0
0.2
0.4
0.6
0.8
1
1.2
1.4
1.6
0
5
10
15
20

a)

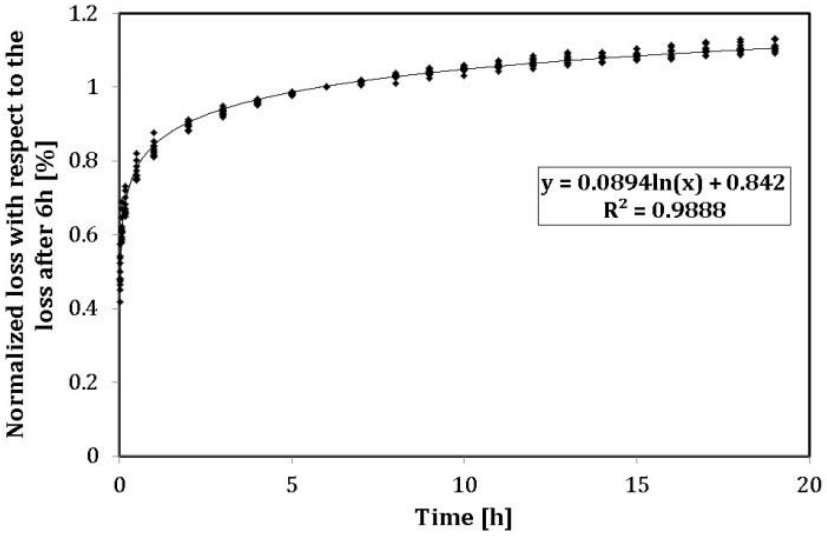
Normalized loss with respect to the loss after 6h [%]
Time [h]
y = 0.0894ln(x) + 0.842
R² = 0.9888
0
0.2
0.4
0.6
0.8
1
1.2
0
5
10
15
20

b)

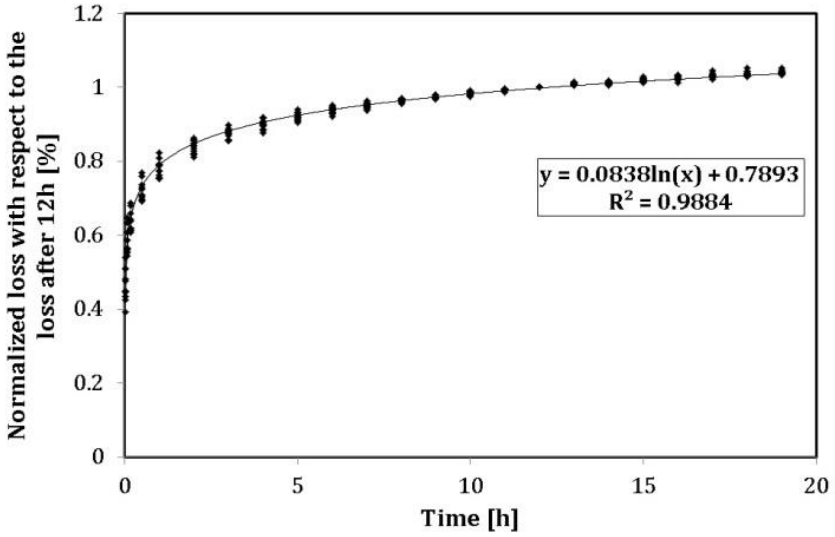

c)

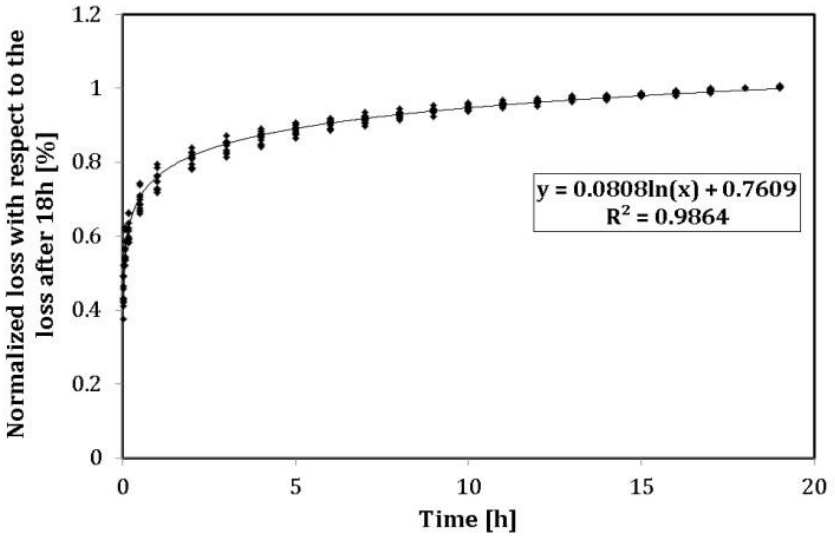

d)

Fig. 3.7 – Regression curves of short term relaxation tests (Flat washers) normalised with respect to the loss occurred in fixed time instants a) 1h; b) 6h; c) 12h; d) 18h.

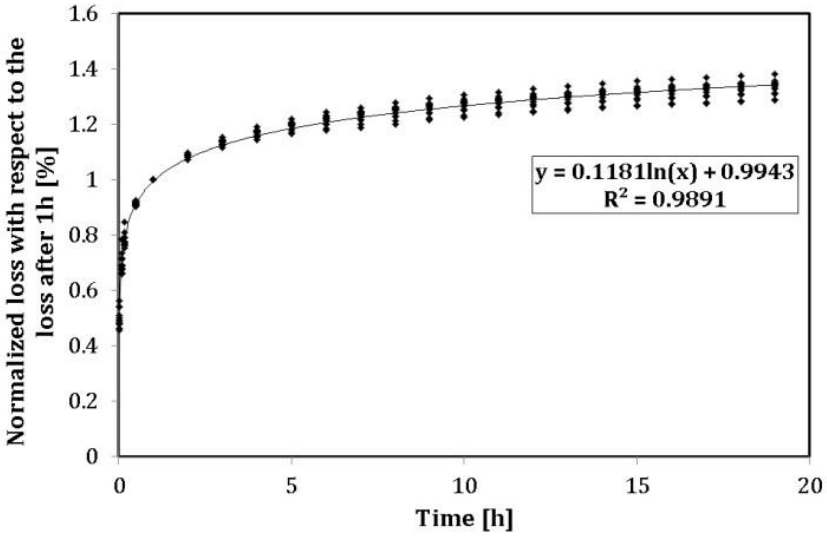
Normalized loss with respect to the loss after 1h [%]
Time [h]
y = 0.1181ln(x) + 0.9943
R² = 0.9891
0
0.2
0.4
0.6
0.8
1
1.2
1.4
1.6
0
5
10
15
20

a)

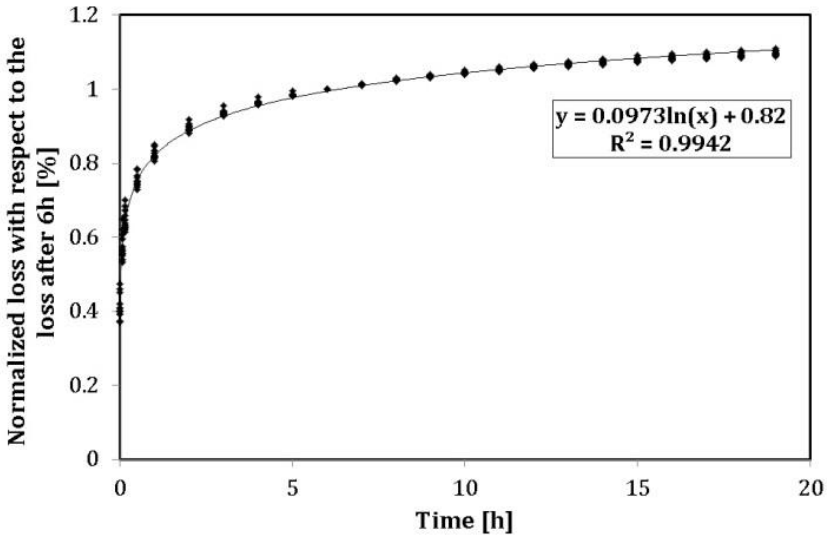
Normalized loss with respect to the loss after 6h [%]
Time [h]
y = 0.0973ln(x) + 0.82
R² = 0.9942
0
0.2
0.4
0.6
0.8
1
1.2
0
5
10
15
20

b)

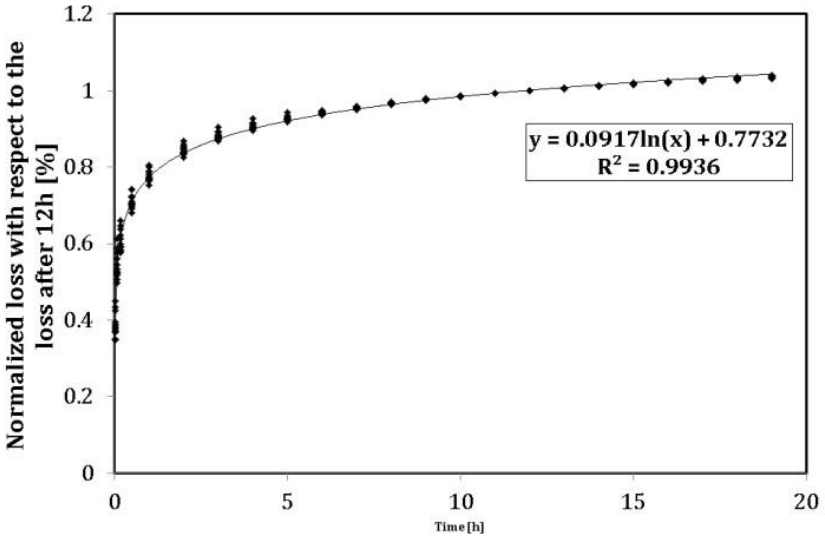

c)

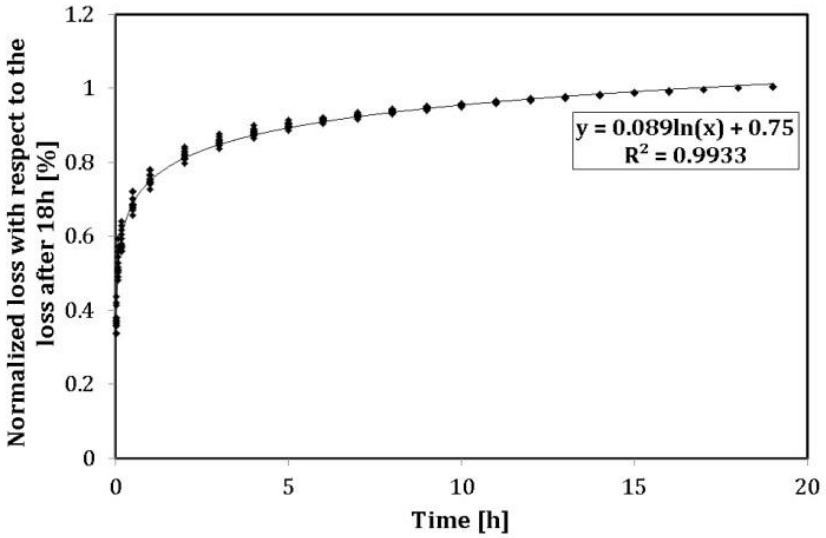

Fig. 3.8 – Regression curves of short term relaxation tests (Disc Springs) normalised with respect to the loss occurred in fixed time instants a) 1h; b) 6h; c) 12h; d) 18h.

Table 3.5. Short term relaxation tests result (Disc Springs)

	μ ***[%]***	***σ*** ***[%]***	***CV***	***Fractile*** ***5% [%]***	***Fractile*** ***95%*** ***[%]***	***Loss at 50 years*** ***(Regression curve)***			***c_1***	***c_2***
						5%	***Mean***	***95%***		
1h	*10.7*	*0.91*	*8.51*	*9.09*	*12.34*	*22.98*	*27.09*	*31.19*	*0.11*	*0.99*
6h	*12.9*	*1.00*	*7.72*	*11.20*	*14.77*	*23.33*	*27.05*	*30.77*	*0.09*	*0.82*
12h	*13.7*	*1.03*	*7.46*	*11.93*	*15.60*	*23.44*	*27.04*	*30.63*	*0.09*	*0.77*
18h	*14.1*	*1.04*	*7.32*	*12.34*	*16.04*	*23.52*	*27.05*	*30.58*	*0.08*	*0.75*

In order to better clarify the role of time-dependent effects on the bolts' pre-load, other four tests have been performed: two on equal specimens with flat washers and two on equal specimens with disc springs. These tests have been extended over a period of 30 days monitoring continuously the pre-load. The results of the tests are shown in Fig.3.9, where the dashed lines report the results of the tests with flat washers and the continuous lines represent those of the specimens with disc springs. Again, it is immediate to note from Fig.3.9 that the specimens employing disc springs showed a higher loss of preload since the beginning. This is probably related to the higher deformability of the assembly. In fact, the higher deformability of the assembly seems to provide, at installation, a higher elastic return of the tightening force. This may, obviously, also depend on the installation procedure that has been carried out; in the current case – manually – with a torque wrench. The same results represented in Fig.3.9, are summarised in Table 3.6, reporting the losses in different time instants, namely at 1h, 6h, 12h, 18h, 15 days, and 30 days. Additionally, in this table, for every test an estimate of the loss of preload at 50 years is reported, performing several regression analyses using the data acquired from the

beginning of the test up to the fixed time instants. This is to check on the approximation obtained in the estimate of the 50-years loss using the data coming from the short-term tests, with respect to the estimate made using the data coming from the mid-term tests.

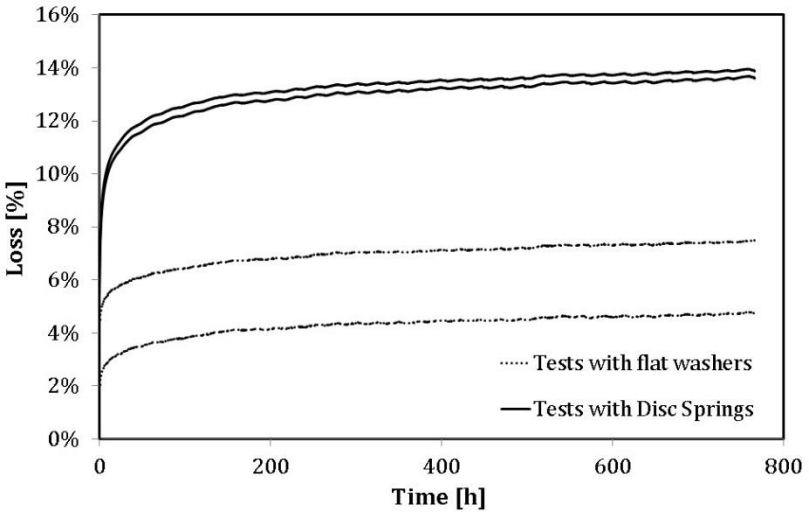

Fig. 3.9 – Medium-term relaxation tests results

From the results reported in Table 3.6, several aspects can be noted. First, as also previously observed, the loss of initial tension with disc springs was evidently higher since the beginning and it did not stabilise as fast as it did for specimens with flat washers. In fact, for specimens with flat washers, the regression curves became practically stable after 12-18h from the tightening, while for specimens employing disc springs, the loss was not completely stabilised even after 30 days. This is evidenced from the extrapolations of the 50-year loss. In fact, for specimens with flat washers the estimate of the loss of initial tension did not change significantly, if considering the data at 6h or 30 days (the regression curve is stabilised already after 6h and does not vary

significantly adding data of the next 29days and 18h). Conversely, for specimens with disc springs the estimate of the loss of preload varies significantly considering the data at 18h or the data at 30 days (the regression curve is not stable and tends to stabilise after a longer period of time because the slope of the curve tends to soften over the time).

Table 3.6. Medium term relaxation tests results.

			1h ***[%]***	***6h*** ***[%]***	***12h*** ***[%]***	***18h*** ***[%]***	***15d*** ***[%]***	***30d*** ***[%]***
Flat washers	***Test 1***	*Loss of preload after #hours/days*	*4.35*	*5.21*	*5.50*	*5.66*	*7.06*	*7.40*
		50 years' loss estimated using the data obtained up to #hours/days	*15.74*	*11.68*	*11.04*	*10.68*	*10.36*	*10.41*
	Test 2	*Loss of preload after #hours/days*	*1.99*	*2.71*	*2.98*	*3.12*	*4.37*	*4.68*
		50 years loss estimated using the data obtained up to #hours/days	*5.00*	*6.35*	*6.75*	*6.74*	*7.48*	*7.33*
Disc Springs	***Test 3***	*Loss of preload after #hours/days*	*6.78*	*9.36*	*10.19*	*10.62*	*13.13*	*13.54*
		50 years loss estimated using the data obtained up to #hours/days	*17.54*	*23.37*	*23.77*	*23.52*	*19.42*	*18.83*
	Test 4	*Loss of preload after #hours/days*	*7.01*	*9.66*	*10.50*	*10.91*	*13.43*	*13.84*
		50 years loss estimated using the data obtained up to #hours/days	*18.03*	*24.01*	*24.28*	*24.03*	*20.32*	*19.22*

Therefore, from the obtained results it seems that short-term tests provide accurate results in estimating the loss of bolts' tension for assemblies with flat washers even after 6 hours and, additionally, the estimate with short-term tests is also slightly on the safe side. Conversely, for assemblies with disc springs, as far as the loss does not stabilise rapidly, it seems that the short-term tests are not accurate, and too conservative to estimate the loss over 50-years. Overall, in all the tests, both with disc springs and with normal washers, about 70% of the loss expected to occur in 50 years ended in 30 days.

The loss of preloading in the bolts all along the life of the structure, due to creep effects, is significant in particular in case of disc spring washers. This aspect has to be properly covered in such a way that the required preload specified above is effectively present, when required, both to ensure the static resistance of the joint and the proper dissipative response under earthquake. For this reason, a higher value of the initial preload has to be installed in the bolts, higher than the targeted one defined above, should be defined in such a way that the "residual" preload, after creep occurs, would be equal to the targeted one.

The percentage of "extra preload" can be obtained by extrapolating the results obtained through the "18 hours" tests. To do so, and according to what is illustrated in EN1090-2 [10], where the extrapolation is based on a "tangent" approach. Obviously, the "18 hours" tests have been performed with a preload of $0,7f_{ub}A_s/\gamma_{M7}$ and not 60% of $0,7f_{ub}A_s/\gamma_{M7}$, what will lead to an overestimation of the "extra preload" to be actually applied in FREEDAM. But, if reference is made to the catalogue "Christian Bauer GMBH" for disc springs, and more specifically in its

figure 26 (amount of relaxation for disc springs according to the level of preload), a linear approximation of the relation between the time effects and the preload may be considered as safe. Consequently, the "extra preload" which will be extrapolated from the "18 hours" will have to be "corrected" by means of a simple proportionality rule that is represented by the following equation:

$$F_{p,ini}\left[1 - L_{50years}\frac{F_{P,ini}}{0{,}7 f_{ub}\, A_s/\gamma_{M7}}\right] = F_d$$

where

$F_{P,ini}$ represents the pre-load force to apply initially;

$L_{50years}$ represents the loss of preload expected after 50 years;

f_{ub} represents the resistance of the steel of the bolts;

A_s represents the effective area of the section of the bolts;

γ_{M7} is a safety factor assumed equal to 1.0;

F_d is the design preload force.

3.3. Conclusions

The accuracy of the tightening procedures proposed by EN 1090-2 [10] and the influence of time-related relaxation effect over the pre-load has been carried out. In the experimental analysis, different bolt assemblies have been tested considering also the possibility to employ the standardised type of European disc springs. Based on the developed work the following conclusions can be drawn:

The torque method as currently codified – even though as already evidenced by Berenbak [15] presents some criticisms and should be improved – seems sufficiently accurate. In fact, with the torque procedure, in all the tightening tests, the bolt target preload was

matched obtaining the expected accuracy. The accuracy did not vary significantly with the type of bolt assembly. In fact, analysing the experimental data statistically revealed that the torque method can be applied to both standard HV assemblies and to assemblies employing disc springs not changing the accuracy;

The combined method has proved to be accurate in achieving the nominal preload. However, despite this, it demonstrated to be more empirical and not accurate enough in limiting the bolt preload below the nominal value of the yield resistance. In fact, following the currently codified procedure, in many cases a preload exceeding the bolt's resistance was applied. This may be due to an imprecise definition of the part-turn rotations indicated in the EN 1090-2 [10]. Additionally, the tests performed have shown that the part-turn rotations suggested by the EN 1090-2 [10] cannot be straightforwardly extended to assemblies with disc springs. This is because, due to the higher deformability of the assembly, a different part-turn rotation should be applied to the assembly. Therefore, a recalibration of the part-turns should be made in order to extend the combined method to assemblies with disc springs;

The short-term tests have revealed that the bolts' loss of initial tension is a relevant effect that deserves to be accounted for in design procedures. To this scope, regression curves of the experimental data have been provided. Overall, the short-term experimental tests have shown that with normal assemblies the loss of preload in 18h is equal, on average, to about 5%, while for assemblies with disc springs it reaches an average value of 14% in 18h. The extrapolation of short-term data led to an estimate of the average loss over 50 years of about 10% and 27% for assemblies with normal HV washers and disc springs,

respectively. In both cases, it was observed that the loss of preload occurring in 18h is about 50% of the total estimated to occur in 50 years;

Overall, from the experimental data, it was observed that both, in case of assemblies with disc springs and normal washers, about 70% of the loss that is expected to occur in 50 years ends in 30 days.

3.4 References

1. Latour M, Piluso V, Rizzano G. (2014). "*Experimental Analysis of Friction Materials for supplemental damping devices*". Construction and Building Materials.
2. Ferrante Cavallaro G., Francavilla A., Latour M., Piluso V., Rizzano G. "*Experimental behaviour of innovative thermal spray coating materials for FREEDAM joints*", Composities Part B Engineering, September 2016.
3. Heistermann C. "Behaviour of pretensioned bolts in friction connections." Licentiate thesis. Lulea, June 2011.
4. Linbo Zhu, Jun Hong, Xiangjun Jiang. "*On controlling preload and estimating anti-loosening performance in threaded fasteners based on accurate contact modelling.*" Tribology International, 2016.
5. Friede R., Lange J. "*Self-loosening of prestressed bolts.*" NSCC,2009.
6. Ramey G., Jenkins R.C. "*Experimental analysis of thread movement in bolted connections due to vibrations.*" Final report research project NAS8-39131. Aubrun University, March 1995. Criteria for preloaded bolts." NASA. Huston, 1998.
7. Friede R., Lange J. "*Loss of preload in bolted connections due to embedding and self-loosening.*" SDSS'Rio 2010.
8. Misiek T. "*Assessment of locking devices for bolted connections – experimental study and evaluation for practical application.*" DSS, 2016

9. Davet G.P. "*Using Belleville springs to maintain bolt preload*" Chardon, 1997.
10. EN 1090-2. "*Execution of steel structures and aluminium structures: technical requirements for steel structures*." CEN, 2008.
11. DIN 6796. "*Conical spring washers for bolted connections*." 2009.
12. EN 14399-1. "*High-strength structural bolting assemblies for preloading - Part 1: General requirements*." CEN, 2015.
13. EN ISO 898-1. "*Mechanical properties of fasteners made of carbon steel and alloy steel - Part 1: Bolts, screws and studs with specified property classes - Coarse thread and fine pitch thread.*"
14. EN 15048-1. "*Non – preloaded structural bolting assemblies. General requirements*". CEN, 2007.
15. Berenbak J. "*Evaluation tightening preloaded bolt assemblies according to EN 1090-2*". CEN/TC 135 WG2, June 2012.
16. EUROCODE 0. "*Basis of structural design.*" CEN, 2010.
17. D'Aniello M., CassianoD., Landolfo R. "*Monotonic and cyclic inelastic tensile response of European preloadable gr10.9 bolt assemblies*" Journal of Constructional Steel Research, January 2016, 124; pp.77-90.
18. EN 14399-3. "*High-strength structural bolting assemblies for preloading - Part 3: System HR – Countersunk head bolt and nut assemblies."* CEN, 2015.
19. EN 14399-4. "*High-strength structural bolting assemblies for preloading - Part 4: System HV – Hexagon fit bolt and nut assemblies.*" CEN, 2015.
20. EN 10088-1. "*Stainless steels- Part 1: List of stainless steels*". CEN, 2005.
21. Latour M., Piluso V., Rizzano G. "*Free from damage beam-to-column joints: Testing and design of DST connections with friction pads*". Engineering Structures, 2015.

22. Latour M, Piluso V, Rizzano G. (2011). "*Experimental analysis of innovative dissipative bolted double split tee beam-to-column connections*". Steel Construction. June;4(2):53-64.
23. EN 14399-2. "*High-strength structural bolting assemblies for preloading - Part 2: Suitability for preloading*". CEN, 2015.
24. EN 14399-6. "*High-strength structural bolting assemblies for preloading - Part 6: Plain chamfered washers*". CEN, 2006.
25. DIN 6796. "*Conical spring washers for bolted connections*". 2009.
26. Ramhormozian S., Clifton G.C., MacRae G.A. "*The Asymmetric Friction Connection with Belleville springs in the Sliding Hinge Joint*". NZSEE Conference, 2014.
27. Ramhormozian S., Clifton G.C., Nguyen H., Cowle K. "*Determination of the required part-turn of the nut with respect to the number of free threads under the loaded face of the nut in fully tensioned high strength friction grip property class 8.8 bolts*". Steel Innovations Conference, 2015.
28. Jianhua Liu, Huajiang Ouyang, Jinfang Peng, ChaoqianZhang, PingyuZhou, Lijun Ma, Minhao Zhu. "*Experimental and numeric studies of bolted joints subjected to axial excitation*". Wear, 2015.
29. Ramhormozian S., Clifton G.C., MacRae G.A. "*The Asymmetric Friction Connection with Belleville springs in the Sliding Hinge Joint*" NZSEE Conference, 2014.

CHAPTER 4

4.1 Design procedure for a FREEDAM connection

The results obtained in the previous chapters are fundamental for the definition of the parameters that are necessary to properly design a FREEDAM connection. In the following, starting from the data available after at the execution of the experimental tests, the design procedure for the design of the friction device will be show.

In detail, three value of the friction coefficient are necessary to satisfy the limit states checks: first of all, a value of the friction coefficient is needed for the serviceability limit state; another value is needed to design the friction damper that represents the dissipative component of the connections; last value of the friction coefficient is important to design the non-dissipative elements of the connection, and it corresponds to the upper bound value.

In case of static loading conditions or in case of frequent seismic event the friction connection has to not start to slip, for this reason the SLS check require the use of the characteristic value of the static friction coefficient.

Regarding the design of the friction damper, it is needed to size the number of the bolts and their tightening torque, to do this the lowest expected value of the dynamic friction coefficient, defined as the characteristic value of the dynamic friction coefficient, has to be considered.

Finally, in order to design the beams and the columns that after the introduction of the FREEDAM connection have to be considered as non-dissipative parts of the structure, it is needed to use the highest expected value of the static friction coefficient, namely the 95% fractile of the static

friction coefficient. In this way, from a statistical point of view, the non-dissipative components are able to withstand without damage until the slippage of the friction damper.

In Table 4.1 the results of the experimental tests shown in the chapter 2, are summarized in terms of effective and actual values of the static friction coefficient.

Table 4.1 - Static friction coefficients for every tests

Material M1				***Material M4***				***Material M6***			
Test n°		$\mu_{0,eff}$	$\mu_{0,act}$	***Test n°***		$\mu_{0,eff}$	$\mu_{0,act}$	***Test n°***		$\mu_{0,eff}$	$\mu_{0,act}$
NV	*60*	*0.82*	*0.84*	*NV*	*39*	*0.64*	*0.65*	*NV*	*49*	*0.64*	*0.65*
NV	*61*	*0.72*	*0.73*	*NV*	*40*	*0.63*	*0.63*	*NV*	*50*	*0.63*	*0.63*
NV	*62*	*0.66*	*0.67*	*NV*	*41*	*0.57*	*0.57*	*NV*	*51*	*0.57*	*0.57*
NV	*63*	*0.75*	*0.77*	*NV*	*42*	*0.54*	*0.55*	*NV*	*52*	*0.54*	*0.55*
NV	*64*	*0.73*	*0.75*	*NV*	*43*	*0.59*	*0.59*	*NV*	*53*	*0.59*	*0.59*
NV	*65*	*0.75*	*0.77*	*NV*	*44*	*0.65*	*0.65*	*NV*	*54*	*0.65*	*0.65*
NV	*66*	*0.62*	*0.62*	*NV*	*45*	*0.58*	*0.59*	*NV*	*55*	*0.58*	*0.59*
NV	*67*	*0.69*	*0.70*	*NV*	*46*	*0.64*	*0.65*	*NV*	*56*	*0.64*	*0.65*
NV	*68*	*0.72*	*0.74*	*NV*	*47*	*0.65*	*0.65*	*NV*	*57*	*0.65*	*0.65*
NV	*69*	*0.67*	*0.69*	*NV*	*48*	*0.53*	*0.53*	*NV*	*58*	*0.53*	*0.53*
MEAN		*0.71*	*0.73*	*MEAN*		*0.76*	*0.79*	*MEAN*		*0.60*	*0.61*
DEV ST		*0.06*	*0.061*	*DEV ST*		*0.04*	*0.041*	*DEV ST*		*0.05*	*0.047*
CV		*0.08*	*0.084*	*CV*		*0.05*	*0.052*	*CV*		*0.08*	*0.077*
Fractile 5%		*0.62*	*0.61*	*Fractile 5%*		*0.69*	*0.72*	*Fractile 5%*		*0.52*	*0.52*
Fractile 95%		*0.81*	*0.85*	*Fractile 95%*		*0.84*	*0.87*	*Fractile 95%*		*0.68*	*0.70*

All these value of the friction coefficient, with also the 5% fractile of the dynamic friction coefficient, evaluated in correspondence of the first

stabilized cycle of test (Fig. 4.1), are needed to design the FREEDAM connection and are summarized in Table 4.2.

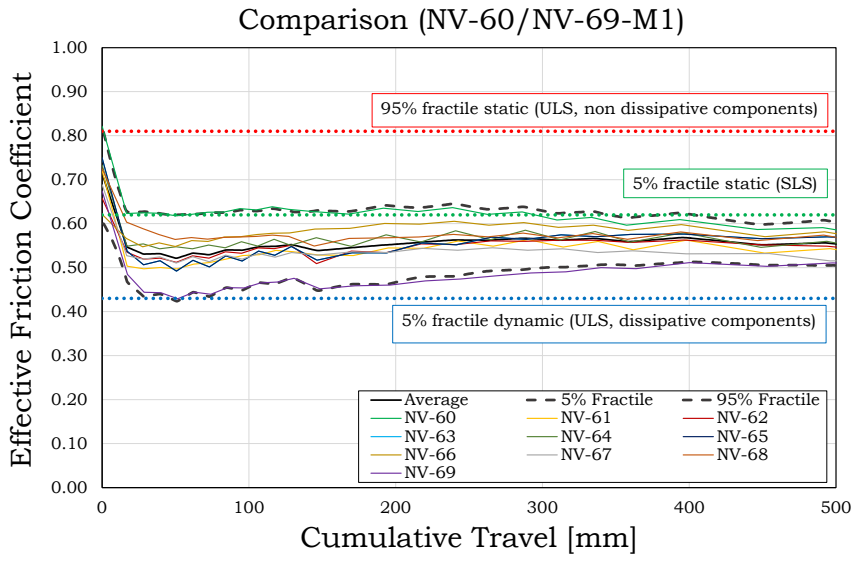

a)

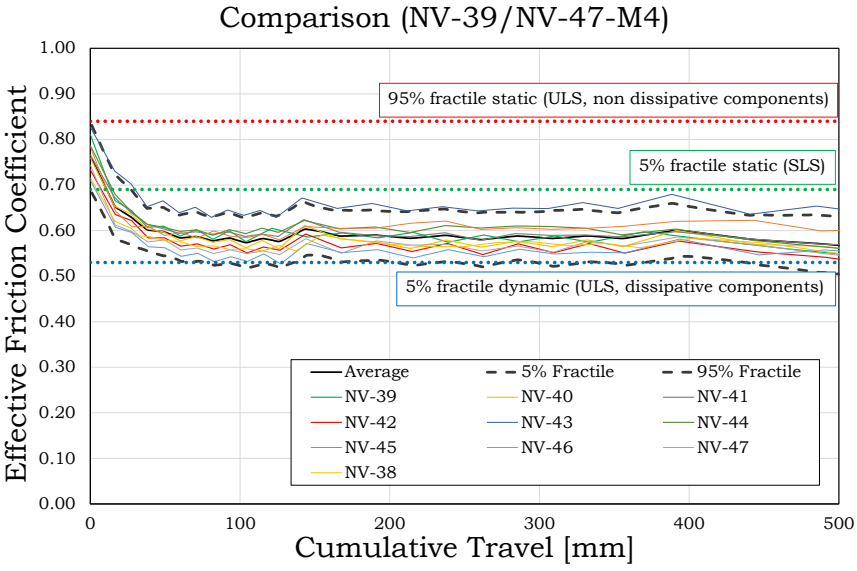

b)

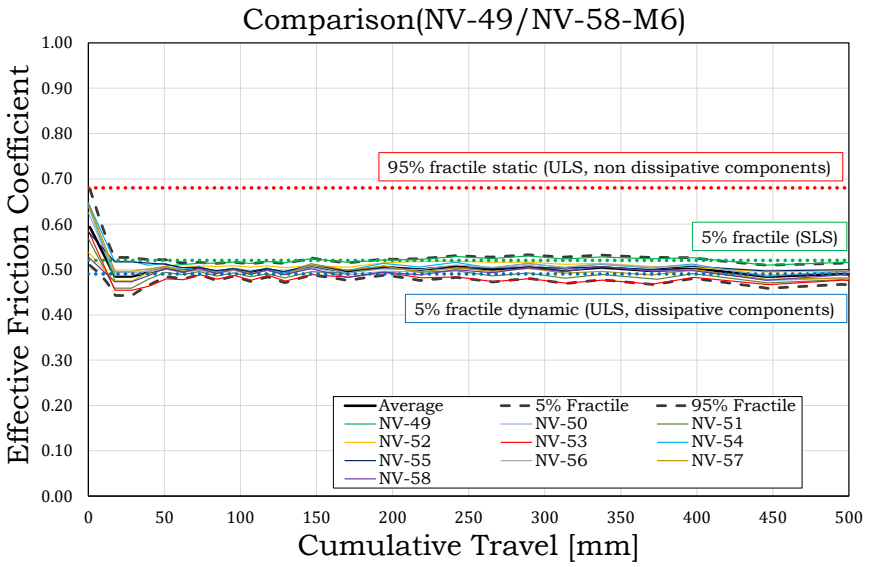

c)

Fig. 4.1 – Design values of the friction coefficient (static or dynamic)

Table 4.2 - Design values of the friction coefficients

Material M1		***Material M4***		***Material M6***	
Design FC	$\mu_{0,d}$	***Design FC***	$\mu_{0,d}$	***Design FC***	$\mu_{0,d}$
Static 5% fractile	*0.62*	*Static 5% fractile*	*0.69*	*Static 5% fractile*	*0.52*
Static 95% fractile	*0.81*	*Static 95% fractile*	*0.84*	*Static 95% fractile*	*0.68*
Dynamic 5% fractile	*0.43*	*Dynamic 5% fractile*	*0.53*	*Dynamic 5% fractile*	*0.49*

One of the first steps is represented by the introduction of the overstrength factor γ_{ov}, given by the ratio between the 95% fractile of the static friction force and the 5% fractile of the dynamic friction force:

$$\gamma_{ov} = \frac{F_{stat,95\%} \cdot n_b \cdot n_s}{\mu_{d.k} \cdot F_{p,k} \cdot n_b \cdot n_s} \tag{4.1}$$

This factor is a simple way to take into account the difference between the static and dynamic friction coefficient. The values of the overstrength factor differentiated for the three tested materials are shown in Table 4.3.

Table 4.3 – Values of the overstrength factor γ_{ov}

	M1	***M4***	***M6***
γ_{ov}	*2.02*	*1.70*	*1.48*

Starting from the classical configuration of a dissipative DST connection, two different joint details have been developed. In both cases the lower T-stub of the DST connection is substituted by a friction damper constituted by metallic plates with one or more friction pads interposed.
The first configuration of the friction device is composed by a haunch with two plates: the upper plate presents normal holes and it is located in correspondence of the bottom beam flange, while the lower plate is realized in Stainless Steel equivalent to AISI 304 with slotted holes and it is bolted to the friction pads and L-stubs by means of 10.9 HV bolts. The second configuration has a particular shape, like a shark fin upside down, with a plate bolted to the lower flange of the beam and welded to the vertical slotted Stainless Steel plate, this one has to be bolted to the friction shims with M20 class 10.9 HV bolts (Fig.4.2). In order to permit the rotation of the beam, in this configuration the friction shims and the angles present vertical slotted holes.
The energy dissipation is provided by the friction device, while all the other elements of the connection remain in the elastic field without exhibit any damage. The main advantage of this joint is represented by the fact that it is possible to fully exploit the beam section by mean the control of the tightening torque applied to the bolts and consequently the force transmitted to the column. In other words, the flexural capacity can

be adjusted to make it close to the value of the nominal bending resistance of the connected beam. In this way the oversizing of the joint components and of the column is significantly reduced.

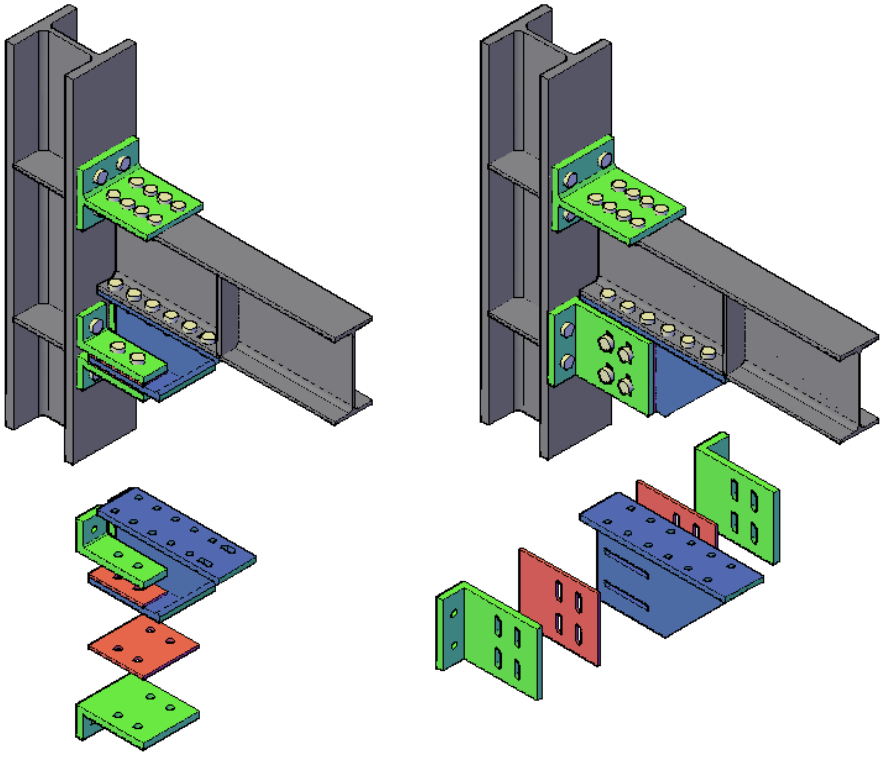

a) b)

Fig. 4.2 – FREEDAM joint configurations: a) horizontal friction device; b) vertical friction device

The energy dissipation is provided by the friction device, while all the other elements of the connection remain in the elastic field without exhibit any damage. The main advantage of this joint is represented by the fact that it is possible to fully exploit the beam section by mean the control of the tightening torque applied to the bolts and consequently the

force transmitted to the column. In other words, the flexural capacity can be adjusted to make it close to the value of the nominal bending resistance of the connected beam. In this way the oversizing of the joint components and of the column is significantly reduced.
The hierarchy criterion has to be applied to the design of the joint according to the formulation provided by Eurocode 3 [1]. This means that the only dissipative component is represented by the friction damper, while the other steel parts that compose the joint (the shear panel, the column web panels in tension and compression, the T-stub/Angles) have to be oversize with respect to the maximum force that the friction damper is able to transmit.
Starting from this consideration, a very simple iterative procedure has been developed in order to design the connection for a bending moment value greater than the beam plastic resistance. The iterative procedure is needed since the ratio between the maximum bending moment that the joint is able to exhibit before the sliding of the friction damper and the plastic strength of the beam depends on the geometric properties of the haunch, which are not known to priori.

Design of the friction damper

In a FREEDAM connection, the slippage force represents the most important parameter able to govern the bending moment transferred from the beam to the column and it is governed by the product of the friction coefficient between the friction pads and the internal plate of the haunch, for the number of the friction interfaces and for the sum of pre-loading force applied by means of the bolts.

The design slip force can be easily estimate dividing the beam plastic resistance $M_{p,b}$ for the lever arm h

$$F_{slip,Ed} = \frac{M_{p,b}}{h} \tag{4.2}$$

The lever arm is defined as the distance between the upper T-stub and the mid-center of the friction damper. Starting from the definition of lever arm, two distinct cases must be considered according to the configuration of the connection.

In the first case the lever arm is given by:

$$h_1 = h_b + h_h \tag{4.3}$$

Where h_b is the beam depth and h_h id the height of the haunch.

In the second case, the mid center of the friction damper coincide with the axis of the bolts, so the lever arm is given by:

$$h_2 = h_b + t + \frac{h_h}{2} \tag{4.4}$$

Where h_b is the beam depth and h_h id the height of the haunch while t is the distance between the upper bound of friction pads and the lower beam flange.

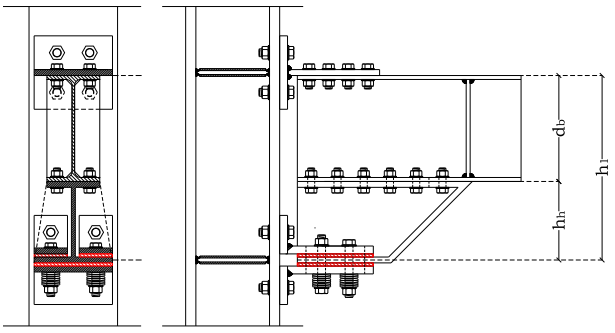

a)

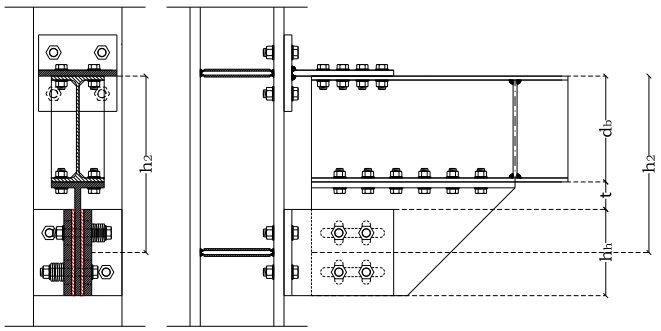

b)

Fig. 4.3 – Lever arm of friction joints: a) configuration n.1; b) configuration n.2

At this point, starting from the relationship that links the sliding force to the dynamic friction coefficient of the friction material, the bolt preloading force F_p, the number of bolts n_b and the number of surfaces in contact n_s:

$$F_{sliding} = \mu_d \cdot F_p \cdot n_b \cdot n_s \tag{4.5}$$

It is possible to evaluate minimum number of bolts:

$$n_{b,min} = \frac{M_{p.b}}{h \cdot \mu_{d,5\%} \cdot F_p \cdot n_s} \tag{4.6}$$

The data inputs are the diameter of the preloaded bolts, the number of surfaces in contact, the value of bolt preload and the 5% fractile of the friction dynamic coefficient (considering the minimum force that allows the slippage of the friction damper).

The design friction resistance and the correspondent value of the bending moment can be easily determined:

$$F_{friction,Rd} = \mu_{d.5\%} \cdot F_p \cdot n_b \cdot n_s \tag{4.7}$$

$$M_{friction,Rd} = F_{friction,Rd} \cdot h \tag{4.8}$$

The last parameter that is needed to design is represented by the length of the slots on the haunch that allows the relative movement between the haunch and the friction pads. Considering the minimum value of the rotational capacity the length of the slots can be determine using the following equation:

$$L_{slot} = (n_b - 1)p + d_b + 2\phi h \tag{4.9}$$

Design of the non-dissipative components

Once the design of the dissipative parts is concluded, non-dissipative elements can be designed by applying the well-known principles of capacity design. In this way, after determining the length of the slotted holes, the size of the friction damper can be evaluated and therefore the distance between the section of the beam that can be plasticized and the flange of the column is easily determined.

The maximum bending moment at the column face $M_{cf,Cd}$ is given by:

$$M_{cf.Cd} = \gamma_{ov} \cdot M_{friction,Rd} \tag{4.10}$$

This value is greater than plastic resistance of the beam due to the possibility to exploit the additional strengthening resulting from the haunch end. For this reason, it is needed to check that the bending moment achievable in correspondence of the axis of the beam plastic hinge is smaller than the plastic resistance of the beam:

$$M_b = M_{cf.Cd} \cdot \frac{L_e - a}{L_e} \leq M_{b.p} \tag{4.11}$$

Where L_e is the shear length of the beam.

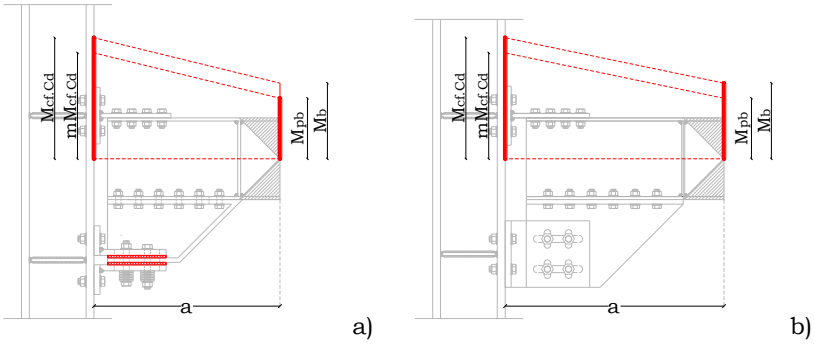

Fig. 4.4 – Distance between the axis of the beam plastic hinge and the column flange: a) configuration n.1; b) configuration n.2

In case that the Eq. 4.11 is not verify, in order to ensure that the beam remains in elastic range. the bending moment of the connection $M_{cf,Cd}$ has to be reduced by means of the reduction of the tightening torque of the bolts of the friction damper. A simple way to reduce the tightening torque is given by the introduction of the ratio between the bending moment M_b and the plastic resistance of the beam.

$$m = \frac{M_{b.p}}{M_b} \tag{4.12}$$

So the Eq. 4.7 turns into:

$$F_{friction,Rd} = \mu_{d.5\%} \cdot (m \cdot F_p) \cdot n_b \cdot n_s \tag{4.13}$$

Finally, the force that the joint has to withstand before that the slippage of the friction damper occurs, results to be equal to:

$$\frac{m \cdot M_{cf,Cd}}{h} = F_{cf,Cd} = \frac{m \cdot M_{friction,Rd} \cdot \gamma_{ov}}{h} \tag{4.14}$$

The other non-dissipative components (T-stub and angles in bending, the haunch, the column web in tension and compression, the column flange

in bending), have to be designed in ordedr to trasmit the maximum force that the dissipative component is able to exhibit.

In conclusion, the procedure to design the joint components can be summarized in the following 9 steps:

Step 1: Evaluation, considering the lowest expected value of the dynamic friction coefficient, namely the characteristic value of the dynamic friction coefficient, of the design friction resistance $F_{friction,Rd}$ of the dissipative component, i.e. the friction device, by means of Eq. 4.13.

Step 2: Design of the length of the slots made on the haunch in order to evaluate the overall dimension of the reinforced part of the joint.

Step 3: Calculation of bending moment $M_{cf,Cd}$ at the column flange, considering the maximum expected value of the static friction coefficient, namely 95% fractile of the static friction coefficient, and check of the resistance of the beam in bending; if not satisfied, the tightening torque of the bolts of the friction damper has to be reduced in order to reduce the force that the joint has to withstand before the slippage of the friction damper.

Step 4: Design of the bolt diameter.

Step 5: Design of the T-stub and L-stubs.

Step 6: Design of the bolts connecting the lower flange of the beam and the flange of the haunch. In order to avoid the slippage of the two surfaces in contact, the bolts have to be preloaded considering the proof value of the tightening torque.

Step 7: Check of the resistance of the column web in shear and design of supplementary web plates if needed. Eurocode 3 [1] introduces a limitation about the thickness of the supplementary plates. In particular, the shear area A_{vc} may be increased no more than b_{stwc}. If a further

supplementary web plate is added on the other side of the web, no further increase of the shear area is allowed. The proposed method does not take into account such limitation.

Step 8: Check of the resistance of the column web in tension and in compression; if needed continuity plates are added and/or supplementary web plates are extended to cover also tension and compression zones.

Step 9: Check of the resistance of the column flange in bending by modelling the tension zone by means of an equivalent T-stub.

4.2. Tests on internal beam-to-column joints

The effectiveness of the FREEDAM connection into the dissipation of the seismic energy deriving from a rare destructive seismic event, avoiding the damage of the structural elements, has been checked performing tests on real scale internal joints. Furthermore, the experimental results, derived from the tests execution, are useful to validate the design procedure adopted for this type of joint. In order to evaluate the influence of scale effects, eight beam-to-column joints equipped with FREEDAM device, varying the geometrical properties of the elements have been tested. The tests results have been also used in order to develop the FE models of the joints, representing the main basis for the calibration of the FE models.

The first phase of the experimental campaign consists in the design of all the joint components of the specimens. As said before, the joint components have been designed according to Eurocode 3 part 1-8 [1], except the friction dampers that have been dimensioned following the procedure shown in the previous paragraph. The experimental campaign

consists in eight tests on internal beam-to-column connection. In detail, two different configurations of the FREEDAM device and two different sizes of the elements have been tested: in case of big size joints IPE450 beams and HEB500 columns have been used, while in case of small size joints IPE270 and HEM220. For all the tests disc spring washers have been used for the bolts of the friction damper. In the following a detailed list of the tests carried out:

- FREEDAM-IN270_CYC-1_M4 (IPE 270-HEM220) is a joint equipped with a friction device realized by means of a haunch with a slotted horizontal steel plate made of 1.4301 Stainless Steel, bolted to the column with mild steel angles and friction shims, all tightened with M20 class 10.9 HV bolts plus 6 disc springs (3s+2p);
- FREEDAM-IN270_CYC-2_M4 (IPE 270-HEM220) is a joint equipped with a friction device realized with a vertical rib made of stainless steel, bolted to the beam flange with a flange plate and bolted to the column by means of mild steel L-stubs and friction shims, tightened with M20 class 10.9 HV bolts plus 6 disc springs (3s+2p);
- FREEDAM-IN450_CYC-1_M4 (IPE 450-HEB500) is a joint equipped with a friction device similar to that of test 1, employing in the bolted assemblies 6 disc springs (3s+2p);
- FREEDAM-IN450_CYC-2_M4 (IPE 450-HEB500) is a joint equipped with a friction device similar to that of test 2, employing in the bolted assemblies 6 disc springs (3s+2p);

According to the design procedure described in the previous chapter, the four joint typologies have been designed. For the sake of simplicity, in the

following only the results of the sizing of the smaller joints for both configurations are illustrated in detail, the same procedure, even if not reported, is repeated identically for the other joints of bigger dimensions.

4.2.1. Design of specimen whit friction pads in horizontal configuration

In this case, the friction damper is composed by friction pads pre-stressed to the haunch, that presents slotted holes in correspondence of the lower stainless steel plate, through M20 class 10.9 HV bolts in horizontal position. (Fig. 4.5)

Thus, starting from the first step, the various design phases are shown below.

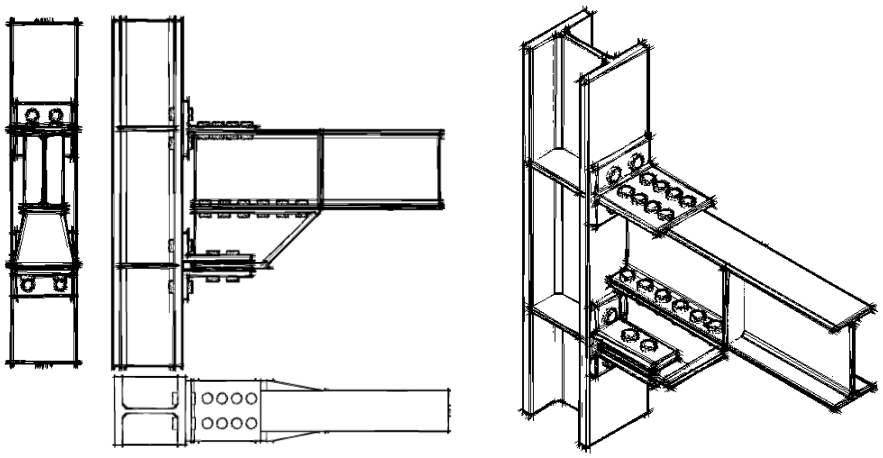

Fig. 4.5 – FREEDAM-CYC01 joint configuration

<u>Step 1:</u> Estimation of the design friction resistance $F_{friction,Rd}$ of the friction device (dissipative component).

The design friction force can be easily derived from the plastic resistance of the beam $M_{p,b}$ (IPE270) and the lever arm h considering a haunch of 220mm height. This force represents the force that the device has to withstand:

$$F_{slip.Ed} = \frac{M_{b.p}}{h} = \frac{171.82}{0.47} = 365.57kN \tag{4.15}$$

At this point from the Eq. 4.16 it is possible to derive the number of bolts strictly necessary:

$$F_{sliding} = \mu_d \cdot F_p \cdot n_b \cdot n_s \tag{4.16}$$

Considering Eq. 4.16 the value of the bolts preload has been determined:

$$F_{p.red} = \frac{F_{slip.Ed}}{\mu_{d,5\%} \cdot n_b \cdot n_s} = \frac{365.57}{0.53 \cdot 4 \cdot 2} \cong 86.21kN \cong 50\%\ F_p \tag{4.17}$$

Recalculating the design friction resistance (Eq. 4.18) the value obtained is obviously equal to $F_{slip,Ed}$, while the correspondent value of the bending moment is equal to the plastic resistance of the beam (Eq. 4.19).

$$F_{friction,Rd} = \mu_{d.5\%} \cdot F_{p,red} \cdot n_b \cdot n_s = 0.53 \cdot 86.21 \cdot 4 \cdot 2 = 365.57\ kN \tag{4.18}$$

$$M_{friction,Rd} = F_{friction,Rd} \cdot h = 365.57kN \cdot 0.47m = 171.82kNm \tag{4.19}$$

<u>Step 2:</u> Design of the length of the slots on the haunch.

The holes on the haunch allows relative slippage of the friction pads on the haunch. The displacement needed at level of the damper is related to the required rotational capacity that can be estimated by means the following equation:

$$L_{slot} = \left(\frac{n_b}{2} - 1\right) \cdot p + d_b + 2\phi h = \\ = (2-1)70 + 20 + 2 \cdot 0.06 \cdot 470 = 146.50mm \ \rightarrow L_{slot} = 150mm \tag{4.20}$$

The minimum length represents the starting value form which it is possible to size the haunch and as a consequence, the distance between column flange and the beam section where the plastic hinge can develop have been determined.

<u>Step 3:</u> Evaluation of the bending moment in correspondence of the column flange and check of the beam in bending.

The maximum bending moment at the column face, $M_{cf,Cd}$ has been determined applying the criterions of the "capacity design" and for this reason the highest expected value of the static friction coefficient has been took in account (non-dissipative components).

$$M_{cf,Cd} = M_{friction,Rd} \cdot \gamma_{ov} = 171.82kNm \cdot 1.70 = 292.09kNm \tag{4.21}$$

In order to assure that the bending moment in correspondence of the axis of the beam plastic hinge is smaller than the plastic resistance of the beam, it is needed to check the following equation:

$$M_b = M_{cf,Cd} \cdot \frac{L_e - a}{L_e} = 292.09kNm \cdot \frac{2890 - 615}{2890} = 229.86kNm$$
$$> M_{b.p} = 171.82kNm \quad (4.22)$$

where L_e is the shear length of the beam equal to 2.89m.

In this way, the additional strengthening due to the presence of the haunch in correspondence of the beam end is take into account.

The pre-load force applied on the steel plated of the friction damper by means pre-loadable bolts has to be reduce until the bending moment of the connection $M_{cf,Cd}$ is lower than the resulting bending moment M_b.

To this scope the m parameter, that represent the reduction coefficient of the pre-load force of the bolts, has been calculate:

$$m = \frac{M_{b.p}}{M_b} = \frac{171.82}{229.86} = 0.75 \quad (4.23)$$

While the reduced design friction resistance is given by:

$$F_{friction,Rd} = \mu_{d.5\%} \cdot \left(m \cdot F_{p,red}\right) \cdot n_b \cdot n_s$$
$$= 0.53 \cdot (0.75 \cdot 86.21) \cdot 4 \cdot 2 = 273.25kN \quad (4.24)$$

Therefore, when the slippage of the friction damper occurs, the maximum force that the joint has to withstand is equal to:

$$F_{cf,Cd} = \frac{0.75 \cdot 171.82 \cdot 1.70}{0.47} = 464.53kN \quad (4.25)$$

The maximum static force estimated using Eq. 4.25, represents the force that the dissipative components (the friction dampers) are able to transmit to the non-dissipative components (T-stubs, angles in bending, haunches, column web in tension and compression, the column flange in bending). In other words, according to the principles of the "*capacity*

design", the non-dissipative components have to be designed in order to resist to the maximum static force above evaluated.

<u>Step 4:</u> Design of the bolts' diameter for the TEE elements and the angles.

According to Eurocode 3 [1], in order to determine the minimum value of the resistant area of the bolts, a check under combined shear and tension have to be performed. Starting from the following actions for the design of the bolts in tensile side:

$$F_{t,Ed} = \frac{F_{cf,Cd}}{n_{b,t}} = \frac{464.53}{4} \cong 116.13kN$$
$$F_{v,Ed} = \frac{F_v}{2\,n_b} = \frac{250}{2 \cdot 4} = 31.25\ kN \tag{4.26}$$

where F_v represents the maximum expected force for the test layout considered. Considering 10.9 class bolts, the minimum value of the resistant area is equal to:

$$A_{res} \geq \frac{\gamma_{M2}}{f_{tb}}\left(\frac{F_{v,Ed}}{\alpha_v} + \frac{F_{t,Ed}}{1.26}\right)$$
$$A_{res} \geq \frac{1.25}{1000}\left(\frac{31250}{0.5} + \frac{116130}{1.26}\right) \cong 193.33\ mm^2 \tag{4.27}$$

and in any case the Eurocode 3 [1] establishes that the minimum value has to be greater than the value estimated considering only the tension action:

$$A_{res} \geq \frac{\gamma_{M2} F_{t,Ed}}{0.9 f_{tb}} = \frac{1.25 \cdot 116130}{0.9 \cdot 1000} \cong 161.30\ mm^2 \tag{4.28}$$

Definitely, M20 bolts have been chosen.

Step 5: Design of the T-stub and L-stubs.

The same criteria used for the design of the bolts have been applied, while in order to check the elements in bending the resistance formulation for mechanism type-1 and type-2 have been taken into account excluding the failure mechanism type-3.

Design of the T-stubs

The first parameter to be calculated is represent by the horizontal distance between the bolts w, which has to be between the following values:

$$\begin{aligned} w_{min} &\cong t_{cw} + 2\, r_c + 1.8 = 26 + 2 \cdot 18 + 1.8 \cdot 21.5 = 100.7 \text{ mm} \\ w_{max} &= b_{cf} - 2.4\, d_0 = 226 - 2.4 \cdot 21.5 = 174.4 \text{ mm} \end{aligned} \quad (4.29)$$

Where t_{cw} is the thickness of the column web, r_c the root radius, do the diameter of the hole and b_{cf} the column width. For this reason, a bolt spacing of the T-stub equal to $w_o = 103.4mm$ has been chosen.
On the other hand, the width of the T-stub has to be smaller than the width of the column, equal to 226mm in this case, and greater than the following value:

$$\begin{aligned} b_{T-stub} &= max\{w + 2.4\, d_0; b_{bf}\} = \\ &= max\{103.4 + 2.4 \cdot 21.5; 135\} = 155\text{mm} \end{aligned} \quad (4.30)$$

Consequently, the width of the end plate is taken equal to 200mm.
Regarding the effective length of the T-stub b_{eff}, the half part of the geometrical length, equal to 100mm, has been considered.
According to the failure mechanism type-1, in order to avoid the collapse of the equivalent T-stub the following value of the thickness of the T-stub is required:

$$F_{2.Rd} = 2\frac{\frac{f_{y.Tstub}}{\gamma_{M0}}\frac{b_{eff}t_{Tstub}^2}{2} + 2\,F_{t.Rd}\,n}{m+n} = F_{cf,Cd} \quad \rightarrow$$

$$t_{Tstub.2} = \sqrt{\frac{2\,\gamma_{M0}}{b_{eff.ep}\,f_{y.Tstub}}\left[\frac{F_{cf,Cd}(m+n)}{2} - 2\,F_{t.Rd}n\right]} = \tag{4.31}$$

$$= \sqrt{\frac{2\cdot 1.05}{100\cdot 355}\left[\frac{464530\,(43+43)}{2} - 2\cdot 176400\cdot 43\right]} \cong 16.45\,mm$$

Where $f_{y,Tstub}$ is the yielding resistance of the plate.

In the same way, to avoid a failure of the T-stub according to the mechanism type-2 the following value of the thickness of the T-stub is required:

$$F_{2.Rd} = 2\frac{\frac{f_{y.Tstub}}{\gamma_{M0}}\frac{b_{eff}t_{Tstub}^2}{2} + 2\,F_{t.Rd}\,n}{m+n} = F_{cf,Cd} \quad \rightarrow$$

$$t_{Tstub.2} = \sqrt{\frac{2\,\gamma_{M0}}{b_{eff.ep}\,f_{y.Tstub}}\left[\frac{F_{cf,Cd}(m+n)}{2} - 2\,F_{t.Rd}n\right]} = \tag{4.32}$$

$$= \sqrt{\frac{2\cdot 1.05}{100\cdot 355}\left[\frac{464530\,(43+43)}{2} - 2\cdot 176400\cdot 43\right]} \cong 16.45\,mm$$

Definitely, the thickness of the T-stub flange has been assumed equal to 20mm.

Regarding the T-stub web, a thickness equal to 15mm has been chosen, greater than the thickness of the beam flange that is 10.2mm.

The number of bolts $n_{b,s}$ needed to connect the T-stub web with the beam flange has been calculated equalling the shear force transmitted by the upper flange $F_{cf,Cd}$ and he the shear resistance of the bolts according to Eurocode 3 [1]:

$$F_{V,Rd} = n_{b,s}\frac{\alpha_v \cdot A_{res} \cdot f_{tb}}{\gamma_{M2}} = F_{cf,Cd} \quad \rightarrow \quad n_{b,s} = \frac{F_{cf,Cd} \cdot \gamma_{M2}}{\alpha_v \cdot A_{res} \cdot f_{tb}} \tag{4.33}$$

Where γ_{M2} is a partial factor, a_v represent a coefficient depending on the bolt class, A_{res} is the nut area and f_{tb} the ultimate resistance.
Considering the fact that the beam size allows a maximum diameter of the holes equal to 19mm, M18 bolts have been chosen for which the minimum number of bolts is equal to:

$$n_{b,s} = \frac{464530 \cdot 1.25}{0.5 \cdot 193 \cdot 1000} = 6.02 \quad \rightarrow \quad n_{b,s} = 8 \tag{4.34}$$

The bolts are tightened in order to take advantage of the friction between the surface in contact of the T-stub web and the beam flange. The friction resistance has to be greater than the action estimated as:

$$F_{fric,Tstub,w} = \mu \cdot F_p \cdot n_s \cdot n_b = 0.5 \cdot 135.10 \cdot 1 \cdot 8 = 540.40kN > F_{cf,Cd} \tag{4.35}$$

Design of the L-stubs

Two different types of L-stubs are used in this configuration of the FREEDAM connection. In a simplified way and for the sake of security, the upper L-stubs equal to the half of the lower ones have been considered. The distance n between the bolt line and the end of the plate is assumed equal to 43mm while the distance m between the bolt axis and the plastic hinge in the beam flange is assumed equal to 35mm. The horizontal distance between the bolts w has to be between the following values:

$$\begin{aligned} w_{min} &\cong t_{cw} + 2\,r_c + 1.8\,d_0 = 26 + 2 \cdot 18 + 1.8 \cdot 21.5 + 15 \\ &= 100.7 \text{ mm} \\ w_{max} &= b_{cf} - 2.4\,d_0 = 226 - 2.4 \cdot 21.5 = 174.4 \text{ mm} \end{aligned} \tag{4.36}$$

In line with the limitations above, the L-stub bolt spacing has been set equal to w_o=115mm.

The minimum value of the L-stub width is equal to:

$$\mathrm{b_{L-stub}} = max\left\{\frac{\mathrm{w} + 2.4\,\mathrm{d_0} - t_{hw}}{2}; \frac{\mathrm{b_{bf}}}{2}\right\} = \\ = max\left\{\frac{115 + 2.4 \cdot 21.5 + 10}{2}; \frac{135}{2}\right\} = 67.5 \text{ mm} \tag{4.37}$$

while the maximum value is equal to:

$$\mathrm{b_{L-stub}} = \frac{b_{c-}t_{hw}}{2} = \frac{226 - 10}{2} = 108mm \tag{4.38}$$

the final value of the L-stub width has been fixed equal to 85mm, that coincides with the effective length.

Aiming to avoid the collapse of the equivalent T-stub, the required thickness for mechanism type-1 and type-2 are given by:

$$F_{1,Rd} = \frac{b_{eff}t_{Lstub}^2}{2 \cdot m}\frac{f_{y.Lstub}}{\gamma_{M0}} = \frac{F_{cf,Cd}}{4} \rightarrow \\ t_{Lstub.1} = \sqrt{\frac{m\,F_{cf,Cd}\,\gamma_{M0}}{2 \cdot\ b_{eff.Lstub} \cdot f_{y,Lstub}}} = \sqrt{\frac{35 \cdot 464530 \cdot\ 1.05}{2 \cdot\ 85 \cdot 355}} \cong 16.82\ mm \tag{4.39}$$

$$F_{2.Rd} = \frac{\frac{f_{y.Lstub}b_{eff}t_{Lstub}^2}{\gamma_{M0}} + F_{t.Rd}\,n}{m+n} = \frac{F_{cf,Cd}}{4} \rightarrow \\ t_{Lstub.2} = \sqrt{\frac{4\,\gamma_{M0}}{b_{eff.ep}\,f_{y.Lstub}}\left[\frac{F_{cf,Cd}(m+n)}{4} - F_{t.Rd}n\right]} = \tag{4.40}$$

$$= \sqrt{\frac{4 \cdot 1.05}{85 \cdot 355}\left[\frac{464530\ (35+43)}{4} - 176400 \cdot 43\right]} \cong\ 14.32\ mm$$

Therefore, a 20mm thickness has been assumed for the L-stub flange/web.

<u>Step 7:</u> Design of the bolted connection between the beam lower flange and the upper flange of the haunch.

The first phase consists into the evaluation of the acting force on the connection:

$$F_{t,Ed} = \frac{F_{cf,Cd} \cdot h_h}{\sum_i d_i^2} \cdot d_i \qquad F_{v,Ed} = \frac{F_{cf,Cd}}{n_{b.h}} \tag{4.41}$$

Where d_i is the distance between the i^{th} bolt from the rotation center. According to the code provisions and the technological requirements, the bolts position has been defined. Considering that the most stressed bolt is the farthest from the column flange, the maximum force on the bolt has been estimated in the following:

$$F_{t,Ed} = \frac{F_{cf,Cd} \cdot h_h}{\sum_i d_i^2} \cdot d_i = \frac{464530 \cdot 200}{324595} \cdot 370 = 52950N$$
$$F_{v,Ed} = \frac{F_{cf,Cd}}{n_{b.h}} = \frac{464530}{2 \cdot 6} = 37710N \tag{4.42}$$

At this point, the minimum value of the resistant area of the bolts has been determined by means of the check under combined shear and tension, according to Eurocode 3 [1]. In particular:

$$A_{res} \geq \frac{\gamma_{M2}}{f_{tb}} \left(\frac{F_{v,Ed}}{\alpha_v} + \frac{F_{t,Ed}}{1.26} \right) \tag{4.43}$$

$$A_{res} \geq \frac{1.25}{1000} \left(\frac{37710}{0.5} + \frac{52950}{1.26} \right) \cong 149.30\, mm^2 \; > 193 mm^2 = A_{res,M18}$$

The check is satisfied for M18 bolts.

Step 8: **Check of the column web in shear.**

The resistance of the column web panel has been estimated starting from the shear resistant area of the section.

$$A_{vc} = A - 2\,b_{cf}\,t_{cf} + (t_{cw} + 2r_c)t_{cf} = \\ = 14940 - 2 \cdot 226 \cdot 26 + (15.5 + 2 \cdot 18) \cdot 26 = 4527\ mm^2 \tag{4.44}$$

$$V_{wp,Rd} = \frac{0.9 \cdot A_{vc} \cdot f_{y,cw}}{\sqrt{3}\ \cdot \gamma_{M0}} = \frac{0.9 \cdot 4527 \cdot 355}{\sqrt{3} \cdot 1.05} \cong 835\ \text{kN} \tag{4.45}$$

Comparing the shear resistance of the column web panel with the action $F_{cf,Cd}$, the resistance results greater than the action, so no supplementary web plates are needed.

Step 9: Check of the column web in tension and compression.

The resistance of the column web in compression is given by:

$$F_{cwc.Rd} = \omega \cdot k_{wc} \cdot b_{eff.cwc}\ \cdot t_{cw} \cdot \frac{f_{y.cw}}{\gamma_{M0}} = \\ = \frac{0.67 \cdot 1 \cdot 280 \cdot 15.5\ \cdot\ 355}{1.05} \cong 938\ \text{kN} \tag{4.46}$$

Where ω take in account the interaction with the column web panel and k_{wc} depends on the effective longitudinal compressive stress $\sigma_{com,Ed}$ due to the axial force and the bending moment on the column web resistance. These coefficients are given by:

$$\omega = \frac{1}{\sqrt{1 + 1.3\left(\frac{b_{eff.cwc} \cdot t_{cw}}{A_{vc}}\right)^2}} = \frac{1}{\sqrt{1 + 1.3\left(\frac{280 \cdot 15.5}{4527}\right)^2}} = 0.67 \tag{4.47}$$

$$k_{wc} = 1 \quad \text{when} \quad \sigma_{com,Ed} \leq 0.7 f_{y,wc}$$

While $b_{eff,cwc}$ represents the effective length of the column web, determined as follows:

$$b_{eff.cwc} = t_{Lstub,w} + 5(t_{fc} + r_c) + 2\,t_{T-Lstub} = \\ = 20 + 5(26 + 18) + 2 \cdot 20 = 280 \text{ mm} \quad (4.48)$$

Continuity plates are not required because the resistance is greater than the action $F_{cf,Cd}$.

Step 10: Check of the resistance of the column flange in bending using the equivalent T-stub model.

The equivalent T-stub in tension model for bolted connection represents a simple way to design the resistance of the column flange in bending. Using the following equations, the resistances for mechanism type-1 and type-2 have been evaluated:

$$F_{1,Rd} \geq F_{cf,Cd} \qquad F_{2,Rd} \geq F_{cf,Cd} \quad (4.49)$$

where

$$F_{1,Rd} = 2\frac{b_{eff} t_{cf}^2}{m}\frac{f_{y.cf}}{\gamma_{M0}} \quad \text{and} \quad F_{2.Rd} = 2\frac{\frac{f_{y.cf}}{\gamma_{M0}}\frac{b_{eff} t_{cf}^2}{2} + 2\,F_{t.Rd}\,n}{m+n} \quad (4.50)$$

with b_{eff} equal to:

$$b_{eff} = min\{2\pi m_c\,;\, 4m_c + 1.25e; p\} = \\ = min\,\{2\pi \cdot 26\,; 4 \cdot 26 + 1.25 \cdot 61.3; 101\} \cong 101\,mm \quad (4.51)$$

Considering n=min {e; e_{Lstub}; 1.25m00$_c$} = min {6.13; 48.3; 1.25 ·26} = 32.5mm, it is simple to derive the design resistances for mechanism type-1 and type-2 as follows:

$$F_{1,Rd} = 2\frac{f_{y.cf}\, b_{eff.cfb}\, t_{cf}^2}{\gamma_{M0}\, m_c} = 2\frac{355 \cdot 101 \cdot 20^2}{1.05 \cdot 26} \cong 1051 \text{ kN} \geq F_{cf,Cd} \quad (4.52)$$

$$F_{2.Rd} = 2\frac{f_{y.cf}\frac{b_{eff.cfb}t_{cf}^2}{2} + 2\,F_{t.Rd}\,n}{\gamma_{M0}(m_c + n)} =$$

$$= 2\frac{355\frac{101\cdot 20^2}{2} + 2\cdot 176400\cdot 32.5}{1.05(26+32.5)} \cong 607\ \text{kN} \geq F_{cf,Cd}$$

Even if, in nay condition, the design resistances are greater than the action $F_{cf,Cd}$, the continuity plates have been insered in order to avoid the column deformation.

Regarding the falilure mechanism type-3, it has been exclude due to the design procedure adopted for the bolts.

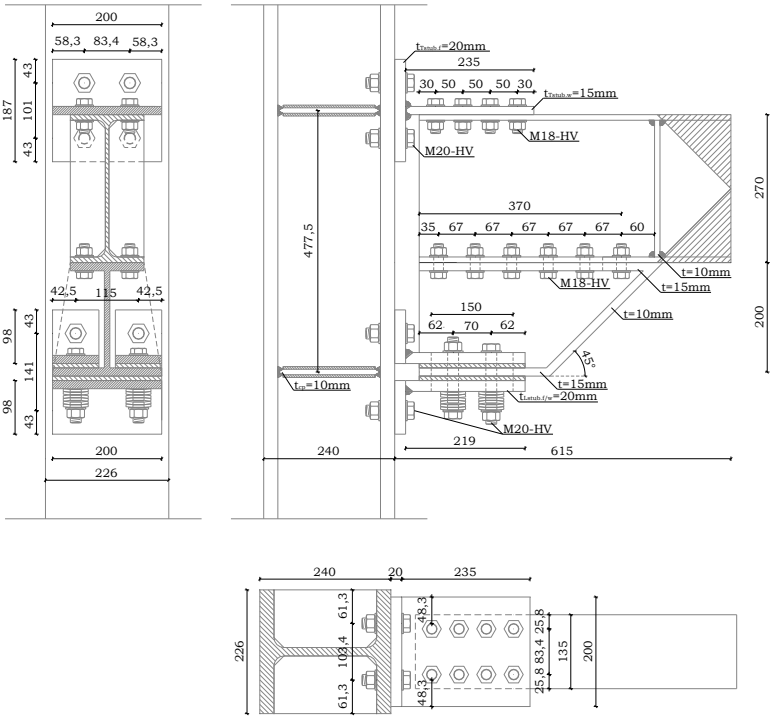

Fig. 4.6 – Geometry of the specimen FREEDAM-CYC01

4.2.2. Design of specimen whit friction pads in vertical configuration

The main difference respect to the previous configuration of the FREEDAM joint consist in the fact that the friction surfaces are vertical. In practice, there is a vertical slotted Stainless steel plate welded to another steel plate that is bolted to the bottom beam flange, that is bolted to the friction shims using M20 class 10.9 HV bolts by means of angles with vertical slotted holes. The slotted holes on the angles are needed in order to allow the rotation of the beam.

The design procedure is exactly the same used for the FREEDAM joint with friction surface in horizontal configuration. In the following the design procedure is reported again as a consequence of the fact that, compared to the previous case, the lever arm has changed.

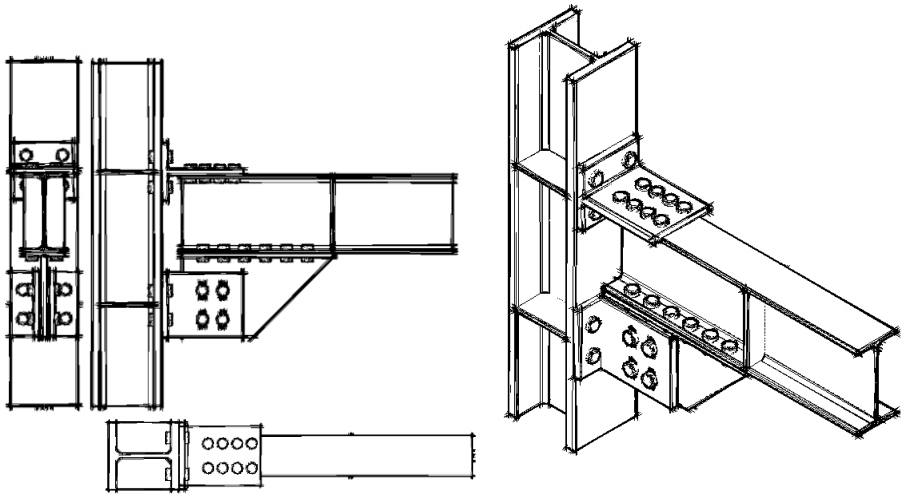

Fig. 4.7– FREEDAM-CYC02 joint configuration

<u>Step 1:</u> Estimation of the design friction resistance $F_{friction,Rd}$ of the friction device (dissipative component).

The design friction force that the device has to withstand is equal to:

$$F_{slip.Ed} = \frac{M_{b.p}}{h} = \frac{171.82}{0.45} = 381.82kN \tag{4.53}$$

Considering that the height of the haunch is equal to 200mm.
At this point from the Eq. 4.53 it is possible to derive the number of bolts strictly necessary:

$$F_{sliding} = \mu_d \cdot F_p \cdot n_b \cdot n_s \tag{4.54}$$

$$n_{b,min} = \frac{F_{slip.Ed}}{\mu_{d,5\%} \cdot F_p \cdot n_s} = \frac{381.82}{0.53 \cdot 171.50 \cdot 2} = 2.10 \qquad \rightarrow n_b = 4 \tag{4.55}$$

Considering Eq. 4.56 the value of the bolts preload has been determined:

$$F_{p.red} = \frac{F_{slip.Ed}}{\mu_{d,5\%} \cdot n_b \cdot n_s} = \frac{381.82}{0.53 \cdot 4 \cdot 2} \cong 90.05kN \cong 53\%\ F_p \tag{4.56}$$

Recalculating the design friction resistance (Eq. 4.57) the value obtained is obviously equal to $F_{slip,Ed}$, while the correspondent value of the bending moment is equal to the plastic resistance of the beam (Eq. 4.58).

$$F_{friction,Rd} = \mu_{d.5\%} \cdot F_{p,red} \cdot n_b \cdot n_s = 0.53 \cdot 90.05 \cdot 4 \cdot 2 = 381.82\ kN \tag{4.57}$$

$$M_{friction,Rd} = F_{friction,Rd} \cdot h = 381.82kN \cdot 0.45m = 171.82kNm \tag{4.58}$$

The design flexural resistance is the same for both configurations even though the dimension of the haunch and consequently the lever arm change.

Step 2: Design of the length of the slots on the haunch

In this configuration the relative rotation between the beam and column is allowed by the presence of the horizontal slots on the haunch and the vertical slots on the L-stubs. Starting from the value of the rotational capacity required for the joint it is possible to derive length of the slots as follows:

$$L_{slot,h} = \left(\frac{n_b}{2} - 1\right) \cdot p + d_b + 2\phi h_h = \tag{4.59}$$

$$= (2-1)70 + 20 + 2 \cdot 0.06 \cdot 500 = 150mm \;\rightarrow L_{slot} = 163mm$$

$$L_{slot,v} = d_b + 2\phi h_v = \tag{4.60}$$

$$= 20 + 2 \cdot 0.06 \cdot 210 = 45.2.mm \;\rightarrow L_{slot} = 61.5mm$$

Where h_h corresponds to the distance between the center of compression and the bottom row of the bolts in the friction device., while h_v is the vertical distance between the upper T-stub and the farthest bolt from it (Fig. 4.8).

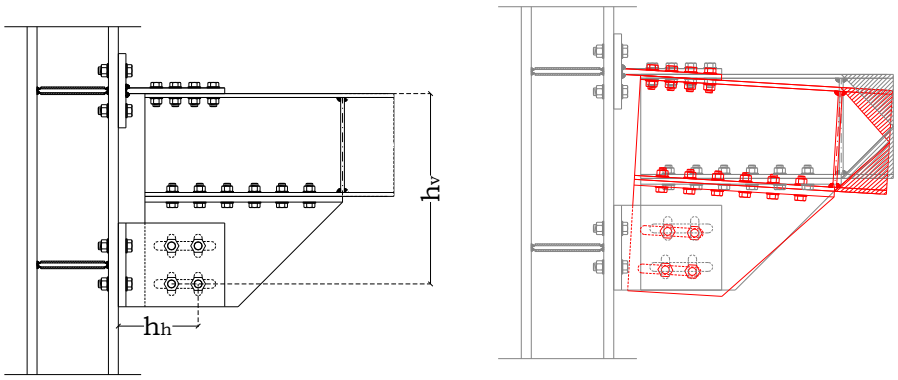

Fig. 4.8 – Rigid deformation of the FREEDAM-CYC02 joint

The minimum length represents the starting value form which it is possible to size the haunch and as a consequence, the distance between column flange and the beam section where the plastic hinge can develop have been determined.

<u>Step 3:</u> Evaluation of the bending moment in correspondence of the column flange and check of the beam in bending.

The maximum bending moment at the column face, $M_{cf,Cd}$ has been determined applying the criterions of the "*capacity design*" and for this reason the highest expected value of the static friction coefficient has been took in account (non-dissipative components).

$$M_{cf,Cd} = M_{friction,Rd} \cdot \gamma_{ov} = 171.82kNm \cdot 1.70 = 291.38kNm \tag{4.61}$$

In order to assure that the bending moment in correspondence of the axis of the beam plastic hinge is smaller than the plastic resistance of the beam, it is needed to check the following equation:

$$M_b = M_{cf,Cd} \cdot \frac{L_e - a}{L_e} = 291.38kNm \cdot \frac{2890 - 725}{2890} = 218.21kNm > M_{b.p} = 178.82\ kNm \tag{4.62}$$

where L_e is the shear length of the beam equal to 2.89m.
In this way, the additional strengthening due to the presence of the haunch in correspondence of the beam end is take into account.
The pre-load force applied on the steel plated of the friction damper by means pre-loadable bolts has to be reduce until the bending moment of the connection $M_{cf,Cd}$ is lower than the resulting bending moment M_b.

To this scope the m parameter, that represent the reduction coefficient of the pre-load force of the bolts, has been calculate:

$$m = \frac{M_{b.p}}{M_b} = \frac{171.82}{218.21} = 0.79 \tag{4.63}$$

While the reduced design friction resistance is given by:

$$\begin{aligned} F_{friction,Rd} &= \mu_{d.5\%} \cdot \left(m \cdot F_{p,red}\right) \cdot n_b \cdot n_s \\ &= 0.53 \cdot (0.79 \cdot 90.05) \cdot 4 \cdot 2 = 300.65kN \end{aligned} \tag{4.64}$$

Therefore, when the slippage of the friction damper occurs, the maximum force that the joint has to withstand is equal to:

$$F_{cf,Cd} = \frac{0.79 \cdot 171.82 \cdot 1.70}{0.47} = 509.86kN \tag{4.65}$$

The maximum static force estimated using Eq. 4.65, represents the force that the dissipative components (the friction dampers) are able to transmit to the non-dissipative components (T-stubs, angles in bending, haunches, column web in tension and compression, the column flange in bending). In other words, according to the principles of the "capacity design", the non-dissipative components have to be designed in order to resist to the maximum static force above evaluated.

<u>Step 4:</u> Design of the bolts' diameter for the TEE elements and the angles.

According to Eurocode 3 [1], in order to determine the minimum value of the resistant area of the bolts, a check under combined shear and tension have to be performed.

Starting from the following actions for the design of the bolts in tensile side:

$$F_{t,Ed} = \frac{F_{cf,Cd}}{n_{b,t}} = \frac{509.86}{4} \cong 127.46kN$$
$$F_{v,Ed} = \frac{F_v}{2\,n_b} = \frac{250}{2 \cdot 4} = 31.25\ kN \tag{4.66}$$

where F_v represents the maximum expected force for the test layout considered.

Considering 10.9 class bolts, the minimum value of the resistant area is equal to:

$$A_{res} \geq \frac{\gamma_{M2}}{f_{tb}}\left(\frac{F_{v,Ed}}{\alpha_v} + \frac{F_{t,Ed}}{1.26}\right)$$
$$A_{res} \geq \frac{1.25}{1000}\left(\frac{31250}{0.5} + \frac{127460}{1.26}\right) \cong 204.57\ mm^2 \tag{4.67}$$

and in any case the Eurocode 3 [1] establishes that the minimum value has to be greater than the value estimated considering only the tension action:

$$A_{res} \geq \frac{\gamma_{M2} F_{t,Ed}}{0.9 f_{tb}} = \frac{1.25 \cdot 127650}{0.9 \cdot 1000} \cong 177.04\ mm^2 \tag{4.68}$$

Definitely, M20 bolts have been chosen.

<u>Step 5:</u> Design of the T-stub and L-stubs.

The same criteria used for the design of the bolts have been applied, while in order to check the elements in bending the resistance formulation for

mechanism type-1 and type-2 have been taken into account excluding the failure mechanism type-3.

Design of the T-stubs

The first parameter to be calculated is represent by the horizontal distance between the bolts w, which has to be between the following values:

$$\begin{aligned} w_{min} &\cong t_{cw} + 2\,r_c + 1.8\,d_0 = 26 + 2\cdot 18 + 1.8\cdot 21.5 = 100.7 \text{ mm} \\ w_{max} &= b_{cf} - 2.4\,d_0 = 226 - 2.4\cdot 21.5 = 174.4 \text{ mm} \end{aligned} \tag{4.69}$$

where t_{cw} is the thickness of the column web, r_c the root radius, do the diameter of the hole and b_{cf} the column width. For this reason, a bolt spacing of the T-stub equal to w_o=*123.4mm* has been chosen.
On the other hand, the width of the T-stub has to be smaller than the width of the column, equal to 226mm in this case, and greater than the following value:

$$\begin{aligned} b_{T-stub} &= max\{w + 2.4\,d_0; b_{bf}\} = \\ &= max\{123.4 + 2.4\cdot 21.5; 135\} = 175 \text{ mm} \end{aligned} \tag{4.70}$$

Consequently, the width of the end plate is taken equal to 200mm.
Regarding the effective length of the T-stub b_{eff}, the half part of the geometrical length, equal to 100mm, has been considered.
According to the failure mechanism type-1, in order to avoid the collapse of the equivalent T-stub the following value of the thickness of the T-stub is required:

$$F_{1,Rd} = 2\frac{b_{eff}\,t_{Tstub}^2}{m}\frac{f_{y.Tstub}}{\gamma_{M0}} = F_{cf,Cd} \;\rightarrow \tag{4.71}$$

$$t_{Tstub.1} = \sqrt{\frac{m\, F_{cf,Cd}\, \gamma_{M0}}{2 \cdot\ b_{eff.Tstub} \cdot f_{y,Tstub}}} = \sqrt{\frac{45 \cdot 509860 \cdot\ 1.05}{2 \cdot\ 100 \cdot 355}} \cong 17.98\ mm$$

Where $f_{y,Tstub}$ is the yielding resistance of the plate.

In the same way, to avoid a failure of the T-stub according to the mechanism type-2 the following value of the thickness of the T-stub is required:

$$F_{2.Rd} = 2\frac{\frac{f_{y.Tstub}}{\gamma_{M0}}\frac{b_{eff}t_{Tstub}^2}{2} + 2\, F_{t.Rd}\, n}{m+n} = F_{cf,Cd} \quad \rightarrow$$

$$t_{Lstub.2} = \sqrt{\frac{2\, \gamma_{M0}}{b_{eff.ep}\, f_{y.Tstub}}\left[\frac{F_{cf,Cd}(m+n)}{2} - 2\, F_{t.Rd} n\right]} = \qquad (4.72)$$

$$= \sqrt{\frac{2 \cdot 1.05}{100 \cdot 355}\left[\frac{509680\ (45+45)}{2} - 2 \cdot 176400 \cdot 45\right]} \cong\ 19.95\ mm$$

Definitely, the thickness of the T-stub flange has been assumed equal to 20mm.

Regarding the T-stub web, a thickness equal to 15mm has been chosen, greater than the thickness of the beam flange that is 10.2mm.

The number of bolts $n_{b,s}$ needed to connect the T-stub web with the beam flange has been calculated equalling the shear force transmitted by the upper flange $F_{cf,Cd}$ and he the shear resistance of the bolts according to Eurocode 3 [1]:

$$F_{V,Rd} = n_{b,s}\frac{\alpha_v\ \cdot A_{res} \cdot f_{tb}}{\gamma_{M2}} = F_{cf,Cd} \quad \rightarrow \quad n_{b,s} = \frac{F_{cf,Cd} \cdot \gamma_{M2}}{\alpha_v\ \cdot A_{res} \cdot f_{tb}} \qquad (4.73)$$

Where γ_{M2} is a partial factor, a_v represent a coefficient depending on the bolt class, Ares is the nut area and f_{tb} the ultimate resistance.

Considering the fact that the beam size allows a maximum diameter of the holes equal to 19mm, M18 bolts have been chosen for which the minimum number of bolts is equal to:

$$n_{b,s} = \frac{509680 \cdot 1.25}{0.5 \cdot 193 \cdot 1000} = 6.60 \quad \rightarrow \quad n_{b,s} = 8 \tag{4.74}$$

The bolts are tightened in order to take advantage of the friction between the surface in contact of the T-stub web and the beam flange. The friction resistance has to be greater than the action estimated as:

$$F_{fric,Tstub,w} = \mu \cdot F_p \cdot n_s \cdot n_b = 0.5 \cdot 135.10 \cdot 1 \cdot 8 = 540.40kN > F_{cf,Cd} \tag{4.75}$$

Design of L-stubs

In this configuration of the FREEDAM connection the distance n between the bolt line and the end of the plate is assumed equal to *40.5mm* while the distance m between the bolt axis and the plastic hinge in the beam flange is assumed equal to *37mm*. The horizontal distance between the bolts w has to be between the following values:

$$\begin{aligned} w_{min} &\cong t_{cw} + 2\,r_c + 1.8\,d_0 = 26 + 2 \cdot 18 + 1.8 \cdot 21.5 + 15 \\ &= 100.7 \text{ mm} \\ w_{max} &= b_{cf} - 2.4\,d_0 = 226 - 2.4 \cdot 21.5 = 174.4 \text{ mm} \end{aligned} \tag{4.76}$$

In line with the limitations above, the L-stub bolt spacing has been set equal to w_0*=145mm*.

The value of the L-stub width is taken equal to 110mm, that is coincident with the effective length.

$$F_{1,Rd} = \frac{b_{eff}\, t_{Lstub}^2}{2 \cdot m} \frac{f_{y.Lstub}}{\gamma_{M0}} = \frac{F_{cf,Cd}}{4} \rightarrow$$

$$t_{Lstub.1} = \sqrt{\frac{m\, F_{cf,Cd}\, \gamma_{M0}}{2 \cdot\ b_{eff.Lstub} \cdot f_{y,Lstub}}} = \sqrt{\frac{37 \cdot 509860 \cdot\ 1.05}{2 \cdot\ 110 \cdot 355}} \cong 15.54\ mm \quad (4.77)$$

Aiming to avoid the collapse of the equivalent T-stub, the required thickness for mechanism type-1 and type-2 are given by:

$$F_{2.Rd} = \frac{\frac{f_{y.Lstub}}{\gamma_{M0}} \frac{b_{eff}\, t_{Lstub}^2}{4} + \ F_{t.Rd}\, n}{m + n} = \frac{F_{cf,Cd}}{4} \rightarrow$$

$$t_{Lstub.2} = \sqrt{\frac{4\, \gamma_{M0}}{b_{eff.ep}\, f_{y.Lstub}} \left[\frac{F_{cf,Cd}(m+n)}{4} - \ F_{t.Rd} n\right]} = \quad (4.78)$$

$$= \sqrt{\frac{4 \cdot 1.05}{110 \cdot 355} \left[\frac{509680\ (37 + 40.5)}{4} - 176400 \cdot 40.5\right]} \cong 16.74 mm$$

Therefore, a 20mm thickness has been assumed for the L-stub flange/web.

<u>Step 7:</u> Design of the bolted connection between the beam lower flange and the upper flange of the haunch.

The first phase consists into the evaluation of the acting force on the connection:

$$F_{t,Ed} = \frac{F_{cf,Cd} \cdot h_h}{\sum_i d_i^2} \cdot d_i \qquad F_{v,Ed} = \frac{F_{cf,Cd}}{n_{b.h}} \quad (4.79)$$

Where d_i is the distance between the *i-th* bolt form the rotation center.

According to the code provisions and the technological requirements, the bolts position has been defined. Considering that the most stressed bolt is the farthest from the column flange, the maximum force on the bolt has been estimated in the following:

$$F_{t,Ed} = \frac{F_{cf,Cd} \cdot h_h}{\sum_i d_i^2} \cdot d_i = \frac{509680 \cdot 180}{473055} \cdot 432.6 = 41960N$$
$$F_{v,Ed} = \frac{F_{cf,Cd}}{n_{b.h}} = \frac{509680}{2 \cdot 6} = 42490N \quad (4.80)$$

At this point, the minimum value of the resistant area of the bolts has been determined by means of the check under combined shear and tension, according to Eurocode 3 [1]. In particular:

$$A_{res} \geq \frac{\gamma_{M2}}{f_{tb}} \left(\frac{F_{v,Ed}}{\alpha_v} + \frac{F_{t,Ed}}{1.26} \right)$$
$$A_{res} \geq \frac{1.25}{1000} \left(\frac{42490}{0.5} + \frac{41960}{1.26} \right) \cong 147.90\ mm^2 \ > 193 mm^2 = A_{res,M18} \quad (4.81)$$

The check is satisfied for M18 bolts.

<u>Step 8:</u> Check of the column web in shear.

The resistance of the column web panel has been estimated starting from the shear resistant area of the section.

$$A_{vc} = A - 2\, b_{cf}\, t_{cf} + (t_{cw} + 2r_c) t_{cf} =$$
$$= 14940 - 2 \cdot 226 \cdot 26 + (15.5 + 2 \cdot 18) \cdot 26 = 4527\ mm^2 \quad (4.82)$$

$$V_{wp,Rd} = \frac{0.9 \cdot A_{vc} \cdot f_{y,cw}}{\sqrt{3} \cdot \gamma_{M0}} = \frac{0.9 \cdot 4527 \cdot 355}{\sqrt{3} \cdot 1.05} \cong 835\ \text{kN} \quad (4.83)$$

Comparing the shear resistance of the column web panel with the action $F_{cf,Cd}$, the resistance results greater than the action, so no supplementary web plates are needed.

Step 9: Check of the column web in tension and compression.

The resistance of the column web in compression is given by:

$$F_{cwc.Rd} = \omega \cdot k_{wc} \cdot b_{eff.cwc} \cdot \mathrm{t_{cw}} \cdot \frac{f_{y.cw}}{\gamma_{M0}} = \\ = \frac{0.68 \cdot 1 \cdot 275 \cdot 15.5 \cdot 355}{1.05} \cong 978 \text{ kN} \tag{4.84}$$

Where ω take in account the interaction with the column web panel and k_{wc} depends on the effective longitudinal compressive stress $\sigma_{com,Ed}$ due to the axial force and the bending moment on the column web resistance. These coefficients are given by:

$$\omega = \frac{1}{\sqrt{1 + 1.3\left(\frac{b_{eff.cwc} \cdot \mathrm{t_{cw}}}{A_{vc}}\right)^2}} = \frac{1}{\sqrt{1 + 1.3\left(\frac{275 \cdot 15.5}{4527}\right)^2}} = 0.68 \tag{4.85}$$

$$k_{wc} = 1 \quad \text{when} \quad \sigma_{com,Ed} \leq 0.7 f_{y,wc}$$

While $b_{eff,cwc}$ represents the effective length of the column web, determined as follows:

$$b_{eff.cwc} = t_{Tstub,w} + 5\left(t_{fc} + r_c\right) + 2\, t_{Tstub} = \\ = 15 + 5(26 + 18) + 2 \cdot 20 = 275 \text{ mm} \tag{4.86}$$

Continuity plates are not required because the resistance is greater than the action $F_{cf,Cd}$.

Step 10: Check of the resistance of the column flange in bending using the equivalent T-stub model.

The equivalent T-stub in tension model for bolted connection represents a simple way to design the resistance of the column flange in bending. Using the following equations, the resistances for mechanism type-1 and type-2 have been evaluated:

$$F_{1,Rd} \geq F_{cf,Cd} \qquad F_{2,Rd} \geq F_{cf,Cd} \tag{4.87}$$

where

$$F_{1,Rd} = 2\frac{b_{eff}t_{cf}^2}{m}\frac{f_{y.cf}}{\gamma_{M0}} \quad \text{and} \quad F_{2.Rd} = 2\frac{\frac{f_{y.cf}}{\gamma_{M0}}\frac{b_{eff}t_{cf}^2}{2} + 2\,F_{t.Rd}\,n}{m+n} \tag{4.88}$$

with b_{eff} equal to:

$$\begin{gathered} b_{eff} = min\{2\pi m_c\,;\, 4m_c + 1.25e; p\} = \\ = min\,\{2\pi \cdot 36\,;4 \cdot 36 + 1.25 \cdot 51.3; 105\} \cong 105\,mm \end{gathered} \tag{4.89}$$

Considering $n=min\{e; e_{Lstub}; 1.25m_c\}=min\{6.13; 48.3; 1.25 \cdot 26\}=32.5mm$, it is simple to derive the design resistances for mechanism type-1 and type-2 as follows:

$$F_{1,Rd} = 2\frac{f_{y.cf}\,b_{eff.cfb}\,t_{cf}^2}{\gamma_{M0}\,m_c} = 2\frac{355 \cdot 105 \cdot 20^2}{1.05 \cdot 36} \cong 789\ \text{kN} \geq F_{cf,Cd}$$

$$\begin{gathered} F_{2.Rd} = 2\frac{f_{y.cf}\frac{b_{eff.cfb}t_{cf}^2}{2} + 2\,F_{t.Rd}\,n}{\gamma_{M0}(m_c+n)} = \\ = 2\frac{355\frac{105 \cdot 20^2}{2} + 2 \cdot 176400 \cdot 38.3}{1.05(36+38.3)} \cong 729\ \text{kN} \geq F_{cf,Cd} \end{gathered} \tag{4.90}$$

Even if, in nay condition, the design resistances are greater than the action $F_{cf,Cd}$, the continuity plates have been insered in order to avoid the column deformation.
Regarding the falilure mechanism type-3, it has been exclude due to the design procedure adopted for the bolts.

4.2.3 Experimental layout

Description of the tests setup

All the experimental tests have been developed at the laboratory of the University of Coimbra. As specified above, the specimens consist of a steel column and two steel beams equipped with the FREEDAM friction devices in correspondence of the lower flanges (Fig. 4.9).

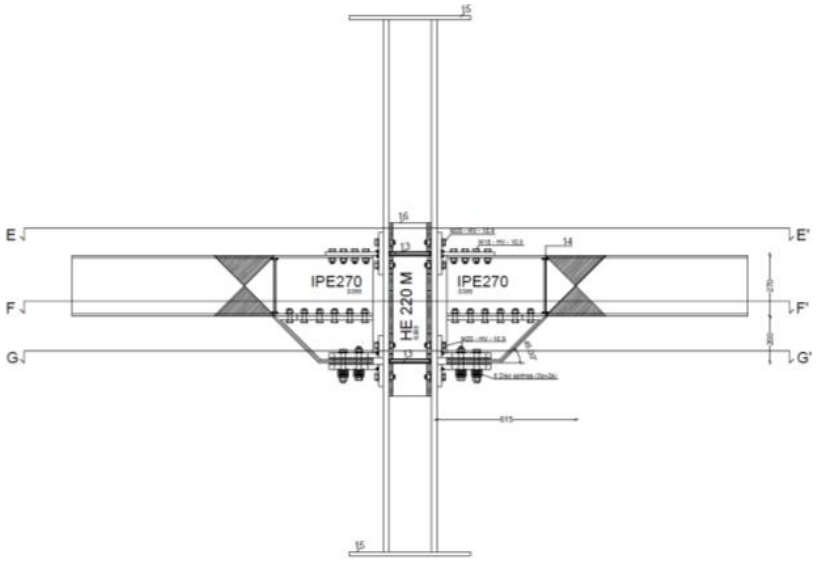

Fig. 4.9 – Internal joint configuration (HE220M / IPE270 - Horizontal pads)

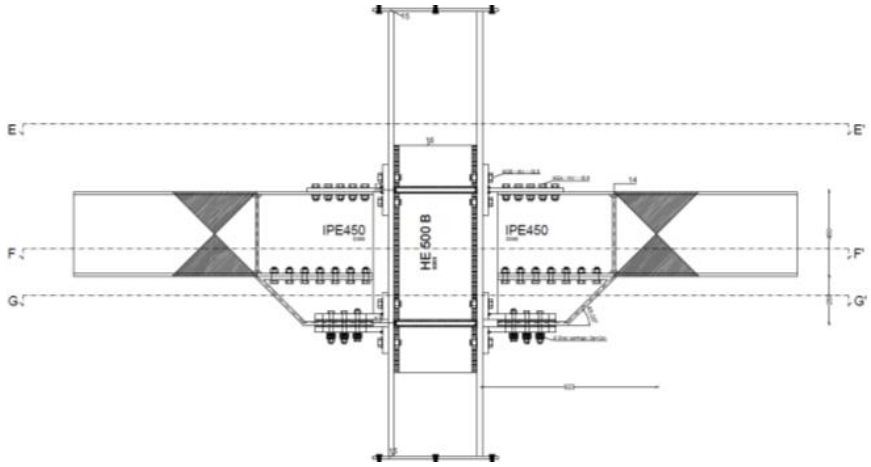

Fig. 4.10 – Internal joint configuration (HE500B / IPE450 – Horizontal pads)

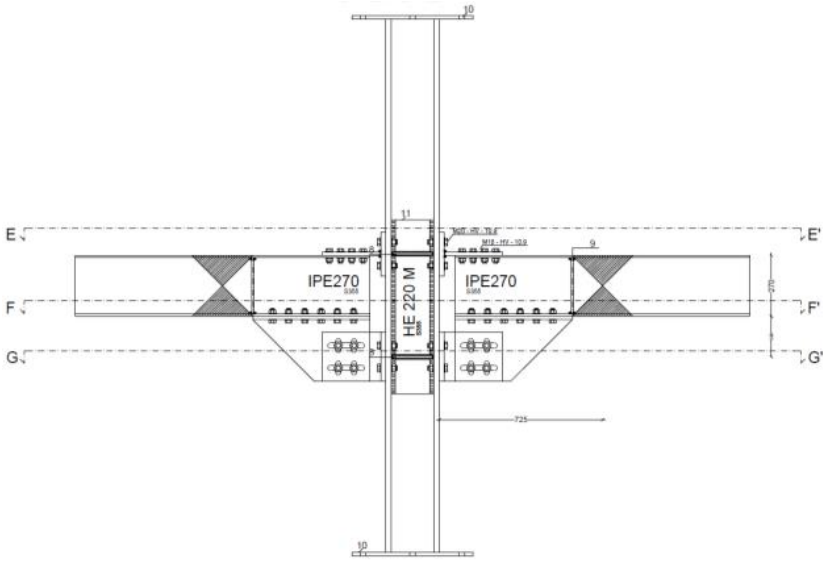

Fig. 4.11 – Internal joint configuration (HE220M / IPE270 - Vertical pads)

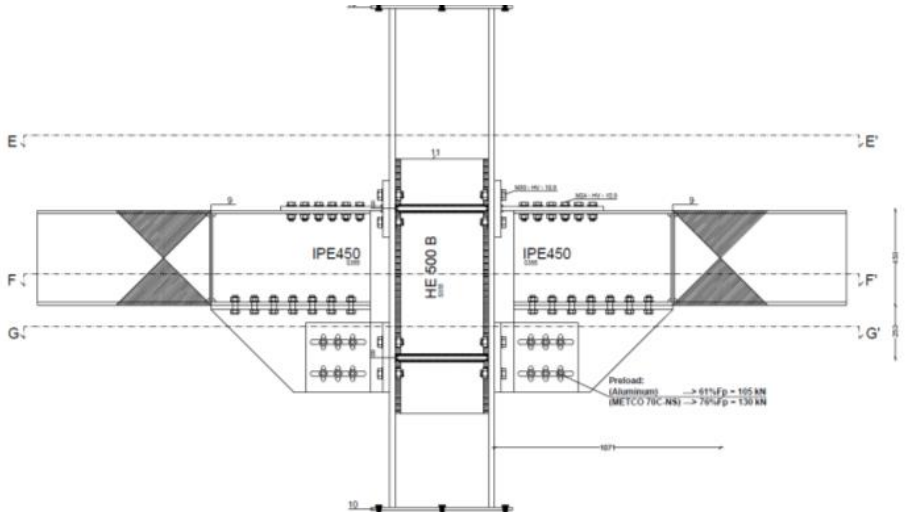

Fig. 4.12 – Internal joint configuration (HE500B / IPE450 - Vertical pads)

The column is supported by a hinge at the bottom. The beam ends are vertically supported allowing the lateral movement of the specimen.

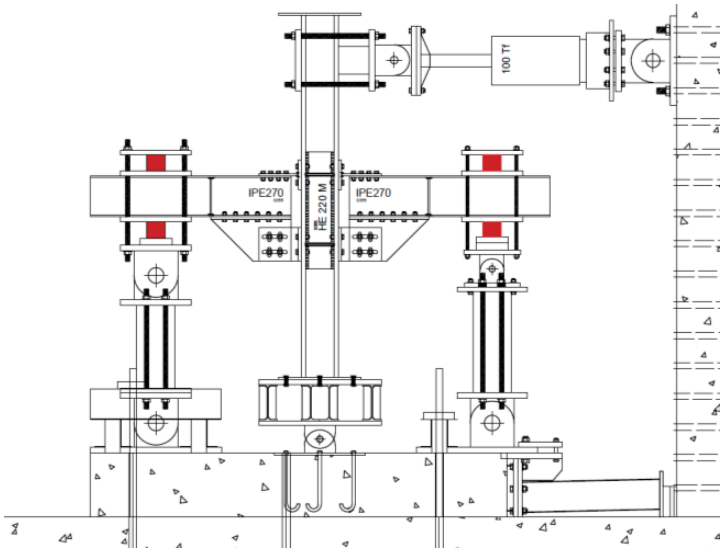

Fig. 4.13 – Test layout for internal joints HE220M-IPE270

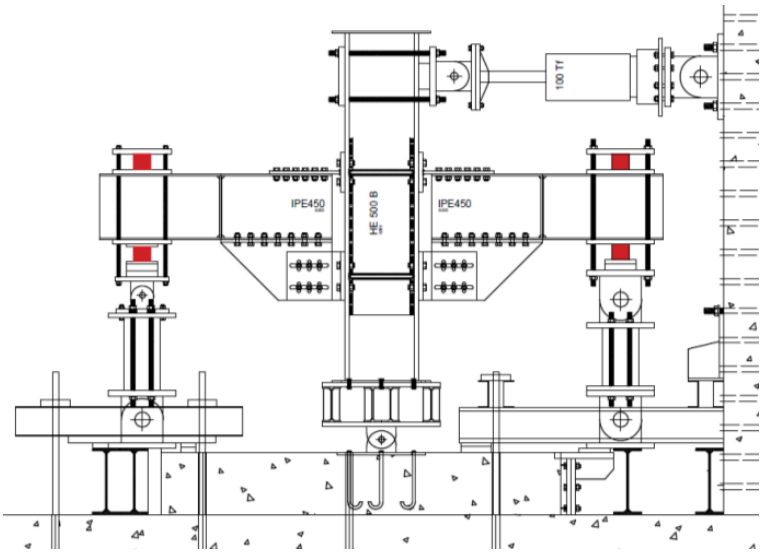

Fig. 4.14 – Test layout for internal joints HE500B-IPE450

The test layouts in Fig. 4.13 and Fig. 4.14 have been verified considering the static scheme in Fig. 4.15 and a maximum force in the actuator equal to 900kN in tension and in compression. In the strong floor laboratory is characterized by the presence of holes, with a diameter of 80mm, spaced according to 1mx1m grid. The holes allow to fix the structures by means of high strength dywidag bars. The actuator is fixed to a rigid and strong vertical wall. The specimen's length between the vertical supports of the beams is $L'_b = 2x1125 = 2250mm$ for the joints with IPE270 beams, while for the joints with IPE450 beams this length is $L''_b = 2 \cdot 1630 = 3260mm$. The column height, for all the specimens, from the bottom hinge to the lateral loading point is $L_c = 2481mm$.

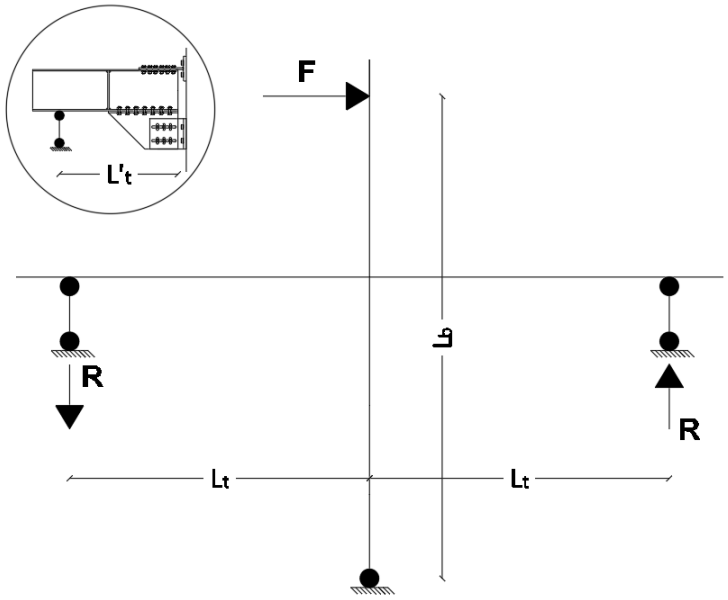

Fig. 4.15 – Static scheme for the calculation of the constraint reactions in the test layout.

The constrain reactions have been estimated using the equation of balance to the rotation around the hinge at the foot of the column (Eq. 4.91 and Eq. 4.92). Finally, the maximum moment in the beam to column connection has been estimated with Eq. 4.93. All the geometric data of the specimens, the reaction of the pendulums and the moment in the joint are summarized in Table 4.4 considering the different layout configurations.

$$F \times L'_c = 2 \times R \times L_t \tag{4.91}$$

$$R = \frac{F \times L'_c}{2 \times L_t} \tag{4.92}$$

$$M_t = R \times L'_t \tag{4.93}$$

Table 4.4 Geometric data, pendulum reactions, moment in the joint.

Configurations with IPE270 beams			***Configurations with IPE450 beams***		
L'_c=2481mm	*L_t=1125mm*	*L'_t=1005mm*	*L'_c=2481mm*	*L_t=1630mm*	*L'_t=1380mm*
R=992kN	*Mt=997kNm*		*R=684kN*	*Mt=945kNm*	

A lateral load has been applied to the top of the column by an actuator operating under displacement control whose maximum load capacity is equal to 1000kN in compression and 900kN in tension with a piston stroke of ± 150mm.

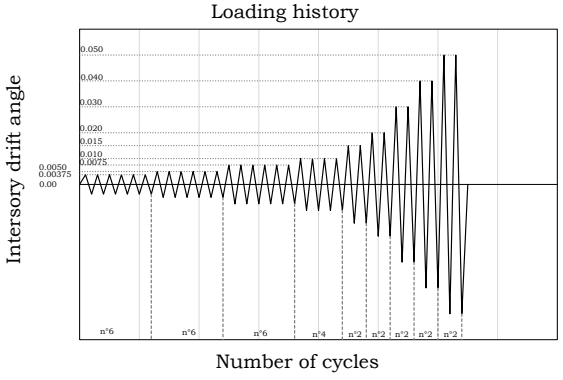

6 cycles at θ = 3.75 mrad
6 cycles at θ = 5 mrad
6 cycles at θ = 7.5 mrad
4 cycles at θ = 10 mrad
2 cycles at θ = 15 mrad
2 cycles at θ = 20 mrad
2 cycles at θ = 30 mrad
2 cycles at θ = 40 mrad
2 cycles at θ = 50 mrad

Fig. 4.16 – Loading protocol according to AISC 341/2010 [2]

The loading program has been planned according to AISC 341/2010 [2] seismic provisions, with a maximum rotation higher than the maximum required provided by Eurocode 8 [3], equal for DCH frames, to 35mrad.
In this test, axial compressive load was not applied to the columns because a very large force is required, and because a low level of compressive force tends to prevent diagonal cracking at the panel zone.

Table 4.5 Preload values for the bolts of the FREEDAM devices.

TEST	Design value of preload	Value of preload and torque applied using torque method according to EN1090-2 [4]
IN270_CYC-1_M4	F'p=0.40xFp=0.38x0,7xfubxAb =65,00kN	1st step: F1=0,75xFp=48,75kN → M1=127Nm
		2nd step: F2=1,10xFp=71,00kN → M2=185Nm
IN270_CYC-2_M4	F'p=0.40xFp=0.40x0,7xfubxAb =71,00kN	1st step: F1=0,75xFp=53,25kN → M1=138Nm
		2nd step: F2=1,10xFp=78,00kN → M2=203Nm
IN450_CYC-1_M4	F'p=0.38xFp=0.38x0,7xfubxAb = 65kN	1st step: F1=0,75xFp=49,00kN → M1=127Nm
		2nd step: F2=1,10xFp=71,00kN → M2=185Nm
IN450_CYC-1_M4	F'p=0.58xFp=0.58x0,7xfubxAb = 100,00kN	1st step: F1=0,75xFp=75,00kN → M1=195Nm
		2nd step: F2=1,10xFp=110,00kN → M2=286Nm

Another important aspect is the definition of the preload in the bolts. From the chapter 2, the value of the friction coefficient and its statistical variability is known. Therefore, the design value of the bolts preload in

the dampers has been evaluated. In Table 4.5 the values of preload for the two steps of the torque method, the procedure adopted to tighten the bolts, are summarized.

During the tests, force, displacements, deformations, torque and temperature are measured (Fig. 4.17 and Fig. 4.18). In detail, each test requires the following instrumentation:

- 1 actuator (Force range: ±900kN; Displacement range: ±150mm; Frequency 1Hz with maximum displacement range +7.02mm/-5.63mm);
- 4 load cells (Maximum capacity 500kN in compression);
- 15 displacement transducers - LVDT (n.4 sensors range ±25mm; n.4 sensors range ±50mm);
- 1 static torque transducer (nominal torque 1000Nm);
- 2 thermocouples;
- 4 annular load cells (capacity 350kN);
- 46 strain gauges (length 6mm, strain limit 5%).

Sensor Layout for specimens with horizontal friction pads

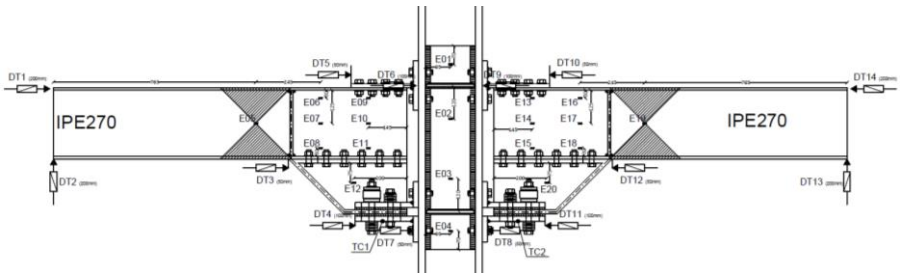

Fig. 4.17 – Sensors' layout scheme

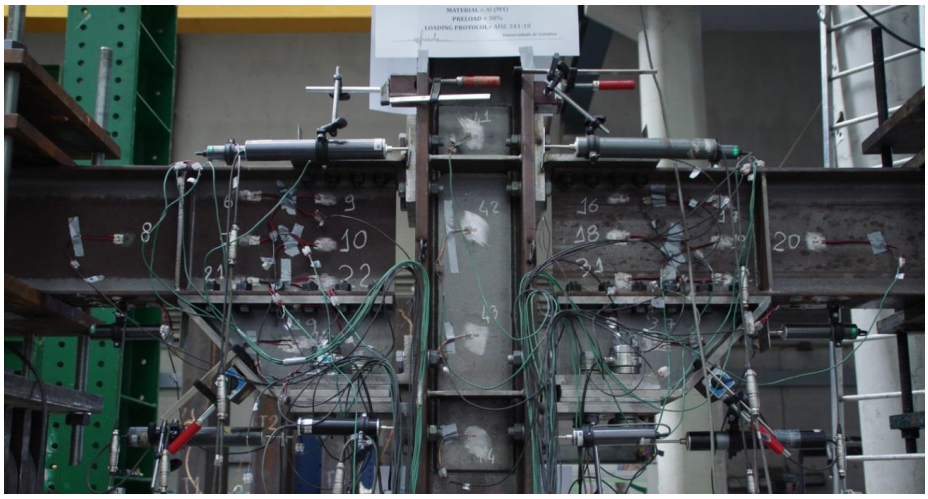

Fig. 4.18 – Sensors' layout

During the tests many parameters have been monitored and acquired, in particular:

- DT n.01 and 14 measure the horizontal displacement at the beam ends;
- DT n.02 and 13 measure the vertical displacement at the beam ends;
- DT n.06 and 09 measure the relative displacement between the T-stub/angles flanges and the column flange;
- DT n.05 and 10 measure eventual slips of the web of the T-stub with respect to the beam flange;
- DT n.03 and 12 measure the eventual displacements between the haunch and the beam;
- DT 07 and 08 measure the relative displacement between the L-stub/angles flanges and the column flange;
- DT 04 and 11 measure the displacement of the friction device.

Sensor Layout for specimens with vertical friction pads

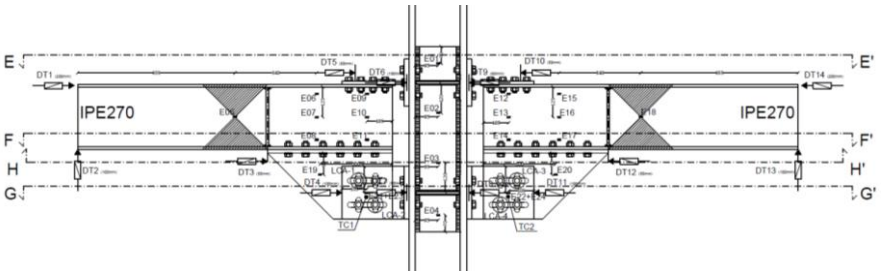

Fig. 4.19 – Sensors' layout scheme

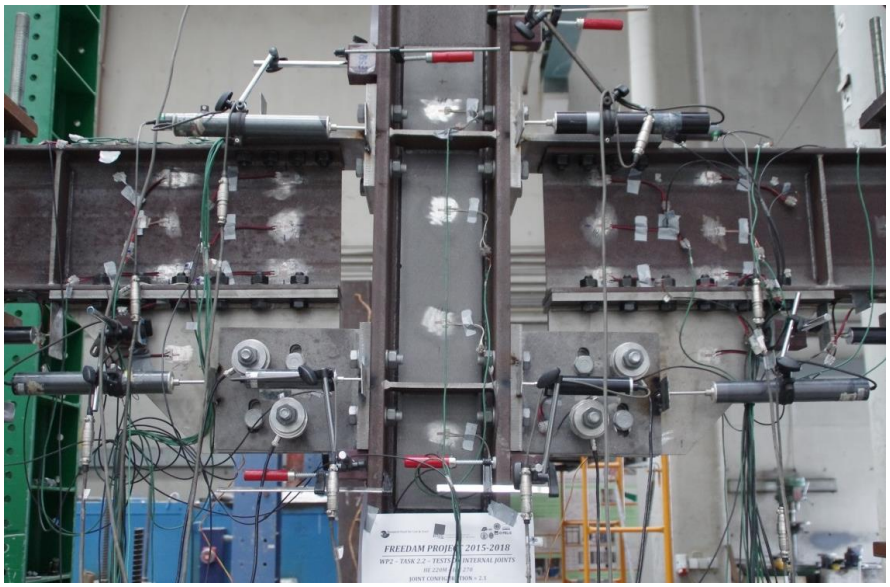

Fig. 4.20 – Sensors' layout

During the tests many parameters have been monitored and acquired, in particular:

- DT n.01 and 14 measure the horizontal displacement at the beam ends;
- DT n.02 and 13 measure the vertical displacement at the beam ends;

- DT n.06 and 09 measure the relative displacement between the T-stub/angles flanges and the column flange;
- DT n.05 and 10 measure eventual slips of the web of the T-stub with respect to the beam flange;
- DT n.03 and 12 measure the eventual displacements between the haunch and the beam;
- DT 07 and 08 measure the relative displacement between the L-stub/angles flanges and the column flange;
- DT 04 and 11 measure the displacement of the friction device.

4.2.4. Coupons tests

In order to know exactly the mechanical properties of the materials which constitute the profiles and the plates used for the production of FREEDAM Internal Joints specimens, an experimental campaign has been conducted on coupons cut from the steel plates and steel profiles.

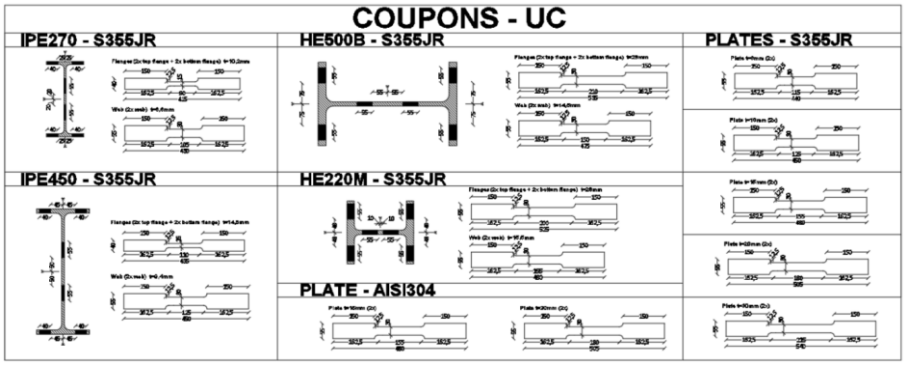

Fig. 4.21 – Geometric characteristics of the coupon to be tested.

The total number of coupons to be tested is 38 (34 realized using S355 steel and 4 using AISI304 stainless steel), in fact for each steel element with different thickness or different initial position in the profile two coupons have been obtained. (Fig. 4.21). Of the 38 tests initially planned 12 tests on coupons obtained from steel and stainless steel plates and 16 tests on coupons obtained from steel profiles were performed.

The tests have been conducted measuring the strain and the displacement. For the displacement it was considered two different measures: the displacement from the stroke and the displacement from the extensometer.

The displacement from the stroke is useful to evaluate the plastic behaviour of the material, while the displacement of the extensometer is more accurate to evaluate the elastic range because it is not affected by the slippage in the clamps of the machine. In diagrams from Fig. 4.22 to Fig. 4.25 the results of the coupon tests are summarized.

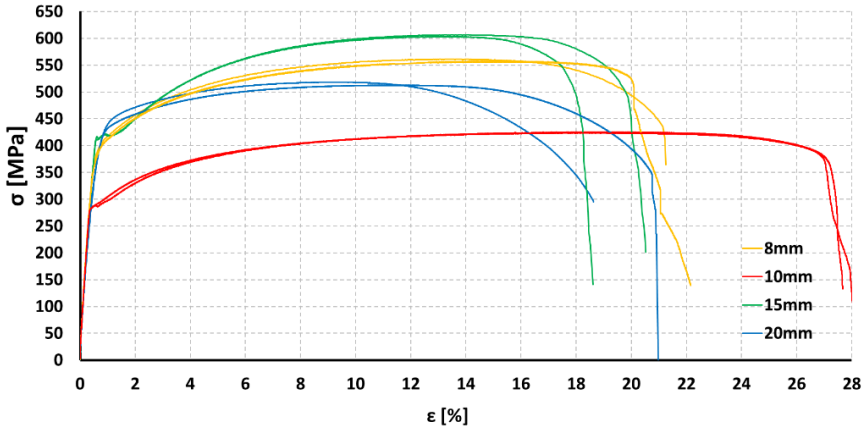

Fig. 4.22 – Stress-strain curves of the coupon tests from S355 steel plates.

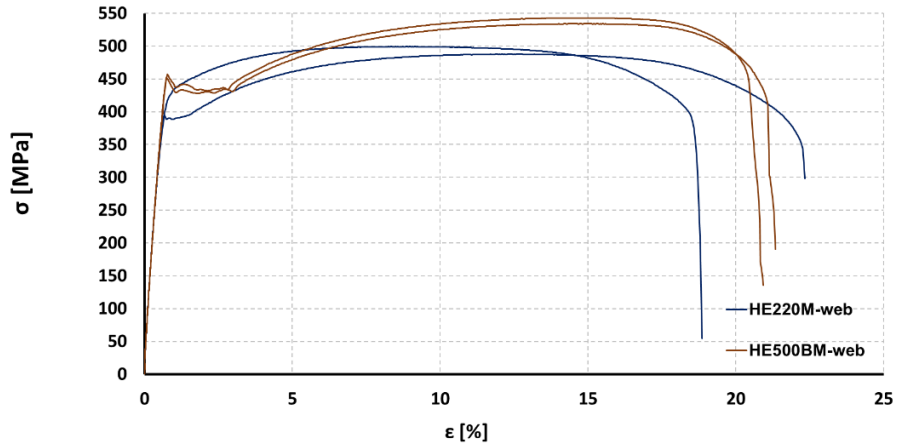

Fig. 4.23– Stress-strain curves of the coupon tests from HE220M and HE500BM profile.

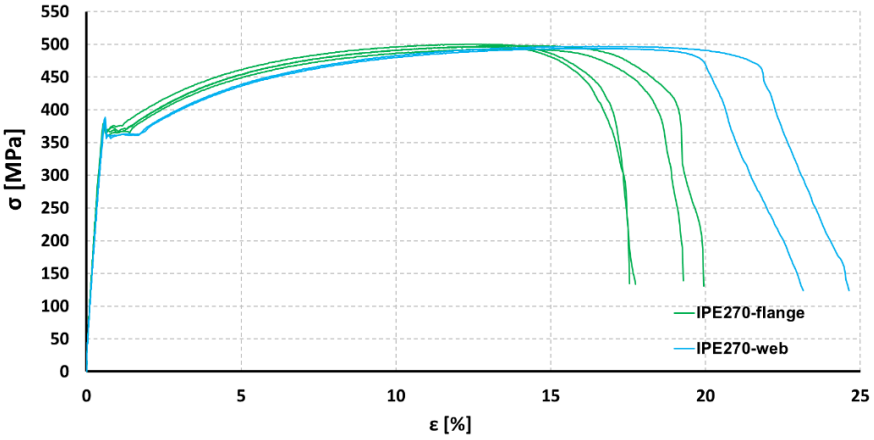

Fig. 4.24 – Stress-strain curves of the coupon tests from IPE270 – S355 steel.

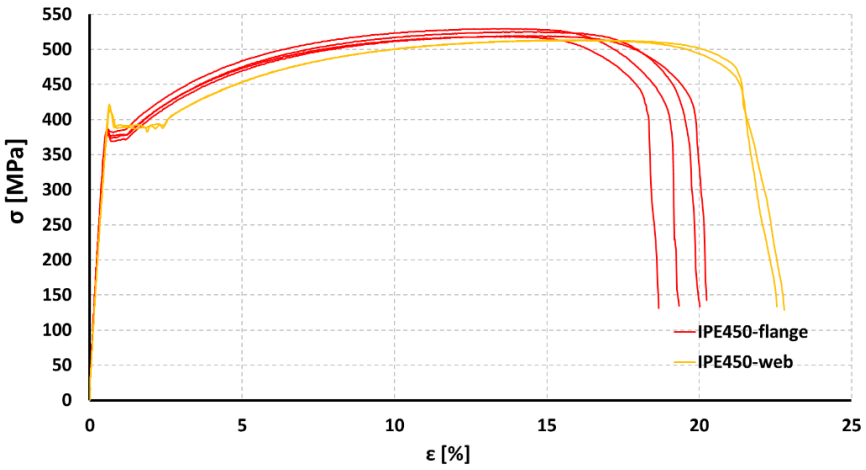

Fig. 4.25 – Stress-strain curves of the coupon tests from IPE450 – S355 steel.

4.2.5. Experimental results

In line with expectations, the test results on internal joints equipped with FREEDAM connections confirm the good behaviour of the connection. In fact, minor yielding has been observed only in T-stubs and L-stubs, while all the other structural elements remain in elastic range without exhibit any damage. The response of the tested joints was very similar, for this reason, in the following the results of one test for each typology are reported.

Main results of TEST FREEDAM-IN270_CYC-1_M4

The global and local behaviour of the FREEDAM-IN270_CYC-1_M4 is in line with the predictions. The friction dampers demonstrated to be able to dissipate the energy avoiding damage in the other components

designed as non-dissipative zone, without significant strength degradation.

Fig. 4.26 – Setup of the test.

Fig. 4.27 – Setup of the test.

Observing the moment-rotation curves (Fig. 4.28 and Fig. 4.29), it is easy to note an asymmetrical behaviour due to the many factors.

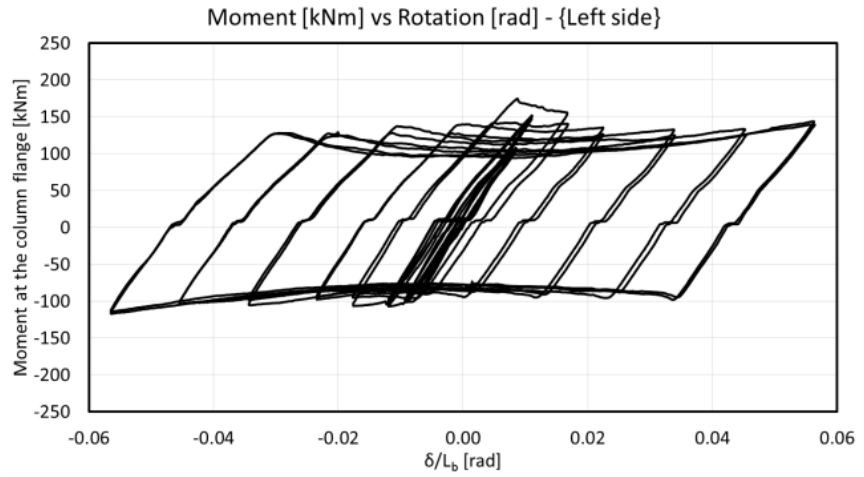

Fig. 4.28 – Moment evaluated at the column's face vs chord rotation – Left side of the joint.

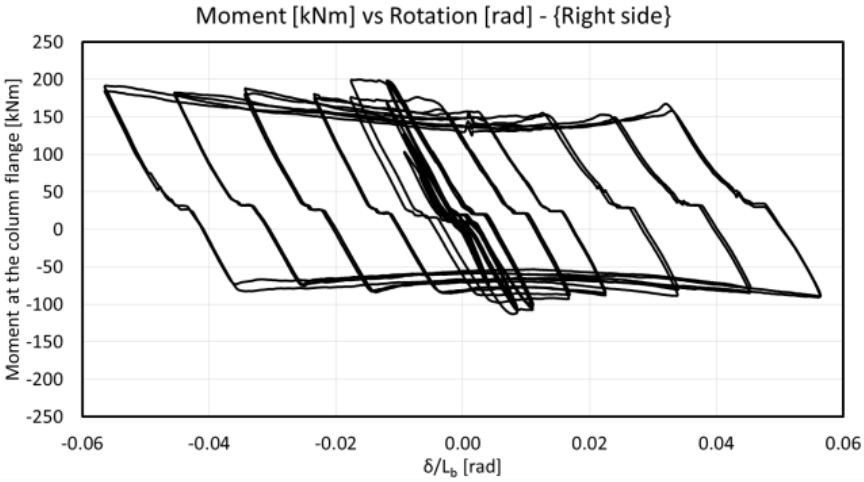

Fig. 4.29 – Moment evaluated at the column's face vs chord rotation – Right side of the joint.

The main reason of this asymmetry is represented by a non-symmetrical layout, in fact the rotation centers of the two pendulums located in correspondence of the beam ends are not perfectly aligned.

It is important to underline that the Moment has been evaluated multiplying the force at the beam end measured by the load cells for the distance from the column flange L'_t, while the chord rotation has been obtained dividing the displacement at level of the actuator "δ" for the distance from the hinge on the bottom L_b.

Another important aspect concerns the difference between maximum bending moment due to hogging or sagging actions, related to a parasite bending of the plates of the friction damper and a variation of the preload in the bolts during under hogging/sagging. Last aspect is represented by the shape of the hysteretic loops: after the first cycles the shape assumed by the curves is stable until the end of the test.

These results are in line with the outcomes of experimental tests performed on the friction materials, in fact, the shapes of the hysteretic loops of the joint was perfectly comparable with that of the shear-lap tests. In fact, the first peaks correspond to the static friction coefficient (higher than the dynamic for the soft materials), while the stabilized cycle corresponds to a slip force of the damper whose value is mainly related to the dynamic value of the friction coefficient.

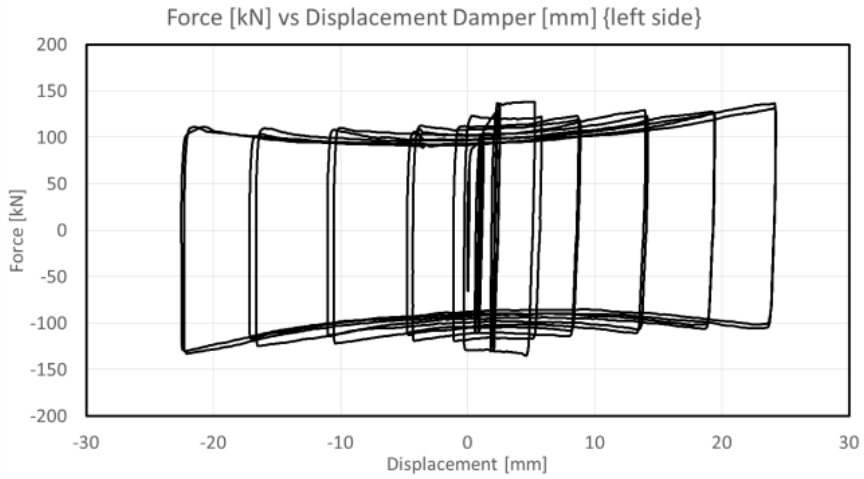

Fig. 4.30 – Force at level of the actuator vs displacement at level of the friction damper – Left

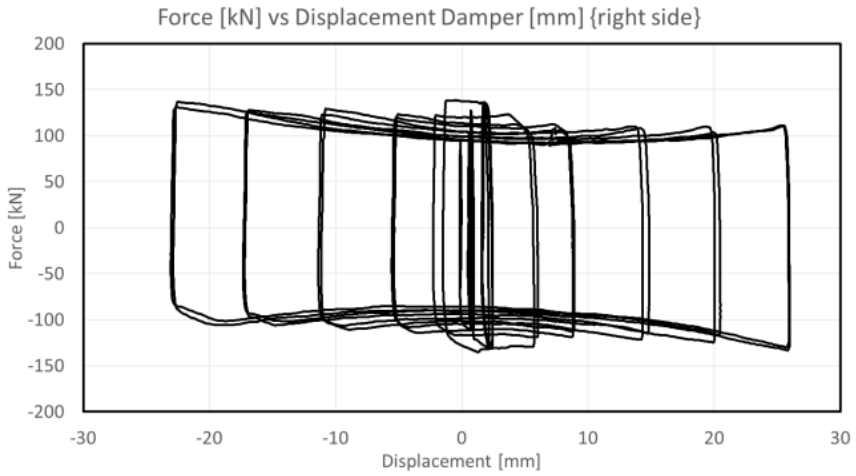

Fig. 4.31 – Force at level of the actuator vs displacement at level of the friction damper – Right

Comparing the friction coefficients evaluated in chapter 2 and the consequent range of slip force values adopted for the design of the joint, with the static and dynamic of slip force values observed during the whole loading history it is easy to verify that the values are compatible. The small differences are due mainly due to the deformations of the L-stubs of the friction dampers during the test, that cause also the oscillations of the bolt preload under hogging/sagging bending moments.
Considering the displacements measured with the LVDT transducers, in particular analysing the curves (Fig. 4.30 and Fig. 4.31) obtained from the force in the actuator and the displacement measured at the T-stub level (in correspondence of the damper) it can be observed that the hysteretic loops in this case assume a rectangular shape, with a significant energy dissipation capacity and almost no degradation both in terms of stiffness and resistance.
In the previews, the variation of the force in the bolts during the tests has been repeatedly mentioned since it significantly affects the behaviour of the FREEDAM connections.
The value of the preload in the bolts of the damper has been monitored by means of four load cells, the diagrams in Fig. 4.32 and Fig. 4.33 show a loss of preload in the bolts at the beginning of the tests that increases as far as the loading cycles increase. Furthermore, it is possible to note the oscillation of the value of the forces in the bolts during the test due to the bending developed in the plates of the dampers.

All the other displacement sensors installed in the connection, as delivered in the following figures, showed that the other joint components practically remained in elastic range (Fig. 4.34 to Fig. 4.41).

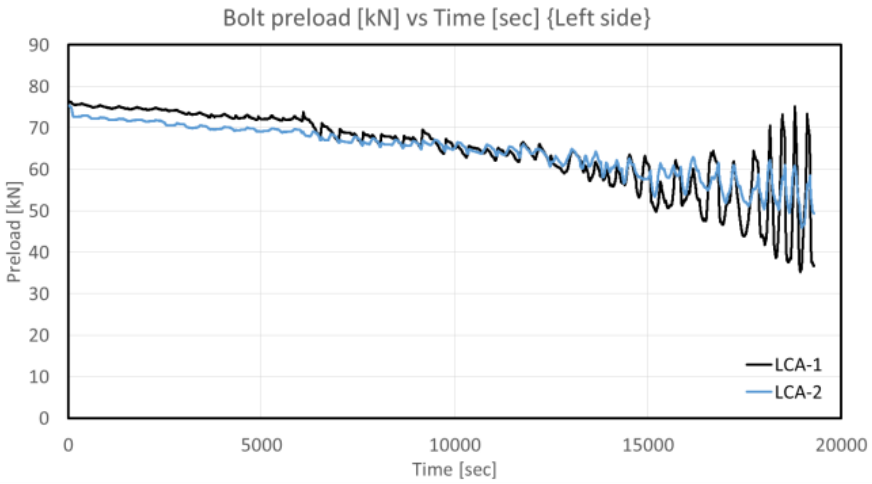

Fig. 4.32 – Bolt preload vs Time - Left side

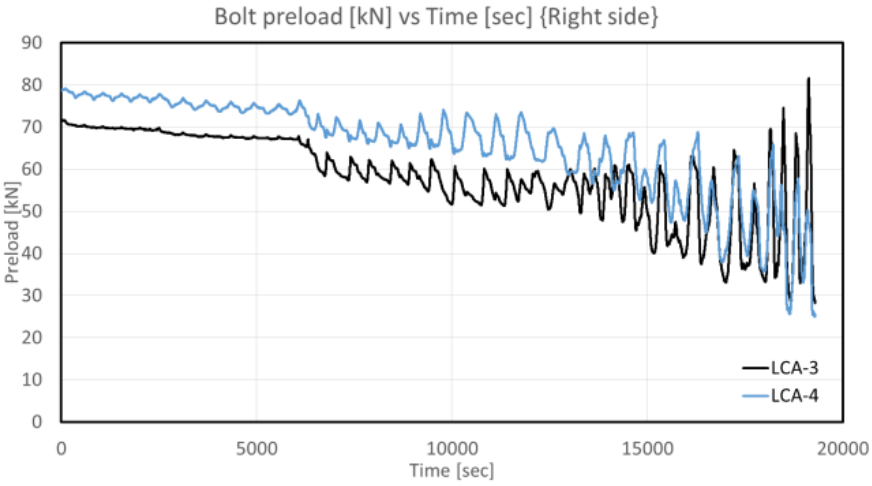

Fig. 4.33 – Bolt preload vs Time - Right side

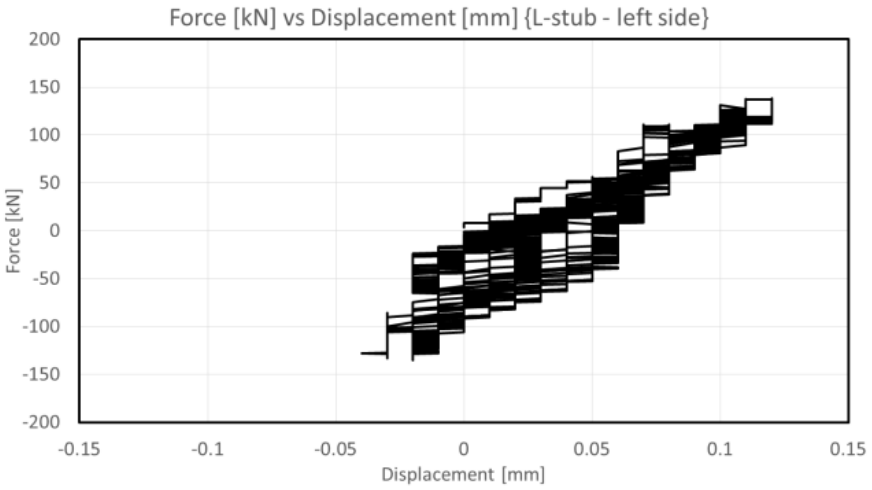

Fig. 4.34 – Force vs Relative displacement between L-stub and column – Left side

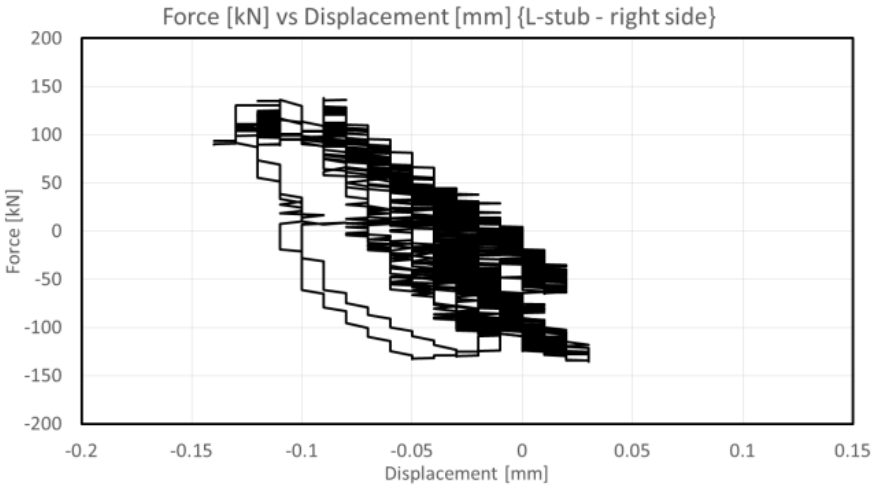

Fig. 4.35 – Force vs Relative displacement between L-stub and column - Right side

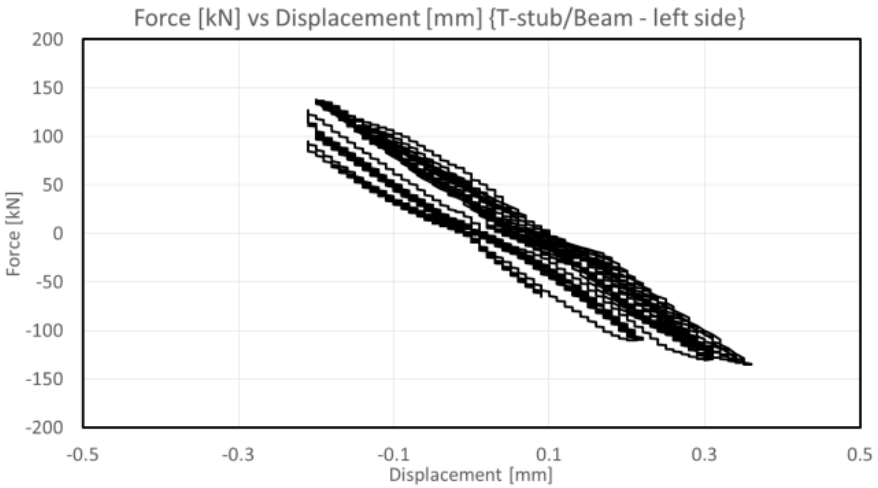

Fig. 4.36 – Force vs Relative displacement between T-stub and beam - Left side

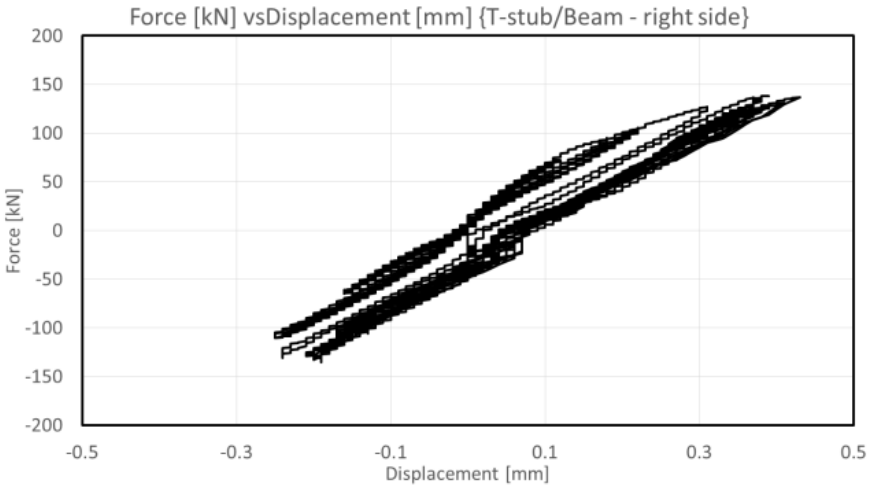

Fig. 4.37 – Force vs Relative displacement between T-stub and beam - Right side

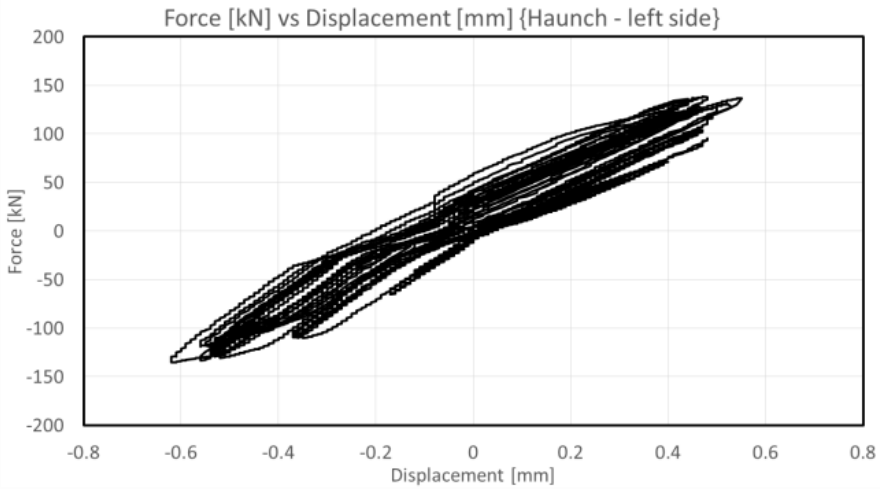

Fig. 4.38 – Force vs Relative displacement between Haunch and Beam - Left side

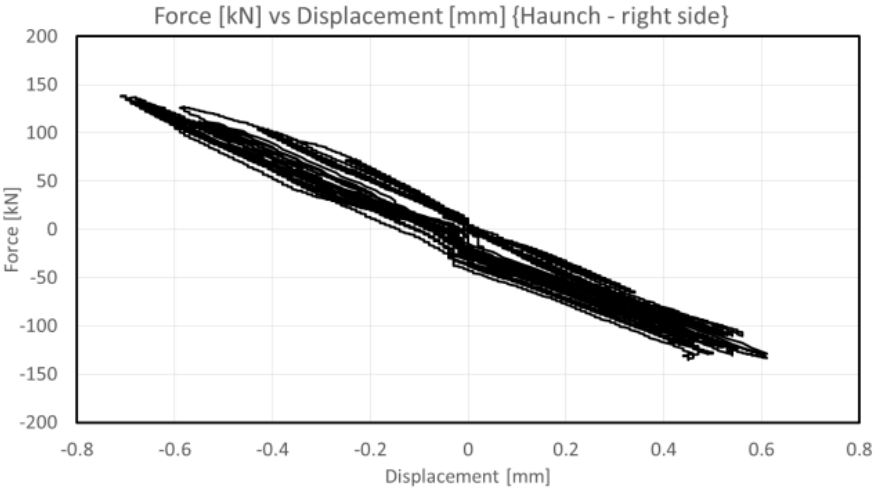

Fig. 4.39 – Force vs Relative displacement between Haunch and Beam - Right side

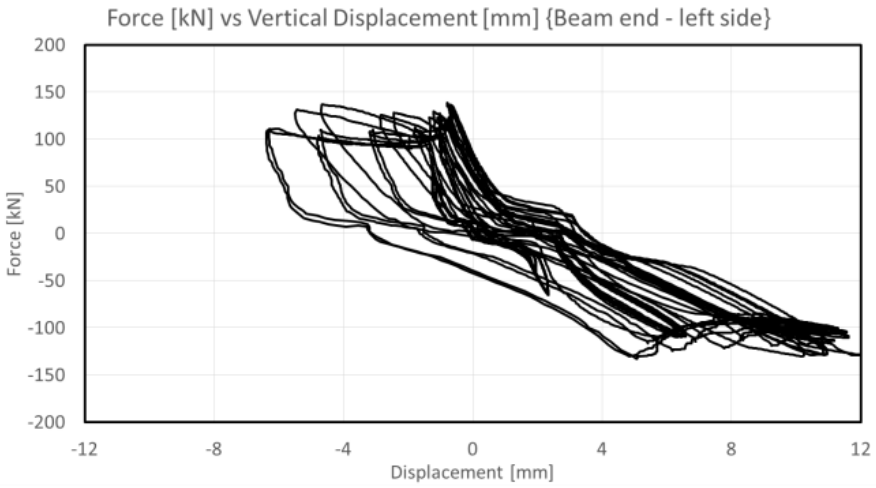

Fig. 4.40 – Force vs Vertical Displacement at the beam end - Left side

Fig. 4.41 – Force vs Vertical Displacement at the beam end - Right side

Main results of TEST FREEDAM-IN270_CYC-2_M4

The global and local behaviour of the FREEDAM-IN270_CYC-2_M4 is in line with the predictions. The friction dampers demonstrated to be able to dissipate the energy avoiding damage in the other components designed as non-dissipative zone, without significant strength degradation. Observing the moment-rotation curves (Fig. 4.44 and Fig. 4.45), it is easy to note an asymmetrical behaviour due to the many factors. The main reason of this asymmetry is represented by a non-symmetrical layout, in fact the rotation centers of the two pendulums located in correspondence of the beam ends are not perfectly aligned.
Considering the displacements measured with the LVDT transducers, in particular analysing the curves (Fig. 4.46 and Fig. 4.47) obtained from the force in the actuator and the displacement measured at the T-stub level (in correspondence of the damper) it can be observed that the hysteretic loops in this case assume a rectangular shape, with a significant energy dissipation capacity and almost no degradation both in terms of stiffness and resistance.

In the previews, the variation of the force in the bolts during the tests has been repeatedly mentioned since it significantly affects the behaviour of the FREEDAM connections. The value of the preload in the bolts of the damper has been monitored by means of four load cells, the diagrams in Fig. 4.48 and 4.49 show a loss of preload in the bolts at the beginning of the tests that increases as far as the loading cycles increase. Furthermore, it is possible to note the oscillation of the value of the forces in the bolts during the test due to the bending developed in the plates of the dampers.

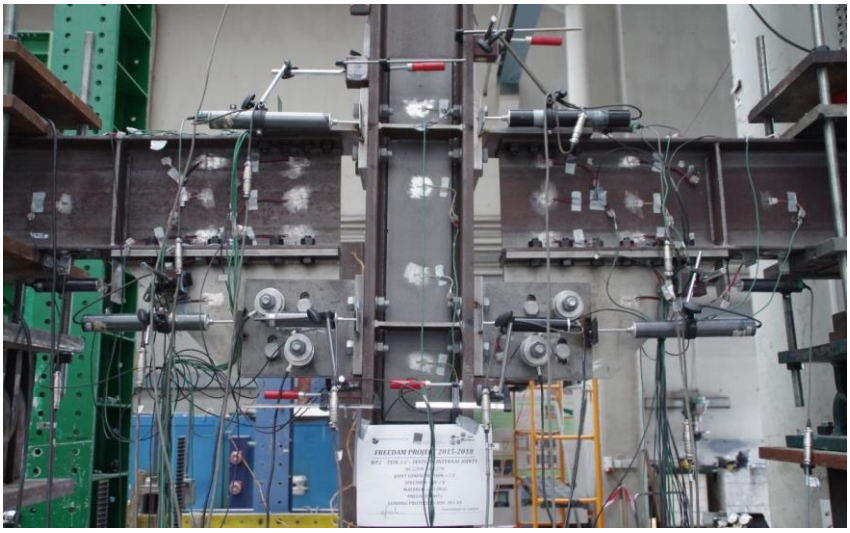

Fig. 4.42 – Setup of the test.

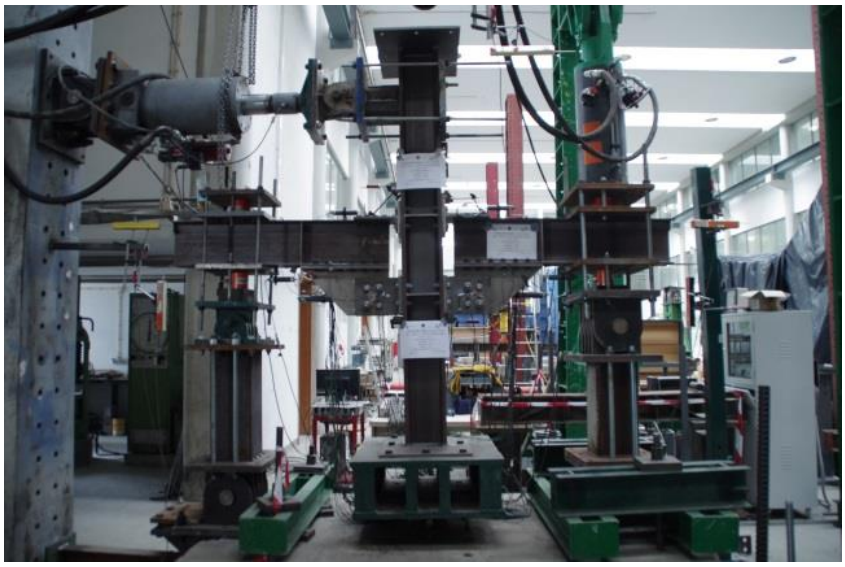

Fig. 4.43 – Setup of the test.

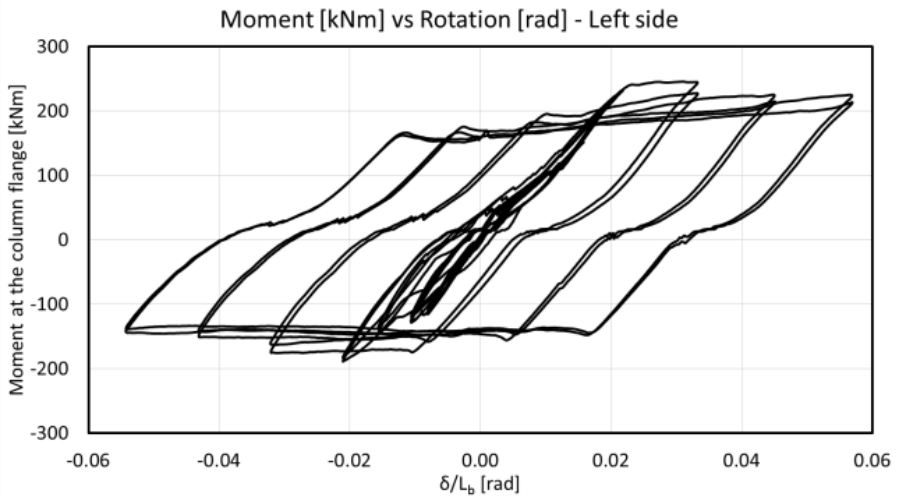

Fig. 4.44 – Moment evaluated at the column's face vs chord rotation – Left side of the joint.

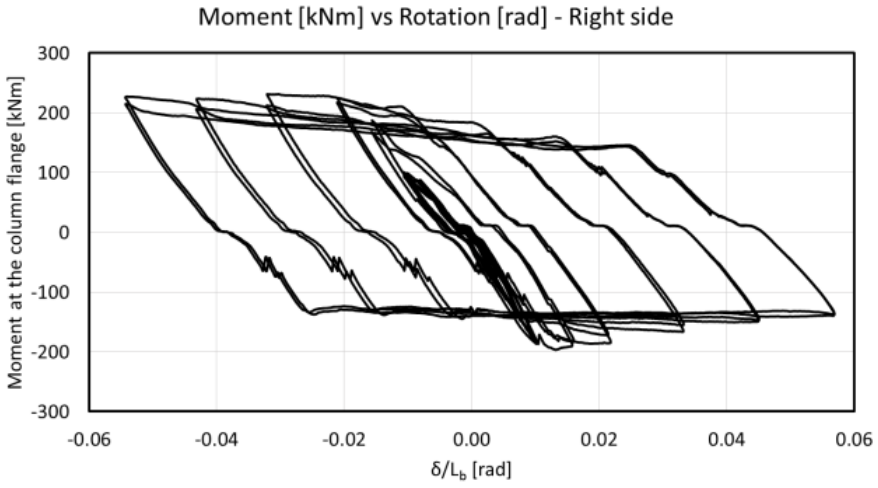

Fig. 4.45 – Moment evaluated at the column's face vs chord rotation – Right side of the joint.

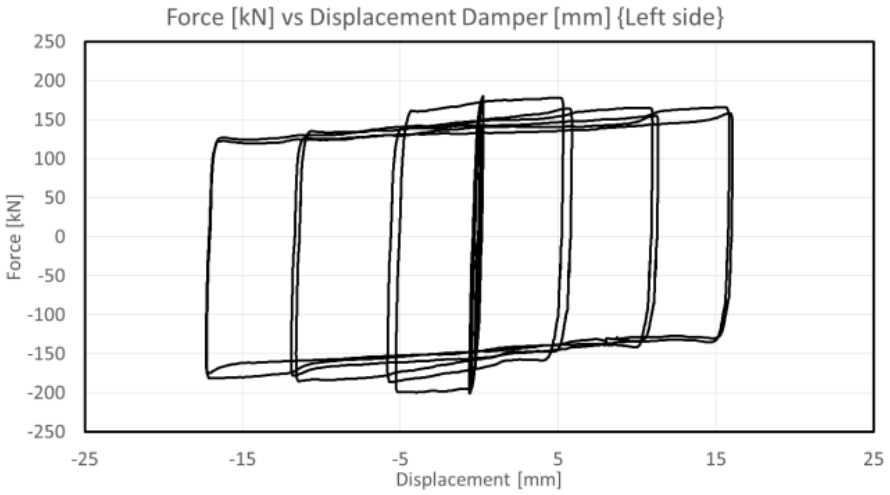

Fig. 4.46 – Force at level of the actuator vs displacement at level of the friction damper – Left.

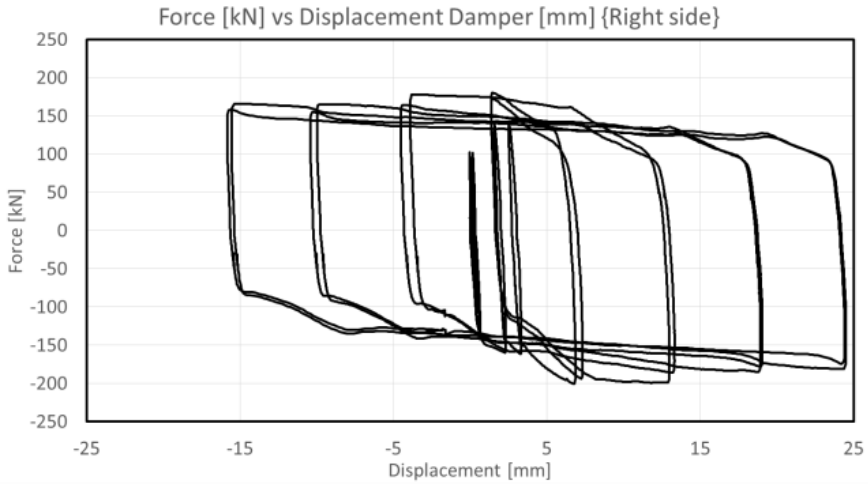

Fig. 4.47 – Force at level of the actuator vs displacement at level of the friction damper – Right

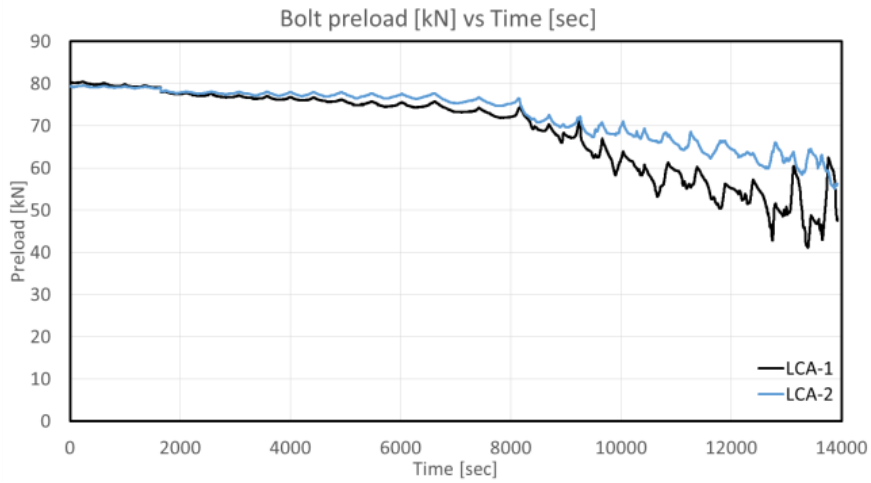

Fig. 4.48 – Bolt preload vs Time - Left side

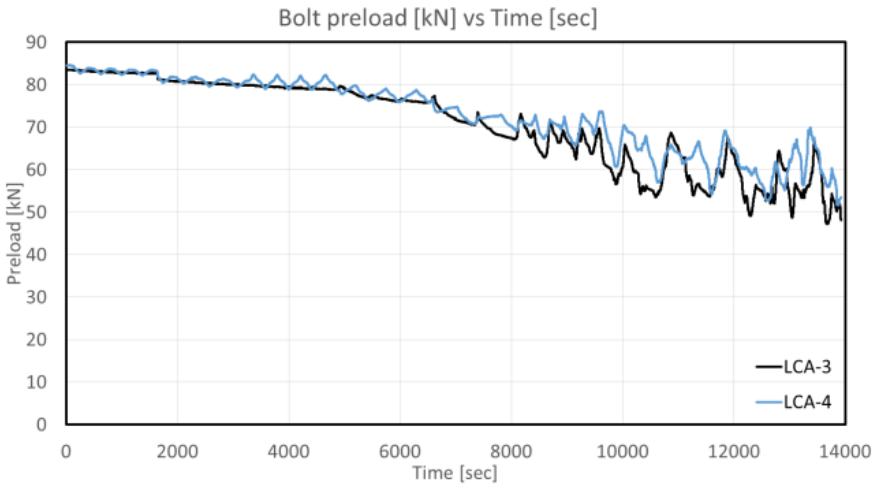

Fig. 4.49 – Bolt preload vs Time - Right side

All the other displacement sensors installed in the connection, as delivered in the following figures, showed that the other joint components practically remained in elastic range (Fig. 4.50 to Fig. 4.57).

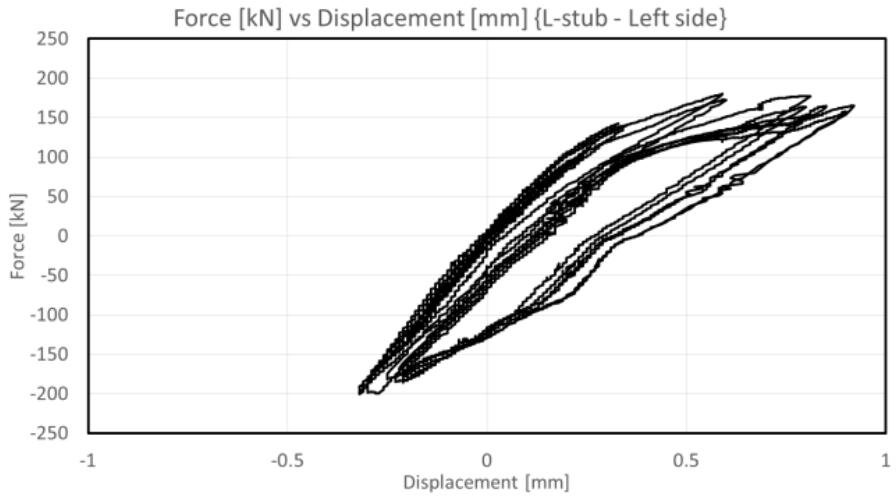

Fig. 4.50 – Force vs Relative displacement between L-stub and column - Left side

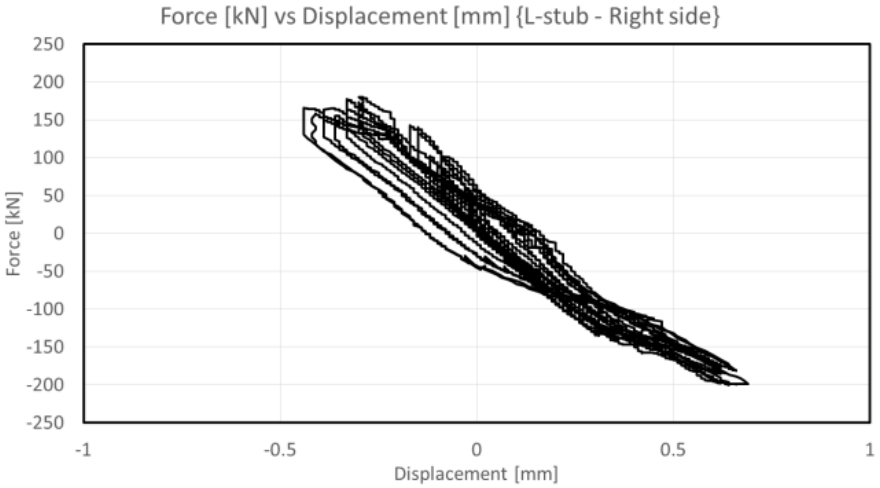

Fig. 4.51 – Force vs Relative displacement between L-stub and column - Right side

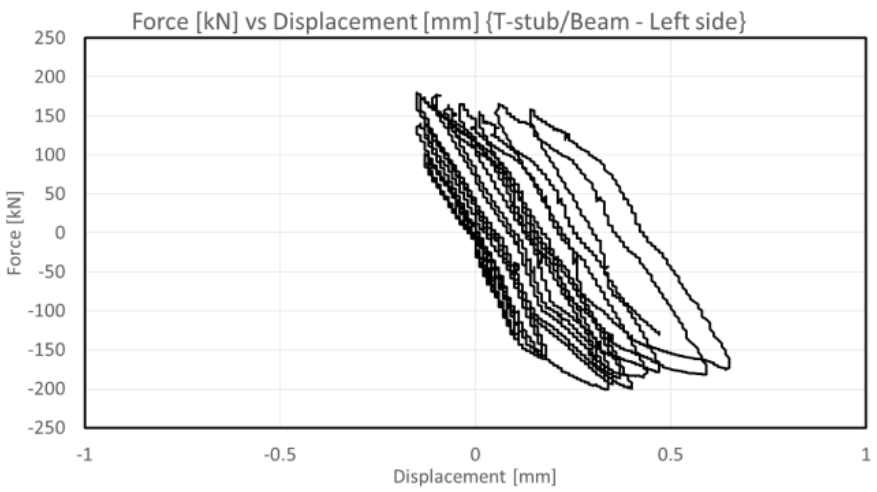

Fig. 4.52 – Force vs Relative displacement between T-stub and beam - Left side

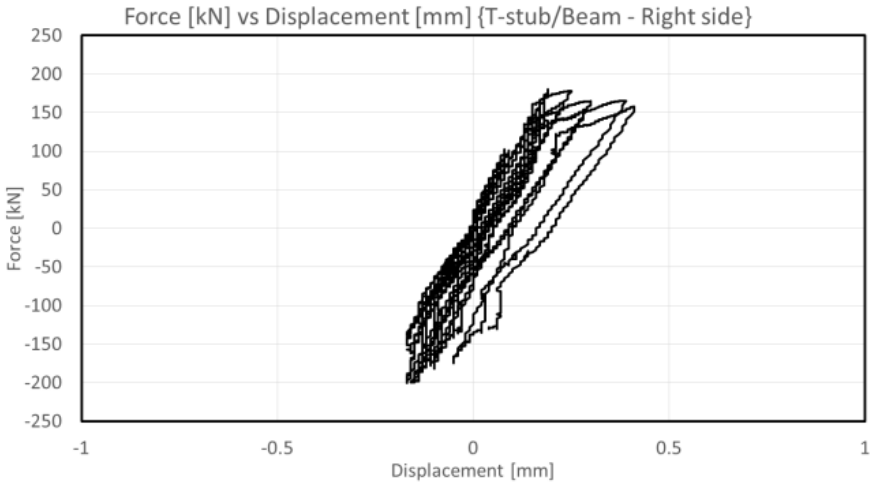

Fig. 4.53 – Force vs Relative displacement between T-stub and beam - Right side

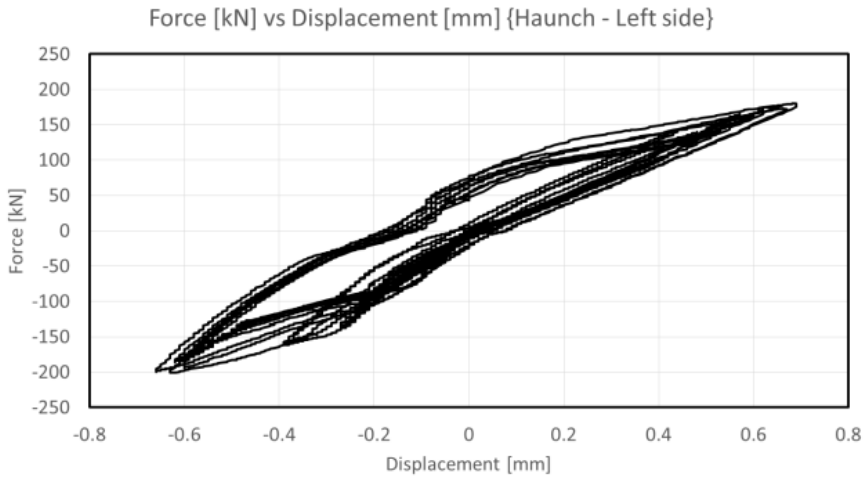

Fig. 4.54 – Force vs Relative displacement between Haunch and Beam - Left side

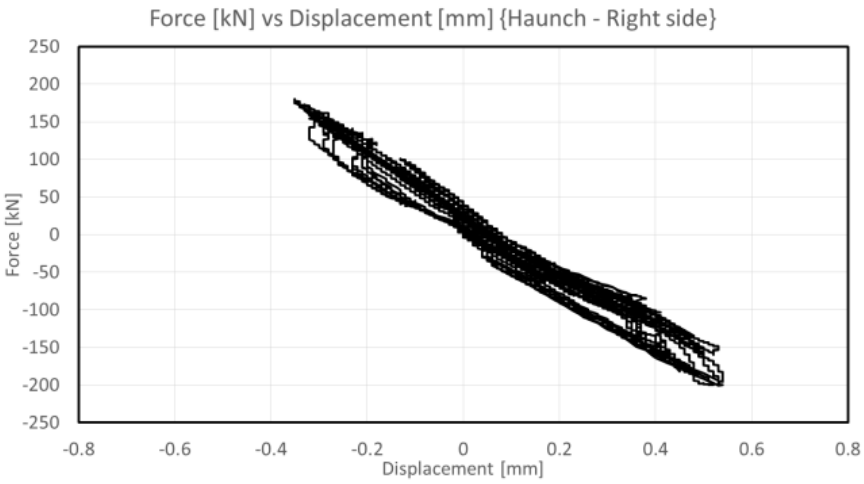

Fig. 4.55 – Force vs Relative displacement between Haunch and Beam - Right side

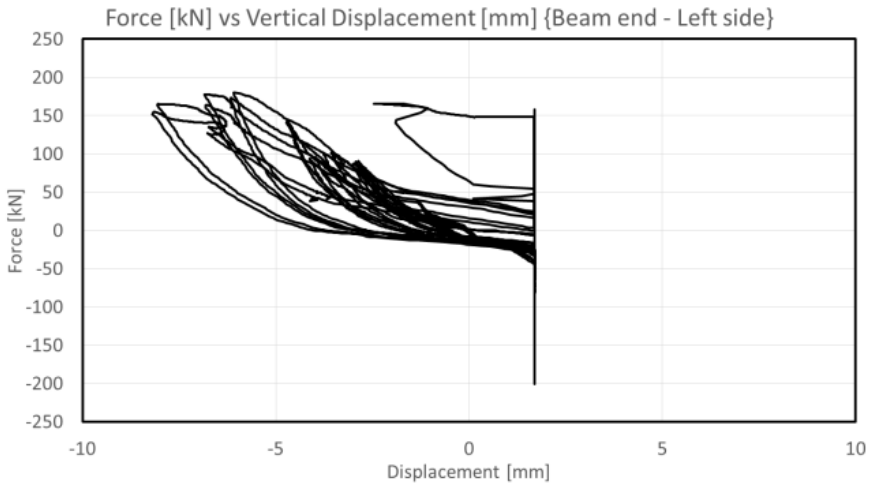

Fig. 4.56 – Force vs Vertical Displacement at the beam end - Left side.

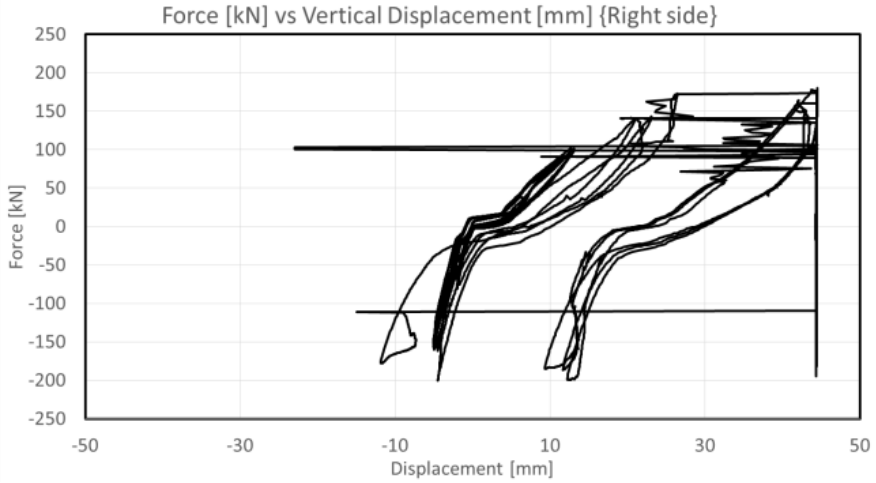

Fig. 4.57 – Force vs Vertical Displacement at the beam end - Right side

Main results of TEST FREEDAM-IN450_CYC-1_M4

The global and local behaviour of the FREEDAM-IN450_CYC-1_M4 is in line with the predictions.

Considering the displacements measured with the LVDT transducers, in particular analysing the curves (Fig. 4.62 and Fig. 4.63) obtained from the force in the actuator and the displacement measured at the T-stub level (in correspondence of the damper) it can be observed that the hysteretic loops in this case assume a rectangular shape, with a significant energy dissipation capacity and almost no degradation both in terms of stiffness and resistance.

In the previews, the variation of the force in the bolts during the tests has been repeatedly mentioned since it significantly affects the behaviour of the FREEDAM connections. The value of the preload in the bolts of the damper has been monitored by means of four load cells, the diagrams in Fig. 4.64 and Fig. 4.65 show a loss of preload in the bolts at the beginning of the tests that increases as far as the loading cycles increase. Furthermore, it is possible to note the oscillation of the value of the forces in the bolts during the test due to the bending developed in the plates of the dampers.

All the other displacement sensors installed in the connection, as delivered in the following figures, showed that the other joint components practically remained in elastic range (Fig. 4.66 to Fig. 4.73).

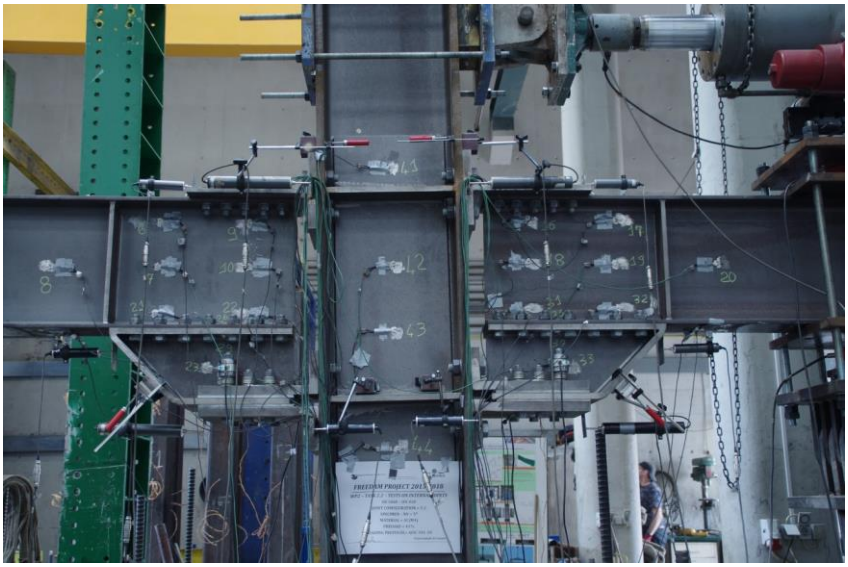

Fig. 4.58 – Setup of the test.

Fig. 4.59 – Setup of the test.

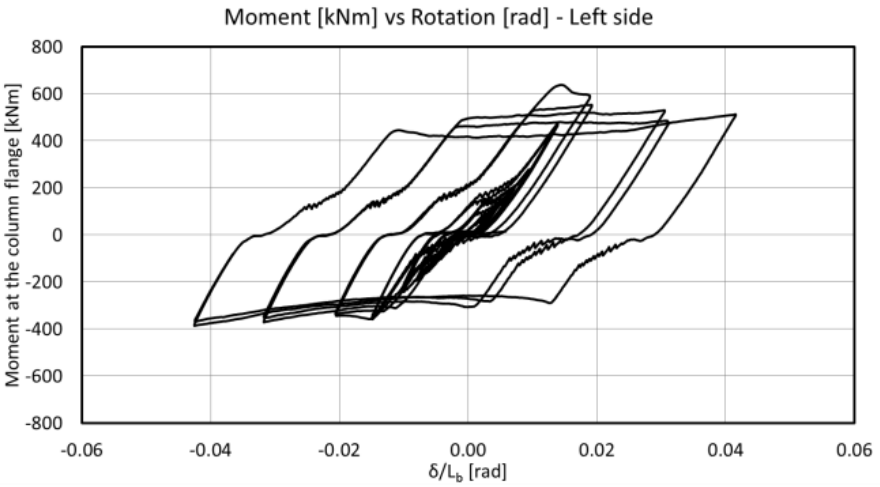

Fig. 4.60 – Moment evaluated at the column's face vs chord rotation – Left side of the joint.

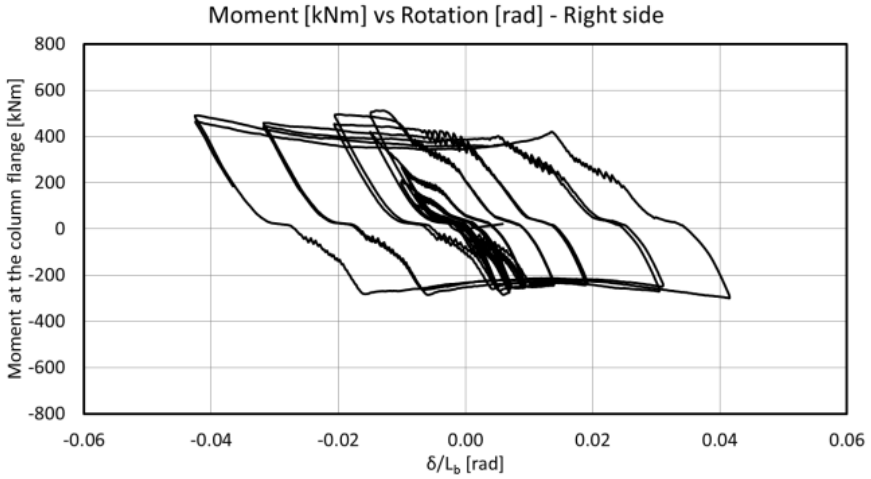

Fig. 4.61 – Moment evaluated at the column's face vs chord rotation – Right side of the joint.

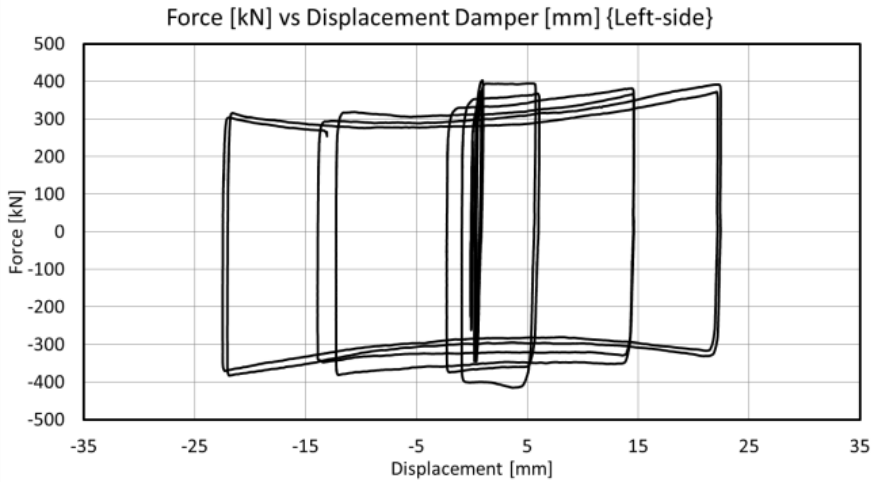

Fig. 4.62 – Force at level of the actuator vs displacement at level of the friction damper – Left.

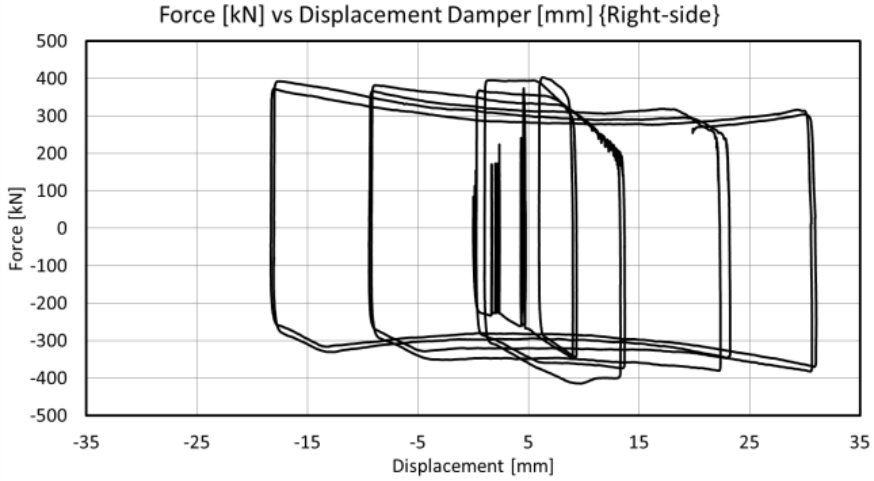

Fig. 4.63 – Force at level of the actuator vs displacement at level of the friction damper – Right

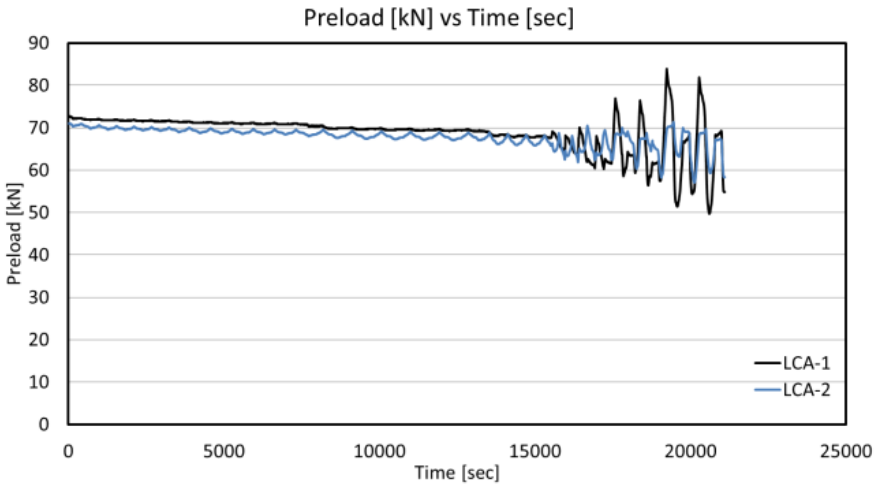

Fig. 4.64 – Bolt preload vs Time - Left side.

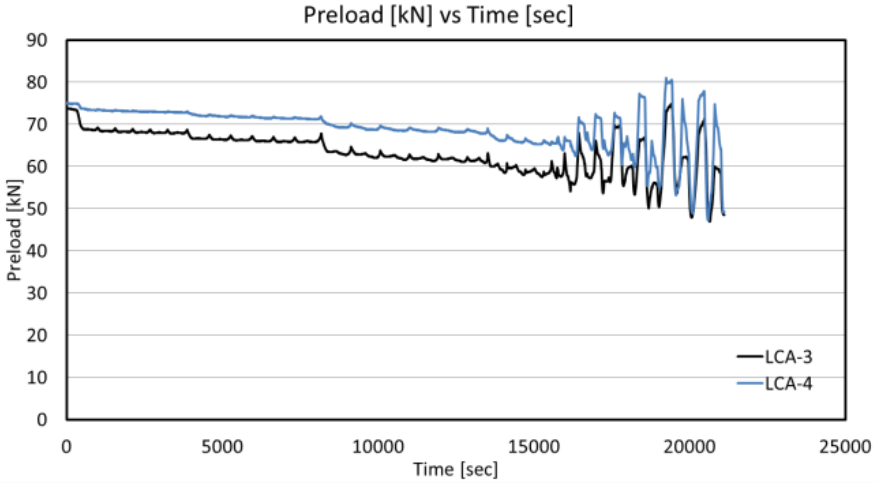

Fig. 4.65 – Bolt preload vs Time - Right side

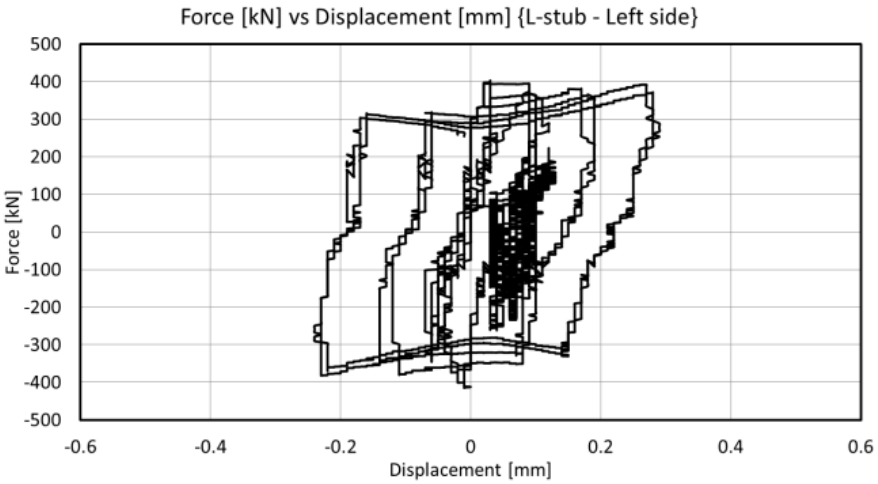

Fig. 4.66 – Force vs Relative displacement between L-stub and column - Left side.

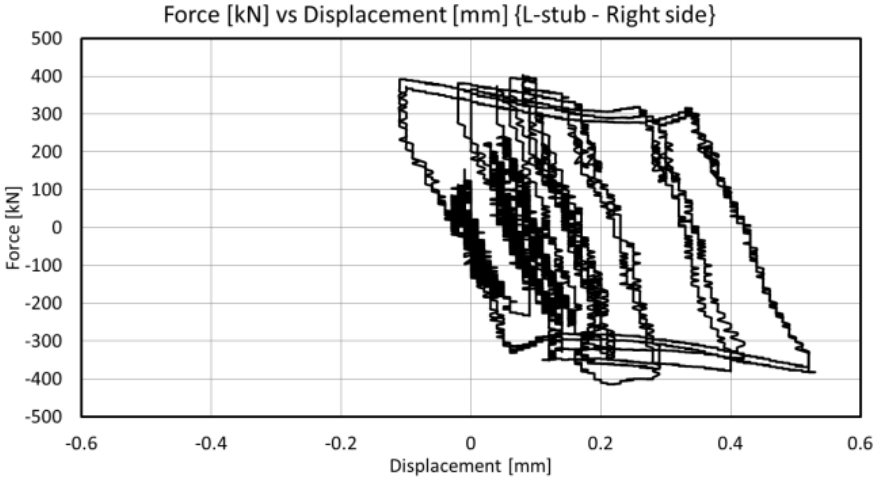

Fig. 4.67 – Force vs Relative displacement between L-stub and column - Right side

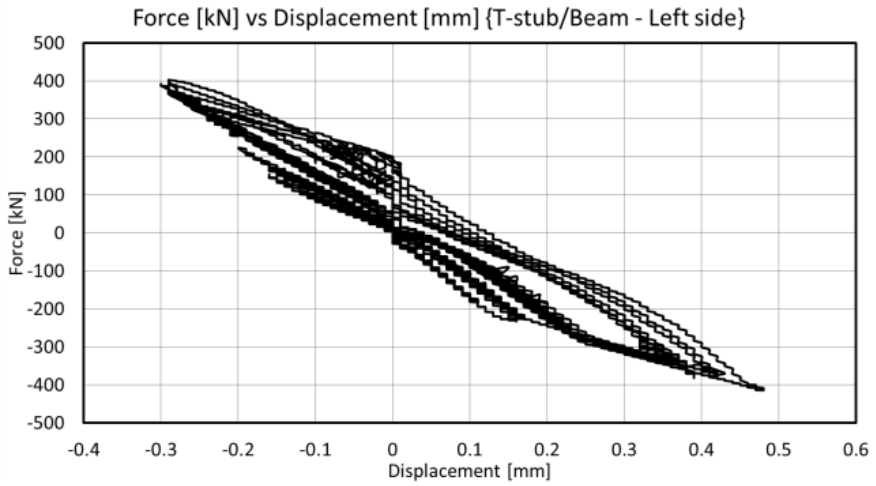

Fig. 4.68 – Force vs Relative displacement between T-stub and beam - Left side.

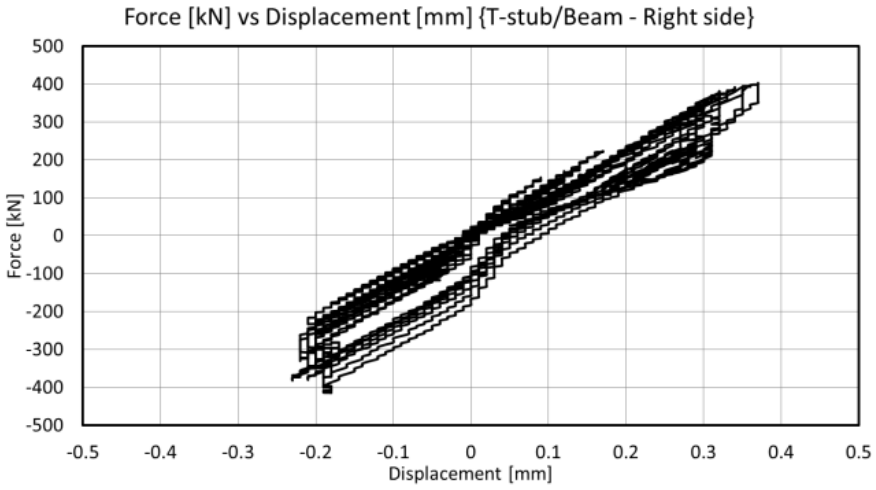

Fig. 4.69 – Force vs Relative displacement between T-stub and beam - Right side

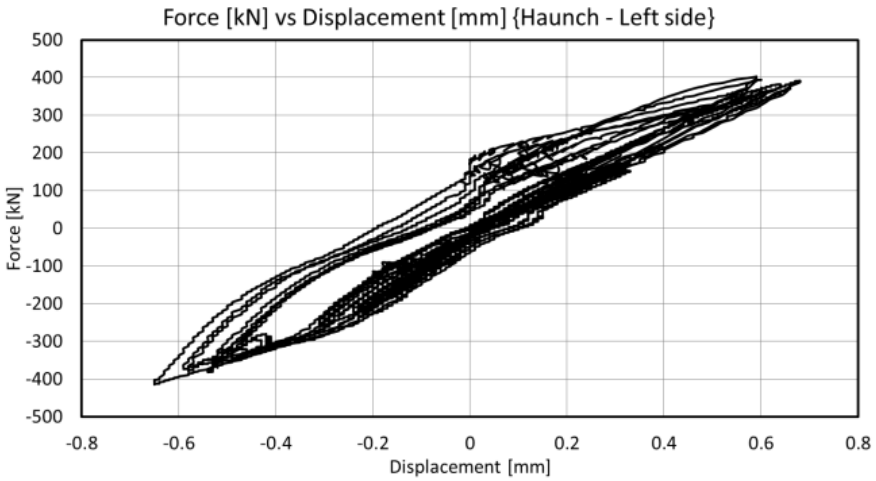

Fig. 4.70 – Force vs Relative displacement between Haunch and Beam - Left side.

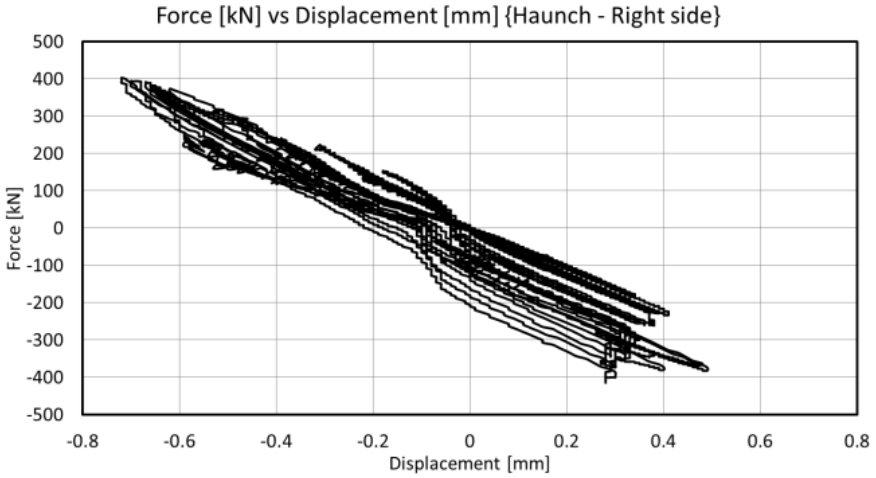

Fig. 4.71 – Force vs Relative displacement between Haunch and Beam - Right side

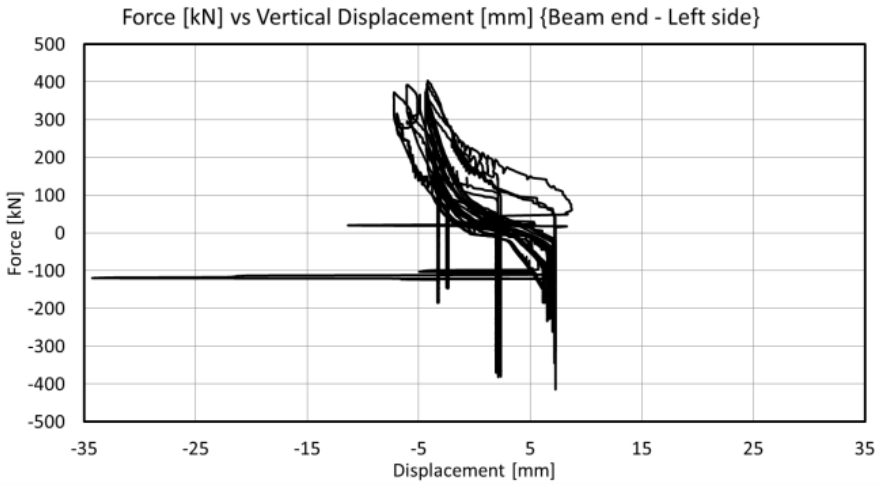

Fig. 4.72 – Force vs Vertical Displacement at the beam end - Left side

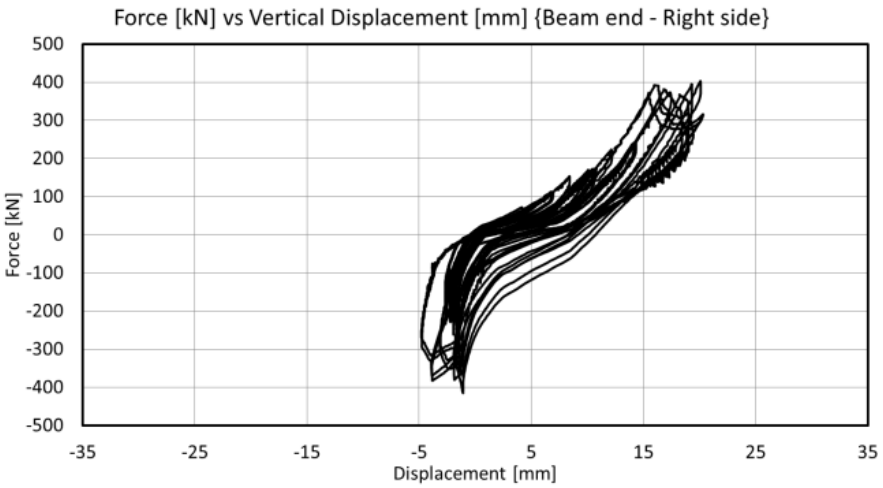

Fig. 4.73 – Force vs Vertical Displacement at the beam end - Right side

Main results of TEST FREEDAM-IN450_CYC-2_M4

The global and local behaviour of the FREEDAM-IN450_CYC-2_M4 is in line with the predictions.

Considering the displacements measured with the LVDT transducers, in particular analysing the curves (Fig. 4.78 and Fig. 4.79) obtained from the force in the actuator and the displacement measured at the T-stub level (in correspondence of the damper) it can be observed that the hysteretic loops in this case assume a rectangular shape, with a significant energy dissipation capacity and almost no degradation both in terms of stiffness and resistance.

In the previews, the variation of the force in the bolts during the tests has been repeatedly mentioned since it significantly affects the behaviour of the FREEDAM connections. The value of the preload in the bolts of the damper has been monitored by means of four load cells, the diagrams in Fig. 4.80 and Fig. 4.81 show a loss of preload in the bolts at the beginning of the tests that increases as far as the loading cycles increase. Furthermore, it is possible to note the oscillation of the value of the forces in the bolts during the test due to the bending developed in the plates of the dampers.

All the other displacement sensors installed in the connection, as delivered in the following figures, showed that the other joint components practically remained in elastic range (Fig. 4.82 to Fig. 4.89).

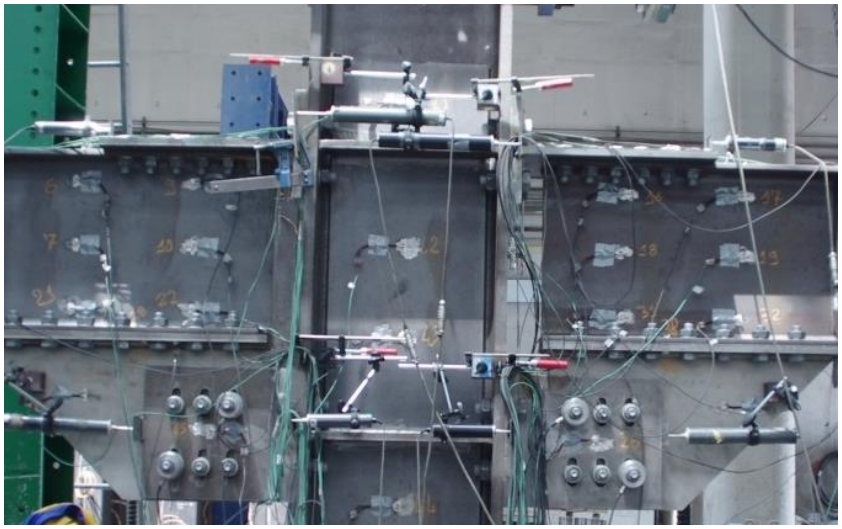

Fig. 4.74 – Setup of the test.

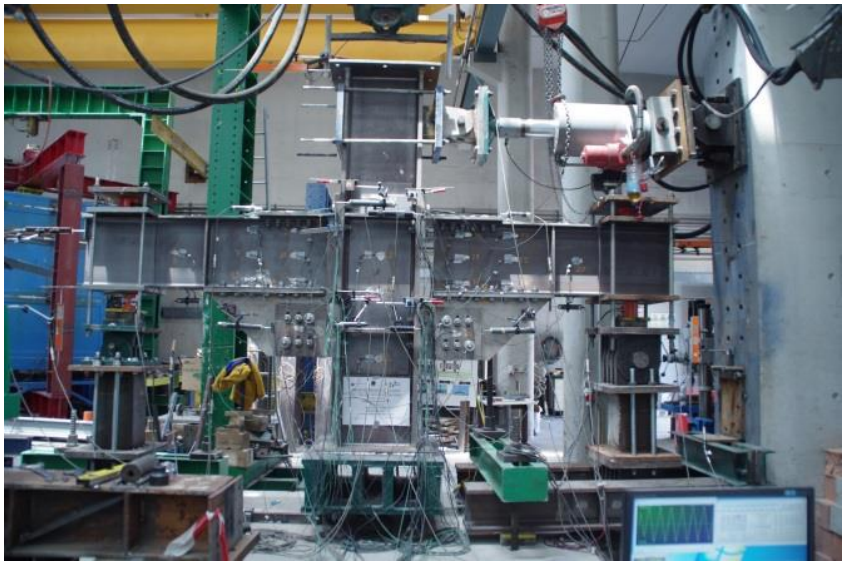

Fig. 4.75 – Setup of the test.

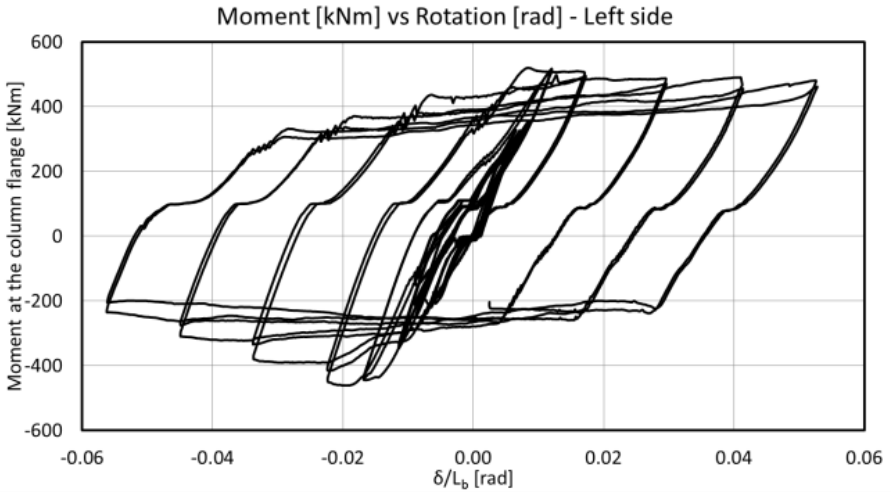

Fig. 4.76 – Moment evaluated at the column's face vs chord rotation – Left side of the joint.

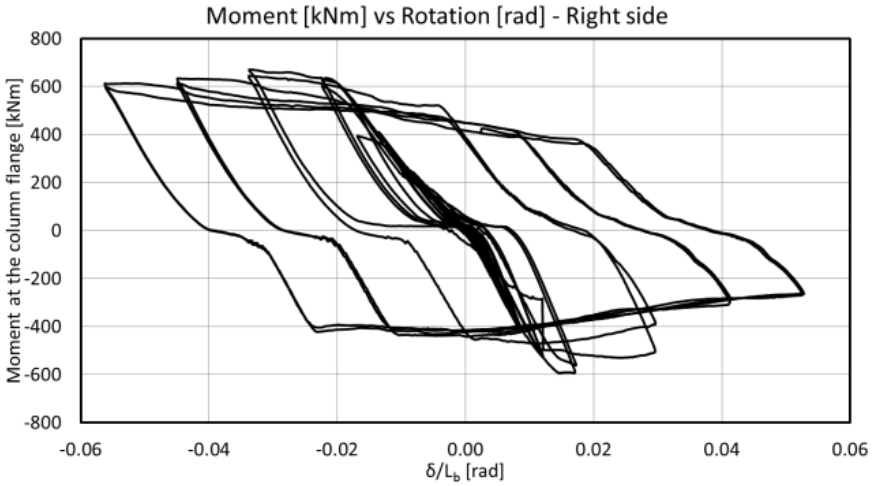

Fig. 4.77– Moment evaluated at the column's face vs chord rotation – Right side of the joint.

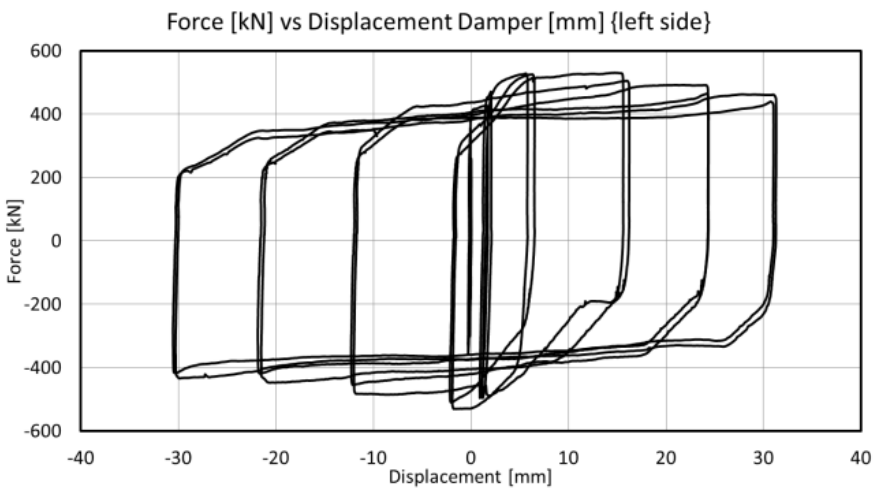

Fig. 4.78 – Force at level of the actuator vs displacement at level of the friction damper – Left.

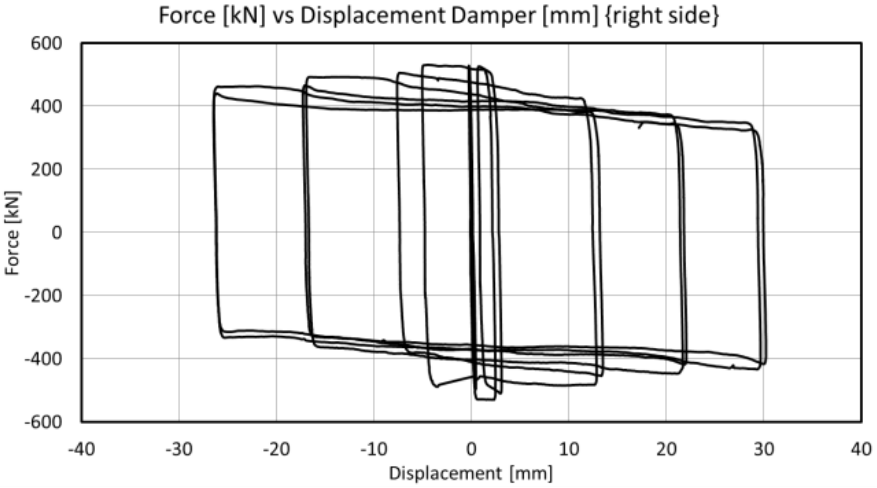

Fig. 4.79 – Force at level of the actuator vs displacement at level of the friction damper – Right

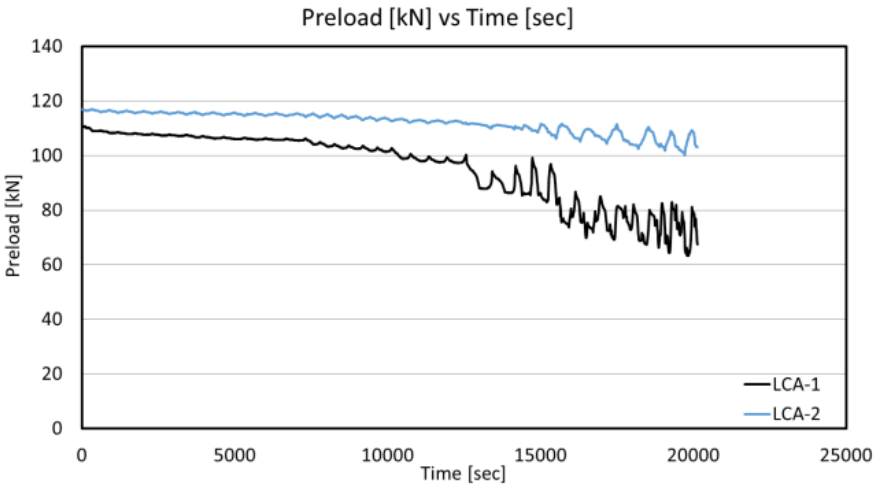

Fig. 4.80 – Bolt preload vs Time - Left side

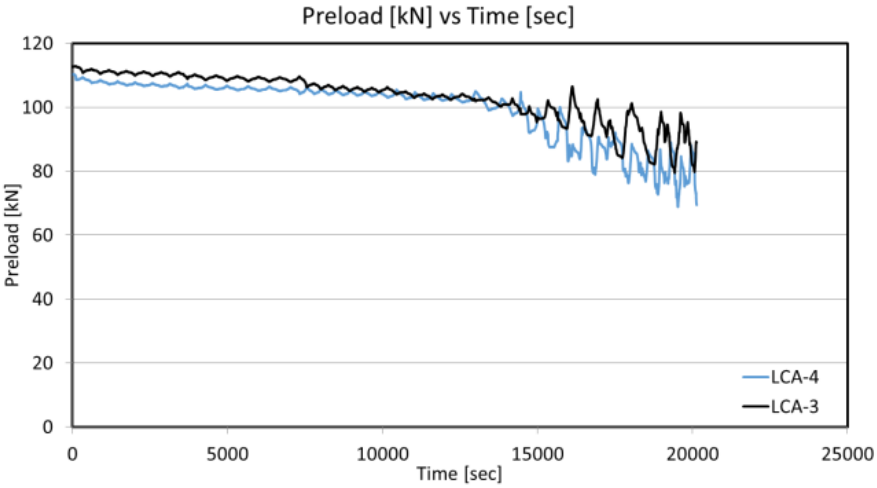

Fig. 4.81 – Bolt preload vs Time - Right side

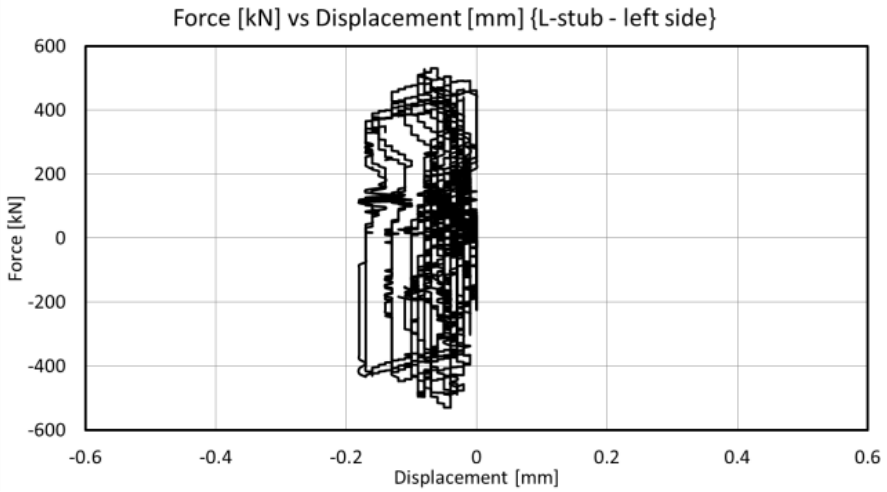

Fig. 4.82 – Force vs Relative displacement between L-stub and column - Left side

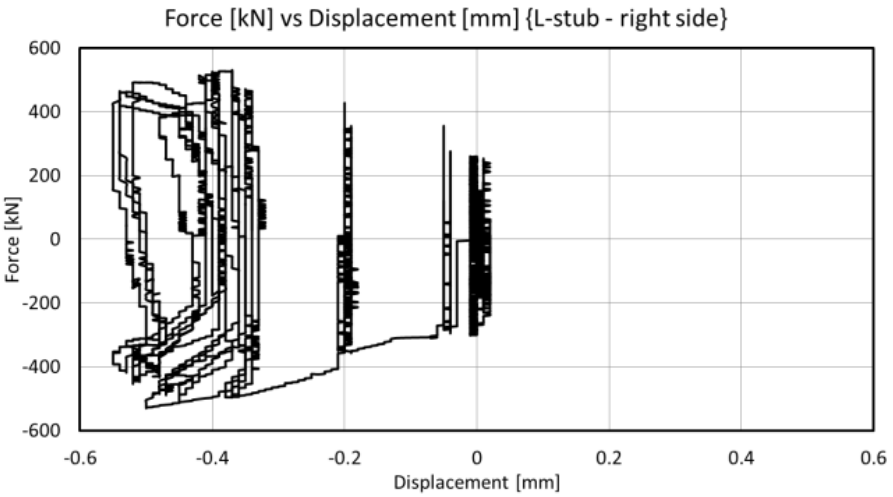

Fig. 4.83 – Force vs Relative displacement between L-stub and column - Right side

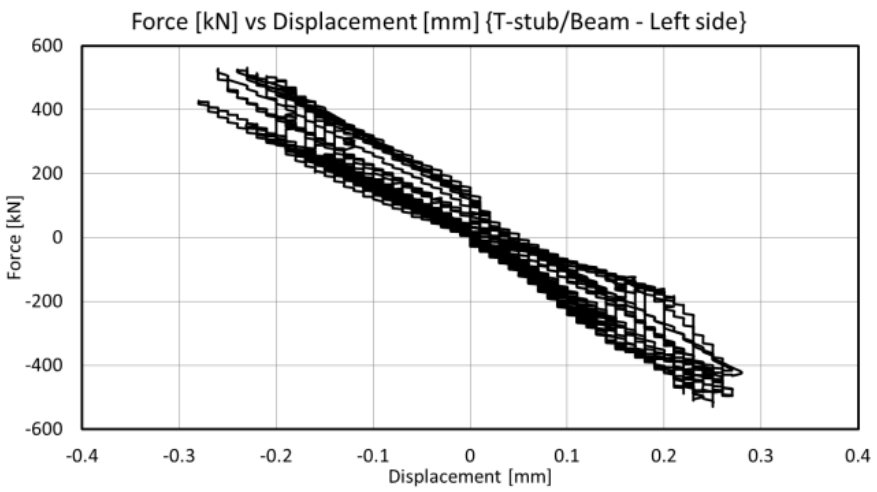

Fig. 4.84 – Force vs Relative displacement between T-stub and beam - Left side.

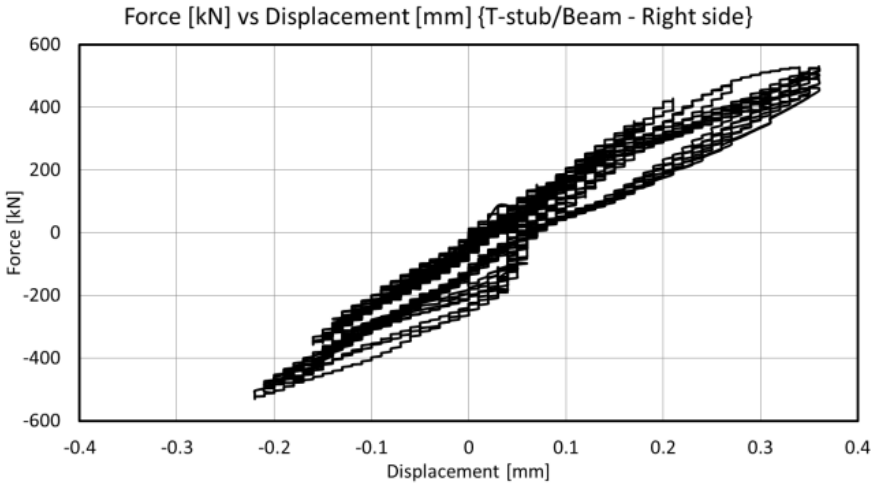

Fig. 4.85 – Force vs Relative displacement between T-stub and beam - Right side

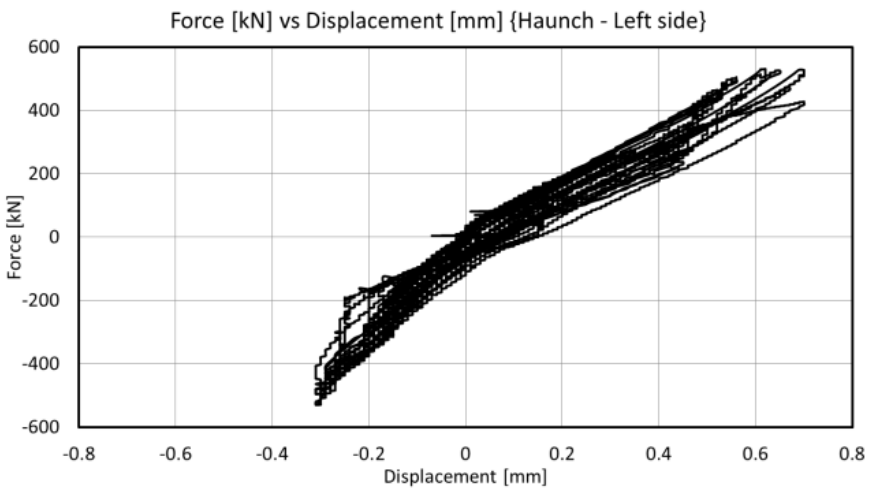

Fig. 4.86 – Force vs Relative displacement between Haunch and Beam - Left side.

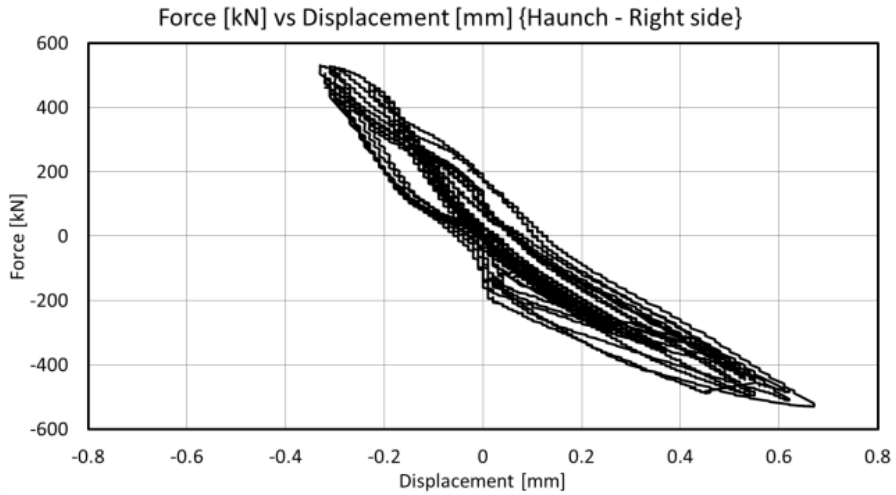

Fig. 4.87 – Force vs Relative displacement between Haunch and Beam - Right side

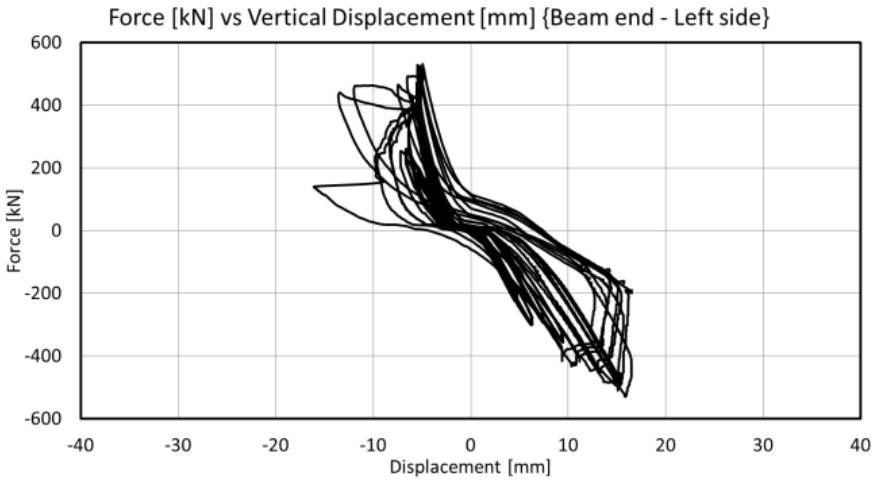

Fig. 4.88 – Force vs Vertical Displacement at the beam end - Left side.

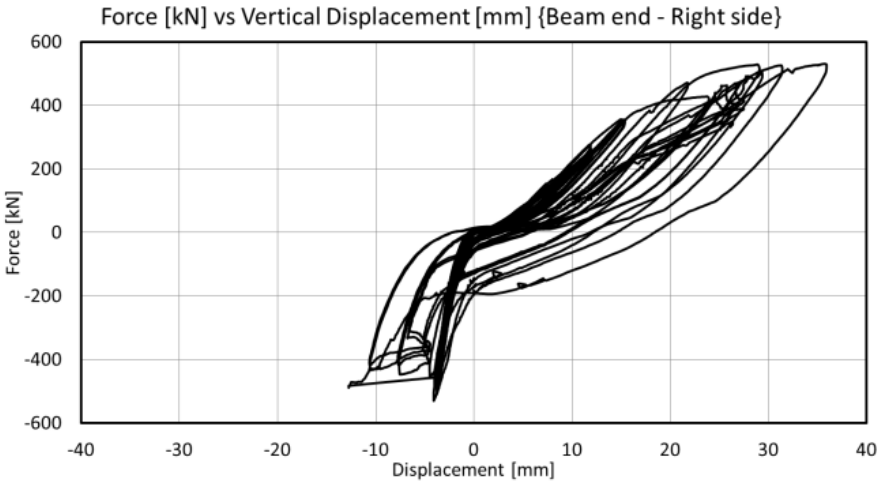

Fig. 4.89 – Force vs Vertical Displacement at the beam end - Right side

4.3. FE Models

4.3.1. Introduction to the finite element simulations

The main objectives of these FE models is to reproduce the response of beam-to-column joints equipped with friction devices and to offer insights on the sensitivity of the joint response with regards to the main parameters determining the joint capacity.

In particular, three dimensional finite element models of the tested joints were created using the advanced software package ABAQUS v6.14.4, and analysed considering the real experimental conditions (for the calibration of the model) and the key parameters that influence the device response.

4.3.2. Geometry description and modelling assumptions

Two internal joint configurations of the tests performed in the experimental campaign have been modelled.

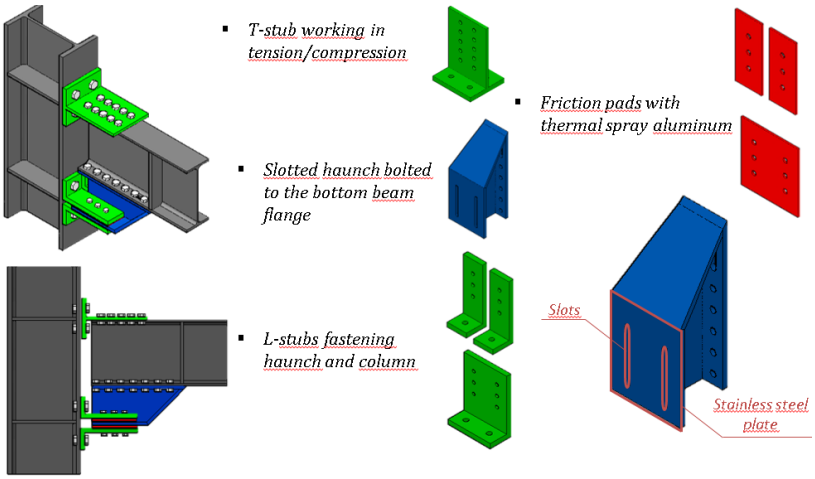

Fig. 4.90 – FREEDAM connection with horizontal friction pads

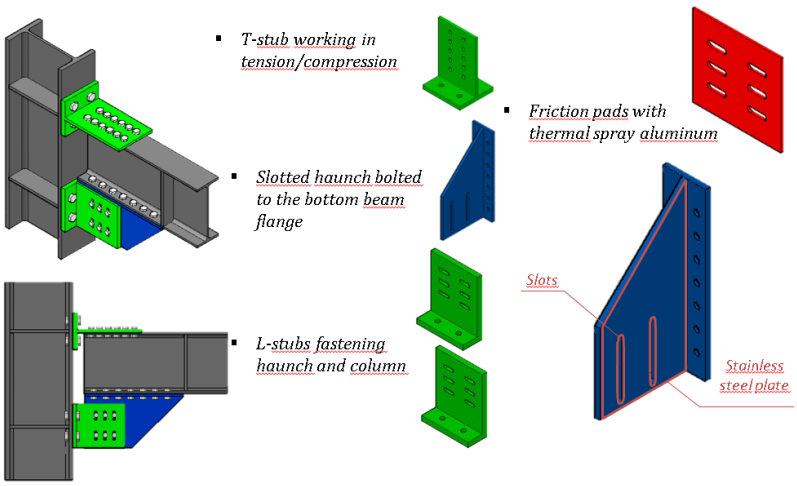

Fig. 4.91 – FREEDAM connection with vertical friction pads

In particular, the joints of smaller dimension equipped in one case with friction pads in horizontal configuration and in the second case in vertical configuration have been modelled.

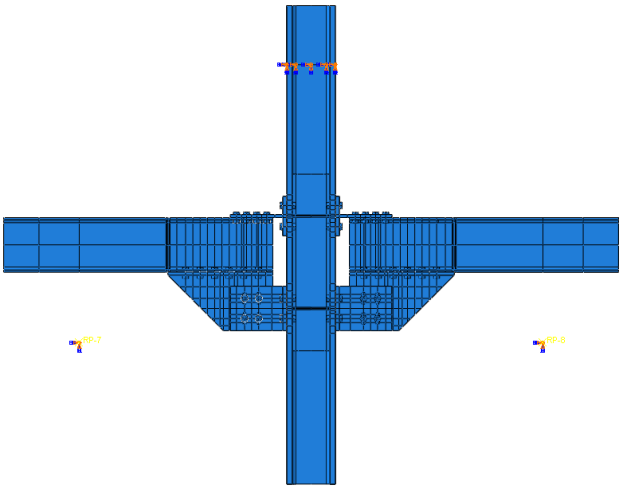

Fig. 4.92 – FE model of the Internal joint equipped with FREEDAM connection

Abaqus v6.14.4 is used to carry out the finite element simulations. The geometrical features of the examined joints are reported in Fig. 4.90 and 4.91. Structured mesh technique is used and the finite element type C3D8R (an 8-node linear brick with reduced integration) is adopted for steel beams, columns and high strength bolts.

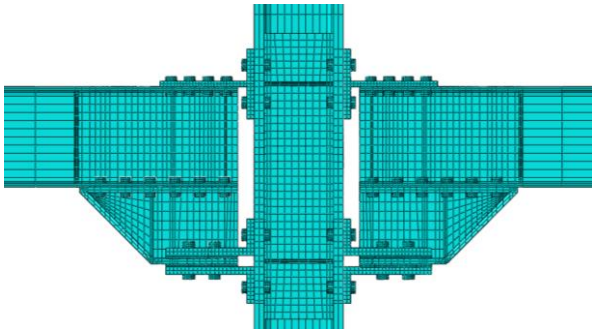

Fig. 4.93 – FE model - mesh

In Fig. 4.92 an example the FE model (basic view) for assembly with friction pads in vertical is shown, while in Fig. 4.93 a detail of the FE model (meshed view) for the assembly with friction pads in horizontal position is shown. Bolts were modelled by meshing a solid cylinder having the nominal circular gross area of the bolt.

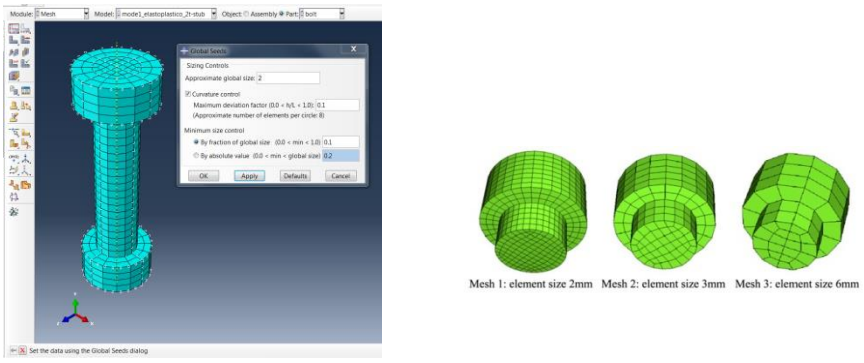

Fig. 4.94 – FE model - bolts

The interactions between the surfaces in contact (e.g. bolt-to-plates, plate-to-plate) are modelled considering both "Normal" and "Tangential" behaviour. The former is implemented considering "Hard Contact", while the latter is modelled differently for the steel–to-steel interfaces and for the friction pad-to-steel interfaces. The main difference between the two types of contacts is the definition of the friction coefficient. For the steel-to-steel surfaces a constant value equal to 0.3 is considered, while the dynamic friction coefficients obtained from lap-shear tests with the friction material considered are used for the friction damper (Table 4.2). The clamping of the bolts is modelled by means of the "Bolt load" option available in the FE software. For the bolts belonging to the friction device, the values from Table 4.5 were used, in order to be consistent with the design and experimental assumptions. All other bolts were fully preloaded, as recommended by EN1993 1-8 [1].

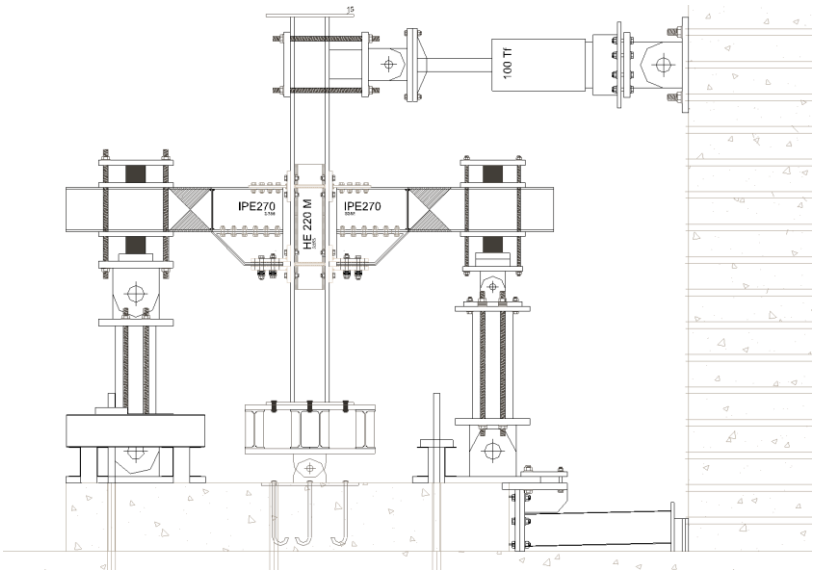

Fig. 4.95 – Test layout for internal joints with HE220M column and IPE270 beams

The boundary conditions are modelled to be representative of those adopted for the experimental set-up (see Figs. 4.95 - 4.97). Both column ends have translational and rotational degrees of freedom restrained with the exception of the in-plane rotation, and the beam is restrained to prevent the lateral-torsional buckling.

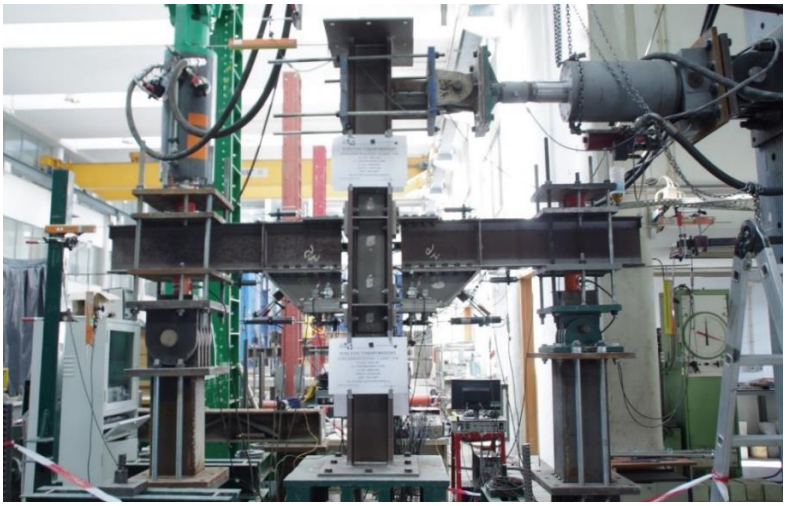

Fig. 4.96 – Specimen during the test

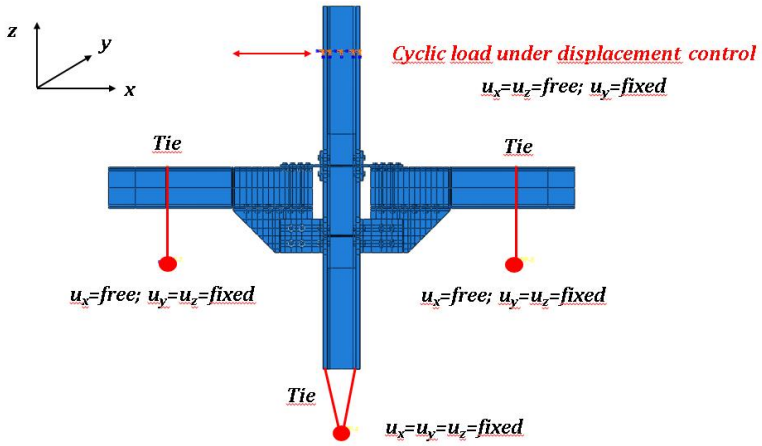

Fig. 4.97 – Boundary conditions for the FE model

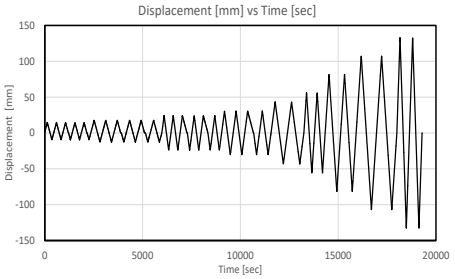

V [mm/sec]	Step	θ [rad]	n° cicli
0,5	1	0.00375	6
	2	0.005	6
1	3	0.0075	6
	4	0.01	4
2	5	0.015	2
	6	0.02	2
	7	0.03	2
	8	0.04	
4	9	0.05	2
	10	0.06	2
	11	0.07	2
6	12	0.08	2
	13	0.09	2
	14	0.10	2
	15	0.11	2

Fig. 4.98 – Loading protocol according to AISC 341/2010 [2]

The loads are applied in the section corresponding to the actual position of the actuator. The cyclic displacement histories are alternatively applied. The AISC 341-10 [2] (Fig. 4.98) loading protocol is used for cyclic tests and numerical analyses.

4.3.3. Monitored parameters

Throughout the numerical investigations, the following parameters were monitored:

- The Bending moment-chord rotation (M - θ) curve evaluated based on Fig. 4.99;
- The equivalent plastic deformations (PEEQ) in the FEAs;
- The variation of bending moment with the investigated parameter

$$\Gamma^{(+)} = 1 + \frac{M_{o.5N_b}^{(+)} - M_{N_b}^{(+)}}{M_{N_b}^{(+)}} \tag{4.94}$$

$$\Gamma^{(-)} = 1 + \frac{M_{o.5N_b}^{(-)} - M_{N_b}^{(-)}}{M_{N_b}^{(-)}} \tag{4.95}$$

- The variation of bending moment under hogging and sagging

$$\Delta M^{(+/-)}/M^{(-)} = 1 + \frac{M^{(-)} - M^{(+)}}{M^{(-)}} \tag{4.96}$$

where:

Γ(+) and *Γ(-)* are the hogging and sagging bending moment capacity variation, respectively, considering alternatively the change in the parameter from the design value (N_b or $\mu_{5\%}$) to the predefined values ($0.5N_b$ and $1.5N_b$ for clamping force or μ_{avg} and $\mu_{95\%}$ for the friction coefficient).

M(+) and *M(-)* are the sagging and hogging bending moments. The subscripts depict the analysis from which the bending moment is taken, e.g. with clamping force equal to either N_b or $0.5N_b$.

ΔM (+/-)/M (-) depicts the differences between the bending moment under hogging and sagging loading conditions.

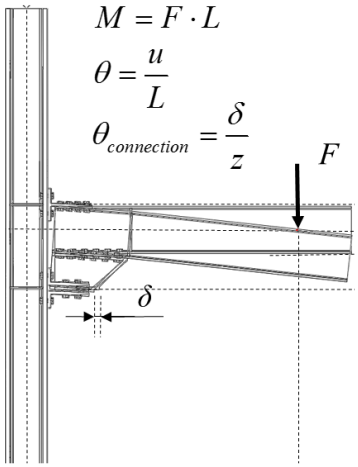

Fig. 4.99 – Static scheme for the evaluation of the bending moment

4.3.4. Experimental results vs. FE analyses

In order to evaluate the fitness of the modelling assumptions, the results of preliminary analyses simulating the experimental conditions (i.e. the design friction coefficient is the dynamic 5% fractile equal to 0.53 and damper-side bolt clamping considered as in Table 4.5) are compared with the results of experimental tests performed at University of Coimbra.

As it can be recognized observing the results reported in the following, the simulated response accurately reproduces the experimental behaviour. In particular, for the small joint assemblies, the overall response (in terms of M - θ), the friction device response ($M - \theta$ connection) and the observable plastic deformation at the assembly level, find very good matches when comparing the experimental results with the numerical analyses.

The limited PEEQ concentrations at the base of the Tee and L-stubs' webs can be explained by the fact that the nominal S355 steel properties were used, instead of the actual ones. As during the experiments, no damage was observed in these regions, it can be safely assumed that the material has higher strength and subsequent analyses with the real material properties can prove this.

Another observation made based on the moment-rotation curves, valid for all models, is that the models do not reproduce the first cycles due to the simplified friction interaction law, where static friction coefficient is not accounted for. However, this is deemed to be of minor importance in the assembly response.

Horizontal configuration

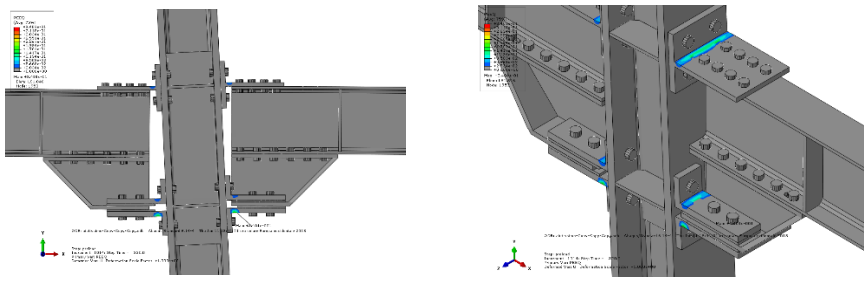

Fig. 4.100 – Plastic deformation in the connection

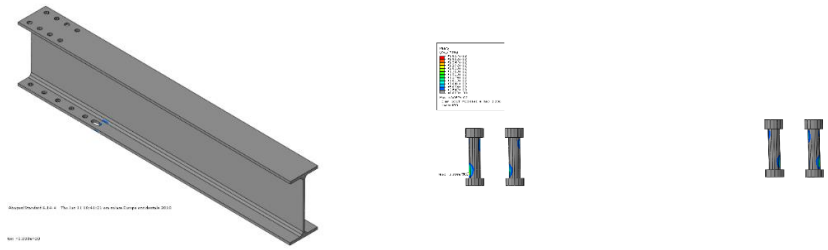

Fig. 4.101 – Plastic deformation for the beam and the bolts

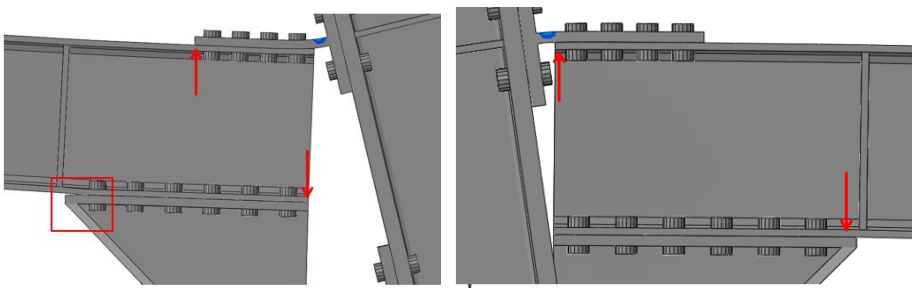

Fig. 4.102 – Schemes of the forces on the part of the connection during the test

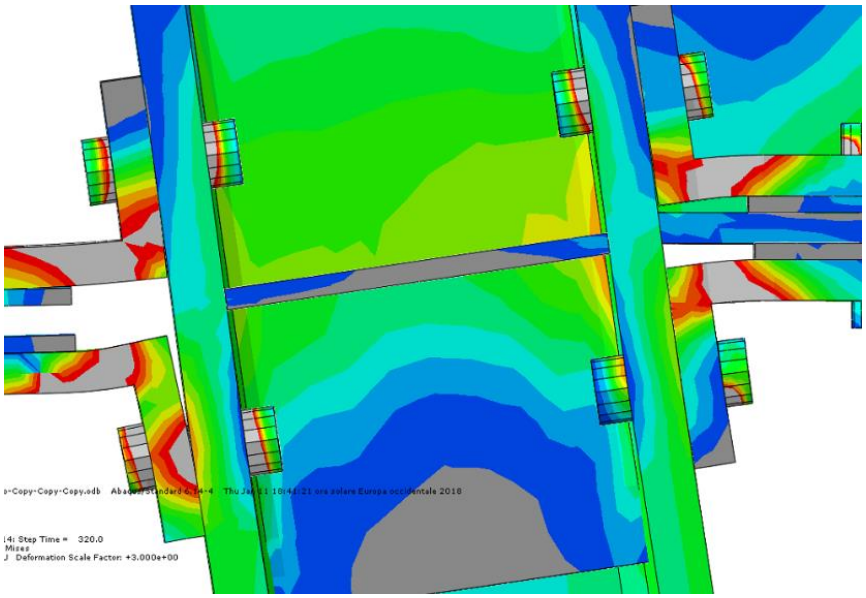

Fig. 4.103 – Stresses in the nodal area

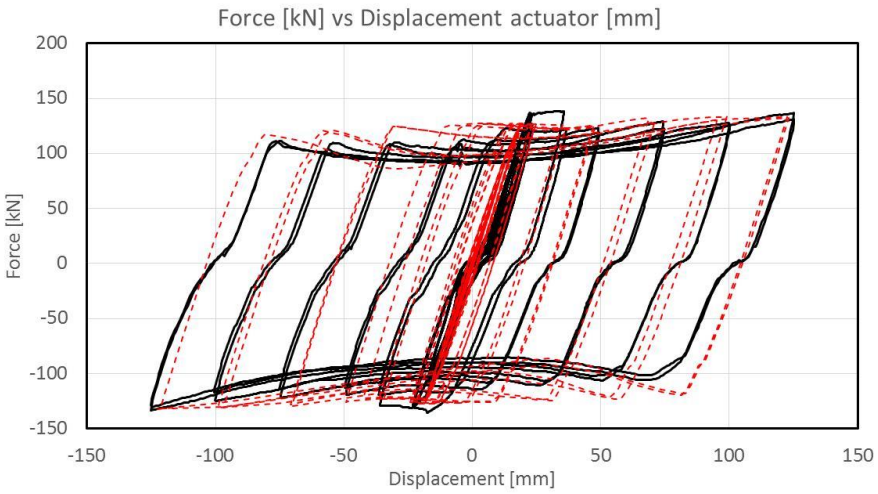

Fig. 4.104 – Comparison between experimental results and FE model (Actuator)

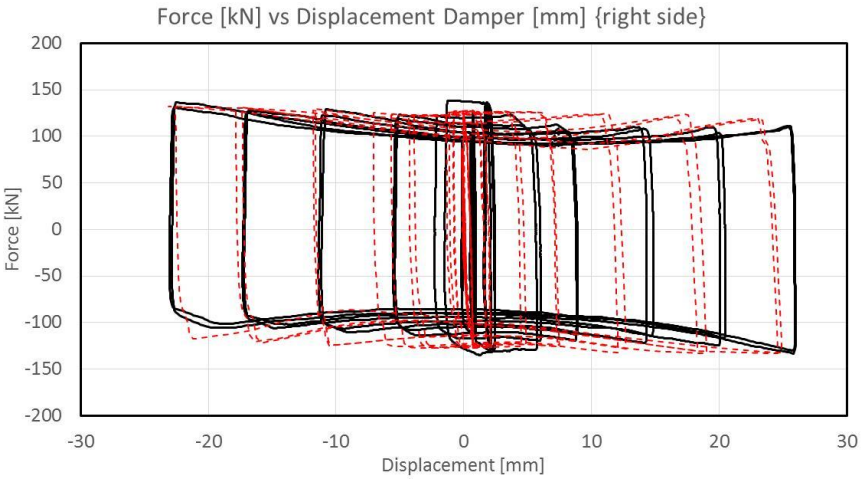

Fig. 4.105 – Comparison between experimental results and FE model (Damper-Right side)

Vertical configuration

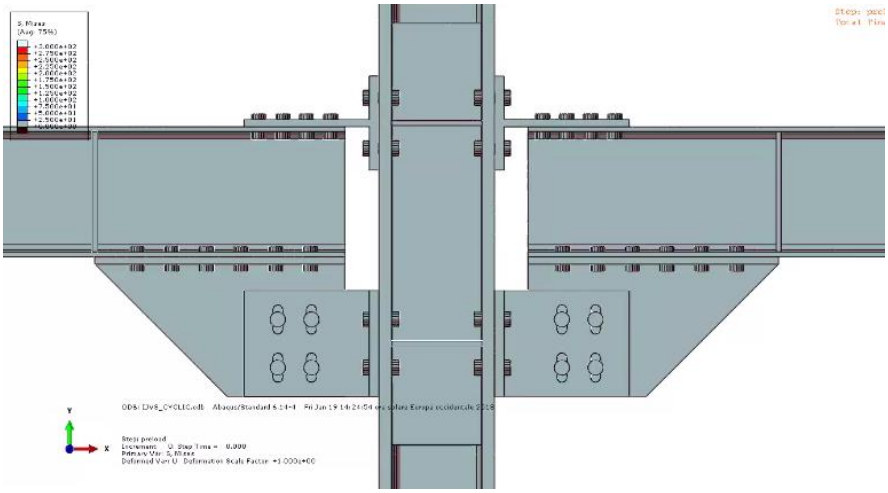

Fig. 4.106 – FE model – vertical configuration

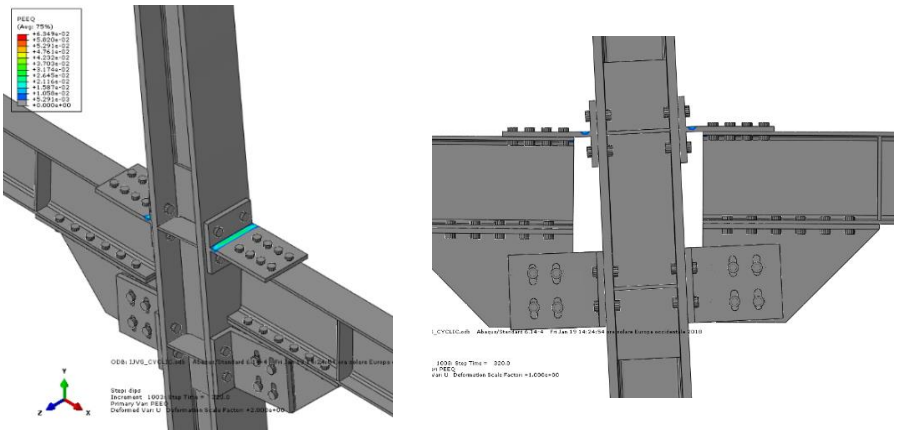

Fig. 4.107 – Plastic deformation in the connection

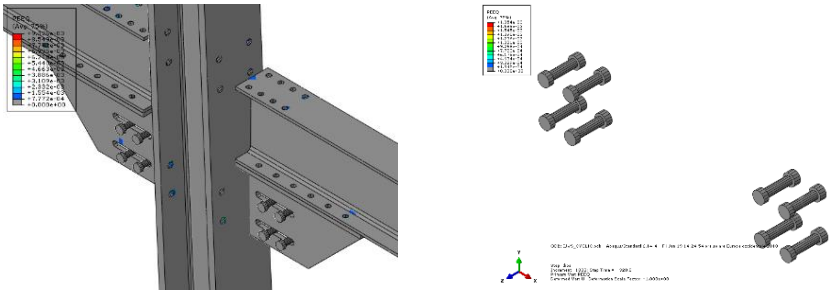

Fig. 4.108 – Plastic deformation for the beam and the bolts

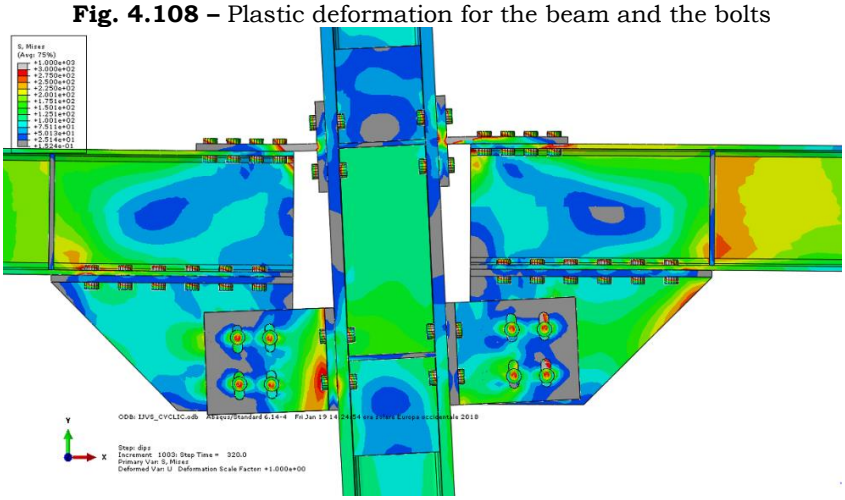

Fig. 4.109 – Stresses in the nodal area”

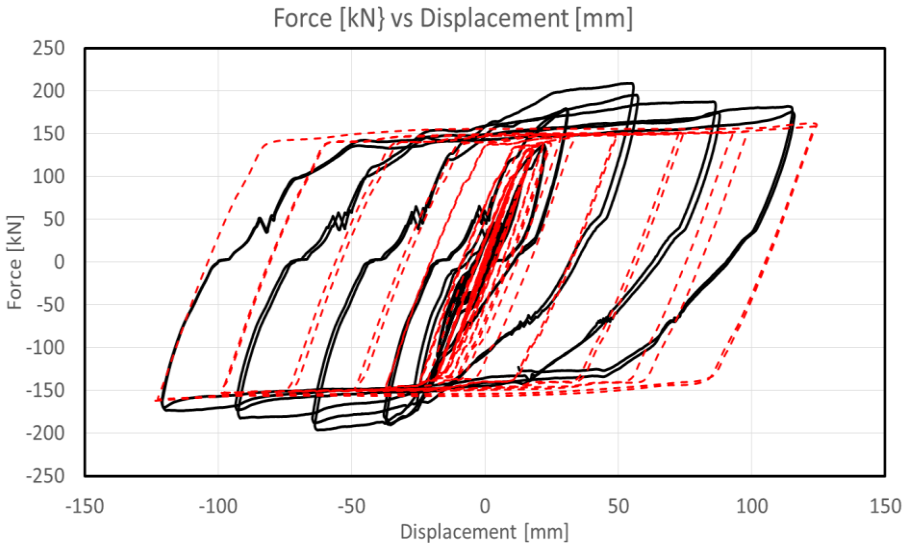

Fig. 4.110 – Comparison between experimental results and FE model (Actuator)

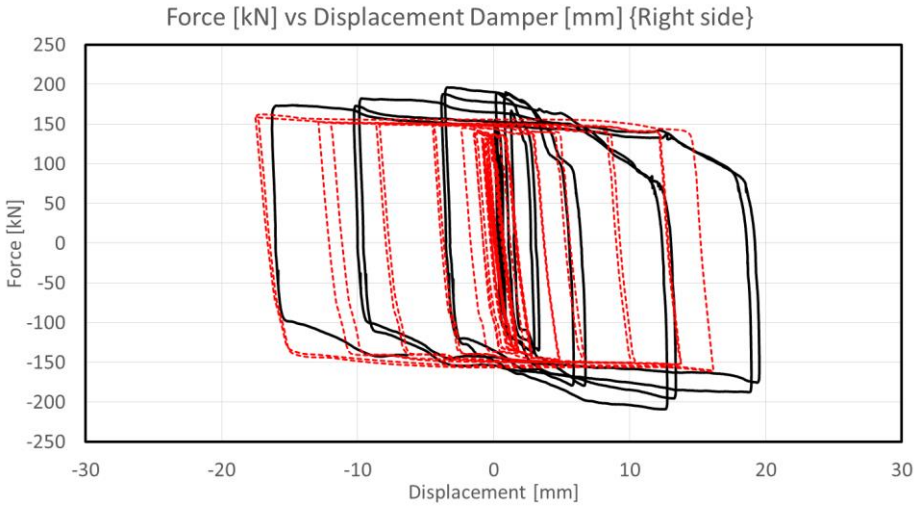

Fig. 4.111 – Comparison between experimental results and FE model (Damper-Right side)

Remarks

The FE models developed in ABAQUS are successful in simulating the response of the internal joints. The numerical models are able to reproduce faithfully the kinematic response of the connection and to predict with a sufficient level of accuracy the overall local response;
Small plasticization arises in the two different configurations. Overall, it seems that the configuration with vertical dampers undergo a lower damage which is concentrated in the T-stub web. The configuration with horizontal dampers provides a higher plastic engagement which, in addition, regards not only the T-stubs but also L-stubs and bolts;

4.4 Conclusions

According to the project prevision, eight cruciform tests have been executed. From the analysis of the results it is possible to derive the following conclusions:
The behaviour of the specimens is characterized by hysteretic loops quite regular, with a limited degradation in terms of energy dissipation, strength and stiffness;
The component method integrated with the results obtained in previous chapters, that represents the base of the design procedure adopted for this innovative connections, seems to be able to accurately described the behaviour of the joint in terms of resistance;
The energy dissipated by the dampers both in horizontal than vertical configuration seems to be in line with the prevision. For this reason, the two solutions can be considered equivalent in terms of hysteretic response;

The damage of the structural elements can be considered negligible, according to the design objectives.

4.5 References

1. CEN: "*Eurocode 3: Design of Steel Structures – Part 1-8: Design of Joints*", EN 1993-1-8, 2005.
2. American Institute of Steel Construction, *ANSI/AISC 341-10*, AISC, 2010.
3. EUROCODE 8, "*Design of structures for earthquake – part 1: General rules, seismic actions and rules for buildings"*, CEN, 2003.
4. EN 1090-2. "*Execution of steel structures and aluminium structures: technical requirements for steel structures*." CEN, 2008.

CHAPTER 5

5.1 Introduction to pseudo-dynamic tests

The greatest concern regarding seismic tests carried out on structures or their components is whether the loading conditions imposed on test samples are representative of those that can actually occur during an earthquake.

It is clear that the test that best evaluates the real behaviour of a structure is the dynamic test on a vibrating table, but it requires sophisticated and expensive equipment; an alternative, instead, would be to resort to an analysis that makes it possible to study the behaviour of a structure in the most reliable way possible, but which at the same time requires less sophisticated equipment than a dynamic test. A test method that allows to satisfy the previous requests is the pseudo-dynamic one, as it allows to analyse the behaviour of a structure subjected to dynamic actions by resorting to the equipment of a quasi-static test.

Instead of using vibrating tables, in a pseudo-dynamic test the following equipment is request:

- hydraulic actuators that allow the structure to be loaded;
- contrast frames acting as constraint devices and to which the actuators are connected;
- transducers for displacement measurements.

The pseudo-dynamic tests reproduce the seismic effects by combining quasi-static experimental techniques with numerical simulations. During a test, a software implements a nonlinear dynamic analysis in order to determine the load stories to be imposed on the specimen.

The tests are conducted applying the loading history slowly, by means of actuators; in this way it is possible to proceed similarly to the tests

performed using a vibrating table, taking into account geometric nonlinearities, interactions along the three dimensions of space and soil-structure interactions.

The technical and theoretical bases that have led to the development of this type of tests have been improved since the end of the 80s by the U.S. - Japan Cooperative Earthquake Research Program.

These studies were conducted in Japan at the Tsukuba Building Research and in the United States at Berkeley, University of California, and at Ann Arbor, University of Michigan.

The pseudo-dynamic method can be applied to:

- the check of analytical models developed to represent the non-linear behaviour of materials and structural elements, comparing the different types of connections and construction details;
- the evaluation of the seismic response of complex structures;
- the check and the calibration of the code provisions.

This method requires interfacing both with data and parameters resulting from a truly numerical forecast analysis and with experimental data; in practice, the phase of numerical analysis and the evaluation phase of experimental data are not distinct, but there is a cyclic correlation between the two phases. For this reason, this test is numerical-experimental. In particular, a non-linear dynamic analysis is used to integrate the equations of motion of a non-linear system with many degrees of freedom (MDOF).

In the literature there are some aspects that prevent a widespread use in practice:

- the choice of parameters affects the results of the analysis;

- numerous analyses are required using different accelerograms to obtain a representative result of the expected response;
- the accuracy of the analysis is to the detriment of simplicity and speed of execution;
- the interpretation of the results is complex and onerous.

The structure is schematized as a system with n degrees of freedom in correspondence with which the masses are assigned and the displacements evaluated with the calculation routine are imposed: this type of test is effective if the masses are discretized, not uniformly distributed and therefore with this test cannot be studied structures such as pylons, monuments or towers.

The objective of the pseudo-dynamic tests is to obtain in a quasi-static way the history of displacement of the structure subjected to dynamic action and in addition, it is possible to inspect the structure at any time, stopping the test.

The test is carried out using a code that allows to evaluate at every step the values of the displacements that are applied to the structure through the hydraulic actuators.

Inertial and viscous forces are numerically simulated by means of discrete modeling using the finite element analysis method, while internal forces and hysteretic damping are measured directly on the structure.

These are input data for calculating the displacements to the next step, representing a problem of integration to the step of the equations of motion. The test procedure is discontinuous and between two successive loading steps the structure remains stationary for the time necessary to measure the reaction forces. Therefore, due to the static nature of this method, it is called "pseudo-dynamic".

To perform a pseudo-dynamic test, it is necessary to define the viscous damping on the basis of literature data, even if during the actual test, with the behavior of the structure pushed in the plastic field, the hysteretic damping will tend to prevail over the viscous.
Since the test is quasi-static the speed with which the structure is deformed is low, in the plastic field the strength and stiffness are lower than those that develop during the real earthquake; these differences may be due to the phenomenon of relaxation (in reality not very significant for steel structures).
To solve this drawback, a method called fast on line testing has recently been proposed, which requires high-speed data acquisition systems: the actuators are in continuous motion, i.e. they do not stop to record the measurements, and it is assumed that the exceeding of the final position at the end of each loading or unloading phase does not affect the correctness of the results. The reaction forces are measured at each sampling period of the digital servo controller and the motion equations are integrated at the sampling rate; in this way there are no interruptions for the displacements imposed on the structure and the risks related to a consequent problematic in the acquisition of the reaction forces themselves are avoided.
In this way it is possible to extend the field of application of the pseudo-dynamic test also to structures sensitive to the strain-rate or equipped with isolators or dissipating instruments.
While in a classic pseudo-dynamical test there are no temporal requirements to be respected since the algorithm and the recording of the actuators are processes that alternate one at a time, in fast pseudo-dynamics, however, a synchrony between the two previous phases is required. imposing a period of binding control.

This causes the occurrence of the need to perform the calculations in reduced time intervals and below two aspects of literature are highlighted that may invalidate the success of the test:

- in case of complexity of the tested structure there can be problems of convergence already in the phase in which the behavior of the structure is still elastic;
- due to the reduced integration step it is preferable to use the central differences method, without however obtaining the security of avoiding instability phenomena, unless an explicit algorithm is used for the experimental part and an implicit one for the analytical part.

5.1.1. Procedure of a pseudo-dynamic test

The pseudo-dynamic method is based on a numeric-experimental numerical integration procedure at the step of the equations of motion.
The displacement at the base and the inertial and damping characteristics of the structure are numerically specified as in conventional dynamic analyzes, but instead of using a mathematical model to determine the characteristics of the reaction forces, these are measured directly on the sample.
The laboratory test inevitably requires a model of the test sample comprising the loads and the boundary conditions; therefore, it has been assumed:

- that the structure is discretized in space in a finite number of degrees of freedom;
- that the masses are concentrated in confined positions;
- only a few components of basic excitation are necessary.

The dynamic effects are taken into account through the equations of motion, while the calculated displacements are imposed on the sample through the actuators.

The method can be generalized to consider the three-dimensional response for multi-freedom systems:

$$[M]\{a_i\} + [C]\{v_i\} + \{R_i\} + [K_g]\{d_i\} = -[M][B]\{a_{gi}\} \quad (5.1)$$

where:

$[M]$ and $[C]$ are the mass and damping matrices respectively;

$\{R_i\}$ is the vector that includes the reaction forces;

$[K_g]$ is the matrix of the geometric stiffness used to compensate the loads not really present on the structure during the test;

$\{a_i\}$, $\{v_i\}$ e $\{d_i\}$ are respectively the vectors of accelerations, velocities and displacements of the degrees of freedom of the structure at time i;

$\{a_{gi}\}$ is the vector of ground accelerations at time i in each direction considered;

$[B]$ is the transformation matrix of ground acceleration; the component B_{ij} corresponds to the acceleration in correspondence with the degree of freedom i when the structure acts as a rigid body due to a unitary acceleration to the ground of component j (in the case of a flat test with a single component of horizontal ground displacement $[B]$ is a unit vector).

The equations of motion are integrated numerically at each step to determine the displacement d_{i+1} at the end of each step.

This calculation is based on the accelerations, the speeds and the displacements calculated at the beginning of each step and through the

matrices and vectors specified by the user: $[M]$, $[C]$, $[K_g]$, $[B]$, $\{a_g\}$, and also considering the forces acting on the structure.

Once the required displacements have been evaluated on the basis of the equation of motion, they are imposed to the structure by the actuators and the reaction forces are measured; this process is repeated recursively until the complete seismic response is evaluated.

Explicit numerical integration procedures are used, which have the advantage over implicit not having to evaluate the tangent stiffness of the sample according to a numerical procedure, but starting directly from the measured reaction force.

In order for these methods to be stable, an integration time of less than $1/\pi$ times the greatest vibration period of the structure is required.

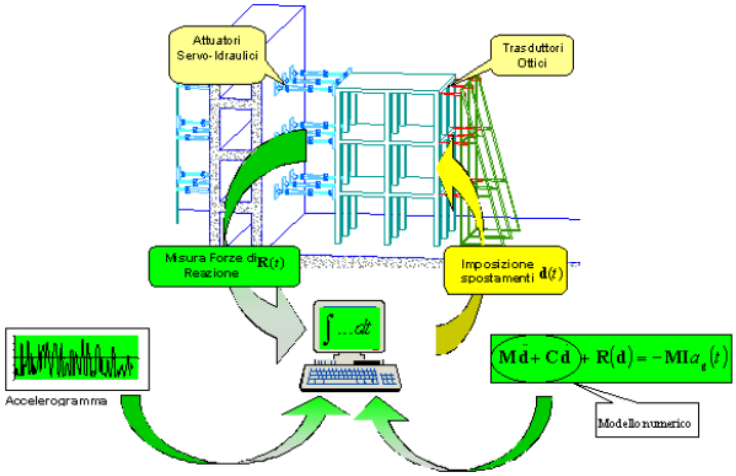

Fig. 5.1 – Scheme of the numerical-experimental procedure for a pseudo-dynamic test.

5.1.2. Advantages and disadvantages of pseudo-dynamic tests

As already specified, the first benefit of the pseudo-dynamic tests is the same that led to its introduction: it is possible to perform quasi-static tests that allow to simulate the dynamic behavior of structures or structural components but with the advantage of using less sophisticated equipment and therefore less expensive.
Moreover, the possibility of simulating the presence of the masses on the various decks, without actually being present, makes it possible to make the preparation of such tests more rapid, economical and safe.
Because of the quasi-static nature of this type of test and the consequent reduced speed with which the structure is affected by the accelerogram, it is possible to observe what happens to the different parts of the structure during the test, which would not be possible in the case of tests dynamics on a vibrating table. Using a numerical procedure to integrate the equations of motion at the same time, it is possible to simultaneously simulate accelerograms along two orthogonal directions.
The disadvantages of the pseudo-dynamic tests are related to the fact that more attention is required in the definition of the parameters involved in the calculation routine
It is important to consider the strain-rate (speed of deformation of a material over time) to understand if the pseudo-dynamic test is able to simulate the real inelastic response of a structure subjected to an earthquake; for this reason, as already specified above, it is possible
expect elastic forces lower than the real ones. However, for steel structures with a fundamental vibration period of more than *0.10sec* it is

expected that the effects of strain rate can be considered negligible, whereas for the structures in reinforced concrete it is necessary to study such effects.

Some disadvantages are related to the accuracy of the numerical procedure due to possible truncations of the quantities involved and any divergent solutions. A not inconsiderable cause of error is related to the experimental measures introduced in the integration of the equations of motion; in fact, the reaction forces measured by the actuators can be influenced by measurement errors that can accumulate during the test, thus affecting the result.

In summary, the limits of this method are linked to the following assumptions:

- the dynamic response of the structure is described by the previous equation of motion;
- the equations are reliable and resolved in an accurate manner;
- the calculated displacements are imposed on the structure with sufficient precision.

5.2. Design of the structure for the pseudo-dynamic test

In a first, strictly numerical phase, the main structural elements of the single-span frame corresponding to the main bracing structural element of the building being analyzed were designed. This design is based on the requirement to ensure that the expected collapse mechanism is global

5.2.1. Definition of loads and masses

The loads acting on the structure do not derive from a specific analysis, but, even if realistic, have been commensurate with the capacity of the equipment available in the laboratory, or of the inflatable boats that can be filled with water.

Since the specimen to be made in the laboratory, in order to avoid contrasting structures out of floors, will be made with two frames of characteristics equal to those of the bracing structure of the building in question connected to each other by a deck with corrugated metal and slab in reinforced concrete, the study is carried out by assimilating the behaviour of the real frames, characterized by a 4m wheelbase, to that of the test structure, characterized by an interaxis of frames equal to 2m.

This has an important consequence: the loads distributed per unit of area in the real scheme are half of those to be adopted in the laboratory.

Therefore, it is the loads that can be adopted in the laboratory to also influence those to be considered in the evaluation of the masses.

In the laboratory loads can be applied with rubber dinghies filled with water; in particular:

- at the first level the boats can reach a height of 85cm, and therefore the loads per unit area are worth $7.50 kN/m^2$;
- on the second level, the rafts can reach a height of 60cm, and therefore the loads per unit area are worth $5.00 \mathrm{kN}/m^2$.

It is also necessary to consider the load deriving from the weight of the sheet that constitutes the rigid deck of the frame: $2.00 kN/m^2$.

In summary, the characteristic loads to be applied to the laboratory frame are:

Table 5.1 – Loads applied to the frame

Level	***q_k (kN/m²)***
1	*9.50*
2	*7.00*

Since the area of influence of the starting multi-sample structure is twice that of the laboratory one, then half loads are applied to the multi-span structure:

Table 5.2 – Loads applied to the multi-span structure

Level	***q_k (kN/m²)***
1	*4.75*
2	*3.50*

This is important for the assessment of the masses at the two decks.
The area of the deck is obtained:

$$A_{impalcato\ tipo} = (4\ m)^2 \cdot 9 = 144{,}00\ m^2 \tag{5.2}$$

The total loads at the two levels can be evaluated:

$$Q_i = q_i A_i$$

$$Q_1 = 4{,}75\ \frac{kN}{m^2} \cdot 144{,}00\ m^2 = \ 684{,}00\ kN \tag{5.3}$$

$$Q_2 = 3{,}50\ \frac{kN}{m^2} \cdot 144{,}00\ m^2 = \ 504{,}00\ kN$$

It is now necessary to derive both the masses deriving from the uniformly distributed loads acting as well as from the structural elements (beams and columns) assumed in the reference multi-sample structure.
In particular, in a first phase the masses deriving from the distributed loads are evaluated:

$$m_{floor\ i} = \frac{Q_i}{g}$$

$$m_{floor,1} = 69{,}72\ tonn \tag{5.4}$$

$$m_{floor,2} = 51{,}38\ tonn$$

The masses are distributed equally between the seismic-resistant frames:

$$m_{i,frame} = \frac{m_{floor,i}}{4}$$

$$m_{1,frame} = 17{,}43\ tonn \tag{5.5}$$

$$m_{2,frame} = 12{,}84\ tonn$$

In the mechanical model representative of the frame, it is decided to assign specific masses at the end nodes of each deck, therefore:

$$m_{i,joint} = \frac{m_{i,\ frame}}{2}$$

$$m_{1,joint} = 8{,}715\ tonn \tag{5.6}$$

$$m_{2,joint} = 6{,}42\ tonn$$

The multi-sample structure of reference is characterized by having a considerable number of structural elements that contribute in a non-negligible way to the evaluation of the nodal masses.

The types of beams are:

- IPE-270, with a distributed mass equal to $0.035 ton/m$;
- IPE-140, with a distributed mass equal to $0.013 ton/m$;
- HEB-140, with a distributed mass equal to $0.033 ton/m$

The types of columns are:

- HEB-200, with distributed mass equal to $0.060\ ton/m$;

- HEB-140, with a distributed mass equal to 0.033 ton/m.

Based on this information and a hypothetical numerical evaluation of beams and columns, it is possible to derive:

$$m_{1,joint,beams\ and\ columns} = 0{,}835\ ton$$
$$m_{2,joint,beams\ and\ columns} = 0{,}707\ ton \quad (5.7)$$

It has been preferred to define at a preliminary stage the masses relative to the structural elements so that they can be assigned to the SeismoStruct software, used to perform the analyzes, without the software automatically calculating them.

Finally, the nodal masses to be assigned to the structural model are:

$$m_{1,joint} = 9{,}550\ ton$$
$$m_{2,joint} = 7{,}127\ ton \quad (5.8)$$

At this point it is possible to proceed with the frame design using the control theory of the collapse mechanism.

The solutions obtained by applying two versions of the control theory of the collapse mechanism represent one the development of the other: one: in fact, one derive form an iteration, while the other provides a solution in a closed form.

5.2.2. Frame design with the iterative procedure of the theory of control of the collapse mechanism

The following figures show the structure in the studio (respectively the section of the frame and a plan to highlight the elements of the deck).

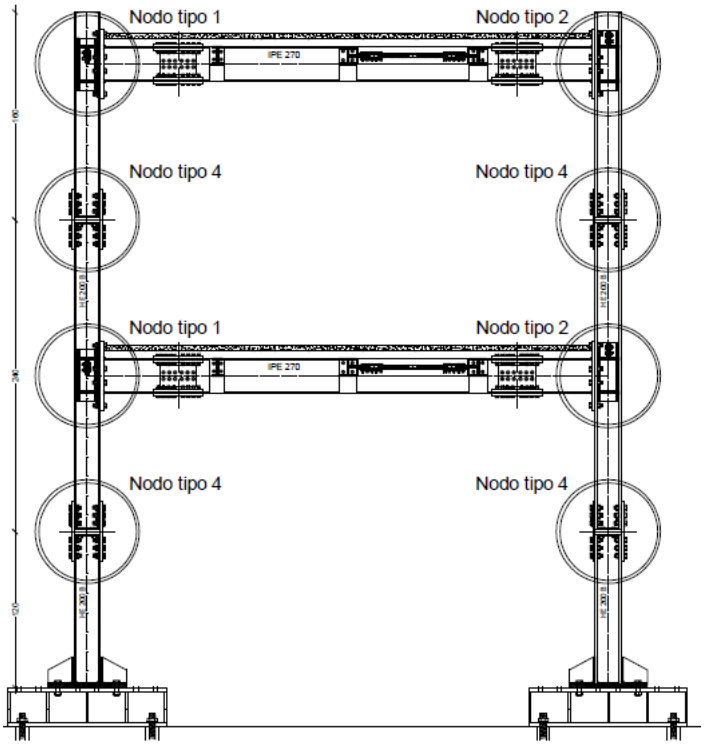

Fig. 5.2 – Longitudinal section of the frame

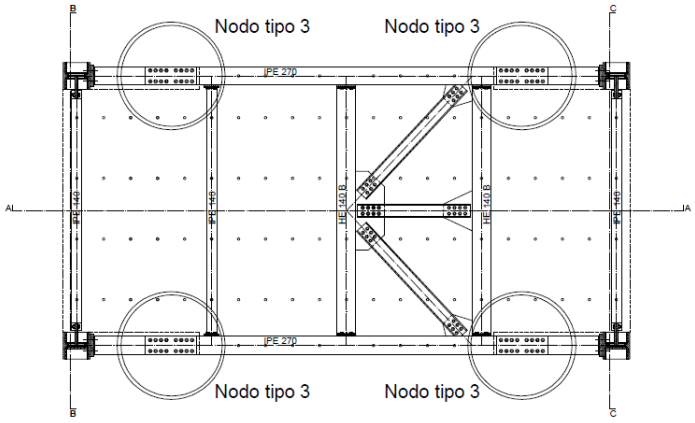

Fig. 5.3 – Floor scheme

The characteristics of the material, a steel *S355*, are:

$$f_{yk} = 355\ N/mm^2$$
$$f_{tk} = 510\ N/mm^2 \tag{5.9}$$

From tests carried out on the material, defining k and δ respectively the mean square deviation and the coefficient of variation:

$$f_m = \frac{f_{yk}}{1 - k \cdot \delta} = \frac{355\ N/mm^2}{1 - 1{,}64 \cdot 0{,}09} = 416{,}47 \frac{N}{mm^2} \cong 415{,}00 \frac{N}{mm^2} \tag{5.10}$$

The loads are applied to the structure by rubber boats full of water, while the sheets act as a rigid deck.

Table 5.3 – Total loads applied to the frame

	Load [kN/m²]	***Weight of the corrugated metal sheets [kN/m²]***	***Total [kN/m²]***
Level 1	*7,50*	*2,00*	*9,50*
Level 2	*5,00*	*2,00*	*7,00*

Seismic actions are seen by the structural system as horizontal forces distributed between the two decks in function:

- of the first vibration mode of the structure (triangular distribution);
- of the floor masses (uniform distribution).

To dimension the beams, the moment in the joints at a last rotation equal to θ_u*=0.045rad* has be taken into account, in order to ensure the plasticization of the node but not the ends of the beams.

A maximum stress moment is assumed at the ends of the beams equal to 168kNm; this value was obtained from laboratory tests and represents

the bending moment at whose value the previous limit rotation is obtained.

$$\Phi_{a,i} = \frac{m_i \cdot h_i}{\sum_{i=1}^{n.floor}(m_i \cdot h_i)}$$

$$\Phi_{b,i} = \frac{m_i}{\sum_{i=1}^{n.floor} m_i}$$

$$m_{1,} = 19{,}100 tonn$$

$$m_2 = 14{,}254 tonn \qquad (5.11)$$

$$\Phi_{a,1} = 0{,}40$$

$$\Phi_{a,2} = 0{,}60$$

$$\Phi_{b,1} = 0{,}57$$

$$\Phi_{b,2} = 0{,}43$$

Therefore, an IPE270 profile is adopted.

$$W_{pl} = 484{,}00\ cm^3$$

$$M_{pl,beam} = W_{pl} \cdot f_{yk} = 484 \cdot 10^3 mm^3 \cdot 355 \frac{N}{mm^2} = 171{,}82\ kNm \qquad (5.12)$$

The columns must be sized in such a way as to guarantee a global breaking mechanism, which is optimal because it allows to maximize the

number of plastic hinges necessary to transform the structure into a kinematic mechanism.

5.2.3. Overview collapse mechanisms

There are three possible collapse mechanisms and they are listed below together with the global mechanism.

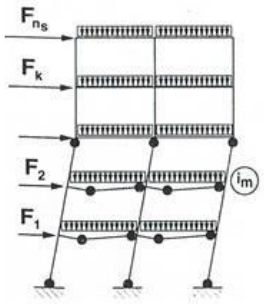

Fig. 5.4 – Mechanism type 1

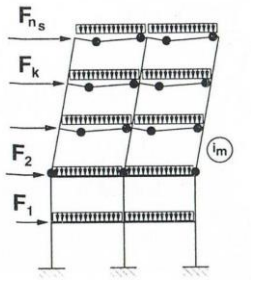

Fig. 5.5 – Mechanism type 2

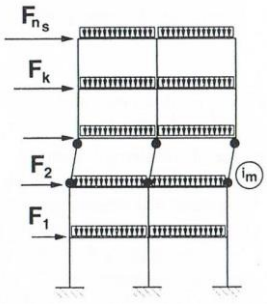

Fig. 5.6 – Mechanism type 3

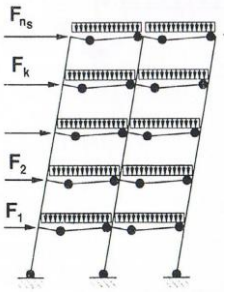

Fig. 5.7 – Global mechanism

If the structure consists of n_s floors, each mechanism is characterized by *ns* mechanism indices; so there are $3 \cdot n_s$ significant breaking mechanisms.

In particular, the kinematic theorem of plastic collapse is used, which in the case in question is set out as follows:

"*The plastic module of the column section can be defined so that the cinematically permissible multiplier corresponding to the global mechanism is smaller than the cinematically admissible multipliers corresponding to the other* $3 \cdot n_{s-1}$ *mechanisms*".

The equilibrium curve of the mechanism is expressed as:

$$\alpha_c = \alpha - \gamma \cdot \delta \tag{5.13}$$

α is the cinematically admissible multiplier of the horizontal forces.

γ is the inclination of the equilibrium curve of the mechanism.

The horizontal forces depend on α while vertical loads are constant.

To derive the previous report, the virtual jobs must be evaluated, and therefore it is necessary to know the movements.

It starts with the evaluation of the displacement movements, referring to the following representative image of a rigid movement of the structural elements:

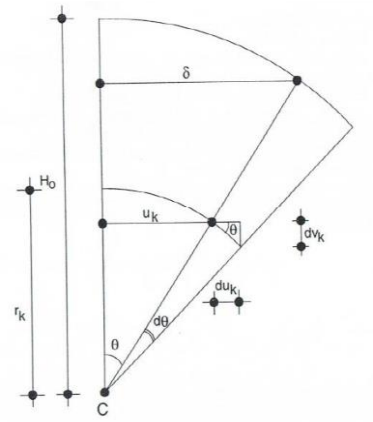

Fig. 5.8 – Rigid movement of structural elements

where:

r_k is the distance of the *k-th* plane from the center of rotation *C*.

ϑ is the rotation angle.

H_0 is the sum of the inter-story heights of the planes involved in the generic mechanism.

u_k is the horizontal displacement of the *k-th* plane involved in the generic mechanism.

du_k and dv_k are the horizontal and vertical virtual displacements.

$$\begin{aligned} u_k &= r_k \cdot \sin\vartheta \\ du_k &= r_k \cdot \cos\vartheta \, d\vartheta \cong r_k \cdot d\vartheta \\ dv_k &= du_k \cdot \sin\vartheta \\ \sin\vartheta &= \frac{\delta}{H_0} \end{aligned} \tag{5.14}$$

Substituting the formulation of *duk* in *dvk* and also *sen* (θ), we have:

$$dv_k = r_k \cdot d\vartheta \cdot \frac{\delta}{H_0} \tag{5.15}$$

where:

$$r_k = s \tag{5.16}$$

while the vertical virtual displacement is:

$$dv_k = \frac{\delta}{H_0} \cdot s \cdot d\vartheta \tag{5.17}$$

The virtual work performed by horizontal forces is:

$$\alpha \cdot F \cdot du_k = \alpha \cdot F \cdot s \cdot d\vartheta \tag{5.18}$$

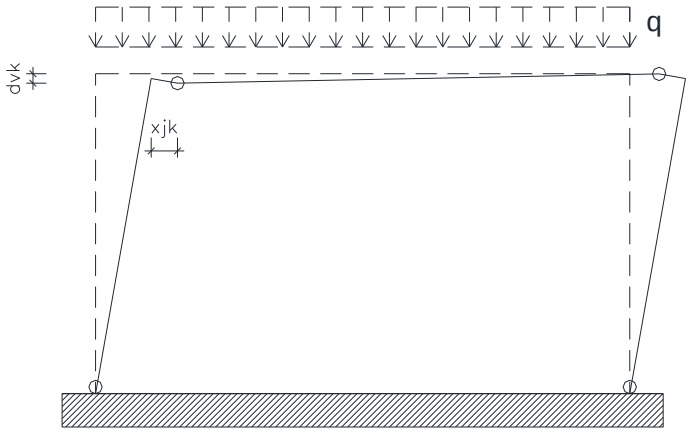

Fig. 5.9 – Global mechanism

Work performed by uniformly distributed loads:

$$dv_k = u_{jk} \cdot d\vartheta$$
$$q\frac{L}{2}\frac{dv_k}{2} = qL\frac{x_{jk}}{2} \cdot d\vartheta = q \cdot D_{jk} \cdot d\vartheta \tag{5.19}$$

Considering:

$$D_{jk} = \frac{L \cdot x_{jk}}{2} \tag{5.20}$$

Work accomplished by the plastic hinges of the columns:

$$C \cdot R_c \cdot d\vartheta \tag{5.21}$$

where

C is the potential torque or plastic moment;

R_c takes into account the number of plasticized sections of an auction.

Work performed by the plastic hinges of the beams:

$$R_b \cdot B_{jk} \cdot d\vartheta \tag{5.22}$$

where R_b =1 if the beam participates in the mechanism, otherwise R_b=0.

$$B = \frac{m_s + m_d}{2} M_b \tag{5.23}$$

General equations of the virtual works starting from a particular case:

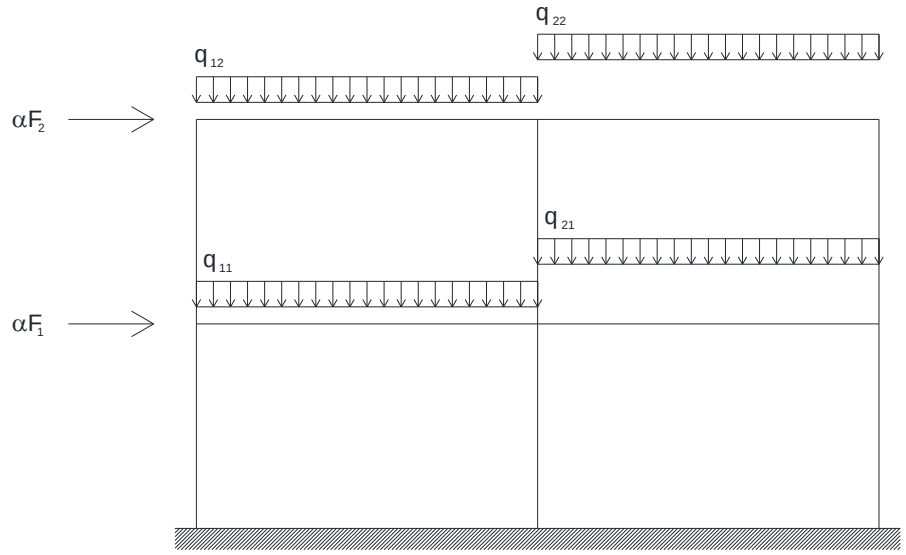

Fig. 5.10 – Two floors two spans frame

External virtual work

$$W_e = \alpha F_1 s_1 \cdot d\vartheta + \alpha F_2 s_2 \cdot d\vartheta + (q_{11}D_{11} + q_{21}D_{21} + q_{12}D_{12} + q_{22}D_{22})$$

$$W_e = \alpha [F_1 \quad F_2] \begin{bmatrix} s_1 \\ s_2 \end{bmatrix} \cdot d\vartheta + tr\left\{ \begin{bmatrix} q_{11} & q_{21} \\ q_{12} & q_{22} \end{bmatrix} \begin{bmatrix} D_{11} & D_{12} \\ D_{21} & D_{22} \end{bmatrix} \right\} \cdot d\vartheta$$

$$W_e = \alpha \underline{F}^T \underline{s} \cdot d\vartheta + tr\left(\underline{\underline{q}}^T \underline{\underline{D}}\right) \cdot d\vartheta \tag{5.24}$$

$$W_e = \left[\alpha \underline{F}^T \underline{s} + tr\left(\underline{\underline{q}}^T \underline{\underline{D}}\right)\right] \cdot d\vartheta$$

Internal virtual work:

$$W_i = (R_{c11}C_{11} + R_{c12}C_{12} + R_{c21}C_{21} + R_{c22}C_{22} + R_{c31}C_{31} + R_{c32}C_{32})d\vartheta + 2(R_{b11}B_{11} + R_{b12}B_{12} + R_{b21}B_{21} + R_{b22}B_{22})d\vartheta$$

$$W_i = tr\left\{ \begin{bmatrix} C_{11} & C_{21} & C_{31} \\ C_{12} & C_{22} & C_{32} \end{bmatrix} \begin{bmatrix} R_{c11} & R_{c12} \\ R_{c21} & R_{c22} \\ R_{c31} & R_{c32} \end{bmatrix} \right\} \cdot d\vartheta +$$

$$+2 \cdot tr\left\{ \begin{bmatrix} B_{11} & B_{21} \\ B_{12} & B_{22} \end{bmatrix} \begin{bmatrix} R_{b11} & R_{b12} \\ R_{b21} & R_{b22} \end{bmatrix} \right\} \cdot d\vartheta \tag{5.25}$$

$$W_i = tr\left(\underline{\underline{C}}^T \underline{\underline{R}}_c\right) \cdot d\vartheta + 2 \cdot tr\left(\underline{\underline{B}}^T \underline{\underline{R}}_b\right) \cdot d\vartheta$$

$$W_i = \left[tr\left(\underline{\underline{C}}^T \underline{\underline{R}}_c\right) + 2 \cdot tr\left(\underline{\underline{B}}^T \underline{\underline{R}}_b\right)\right] \cdot d\vartheta$$

The total load acting on the *k-th* floor is:

$$V_k = \sum_{j=1}^{n_b} q_{jk} L_j \tag{5.26}$$

Work of vertical loads due to the effects of the second order:

$$W_v = \underline{V}^T \underline{s} \frac{\delta}{H_0} \cdot d\vartheta \tag{5.27}$$

Neglecting the second order effects

$$W_e = W_i$$

$$\left[\alpha \underline{F}^T \underline{s} + tr\left(\underline{\underline{q}}^T \underline{\underline{D}}\right)\right] \cdot d\vartheta = \left[tr\left(\underline{\underline{C}}^T \underline{\underline{R}}_c\right) + 2 \cdot tr\left(\underline{\underline{B}}^T \underline{\underline{R}}_b\right)\right] \cdot d\vartheta$$

$$\left[\alpha \underline{F}^T \underline{s} + tr\left(\underline{\underline{q}}^T \underline{\underline{D}}\right)\right] = \left[tr\left(\underline{\underline{C}}^T \underline{\underline{R}}_c\right) + 2 \cdot tr\left(\underline{\underline{B}}^T \underline{\underline{R}}_b\right)\right] \tag{5.28}$$

$$\alpha = \frac{tr\left(\underline{\underline{C}}^T \underline{\underline{R}}_c\right) + 2 \cdot tr\left(\underline{\underline{B}}^T \underline{\underline{R}}_b\right) - tr\left(\underline{\underline{q}}^T \underline{\underline{D}}\right)}{\underline{F}^T \underline{s}}$$

Taking into account the second order effects

$$W_i = W_e + W_v$$

$$\begin{aligned} &\left[tr\left(\underline{\underline{C}}^T \underline{\underline{R}}_c\right) + 2 \cdot tr\left(\underline{\underline{B}}^T \underline{\underline{R}}_b\right)\right] \cdot d\vartheta \\ &\qquad = \left[\alpha_c \underline{F}^T \underline{s} + tr\left(\underline{\underline{q}}^T \underline{\underline{D}}\right)\right] \cdot d\vartheta + \underline{V}^T \underline{s} \frac{\delta}{H_0} \cdot d\vartheta \end{aligned} \tag{5.29}$$

$$tr\left(\underline{\underline{C}}^T \underline{\underline{R}}_c\right) + 2 \cdot tr\left(\underline{\underline{B}}^T \underline{\underline{R}}_b\right) = \alpha_c \underline{F}^T \underline{s} + tr\left(\underline{\underline{q}}^T \underline{\underline{D}}\right) + \underline{V}^T \underline{s} \frac{\delta}{H_0}$$

$$\alpha_c = \frac{tr\left(\underline{\underline{C}}^T \underline{\underline{R}}_c\right) + 2 \cdot tr\left(\underline{\underline{B}}^T \underline{\underline{R}}_b\right) - tr\left(\underline{\underline{q}}^T \underline{\underline{D}}\right)}{\underline{F}^T \underline{s}} - \frac{1}{H_0} \frac{\underline{V}^T \underline{s}}{\underline{F}^T \underline{s}} \delta$$

but placing:

$$\alpha = \frac{tr\left(\underline{\underline{C}}^T \underline{\underline{R}}_c\right) + 2 \cdot tr\left(\underline{\underline{B}}^T \underline{\underline{R}}_b\right) - tr\left(\underline{\underline{q}}^T \underline{\underline{D}}\right)}{\underline{F}^T \underline{s}} \tag{5.30}$$

$$\gamma = \frac{1}{H_0}\frac{\underline{V}^T\underline{s}}{\underline{F}^T\underline{s}}$$

The multiplier of the horizontal loads is obtained considering also the effects of the second order:

$$\alpha_c = \alpha - \gamma\delta \tag{5.31}$$

For the global mechanism:

$$\alpha = \frac{\underline{M}_{c1}^T\underline{I} + 2\cdot tr\left(\underline{\underline{B}}^T\underline{\underline{R}}_b{}^{(g)}\right) - tr\left(\underline{\underline{q}}^T\underline{\underline{D}}_v^{(g)}\right)}{\underline{F}^T\underline{s}^{(g)}} \tag{5.32}$$

with:

$$\underline{s}^{(g)} = \underline{h} \tag{5.33}$$

For the *i-th* mechanism of type-1:

$$\begin{gathered}\underline{s}^{(1)T} = \{h_1; h_2; \dots; h_{im}; h_{im}\} \\ H_0 = h_{im} \\ \alpha_{im}^{(1)} = \frac{\underline{M}_{c,im}^T\underline{I} + 2\cdot tr\left(\underline{\underline{B}}^T\underline{\underline{R}}_{b,im}{}^{(1)}\right) - tr\left(\underline{\underline{q}}^T\underline{\underline{D}}_{v,im}^{(1)}\right)}{\underline{F}^T\underline{s}_{im}{}^{(1)}}\end{gathered} \tag{5.34}$$

For the *i-th* mechanism of type-2:

$$\begin{gathered}\underline{s}^{(2)T} = \{0; 0; \dots; h_{im} - h_{im-1}; h_{im+1} - h_{im}; \dots\} \\ H_0 = h_{ns} - h_{im-1} \\ \alpha_{im}^{(2)} = \frac{\underline{M}_{c,im}^T\underline{I} + 2\cdot tr\left(\underline{\underline{B}}^T\underline{\underline{R}}_{b,im}{}^{(2)}\right) - tr\left(\underline{\underline{q}}^T\underline{\underline{D}}_{v,im}^{(2)}\right)}{\underline{F}^T\underline{s}_{im}{}^{(2)}}\end{gathered} \tag{5.35}$$

For the *i-th* mechanism of type-3:

$$\underline{s}^{(3)T} = \{0; 0; \dots; h_{im} - h_{im-1}; \dots\}$$

$$H_0 = h_{im} - h_{im-1} \tag{5.36}$$

$$\alpha_{im}^{(3)} = \frac{2 \cdot \underline{M}_{c,im}^{T} \underline{I}}{\underline{F}^{T} \underline{s}_{im}{}^{(3)}}$$

In order to obtain the overall structure breakage mechanism, the cross section must be dimensioned in such a way that, according to the lower limit theorem, the cinematically permissible horizontal force multiplier corresponding to the global mechanism is the minimum among all cinematically permissible multipliers. This is true if the material has a rigid-plastic behavior. The real behavior is elastic-plastic and originates the effects of the second order that cannot be neglected.

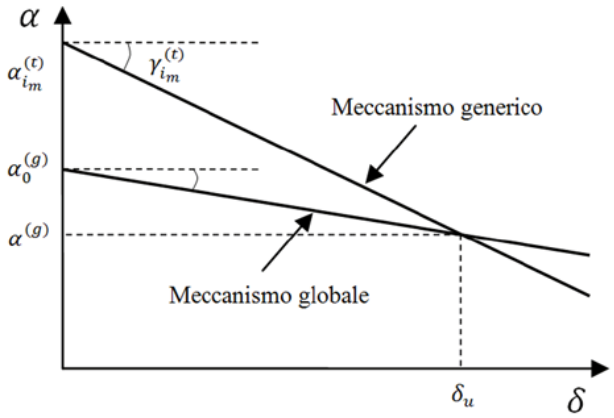

Fig. 5.11 – Equilibrium curves for the different mechanisms

The influence of the second order effects can be taken into account by imposing that the equilibrium curve of the global mechanism is found below those of all the other mechanisms:

$$\alpha^{(g)} - \gamma^{(g)}\delta_u \leq \alpha_{im}^{(t)} - \gamma_{im}^{(t)}\delta_u \tag{5.37}$$

The conditions to avoid the type 1 mechanism must be considered:

$$\begin{aligned} &\frac{\underline{M}_{c1}^T \underline{I} + 2 \cdot tr\left(\underline{\underline{B}}^T \underline{\underline{R}}_b{}^{(g)}\right) - tr\left(\underline{\underline{q}}^T \underline{\underline{D}}_v^{(g)}\right)}{\underline{F}^T \underline{S}^{(g)}} - \frac{\delta_u}{h_{ns}} \frac{\underline{V}^T \underline{S}^{(g)}}{\underline{F}^T \underline{S}^{(g)}} \leq \\ &\leq \frac{\underline{M}_{c,im}^T \underline{I} + 2 \cdot tr\left(\underline{\underline{B}}^T \underline{\underline{R}}_{b,im}{}^{(1)}\right) - tr\left(\underline{\underline{q}}^T \underline{\underline{D}}_{v,im}^{(1)}\right)}{\underline{F}^T \underline{S}_{im}{}^{(1)}} - \frac{\delta_u}{h_{im}} \frac{\underline{V}^T \underline{S}_{im}{}^{(1)}}{\underline{F}^T \underline{S}_{im}{}^{(1)}} \end{aligned} \tag{5.38}$$

At this point, the following quantities are needed to introduce.

Internal work done by beams:

$$\mu^{(g)} = 2 \cdot tr\left(\underline{\underline{B}}^T \underline{\underline{R}}_b{}^{(g)}\right) \tag{5.39}$$

Work of vertical loads due to the effects of the second order:

$$v^{(g)} = \frac{1}{h_{ns}} \underline{V}^T \underline{S}^{(g)} \tag{5.40}$$

External work due to uniformly distributed loads on beams:

$$\tau^{(g)} = tr\left(\underline{\underline{q}}^T \underline{\underline{D}}_v^{(g)}\right) \tag{5.41}$$

Relationship between the internal work that the beams perform in the *i-th* mechanism of type-1 and that developed in the global mechanism:

$$\xi_{im}^{(1)} = \frac{2 \cdot tr\left(\underline{\underline{B}}^T \underline{\underline{R}}_{b,im}{}^{(1)}\right)}{2 \cdot tr\left(\underline{\underline{B}}^T \underline{\underline{R}}_b{}^{(g)}\right)} \tag{5.42}$$

Relationship between the external work that the horizontal forces play in the *i-th* mechanism of type-1 and that performed in the global mechanism:

$$\lambda_{im}^{(1)} = \frac{\underline{F}^T \underline{s}_{im}{}^{(1)}}{\underline{F}^T \underline{s}^{(g)}} \tag{5.43}$$

Relationship between the external work that the uniformly distributed loads perform in the *i-th* mechanism of type-1 and that performed in the global mechanism:

$$\zeta_{im}^{(1)} = \frac{tr\left(\underline{\underline{q}}^T \underline{\underline{D}}_{v,im}^{(1)}\right)}{tr\left(\underline{\underline{q}}^T \underline{\underline{D}}_{v}^{(g)}\right)} \tag{5.44}$$

Ratio between the slope of the equilibrium curve of the *i-th* mechanism of type 1 and that of the global mechanism:

$$\Delta_{im}^{(1)} = \frac{\underline{F}^T \underline{s}^{(g)}}{\underline{F}^T \underline{s}_{im}{}^{(1)}} \frac{\frac{1}{h_{im}} \underline{V}^T \underline{s}_{im}{}^{(1)}}{\frac{1}{h_{ns}} \underline{V}^T \underline{s}^{(g)}} \tag{5.45}$$

Obtaining

$$\begin{aligned} &\underline{M}_{c1}^T \underline{I}\left(1 - \frac{1}{\lambda_{im}^{(1)}}\right) + \mu^{(g)}\left(1 - \frac{\xi_{im}^{(1)}}{\lambda_{im}^{(1)}}\right) + v^{(g)} \delta_u\left(\Delta_{im}^{(1)} - 1\right) + \\ &+\tau^{(g)}\left(\frac{\xi_{im}^{(1)}}{\lambda_{im}^{(1)}} - 1\right) \leq \frac{1}{\lambda_{im}^{(1)}} \underline{M}_{c,im}^T \underline{I} \end{aligned} \tag{5.46}$$

It is possible to introduce the parameter ρ_{im} which represents the sum of the reduced plastic moments of the columns of the *i-th* floor and the same sum corresponding to the columns of the first floor:

$$\rho_{im} = \frac{\underline{M}_{c,im}^T \underline{I}}{\underline{M}_{c1}^T \underline{I}}$$

$$\rho_{im}^{(1)} \geq \frac{\left(1 - \frac{1}{\lambda_{im}^{(1)}}\right)\sum_{i=1}^{n_c} M_{c,i1} + \mu^{(g)}\left(1 - \frac{\xi_{im}^{(1)}}{\lambda_{im}^{(1)}}\right) + \nu^{(g)}\delta_u\left(\Delta_{im}^{(1)} - 1\right) + \tau^{(g)}\left(\frac{\xi_{im}^{(1)}}{\lambda_{im}^{(1)}} - 1\right)}{\frac{1}{\lambda_{im}^{(1)}}\sum_{i=1}^{n_c} M_{c,i1}} \tag{5.47}$$

i_m = 1, 2, 3, …, n_s.

The conditions to avoid the type 2 failure mechanism must be considered:

$$\frac{\underline{M}_{c1}^T \underline{I} + 2 \cdot tr\left(\underline{\underline{B}}^T \underline{\underline{R}}_b{}^{(g)}\right) - tr\left(\underline{q}^T \underline{\underline{D}}_v^{(g)}\right)}{\underline{F}^T \underline{s}^{(g)}} - \frac{\delta_u}{h_{ns}} \frac{\underline{V}^T \underline{s}^{(g)}}{\underline{F}^T \underline{s}^{(g)}} \leq$$

$$\leq \frac{\underline{M}_{c,im}^T \underline{I} + 2 \cdot tr\left(\underline{\underline{B}}^T \underline{\underline{R}}_{b,im}{}^{(2)}\right) - tr\left(\underline{q}^T \underline{\underline{D}}_{v,im}^{(2)}\right)}{\underline{F}^T \underline{s}_{im}{}^{(2)}} - \frac{\delta_u}{h_{ns} - h_{im-1}} \frac{\underline{V}^T \underline{s}_{im}{}^{(2)}}{\underline{F}^T \underline{s}_{im}{}^{(2)}} \tag{5.48}$$

The same parameters of the case of mechanism 2 are introduced:

$$\xi_{im}^{(2)} = \frac{2 \cdot tr\left(\underline{\underline{B}}^T \underline{\underline{R}}_{b,im}{}^{(2)}\right)}{2 \cdot tr\left(\underline{\underline{B}}^T \underline{\underline{R}}_b{}^{(g)}\right)}$$

$$\lambda_{im}^{(2)} = \frac{\underline{F}^T \underline{s}_{im}{}^{(2)}}{\underline{F}^T \underline{s}^{(g)}}$$

$$\zeta_{im}^{(2)} = \frac{tr\left(\underline{q}^T \underline{\underline{D}}_{v,im}^{(2)}\right)}{tr\left(\underline{q}^T \underline{\underline{D}}_v^{(g)}\right)} \tag{5.49}$$

$$\underline{M}_{c1}^T \underline{I} + \mu^{(g)}\left(1 - \frac{\xi_{im}^{(2)}}{\lambda_{im}^{(2)}}\right) + \nu^{(g)}\delta_u\left(\Delta_{im}^{(2)} - 1\right) + \tau^{(g)}\left(\frac{\xi_{im}^{(2)}}{\lambda_{im}^{(2)}} - 1\right) \leq \frac{1}{\lambda_{im}^{(2)}} \underline{M}_{c,im}^T \underline{I}$$

$$\rho_{im}^{(1)} \geq \frac{\sum_{i=1}^{n_c} M_{c,i1} + \mu^{(g)}\left(1 - \frac{\xi_{im}^{(2)}}{\lambda_{im}^{(2)}}\right) + v^{(g)}\delta_u\left(\Delta_{im}^{(2)} - 1\right) + \tau^{(g)}\left(\frac{\xi_{im}^{(2)}}{\lambda_{im}^{(2)}} - 1\right)}{\frac{1}{\lambda_{im}^{(2)}}\sum_{i=1}^{n_c} M_{c,i1}}$$

$i_m = 1, 2, 3, \ldots, n_s.$

The conditions to avoid the type 3 mechanism must be considered:

$$\frac{\underline{M}_{c1}^T \underline{I} + 2 \cdot tr\left(\underline{\underline{B}}^T \underline{\underline{R}}_b{}^{(g)}\right) - tr\left(\underline{q}^T \underline{\underline{D}}_v^{(g)}\right)}{\underline{F}^T \underline{S}^{(g)}} - \frac{\delta_u}{h_{ns}} \frac{\underline{V}^T \underline{S}^{(g)}}{\underline{F}^T \underline{S}^{(g)}} \leq$$

$$\leq \frac{2\underline{M}_{c,im}^T \underline{I}}{\underline{F}^T \underline{S}_{im}{}^{(3)}} - \frac{\delta_u}{h_{im} - h_{im-1}} \frac{\underline{V}^T \underline{S}_{im}{}^{(3)}}{\underline{F}^T \underline{S}_{im}{}^{(3)}} \tag{5.50}$$

The relationship between the external work that the horizontal forces play in the *n-th* mechanism of type-3 and that performed in the global mechanism:

$$\lambda_{im}^{(1)} = \frac{\underline{F}^T \underline{S}_{im}{}^{(3)}}{\underline{F}^T \underline{S}^{(g)}}$$

$$\Delta_{im}^{(3)} = \frac{\underline{F}^T \underline{S}^{(g)}}{\underline{F}^T \underline{S}_{im}{}^{(3)}} \frac{\frac{1}{h_{im} - h_{im-1}} \underline{V}^T \underline{S}_{im}{}^{(3)}}{\frac{1}{h_{ns}} \underline{V}^T \underline{S}^{(g)}}$$

$$\underline{M}_{c1}^T \underline{I} + \mu^{(g)} + v^{(g)}\delta + \tau^{(g)} \leq \frac{1}{\lambda_{im}^{(3)}} \underline{M}_{c,im}^T \underline{I} - v^{(g)}\delta_u \Delta_{im}^{(3)} \tag{5.51}$$

$$\rho_{im}^{(3)} \geq \frac{\sum_{i=1}^{n_c} M_{c,i1} + \mu^{(g)} + v^{(g)}\delta_u\left(\Delta_{im}^{(3)} - 1\right) - \tau^{(g)}}{\frac{2}{\lambda_{im}^{(3)}}\sum_{i=1}^{n_c} M_{c,i1}}$$

Numerical application of the control theory of the collapse mechanism

The formulations preceding the case of the structure in question are particularized:

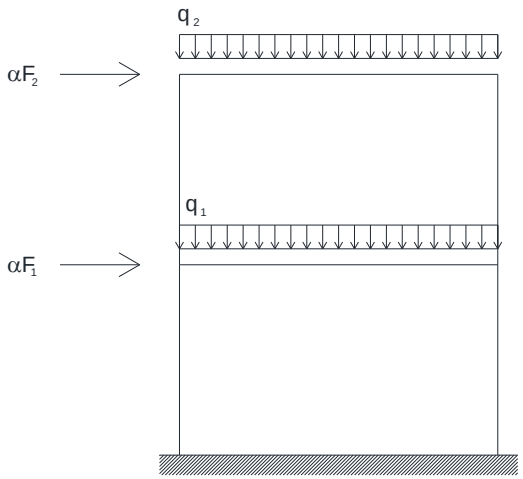

Fig. 5.12 – Two floors, single span frame with distributed and concentrated force.

Type-1 mechanism

Case of ι_m = 1:

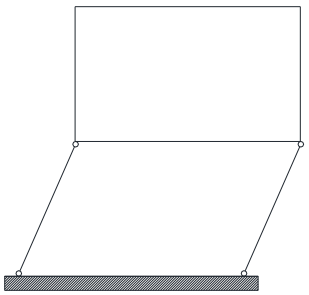

Fig. 5.13 – Index of mechanism 1 - Mechanism type-1.

As no plastic hinges are formed at the ends of the beams, they do not work:

$$\xi = 0$$

$$\lambda = \frac{F_1 h_1 + F_2 h_1}{F_1 h_1 + F_2 h_2} \tag{5.52}$$

As uniformly distributed loads do not work:

$$\zeta = 0 \tag{5.53}$$

Case of $\imath_m$ = 2:

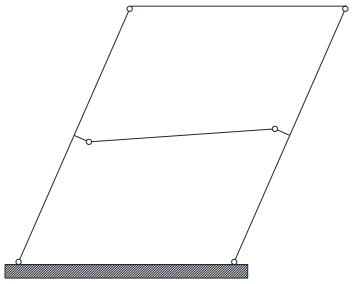

Fig. 5.14 – Index of mechanism 2 - Mechanism type-1.

$$\xi = \frac{2M_b}{4M_b} = 0{,}50$$

$$\lambda = \frac{F_1 h_1 + F_2 h_2}{F_1 h_1 + F_2 h_2} = 1{,}00 \tag{5.54}$$

$$\zeta = \frac{q_1 \frac{L}{2}}{q_1 \frac{L}{2} + q_2 \frac{L}{2}}$$

Type-2 mechanism

Case of $\imath_m$ = 1:

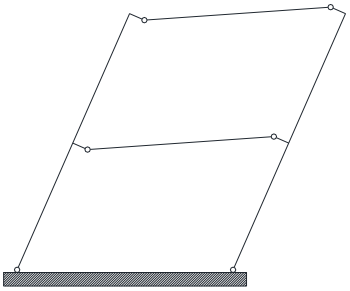

Fig. 5.15 – Index of mechanism 1 - Mechanism type-2 (Coincident with global mechanism).

$$\xi = \frac{4M_b}{4M_b} = 1{,}00$$

$$\lambda = \frac{F_1 h_1 + F_2 h_2}{F_1 h_1 + F_2 h_2} = 1{,}00 \qquad (5.55)$$

$$\zeta = \frac{q_1 \frac{L}{2} + q_2 \frac{L}{2}}{q_1 \frac{L}{2} + q_2 \frac{L}{2}} = 1{,}00$$

This case corresponds to the global mechanism because the plastic hinges are formed at the ends of the beams and at the foot of the columns.

Case of i_m = 2:

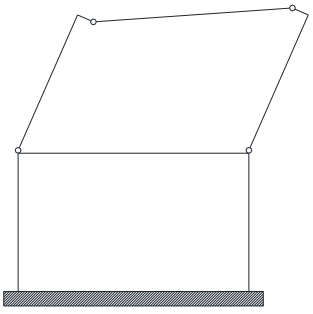

Fig. 5.16 – Index of mechanism 2 - Mechanism type-2.

$$\xi = \frac{2M_b}{4M_b} = 0{,}50$$
$$\lambda = \frac{F_2(h_2 - h_1)}{F_1 h_1 + F_2 h_2} \qquad (5.56)$$
$$\zeta = \frac{q_2 \frac{L}{2}}{q_1 \frac{L}{2} + q_2 \frac{L}{2}}$$

Type-3 mechanism

Case of i_m = 1:

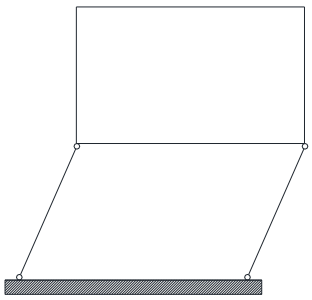

Fig. 5.17 – Index of mechanism 1 - Mechanism type-3.

As no plastic hinges are formed at the ends of the beams, they do not work:

$$\xi = 0$$
$$\lambda = \frac{F_1 h_1 + F_2 h_1}{F_1 h_1 + F_2 h_2} \qquad (5.57)$$

As uniformly distributed loads do not work:

$$\zeta = 0 \qquad (5.58)$$

This case is similar to the one concerning the mechanism index 1 of mechanism 1.

Case of $\acute{\imath}_m$ = 2:

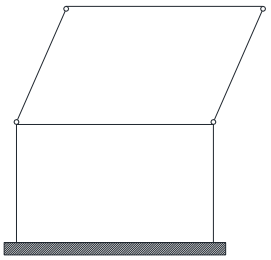

Fig. 5.18 – Index of mechanism 2 - Mechanism type-3.

$$\xi = 0$$

$$\lambda = \frac{F_2(h_2 - h_1)}{F_1 h_1 + F_2 h_2} \tag{5.59}$$

It is important to assure that the collapse mechanism is global type. In this case the last move is:

$$\delta_u = \vartheta_{pu} h_{ns} \tag{5.60}$$

where:

θ_{pu} has been set at *0.045rad*;

h_{ns} is the overall height of the structure;

The parameters ξ, λ, ζ are calculated for each mechanism index and for each mechanism.

Table 5.4 – Parameters ξ, λ, ζ calculated or each mechanism

Mechanism	i_m	ξ	λ_a	λ_b	ζ
Type 1	1	0.00	0.63	0.70	0.00
	2	0.50	1.00	1.00	0.58
Type 2	1	1.00	1.00	1.00	1.00
	2	0.50	0.37	0.30	0.42
Type 3	1	0.00	0.63	0.70	0.00
	2	0.00	0.37	0.30	0.00
Global	-	1.00	1.00	1.00	1.00

The parameters $\Delta_{im}(t)$ relative to the effects of the second order are calculated for each mechanism index, for each mechanism and for each distribution of horizontal actions. The subscript *a* indicates a distribution of seismic actions of a decking similar to the first mode of vibrating of the structure. The subscript *b* indicates a distribution of seismic actions of a slab similar to the masses. The slopes of the equilibrium curves of the considered mechanisms are calculated.

Table 5.5 – Parameters $\Delta_{im}(t)$ calculated or each mechanism

Mechanism	i_m	$\Delta\alpha$	$\Delta\beta$	$\sigma_1(\mu)$	$\sigma_2(\mu)$	$H_0(\mu)$	γ_α	γ_β
Type 1	1	2.25	2.00	2.40	2.40	2.40	27.50	27.50
	2	1.00	1.00	2.40	4.80	4.80	12.25	13.72
Type 2	1	1.00	1.00	2.40	4.80	4.80	12.25	13.72
	2	1.59	1.99	0.00	2.40	2.40	19.48	27.30
Type 3	1	2.25	2.00	2.40	2.40	2.40	27.50	27.50
	2	1.59	1.99	0.00	2.40	2.40	19.48	27.30
Global	-	1.00	1.00	2.40	4.80	4.80	-	-

An attempt value of the reduced plastic moment of the columns is required, for example 25% higher than the plastic moment of the beams

or the first plastic moment from the catalogs of the columns and more than 25% of that of the beams. In this case the second solution has been preferred and the a_t multiplier, corresponding to the global mechanism, has been evaluated in correspondence of the last selected displacement:

$$\alpha_t = \alpha^{(g)} - \gamma^{(g)}\delta_u \tag{5.61}$$

The limit values are calculated: $\rho_{im}^{(1)}$, $\rho_{im}^{(2)}$, $\rho_{im}^{(3)}$.

Table 5.6 – Parameters a calculated or each mechanism

Mechanism	i_m	*Mc [kNm]*	$\alpha_\alpha^{(\gamma)}$	$\alpha_\beta^{(\gamma)}$	$\gamma_\alpha^{(\gamma)}$	$\gamma_\beta^{(\gamma)}$	$\mu^{(\gamma)}$	$\nu^{(\gamma)}$	$\tau^{(\gamma)}$
Type 1	***1***	*228.09*	-	-	-	-	-	-	-
	2	-	-	-	-	-	-	-	-
Type 2	***1***	-	-	-	-	-	-	-	-
	2	-	-	-	-	-	-	-	-
Type 3	***1***	-	-	-	-	-	-	-	-
	2	-	-	-	-	-	-	-	-
Global		-	*297.40*	*333.13*	*12.25*	*13.72*	*685.01*	*47.00*	*0.00*

Table 5.7 – Parameters ρ_{im} calculated or each mechanism

Mechanism	i_m	$\rho_\alpha^{(1)}$	$\rho_\beta^{(1)}$	$\rho_\alpha^{(2)}$	$\rho_\beta^{(2)}$	$\rho_\alpha^{(3)}$	$\rho_\beta^{(3)}$
Type 1	***1***	*0.58*	*0.77*	-	-	-	-
	2	*0.75*	*0.75*	-	-	-	-
Type 2	***1***	-	-	*1.00*	*1.00*	-	-
	2	-	-	*0.19*	*0.00*	-	-
Type 3	***1***	-	-	-	-	*0.79*	*0.88*
	2	-	-	-	-	*0.47*	*0.38*
Global		-	-	-	-	-	-

The values ρ_{im} are calculated for each floor; these values prevent a failure mode corresponding to the three types of collapse mechanisms examined. The satisfaction of the technological condition is checked:

$$\rho_1 \geq \rho_2 \geq \rho_3 \geq \ldots \geq \rho_{ns} \tag{5.62}$$

Table 5.8 – Parameters ρ_{im} calculated or each analysis type

$\rho(\tau)$	1st mode (a)			Masses (b)				
i_m	Type 1	Type 2	Type 3	Type 1	Type 2	Type 3	1st mode (a)	Masses (b)
1	0.58	1.00	0.79	0.77	1.00	0.88	1.00	1.00
2	0.75	0.19	0.47	0.75	0.00	0.38	0.75	0.75

Table 5.9 – Checks of the ρ_{im} parameter

Check	Check
$\rho_\alpha^{(1)} > \rho_\alpha^{(2)}$	$\rho_\beta^{(1)} > \rho_\beta^{(2)}$
Satisfied	Satisfied

The values of the corresponding kinematic multipliers are calculated $\alpha_{im}^{(1)}$, $\alpha_{im}^{(2)}$, $\alpha_{im}^{(3)}$.

Table 5.10 – Kinematic multipliers

		Type 1		Type 2		Type 3	
	i_m	1st mode (a)	Masses (b)	1st mode (a)	Masses (b)	1st mode (a)	Masses (b)
α_{im}	1	380.15	380.15	297.40	333.13	380.15	380.15
α_{im}	2	327.03	366.31	555.74	778.70	634.84	889.53

The last multiplier is calculated as the minimum among all the cinematically permissible multipliers, including the influence of the second order effects for a last assigned displacement:

$$\alpha_u = min\left\{\alpha_{im}^{(t)} - \gamma_{im}^{(t)}\delta_u; i_m = 1,2,\dots,n_s; t = 1,2,3\right\} \quad (5.63)$$

Table 5.11 – Minimum values of the kinematic multipliers

		Type 1		***Type 2***		***Type 3***	
	i_m	***1st mode***	***Masses***	***1st mode***	***Masses***	***1st mode***	***Masses***
		(a)	***(b)***	***(a)***	***(b)***	***(a)***	***(b)***
$\alpha_u^{(t)}$	***1***	*374.21*	*374.21*	*294.76*	*330.17*	*374.21*	*374.21*
$\alpha_u^{(t)}$	***2***	*324.38*	*363.35*	*551.53*	*772.81*	*630.63*	*883.63*

If

$$\left|\alpha_g - \alpha_t\right| > 0 \quad (5.64)$$

then the multiplicative coefficient of the plastic moment of the beam is modified and the previous operations starting from the definition of α_t.
If

$$\left|\alpha_g - \alpha_t\right| = 0 \quad (5.65)$$

then convergence is reached.

Table 5.12 – Checks of the kinematic multipliers

$\alpha_{a,u}$=	*294.76*	$\alpha_{b,u}$=	*330.17*
$\alpha_{a,u}^{(g)}$=	*294.76*	$\alpha_{b,u}^{(g)}$=	*330.17*
Δ =	*0.00*	Δ =	*0.00*

As can be seen from the data in the table, in this case the convergence is achieved.

Then the normal stresses to the collapse of the columns of the first floor are calculated.

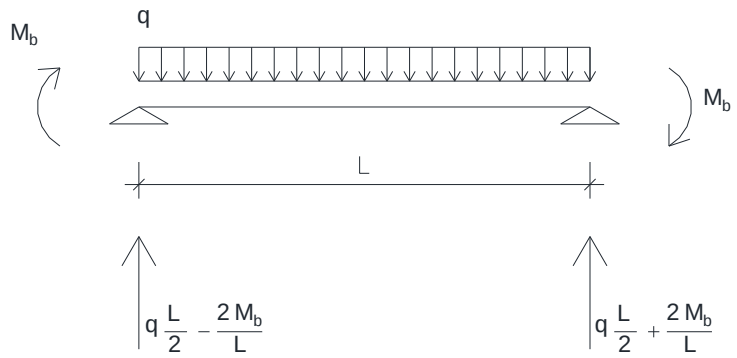

Fig. 5.19 – Scheme of the beam for the evaluation of the axial forces in the columns.

$$N_{c,1i} = q_1 \frac{L}{2} + q_2 \frac{L}{2} + \frac{4M_b}{L} \tag{5.66}$$

The reduced plastic moment of each column can be obtained once the normal collapse stresses in the columns are known in the hypothesis of a global mechanism.

$$M_{c,ik} = \rho_k \frac{N_{ik}}{\sum_{i=1}^{n_c} N_{ik}} \sum_{i=1}^{n_c} M_{c,i1} \tag{5.67}$$

N_{ik} is the normal effort of the *i-th* column of the *k-th* plane.

Table 5.13 – Columns checks

Level:	1	2
$N_{c,1i}$ [kN] =	204.25	99.63
ρ_1 =	1.00	0.75
Mc,1k [kNm] =	228.09	171.25
$W_{pl,\ HE200B}$ [mm3] =	642500.00	642500.00
$M_{pl,\ HE200B}$ [kNm] =	228.09	228.09
Check:	Satisfied	Satisfied

5.2.4. Design of the frame with the procedure in closed form of the control theory of the collapse mechanism.

Recently, a new procedure has been proposed on the control of the collapse mechanism that has the peculiarity of not being iterative, but can be expressed in a closed form.

It is important that the collapse mechanism of a structure corresponds to the global one; in this way, in fact, they are used as dissipative zones:

- the ends of the beams, more ductile being subjected to null normal stresses;
- the sections placed at the base of the frame columns.

With the current legislation reference is made to the design criterion based on the hierarchy of resistance; this criterion, however, fails to guarantee a global collapse mechanism, but only allows avoiding the soft plane mechanism.

Probably the most important reason that leads to the failure of the beam-column hierarchy criterion is that the variation and the trend of the

bending moments during the seismic event can be very different from what is assumed by the norm.

The lack of knowledge of the real evolution of the distribution of plastic hinges causes such important uncertainties to decree the inadequacy of the beam-column hierarchy criterion in order to obtain a global collapse mechanism. Therefore, it is possible to resort to the theory of control of the collapse mechanism, already proposed in the previous phase for the frame design, and now revived in order to obtain a solution in a closed form following a recent updating work. In fact, it is necessary to satisfy the design conditions to prevent unwanted collapse mechanisms without iterations.

The theory of control of the collapse mechanism is based on the upper limit theorem of plastic collapse. An important hypothesis is that of assuming a rigid-plastic behavior of the structure, that is to say neglecting the lateral displacements that occur before the complete development of the collapse mechanism. Moreover, the relevant lateral displacements produce non-negligible effects of the second order.

For each mechanism of collapse, the equilibrium curve of the mechanism is obtained by equalizing the work of external forces with the internal one due to the plastic hinges that originate as a result of this mechanism, but also including the effects of the second order in the external forces.

To ensure that the plastic hinges are formed at the ends of the beams, it must be:

$$q_{jk} \leq \frac{4M_{b,jk}}{L_j^2} \tag{5.68}$$

j is the span index, while k is the plan index.

The basic reference scheme after the formation of plastic hinges is:

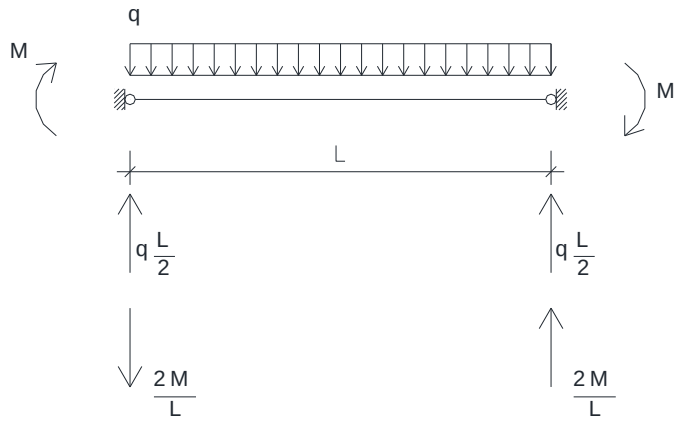

Fig. 5.20 – Static scheme that assure that the plastic hinges develop at the beam ends.

$$q\frac{L}{2} \leq \frac{2M}{L} \quad \rightarrow \quad q \leq \frac{4M}{L^2} \tag{5.69}$$

For the global mechanism the work of external forces due to a virtual rotation $d\vartheta$ of the plastic hinges of the column, starting from a deformed configuration characterized by a rotation θ is:

$$W_e = \alpha \sum_{k=1}^{n_s} F_k(h_k \cdot d\vartheta) + \frac{\delta}{h_{ns}} \sum_{k=1}^{n_s} V_k(h_k \cdot d\vartheta) \tag{5.70}$$

where:

α is the multiplier of horizontal forces;

F_k and h_k are, respectively, the seismic force applied to the k-th plane and the elevation of the same plane with respect to the foundation level;

h_{ns} is the value of h_k at the level of the last floor;

δ is the maximum horizontal displacement at the top of the structure;
V_k is the total vertical load acting on the *k-th* floor.
The first term to the second member of the previous equation represents the external work due to the horizontal seismic forces, while the second term is the work of the second order due to the vertical loads.
The vector of vertical virtual displacements is:

$$dv_k = du_k \frac{\delta}{h_{ns}} = \frac{\delta}{h_{ns}} h_k \cdot d\vartheta \tag{5.71}$$

where dv_k represents the virtual vertical displacement at the *k-th* floor.
The internal work due to the virtual rotation of the plastic hinges is:

$$W_i = \left(\sum_{i=1}^{n_s} M_{c,i1} + 2 \sum_{k=1}^{n_s} \sum_{j=1}^{n_b} M_{b,jk} \right) \cdot d\vartheta \tag{5.72}$$

where:
$M_{c,ik}$ is the reduced plastic moment of the *i-th* column of the *k-th* plane, due to the presence of the normal stress, (in the case under examination $k = 1$).
n_c, n_b, n_s are, respectively, the number of columns, beams and planes.
Equating W_e and W_i:

$$W_e = W_i$$

$$\alpha \sum_{k=1}^{n_s} F_k (h_k \cdot d\vartheta) + \frac{\delta}{h_{ns}} \sum_{k=1}^{n_s} V_k (h_k \cdot d\vartheta) = \left(\sum_{i=1}^{n_s} M_{c,i1} + 2 \sum_{k=1}^{n_s} \sum_{j=1}^{n_b} M_{b,jk} \right) \cdot d\vartheta \tag{5.73}$$

$$\alpha = \frac{\sum_{i=1}^{n_s} M_{c,i1} + 2 \sum_{k=1}^{n_s} \sum_{j=1}^{n_b} M_{b,jk}}{\sum_{k=1}^{n_s} F_k h_k} - \frac{1}{h_{ns}} \frac{\sum_{k=1}^{n_s} V_k h_k}{\sum_{k=1}^{n_s} F_k h_k} \delta$$

The equilibrium curve of the mechanism is a straight line and it can be written as:

$$\alpha = \alpha_0 - \gamma\delta \tag{5.74}$$

Where a_0 is the cinematically permissible multiplier of the horizontal forces in accordance with a rigid-plastic analysis of the first order, and γ is the slope of the equilibrium curve of the mechanism.

The formulations of a_0 and γ are reported for the different types of collapse mechanisms.

Global mechanism:

$$\alpha_0^{(g)} = \frac{\sum_{i=1}^{n_c} M_{c,i1} + 2\sum_{k=1}^{n_s}\sum_{j=1}^{n_b} M_{b,jk}}{\sum_{k=1}^{n_s} F_k h_k}$$

$$\gamma^{(g)} = \frac{1}{h_{ns}} \frac{\sum_{k=1}^{n_s} V_k h_k}{\sum_{k=1}^{n_s} F_k h_k} \tag{5.75}$$

Mechanism type-1:

$$\alpha_{im}^{(1)} = \frac{\sum_{i=1}^{n_c} M_{c,i1} + 2\sum_{k=1}^{i_m-1}\sum_{j=1}^{n_b} M_{b,jk} + \sum_{i=1}^{n_c} M_{c,i,im}}{\sum_{k=1}^{i_m} F_k h_k + h_{im}\sum_{k=i_m+1}^{n_s} F_k}$$

$$\gamma_{im}^{(1)} = \frac{1}{h_{im}} \frac{\sum_{k=1}^{i_m} V_k h_k + h_{im}\sum_{k=i_m+1}^{n_s} F_k}{\sum_{k=1}^{i_m} F_k h_k + h_{im}\sum_{k=i_m+1}^{n_s} F_k} \tag{5.76}$$

Mechanism type-2:

$$\alpha_{im}^{(2)} = \frac{\sum_{i=1}^{n_c} M_{c,i,im} + 2\sum_{k=i_m}^{n_s}\sum_{j=1}^{n_b} M_{b,jk}}{\sum_{k=i_m}^{n_s} F_k\,(h_k - h_{im-1})}$$

$$\gamma_{im}^{(2)} = \frac{1}{h_{ns} - h_{im-1}} \frac{\sum_{k=i_m}^{n_s} V_k\,(h_k - h_{im-1})}{\sum_{k=i_m}^{n_s} F_k\,(h_k - h_{im-1})} \tag{5.77}$$

Mechanism type-3:

$$\alpha_1^{(3)} = \frac{2\sum_{i=1}^{n_c} M_{c,i1}}{h_1 \sum_{k=1}^{n_s} F_k} \quad per\ i = 1$$

$$\alpha_{im}^{(3)} = \frac{2\sum_{i=1}^{n_c} M_{c,i,im}}{(h_{im} - h_{im-1})\sum_{k=i_m}^{n_s} F_k} \quad per\ i > 1 \tag{5.78}$$

$$\gamma_{im}^{(3)} = \frac{1}{h_{im} - h_{im-1}} \frac{\sum_{k=i_m}^{n_s} V_k}{\sum_{k=i_m}^{n_s} F_k}$$

The slope of the equilibrium curve of the mechanism draws its minimum value when the collapse mechanism that develops is the global one.

In accordance with the kinematic theorem of plastic collapse extended to the concept of equilibrium curve of the mechanism, the design condition that must be satisfied to avoid unwanted collapse mechanisms requires that the equilibrium curve corresponding to the global mechanism be located below those corresponding to the undesired mechanisms, up to a maximum top displacement δ_u compatible with the local ductility resources of the structure.

The solution in closed form is obtained by following a series of steps.

- Select a project shift δ_u compatible with the local ductility resources of the structure.

In this case it is assumed $\vartheta = 0{,}045\, rad$, considering that $h_{ns} = 4{,}80\, m$, it follows that $\delta_u = 0{,}216\, m$.

- The slopes of the equilibrium curves of the collapse mechanisms $\gamma_{im}^{(t)}$ have been calculated through the previous relationships.
  For a distribution similar to the first vibration mode of the structure:

Table 5.14 – Parameters $\gamma_{im}^{(t)}$ (vibration mode)

	γ_{im} [cm^{-1}]		
i_m	**Mechanism 1**	**Mechanism 2**	**Mechanism 3**
2	*0.122*	*0.195*	*0.195*
1	*0.275*	*0.122*	*0.275*

$$\gamma^{(g)}[cm^{-1}] = 0{,}122 \tag{5.79}$$

For a distribution according to the distribution of the masses:

Table 5.15 – Parameters $\gamma_{im}^{(t)}$ (masses)

	γ_{im} [cm^{-1}]		
i_m	**Mechanism 1**	**Mechanism 2**	**Mechanism 3**
2	*0.137*	*0.273*	*0.273*
1	*0.275*	*0.137*	*0.275*

$$\gamma^{(g)}[cm^{-1}] = 0{,}137 \tag{5.80}$$

- With this step it is possible to design the sections of the beams and columns on the first floor. In the case in question, as was specified in the previous one design procedure, from experimental data we deduce a maximum expected moment at the ends of the

beams equal to *168kNm* and therefore IPE270 sections are adopted.

Then the sum of the plastic moments of the columns required on the first floor is obtained (and reduced due to the simultaneous action of the axial stress) to prevent unwanted collapse mechanisms, with the following formula:

$$\sum_{i=1}^{n_c} M_{c,i1} \geq \frac{2\sum_{k=1}^{n_s}\sum_{j=1}^{n_b} M_{b,jk} + \left(\gamma_1^{(3)} - \gamma^{(g)}\right)\delta_u \sum_{k=1}^{n_s} F_k h_k}{2\dfrac{\sum_{k=1}^{n_s} F_k h_k}{h_1 \sum_{k=1}^{n_s} F_k} - 1} \tag{5.81}$$

This relationship is obtained from the design condition:

$$\alpha_0^{(g)} - \gamma^{(g)}\delta_u \leq \alpha_{im}^{(t)} - \gamma^{(t)}\delta_u \tag{5.82}$$

With $i_m=1$ and $t=1$ or $t=3$, il meccanismo di tipo 1 ed il meccanismo di tipo 3 risultano coincidenti.

Moreover, the previous relationship is valid when the frame is perpendicular to the secondary beams of the deck.

$$\sum_{i=1}^{n_c} M_{c,i1,a} = 339{,}37\ kNm$$

$$\sum_{i=1}^{n_c} M_{c,i1,b} = 396{,}01\ kNm \tag{5.83}$$

- The axial stress of the columns in a collapsed condition is calculated as:

$$\sum_{i=1}^{n_c} N_{c,i,a} = 237{,}82\ kN$$
$$\sum_{i=1}^{n_c} N_{c,i,b} = 237{,}82\ kN \qquad (5.84)$$

Table 5.16 – Axial load of the columns

Level	***N_q (kN)***	***N_f (kN)***	***N_{tot} (kN)***
2	$q_2 \frac{L}{2} = 14{,}00$	$\frac{2M_b}{L} = 85{,}81$	$N_q + N_f = 99{,}81$
1	$q_1 \frac{L}{2} + N_2 = 33{,}00$	$\frac{2M_b}{L} = 85{,}81$	$N_q + N_f = 118{,}81$

$$\sum_{i=1}^{n_c} N_{c,i,a,b} = 2 \cdot 118{,}91\ kN = 237{,}82\ kN \qquad (5.85)$$

- The sum of the plastic moments required on the first floor is distributed between the columns proportionally to the axial force causing the collapse, that is by means of a distribution coefficient defined as the ratio of normal stress to collapse in the single column and the sum of normal stresses to the collapse of the columns of the first floor. Therefore, it is possible to design the different sections of the columns

Table 5.17 – Design of the columns sections

N_{tot} [kN]	***$M_{req,c,a}$ [kNm]***	***$W_{pl,eq}$ [cm³]***	***Section***	***$M_{pl,section}$ [kNm]***
118,91	$\frac{N_{c,i}}{\sum_{i=1}^{n_c} N_{c,i}} \sum_{i=1}^{n_c} M_{c,i1} = 169{,}68$	$\frac{M}{f_{yk}}$	*HE200B*	*228,10*
N_{tot} [kN]	***$M_{req,c,b}$ [kNm]***	***$W_{pl,eq}$ [cm³]***	***Section***	***$M_{pl,section}$ [kNm]***
118,91	$\frac{N_{c,i}}{\sum_{i=1}^{n_c} N_{c,i}} \sum_{i=1}^{n_c} M_{c,i1} = 198{,}00$	$\frac{M}{f_{yk}}$	*HE200B*	*228,10*

$$\sum_{i=1}^{n_c} M^*_{c,i1} = 2 \cdot 228{,}10\ kNm = 456{,}21\ kNm \tag{5.86}$$

The equilibrium curve of the mechanism can be calculated using this last value, the one corresponding to the actual sections present because they take into account an additional resistance with respect to the minimum required. Therefore, it is possible to calculate:

$$\begin{aligned} \alpha_a^{(g)} &= 295{,}36 \\ \alpha_b^{(g)} &= 330{,}84 \end{aligned} \tag{5.87}$$

- The sum of the plastic moments of the columns is calculated (reduced due to the simultaneous presence of the normal stress) required to avoid unwanted collapse mechanisms.

Mechanism type-1:

$$\sum_{i=1}^{n_c} M^{(1)}_{c,i,im} \geq \left(\alpha^{(g)} + \gamma_{im}^{(1)}\delta_u\right)\left(\sum_{k=1}^{i_m} F_k h_k + h_{im} \sum_{k=i_m+1}^{n_s} F_k\right) + - \sum_{i=1}^{n_c} M^*_{c,i1} - 2\sum_{k=1}^{i_m-1}\sum_{j=1}^{n_b} M_{b,jk} \tag{5.88}$$

Mechanism type-2:

$$\sum_{i=1}^{n_c} M^{(2)}_{c,i,im} \geq \left(\alpha^{(g)} + \gamma_{im}^{(2)}\delta_u\right) \sum_{k=i_m}^{n_s} F_k\,(h_{im} - h_{im-1}) + -2\sum_{k=i_m}^{n_s}\sum_{j=1}^{n_b} M_{b,jk} \tag{5.89}$$

Mechanism type-3:

$$\sum_{i=1}^{n_c} M^{(3)}{}_{c,i,im} \geq \left(\alpha^{(g)} + \gamma_{im}^{(3)} \delta_u\right) \frac{h_{im} - h_{im-1}}{2} \sum_{k=i_m}^{n_s} F_k \qquad (5.90)$$

- Calculation of the summation of the plastic moments of the columns required on each floor, to avoid all unwanted collapse mechanisms, such as the maximum value among those calculated previously.

$$\sum_{i=1}^{n_c} M_{\,c,i,im} = max\left\{\sum_{i=1}^{n_c} M^{(1)}{}_{c,i,im}\,; \sum_{i=1}^{n_c} M^{(2)}{}_{c,i,im}\,; \sum_{i=1}^{n_c} M^{(3)}{}_{c,i,im}\right\} \qquad (5.91)$$

Table 5.18 – Plastic moments of the columns

	$\sum_{i=1}^{n_c} \boldsymbol{M}_{\,c,i,im,a}$ $[\boldsymbol{kNm}]$			
$\boldsymbol{i_m}$	***Mechanism 1***	***Mechanism 2***	***Mechanism 3***	***Maximum***
2	*343,64*	*86,88*	*215,26*	*343,64*
1	*266,91*	*456,21*	*361,56*	*456,21*
	$\sum_{i=1}^{n_c} \boldsymbol{M}_{\,c,i,im,b}$ $[\boldsymbol{kNm}]$			
$\boldsymbol{i_m}$	***Mechanism 1***	***Mechanism 2***	***Mechanism 3***	***Maximum***
2	*343,64*	*1,73*	*172,69*	*343,64*
1	*352,06*	*456,21*	*404,13*	*456,21*

- The sums of the required plastic moments of the columns on each floor, reduced by the simultaneous action of the normal stress,

are distributed among all the columns of the plane proportionally to the axial stress acting as collapse.

Table 5.19 – Check of the column sections

Level	N_{tot} ***[kN]***	$M_{req,c}$ ***[kNm]***	$W_{pl,eq}$ ***[cm³]***	***Section***	$M_{pl,sezione}$ ***[kNm]***
2	*99,91*	*171,82*	*484,00*	*HEB200*	*228,10*
1	*118,91*	*228,10*	*642,55*	*HEB200*	*228,10*

Check of the frame according to the Eurocode 8 [1]

The type of soil must be specified so that the frame can be designed to support seismic actions: a type B soil has been chosen with $\frac{a_g}{g} = 0{,}35$

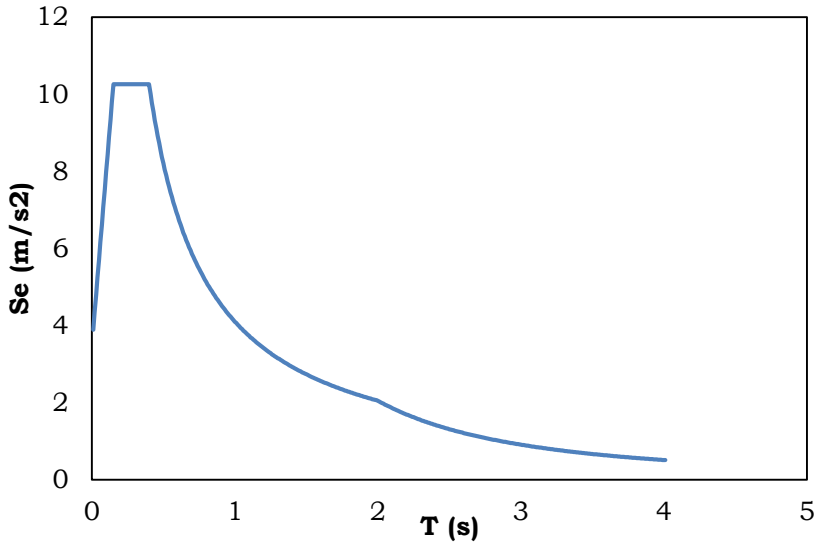

Fig. 5.21 – Spectrum according to Eurocode 8 [1]

The structure can be designed according to a ductility class: low, medium, high. Based on this choice, distinct structural factors can be defined:

Design concept	Structural ductility class	Range of the reference values of the behaviour factor q
Concept a) Low dissipative structural behaviour	DCL (Low)	≤ 1,5 - 2
Concept b) Dissipative structural behaviour	DCM (Medium)	≤ 4 also limited by the values of Table 6.2
	DCH (High)	only limited by the values of Table 6.2

Fig. 5.22 – Behaviour factors according to Eurocode 8 [1]

Since with this activity it is planned to test dissipative nodes, the structure in the high ductility class is designed and, therefore, according to the previous tables it is possible to define:

$$\frac{\alpha_u}{\alpha_1} = 1{,}20$$
$$q = 5\frac{\alpha_u}{\alpha_1} = 6{,}00 \tag{5.92}$$

The base shear has to be evaluated using the following relationship:

$$F_b = \frac{S_e \cdot m \cdot \lambda \cdot \delta}{q} \tag{5.93}$$

where δ is a parameter that allows to consider accidental eccentricity:

$$\delta = 1 + 0.6\frac{x}{L_e} sss \tag{5.94}$$

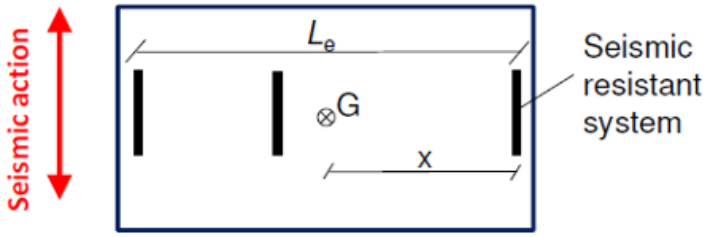

Fig. 5.23 – Scheme for the accidental eccentricity

where x is the distance between the frame under examination and the center of gravity of the masses, while L_e is the distance between the furthest seismo-resistant frames.

Table 5.20 – Base shear

m [kg] =	*33354.00*
λ =	*0.85*
S_e [m/s²] =	*10.26*
d =	*1.30*
F_b [kN] =	*63.02*

Subsequently, with reference to the shear at the base, the floor forces are evaluated, which are defined without a division similar to the first vibration mode of the structure:

$$F_i = F_b \frac{z_i m_i}{\sum z_i m_i} \tag{5.95}$$

Table 5.21 – Floor forces

i_m	***z [m]***	***m [kg]***	***z·m [kgm]***	***F [kN]***
1	*2.40*	*19100.00*	*45840.00*	*25.28*
2	*4.80*	*14254.00*	*68419.20*	*37.74*
Total	-	*33354.00*	*114259.20*	*63.02*

The structural elements have already been designed in the previous paragraphs, while in the following it is proposed to verify the satisfaction of the requests in terms of collapse and service conditions by adopting a procedure proposed by Eurocode 8 [1].
For beams, it is necessary to check:

$$\frac{M_{Ed}}{M_{pl,Rd}} \leq 1{,}00$$

$$\frac{N_{Ed}}{N_{pl,Rd}} \leq 0{,}15 \qquad (5.96)$$

$$\frac{V_{Ed}}{V_{pl,Rd}} = \frac{V_{Ed,G} + V_{Ed,M}}{V_{pl,Rd}} \leq 0{,}50$$

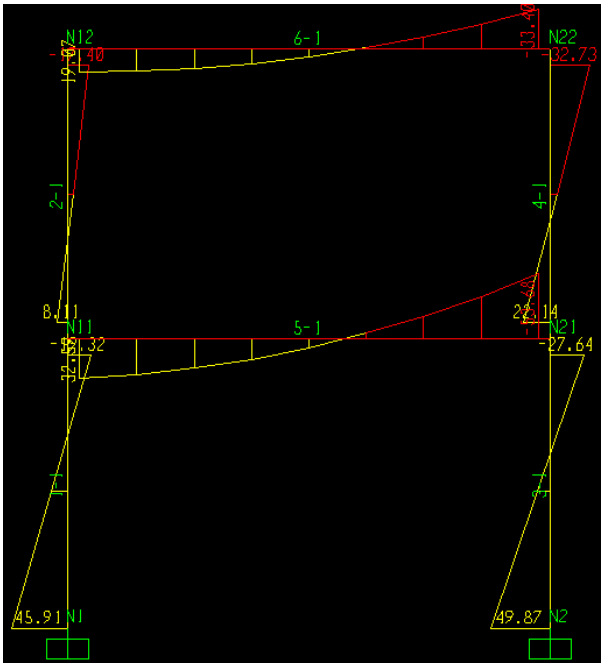

Fig. 5.24 – Bending moment for the check of the beams

The analyzes are carried out using the SAP2000 software and the bending moments diagram due to the weight of the structural elements, the uniformly distributed loads and the horizontal forces is as in Fig.5.24.
The previous limits are respected.
It is also necessary to verify that the beam, seen as hinged at the ends, has a not excessive displacement in the center line:

$$\delta_{max} = \frac{5}{384}\frac{ql^4}{EI} = 2.60\ mm$$
$$\delta_{limite} = \frac{L}{250} = 16.00\ mm \qquad (5.97)$$

The check is widely satisfied.

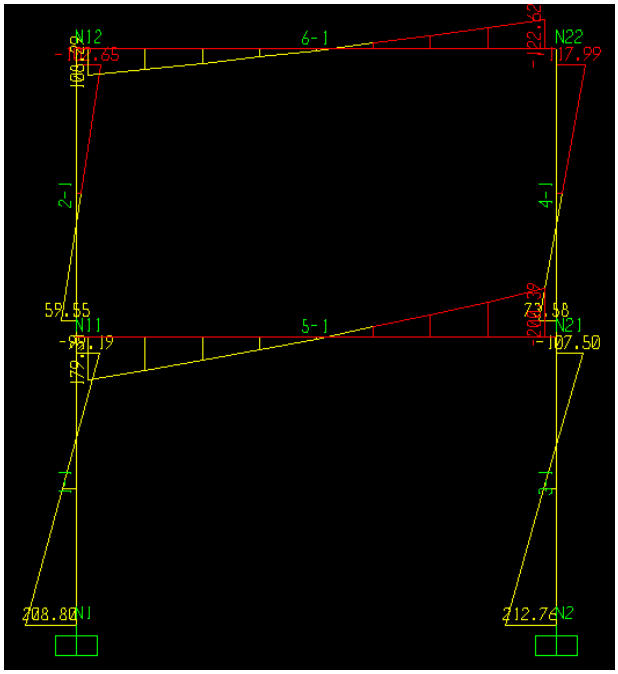

Fig. 5.25 – Bending moment for the check of the columns

Table 5.22 – Loads applied to the frame

i_m	z [m]	m [kg]	$z \cdot m$ [kgm]	F [kN]	$1.1\gamma_{ov}\Omega$	F [kN]
1	2.40	19100	45840.00	25.28	4.40	111.28
2	4.80	14254	68419.20	37.74	4.40	166.09
Tot.	-	33354	114259.20	63.02	-	-

In order to check the columns, the horizontal forces at level of the floor have to be amplified by means of three coefficients:

- 1.10, which allows to consider the phenomenon of hardening;
- γ_{ov}, an over-durability factor that is 1.25;

Ω, which is the minimum value of $\Omega_i = M_{pl,Rd,i}/M_{Ed,i}$ of all the beams in which the dissipative devices are positioned; $M_{Ed,i}$ is the design value of the bending moment of the beam in seismic conditions, while $M_{pl,Rd,i}$ is the corresponding plastic moment; in the case in question, this value is 3.20.

At this point the checks for the columns are performed:

$$\frac{N_{Ed}}{\frac{\chi_y N_{Rk}}{\gamma_{M1}}} + k_{yy}\frac{M_{y,Ed}+\Delta M_{y,Ed}}{\chi_{LT}\frac{M_{y,Rk}}{\gamma_{M1}}} + k_{yz}\frac{M_{z,Ed}+\Delta M_{z,Ed}}{\frac{M_{z,Rk}}{\gamma_{M1}}} \le 1$$

$$\frac{N_{Ed}}{\frac{\chi_z N_{Rk}}{\gamma_{M1}}} + k_{zy}\frac{M_{y,Ed}+\Delta M_{y,Ed}}{\chi_{LT}\frac{M_{y,Rk}}{\gamma_{M1}}} + k_{zz}\frac{M_{z,Ed}+\Delta M_{z,Ed}}{\frac{M_{z,Rk}}{\gamma_{M1}}} \le 1 \qquad (5.98)$$

In this case the resistance checks are satisfied because from the previous formulations a value around 0.90 has been obtained.

The verification is also satisfied that for each node the sum of the plastic moments of the columns is 30% greater than the sum of the plastic moments of the beams that flow into the same node.
The influence of the effects of the second order must also be assessed.

$$\vartheta = \frac{P \cdot d_r}{V \cdot h} \tag{5.99}$$

Where:
P is the total gravitational load above the plane under seismic conditions;
d_r is the relative displacement of the plan evaluated as the average of the lateral displacements to the head and to the foot of the considered plane;
V is the seismic force;
h is the height of inter-floor.
The effects of the second order are negligible if $\vartheta \leq 0{,}10$ and to be taken into account with a multiplicative coefficient of the plan forces equal to $1/(1-\vartheta)$ if $0{,}10 \leq \vartheta \leq 0{,}20$, in any case, ϑ can not be greater than 0.30.
It is possible to observe that the effects of the second order are negligible:

Table 5.23 – Second order effects

i_m	z [m]	P [kN]	d_r [m]	V [kN]	h [m]	θ
1	2.40	66.00	0.035826	63.02	2.40	0.01563
2	4.80	28.00	0.036192	37.74	2.40	0.01118

In the following the check in terms of damage is reported. For this check it is necessary to evaluate the drift of the floors at the two levels and compare them with the values reported by the Eurocode 8 [1] to proceed to a classification of the type of non-structural elements that can be adopted for the structure under consideration.

The drift limits are:

- $vd_t \leq 0{,}005 \cdot h$ for buildings which have non-structural elements of fragile material connected to the structure;
- $vd_t \leq 0{,}075 \cdot h$ for buildings having ductile non-structural elements;
- $vd_t \leq 0{,}010 \cdot h$ for buildings without non-structural elements or having non-structural elements fixed so as not to interfere with structural deformations.

Table 5.24 – Drift limits

i_m	s [m]	s_{ass} [mm]	s_{rel} [mm]	vs_{rel} [mm]
1	0.005971	35.83	35.83	17.91
2	0.012003	72.02	36.19	18.10

Table 5.25 – Checks of the drift

i_m	vs_{rel} [mm]	s_{lim} – Case C [mm]	Check
1	17.91	24.00	OK
2	18.10	24.00	OK

5.2.5. Design of the benchmark beam-to-column joint and experimental behaviour

The joint with RBSs (Fig. 5.26), used in the FREEDAM project for the benchmark 3D building mock-up with classical connections, was already tested in Iannone et al. [2] (in the original work it was labeled EEP-DB-CYC 03).

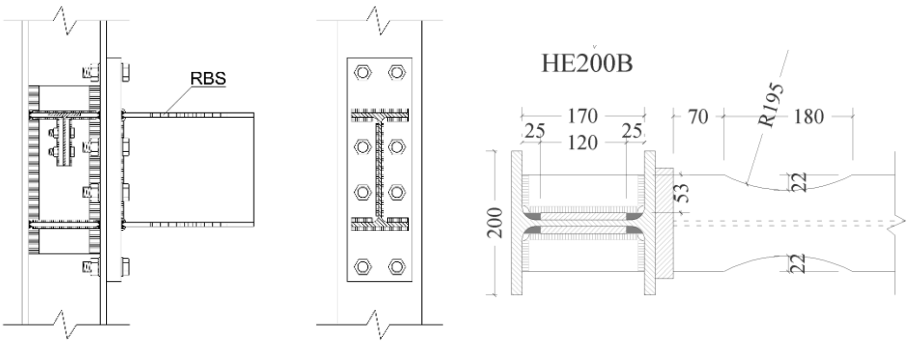

Fig. 5.26 – Benchmark case: Beam-to-Column Connection with RBS

Such connection, was designed according to the principles hereinafter reported. The three parameters to be designed for the RBS are the distance of the reduced section zone from the face of the column flange (a), the length of the reduced section zone (b) and the flange reduction width (c) (Fig. 5.27).

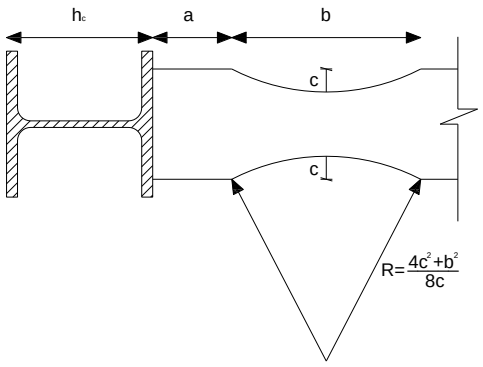

Fig. 5.27 – Design parameters for RBS connections

The first two parameters should be chosen as little as possible in order to minimize the stepping up of the moment due to the distance between

the plastic hinge and the column face. At the same time the RBS center should be not too far away to allow the complete yielding of beam flanges along the end section zone whose length should be sufficient to avoid plastic strain concentrations. A detailed discussion about the dimensioning of the amount of flange reduction (c) and of the distance between the center of RBS zone and the face of the column flange is given in (Montuori and Piluso, 1997 [3]), where also the influence of the uniform load acting on the beam is taken into account. However, structural schemes adopted for testing beam-to-column connections are more simple than real structures, because the beam uniform load is missing. For this reason, the simple design procedure suggested in (Moore et al.,1999 [4]) can be adopted without any trouble. In particular, it is suggested to use values of the two parameters *a* and *b* according to the following ranges:

$$\begin{aligned} 0.5b_f \le a \le 0.75b_f \\ 0.65d_f \le b \le 0.85d_f \end{aligned} \tag{5.100}$$

The last parameter to be considered is the amount of flange reduction (c) which controls the maximum bending moment at the RBS and, as consequence, the maximum moment at the face of the column flange. The value of *c* should be limited in order to obtain a moment at the column face in a range contained in the 85-100% of the beam cross section plastic moment. According to past experiences, Engelhardt et al. [5] suggest to avoid the use of these kinds of connections for reductions greater than 50%. Therefore, *c* must not be greater than $0.25b_f$.

The design procedure usually is iterative, because the moment at the column face can be evaluated only after the choice of the three

geometrical parameters, so that the fulfilment of suggested limits can be checked. In addition, the beam-column hierarchy criterion and the absence of shear mechanisms have to be checked. With reference to IPE270 section of tested specimens, after few iterations the design parameters have been identified: $a = 70mm$, $b = 180mm$ and $c = 22mm$. In particular, the amount of flange reduction (c) has been determined so that the plastic moment is equal to the desired joint resistance. In this case, this is equal to 100kNm. In fact, considering the reduction of 22 mm, the plastic moment of RBS is given by:

$$M_{pl,RBS} = W_{pl,RBS} f_y = \left[W_{pl,b} - 2ct_{bf}\left(d_b - t_{bf}\right)\right] f_y = \\ = \left[484000 - 2 \cdot 22 \cdot 10 \cdot \left(270 - 10\right)\right] \cdot 275 = 101640000 Nmm \cong 101.6 kNm \quad (5.101)$$

The design of the other elements of the connection, which have to remain in elastic range, has been carried out taking into account two effects: the strain hardening of steel, considered by a 1.15 factor and the expected yield strength herein assumed equal to $1.13f_y$, resulting from a coefficient of variation equal to 0.07. Therefore, the expected resistance of RBS at its center line was evaluated as:

$$M_{RBS,E} = 1.15 W_{pl,RBS} f_{y,E} = 1.15 \cdot 369600 \cdot 1.13 \cdot 275 = 132081180 Nmm \cong \\ \cong 132.1\ kNm \quad (5.102)$$

Starting from the knowledge of the expected moment at the RBS center, it was possible to evaluate the bending moment acting at the column face to check that it is contained in the stated limits and to design the end-plate and the shear panel in order remain in elastic range. To this scope it is necessary to evaluate the shear force acting at the RBS centerline,

that is given by the ratio between the maximum moment expected at the reduced section zone given by Eq. 5.103 and the beam length up to the "dog-bone" centerline:

$$V_{RBS,E} = \frac{M_{RBS,E}}{\left(L_b - a - \frac{b}{2}\right)} = \frac{132081180}{\left(1460 - 70 - \frac{180}{2}\right)} = 101601N \cong 101.6 \ kN \tag{5.103}$$

where L_b is the beam length. Neglecting the end-plate thickness, the moment acting on the column face and the plastic moment of the beam can be evaluated by means of the following expressions:

$$M_c = M_{RBS,E} + V_{RBS,E}\left(a + \frac{b}{2}\right) = 132081180 + 101601\left(70 + \frac{180}{2}\right) = \tag{5.104}$$

$$= 148337340Nmm \cong 148.3 \ kNm$$

$$M_b = W_{pl,b} f_{y,E} = 484000 \cdot 1.13 \cdot 275 = 150403000 \ Nmm \cong 150.4 \ kNm \tag{5.105}$$

Therefore, being $M_c / M_b \cong 1$, the suggested limit of 85%-100% is satisfied. It is easy to check that the strong column-weak beam requirement is also satisfied, being the sum of the plastic moments of columns, reduced to account for the influence of the axial load, greater than the bending moment M_c transmitted by the RBS to the column face. Considering these actions, the shear panel and the end-plate were designed so as to be over-resistant using the formulations contained in EC3 part 1.8 [6].

The beam-to-column connection with RBS used in the 3D building mock-up was tested in Iannone et al. [2] and more details on the experimental program carried out on this connection can be found in the original work.

The RBS beam-joint, accordingly with the design procedure was characterized by the typical failure mechanism of steel members with H section shape. In particular, after yielding of flanges and web and the attainment of the maximum flexural resistance, flange local buckling occurred accompanied by beam web buckling due to compatibility between flange and web out-of-plane displacements (Fig. 5.28).

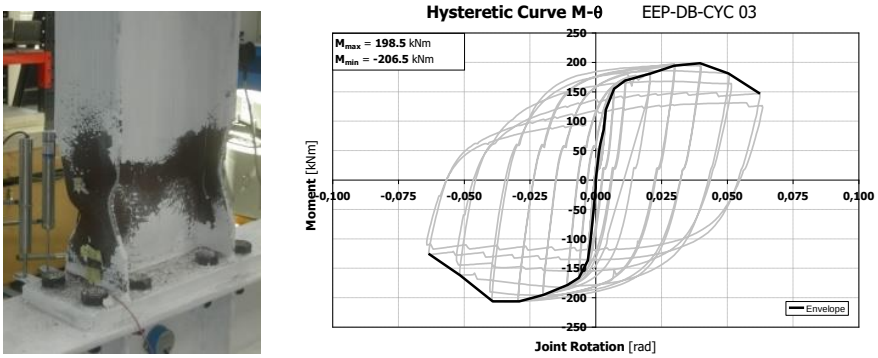

Fig. 5.28 – Cyclic behaviour of the beam-to-column joint with RBS tested in Iannone et al., (2008) [2]

The shape of the cycles of the whole joint was, as expected, wide and stable, guaranteeing a good energy dissipation capacity and significant plastic rotation supply.

5.2.6. Design of FREEDAM connection

The design procedure is quite similar to the one used in chapter 4. In the following the design procedure is reported in order to define the geometrical dimensions of the connection for the real scale frame.

<u>Step 1:</u> Estimation of the design friction resistance $F_{friction,Rd}$ of the friction device (dissipative component)

The design friction force that the device has to withstand is equal to:

$$F_{cf,Sd} = \frac{0.60 \cdot M_{Rd,IPE270}}{z} = \frac{0.60 \cdot 171.8 \cdot 10^3}{440} = 234\ kN \qquad (5.106)$$

Where z is equal to 440mm.

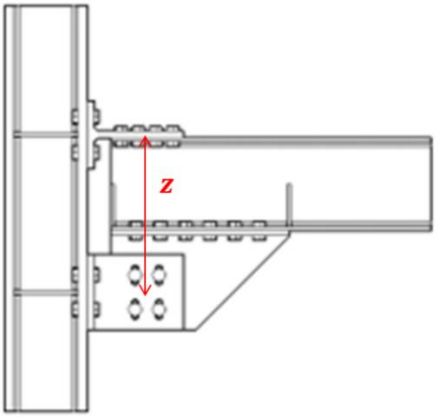

Fig. 5.29 – Lever arm scheme

At this point from the Eq. 5.107 it is possible to derive the number of bolts strictly necessary:

$$F_{cf,Seismic,d} = \frac{\mu_{dyn,5\%} \cdot F_p \cdot n_{b,min,1} \cdot n_s}{\gamma_{M3} \cdot \gamma_{creep}} \qquad (5.107)$$

$$n_{b,min} = \frac{F_{cf,d} \cdot \gamma_{M3} \cdot \gamma_{creep}}{\mu_{dyn,5\%} \cdot F_p \cdot n_s} = \frac{234 \cdot 1.10 \cdot 1.15}{0.53 \cdot 109.90 \cdot 2} = 2.54 \qquad (5.108)$$

The number of bolts is fix equal to 4.

Considering Eq. 5.109 the value of the bolts preload has been determined:

$$F_{p,red} = \frac{234}{0.53 \cdot 4 \cdot 2} = 55.60\ kN \tag{5.109}$$

Recalculating the design friction resistance (Eq. 5.109) the value obtained is obviously equal to $F_{slip,Ed}$, while the correspondent value of the bending moment is equal to the plastic resistance of the beam (Eq. 5.110).

$$F_{friction,Rd} = \mu_{dyn,5\%} \cdot F_{p,red} \cdot n_b \cdot n_s = 234.30\ kN \tag{5.110}$$

$$M_{friction,Rd} = 234.30\ kN \cdot 0.44\ m = 103\ kNm \tag{5.111}$$

<u>Step 2:</u> Design of the length of the slots on the haunch

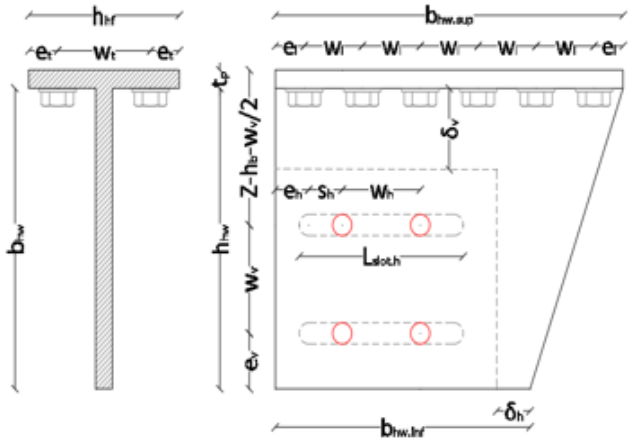

Fig. 5.30 – Geometrical parameters

In Fig. 5.30 the parameters that allow to define the geometric characteristics required are shown

In detail, the geometrical parameters assume the following values:

$$w_h = k_{wh} \cdot d_0 \tag{5.112}$$

$$e_h = k_{eh} \cdot d_0 \tag{5.113}$$

$$w_v = k_{vh} \cdot d_0 \tag{5.114}$$

$$e_v = k_{ev} \cdot d_0 \tag{5.115}$$

considering the following assumptions:

- $k_{wh} = 3.50$;
- $k_{eh} = 1.50$;
- $k_{wv} = 5.00$;
- $k_{ev} = 2.50$.

The length of the horizontal slots is fixed in $170mm$ to assure a rotation of $50mrad$, which is greater than the minimum required:

$$\begin{aligned} l_{slot,h} = 170\,mm \; &> l_{slot,h,min} \\ &= \left(\frac{4}{2} - 1\right) \cdot 63 + 17 + 2 \cdot 0.05 \cdot \left(440 + \frac{90}{2}\right) \\ &= 140\,mm \end{aligned} \tag{5.116}$$

<u>Step 3:</u> Evaluation of the bending moment in correspondence of the column flange and check of the beam in bending.

According to the second principle of capacity design, the moment acting at the column flange is evaluated by considering a coefficient of over-resistance $\gamma_{ov} = 1.78$:

$$M_{cf,Rd} = M_{friction,Rd} \cdot \gamma_{ov} = 183\ kNm \tag{5.117}$$

The design resistance is equal to:

$$F_{friction,Rd} = \frac{M_{cf,Rd}}{z} = \frac{183}{0.44} = 416.91\ kN \tag{5.118}$$

Considering a distributed load applied on the beam equal to 9.50 kN/m, a beam length of 4.00m and the height of the column, 200mm, the design shear is:

$$V_{Ed} = \frac{2 \cdot 183}{4 - 0.10} + 9.5\frac{4 - 0.10}{2} = 114.60\ kNm \tag{5.119}$$

<u>Step 4:</u> Design of the bolts' diameter for the TEE elements and the angles.

<u>Project of the flange of the T-stub and the bolts</u>

To design the diameter of the tensioning bolts, both tension and shear actions have to be considered:

$$F_{t,Ed} = \frac{F_{friction,Rd}}{n_b} = \frac{416.91}{4} = 104.23\ kN \tag{5.120}$$

$$F_{v,Ed} = \frac{V_{Ed}}{2 \cdot n_b} = \frac{114.60}{8} = 14.32\ kN \tag{5.121}$$

To design the resistant area of the bolts, the following formulation proposed by the Eurocode 3 [6] is used:

$$A_{res,min} = max\left[\frac{\gamma_{M2}}{f_{ub}}\left(\frac{F_{v,Ed}}{\alpha_v} + \frac{F_{t,Ed}}{1.26}\right); \frac{\gamma_{M2} \cdot F_{t,Ed}}{0.9 \cdot f_{ub}}\right] = 144.76\, mm^2 \qquad (5.122)$$

M24 bolts have been chosen, characterized by a resistant area of $353 mm^2$.

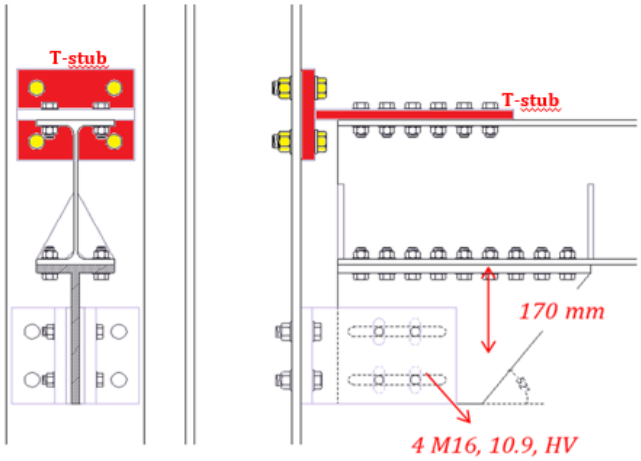

Fig. 5.31 – Geometrical parameters –T-stub

The horizontal distance between the bolts must meet the following limits:

$$w_{T,h,min} = max\{t_{wc} + 2r_c + 1.8d_0; b_b - 2 \cdot e\} = 91.8\, mm \qquad (5.123)$$

$$w_{T,h,max} = b_c - 2.4d_0 = 137.6\, mm \qquad (5.124)$$

where

b_c is the width of the column.

r_c is the radius of the arc that connects the flange and the core of the column.

e represents the horizontal and vertical distance of the bolt from the free edge and is $1.2d_0$.

Despite the previous limits are not respected, a distance between the bolts equal to $81mm$ has been adopted.
The width of the T-stub is equal to:

$$b_T = 2e_{T,f} + w_{T,h} = 195\ mm \tag{5.125}$$

$$b_{eff} = min\{b_{eff,1}; b_{eff,2}; 0.5b_T\} = 97.5\ mm \tag{5.126}$$

The width of the T-stub is fixed at the value of $30mm$.

Design of the horizontal plate of the T-stub and bolts.

To avoid the interaction between shear and bending moment at the base of the T-stub:

$$t_{T-stub,w} = \frac{V_{Ed} \cdot \sqrt{3} \cdot \gamma_{M0}}{0.5 \cdot b_t \cdot f_{y,T}} = 5.73\ mm \tag{5.127}$$

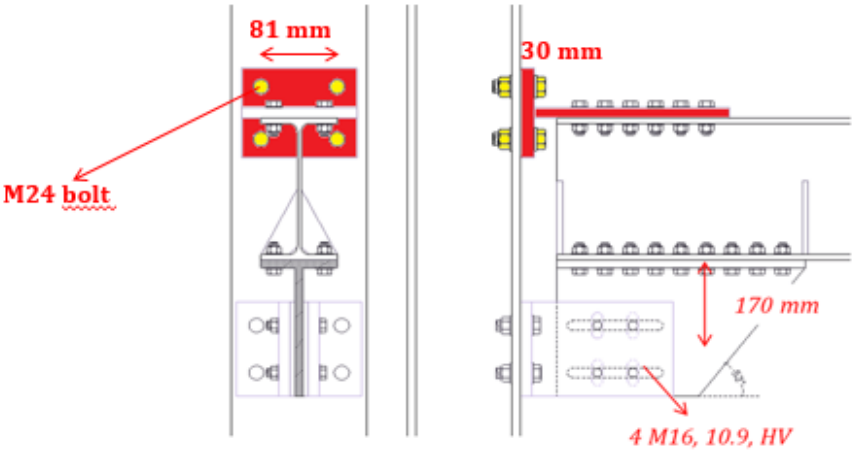

Fig. 5.32 – T-stub flange

the following assumption is considered:

$$t_{T-stub,w} = 15\ mm \tag{5.128}$$

It is also assumed that the width of the core of the T-stub is equal to the width of the flange.

Having set the diameter of the bolts to 16 mm, the number of bolts working in shear can be determined by considering the action they can transmit:

$$n_{b,min} = \frac{F_{friction,Rd} \cdot \gamma_{M2}}{\alpha_v \cdot A_{res} \cdot f_{ub}} = 8.37 \tag{5.129}$$

The number of bolts is rounded to 12.

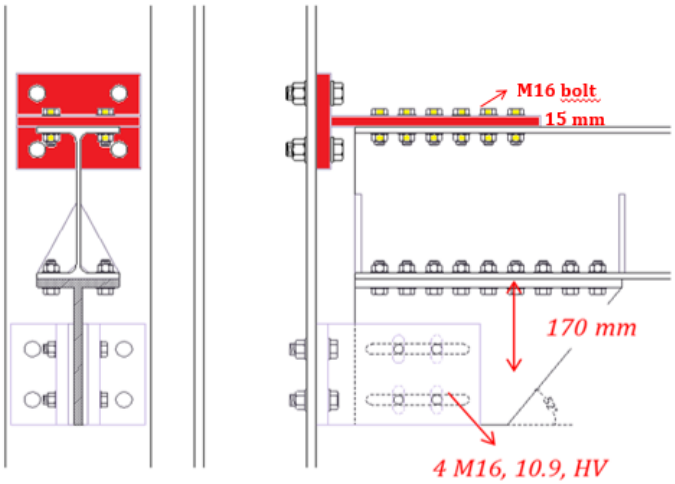

Fig. 5.33 – T-stub web

The distance between the beam and the column must be defined in such a way as to allow the joint to rotate the project, typically assumed to be

equal to 50$mrad$ to take into account the demand for local ductility. Furthermore, this distance should be sized so as to provide sufficient ductility to the plastic hinge formed at the core of the T-stub in case of seismic events.

This distance must be greater than $t_{T,f} + 2 \cdot t_{T,w}$. Therefore, to satisfy both the previous requests:

$$n_{b,min} = \frac{F_{friction,Rd} \cdot \gamma_{M2}}{\alpha_v \cdot A_{res} \cdot f_{ub}} = 8.37 \qquad (5.130)$$

<u>Step 5:</u> Design of the haunch.

<u>Flange</u>

The geometry of the flange is defined by means of a "trial and error" procedure, by fixing, iteratively, the number of rows of bolts, the pitch, the diameter of the bolts and the distance of the terminal rows of the bolts from the edge.

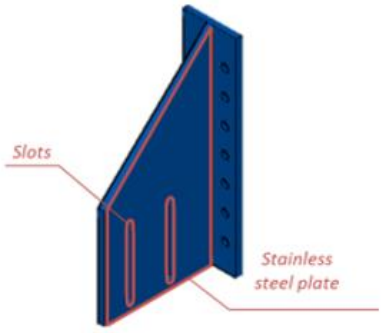

Fig. 5.34 – Haunch

In this case two rows of M16 bolts are adopted, with a longitudinal pitch of $2.4d_0 = 45\ mm$ and a distance from the free edge of $1.5d_0 = 22.5\ mm$
The control of the bolts that connect the flange of the additional element to the flange of the beam will be performed with the previous hypotheses.

$$F_{t,Ed} = \frac{F_{friction,Rd} \cdot h_h}{\sum_i d_i^2} \cdot d_{max} = 43.26\ kN \tag{5.131}$$

$$F_{v,Ed} = \frac{F_{friction,Rd}}{n_{b,h}} = 29.78\ kN \tag{5.132}$$

where
h_h represents half height of the additional plate;
d_i is the distance of the bolt i from the center of rotation.

Web

Considering the tensile failure:

$$t_{hw} \geq \frac{F_{friction,Rd} \cdot \gamma_{M0}}{(h_w - 2 \cdot d_0) \cdot f_y} = 9.50\ mm \tag{5.133}$$

It is assumed:

$$t_{hw} = 15\ mm \tag{5.134}$$

Step 6: Design of the L-stubs

Flange: Design of bolts and plate

$$F_{t,Ed} = \frac{F_{friction,Rd}}{n_b} = 104.23\ kN \tag{5.135}$$

$$F_{v,Ed} = \frac{F_{friction,Rd}}{2 \cdot n_b} = 14.32\ kN \tag{5.136}$$

The resistant area of the bolts must be greater than the value determined considering the combined action of shear and tension and the value determined for tension only:

$$A_{res,min} = max\left[\frac{\gamma_{M2}}{f_{ub}}\left(\frac{F_{v,Ed}}{\alpha_v} + \frac{F_{t,Ed}}{1.26}\right); \frac{\gamma_{M2} \cdot F_{t,Ed}}{0.9 \cdot f_{ub}}\right] = 144.76\ mm^2 \tag{5.137}$$

The bolts diameter is fixed to 20mm.

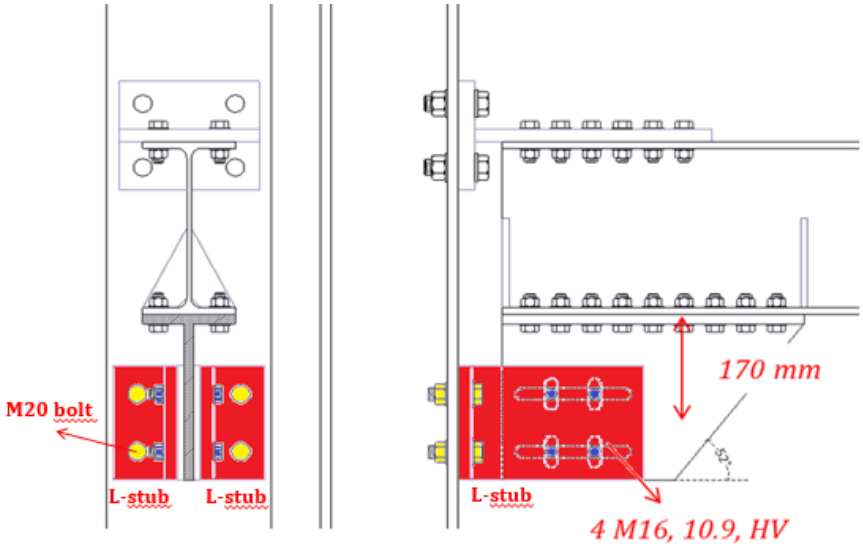

Fig. 5.35 – L-stubs

Web: design of the slotted holes

$$stroke_{v,D} = \varphi \cdot \left(gap + e_{L,f,h} + w_{L,f,h} + stroke_{h,A}\right) = 11.67\,mm \tag{5.138}$$

$$L_{slot,v,min} = 2 \cdot stroke_{v,D} + d_0 = 2 \cdot 9.98 + 18 = 41.34\,mm \rightarrow 50\,mm \tag{5.139}$$

Step 7 Checking the resistance of the beam

The bending moment at the column flange, $M_{cf,Rd}$, should be greater than the plastic resistant moment of the beam.
Therefore it is essential to evaluate the bending moment at the presumed position of the plastic hinge $M_{b,Ed}$. The beam, in this case, is a non-dissipative zone and must be controlled by the following relation:

$$M_{b,Ed} = M_{cf,Rd}\frac{L_e - b}{L_e} = 183\frac{2.18 - 0.245}{2.18} = 162.43 \leq M_{b,Rd} \tag{5.140}$$

where L_e is an equivalent length for shear and it can be evaluated as:

$$L - 2a - \frac{M_{cf,Rd}}{V_{Ed}} = 2.18\,m \tag{5.141}$$

while b is the length of the additional plate to increase the beam height.

5.3. Definition of a set of accelerograms

In this phase it is necessary to define the accelerogram to be used for the pseudo dynamic test. It must be specified that in order to perform nonlinear dynamic analyzes it is not possible to choose an accelerogram in an arbitrary manner, but one must refer to a set of accelerograms. Strictly speaking, a choice between natural accelerograms (i.e. those actually registered) and artificial ones (recordings of seismic events actually occurred but suitably modified in the frequency domain to have a response spectrum that is as similar as possible to a reference spectrum) is allowed.

From some publications (Caraballo and Cornell, 2000 [7] it has been shown that using artificial accelerograms the number of cycles or the energy of the signal can be very different from those of a real recording and, therefore, can lead to a statistically incorrect estimate of the non-linear response. For these reasons it has been decided to resort to mainly natural registrations properly scaled in terms of peak acceleration to the ground only to minimize the dispersion of the spectra with respect to the reference spectrum. No other manipulations have been made.

A set of accelerograms consists of:

- three accelerograms, then the effects on the structure (stresses, displacements, etc.) must be evaluated in terms of the envelopes obtained from the analyzes;
- seven accelerograms, then the effects on the structure can be represented by the means of the maximum values obtained in the analyzes assuming that the seismic events propagate only along a preferential direction;

- fourteen accelerograms, then the effects on the structure can be represented by the means of the maximum values obtained from the analyzes with simulated events acting along two orthogonal directions.

As already specified, the standards require that for the set of accelerograms chosen the average response spectrum is compatible with a reference spectrum: for a 5% equivalent viscous damping the average spectral ordinance must not be less than 90% of the corresponding reference elastic spectrum in the range $0{,}15\,s \div 2{,}00\,s$ or $0{,}15\,s \div 2 \cdot T$ in which T is the fundamental period of vibration of the structure in the elastic field. Below is a table with the set of nine accelerograms chosen:

Table 5.26 – Loads applied to the frame

Earthquake	***ΔT [s]***	***Duration [s]***	***a_g/g***
1.Coalinga	*0.01*	*29.99*	*0.17*
2.Helena	*0.01*	*39.99*	*0.15*
3.Imperial_Valley	*0.01*	*28.35*	*0.37*
4.Kobe	*0.01*	*40.95*	*0.25*
5.Landers	*0.02*	*50.00*	*0.17*
6.Northridge	*0.01*	*39.99*	*0.25*
7.Santa_Barbara	*0.01*	*12.57*	*0.10*
8.Spitak	*0.01*	*19.89*	*0.20*

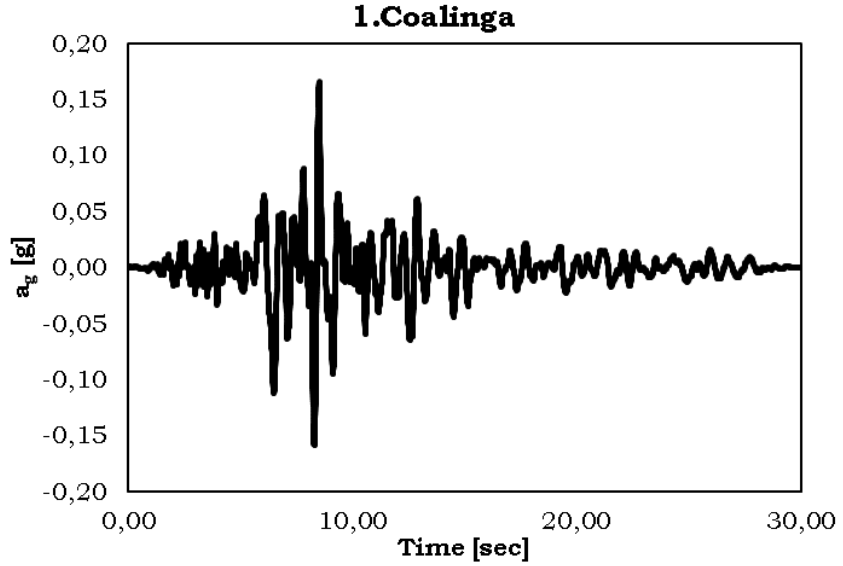

Fig. 5.36 – Coalinga accelerogram

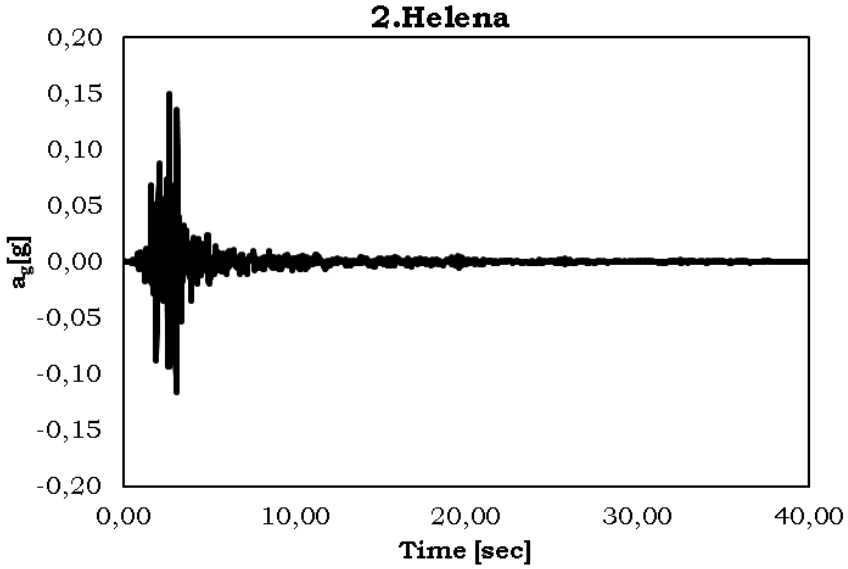

Fig. 5.37 – Helena accelerogram

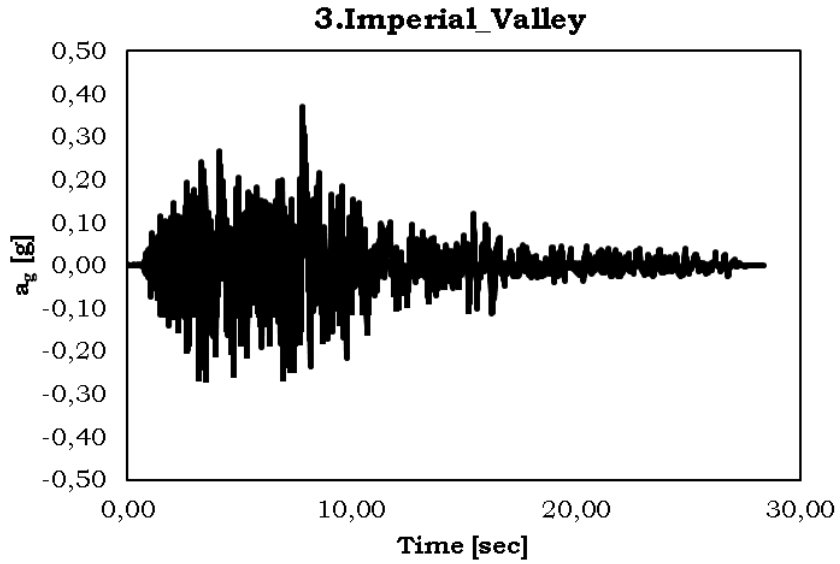

Fig. 5.38 – Imperial Valley accelerogram

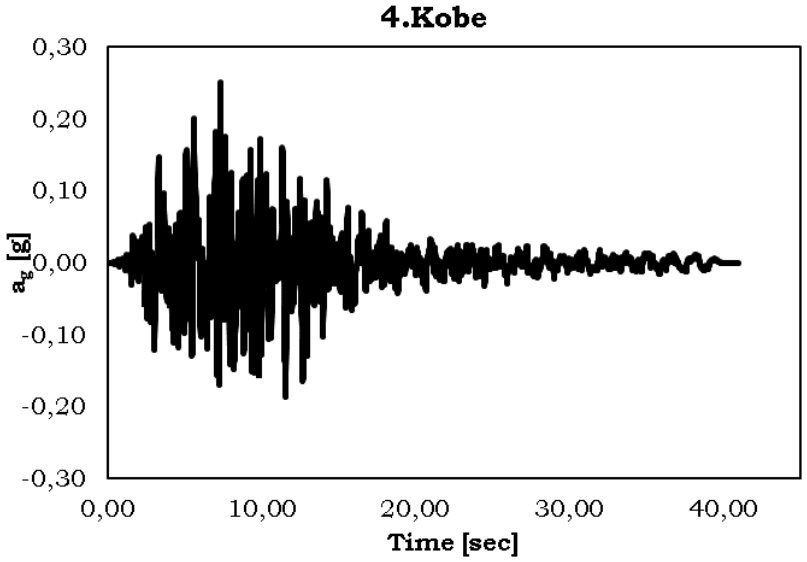

Fig. 5.39 – Kobe accelerogram

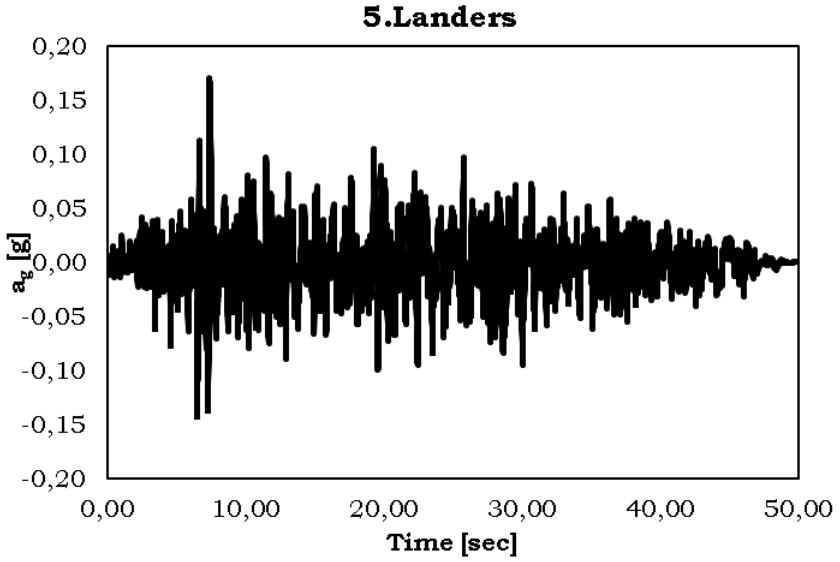

Fig. 5.40 – Landers accelerogram

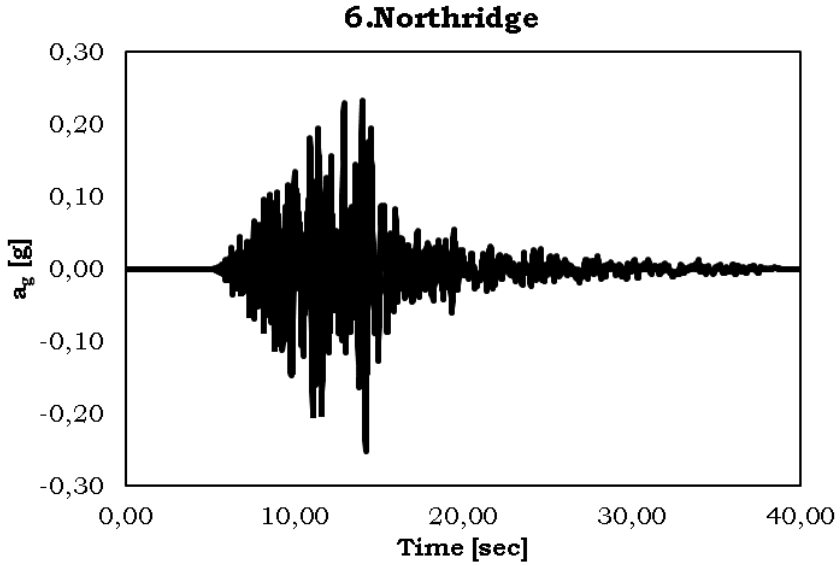

Fig. 5.41 – Northridge accelerogram

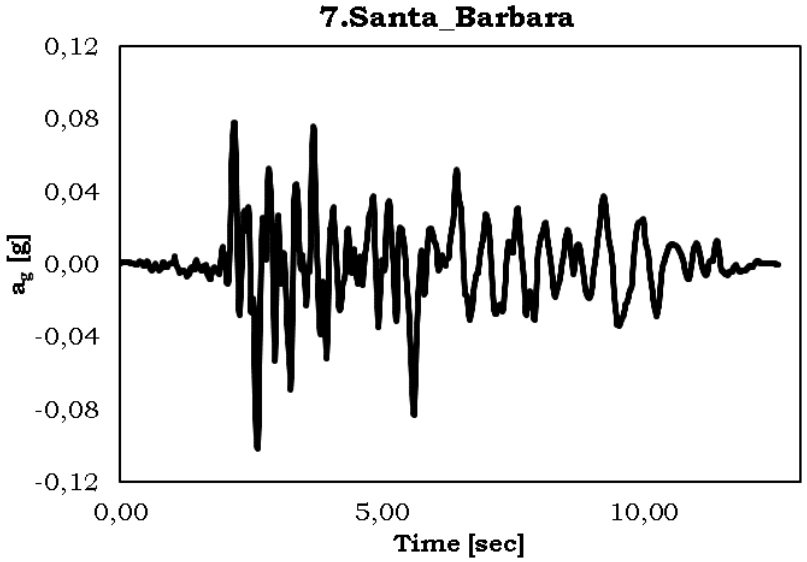

Fig. 5.42 – Santa Barbara accelerogram

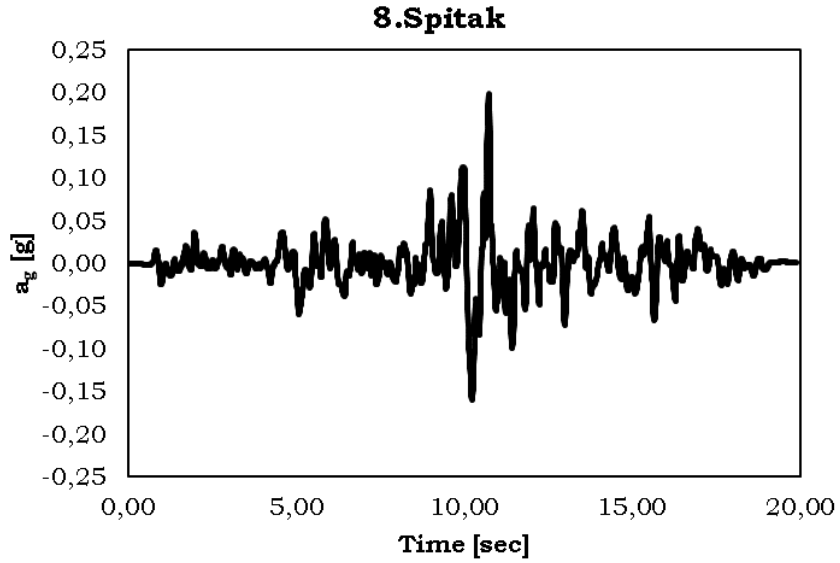

Fig. 5.43 – Spitak accelerogram

The characteristics of the reference spectrum have to be specified. In general, this spectrum is obtained by using the following formulations:

$$0 \le T \le T_B: S_e(T) = a_g \cdot S \cdot \left[1 + \frac{T}{T_B} \cdot (2{,}5 \cdot \eta - 1)\right] \quad (5.142)$$

$$T_B \le T \le T_C: S_e(T) = a_g \cdot S \cdot 2{,}5 \cdot \eta \quad (5.143)$$

$$T_C \le T \le T_D: S_e(T) = a_g \cdot S \cdot 2{,}5 \cdot \eta \cdot \left[\frac{T_C}{T}\right] \quad (5.144)$$

$$T_D \le T \le 4{,}00\ sec: \ S_e(T) = a_g \cdot S \cdot 2{,}5 \cdot \eta \cdot \left[\frac{T_C T_D}{T^2}\right] \quad (5.145)$$

where

$S_e(T)$is the elastic response spectrum;

T is the period of vibration of a linear system with only one degree of freedom;

a_g is the design acceleration of the terrain;

T_B is the lower limit of the period of the constant portion of the acceleration spectrum;

T_C is the upper limit of the period of the constant stretch of the acceleration spectrum;

T_D is the value that defines the beginning of the constant displacement response segment of the spectrum;

S is the ground coefficient;

η is the correction coefficient of the damping with a reference value of $\eta = 1$ for a viscous damping of 5%.

Using the SeismoSpect software, the response spectra of the nine accelerograms and the reference spectrum of the Eurocode 8 [1] are defined.

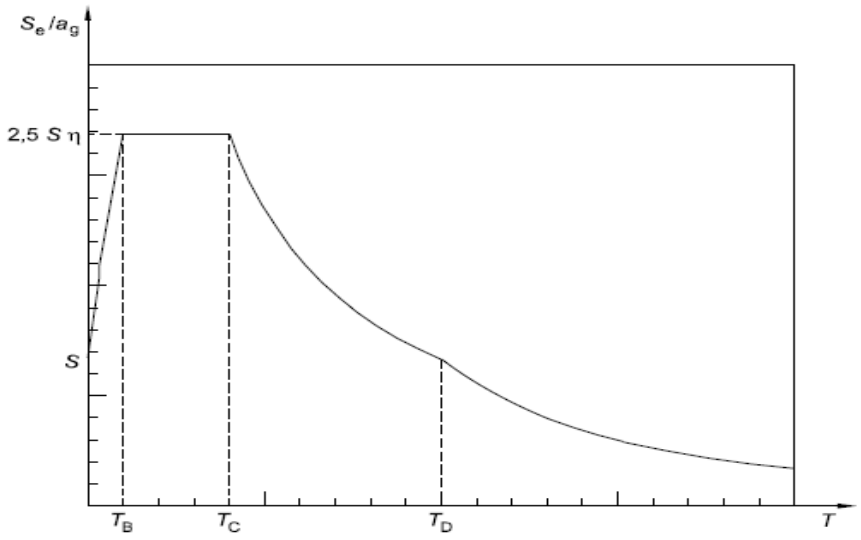

Fig. 5.44 – Elastic spectrum

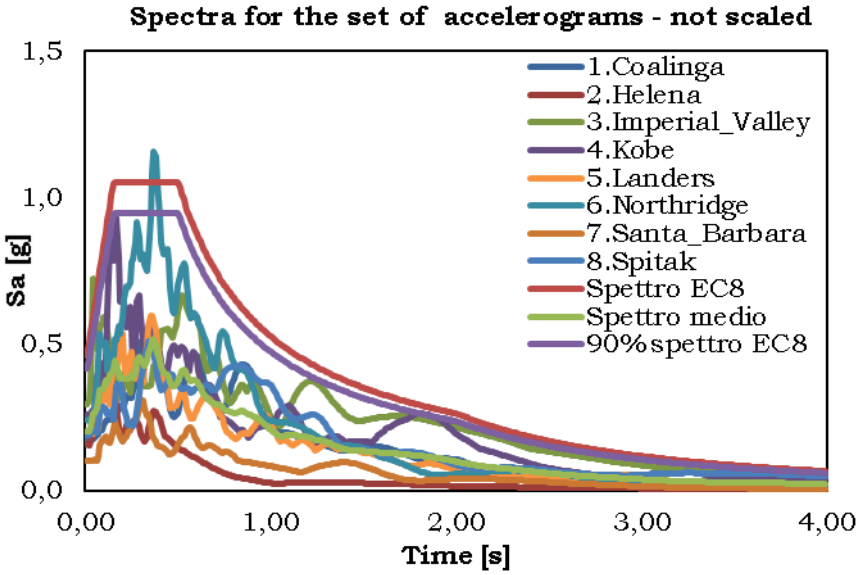

Fig. 5.45 – Elastic spectra not scaled

It is evident that with natural accelerograms it is not possible to obtain a medium spectrum respectful of the provisions of the rules and therefore it is necessary, as already anticipated, to scale the accelerograms

To perform this operation, it is necessary to know the vibration period of the structure and therefore a model has been preliminarily realized in SeismoStruct that allows to evaluate the missing information. It is specified that the vibration period of the structure is variable depending on the type of nodal connection taken into consideration, but the variability is between 0.40 ÷ 0.50 *s*.

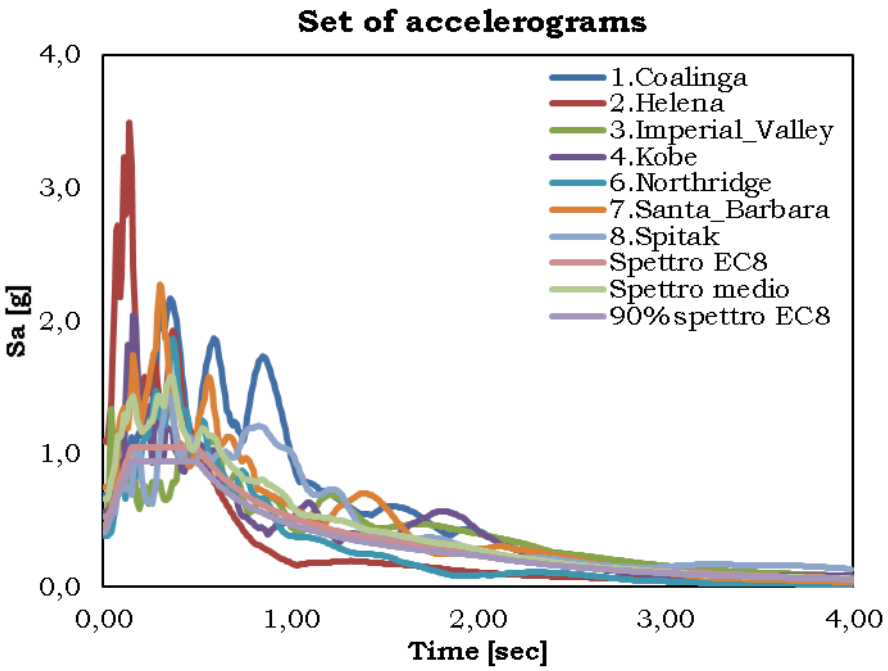

Fig. 5.46 –Set of accelerograms

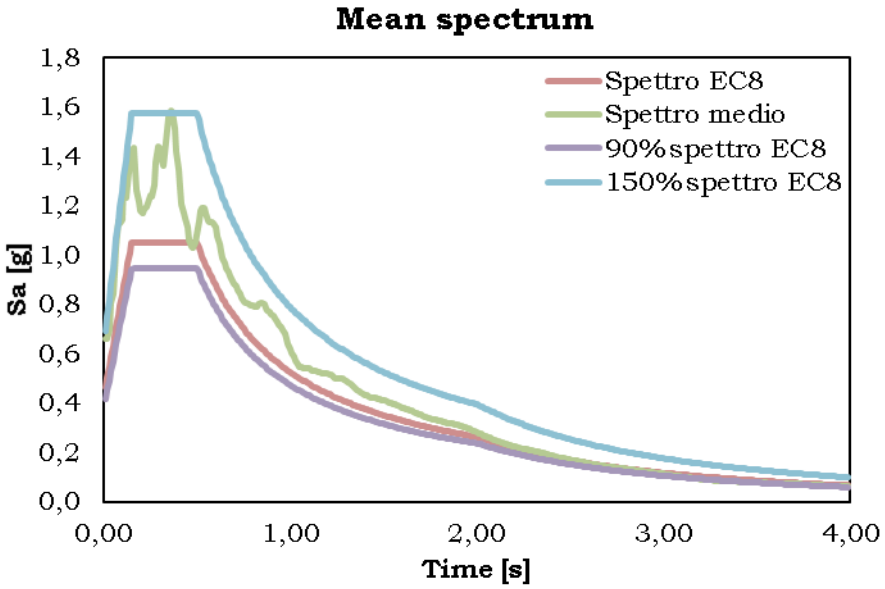

Fig. 5.47 –Mean spectrum for the set of accelerograms

5.4. Structural model in SeismoStruct

The SeismoStruct software is used to create a mathematical model of the structure in question. In this chapter the salient phases that led to the development of this model are reviewed.

The reference material is S355 steel with a bilinear strain-strain bond, as shown in Fig. 5.48, neglecting the specific weight so that the structural model does not automatically take into account the masses, that the calculation code with which it is conducted the pseudo-dynamic test is not able to evaluate.

In addition to the material S355 a material has been defined with the same characteristics but with exclusively elastic behavior.

The IPE270 and HEB200 sections have been defined that have been made to fall within the range of inelastic force-based elements so that the software can perform the analysis by dividing the frame elements into five sections and discretizing each in 150 fibers.

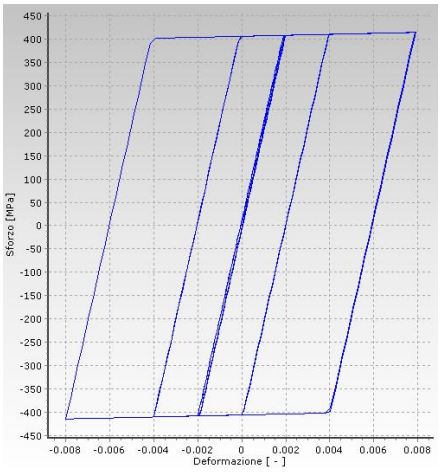

Fig. 5.48 – Hysteresis loops for Steel S355

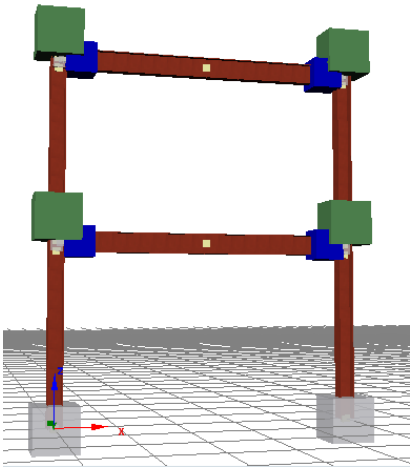

Fig. 5.49 – Seismostruct model

Concentrated masses were assigned using the *lmass* command. Since the present model is of concentrated plasticity, link elements are provided to define the behavior of the beam-to-column connections.

5.4.1. Seismostruct model for frame equipped with FREEDAM connections

The Fig. 5.50 shows how the different members of the structure equipped with FREEDAM devices have been differentiated using the Seismostruct software.

The inelastic frame elements based on the forces corresponding to beams and columns are highlighted in red. While the rigid sections are indicated in green at the intersection of the beams and columns axes: it is specified that in the model the behavior of the rigid elements converging in a node has been realized by means of internal constraint "Rigid connection" which binds some degrees of freedom of the slave nodes to a master node (i.e. there is a rigid arm connecting the slave nodes to the master node). Finally, the yellow crosses identify the positions in which there are pairs of physically coincident structural nodes and in correspondence of which the link elements are allocated.

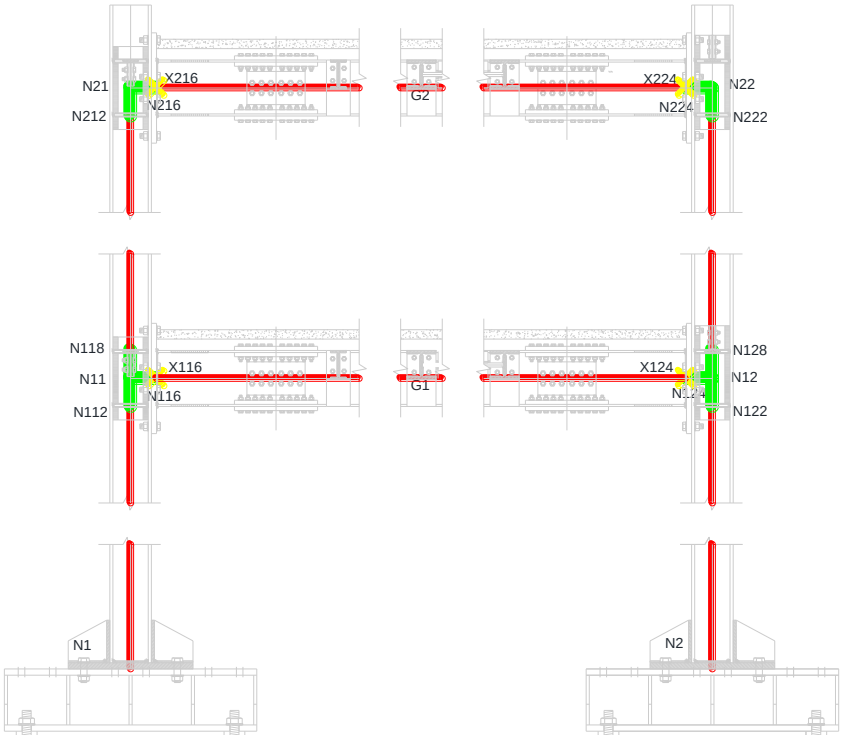

Fig. 5.50 – Structural scheme of the model

The "Rigid diaphragm" option was used for scaffolding nodes to define their rigid behavior.

The concentrated plasticity zone has been modeled by means of two bilinear link elements arranged in parallel.

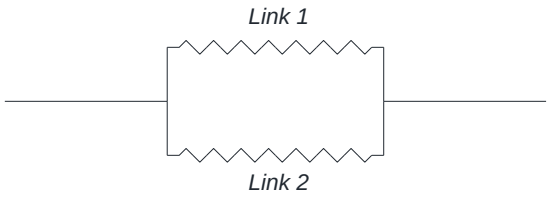

Fig. 5.51 – Plasticity model

The FREEDAM device is characterized by a hysteretic curve similar to that shown in the Fig. 5.52, with a first rigid section which reaches a certain value of the moment and then the successive cycles reach a maximum moment in absolute value lower than that defined in the first elastic stretch, due to the fact that the static friction is higher than dynamic friction.

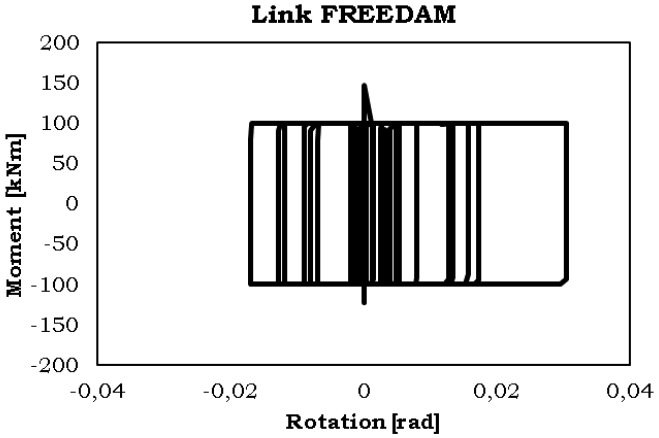

Fig. 5.52 – Hysteresis curve for the FREEDAM connection

Once the sliding starts, i.e. after the static friction has been exceeded, the coefficient of friction that defines the displacements of the device is the dynamic one, lower than the static one and therefore able to induce lower maximum moments in absolute terms. The values of these moments depend on the coefficient of friction; since this parameter is a variable that cannot be determined a priori, it is necessary to consider both the conditions: maximum and minimum coefficient of friction:

Maximum static friction:

- static moment equal to $183kNm$;
- dynamic moment equal to $124kNm$.

Minimum static friction:

- static moment equal to $153kNm$;
- dynamic moment equal to $100kNm$.

In order to model the first section to be able to simulate a rigid behavior, it is necessary to adopt the provisions of the Eurocode 8 [1].

Depending on the slope of the moment-rotation curve of the joint, three zones are defined:

- zone 1, for which the connection can be considered rigid, if $S_{j,ini} \geq k_b E I_b / L_b$, where $k_b = 8$ for frames equipped with bracing systems capable of reducing horizontal displacements by at least 80%, or $k_b = 25$ for other frames provided that $K_b/K_c \geq 0{,}10$;;
- zone 2, for which the behavior can be considered semi-rigid;
- zone 3, if $S_{j,ini} \geq 0{,}50 \cdot E I_b / L_b$.

In particular:

- for frames where $K_b/K_c < 0{,}10$, the joints should be classified as semi-rigid;
- K_b is the average value of $I_b/L_b$of all the beams of that floor;

- K_c is the average value of $I_c/L_c$of all the columns of that floor;
- I_b is the moment of inertia of a beam;
- I_c is the moment of inertia of a column;
- L_b is the length of a beam (between the axes of the columns);
- L_c is the inter-floor height of a column.

Table 5.27 – FREEDAM link properties

$E\ [N/mm^2]$ =	210000.00
$I_b\ [mm^4]$ =	57900000.00
$L_b\ [mm]$ =	4000.00
$I_c\ [mm^4]$ =	56960000.00
$L_c\ [mm]$ =	2400.00
$EI_b/L_b\ [Nmm]$ =	3039750000.00
$EI_b/L_b\ (kNm)$ =	3039.75
k_b =	25.00
K_b/K_c =	0.61
Check:	OK
$k_{b,design}$ =	50.00
$k_{b,design}EI_b/L_b\ [kNm]$ =	151987.50

The Table 5.27contains the information used to calibrate the FREEDAM link in the finite element model.

It is specified that a value of *kb* double was adopted compared to that required by Eurocode 8 [1].

The Table 5.28 shows the values adopted for the prediction of the bilinear hysteretic curves to be introduced as input into SeismoStruct. In particular, it is decided to adopt two link elements precisely to model the transition from static to dynamic behavior as long as both are active there

is a division of the bending action between the two depending on the respective stiffness, while when link-2 is not more active, because it has reached its maximum moment, only link-1 will make its contribution.

Table 5.28 – Adopted values for the prediction of the bilinear hysteretic curves

Maximum static friction		
M_{static} [kNm]= 183.00	M_{dyn} [kNm]= 124.00	M_{aux} [kNm]= 59.00
k_{static} [kNm]= 151987.50	k_{dyn} [kNm]= 102986.07	k_{aux} [kNm]= 49001.43
θ_{static} [rad]= 0.001204	θ_{dyn} [rad]= 0.001204	θ_{aux} [rad]= 0.001204
Minimum static friction		
M_{static} [kNm]= 153.00	M_{dyn} [kNm]= 100.00	M_{aux} [kNm]= 53.00
k_{static} [kNm]= 151987.50	k_{dyn} [kNm]= 99338.24	k_{aux} [kNm]= 52649.26
θ_{static} [rad]= 0.0010066	θ_{dyn} [rad]= 0.0010066	θ_{aux} [rad]= 0.0010066

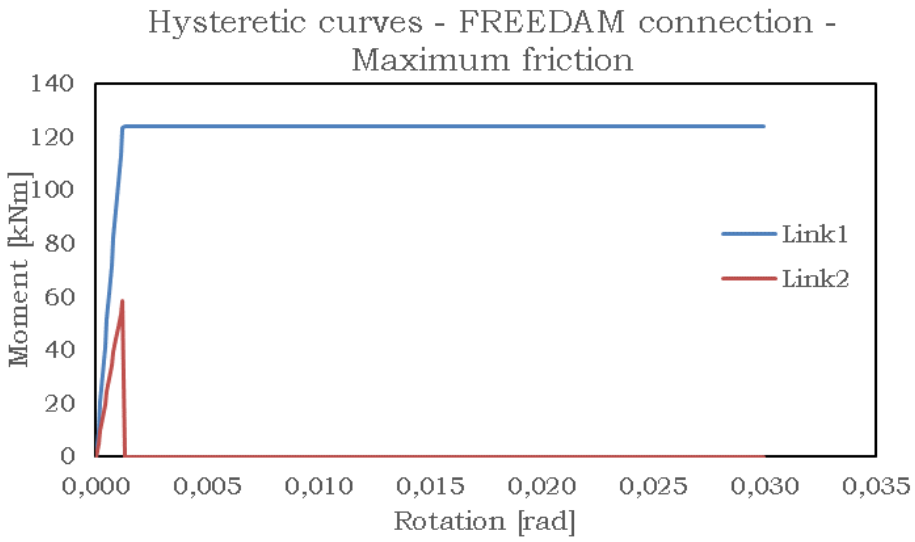

Fig. 5.53 – Hysteretic curves - FREEDAM connection – maximum friction

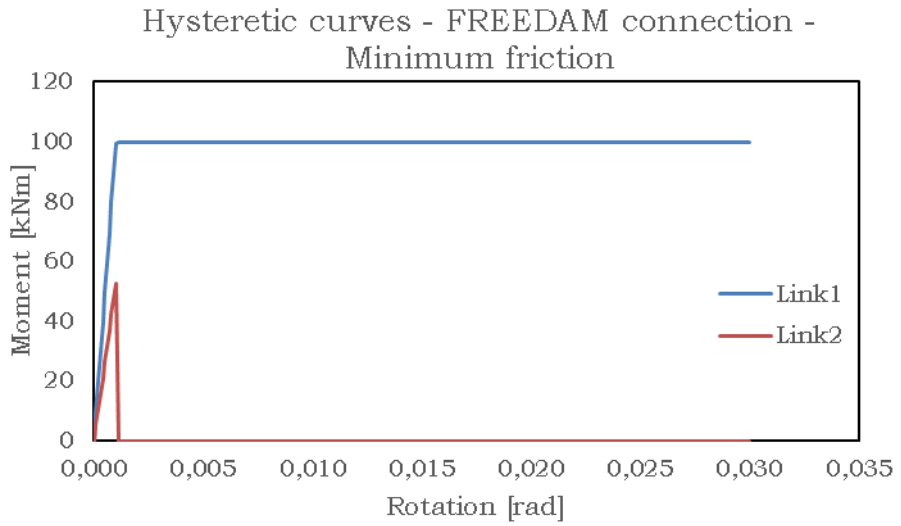

Fig. 5.54 – Hysteretic curves - FREEDAM connection – minimum friction

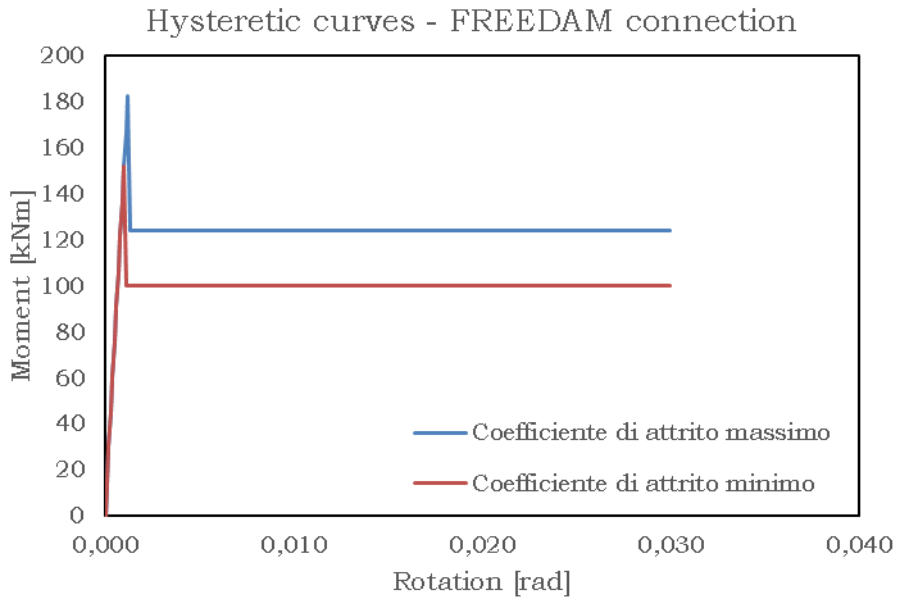

Fig. 5.55 – Hysteretic curves - FREEDAM connection

Starting from the previous hysteretic curves for the minimum and maximum coefficient of friction, with the same rotation the moments of the two links are added together; the results obtained are replied in Fig. 5.55.

5.4.2. Seismostruct model for frame equipped with RBS connections

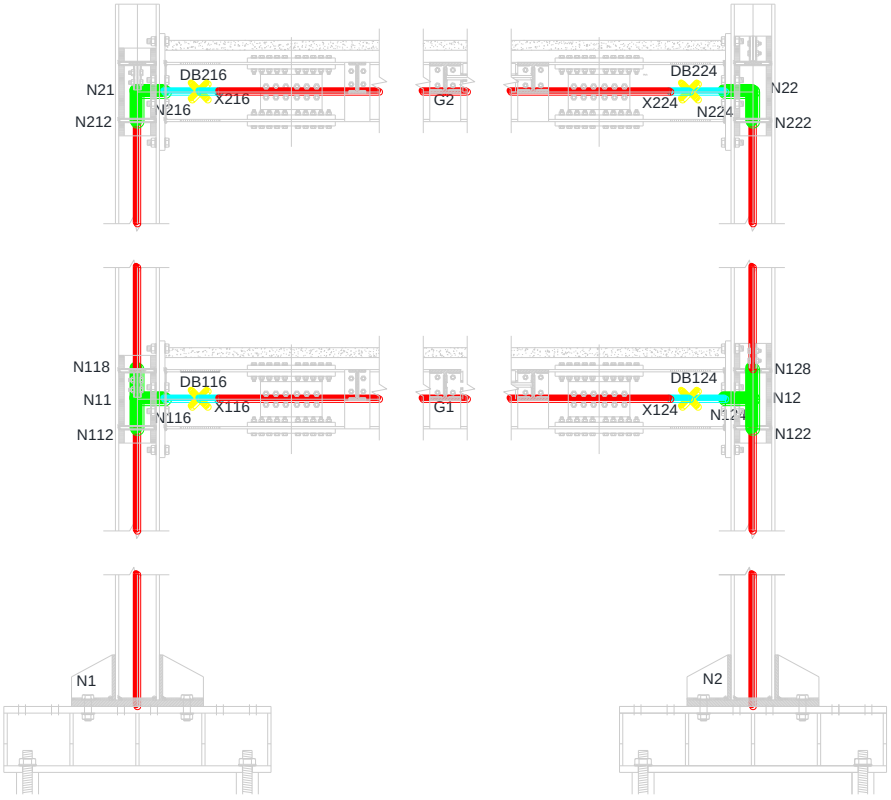

Fig. 5.56 – Seismostruct model

The Fig. 5.56 shows how the different members of the structure equipped with RBS connections have been differentiated using the Seismostruct software. The symbolism is analogous to the case of the connection with FREEDAM devices, except for some differences described in detail in the following. The beam sections to which S355 steel is not assigned as material but an equivalent with indefinitely elastic behavior are indicated in light blue, while the yellow crosses represent the pairs of physically coincident structural nodes where the link elements are allocated.

The parameters that allow defining the characteristics of the smooth link element have been obtained through a calibration with the Multical software starting from an experimental moment-rotation curve obtained following a test conducted on a specimen.

In Fig. 5.57 the schematization related to the execution of the test is shown.

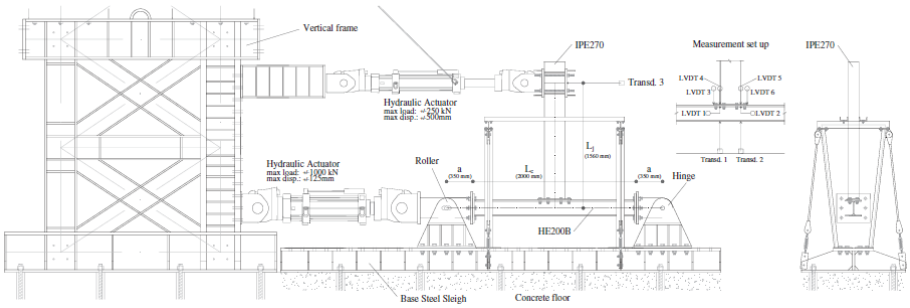

Fig. 5.57 – Test layout

The actuator, by means of the application of a force, imparts a displacement to the end of the cantilever diagram; but from this displacement the contributions relative to the deformability relative to the beam and to the column must be purified.

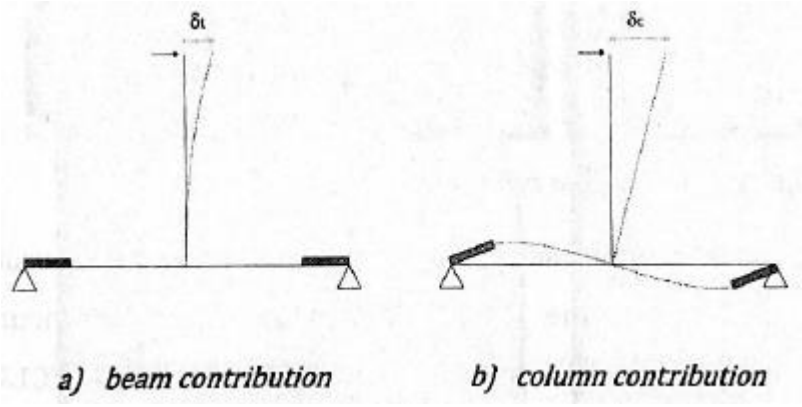

Fig. 5.58 – Deformability of beam and column

$$\delta_{beam} = \frac{FL_{beam}^3}{3EI_{beam}} \tag{5.146}$$

Due to the presence of rigid elements at the ends of the column, the expression becomes:

$$\delta_{column} = \frac{FL_{column}L_{beam}^2}{12EI_{column}}\left[\left(\frac{L_{column}}{L_{column}+2a}\right)^2 + \frac{6a}{L_{column}+2a}\right] \tag{5.147}$$

The displacement required to evaluate the rotation is:

$$\delta_j = \delta_{actuator} - \frac{FL_{beam}^3}{3EI_{beam}} - \frac{FL_{column}L_{beam}^2}{12EI_{column}}\left[\left(\frac{L_{column}}{L_{column}+2a}\right)^2 + \frac{6a}{L_{column}+2a}\right] \tag{5.148}$$

The rotation is obtained by dividing the previous displacement by the distance between the position of the link element (in this case the center of gravity of the dogbone) and the end of the beam:

$$\varphi_j = \frac{\delta_j}{L_{beam} - s_{end-plate} - a_{dog-bone} - \frac{b_{dog-bone}}{2}} \tag{5.149}$$

The moment is evaluated by multiplying the force applied by the actuator by the distance between the position of the link element and the end of the beam:

$$M_j = F\left(L_{beam} - s_{end-plate} - a_{dog-bone} - \frac{b_{dog-bone}}{2}\right) \tag{5.150}$$

The Fig. 5.59 shows:

- the hysteretic curve obtained from the laboratory test;
- the hysteretic curve calibrated by Multical software.

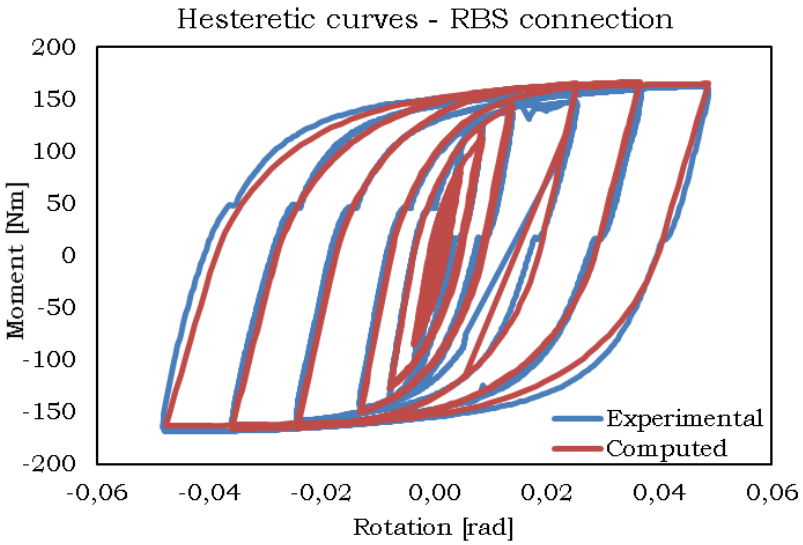

Fig. 5.59 – Hysteretic curves – RBS connection

5.4.3. Numerical simulations using SeismoStruct model

Three types of analysis have been performed:

- modal analysis;
- pushover analysis;
- incremental dynamics analysis (IDA), obtained by progressively increasing the peak acceleration of natural accelerograms to the ground up to obtain rotations of 30*mrad* in at least one link element.

It is specified that for the case of the FREEDAM connection the results of the simulations carried out are considered considering two types of hysteretic curves depending on the maximum and minimum coefficient of friction that can develop in relation to the preload of the bolts.

5.4.4. Modal analysis for the determination of natural periods of vibration of the structure

Modal analyzes have been performed for the types of connection under examination using the SeismoStruct software:

Table 5.29 – Natural vibration periods

	FREEDAM connection	***DB connection***
T_1 **(s) =**	*0.444601*	*0.490172*
T_2 **(s) =**	*0.126383*	*0.131325*

Modal analysis provides the values of the periods of the first and second vibrating modes of the structure, this information is used for:

- define the Rayleigh coefficients to perform incremental dynamic analyzes;

- define the multiplicative coefficients of the accelerograms to obtain a medium spectrum compatible with the design spectrum provided by the Eurocode 8 [1] for a type B soil and a peak ground acceleration of *0.35g*.

Table 5.30 – Scale factors of the accelerograms.

1. Coalinga	***2. Helena***
4.018	*7.031*
3. Imperial_Valley	***4. Kobe***
1.852	*2.174*
5. Landers	***6. Northridge***
3.646	*1.615*
7. Santa_Barbara	***8. Spitak***
7.298	*2.834*

5.4.5. Pushover analysis

Pushover analysis have been performed by assigning horizontal plane forces related to the first vibration mode of the structure and to the distribution of the masses; these distributions have already been evaluated in the design phase, at the time of application of the control theory of the collapse mechanism and therefore the results already obtained are schematically reported:

- distribution similar to the first way to vibrate the structure (triangular distribution);
- distribution similar to the floor masses (uniform distribution).

$$\Phi_{a,i} = \frac{m_i \cdot h_i}{\sum_{i=1}^{n.impalcati}(m_i \cdot h_i)}$$

$$\Phi_{b,i} = \frac{m_i}{\sum_{i=1}^{n.impalcati} m_i}$$

$$m_{1,} = 19{,}100\ tonn$$

$$m_2 = 14{,}254\ tonn \qquad (5.151)$$

$$\Phi_{a,1} = 0{,}40$$

$$\Phi_{a,2} = 0{,}60$$

$$\Phi_{b,1} = 0{,}57$$

$$\Phi_{b,2} = 0{,}43$$

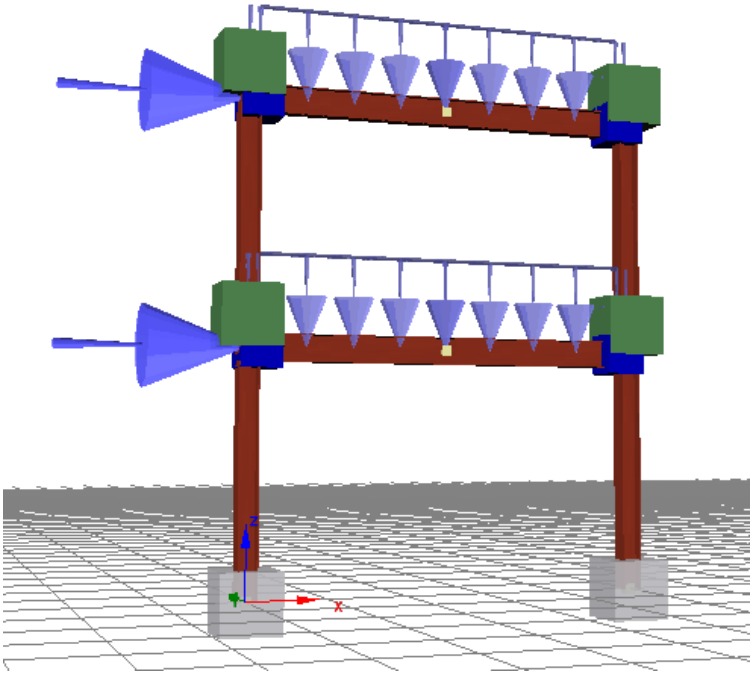

Fig. 5.60 – Load distribution on the frame for the pushover analysis

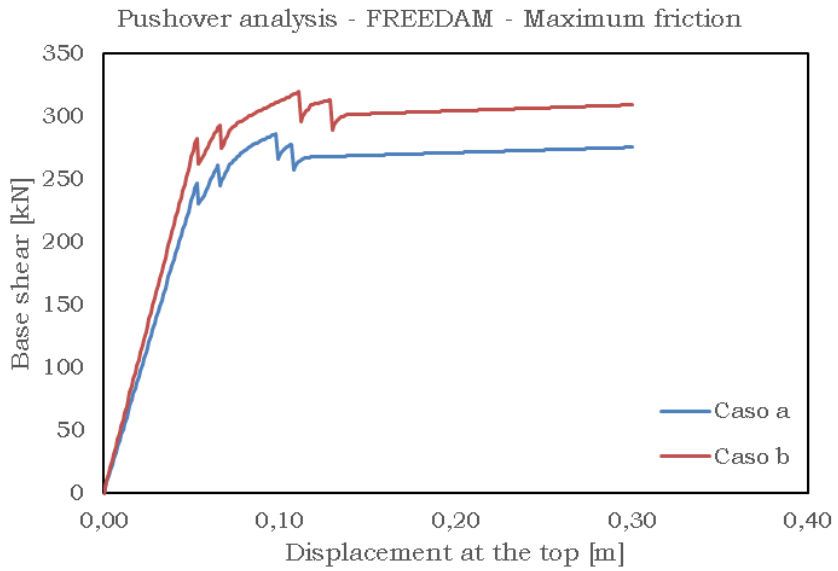

Fig. 5.61 – Pushover analysis - FREEDAM - Maximum friction

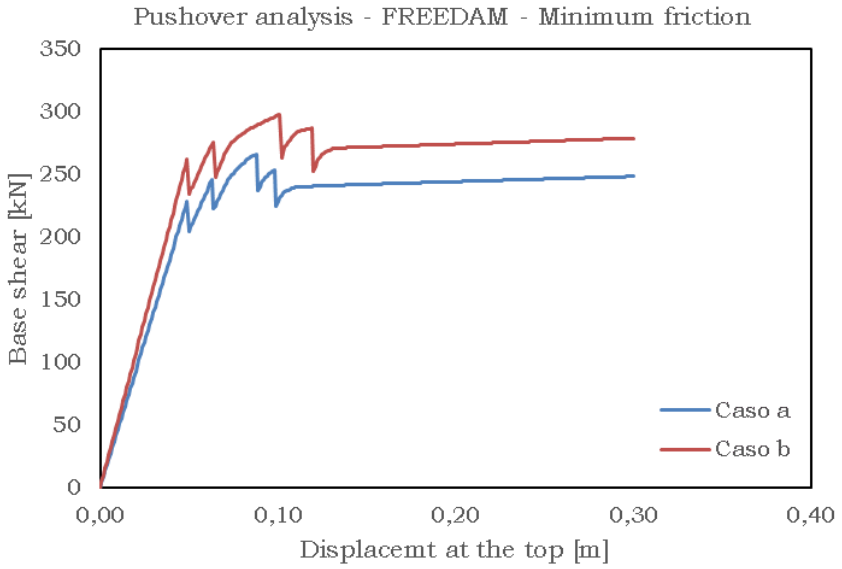

Fig. 5.62 – Pushover analysis - FREEDAM - Minimum friction

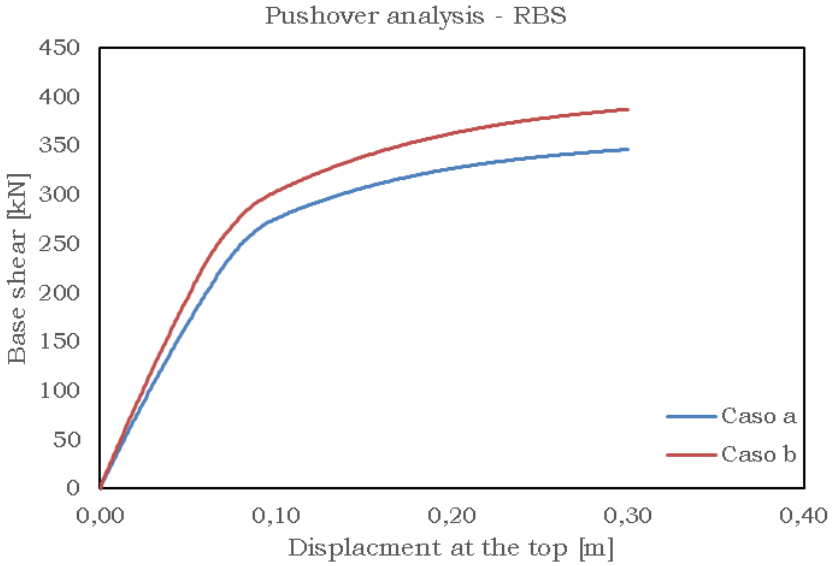

Fig. 5.63 – Pushover analysis - RBS

The pushover analyzes are useful for assessing the behavior of the structure in the nonlinear field, allowing to obtain important information in terms of the questions of force and deformation and the capacities that control the seismic response close to the collapse. The presumed behavior of the structure for severe earthquakes can be assessed in a more accurate way as the structures oscillate according to the first way of vibrating.

Unfortunately, the most obvious limit of the pushover analysis consists in the fact that these are approximated and based on static loads and therefore are not able to represent dynamic phenomena with great accuracy.

In particular, the differences between the prediction of the mechanical behavior of a structure and the reality are more evident when the effects

related to the vibrating modes are greater than the first; this is due to the restrictive assumption at the base of this type of analysis that consists in defining the movements of the plane as independent of time (for this reason if modal forms higher than the first begin to prevail, we are witnessing a behavior very different from that expected).
To remedy these problems two strategies are available:

- adopt different forms of displacement and perform the envelope of the results using a method called Modal Pushover;
- use a lateral force distribution that changes with each step of the analysis, Adaptive Pushover.

5.4.6. Incremental dynamic analysis (IDA)

In the following, the graphs and tables related to incremental dynamic analyzes performed using the SeismoStruct software are reported.
In particular, the cells of the tables are highlighted in such a way as to make visually clear whether the values of forces and displacements are compatible with the capacities of the actuators available.
It is useful to anticipate that the displacements obtained from the simulations are always compatible with the capacities of the actuators, while this is not the case for the plan forces.

Table 5.31 – Capacities of the actuators

	Compression [kN]	***Tension [kN]***
Level 1	*275.40*	*275.40*
Level 2	*275.83*	*189.13*

Since only a two-dimensional frame representing the three-dimensional structure was modeled in SeismoStruct, for the analysis of the following

results it is required to halve the capacities of the actuators, as shown in Table 5.31.

The symbols adopted to highlight the cells have the following meanings:

- underlined and bold, if the values are not compatible with the capacities of actuators;
- underlined, if the values are compatible with the actuators' capacities, but they are too close to the predicted limits;
- normal character, if the values are compatible with the actuator capacities with a large margin of safety.

Coalinga

Table 5.32 – FREEDAM - Maximum friction coefficient - COALINGA

PGA [g]	***Rotation [rad]***	***Displacement (m)***		***Compression [kN]***		***Tension [kN]***	
		Lev. 1	***Lev. 2***	***Lev. 1***	***Lev. 2***	***Lev. 1***	***Lev. 2***
0.10	*0.000*	*0.006*	*0.012*	*23.42*	*34.29*	*20.15*	*29.66*
0.20	*0.000534*	*0.011*	*0.024*	*46.86*	*68.60*	*40.34*	*59.40*
0.30	*0.000752*	*0.017*	*0.037*	*70.32*	*102.98*	*60.69*	*89.46*
0.40	*0.000970*	*0.023*	*0.049*	*93.86*	*137.34*	*81.17*	*119.62*
0.50	*0.011600*	*0.029*	*0.062*	*113.96*	*152.28*	*79.18*	*118.57*
0.60	*0.013964*	*0.036*	*0.076*	*123.05*	*165.57*	*87.16*	*134.38*
0.70	*0.017873*	*0.048*	*0.097*	*148.09*	*185.91*	*113.06*	*132.93*
0.80	*0.021459*	*0.057*	*0.117*	*173.33*	*187.81*	*124.94*	*144.05*
0.90	*0.028702*	*0.070*	*0.150*	*171.48*	*193.08*	*127.31*	*138.89*
1.00	***0.037223***	*0.086*	*0.188*	*164.22*	*189.86*	*141.44*	*142.61*
1.10	***0.046818***	*0.107*	*0.230*	*156.45*	*184.60*	*165.41*	*152.22*

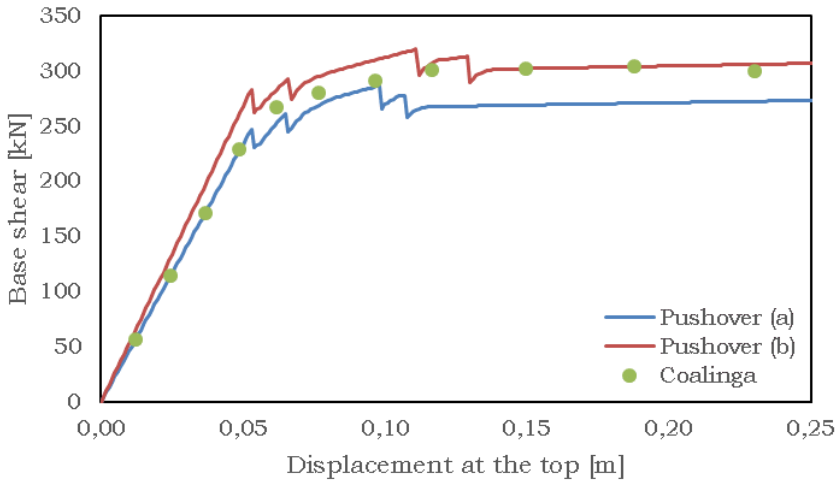

Fig. 5.64 – Base shear vs Displacement at the top – COALINGA Max friction

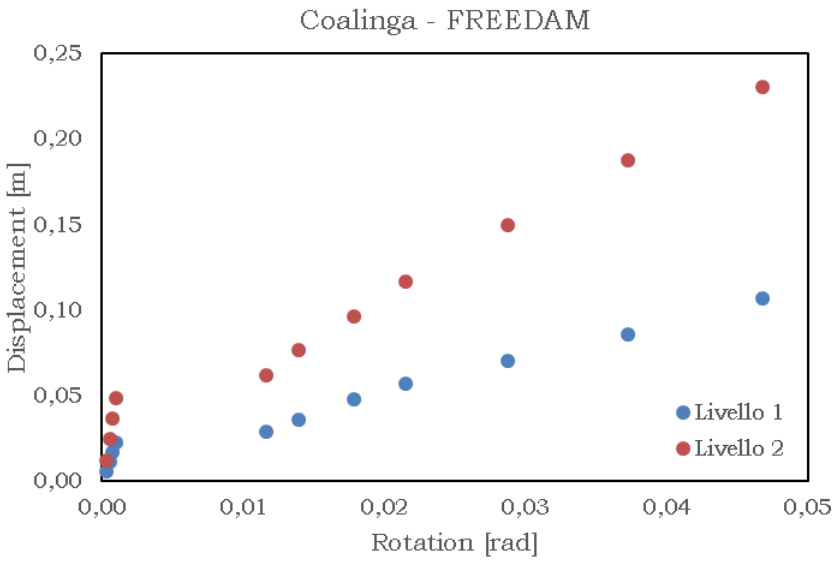

Fig. 5.65 - Displacement vs rotation – COALINGA Max friction

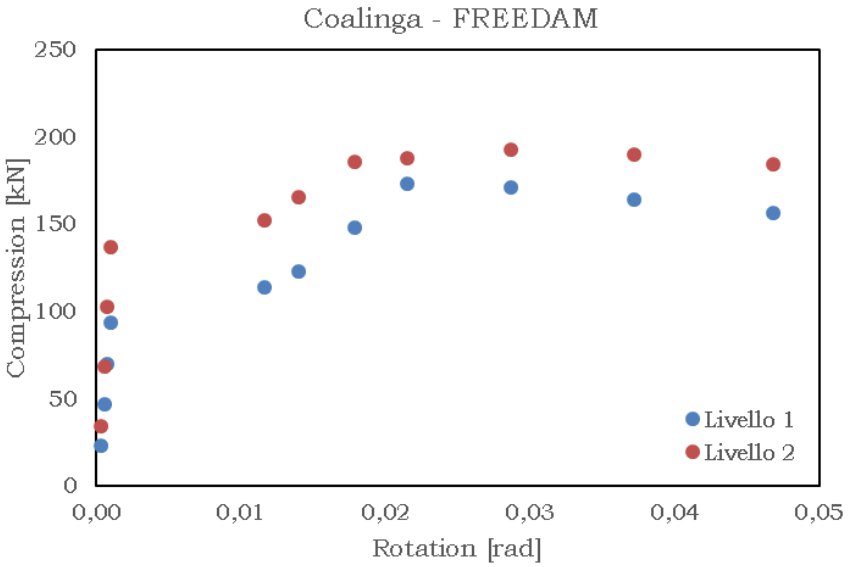

Fig. 5.66 – Compression vs rotation – COALINGA Max friction

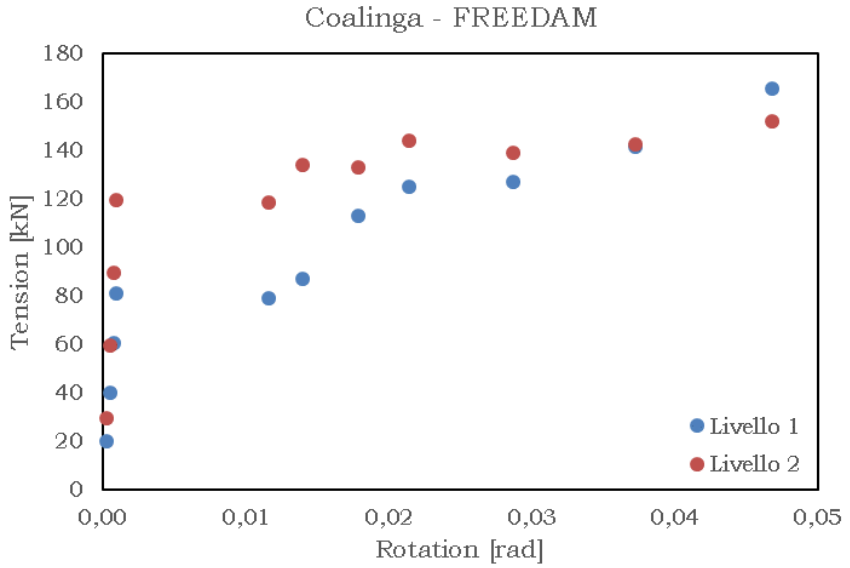

Fig. 5.67 – Tension vs rotation – COALINGA Max friction

Table 5.33 – FREEDAM - Minimum friction coefficient - COALINGA

PGA [g]	***Rotation [rad]***	***Displacement (m)***		***Compression [kN]***		***Tension [kN]***	
		Lev. 1	***Lev. 2***	***Lev. 1***	***Lev. 2***	***Lev. 1***	***Lev. 2***
0.10	*0.00*	*0.006*	*0.012*	*23.42*	*34.29*	*20.15*	*29.66*
0.20	*0.000547*	*0.011*	*0.024*	*46.84*	*68.57*	*40.31*	*59.33*
0.30	*0.000787*	*0.017*	*0.037*	*70.27*	*102.86*	*60.47*	*89.01*
0.40	*0.009256*	*0.023*	*0.049*	*93.72*	*131.71*	*63.11*	*96.08*
0.50	*0.013835*	*0.029*	*0.063*	*103.18*	*148.98*	*81.01*	*111.81*
0.60	*0.016025*	*0.037*	*0.079*	*113.83*	*162.37*	*85.75*	*134.16*
0.70	*0.020715*	*0.047*	*0.103*	*138.91*	*158.47*	*101.41*	*121.13*
0.80	*0.025709*	*0.055*	*0.128*	*166.43*	*168.76*	*113.25*	*137.51*
0.90	*0.031406*	*0.064*	*0.152*	*161.31*	*169.69*	*120.21*	*122.23*
1.00	***0.035152***	*0.071*	*0.169*	*172.55*	*169.85*	*127.28*	*124.92*
1.10	***0.042016***	*0.088*	*0.199*	*156.79*	*167.96*	*179.84*	*141.55*

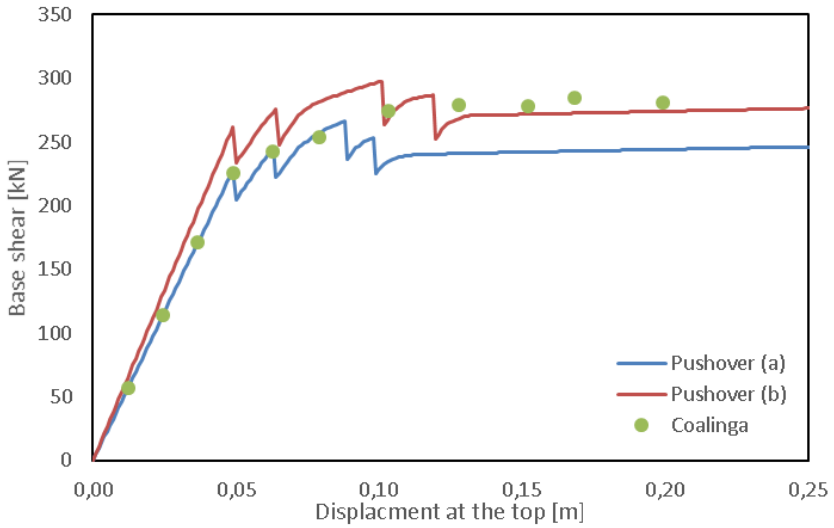

Fig. 5.68 – Base shear vs Displacement at the top – COALINGA min friction

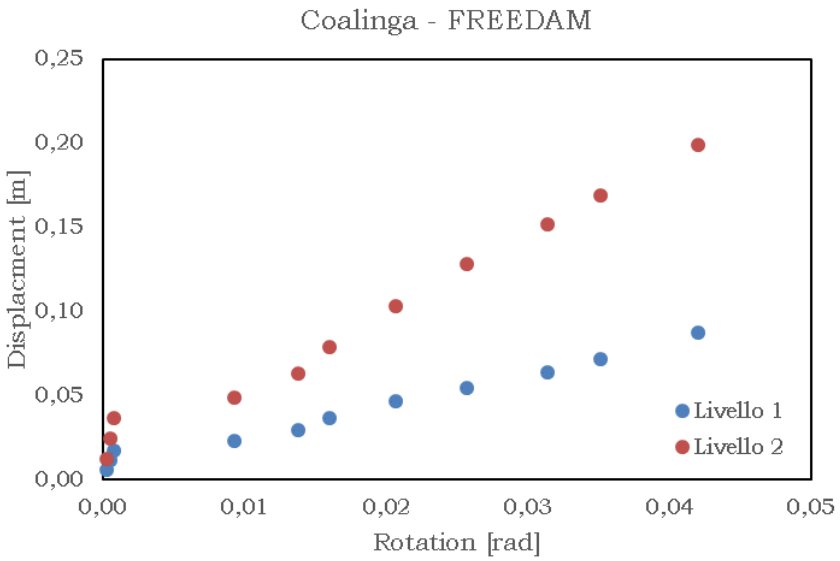

Fig. 5.69 – Displacement vs rotation – COALINGA min friction

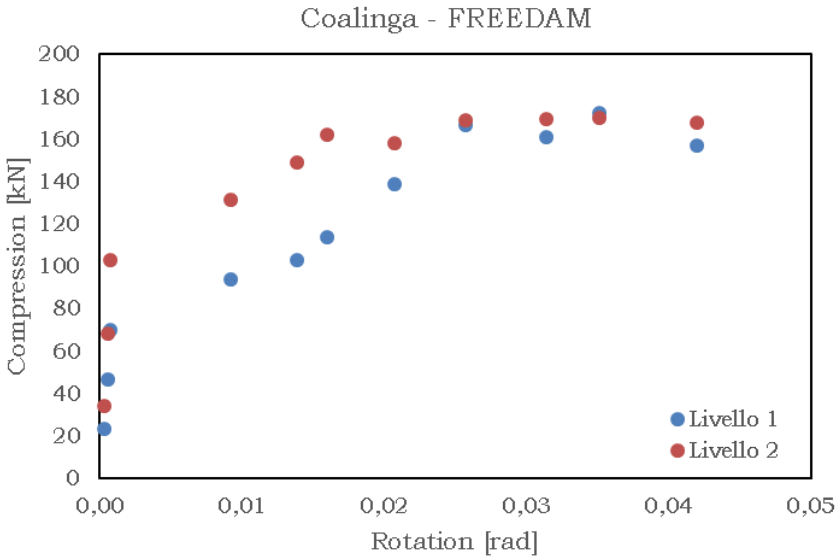

Fig. 5.70 – Compression vs rotation – COALINGA min friction

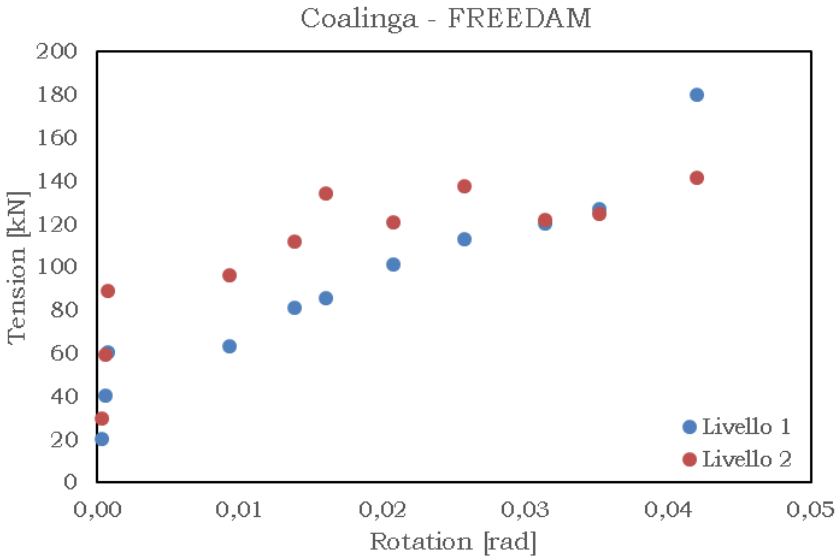

Fig. 5.71 – Tension vs rotation – COALINGA min friction

Table 5.34 – RBS - COALINGA

PGA [g]	***Rotation [rad]***	***Displacement (m)***		***Compression [kN]***		***Tension [kN]***	
		Lev. 1	***Lev. 2***	***Lev. 1***	***Lev. 2***	***Lev. 1***	***Lev. 2***
0.10	*0.002*	*0.006*	*0.013*	*19.00*	*27.15*	*19.88*	*25.42*
0.20	*0.003406*	*0.012*	*0.026*	*38.52*	*55.93*	*40.16*	*48.70*
0.30	*0.005302*	*0.018*	*0.042*	*58.36*	*85.91*	*60.69*	*70.11*
0.40	*0.007646*	*0.025*	*0.058*	*78.23*	*116.66*	*81.55*	*91.56*
0.50	*0.010599*	*0.033*	*0.076*	*98.35*	*147.64*	*102.78*	*113.43*
0.60	*0.013920*	*0.042*	*0.096*	*116.63*	*173.08*	*123.83*	*127.32*
0.70	*0.017645*	*0.056*	*0.117*	*162.68*	*188.01*	*144.61*	*142.96*
0.80	*0.025924*	*0.073*	*0.145*	*189.62*	*199.57*	*164.84*	*150.99*
0.90	*0.032432*	*0.092*	*0.175*	*206.99*	*210.08*	*183.75*	*154.60*
1.00	***0.036864***	*0.110*	*0.208*	*216.01*	*218.57*	*197.69*	*159.57*
1.10	***0.042304***	*0.123*	*0.232*	*220.46*	*221.95*	*211.42*	*169.38*

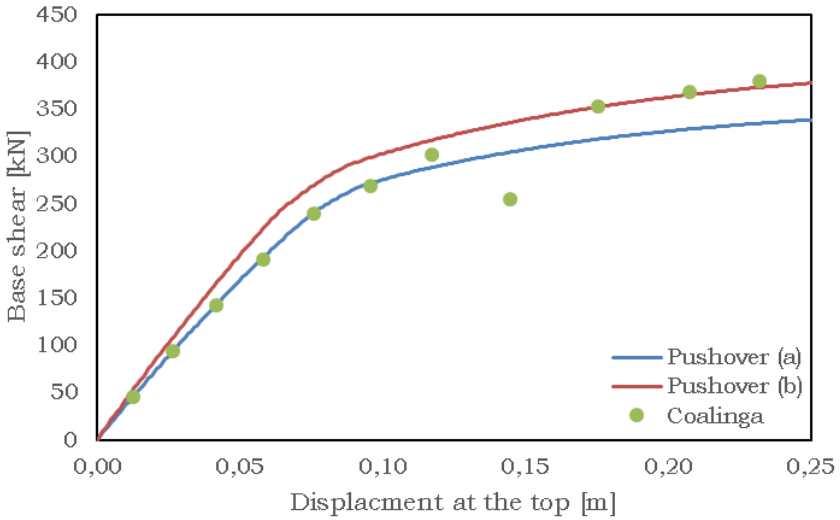

Fig. 5.72 – Base shear vs displacement at the top – COALINGA RBS

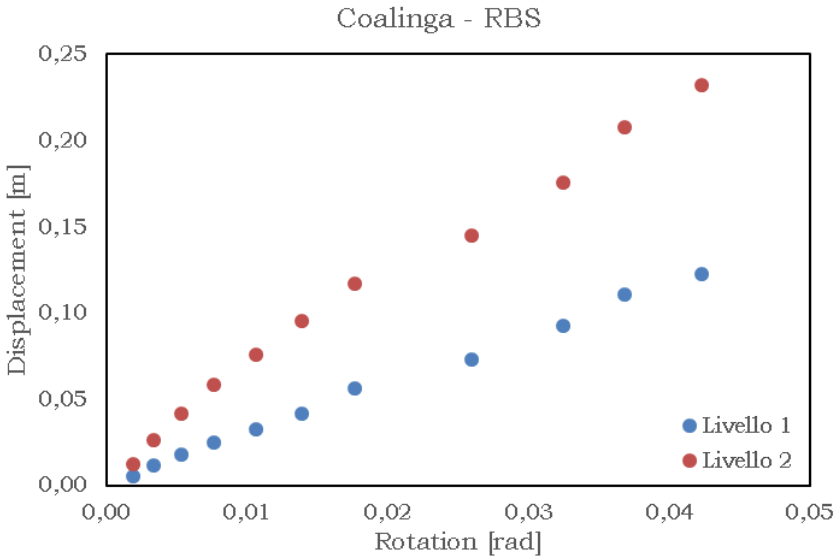

Fig. 5.73 – Displacement vs rotation – COALINGA RBS

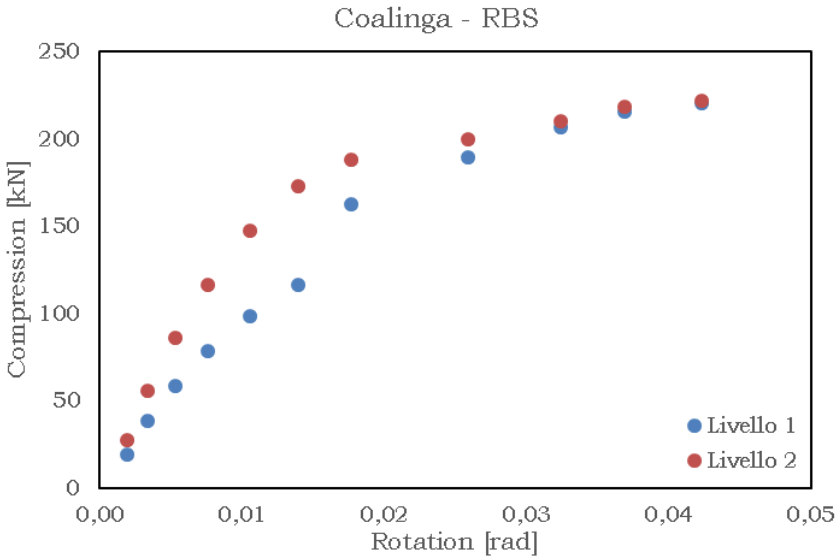

Fig. 5.74 – Compression vs rotation – COALINGA RBS

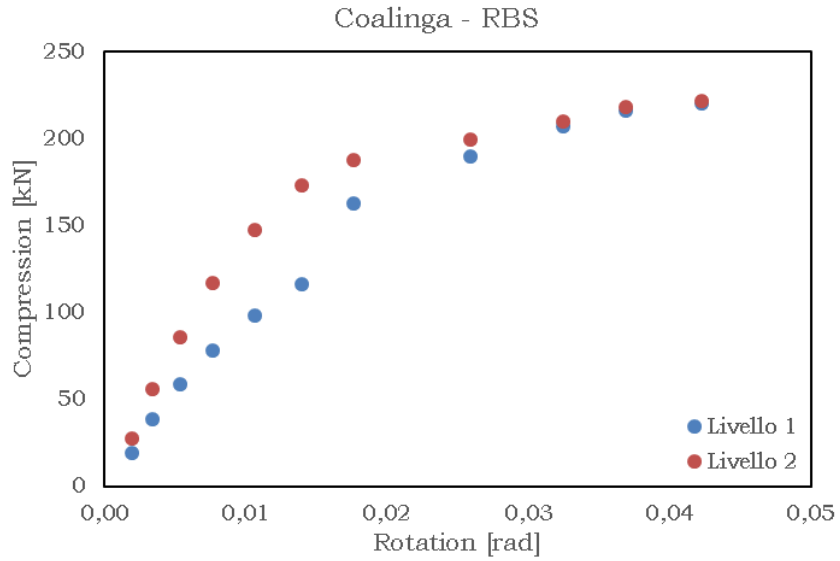

Fig. 5.75– Tension vs rotation – COALINGA RBS

Helena

Table 5.35 – FREEDAM - Maximum friction coefficient - HELENA

PGA [g]	Rotation [rad]	Displacement (m)		Compression [kN]		Tension [kN]	
		Lev. 1	Lev. 2	Lev. 1	Lev. 2	Lev. 1	Lev. 2
0.10	0.000	0.003	0.007	25.88	26.65	20.72	25.73
0.20	0.000351	0.006	0.015	51.76	53.30	41.44	51.45
0.30	0.000486	0.010	0.022	77.67	80.01	62.18	77.24
0.40	0.000616	0.013	0.029	103.66	106.91	83.01	103.16
0.50	0.000746	0.016	0.037	129.67	133.89	103.88	129.11
0.60	0.000876	0.019	0.044	155.77	160.83	124.72	154.99
0.70	0.005209	0.022	0.051	176.14	173.90	142.51	164.86
0.80	0.009009	0.025	0.056	193.23	182.59	159.44	170.37
0.90	0.011863	0.028	0.064	208.63	194.41	173.58	188.71
1.00	0.013725	0.032	0.072	223.29	197.23	189.03	189.84
1.10	0.015155	0.035	0.080	249.02	208.97	208.89	203.16
1.20	0.016293	0.040	0.089	281.84	215.07	229.26	210.52
1.30	0.016304	0.040	0.092	312.59	220.73	255.26	204.96
1.40	0.017422	0.043	0.098	**334.92**	226.93	272.19	209.11
1.50	0.018792	0.047	0.105	**356.57**	234.92	294.36	215.19
1.60	0.020689	0.051	0.114	**377.64**	241.43	312.14	220.59
1.70	0.020980	0.050	0.114	**395.11**	244.68	323.39	**226.00**
1.80	0.023074	0.054	0.123	**417.75**	249.25	**343.14**	**233.67**
1.90	0.024127	0.056	0.127	**438.13**	255.51	**357.93**	**239.77**
2.00	0.024234	0.056	0.128	**459.69**	261.77	**372.28**	**247.70**

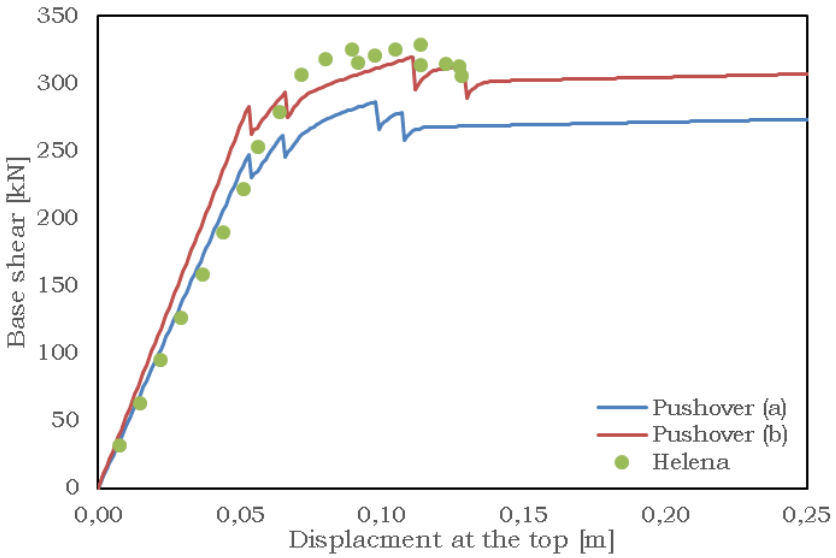

Fig. 5.76 – Base shear vs Displacement at the top – HELENA Max friction

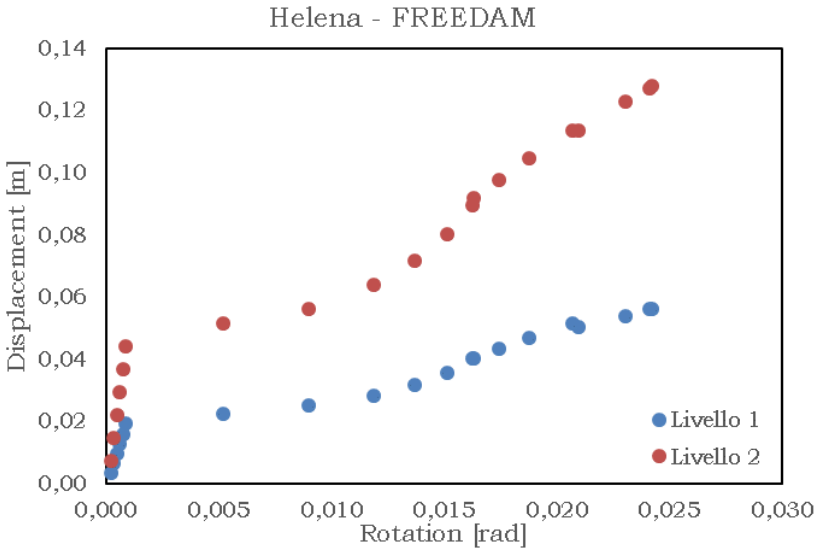

Fig. 5.77 – Displacement vs rotation – HELENA Max friction

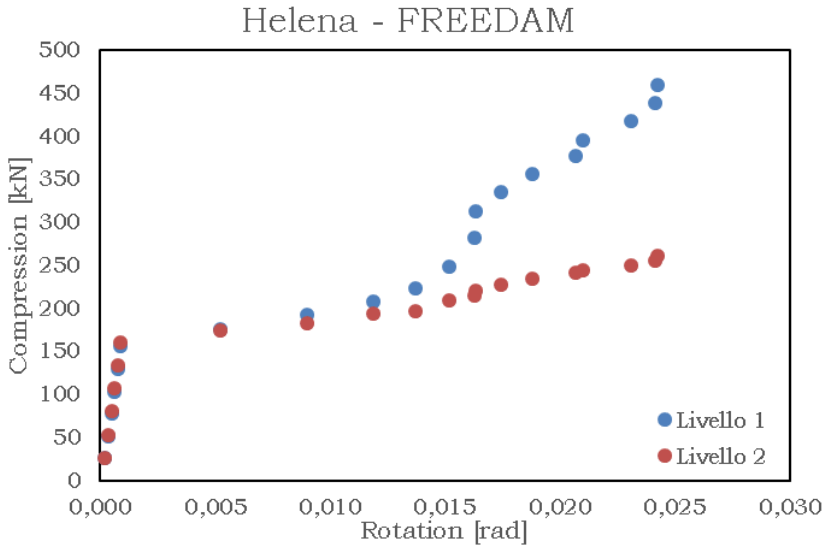

Fig. 5.78 – Compression vs rotation – HELENA Max friction

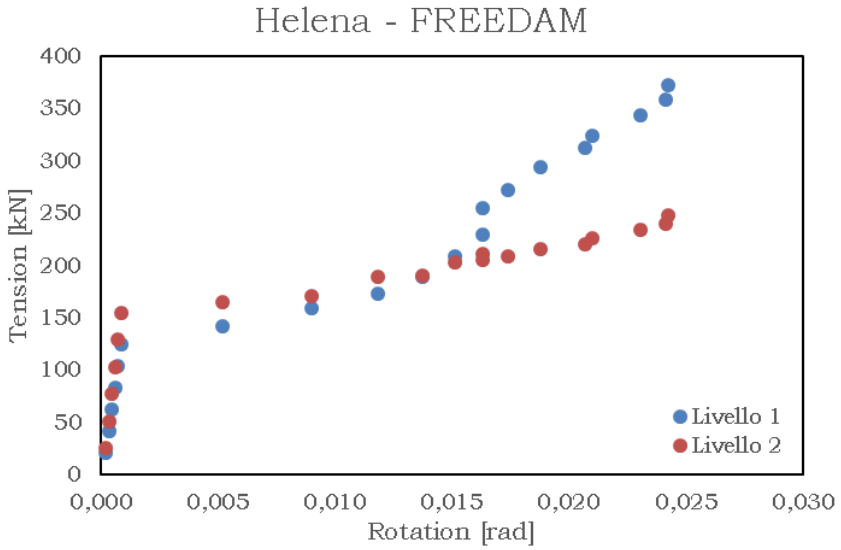

Fig. 5.79 – Tension vs rotation – HELENA Max friction

Table 5.36 – FREEDAM - Minimum friction coefficient - HELENA

PGA [g]	***Rotation [rad]***	***Displacement (m)***		***Compression [kN]***		***Tension [kN]***	
		Lev. 1	***Lev. 2***	***Lev. 1***	***Lev. 2***	***Lev. 1***	***Lev. 2***
0.10	*0.00*	*0.003*	*0.007*	*25.88*	*26.65*	*20.72*	*25.73*
0.20	*0.000351*	*0.006*	*0.015*	*51.76*	*53.30*	*41.44*	*51.45*
0.30	*0.000494*	*0.010*	*0.022*	*77.64*	*79.95*	*62.16*	*77.18*
0.40	*0.000636*	*0.013*	*0.029*	*103.53*	*106.61*	*82.87*	*102.90*
0.50	*0.000778*	*0.016*	*0.037*	*129.42*	*133.26*	*103.58*	*128.62*
0.60	*0.000921*	*0.019*	*0.044*	*155.32*	*159.91*	*124.28*	*154.33*
0.70	*0.009567*	*0.022*	*0.049*	*165.67*	*153.64*	*137.62*	*145.43*
0.80	*0.012485*	*0.025*	*0.057*	*180.71*	*164.14*	*151.27*	*163.27*
0.90	*0.014582*	*0.028*	*0.065*	*195.60*	*173.22*	*164.55*	*185.57*
1.00	*0.014854*	*0.032*	*0.074*	*234.10*	*173.59*	*189.78*	*184.81*
1.10	*0.016475*	*0.036*	*0.083*	*273.67*	*175.73*	*221.05*	*189.42*
1.20	*0.015885*	*0.034*	*0.082*	*294.94*	*182.78*	*237.98*	*188.81*
1.30	*0.017499*	*0.037*	*0.091*	***327.41***	*192.42*	*270.31*	*183.71*
1.40	*0.019891*	*0.040*	*0.101*	***351.54***	*196.53*	*291.24*	*190.62*
1.50	*0.022349*	*0.045*	*0.112*	***371.96***	*200.91*	*306.74*	*194.05*
1.60	*0.022463*	*0.043*	*0.112*	***390.96***	*204.72*	*322.49*	*196.67*
1.70	*0.024242*	*0.047*	*0.120*	***409.52***	*208.51*	***334.88***	*199.42*
1.80	*0.024816*	*0.044*	*0.117*	***437.90***	*224.20*	***354.78***	*208.84*
1.90	*0.025434*	*0.044*	*0.118*	***460.35***	*230.24*	***369.37***	*214.07*
2.00	*0.027177*	*0.046*	*0.123*	***483.68***	*235.59*	***386.74***	*218.86*

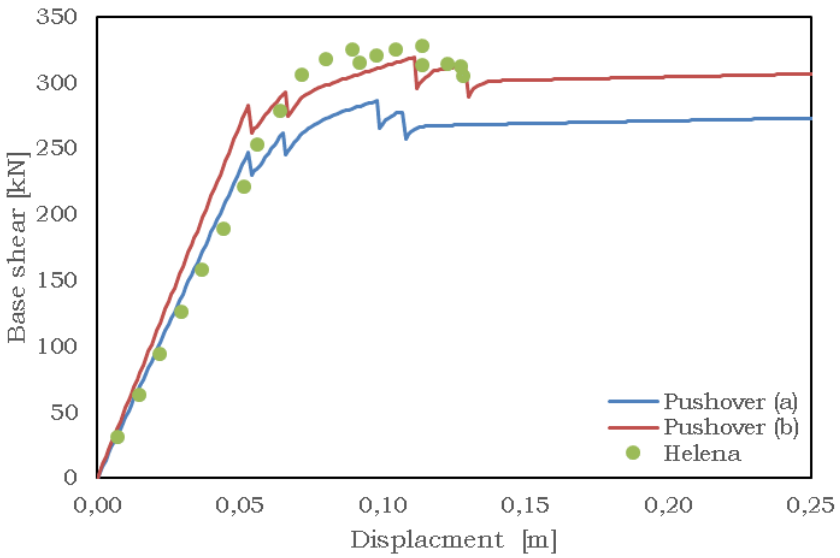

Fig. 5.80 – Base shear vs Displacement at the top – HELENA min friction

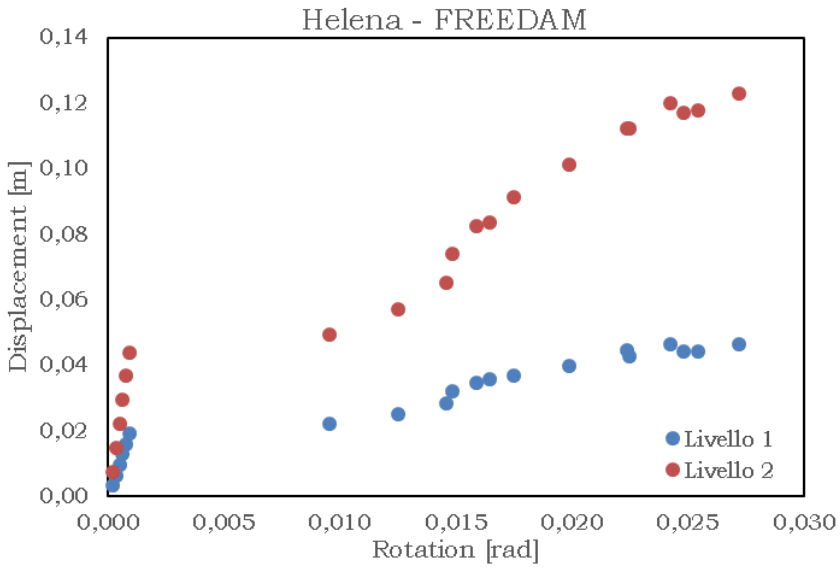

Fig. 5.81 – Displacement vs rotation – HELENA min friction

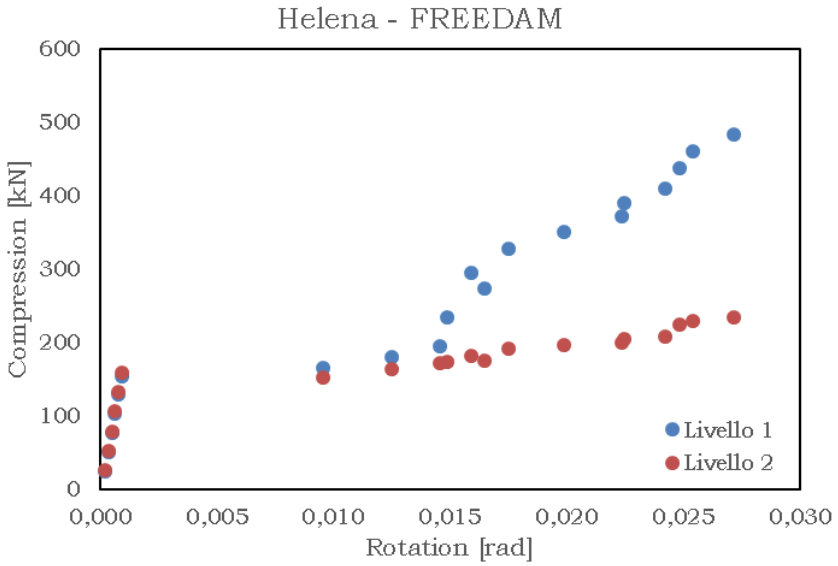

Fig. 5.82 – Compression vs rotation – HELENA min friction

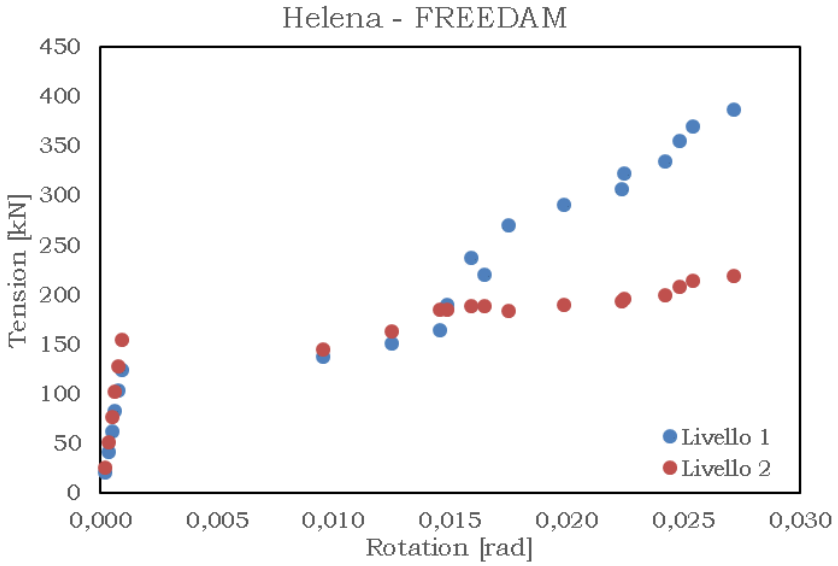

Fig. 5.83 – Tension vs rotation – HELENA min friction

Table 5.37 – RBS - HELENA

PGA [g]	***Rotation [rad]***	***Displacement (m)***		***Compression [kN]***		***Tension [kN]***	
		Lev. 1	***Lev. 2***	***Lev. 1***	***Lev. 2***	***Lev. 1***	***Lev. 2***
0.10	0.001	0.003	0.008	25.43	19.48	26.30	20.93
0.20	0.001513	0.006	0.015	50.34	38.01	52.43	41.23
0.30	0.002223	0.010	0.023	74.89	55.87	78.38	61.06
0.40	0.002973	0.013	0.030	99.00	72.96	104.09	80.34
0.50	0.003780	0.016	0.038	122.74	89.30	129.58	99.08
0.60	0.004651	0.019	0.045	146.10	104.84	154.79	117.20
0.70	0.005587	0.022	0.052	169.08	119.55	179.69	134.71
0.80	0.006593	0.025	0.060	191.65	133.38	204.27	151.52
0.90	0.007684	0.028	0.067	213.82	146.31	228.52	167.63
1.00	0.008844	0.031	0.074	235.59	158.32	252.87	182.95
1.10	0.010075	0.034	0.081	257.17	169.50	277.77	197.89
1.20	0.011339	0.037	0.088	279.58	180.59	304.19	212.14
1.30	0.012598	0.040	0.095	303.85	191.55	**331.93**	**225.72**
1.40	0.013839	0.043	0.102	**333.98**	200.68	**358.23**	**237.19**
1.50	0.015092	0.047	0.109	**362.93**	207.34	**382.51**	**246.18**

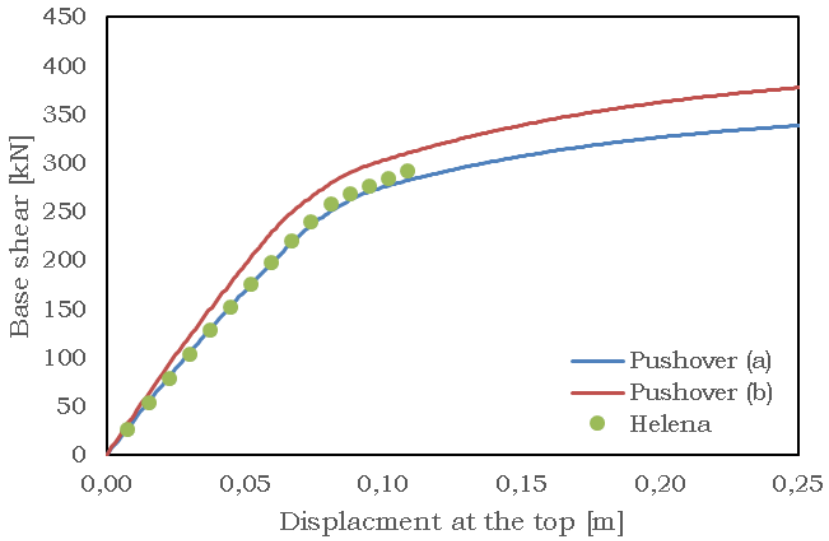

Fig.5.84 – Base shear vs displacement at the top – HELENA RBS

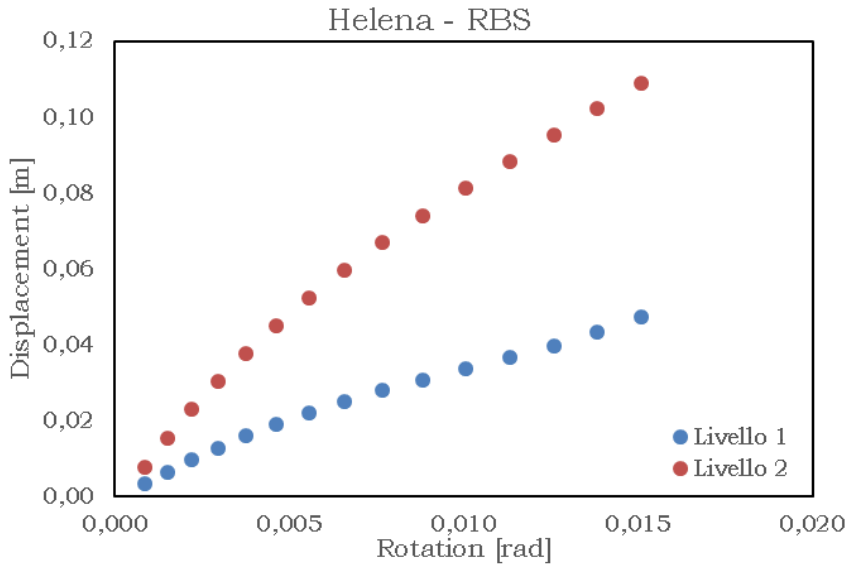

Fig. 5.85 – Displacement vs rotation – HELENA RBS

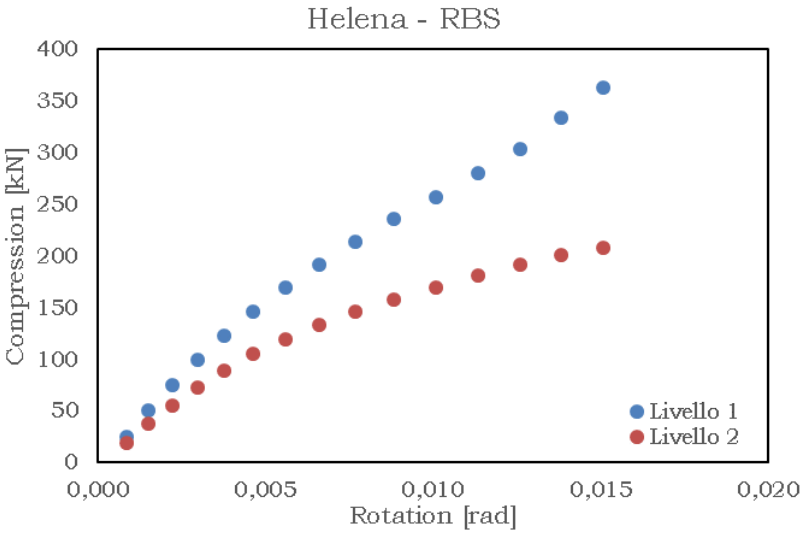

Fig. 5.86 – Compression vs rotation – HELENA RBS

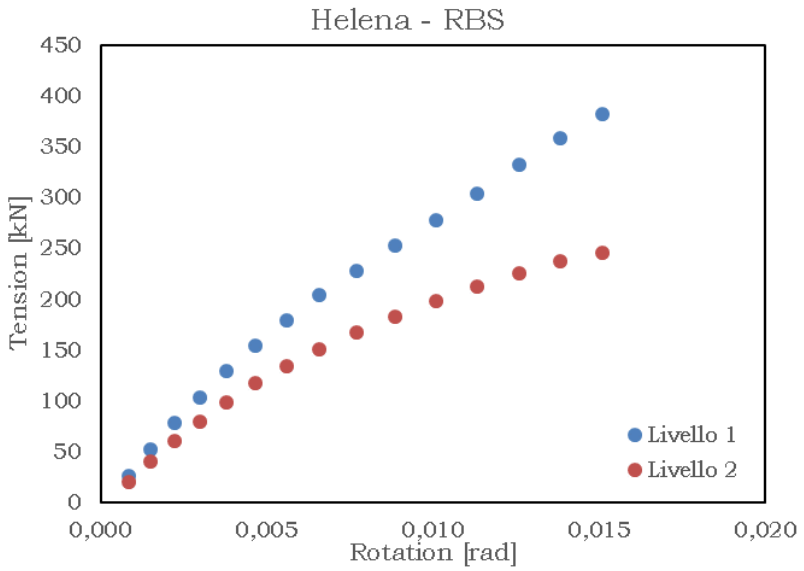

Fig. 5.87 – Tension vs rotation – HELENA RBS

Imperial Valley

Table 5.38 – FREEDAM - Maximum friction coefficient – IMPERIAL VALLEY

PGA [g]	***Rotation [rad]***	***Displacement (m)***		***Compression [kN]***		***Tension [kN]***	
		Lev. 1	***Lev. 2***	***Lev. 1***	***Lev. 2***	***Lev. 1***	***Lev. 2***
0.10	0.000	0.004	0.009	19.80	26.95	22.88	23.54
0.20	0.000416	0.008	0.018	39.61	53.90	45.77	47.08
0.30	0.000576	0.013	0.027	59.47	80.91	68.67	70.74
0.40	0.000736	0.017	0.036	79.41	107.95	91.60	94.43
0.50	0.000895	0.021	0.045	99.37	134.93	114.57	118.08
0.60	0.006000	0.025	0.051	112.21	143.29	137.59	125.15
0.70	0.010715	0.029	0.060	116.87	157.50	149.29	141.14
0.80	0.012863	0.034	0.071	116.29	154.49	154.13	154.57
0.90	0.014688	0.042	0.084	125.58	165.73	145.31	153.60
1.00	0.017406	0.050	0.095	146.32	174.16	160.73	162.94
1.10	0.020746	0.060	0.110	157.94	173.75	180.32	169.76
1.20	0.025664	0.068	0.135	164.29	178.23	190.97	177.27
1.30	0.031577	0.080	0.162	166.97	172.17	202.85	185.56
1.40	**0.037381**	0.093	0.189	161.68	170.60	185.29	184.35

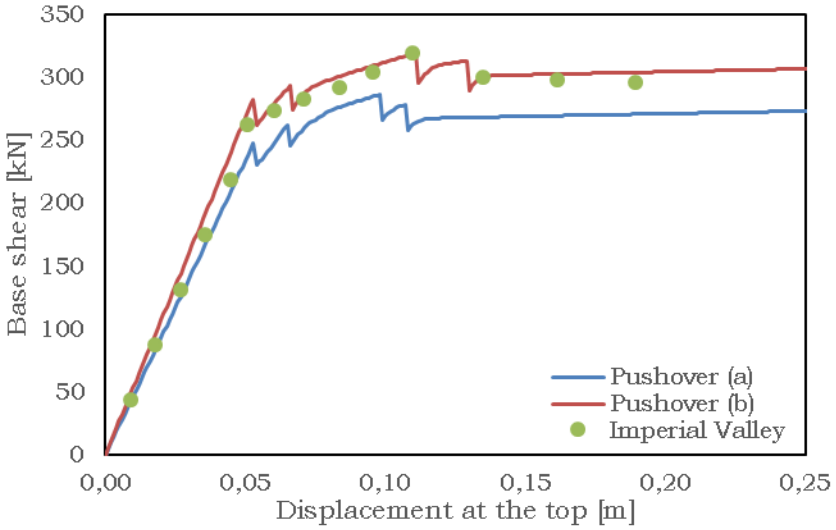

Fig. 5.88 – Base shear vs Displacement at the top – IMPERIAL VALLEY Max friction

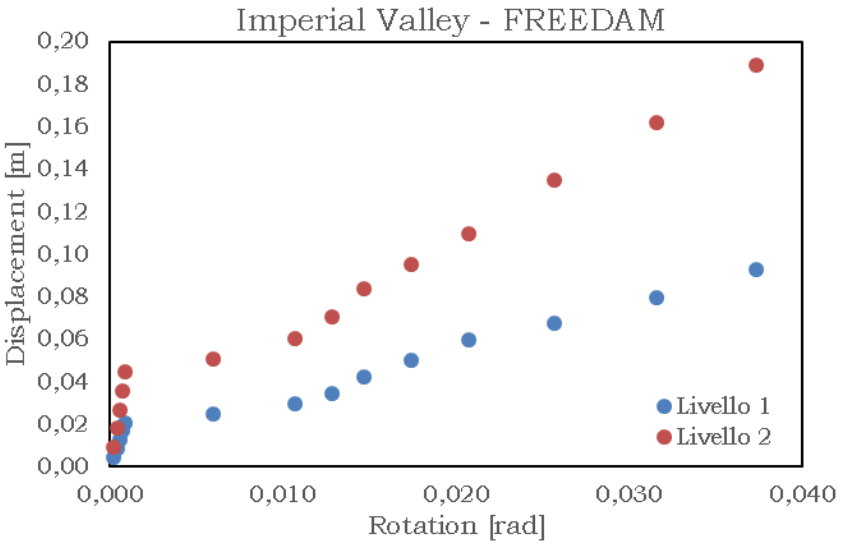

Fig. 5.89 – Displacement vs rotation – IMPERIAL VALLEY Max friction

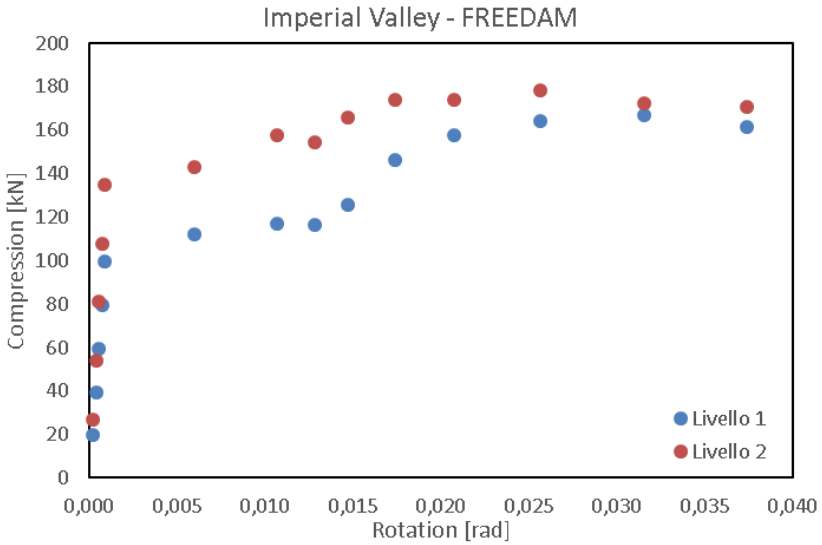

Fig. 5.90 – Compression vs rotation – IMPERIAL VALLEY Max friction

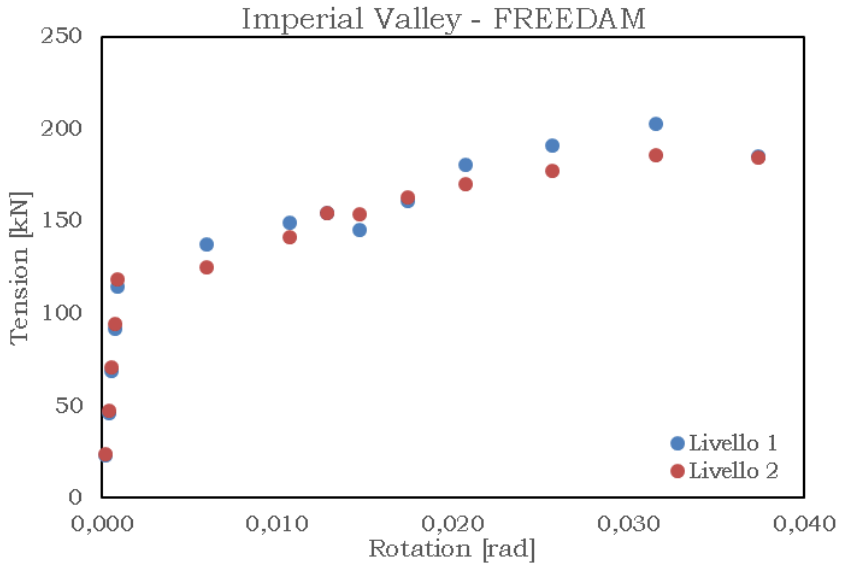

Fig. 5.91 – Tension vs rotation – IMPERIAL VALLEY Max friction

Table 5.39 – FREEDAM - Minimum friction coefficient – IMPERIAL VALLEY

PGA [g]	***Rotation [rad]***	***Displacement (m)***		***Compression [kN]***		***Tension [kN]***	
		Lev. 1	***Lev. 2***	***Lev. 1***	***Lev. 2***	***Lev. 1***	***Lev. 2***
0.10	0.00	0.004	0.009	19.80	26.95	22.88	23.54
0.20	0.000417	0.008	0.018	39.61	53.90	45.77	47.07
0.30	0.000593	0.013	0.027	59.41	80.85	68.65	70.61
0.40	0.000768	0.017	0.036	79.22	107.79	91.54	94.15
0.50	0.000943	0.021	0.045	99.03	134.73	114.42	117.69
0.60	0.010977	0.025	0.051	97.09	130.06	128.49	120.83
0.70	0.013625	0.030	0.062	107.09	149.68	143.53	141.82
0.80	0.015082	0.035	0.074	116.77	141.10	148.88	146.96
0.90	0.017887	0.043	0.087	138.50	151.44	140.87	148.62
1.00	0.020590	0.051	0.103	148.13	136.45	184.85	156.49
1.10	0.024553	0.058	0.122	153.00	148.39	180.29	158.57
1.20	0.029108	0.064	0.144	155.22	147.15	193.13	169.46
1.30	**0.036057**	0.074	0.174	159.92	151.63	188.12	170.28
1.40	**0.043871**	0.094	0.208	165.11	154.47	180.81	159.95

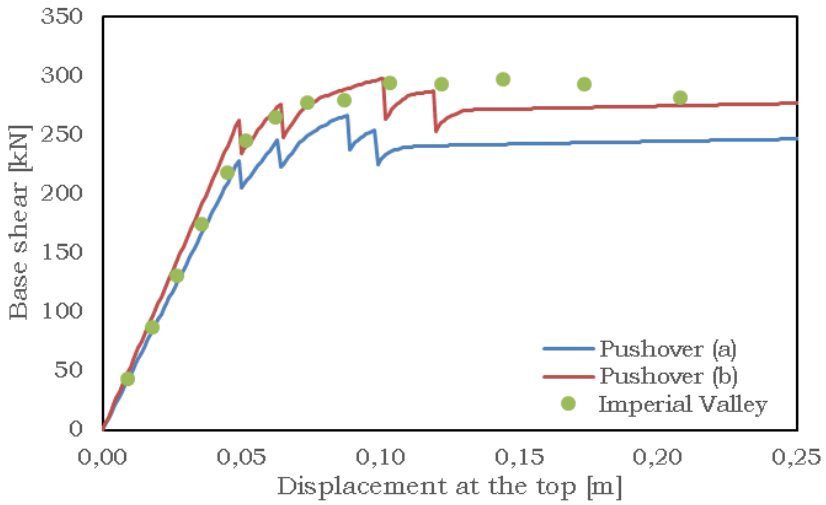

Fig. 5.92 – Base shear vs Displacement at the top – IMPERIAL VALLEY min friction

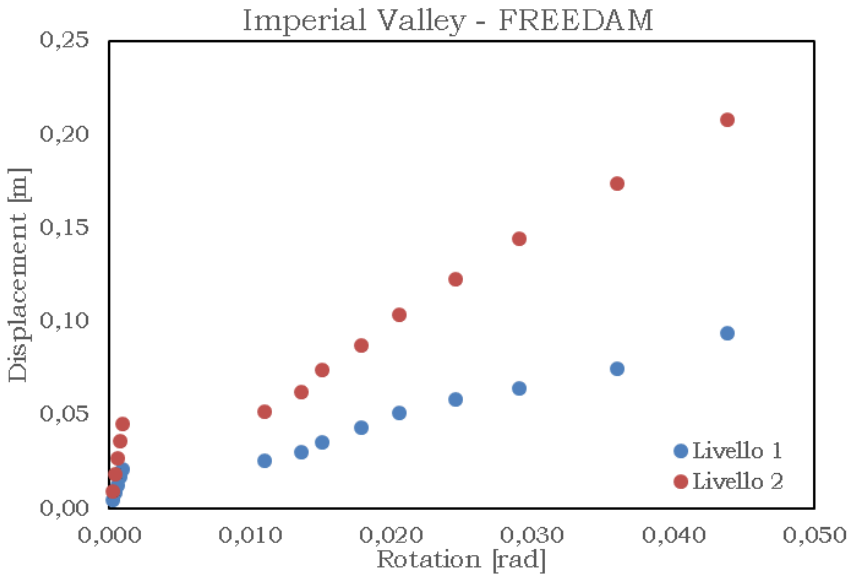

Fig. 5.93 – Displacement vs rotation – IMPERIAL VALLEY min friction

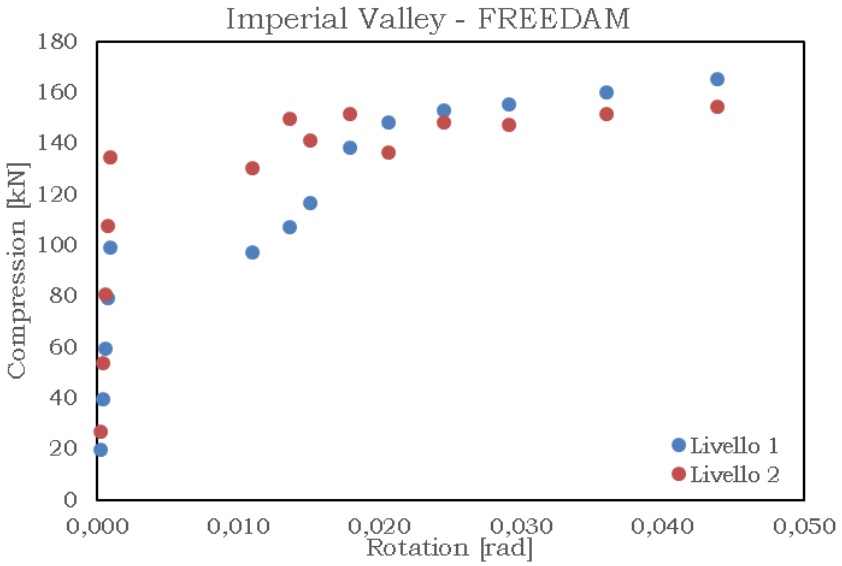

Fig. 5.94 – Compression vs rotation – IMPERIAL VALLEY min friction

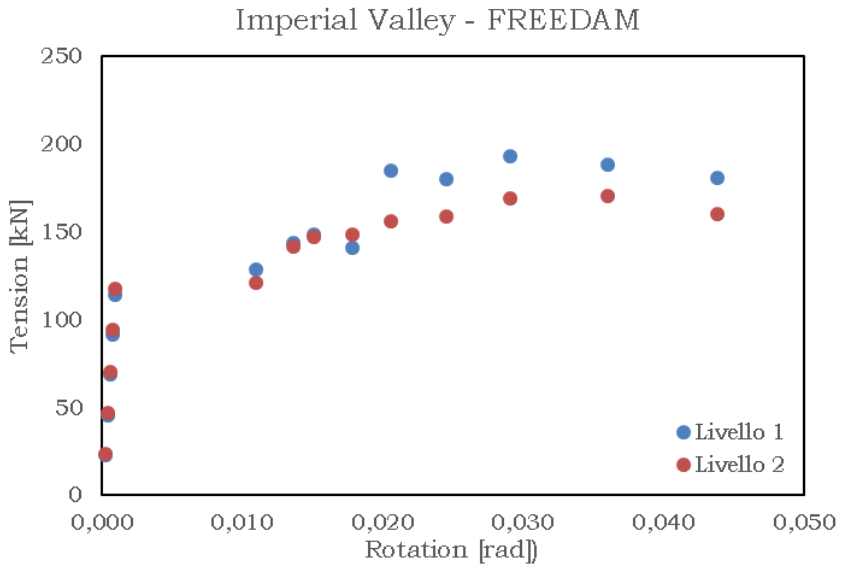

Fig. 5.95 – Tension vs rotation – IMPERIAL VALLEY min friction

Table 5.40 – RBS – IMPERIAL VALLEY

PGA [g]	***Rotation [rad]***	***Displacement (m)***		***Compression [kN]***		***Tension [kN]***	
		Lev. 1	***Lev. 2***	***Lev. 1***	***Lev. 2***	***Lev. 1***	***Lev. 2***
0.10	0.00	0.005	0.011	16.82	26.11	19.91	24.18
0.20	0.002737	0.010	0.022	33.19	51.50	39.31	47.27
0.30	0.003883	0.014	0.032	49.13	76.05	58.36	69.33
0.40	0.005063	0.019	0.043	64.60	99.61	76.94	90.11
0.50	0.006331	0.024	0.053	79.49	122.43	94.91	109.38
0.60	0.007891	0.028	0.063	93.87	143.93	112.34	127.02
0.70	0.009683	0.033	0.073	107.26	163.67	128.72	143.70
0.80	0.011507	0.038	0.085	113.00	176.35	133.09	157.17
0.90	0.013573	0.046	0.097	123.84	182.14	143.01	165.82
1.00	0.016413	0.053	0.111	137.80	183.74	152.82	169.64
1.10	0.019454	0.061	0.124	152.23	183.53	175.77	175.70
1.20	0.022749	0.070	0.138	165.49	182.99	193.34	184.61
1.30	0.026250	0.079	0.153	174.61	181.84	207.18	193.25
1.40	0.030063	0.088	0.169	179.39	181.16	220.35	198.75
1.50	0.034388	0.098	0.187	185.87	183.04	233.20	208.24
1.60	**0.039326**	0.108	0.207	185.93	184.46	244.28	218.68
1.70	**0.045110**	0.119	0.231	187.85	188.25	255.12	**230.46**

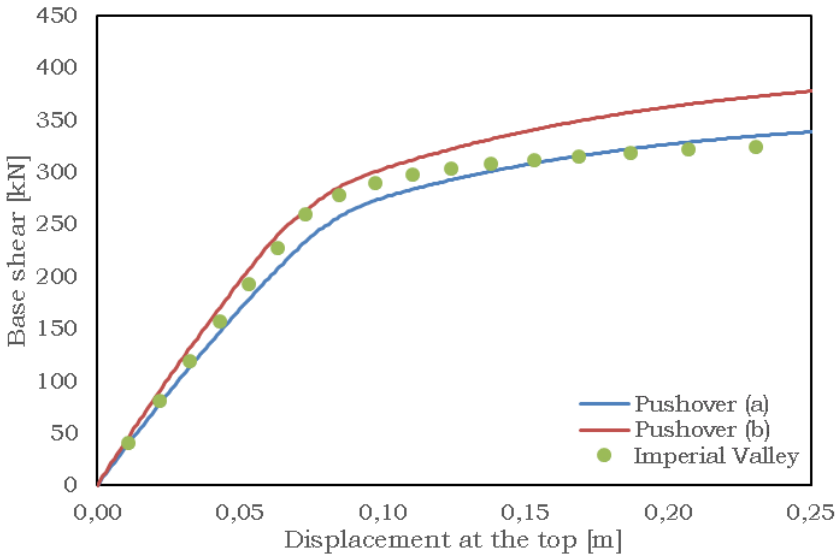

Fig. 5.96 – Base shear vs displacement at the top – IMPERIAL VALLEY RBS

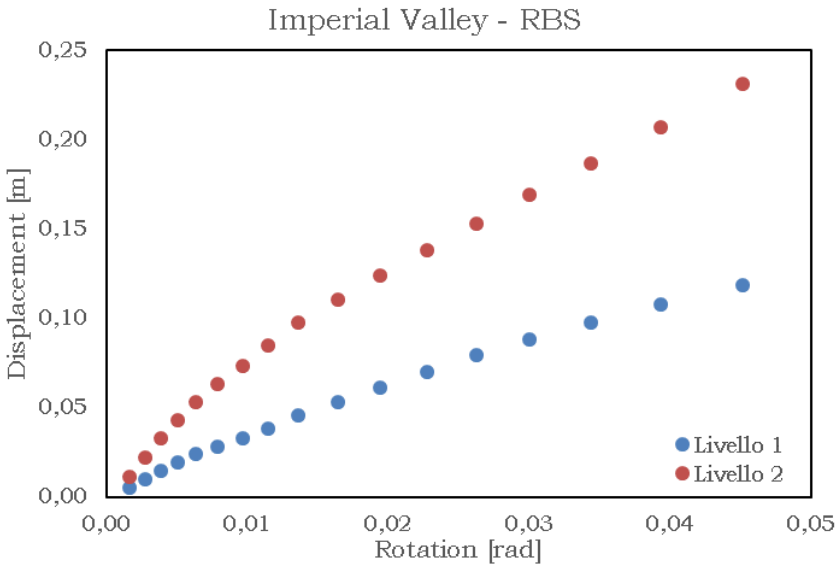

Fig. 5.97 – Displacement vs rotation – IMPERIAL VALLEY RBS

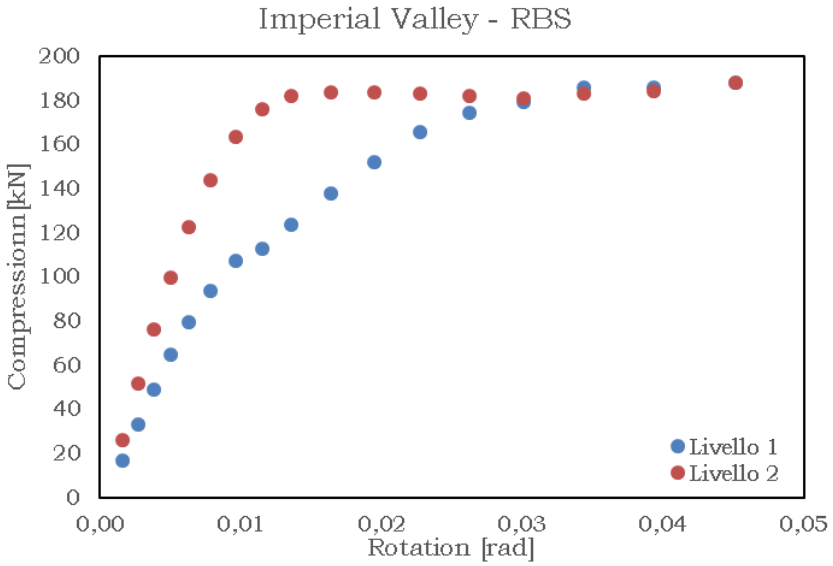

Fig. 5.98 – Compression vs rotation – IMPERIAL VALLEY RBS

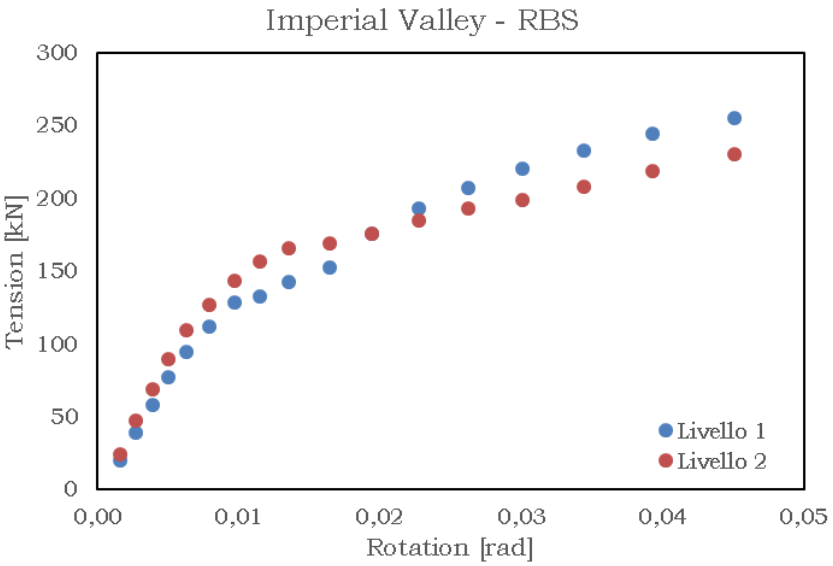

Fig. 5.99 – Tension vs rotation – IMPERIAL VALLEY RBS

Kobe

Table 5.41 – FREEDAM - Maximum friction coefficient - KOBE

PGA	***Rotation***	***Displacement***		***Compression***		***Tension***	
[g]	***[rad]***	***(m)***		***[kN]***		***[kN]***	
		Lev. 1	***Lev. 2***	***Lev. 1***	***Lev. 2***	***Lev. 1***	***Lev. 2***
0.10	0.000	0.005	0.011	28.68	33.91	28.63	29.97
0.20	0.000488	0.011	0.022	57.38	67.83	57.26	59.95
0.30	0.000683	0.016	0.033	86.12	101.85	85.99	90.02
0.40	0.000879	0.021	0.044	114.94	135.96	114.83	120.14
0.50	0.008705	0.026	0.055	138.04	160.10	137.86	149.55
0.60	0.012399	0.032	0.067	157.64	178.39	160.17	169.54
0.70	0.013706	0.039	0.080	183.04	202.10	184.53	180.52
0.80	0.015838	0.045	0.088	208.33	220.59	204.74	185.45
0.90	0.018156	0.052	0.101	233.92	225.07	229.37	189.39
1.00	0.022575	0.060	0.121	252.51	231.33	253.78	193.93
1.10	0.025426	0.066	0.135	267.04	225.68	276.70	198.88
1.20	0.027720	0.071	0.146	273.74	228.89	298.07	204.57
1.30	0.029767	0.075	0.156	283.46	232.75	319.47	207.64
1.40	0.033702	0.083	0.174	294.93	238.93	**338.61**	207.99
1.50	**0.040424**	0.090	0.202	311.11	247.23	**358.57**	210.97

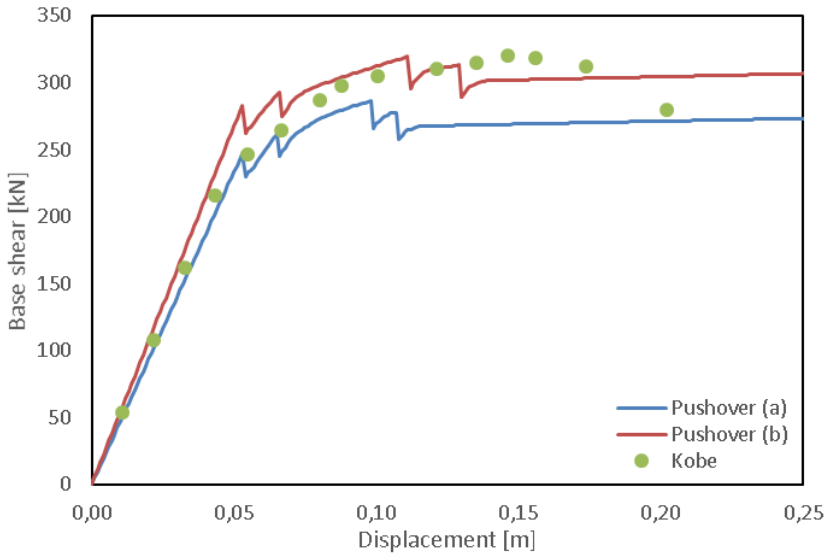

Fig. 5.100 – Load distribution on the frame for the pushover analysis

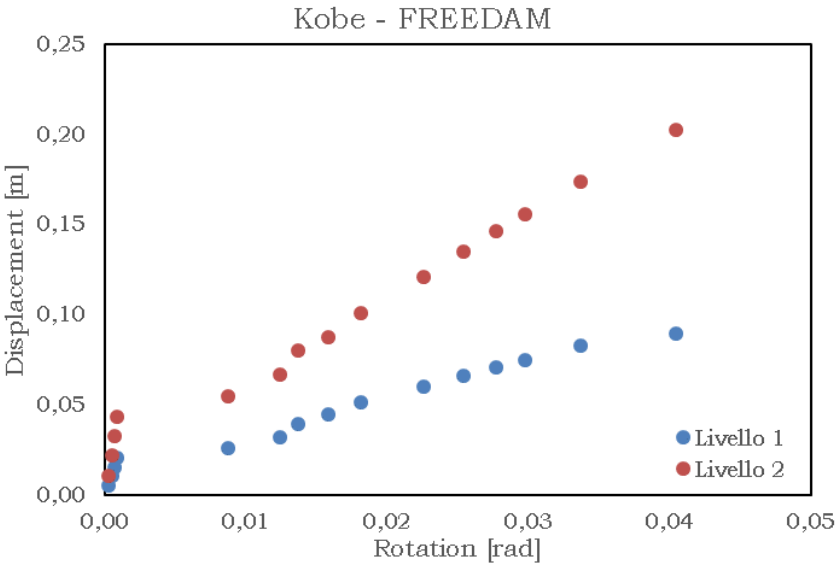

Fig. 5.101 – Load distribution on the frame for the pushover analysis

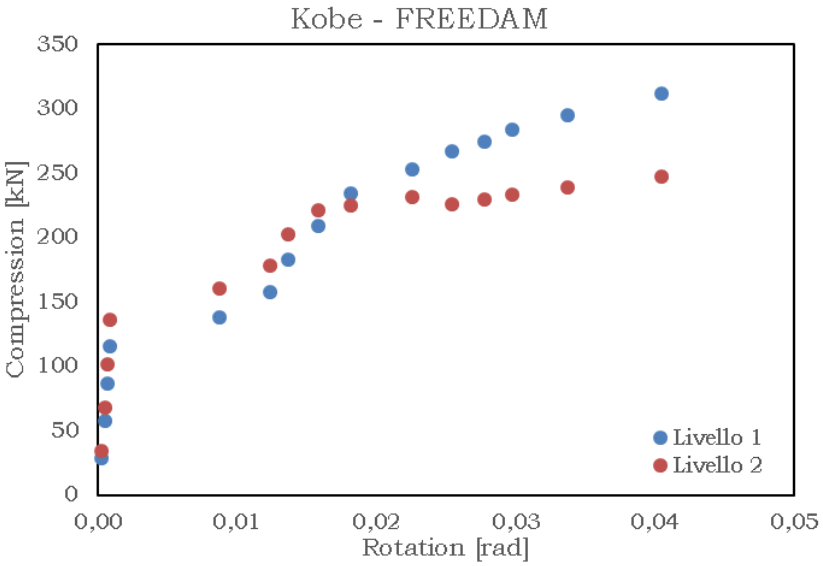

Fig. 5.102 – Load distribution on the frame for the pushover analysis

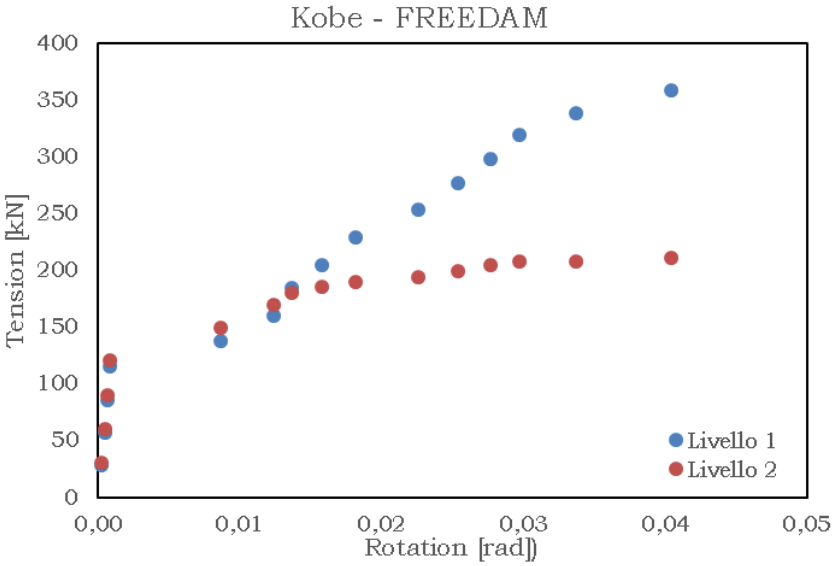

Fig. 5.103 – Load distribution on the frame for the pushover analysis

FREEDAM – Minimum friction coefficient

Table 5.42 – FREEDAM - Minimum friction coefficient - KOBE

PGA [g]	***Rotation [rad]***	***Displacement (m)***		***Compression [kN]***		***Tension [kN]***	
		Lev. 1	***Lev. 2***	***Lev. 1***	***Lev. 2***	***Lev. 1***	***Lev. 2***
0.10	0.00	0.005	0.011	28.68	33.91	28.63	29.97
0.20	0.000496	0.011	0.022	57.37	67.83	57.26	59.94
0.30	0.000711	0.016	0.033	86.06	101.75	85.89	89.91
0.40	0.000926	0.021	0.044	114.74	135.68	114.51	119.88
0.50	0.011985	0.027	0.056	135.16	155.99	135.76	141.58
0.60	0.015195	0.033	0.069	155.40	168.23	156.36	150.61
0.70	0.016886	0.041	0.083	179.18	185.06	176.57	165.60
0.80	0.018599	0.045	0.091	199.91	176.92	202.83	158.89
0.90	0.021385	0.050	0.106	220.73	170.90	228.02	161.85
1.00	0.026159	0.059	0.130	236.21	186.31	253.59	165.75
1.10	0.028389	0.063	0.141	242.47	196.39	275.55	173.74
1.20	0.031907	0.066	0.156	255.60	203.96	294.96	174.87
1.30	0.034714	0.070	0.163	273.65	212.98	316.68	180.54
1.40	**0.038903**	0.079	0.184	298.12	223.88	**337.96**	190.24
1.50	**0.043120**	0.090	0.205	319.74	231.28	**357.22**	199.70

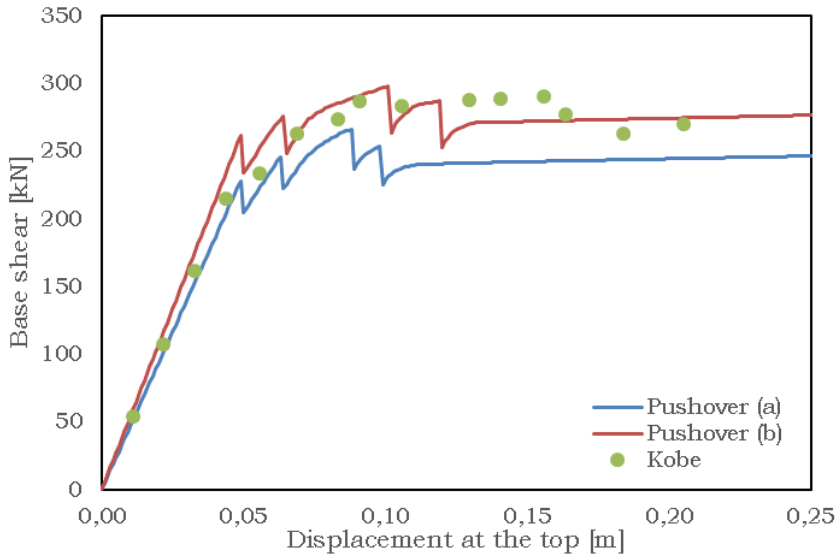

Fig. 5.104 – Base shear vs Displacement at the top – KOBE min friction

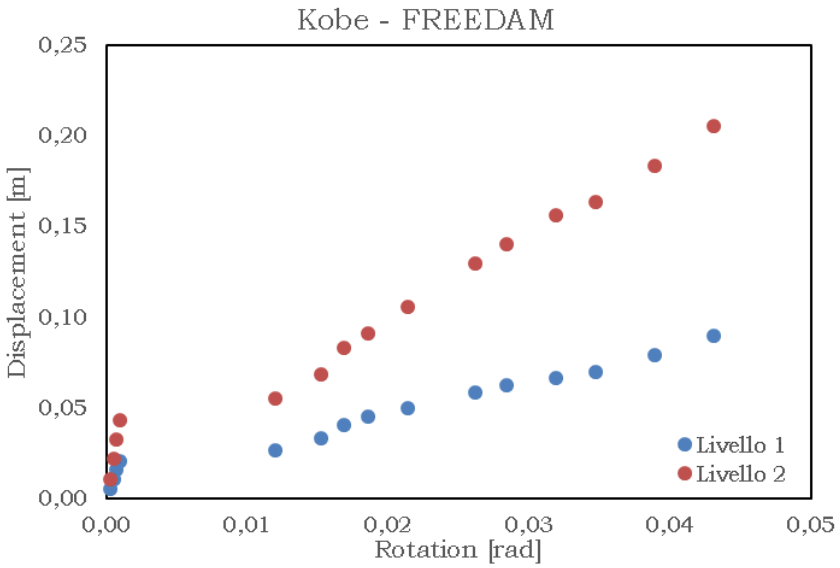

Fig. 5.105 – Displacement vs rotation – KOBE min friction

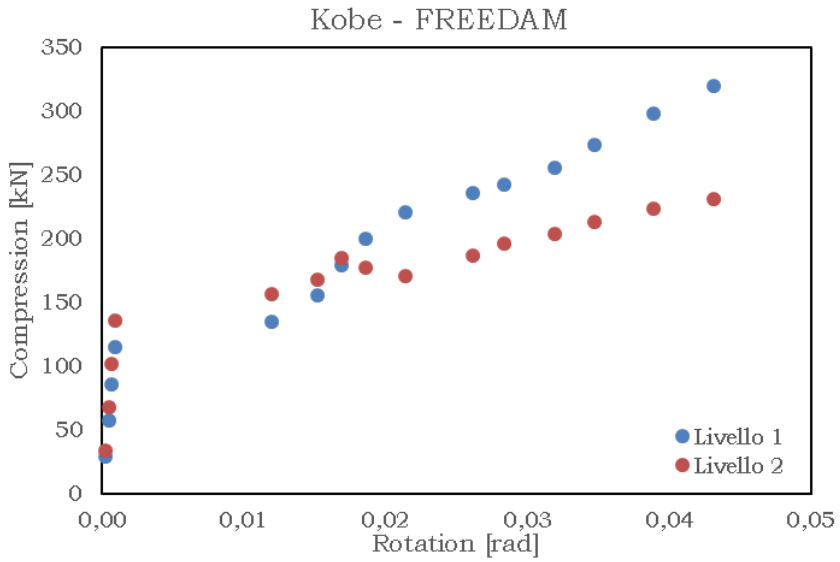

Fig. 5.106 – Compression vs rotation – KOBE min friction

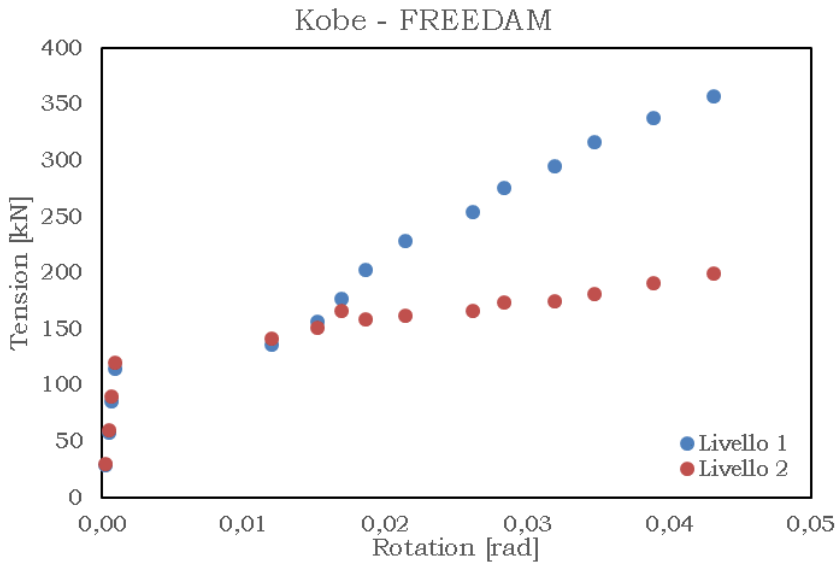

Fig. 5.107 – Tension vs rotation – KOBE min friction

Table 5.43 – RBS - KOBE

PGA [g]	***Rotation [rad]***	***Displacement (m)***		***Compression [kN]***		***Tension [kN]***	
		Lev. 1	***Lev. 2***	***Lev. 1***	***Lev. 2***	***Lev. 1***	***Lev. 2***
0.10	0.00	0.006	0.014	24.86	34.08	27.36	32.94
0.20	0.003335	0.013	0.029	48.28	67.48	53.76	63.96
0.30	0.004979	0.019	0.042	70.71	99.76	79.60	93.63
0.40	0.006782	0.024	0.056	93.75	130.66	105.14	121.84
0.50	0.008806	0.030	0.069	117.10	160.87	130.58	148.46
0.60	0.010938	0.036	0.082	140.30	188.16	156.18	169.13
0.70	0.013026	0.043	0.095	163.24	205.28	182.63	174.25
0.80	0.015127	0.051	0.108	186.18	217.90	209.92	177.28
0.90	0.017598	0.059	0.120	209.49	228.16	237.80	192.96
1.00	0.018931	0.066	0.129	229.78	234.75	266.09	210.30
1.10	0.022217	0.071	0.137	253.53	237.10	295.38	**227.32**
1.20	0.028419	0.076	0.159	277.37	239.38	**325.55**	**237.89**
1.30	0.033697	0.082	0.182	301.07	242.90	**356.16**	**241.64**
1.40	**0.038337**	0.092	0.202	**324.62**	248.09	**386.92**	**242.68**
1.50	**0.042545**	0.100	0.220	**347.00**	264.94	**416.67**	**243.44**

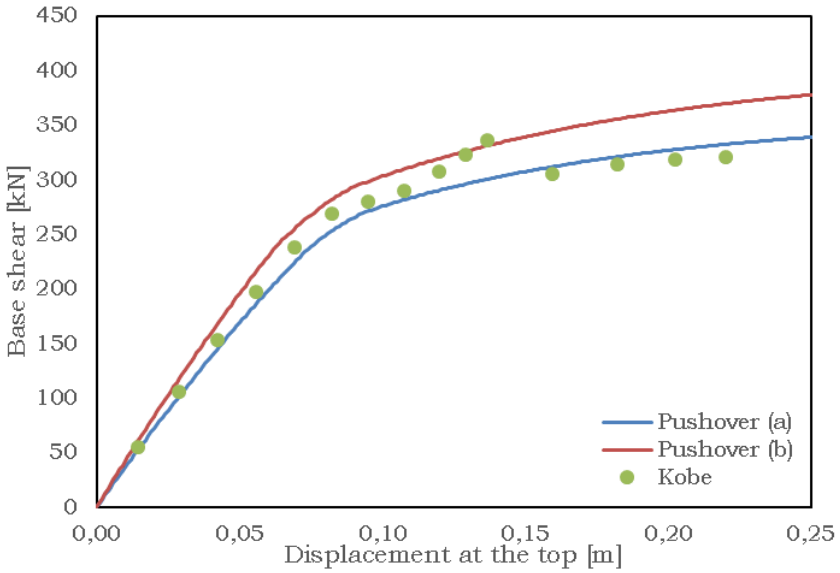

Fig. 5.108 – Base shear vs displacement at the top – KOBE RBS

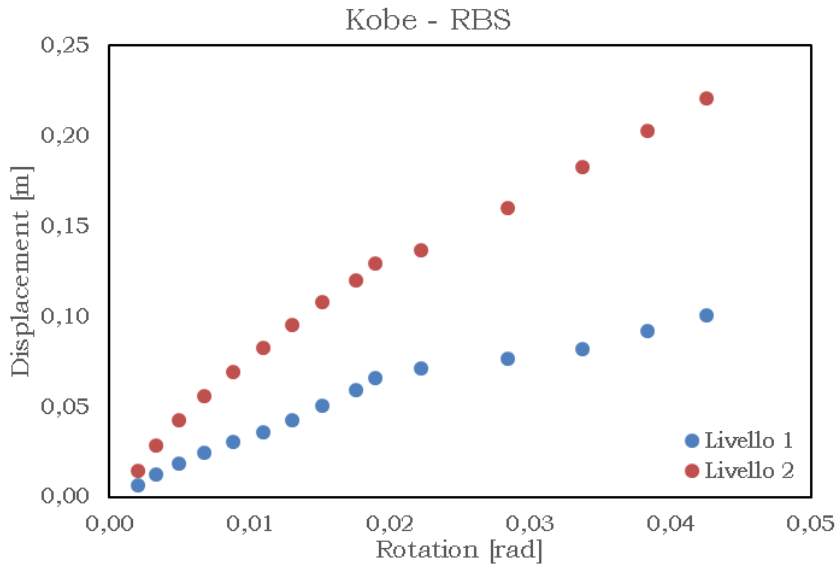

Fig. 5.109 – Displacement vs rotation – KOBE RBS

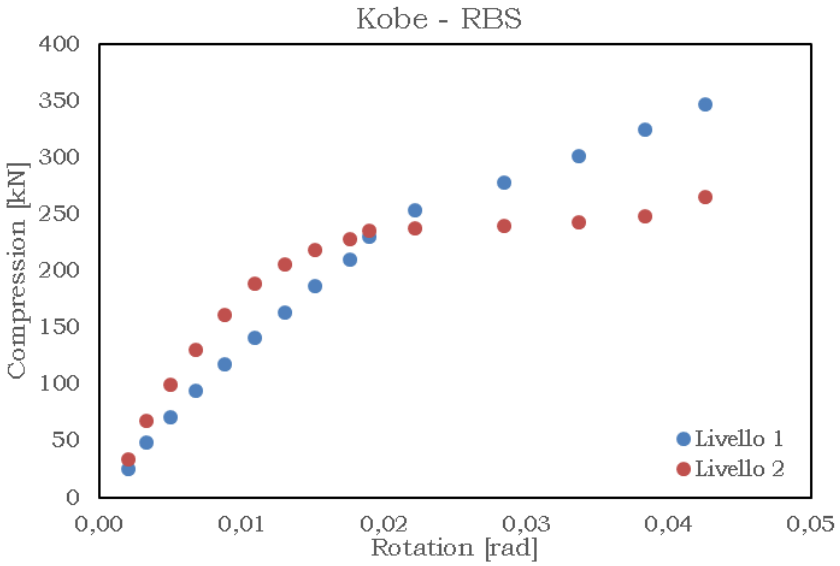

Fig. 5.110 – Compression vs rotation – KOBE RBS

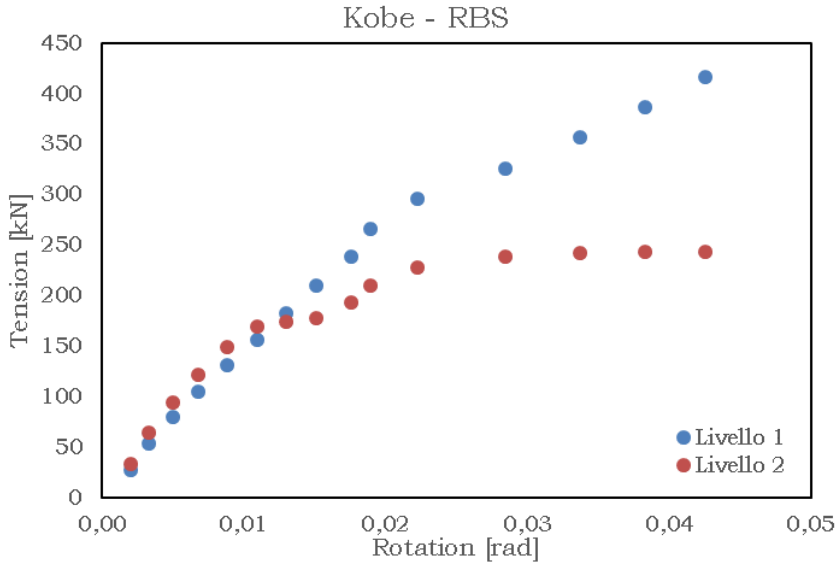

Fig. 5.111 – Tension vs rotation – KOBE RBS

Landers

Table 5.44 – FREEDAM - Maximum friction coefficient - LANDERS

PGA [g]	***Rotation [rad]***	***Displacement (m)***		***Compression [kN]***		***Tension [kN]***	
		Lev. 1	***Lev. 2***	***Lev. 1***	***Lev. 2***	***Lev. 1***	***Lev. 2***
0.10	0.000	0.006	0.012	22.88	31.16	23.70	37.44
0.20	0.000536	0.011	0.025	45.83	62.38	47.40	74.91
0.30	0.000755	0.017	0.037	69.06	93.77	71.15	112.52
0.40	0.000975	0.022	0.049	92.60	125.22	94.92	150.26
0.50	0.009786	0.028	0.062	102.27	135.78	118.83	167.14
0.60	0.014420	0.035	0.077	116.15	163.35	136.03	183.12
0.70	0.017162	0.040	0.087	129.88	181.56	145.40	195.64
0.80	0.019034	0.049	0.104	143.95	189.91	156.08	199.05
0.90	0.024214	0.059	0.128	154.55	203.42	162.15	203.45
1.00	0.030027	0.072	0.154	164.11	209.85	152.69	186.85
1.10	**0.036621**	0.086	0.185	180.13	220.84	174.94	195.43
1.20	**0.042495**	0.099	0.211	193.27	228.59	186.51	207.15
1.30	**0.047812**	0.108	0.233	204.71	225.04	186.92	210.68

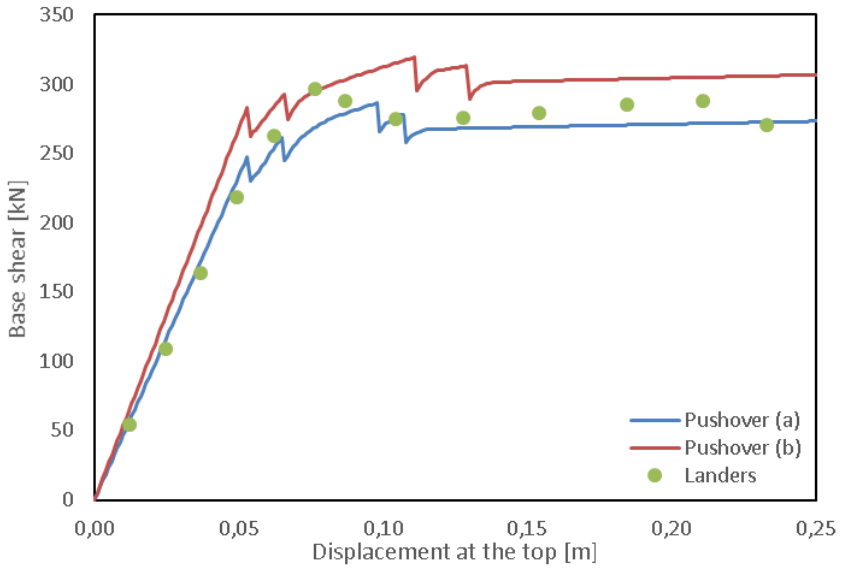

Fig. 5.112 – Base shear vs Displacement at the top – LANDERS Max friction

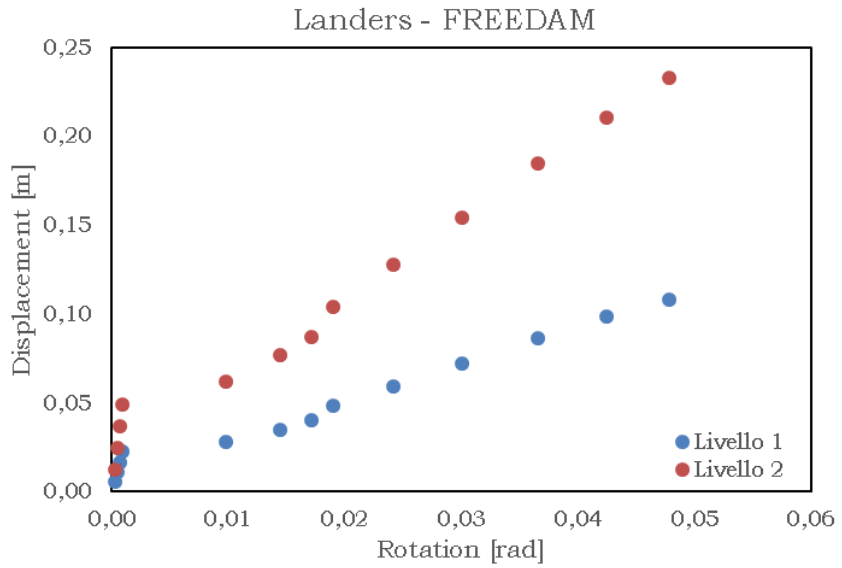

Fig. 5.113 – Displacement vs rotation – LANDERS Max friction

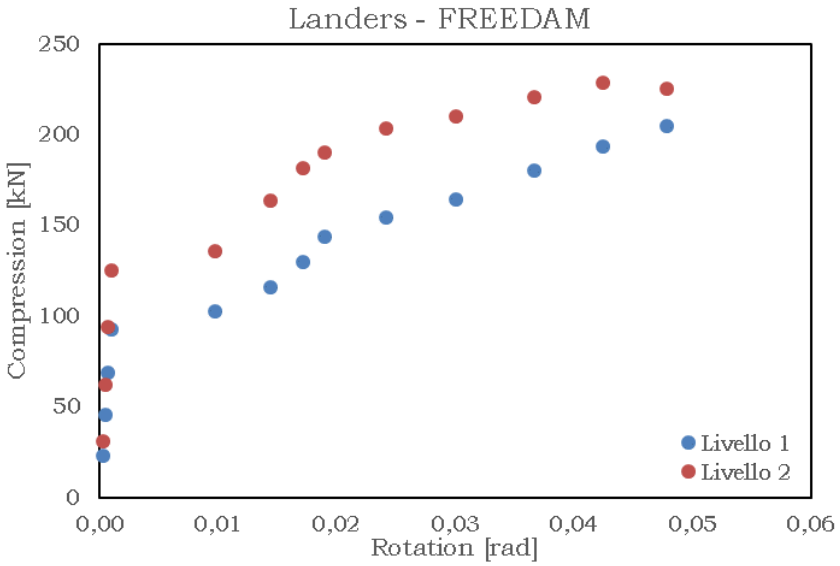

Fig. 5.114 – Compression vs rotation – LANDERS Max friction

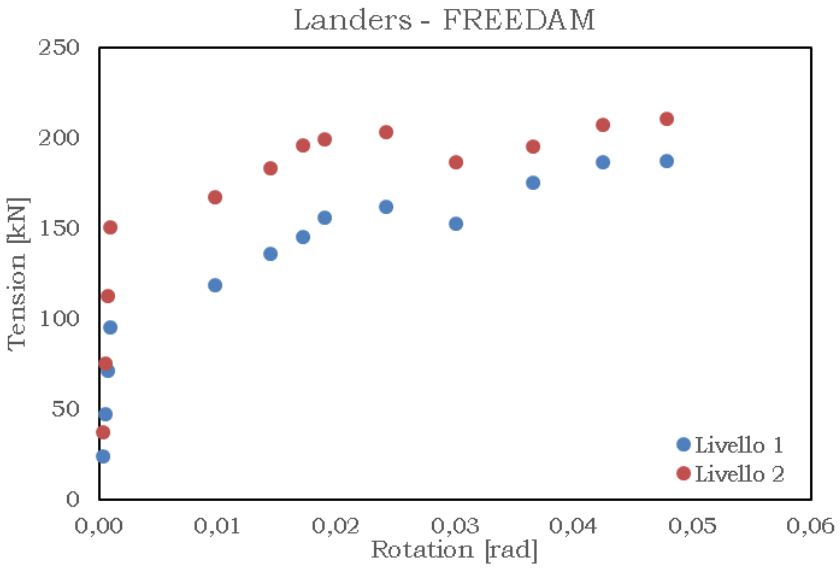

Fig. 5.115 – Tension vs rotation – LANDERS Max friction

FREEDAM – Minimum friction coefficient

Table 5.45 – FREEDAM - Minimum friction coefficient -LANDERS

PGA [g]	***Rotation [rad]***	***Displacement (m)***		***Compression [kN]***		***Tension [kN]***	
		Lev. 1	***Lev. 2***	***Lev. 1***	***Lev. 2***	***Lev. 1***	***Lev. 2***
0.10	0.00	0.006	0.012	22.88	31.16	23.70	37.44
0.20	0.000548	0.011	0.025	45.81	62.32	47.40	74.88
0.30	0.000790	0.017	0.037	68.85	93.51	71.09	112.34
0.40	0.006835	0.022	0.049	81.38	108.04	94.78	145.37
0.50	0.012324	0.029	0.063	94.64	135.09	116.14	151.73
0.60	0.017734	0.035	0.079	111.27	162.17	130.77	168.20
0.70	0.017738	0.040	0.090	122.05	171.09	142.32	162.97
0.80	0.022096	0.047	0.110	132.89	184.29	154.28	167.79
0.90	0.023917	0.051	0.118	148.96	179.12	154.30	170.94
1.00	0.027530	0.058	0.135	161.26	183.48	159.01	177.69
1.10	0.031555	0.066	0.153	181.59	192.25	167.77	191.99
1.20	**0.038379**	0.074	0.178	202.19	192.42	176.38	199.63
1.30	**0.042835**	0.089	0.199	225.45	201.43	187.41	202.12

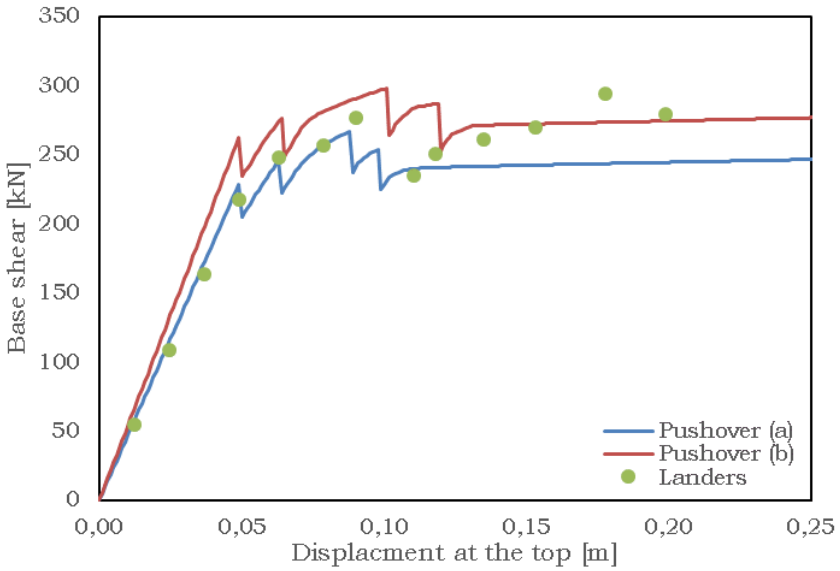

Fig. 5.116 – Base shear vs Displacement at the top – LANDERS min friction

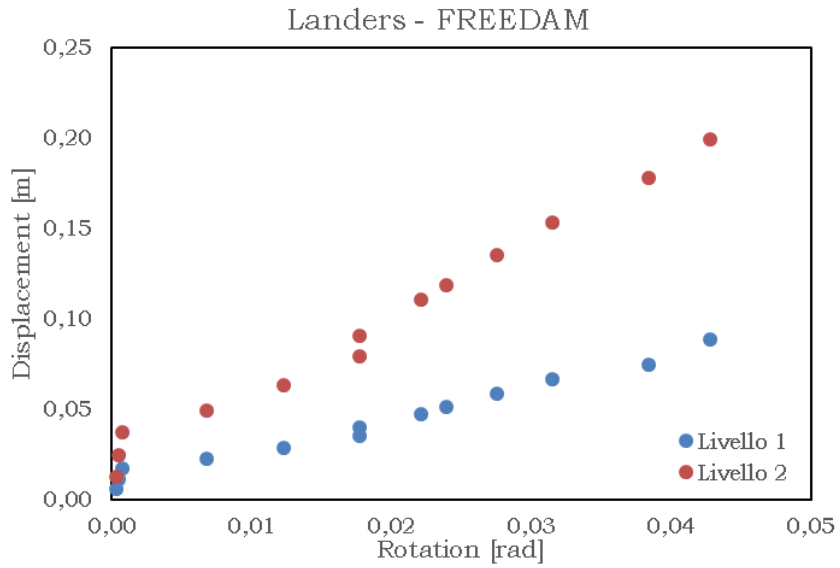

Fig. 5.117 – Displacement vs rotation – LANDERS min friction

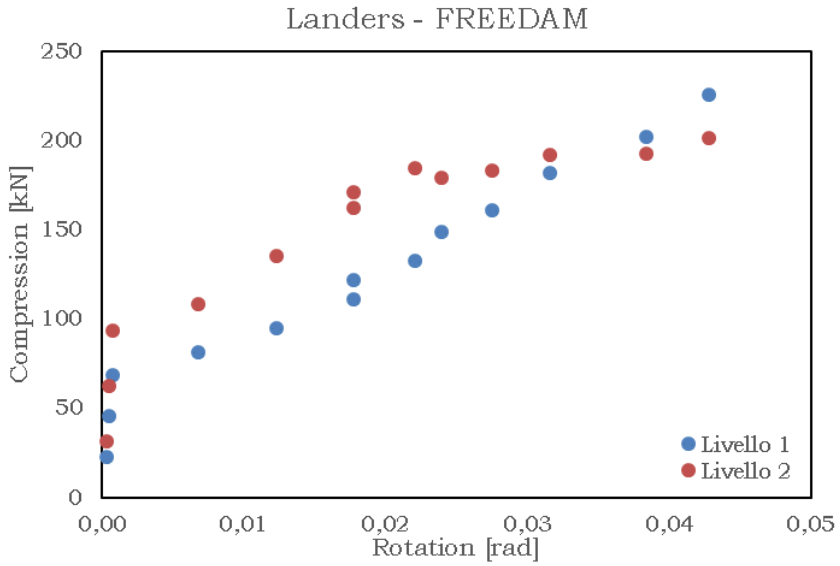

Fig. 5.118 – Compression vs rotation – LANDERS min friction

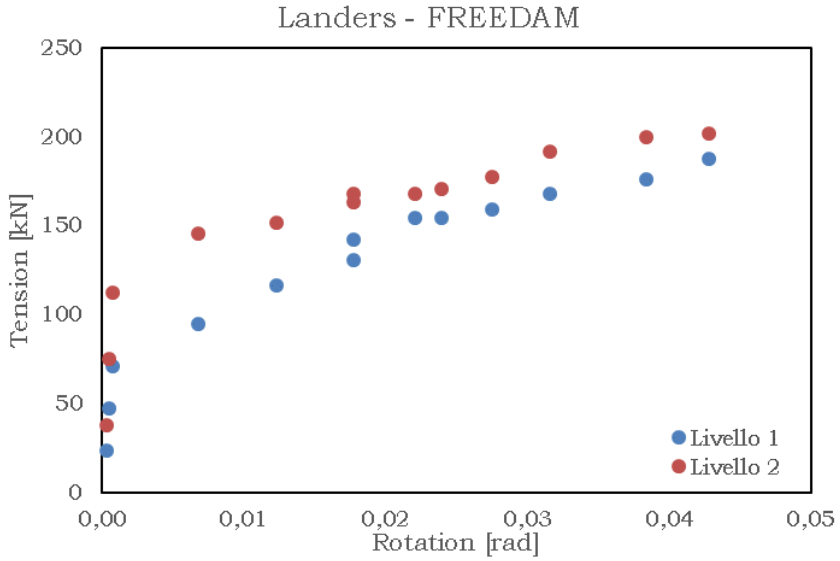

Fig. 5.119 – Tension vs rotation – LANDERS min friction

Table 5.46 – RBS - LANDERS

PGA [g]	***Rotation [rad]***	***Displacement (m)***		***Compression [kN]***		***Tension [kN]***	
		Lev. 1	***Lev. 2***	***Lev. 1***	***Lev. 2***	***Lev. 1***	***Lev. 2***
0.10	0.002	0.006	0.014	17.34	24.78	22.35	29.40
0.20	0.003583	0.012	0.027	34.36	49.58	43.73	57.63
0.30	0.005057	0.018	0.041	51.08	74.15	64.08	84.93
0.40	0.006777	0.024	0.055	67.32	98.20	82.81	110.87
0.50	0.008763	0.030	0.069	83.02	121.62	100.15	135.00
0.60	0.010906	0.036	0.083	99.27	144.02	112.54	158.47
0.70	0.012871	0.043	0.096	116.36	165.06	132.22	178.62
0.80	0.014304	0.050	0.105	137.83	184.83	160.56	193.16
0.90	0.015352	0.053	0.109	162.59	200.83	181.65	200.82
1.00	0.017884	0.058	0.114	197.74	214.32	197.89	209.12
1.10	0.023347	0.063	0.133	224.28	222.75	215.82	214.30
1.20	0.027659	0.070	0.153	234.49	228.48	226.24	218.05
1.30	0.032218	0.082	0.173	244.47	233.50	232.88	221.67
1.40	**0.035722**	0.095	0.189	253.00	237.80	240.26	**225.41**

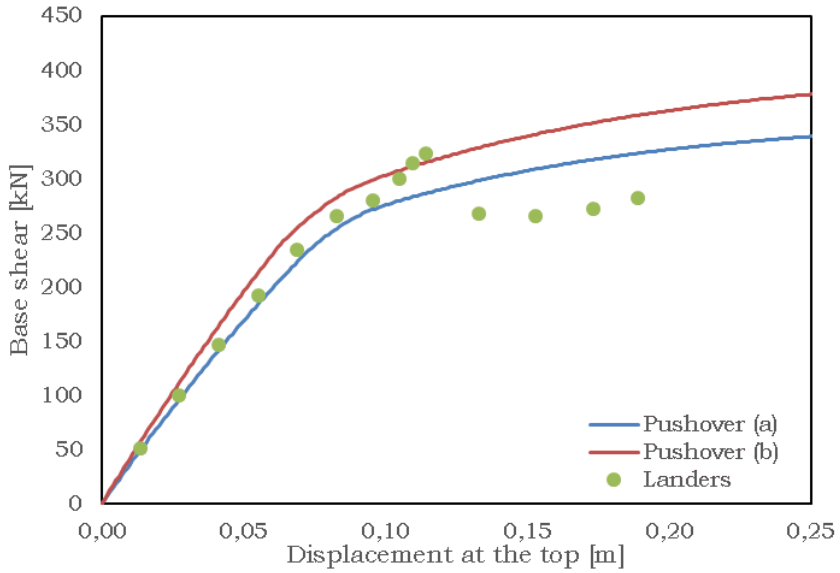

Fig. 5.120 – Base shear vs displacement at the top – LANDERS RBS

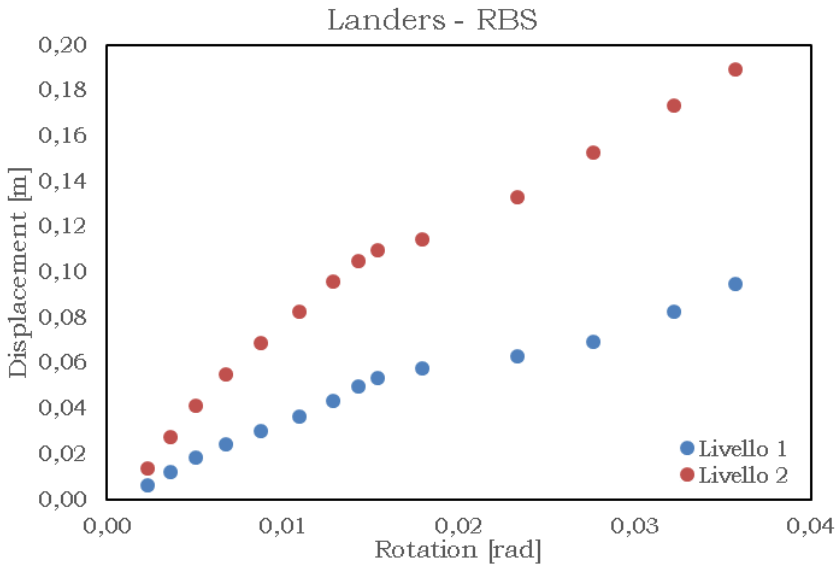

Fig. 5.121 – Displacement vs rotation – LANDERS RBS

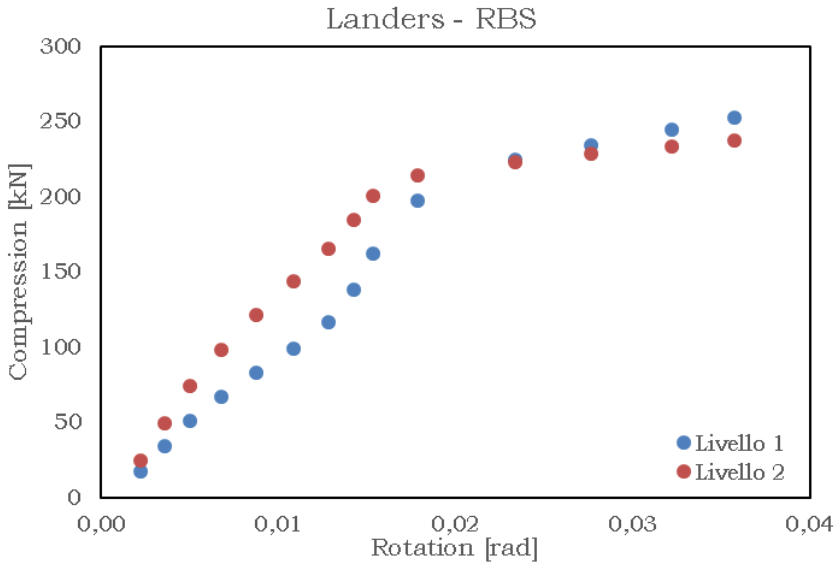

Fig. 5.122 – Compression vs rotation – LANDERS RBS

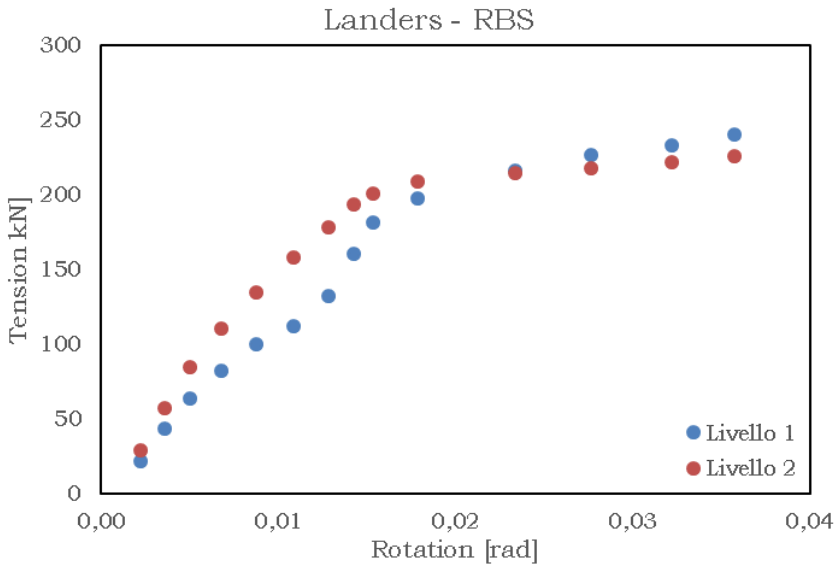

Fig. 5.123 – Load distribution on the frame for the pushover analysis

Northridge

FREEDAM – Maximum friction coefficient

Table 5.47 – FREEDAM - Maximum friction coefficient - NORTHRIDGE

PGA ***[g]***	***Rotation*** ***[rad]***	***Displacement*** ***(m)***		***Compression*** ***[kN]***		***Tension*** ***[kN]***	
		Lev. 1	***Lev. 2***	***Lev. 1***	***Lev. 2***	***Lev. 1***	***Lev. 2***
0.10	0.000	0.009	0.020	31.23	53.55	44.88	55.37
0.20	0.000807	0.019	0.040	62.87	107.46	89.98	110.96
0.30	0.011117	0.028	0.060	91.68	129.01	134.05	145.15
0.40	0.012439	0.034	0.074	107.68	152.64	145.22	167.75
0.50	0.015771	0.042	0.087	124.57	161.68	150.37	181.90
0.60	0.017534	0.050	0.098	149.63	181.18	164.86	178.37
0.70	0.017782	0.047	0.096	174.74	191.93	169.94	165.93
0.80	0.021648	0.055	0.116	182.11	197.19	173.88	177.19
0.90	0.026106	0.063	0.137	191.85	205.42	183.67	180.04
1.00	0.031364	0.074	0.160	196.97	200.15	177.33	176.92
1.10	0.033678	0.079	0.171	231.44	207.58	179.02	190.85
1.20	**0.036338**	0.085	0.183	244.29	213.30	187.68	196.70

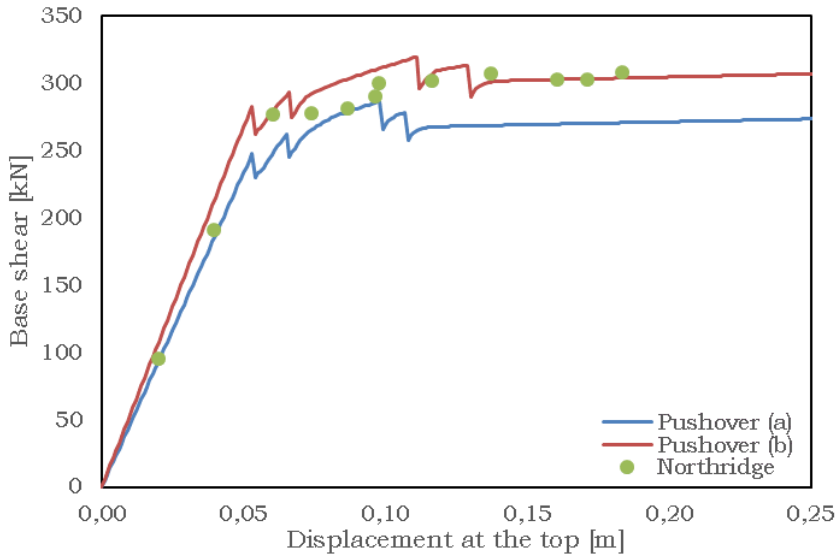

Fig. 5.124 – Base shear vs Displacement at the top – NORTHRIDGE Max friction

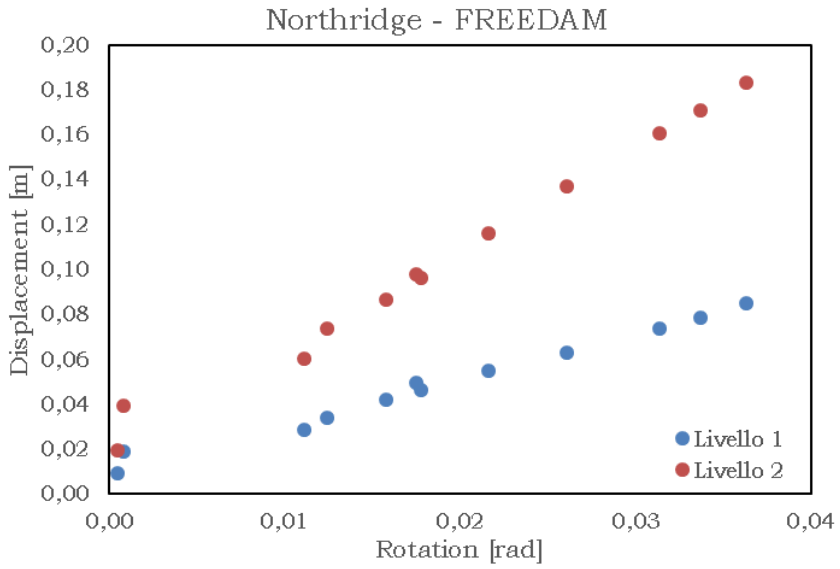

Fig. 5.125 – Displacement vs rotation – NORTHRIDGE Max friction

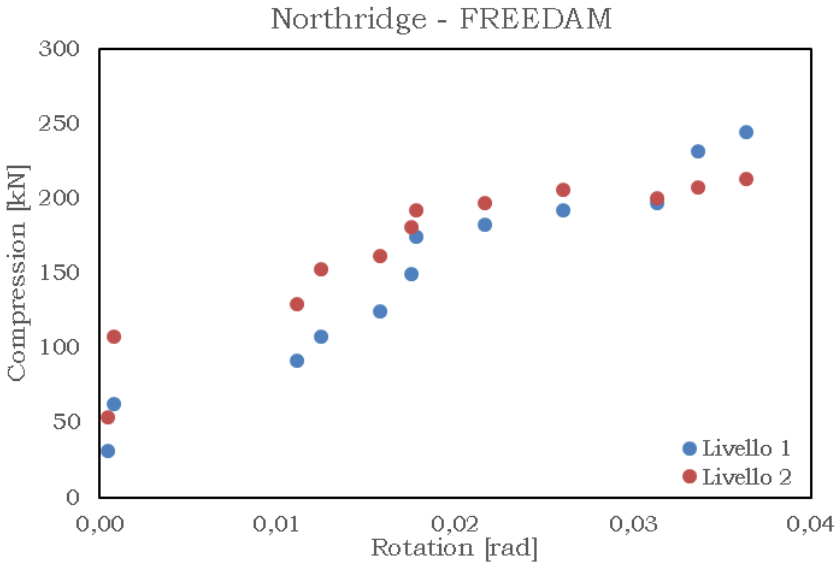

Fig. 5.126 – Load distribution on the frame for the pushover analysis

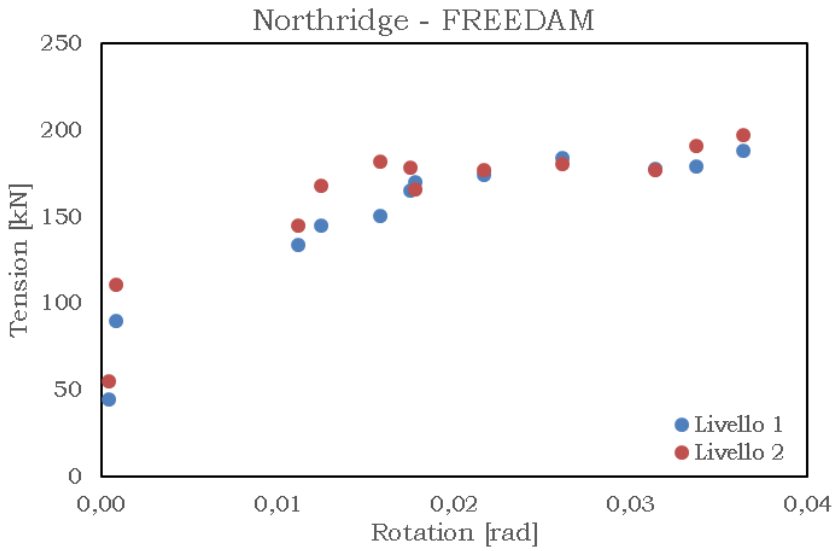

Fig. 5.127 – Load distribution on the frame for the pushover analysis

Table 5.48 – FREEDAM - Minimum friction coefficient - NORTHRIDGE

PGA [g]	***Rotation [rad]***	***Displacement (m)***		***Compression [kN]***		***Tension [kN]***	
		Lev. 1	***Lev. 2***	***Lev. 1***	***Lev. 2***	***Lev. 1***	***Lev. 2***
0.10	0.00	0.009	0.020	31.22	53.53	44.88	55.36
0.20	0.000846	0.019	0.040	62.48	107.09	89.79	110.74
0.30	0.013497	0.029	0.061	91.13	123.30	123.11	145.49
0.40	0.014622	0.034	0.073	100.73	138.01	133.33	157.40
0.50	0.017097	0.040	0.088	124.30	146.04	139.16	163.77
0.60	0.021542	0.048	0.108	149.16	160.19	163.35	168.06
0.70	0.021279	0.043	0.107	157.44	171.59	204.67	163.04
0.80	0.021097	0.046	0.106	164.27	175.13	240.49	186.07
0.90	0.025575	0.052	0.125	181.00	172.67	236.83	188.76
1.00	0.031465	0.065	0.152	192.86	187.06	239.49	187.46
1.10	0.034457	0.072	0.166	199.22	197.31	241.12	197.05
1.20	**0.041586**	0.088	0.198	204.59	208.89	246.68	206.76

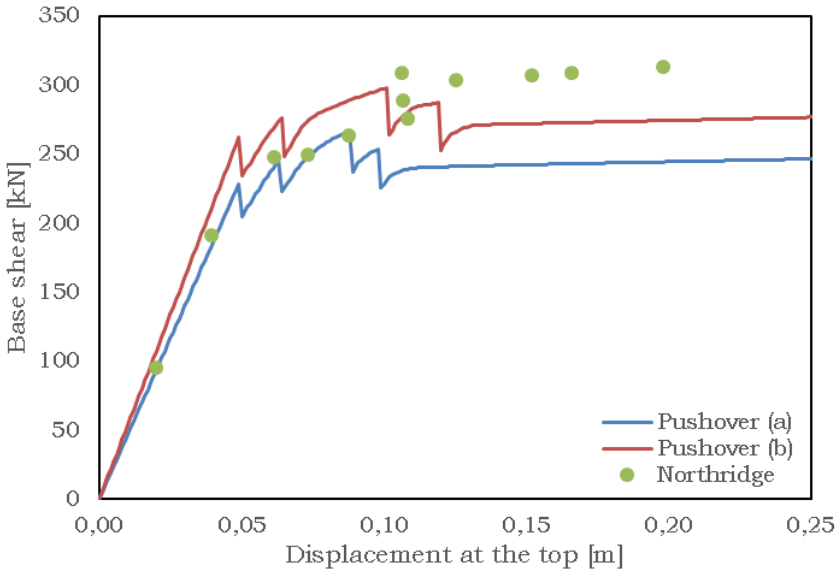

Fig. 5.128 – Base shear vs Displacement at the top – NORTHRIDGE min friction

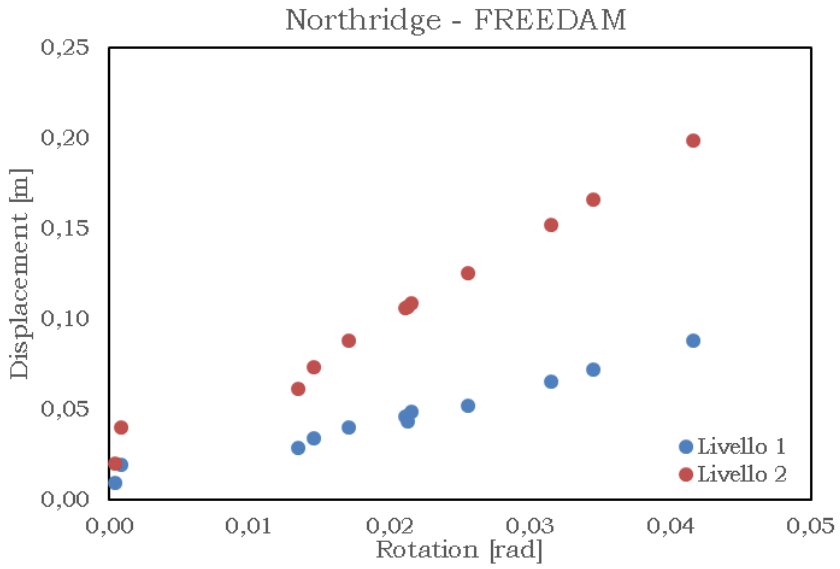

Fig. 5.129 – Displacement vs rotation – NORTHRIDGE min friction

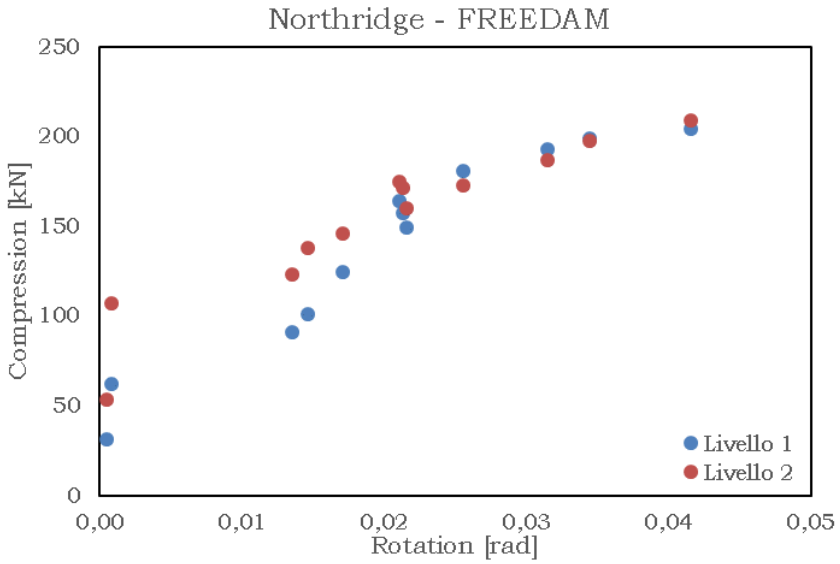

Fig. 5.130 – Compression vs rotation – NORTHRIDGE min friction

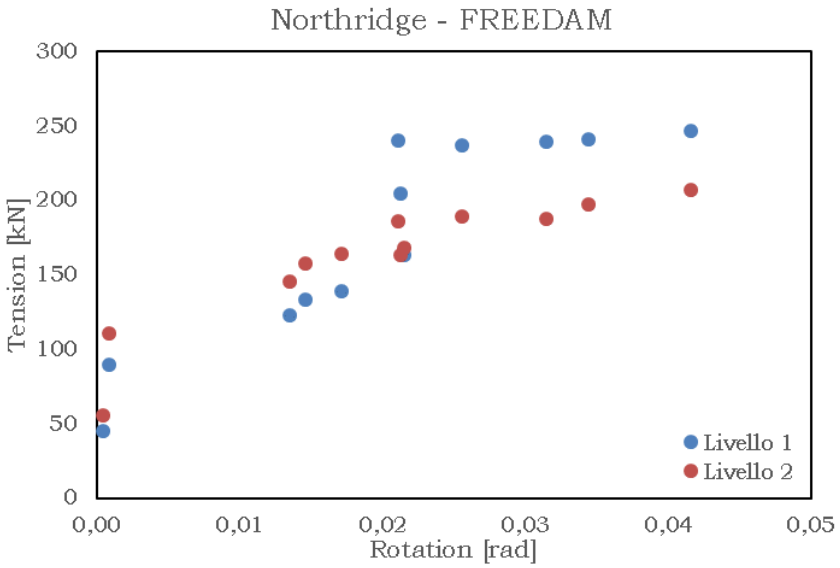

Fig. 5.131 – Tension vs rotation – NORTHRIDGE min friction

Table 5.49 – RBS - NORTHRIDGE

PGA [g]	***Rotation [rad]***	***Displacement (m)***		***Compression [kN]***		***Tension [kN]***	
		Lev. 1	***Lev. 2***	***Lev. 1***	***Lev. 2***	***Lev. 1***	***Lev. 2***
0.10	0.003	0.009	0.021	27.62	44.72	34.40	45.48
0.20	0.004962	0.018	0.041	54.49	85.65	65.63	89.44
0.30	0.007678	0.027	0.062	79.72	121.23	94.00	130.69
0.40	0.010953	0.036	0.083	100.49	148.54	119.64	167.14
0.50	0.014159	0.048	0.103	118.46	156.23	142.08	186.71
0.60	0.017492	0.061	0.122	136.67	182.86	172.67	194.70
0.70	0.019740	0.070	0.134	148.01	203.68	194.01	199.58
0.80	0.020504	0.074	0.139	151.69	216.24	208.33	204.30
0.90	0.020883	0.076	0.141	169.66	225.28	220.40	208.97
1.00	0.022037	0.080	0.147	185.47	232.58	233.24	213.07
1.10	0.024443	0.084	0.156	207.83	241.79	245.75	**224.62**
1.20	0.028295	0.088	0.170	226.34	249.55	256.04	**237.79**
1.30	0.032771	0.093	0.189	251.24	254.72	262.29	**248.54**
1.40	**0.037165**	0.102	0.207	280.03	258.43	266.30	**254.93**
1.50	**0.041164**	0.110	0.224	304.43	260.46	268.91	**263.00**

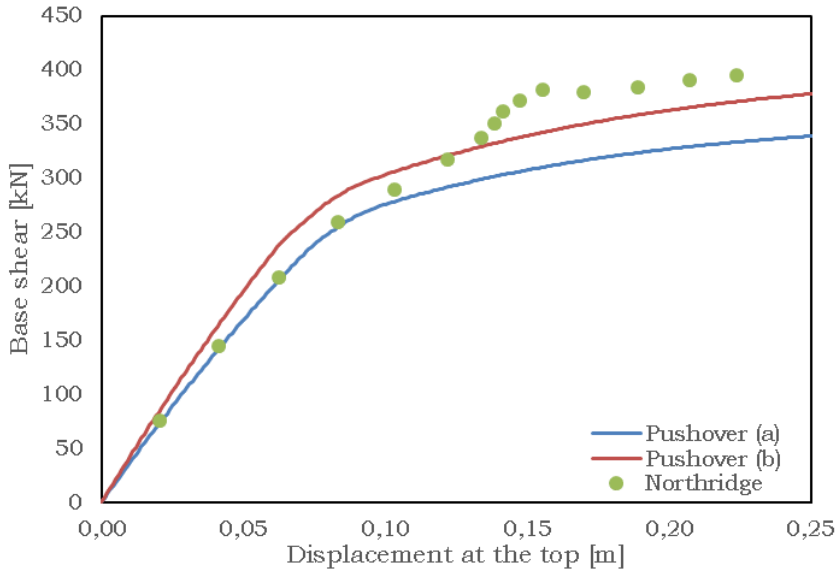

Fig. 5.132 – Base shear vs displacement at the top – NORTHRIDGE RBS

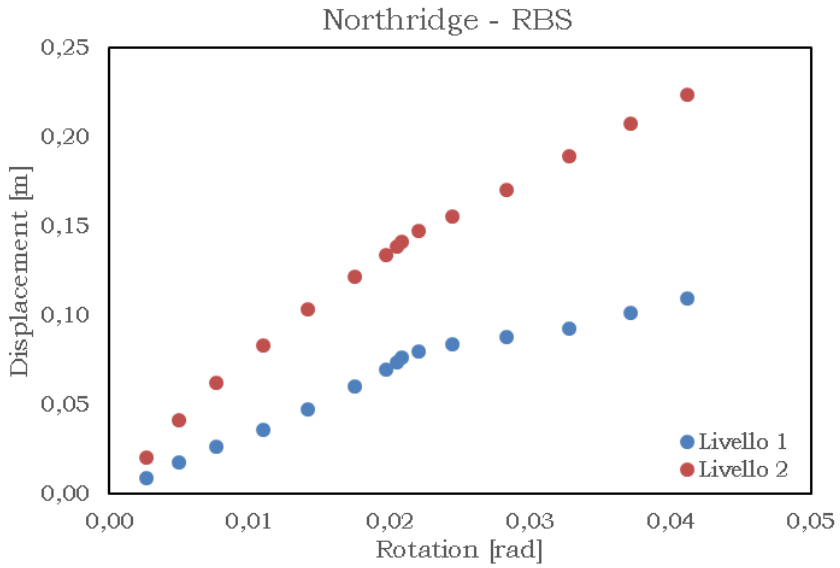

Fig. 5.133 – Displacement vs rotation – NORTHRIDGE RBS

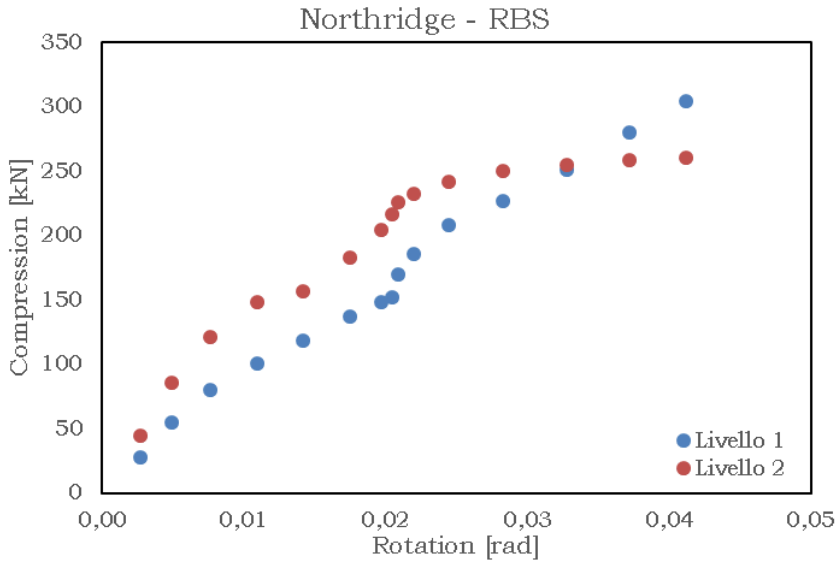

Fig. 5.134 – Compression vs rotation – NORTHRIDGE RBS

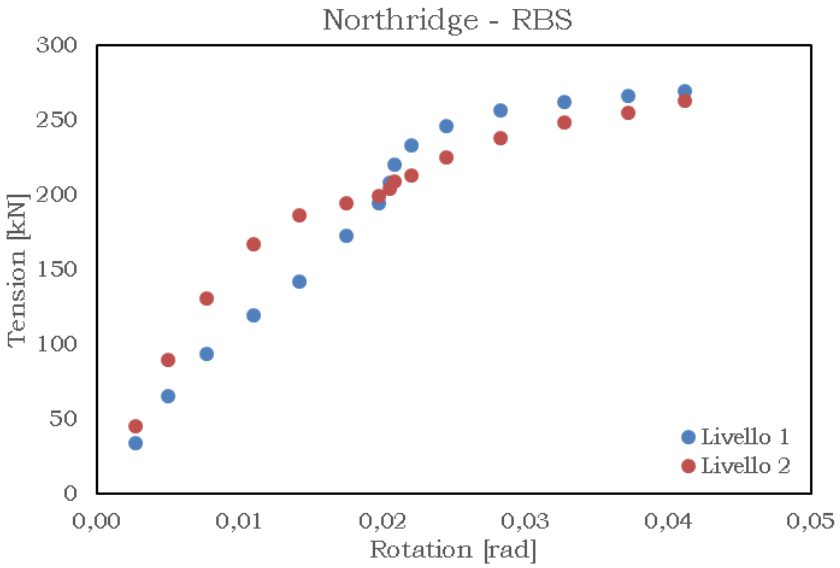

Fig. 5.135 – Tension vs rotation – NORTHRIDGE RBS

Santa Barbara

FREEDAM – Maximum friction coefficient

Table 5.50 – FREEDAM - Maximum friction coefficient – SANTA BARBARA

PGA [g]	***Rotation [rad]***	***Displacement (m)***		***Compression [kN]***		***Tension [kN]***	
		Lev. 1	***Lev. 2***	***Lev. 1***	***Lev. 2***	***Lev. 1***	***Lev. 2***
0.10	0.000	0.003	0.008	16.37	25.46	19.77	26.07
0.20	0.000372	0.007	0.016	32.74	50.92	39.54	52.15
0.30	0.000515	0.010	0.024	49.10	76.44	59.31	78.24
0.40	0.000655	0.014	0.031	65.47	102.14	79.09	104.40
0.50	0.000796	0.017	0.039	81.82	127.97	98.89	130.57
0.60	0.000937	0.021	0.047	98.17	153.78	118.66	156.67
0.70	0.007922	0.024	0.055	114.51	156.21	138.36	176.32
0.80	0.011908	0.028	0.063	130.97	169.69	157.97	185.83
0.90	0.013459	0.031	0.072	147.13	169.80	177.45	192.22
1.00	0.013746	0.032	0.075	163.35	184.58	191.66	204.13
1.10	0.012937	0.033	0.076	182.41	184.19	200.63	210.78
1.20	0.013960	0.038	0.082	194.64	200.36	211.37	216.43
1.30	0.015432	0.041	0.089	211.22	215.65	207.37	200.82
1.40	0.016518	0.044	0.093	274.45	222.45	204.11	208.53
1.50	0.017867	0.048	0.099	297.31	226.71	228.82	**215.44**
1.60	0.022186	0.056	0.119	323.52	203.28	261.67	**228.29**
1.70	0.028403	0.070	0.147	**344.07**	207.95	284.64	**235.37**
1.80	**0.035189**	0.085	0.176	**368.24**	223.72	312.18	**242.91**

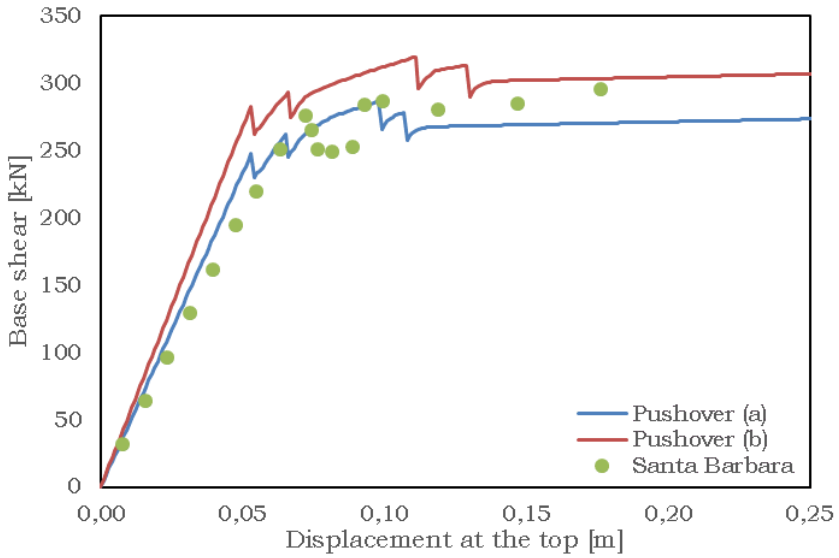

Fig. 5.136 – Base shear vs Displacement at the top – SANTA BARBARA Max friction

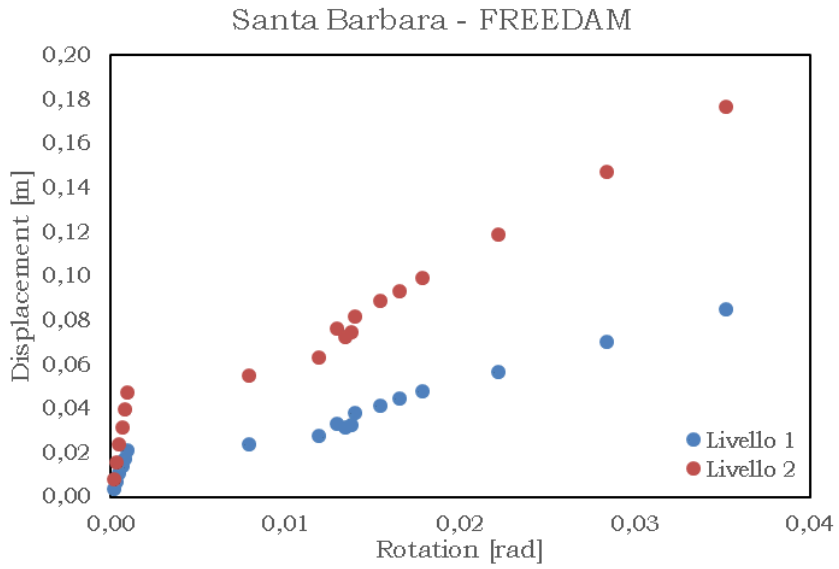

Fig. 5.137 – Displacement vs rotation – SANTA BARBARA Max friction

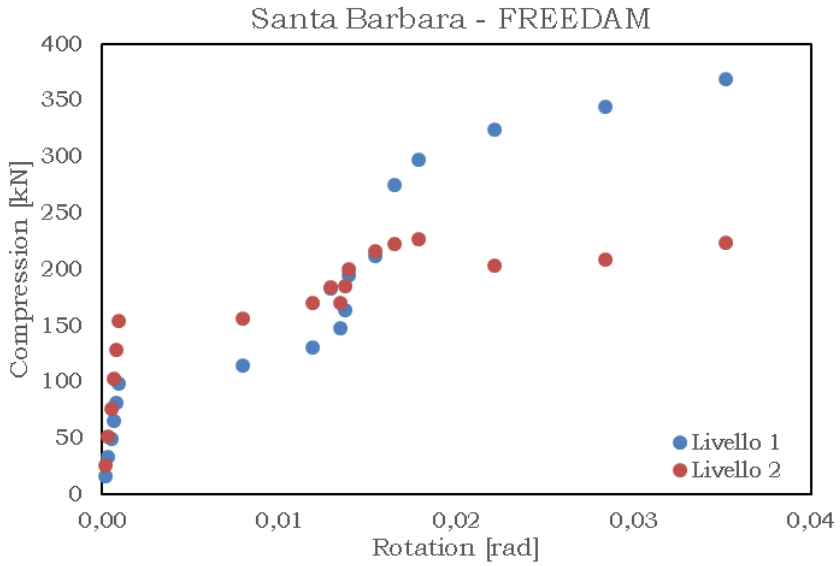

Fig. 5.138 – Compression vs rotation – SANTA BARBARA Max friction

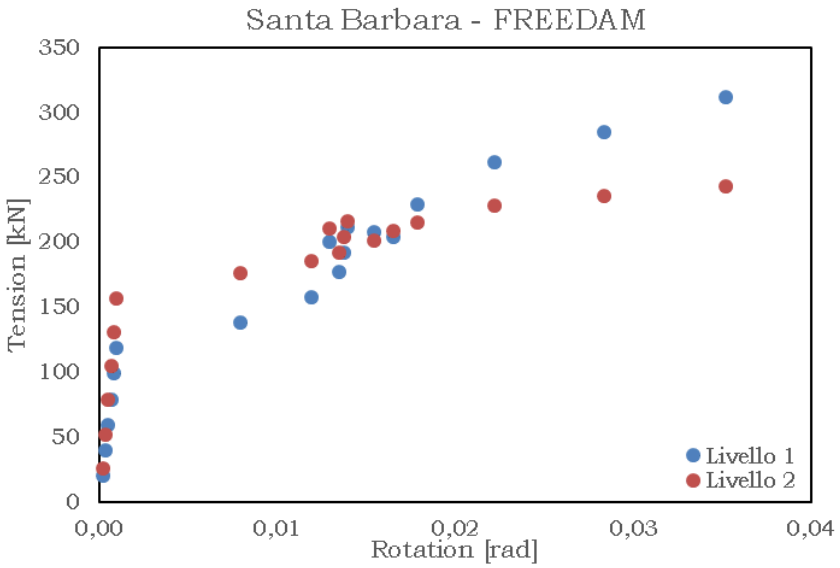

Fig. 5.139 – Tension vs rotation – SANTA BARBARA Max friction

FREEDAM – Minimum friction coefficient

Table 5.51 – FREEDAM - Minimum friction coefficient - SANTA BARBARA

PGA [g]	***Rotation [rad]***	***Displacement (m)***		***Compression [kN]***		***Tension [kN]***	
		Lev. 1	***Lev. 2***	***Lev. 1***	***Lev. 2***	***Lev. 1***	***Lev. 2***
0.10	0.00	0.003	0.008	16.37	25.46	19.77	26.07
0.20	0.000372	0.007	0.016	32.74	50.92	39.54	52.15
0.30	0.000525	0.010	0.024	49.10	76.39	59.31	78.22
0.40	0.000678	0.014	0.031	65.47	101.85	79.08	104.29
0.50	0.000831	0.017	0.039	81.83	127.32	98.84	130.35
0.60	0.000984	0.021	0.047	98.20	152.78	118.60	156.41
0.70	0.012104	0.024	0.056	114.56	142.84	138.34	159.44
0.80	0.014875	0.028	0.064	134.16	153.46	158.01	178.53
0.90	0.015476	0.032	0.074	147.25	169.85	177.57	181.08
1.00	0.012672	0.031	0.067	161.45	163.24	172.22	181.67
1.10	0.014014	0.033	0.073	176.31	180.50	184.79	192.65
1.20	0.015560	0.035	0.080	220.90	195.46	172.98	185.99
1.30	0.018344	0.039	0.093	279.66	187.55	233.94	192.98
1.40	0.023257	0.048	0.115	307.46	183.70	268.71	204.38
1.50	0.027739	0.058	0.135	**327.62**	200.56	290.14	208.30
1.60	0.032087	0.067	0.155	**347.55**	211.31	309.45	212.99
1.70	**0.037195**	0.078	0.178	**364.94**	227.19	**326.31**	214.50
1.80	**0.044736**	0.094	0.212	**375.81**	233.49	**341.60**	219.29

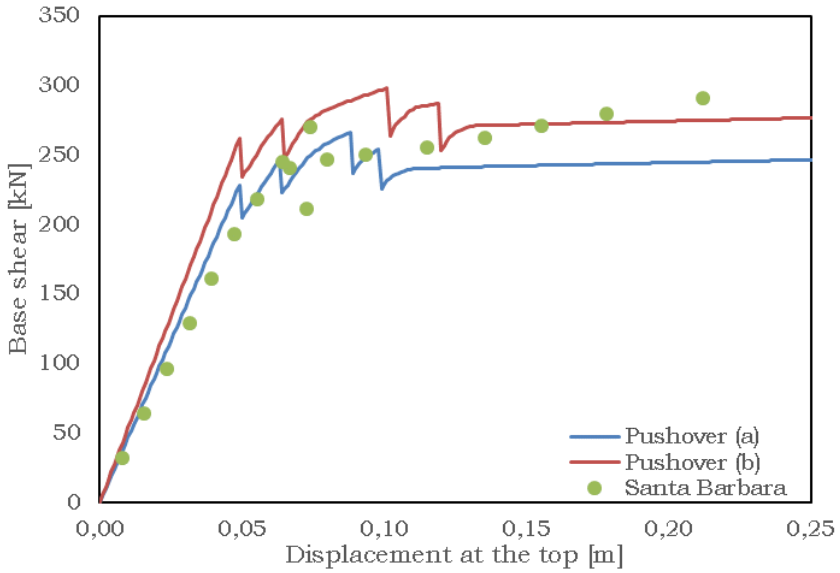

Fig. 5.140 – Base shear vs Displacement at the top – SANTA BARBARA min friction

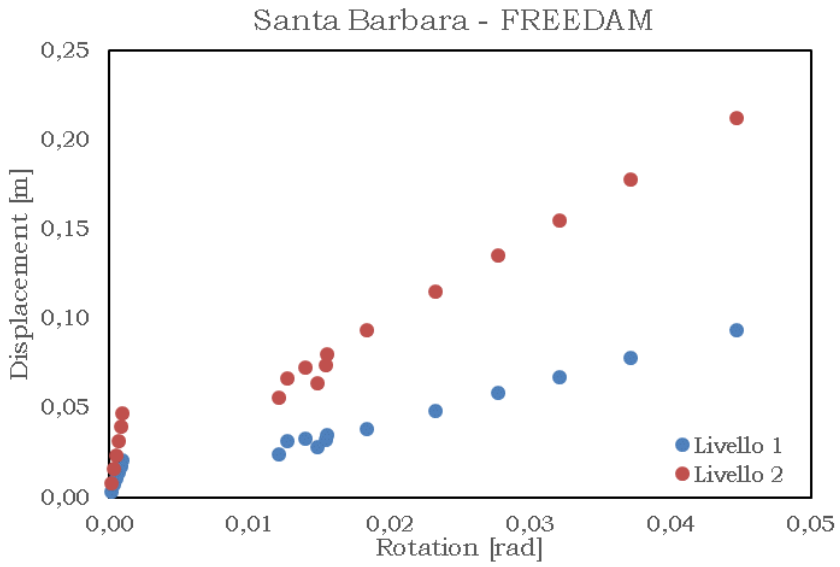

Fig. 5.141 – Displacement vs rotation – SANTA BARBARA min friction

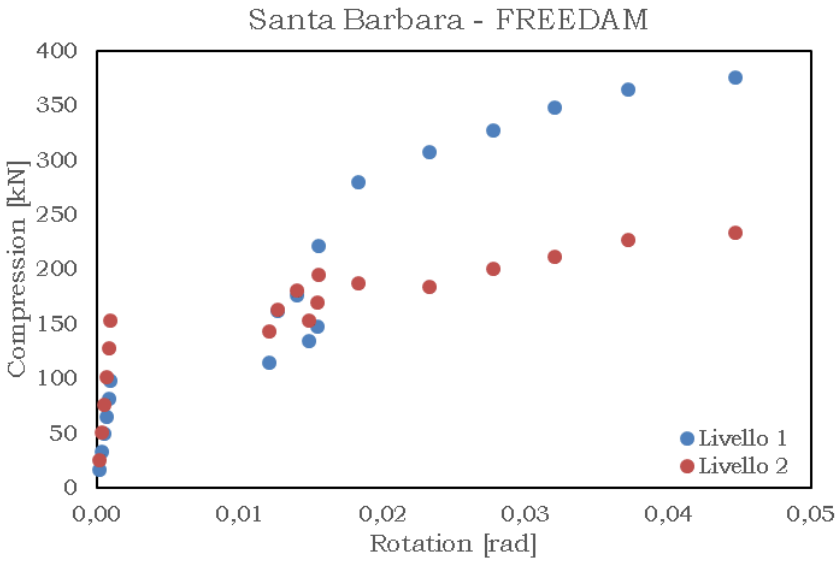

Fig. 5.142 – Compression vs rotation – SANTA BARBARA min friction

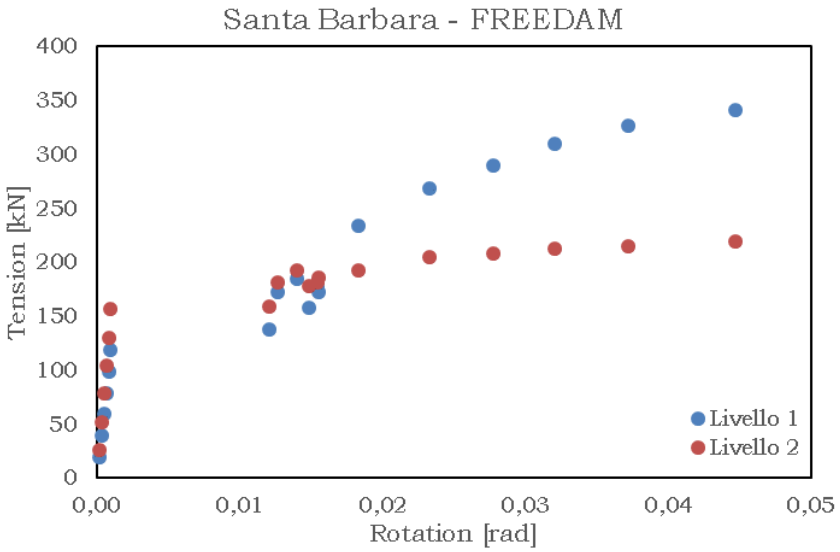

Fig. 5.143 – Tension vs rotation – SANTA BARBARA min friction

EEP-DB-CYC 03

Table 5.52 – RBS – SANTA BARBARA

PGA [g]	***Rotation [rad]***	***Displacement (m)***		***Compression [kN]***		***Tension [kN]***	
		Lev. 1	***Lev. 2***	***Lev. 1***	***Lev. 2***	***Lev. 1***	***Lev. 2***
0.10	0.002	0.005	0.011	22.64	23.97	19.41	25.24
0.20	0.002632	0.010	0.022	45.56	47.27	38.93	50.03
0.30	0.003651	0.014	0.032	68.59	69.77	58.49	74.31
0.40	0.004758	0.019	0.043	91.71	91.52	78.07	98.01
0.50	0.006005	0.024	0.053	114.77	112.06	97.65	121.03
0.60	0.007432	0.028	0.064	137.63	131.56	117.18	143.83
0.70	0.008936	0.032	0.074	160.18	149.91	136.63	165.89
0.80	0.010408	0.037	0.083	182.28	165.18	156.01	187.03
0.90	0.011382	0.040	0.089	204.60	174.48	175.24	207.09
1.00	0.012801	0.043	0.093	223.81	178.22	194.31	**225.93**
1.10	0.013879	0.045	0.098	231.03	194.80	212.99	**242.23**
1.20	0.014391	0.048	0.104	230.92	208.54	227.61	**251.59**
1.30	0.014855	0.051	0.108	228.60	216.69	233.30	**254.90**
1.40	0.016194	0.054	0.114	228.28	220.55	232.77	**255.69**
1.50	0.019063	0.062	0.128	230.04	222.29	229.65	**255.66**
1.60	0.022646	0.072	0.144	233.13	222.55	231.58	**255.92**
1.70	0.027086	0.082	0.164	237.72	228.25	242.13	**257.15**
1.80	0.032859	0.095	0.189	243.56	237.10	252.50	**259.00**
1.90	**0.039849**	0.111	0.219	250.28	245.40	262.82	**261.68**

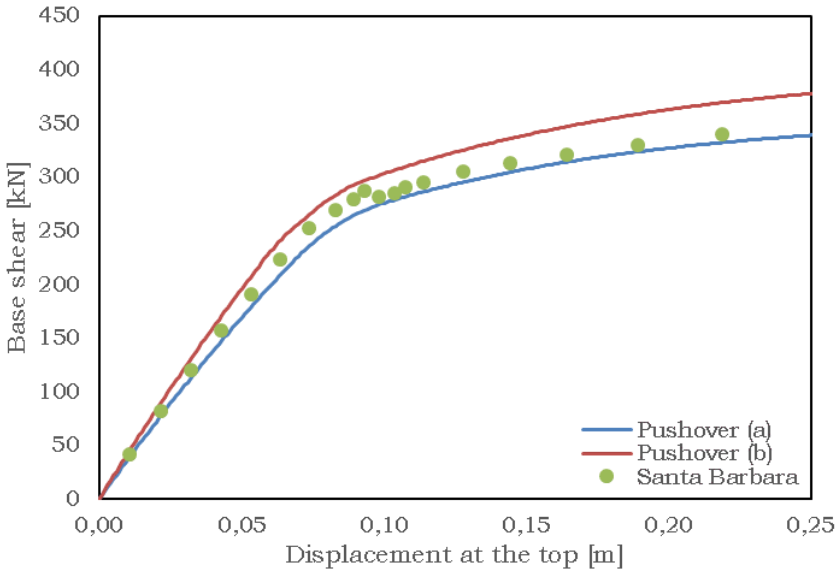

Fig. 5.144 – Base shear vs displacement at the top – SANTA BARBARA RBS

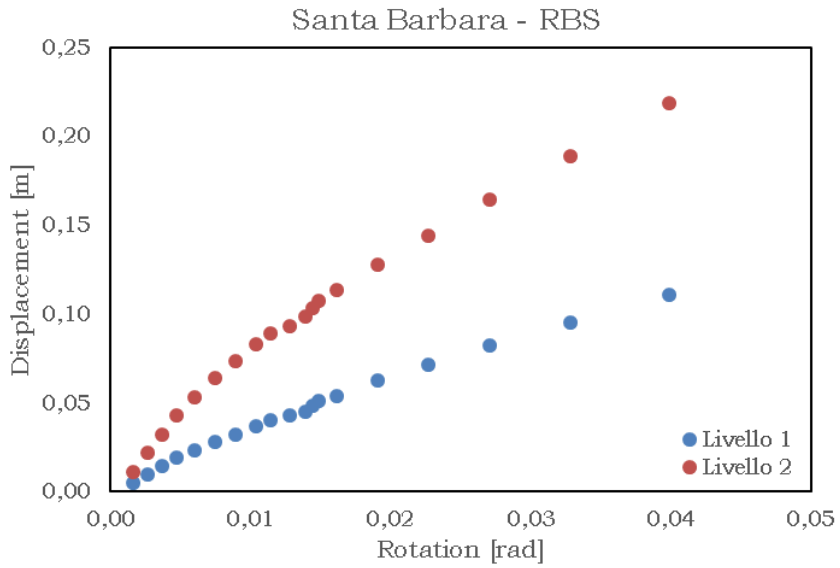

Fig. 5.145 – Displacement vs rotation – SANTA BARBARA RBS

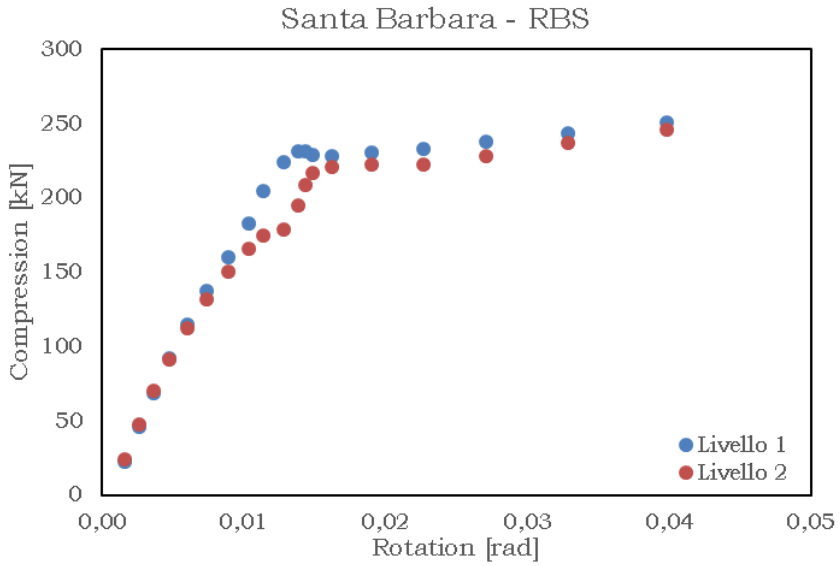

Fig. 5.146 – Compression vs rotation – SANTA BARBARA RBS

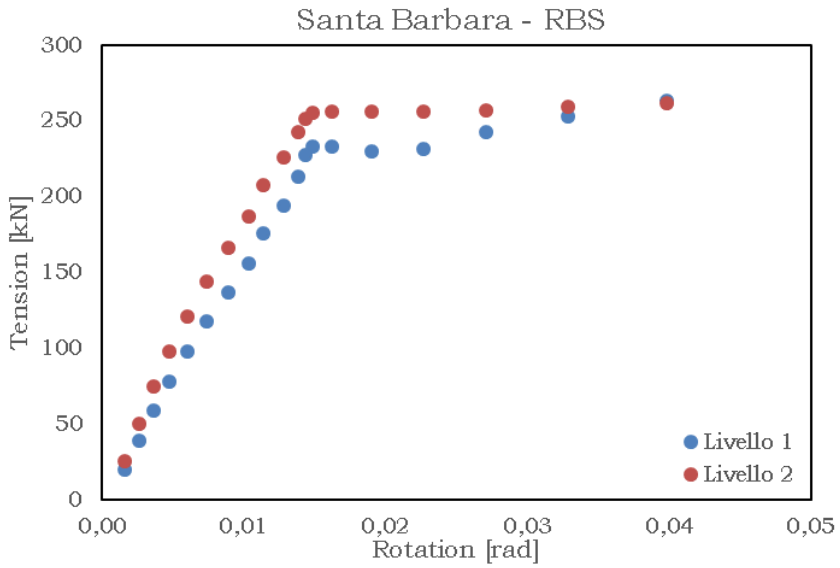

Fig. 5.147 – Tension vs rotation – SANTA BARBARA RBS

Spitak

FREEDAM – Maximum friction coefficient

Table 5.53 – FREEDAM - Maximum friction coefficient - SPITAK

PGA	***Rotation***	***Displacement***		***Compression***		***Tension***	
[g]	***[rad]***	***(m)***		***[kN]***		***[kN]***	
		Lev. 1	***Lev. 2***	***Lev. 1***	***Lev. 2***	***Lev. 1***	***Lev. 2***
0.10	0.000	0.006	0.012	25.26	32.36	15.08	19.60
0.20	0.000518	0.011	0.024	50.52	64.73	30.17	39.20
0.30	0.000728	0.017	0.035	75.81	97.15	45.37	58.82
0.40	0.000938	0.022	0.047	101.10	129.52	60.64	78.63
0.50	0.010445	0.028	0.059	126.20	141.86	66.80	96.16
0.60	0.013614	0.035	0.073	145.86	159.65	79.84	104.90
0.70	0.015886	0.044	0.089	155.35	169.39	95.25	121.77
0.80	0.019499	0.055	0.108	165.13	170.61	130.72	138.57
0.90	0.025058	0.067	0.134	184.52	169.95	148.75	142.53
0.95	0.028646	0.072	0.153	206.03	181.12	171.78	154.19
1.00	0.029157	0.073	0.155	199.80	181.66	167.41	152.42
1.10	**0.035060**	0.083	0.183	215.70	188.30	180.30	168.08

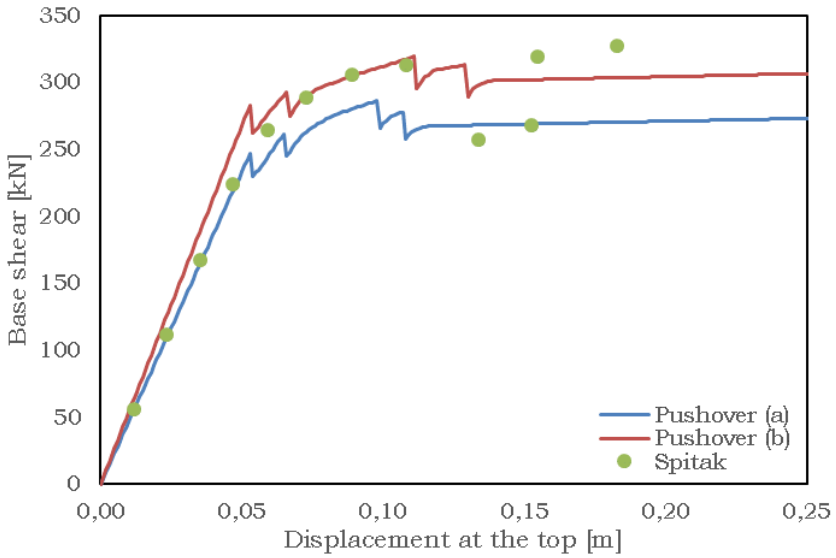

Fig. 5.148 – Base shear vs Displacement at the top – SPITAK Max friction

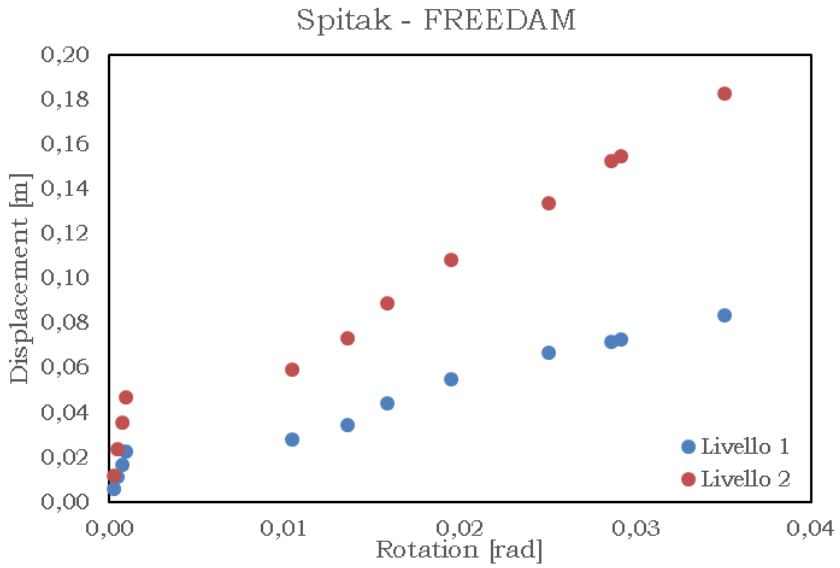

Fig. 5.149 – Displacement vs rotation – SPITAK Max friction

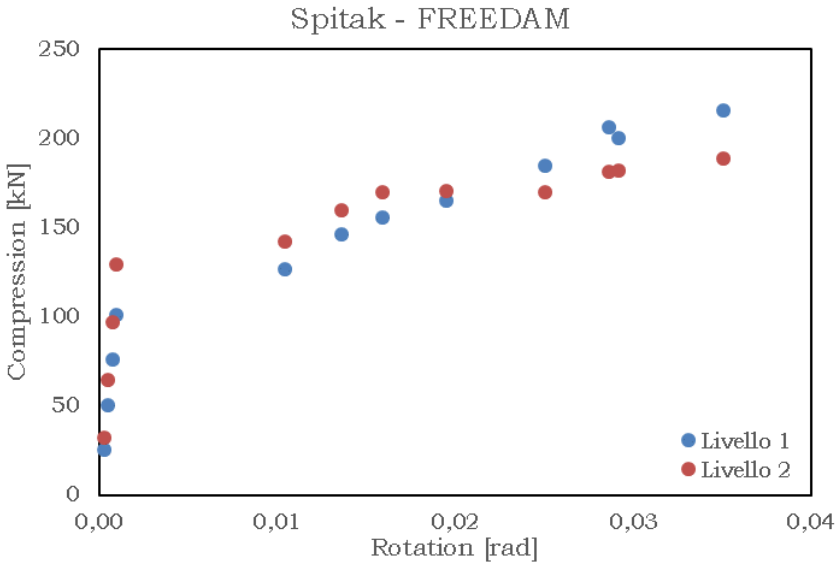

Fig. 5.150 – Compression vs rotation – SPITAK Max friction

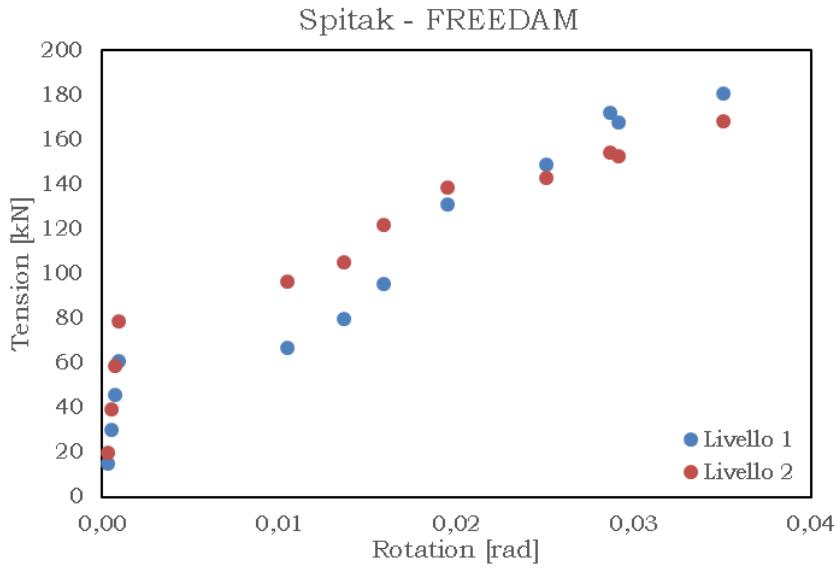

Fig. 5.151 – Tension vs rotation – SPITAK Max friction

FREEDAM – Minimum friction coefficient

Table 5.54 – FREEDAM - Minimum friction coefficient - SPITAK

PGA [g]	***Rotation [rad]***	***Displacement (m)***		***Compression [kN]***		***Tension [kN]***	
		Lev. 1	***Lev. 2***	***Lev. 1***	***Lev. 2***	***Lev. 1***	***Lev. 2***
0.10	0.00	0.006	0.012	25.26	32.36	15.08	19.60
0.20	0.000529	0.011	0.024	50.51	64.71	30.16	39.21
0.30	0.000761	0.017	0.035	75.78	97.07	45.24	58.82
0.40	0.000992	0.022	0.047	101.04	129.42	60.32	78.44
0.50	0.013031	0.029	0.061	122.35	141.90	66.78	93.23
0.60	0.015439	0.036	0.077	139.45	155.67	94.08	104.61
0.70	0.018904	0.045	0.095	150.69	157.59	124.84	109.34
0.80	0.024292	0.055	0.120	164.52	158.89	145.10	123.05
0.90	0.028611	0.060	0.141	189.91	167.62	165.20	146.41
0.95	0.032112	0.066	0.156	182.45	167.49	157.99	153.03
1.00	**0.035499**	0.074	0.170	185.95	168.53	169.14	156.73
1.10	**0.044628**	0.099	0.212	189.49	168.09	203.49	157.56

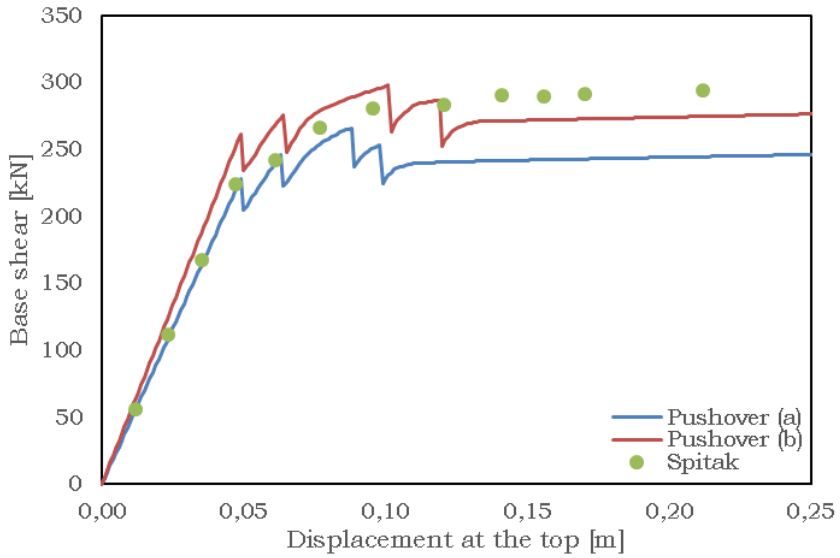

Fig. 5.152 – Base shear vs Displacement at the top – SPITAK min friction

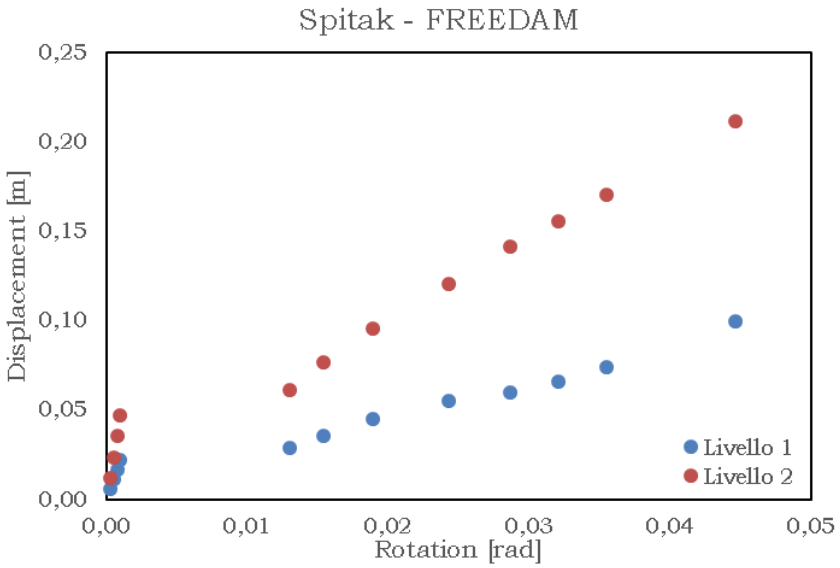

Fig. 5.153 – Load distribution on the frame for the pushover analysis

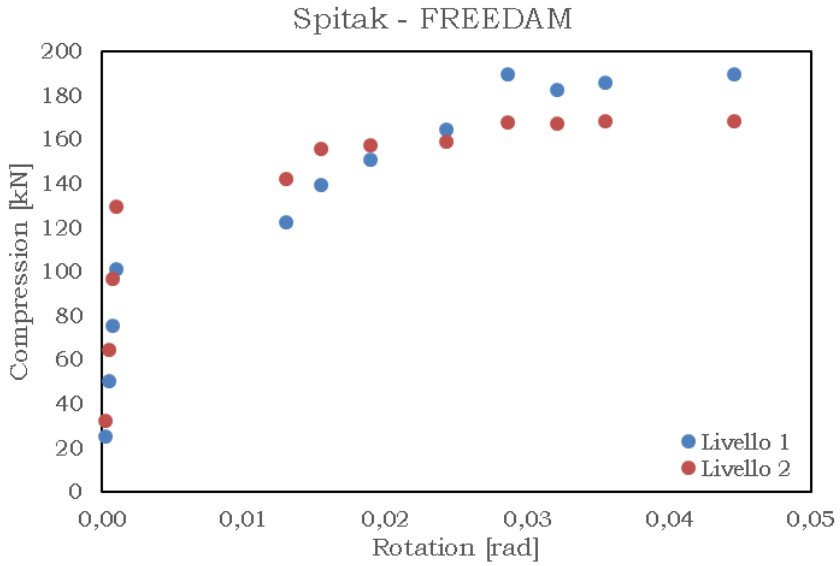

Fig. 5.154 – Load distribution on the frame for the pushover analysis

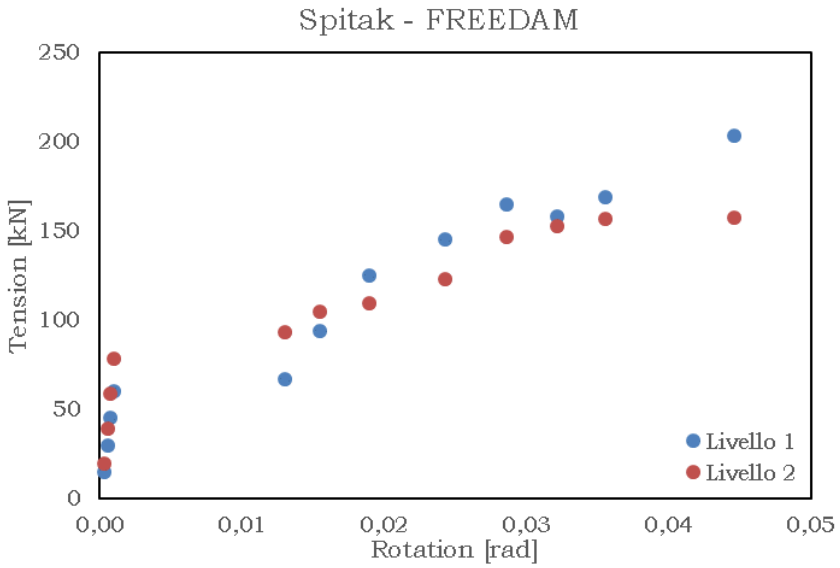

Fig. 5.155 – Load distribution on the frame for the pushover analysis

Table 5.55 – RBS - SPITAK

PGA [g]	***Rotation [rad]***	***Displacement (m)***		***Compression [kN]***		***Tension [kN]***	
		Lev. 1	***Lev. 2***	***Lev. 1***	***Lev. 2***	***Lev. 1***	***Lev. 2***
0.10	0.002	0.006	0.014	21.17	31.86	18.56	21.19
0.20	0.003320	0.012	0.028	41.95	62.72	38.10	41.48
0.30	0.004990	0.018	0.042	62.42	92.54	58.61	61.00
0.40	0.006914	0.024	0.057	82.78	121.14	80.49	79.79
0.50	0.009184	0.030	0.071	102.99	148.21	103.69	97.51
0.60	0.011706	0.037	0.086	123.20	173.24	132.64	115.04
0.70	0.014243	0.046	0.101	155.60	189.38	172.95	131.87
0.80	0.017325	0.057	0.117	180.99	197.16	196.18	145.69
0.90	0.020452	0.069	0.135	194.96	201.71	218.31	166.07
1.00	0.024485	0.081	0.155	200.30	204.17	239.57	191.55
1.10	0.029404	0.094	0.177	201.63	205.18	257.22	211.36
1.20	0.035173	0.108	0.202	202.19	205.25	273.51	227.81
1.30	**0.041634**	0.121	0.229	206.37	205.16	291.56	**240.48**

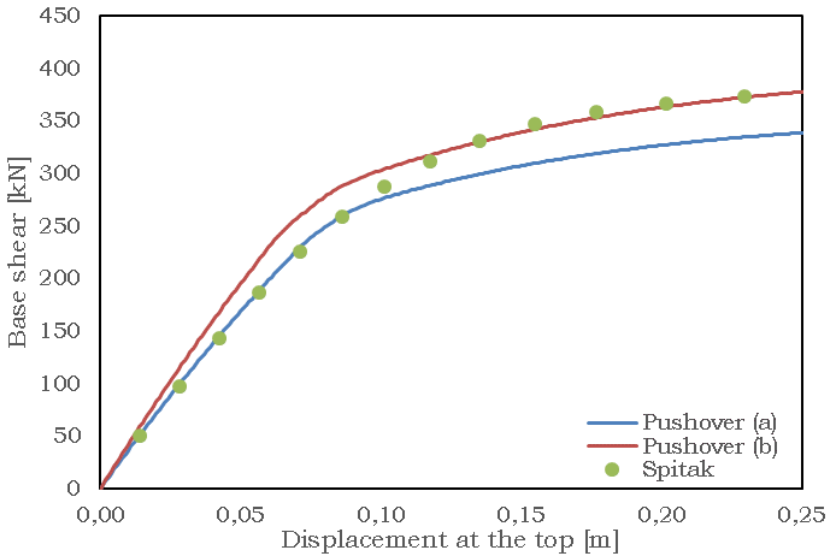

Fig. 5.156 – Base shear vs displacement at the top – SPITAK RBS

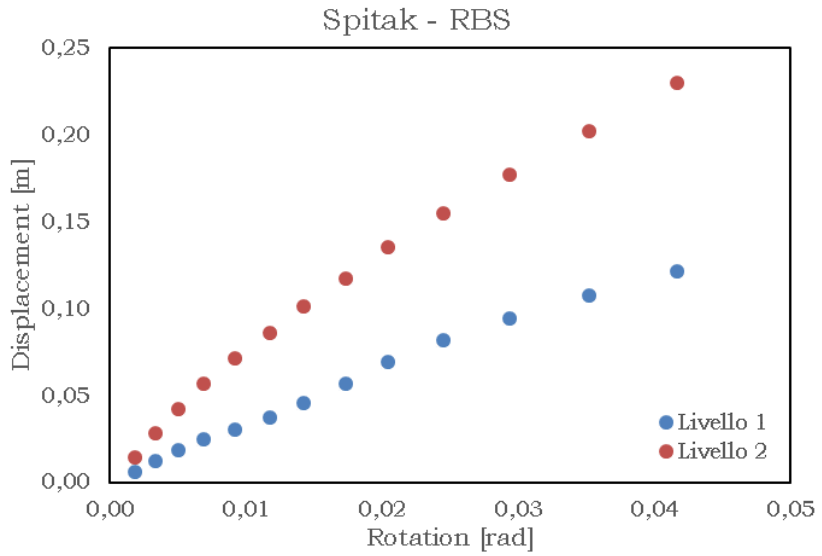

Fig. 5.157 – Displacement vs rotation – SPITAK RBS

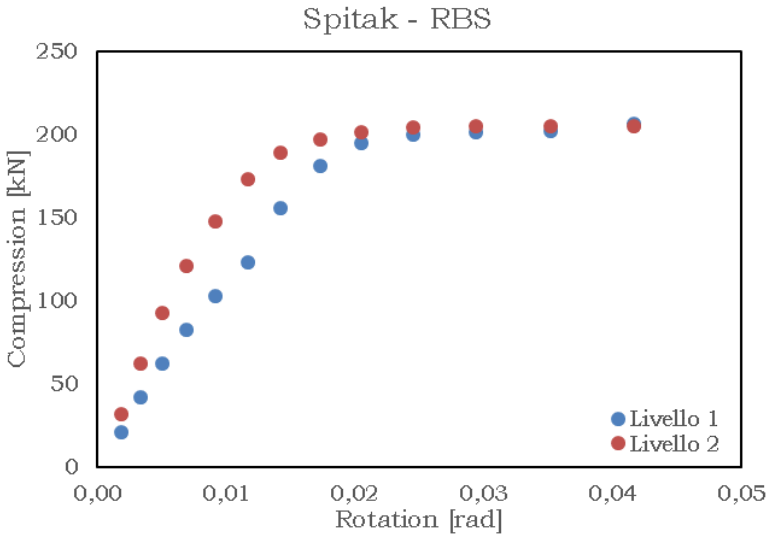

Fig. 5.158 – Compression vs rotation – SPITAK RBS

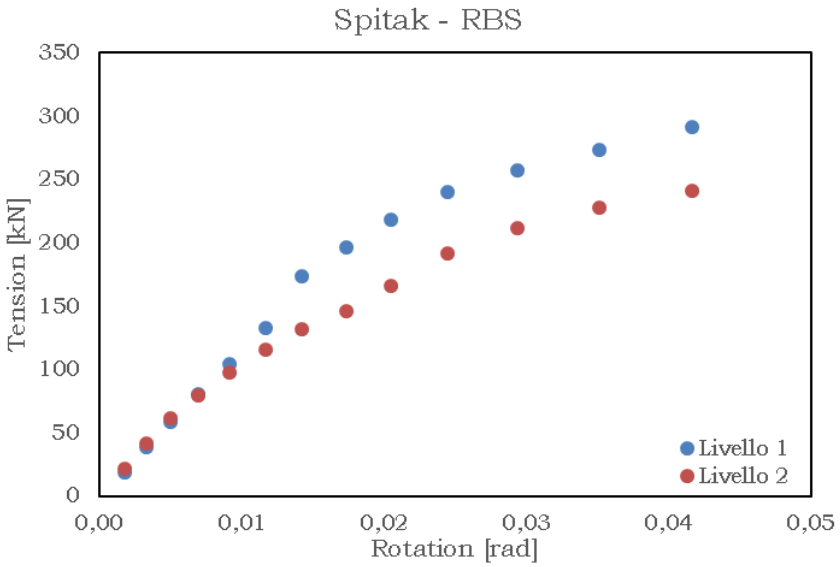

Fig. 5.159 – Tension vs rotation – SPITAK RBS

5.4.7. Remarks

It is possible to observe that the natural periods of vibration decrease from the RBS to the FREEDAM connection due to the greater stiffness that the latter provides to the structure.

The pushover curves of the RBS connection have a monotonous behavior, while those of the FREEDAM connection have discontinuities in numbers equal to the number of link elements: this behavior is due to the type of hysteretic curve adopted for the FREEDAM connection.

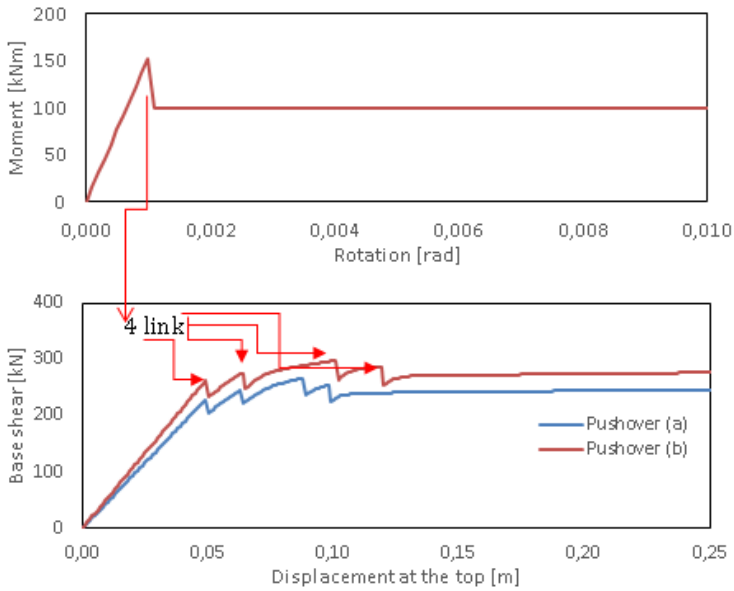

Fig. 5.160 – Consequences of the use of link elements for modelling FREEDAM connections on pushover curves

From the comparison of the pushover curves for the two types of connections it is possible to observe the truthfulness of the hypothesis made regarding the greater rigidity of the FREEDAM node system with respect to the RBS connection.

It is specified that for the FREEDAM connection in the design phase the static resistance has been overestimated by 50% compared to the dynamics, while from the simulations an overestimation of 10% is observed; on the basis of this attenuation effect it is possible to hypothesize to model the link elements only on the basis of the dynamic resistance without significant changes in terms of results.

Diagramming the shear at the base versus the displacement at the top of the incremental dynamic analysis, it is possible to observe the similarity with the pushover curves.

Because of the type of hysteretic curve chosen for the FREEDAM connection it is possible to observe that in the displacement-rotation diagrams, compression-rotation force, tension-rotation there are two traits: the first in which the behavior is elastic and the second plastic.

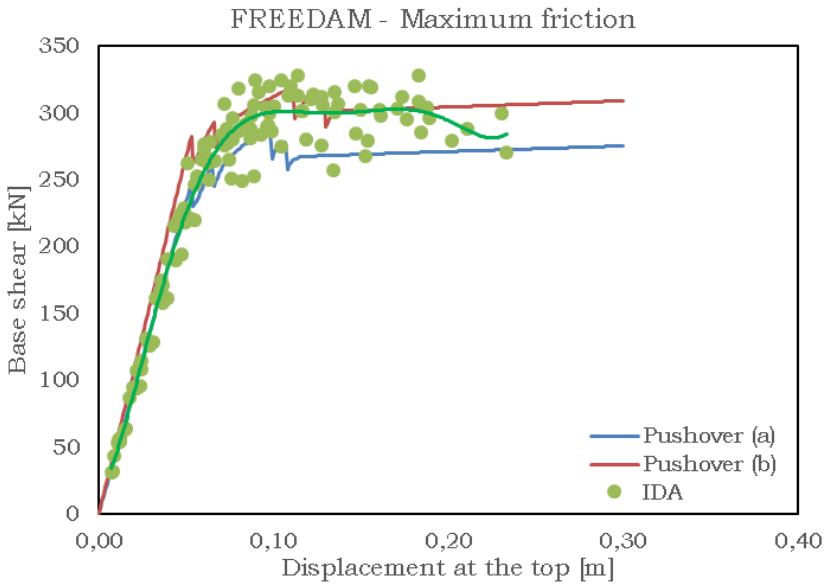

Fig. 5.161 – Base shear vs displacement – FREEDAM Max. friction

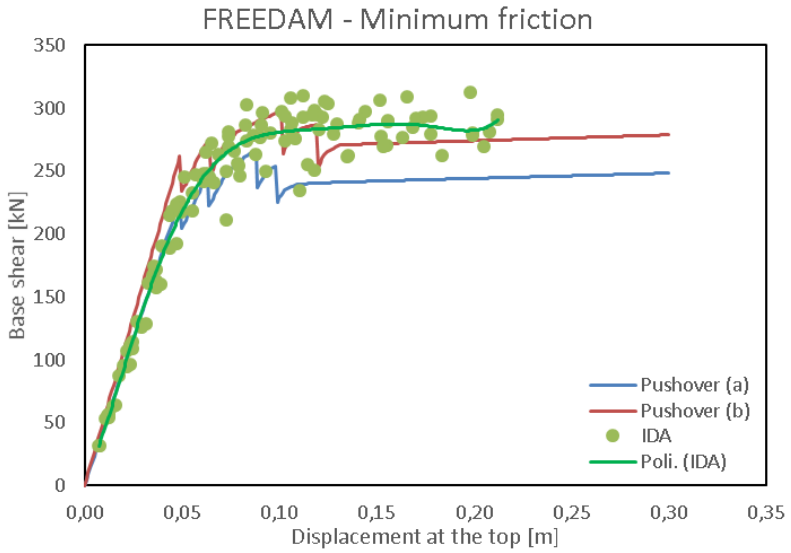

Fig. 5.162 – Base shear vs displacement – FREEDAM min friction

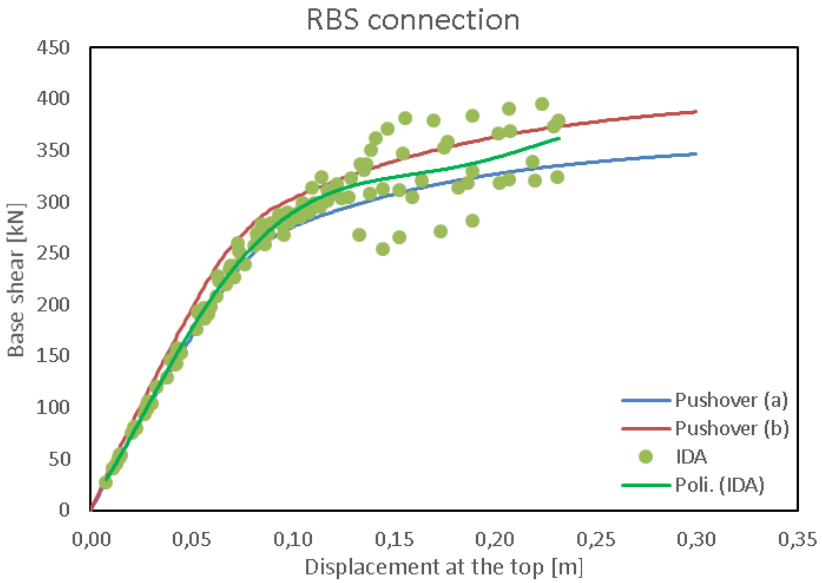

Fig. 5.163 – Base shear vs displacement - RBS

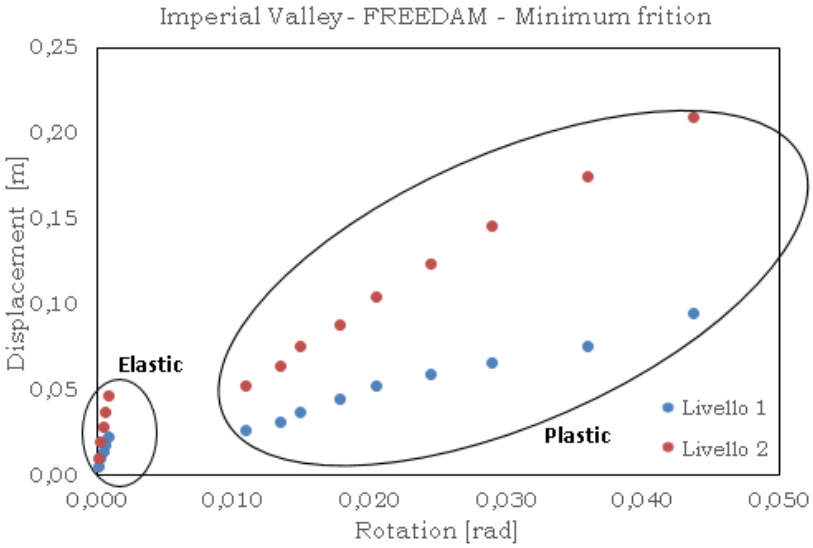

Fig. 5.164 – Displacement vs rotation – FREEDAM min friction

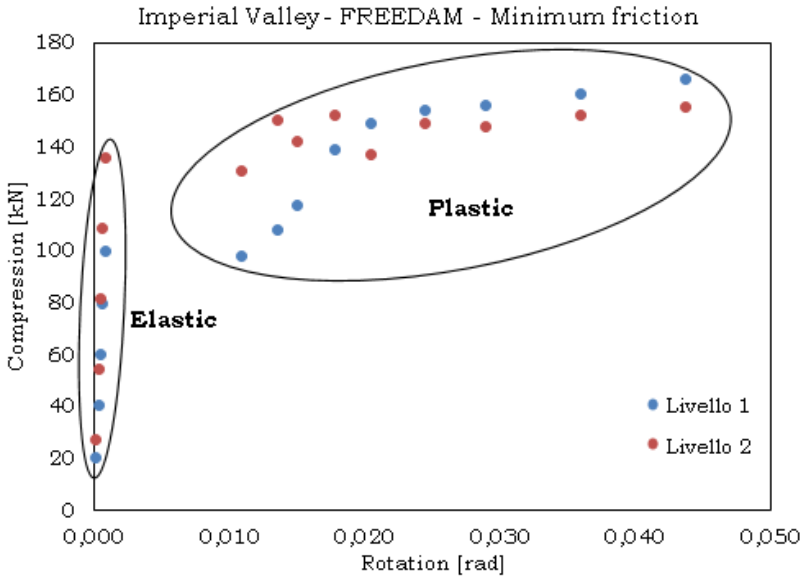

Fig. 5.165 – Compression vs rotation – FREEDAM min friction

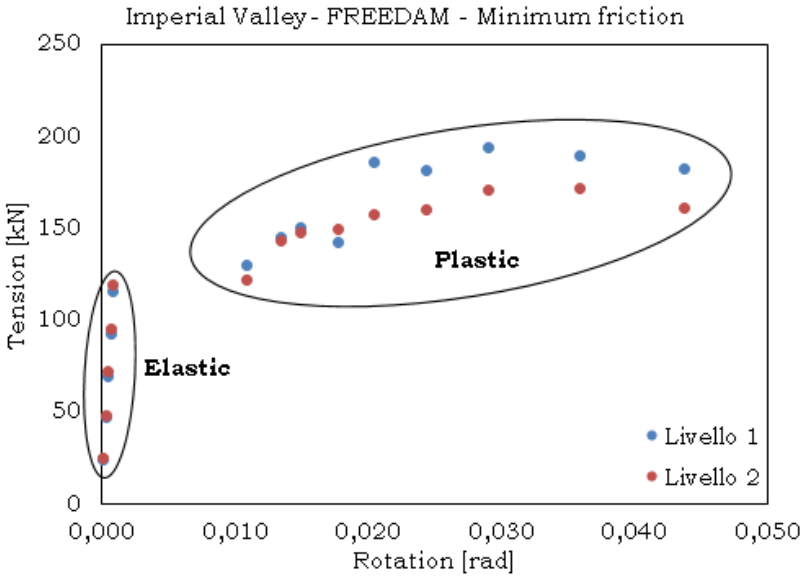

Fig. 5.166 – Tension vs rotation – FREEDAM min friction

By way of example, the differences observed between the RBS connection and the FREEDAM connection with minimum friction are shown for all the accelerograms.

It is possible to observe differences in terms of base shear of about $100kN$ in favor of the RBS connection for the following accelerograms:

- Coalinga;
- Northridge;
- Spitak.

For Santa Barbara this difference decreases to $20kN$, while for the other accelerograms there are no significant differences.

Between the two types of connections there are no significant differences in terms of displacements.

The following are the differences in terms of compressive forces, which the actuators must provide, for the two types of connections.

- Coalinga: +50kN - RBS connection.
- Helena: +150kN - RBS connection.
- Imperial Valley: +40kN - RBS connection.
- Kobe: +50kN - RBS connection.
- Landers: +50kN - RBS connection.
- Northridge: +100kN - RBS connection.
- Santa Barbara: +100kN - FREEDAM connection.
- Spitak: there are no significant differences.
- Artificial accelerogram: there are no significant differences.

The following are the differences in terms of tension forces, which the actuators must provide, for the two types of connections.

- Coalinga: +50kN - RBS connection.
- Helena: +200kN - RBS connection.
- Imperial Valley: +50kN - RBS connection.
- Kobe: +50kN - RBS connection.
- Landers: +50kN - RBS connection.
- Northridge: there are no significant differences.
- Santa Barbara: +100kN - FREEDAM connection.
- Spitak: +100kN - RBS connection.
- Artificial accelerogram: +50kN - FREEDAM connection.

Starting from Table 5.56 to Table 5.58, a summary of the results has been reported:

Table 5.56 – FREEDAM Maximum friction - summary

	PGA [g]	***Rotation [rad]***	***Displacement [m]***		***Compression [kN]***		***Tension [kN]***	
			Level 1	***Level 2***	***Level 1***	***Level 2***	***Level 1***	***Level 2***
Coalinga	*0.90*	*0.0287*	*0.070*	*0.150*	*171.48*	*193.08*	*127.31*	*138.89*
Helena	*2.00*	*0.0242*	*0.056*	*0.128*	***459.69***	*261.77*	***372.28***	***247.70***
Imperial Valley	*1.30*	*0.0315*	*0.080*	*0.162*	*166.97*	*172.17*	*202.85*	*185.56*
Kobe	*1.30*	*0.0297*	*0.075*	*0.156*	*283.46*	*232.75*	*319.47*	*207.64*
Landers	*1.00*	*0.0300*	*0.072*	*0.154*	*164.11*	*209.85*	*152.69*	*186.85*
Northridge	*1.00*	*0.0313*	*0.074*	*0.160*	*196.97*	*200.15*	*177.33*	*176.92*
Santa Barbara	*1.70*	*0.0284*	*0.070*	*0.147*	***344.07***	*207.95*	*284.64*	***235.37***
Spitak	*1.00*	*0.0291*	*0.073*	*0.155*	*199.80*	*181.66*	*167.41*	*152.42*

Table 5.57 – FREEDAM Minimum friction - summary

	PGA [g]	***Rotation [rad]***	***Displacement [m]***		***Compression [kN]***		***Tension [kN]***	
			Level 1	***Level 2***	***Level 1***	***Level 2***	***Level 1***	***Level 2***
Coalinga	*0.85*	*0.0314*	*0.064*	*0.152*	*161.31*	*169.69*	*120.21*	*122.23*
Helena	*2.00*	*0.0271*	*0.046*	*0.123*	***483.68***	*235.59*	***386.74***	*218.86*
Imperial Valley	*1.20*	*0.0291*	*0.064*	*0.144*	*155.22*	*147.15*	*193.13*	*169.46*
Kobe	*1.20*	*0.0319*	*0.066*	*0.156*	*255.60*	*203.96*	*294.96*	*174.87*
Landers	*1.10*	*0.0315*	*0.066*	*0.153*	*181.59*	*192.25*	*167.77*	*191.99*
Northridge	*1.00*	*0.0314*	*0.065*	*0.152*	*192.86*	*187.06*	*239.49*	*187.46*
Santa Barbara	*1.60*	*0.0320*	*0.067*	*0.155*	***347.55***	*211.31*	*309.45*	*212.99*
Spitak	*0.95*	*0.0321*	*0.066*	*0.156*	*182.45*	*167.49*	*157.99*	*153.03*

Table 5.58 – RBS - summary

	PGA [g]	Rotation [rad]	Displacement [m]		Compression [kN]		Tension [kN]	
			Level 1	Level 2	Level 1	Level 2	Level 1	Level 2
Coalinga	0.90	0.0324	0.092	0.175	206.99	210.08	183.75	154.60
Helena	1.50	0.0150	0.047	0.109	**362.93**	207.34	**382.51**	**246.18**
Imperial Valley	1.40	0.0300	0.088	0.169	179.39	181.16	220.35	198.75
Kobe	1.30	0.0336	0.082	0.182	301.07	242.90	**356.16**	**241.64**
Landers	1.30	0.0322	0.082	0.173	244.47	233.50	232.88	221.67
Northridge	1.30	0.0327	0.093	0.189	251.24	254.72	262.29	**248.54**
Santa Barbara	1.80	0.0328	0.095	0.189	243.56	237.10	252.50	**259.00**
Spitak	1.10	0.0294	0.094	0.177	201.63	205.18	257.22	211.36

5.5. Choice of the accelerogram for the pseudo-dynamic test

The choice of the accelerogram for the pseudo-dynamic test depends mainly on three factors:

- degree of safety against the capacities of the actuators (in fact, if forces greater than the actuators' capacity were required, they would stop working, stopping the test);
- number and width of the expected cycles;
- compatibility of the response spectrum with the reference spectrum proposed by the Eurocode 8 [1] for a type B soil and a peak ground acceleration of *0.35g*.

The first and last of the highlighted aspects have already been dealt with previously, while for the evaluation of the number and width of the cycles the rainflow method is used.

5.5.1. RAINFLOW method

In order to evaluate the number of cycles of the link elements for each type of connection and for each incremental dynamic analysis, the *rainflow* method is adopted.

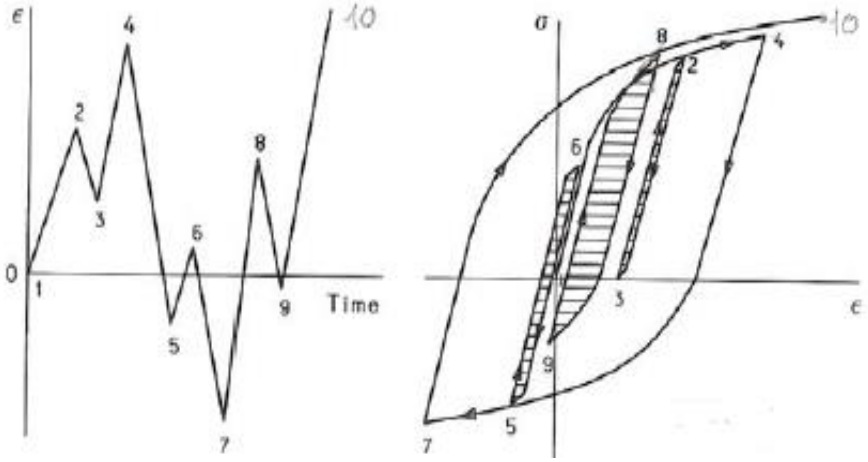

Fig. 5.167 – Deformation vs Time curve and Stress vs strain curve

In this case, the diagram rotation-time has to be considered in order to determine the number of cycles. It is important to modify the diagram rotation-time so as to obtain only the peaks in absolute terms.
The term *rainflow* is due to the fact that the rules that define this method are those that would affect a flow of rain that invests a rotation-time diagram rotated clockwise by *90°*.

The *rainflow* originates from every point of local minimum or maximum and continues in its fall respecting the following three rules:

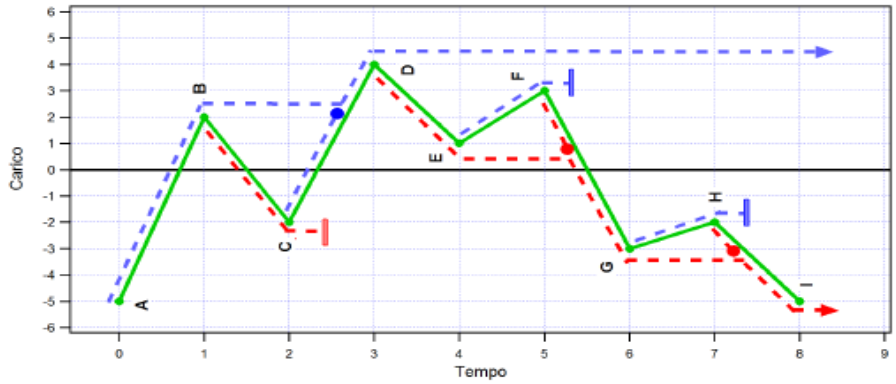

Fig. 5.168 – Rainflow scheme

- starting from a local minimum point, the flow of rain stops when it encounters another local minimum point with ordinate in absolute terms greater than the starting point;
- starting from a local maximum point, the rain flow stops when it encounters another local maximum point with ordinate in absolute terms greater than the original one;
- starting from a minimum or maximum local point, the rain flow stops if it intersects another rain stream with the origin of the same species.

Applying this method to the evaluation of the number and width of the cycles of connections submitted to incremental dynamic tests, it is necessary to specify that the amplitude of the cycle must be understood as half of the amplitudes obtained in the previous example.

For the calculation of the number of cycles of the link elements modeled using the SeismoStruct software, a spreadsheet has been created which,

starting from the hysteretic curve of the link as input, directly provides the number of cycles for each class of defined amplitude and at the same time purifying the rotations of hysteretic curves from elastic contributions. The Table 5.59 shows the results concerning the number of cycles for the different types of connection and the different accelerograms.

The results obtained show that only four accelerograms allow to obtain maximum rotations of at least one link element equal to 30*mrad* without exceeding the capacitances in terms of actuator forces:

- Coalinga;
- Imperial Valley;
- Landers;
- Spitak.

Table 5.59 – FREEDAM Maximum friction – Results

Earthquake	***Amplitude [mrad]***					***Cumulative rotation [mrad]***	***Cumulative displacement [mrad]***
	<3.75	***3.75-7.50***	***7.50-15***	***15-30***	***>30***		
1.Coalinga	*7*	*3*	*1*	*0*	*0*	*42.74*	*18.80*
2.Helena	*22*	*2*	*1*	*1*	*0*	*43.36*	*19.08*
3.Imperial_Valley	*10*	*3*	*3*	*1*	*0*	*66.56*	*29.29*
4.Kobe	*13*	*11*	*4*	*2*	*0*	*152.34*	*67.03*
5.Landers	*30*	*20*	*3*	*1*	*0*	*210.20*	*92.49*
6.Northridge	*10*	*7*	*5*	*2*	*0*	*146.21*	*64.33*
7.Santa_Barbara	*7*	*10*	*8*	*3*	*0*	*206.32*	*90.78*
8.Spitak	*2*	*1*	*3*	*0*	*0*	*39.17*	*17.24*

Table 5.60 – FREEDAM Minimum friction - Results

Earthquake	Amplitude [mrad]					Cumulative rotation [mrad]	Cumulative displacement [mrad]
	<3.75	3.75-7.50	7.50-15	15-30	>30		
1.Coalinga	12	2	2	1	0	66.72	29.36
2.Helena	26	0	2	0	0	30.65	13.48
3.Imperial_Valley	16	4	2	1	0	79.58	35.02
4.Kobe	11	10	5	2	0	169.63	74.64
5.Landers	13	5	4	2	0	107.72	47.40
6.Northridge	13	5	7	3	0	177.21	77.97
7.Santa_Barbara	11	8	10	3	0	230.54	101.44
8.Spitak	0	2	2	1	0	46.05	20.26

Table 5.61 – RBS - Results

Earthquake	Amplitude [mrad]					Cumulative
	<3.75	3.75-7.50	7.50-15	15-30	>30	[mrad]
1.Coalinga	63	7	1	0	0	111.51
2.Helena	11	1	0	0	0	13.74
3.Imperial_Valley	53	6	2	0	0	108.20
4.Kobe	104	7	3	1	0	195.64
5.Landers	111	34	2	2	0	367.91
6.Northridge	57	8	7	2	0	204.00
7.Santa_Barbara	13	12	7	2	0	200.06
8.Spitak	37	2	2	0	0	72.44

The following tables and graphs contain specific details for the four accelerograms under examination.

Coalinga

Table 5.62 – COALINGA – details (A)

	PGA [g]	Rotation [rad]	Displacement [m]		Compression [kN]		Tension [kN]	
			Lev. 1	Lev. 2	Lev. 1	Lev. 2	Lev. 1	Lev. 2
RBS	0.90	0.032432	0.092	0.175	206.99	210.08	183.75	154.60
FREEDAM min	0.85	0.031406	0.064	0.152	161.31	169.69	120.21	122.23
FREEDAM max	0.90	0.028702	0.070	0.150	171.48	193.08	127.31	138.89

Table 5.63 – COALINGA – details (B)

	Amplitude [mrad]					Cumulative rotation [mrad]	Cumulative displacement [mm]
	< 3.75	3.75 - 7.50	7.50- 15	15 – 30	> 30		
RBS	63	7	1	0	0	111.51	-
FREEDAM min	12	2	2	1	0	66.72	29.36
FREEDAM max	7	3	1	0	0	42.74	18.80

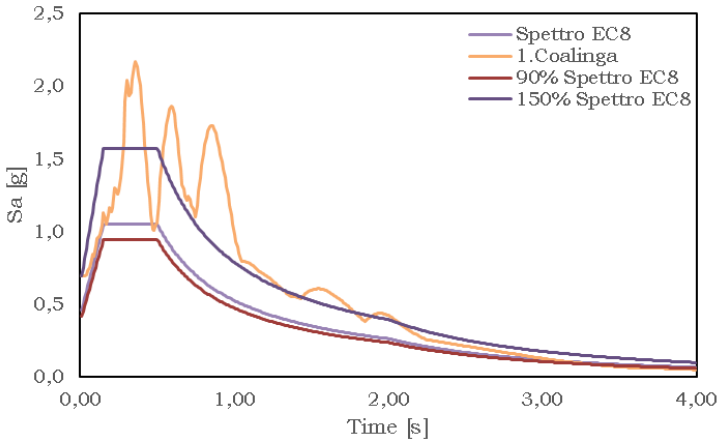

Fig. 5.169 – Spectral acceleration vs time - COALINGA

Imperial Valley

Table 5.64 – IMPERIAL VALLEY – details (A)

	PGA [g]	***Rotation [rad]***	***Displacement [m]***		***Compression [kN]***		***Tension [kN]***	
			Lev. 1	***Lev. 2***	***Lev. 1***	***Lev. 2***	***Lev. 1***	***Lev. 2***
RBS	*1.40*	*0.030063*	*0.088*	*0.169*	*179.39*	*181.16*	*220.35*	*198.75*
FREEDAM min	*1.20*	*0.029108*	*0.064*	*0.144*	*155.22*	*147.15*	*193.13*	*169.46*
FREEDAM max	*1.30*	*0.031577*	*0.080*	*0.162*	*166.97*	*172.17*	*202.85*	*185.56*

Table 5.65 – IMPERIAL VALLEY – details (B)

	Amplitude [mrad]					***Cumulative rotation [mrad]***	***Cumulative displacement [mm]***
	< 3.75	*3.75 - 7.50*	*7.51- 15*	*15 – 30*	*> 30*		
RBS	*53*	*6*	*2*	*0*	*0*	*108.20*	*-*
FREEDAM min	*16*	*4*	*2*	*1*	*0*	*79.58*	*35.02*
FREEDAM max	*10*	*3*	*3*	*1*	*0*	*66.56*	*29.29*

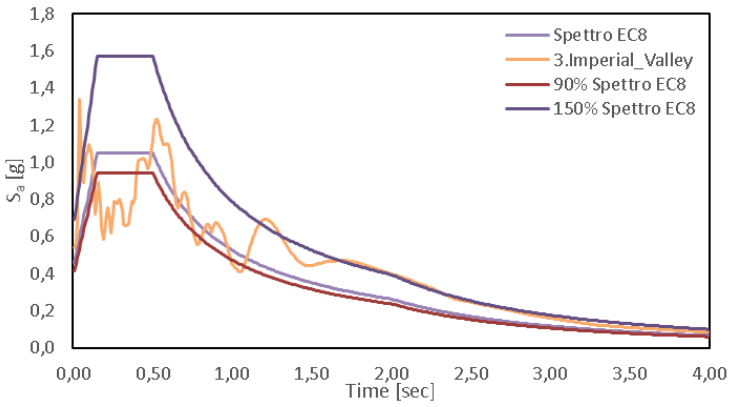

Fig. 5.170 – Spectral acceleration vs time – IMPERIAL VALLEY

Landers

Table 5.66 – LANDERS – details (A)

	PGA [g]	Rotation [rad]	Displacement [m]		Compression [kN]		Tension [kN]	
			Lev. 1	Lev. 2	Lev. 1	Lev. 2	Lev. 1	Lev. 2
RBS	1.30	0.032218	0.082	0.173	244.47	233.50	232.88	221.67
FREEDAM min	1.10	0.031555	0.066	0.153	181.59	192.25	167.77	191.99
FREEDAM max	1.00	0.030027	0.072	0.154	164.11	209.85	152.69	186.85

Table 5.67 – LANDERS – details (B)

	Amplitude [mrad]					Cumulative rotation [mrad]	Cumulative displacement [mm]
	< 3.75	3.75 - 7.50	7.52- 15	15 – 30	> 30		
RBS	111	34	2	2	0	367.91	-
FREEDAM min	13	5	4	2	0	107.72	47.40
FREEDAM max	30	20	3	1	0	210.20	92.49

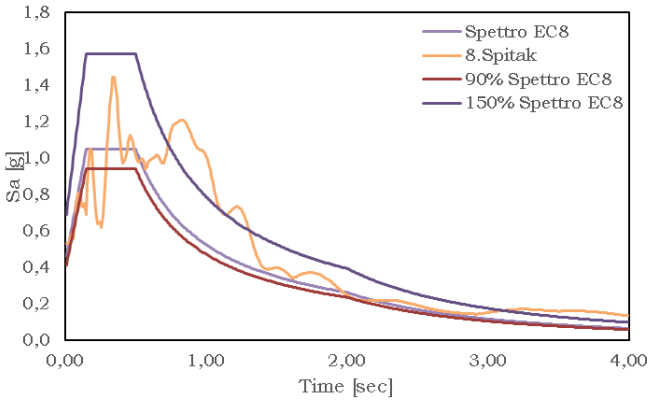

Fig. 5.171 – Spectral acceleration vs time – LANDERS

Spitak

Table 5.68 – SPITAK – details (A)

	PGA [g]	Rotation [rad]	Displacement [m]		Compression [kN]		Tension [kN]	
			Lev. 1	Lev. 2	Lev. 1	Lev. 2	Lev. 1	Lev. 2
RBS	1.10	0.029404	0.094	0.177	201.63	205.18	257.22	211.36
FREEDAM min	0.95	0.032112	0.066	0.156	182.45	167.49	157.99	153.03
FREEDAM max	1.00	0.029157	0.073	0.155	199.80	181.66	167.41	152.42

Table 5.69 – SPITAK – details (B)

	Amplitude [mrad]					Cumulative rotation [mrad]	Cumulative displacement [mm]
	< 3.75	3.75 - 7.50	7.53- 15	15 – 30	> 30		
RBS	37	2	2	0	0	72.44	-
FREEDAM min	0	2	2	1	0	46.05	20.26
FREEDAM max	2	1	3	0	0	39.17	17.24

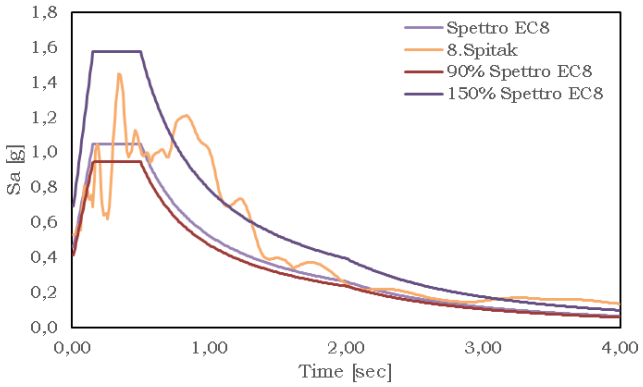

Fig. 5.172 – Spectral acceleration vs time – SPITAK

5.5.2. Final considerations

The Coalinga accelerogram:

- guarantees a large safety margin in terms of the forces that the actuators must impose on the decks;
- guarantees a fair number of cycles for the connections under examination;
- is characterized by a response spectrum that is not compatible with the reference spectrum.

Therefore, this accelerogram is not considered suitable for the pseudo-dynamic test.

The Imperial Valley accelerogram:

- guarantees a good safety margin in terms of the forces that the actuators must impose on the decks;
- guarantees a fair number of cycles for the connections under examination;
- is characterized by a satisfactory response spectrum compatible with the reference spectrum.

Therefore, this accelerogram is considered suitable for the pseudo-dynamic test.

The Landers accelerogram:

- guarantees a safety margin in terms of the forces that the actuators must impose very limited and risky decks for successful completion of the test;
- guarantees a satisfactory number of cycles for the connections in question;

- is characterized by a satisfactory response spectrum compatible with the reference spectrum.

Therefore, this accelerogram is not considered suitable for the pseudo-dynamic test.

The Spitak accelerogram:

- guarantees a safety margin in terms of the forces that the actuators must impose limited deck;
- guarantees an inadequate number of cycles for the connections in question;
- is characterized by a satisfactory response spectrum compatible with the reference spectrum.

Therefore, this accelerogram is not considered suitable for the pseudo-dynamic test.

As noted above, the Imperial Valley accelerogram is chosen to perform the pseudo-dynamic tests.

5.6. Pseudo-dynamic test on specimen equipped with RBS connections

5.6.1. Experimental set-up

Assembly of the specimen

The steel structure has been assembled at the STRENGHT laboratory (STRuctural ENGineering Testing Hall) of the University of Salerno. In the

following some pictures (from Fig. 5.173 to Fig. 5.175) related to the construction phases are shown.

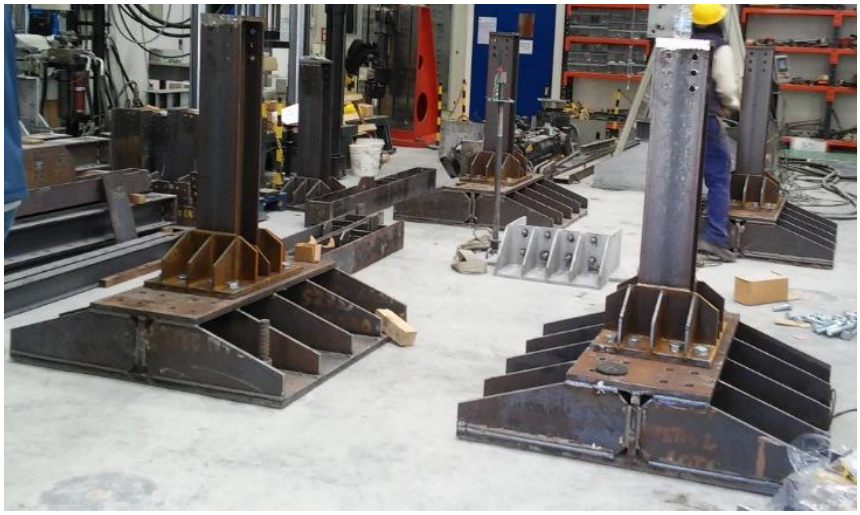

Fig. 5.173 – Column bases

Fig. 5.174 – Columns and beams

Fig. 5.175 – Complete structure

Instrumentation of the specimen for the pseudo-dynamic test

As mentioned previously, the pseudo-dynamic test requires for its execution of less complex devices than those of other dynamic tests (vibrating tables).

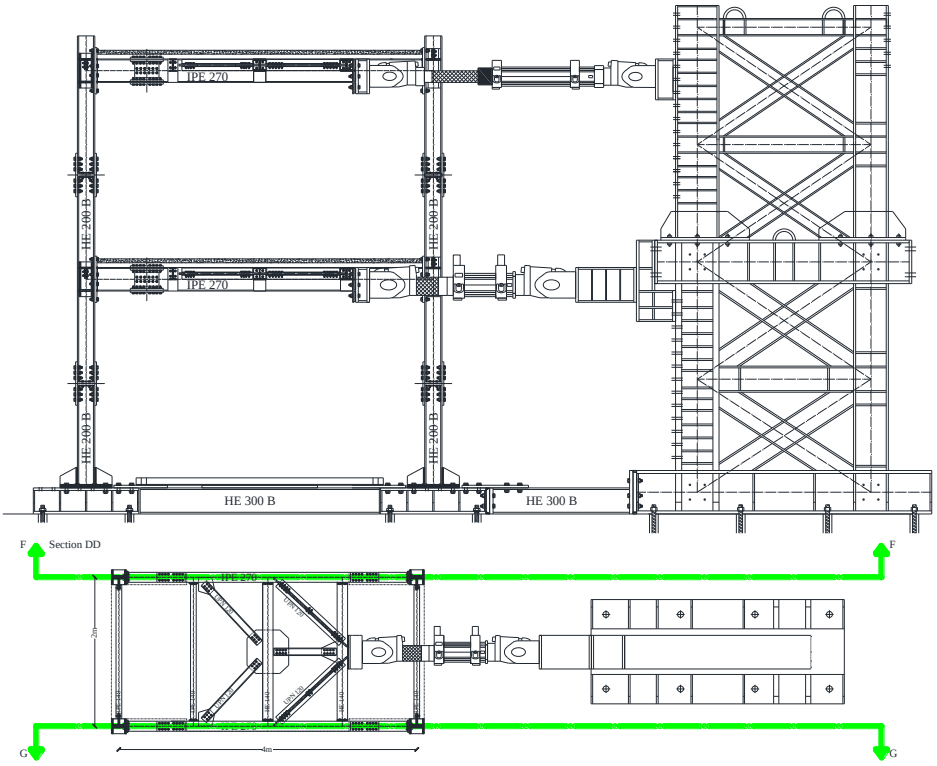

Fig. 5.176 – Experimental test set-up

First of all, actuators are required, which are able to stress the structure by applying perhaps both tensile and compressive forces applied at the two floors. The pseudo-dynamic tests have been performed thanks to two MTS actuators with the following characteristics:

- the actuator located at first level is an MTS 243.45-01, which is able to apply $649\,kN$ in compression and $445\,kN$ in tension; its piston stroke is $\pm 1066\,mm$;
- the actuator located at second level is an MTS 243.60-02, which is able to apply $648\,kN$ in both tension and compression; its piston stroke is $\pm 508\,mm$.

The actuators have been fixed to reaction wall constituted by a rigid steel braced frame.

Both column bases and the steel braced frame are anchored to the laboratory strong floor by means of high strength dywidag bars.

a)

b)

Fig. 5.177 – a) LVDT and wire transducers; b) MTS Temposonic transducer

The measurement of the displacements in correspondence of the two planes has been carried out through displacement transducers: two wire potentiometric transducers and one LVDT (Linear Variable Displacement Transducer) at first level; two wire potentiometric transducers and one MTS Temposonic – Series R transducer at second level.

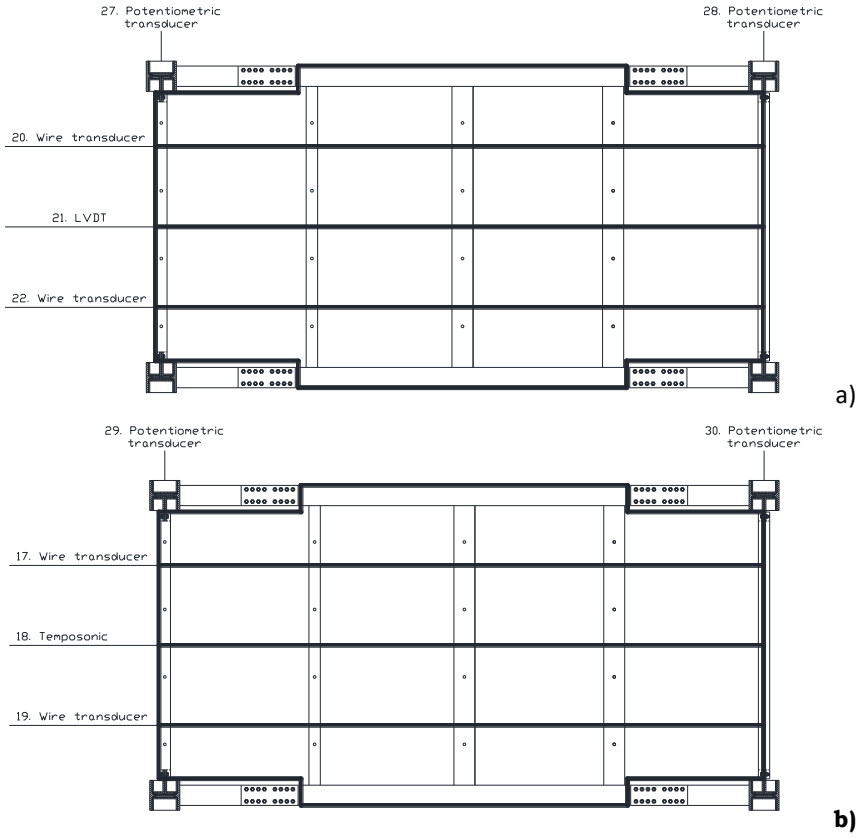

Fig. 5.178 – Transducers layout at the 1st and 2nd level

Regarding the deformations to which the members are subjected, the measure of which is necessary to derive the moment-rotation curves,

have been recorded using strain gauges. Forty-eight strain-gauges have been applied at the top and bottom of first level columns and at beams ends with the aim to assess bending moment for the checked section. In order to ensure their reliability, they have been applied on structural elements supposed to remain in elastic range.

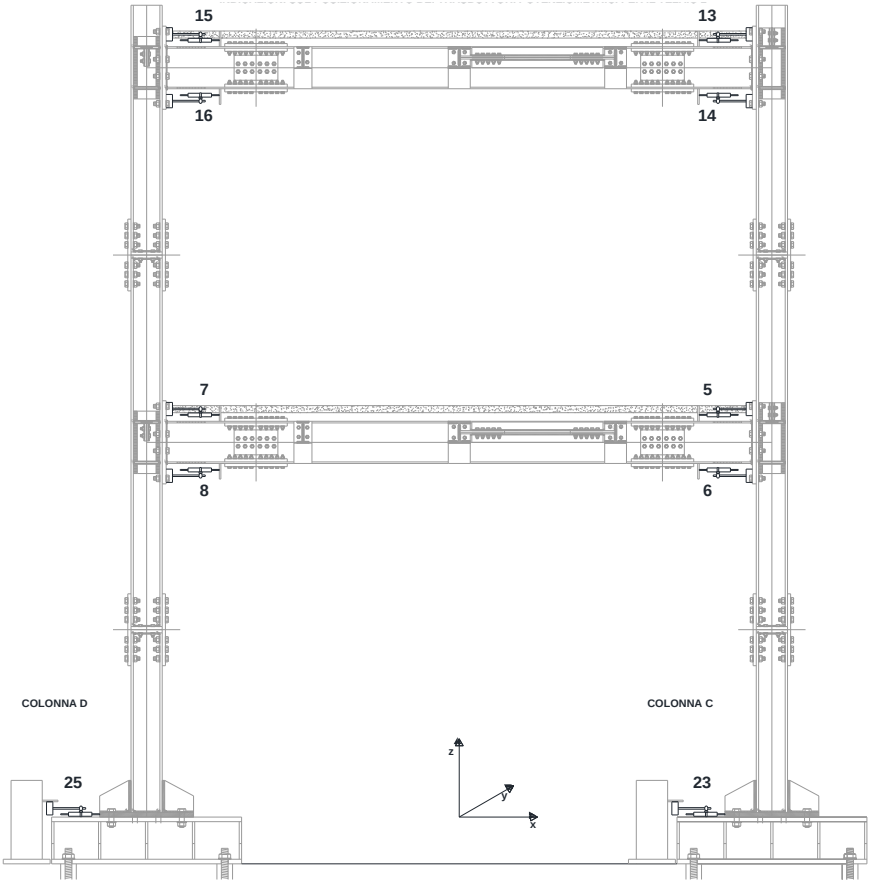

Fig. 5.179 – Displacement transducers on frames

They have been applied to both MRFs, but one of them is more equipped than the other one. In fact the first MRF has 32 strain-gauges, while the other one 16.

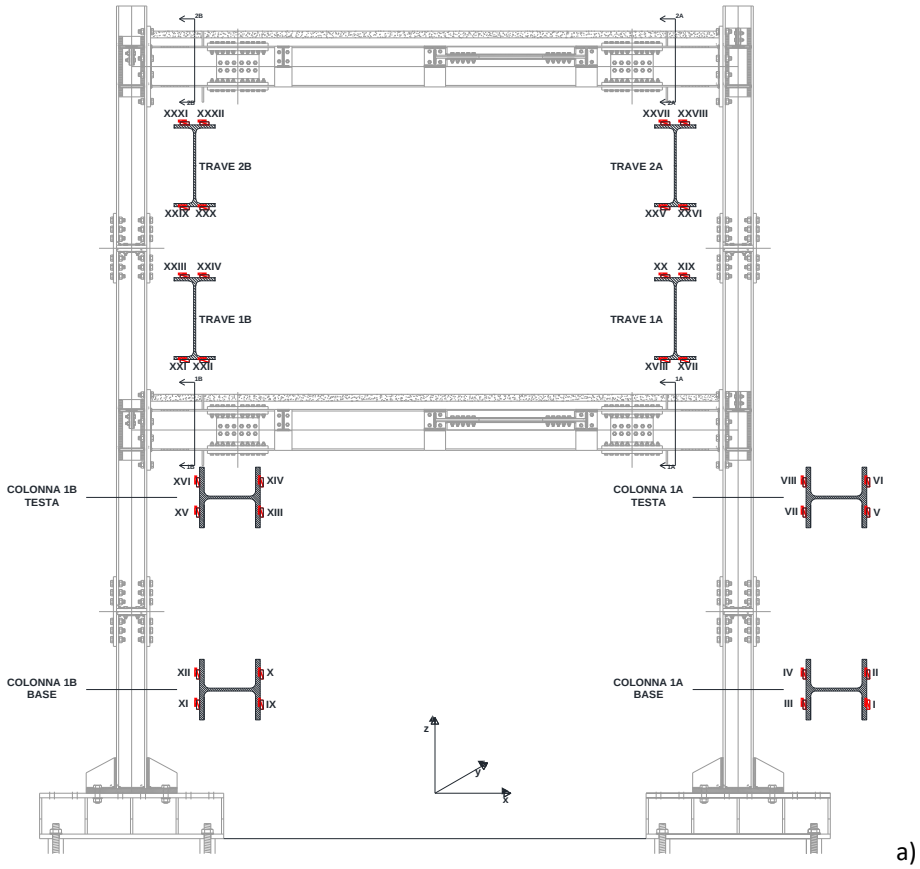

a)

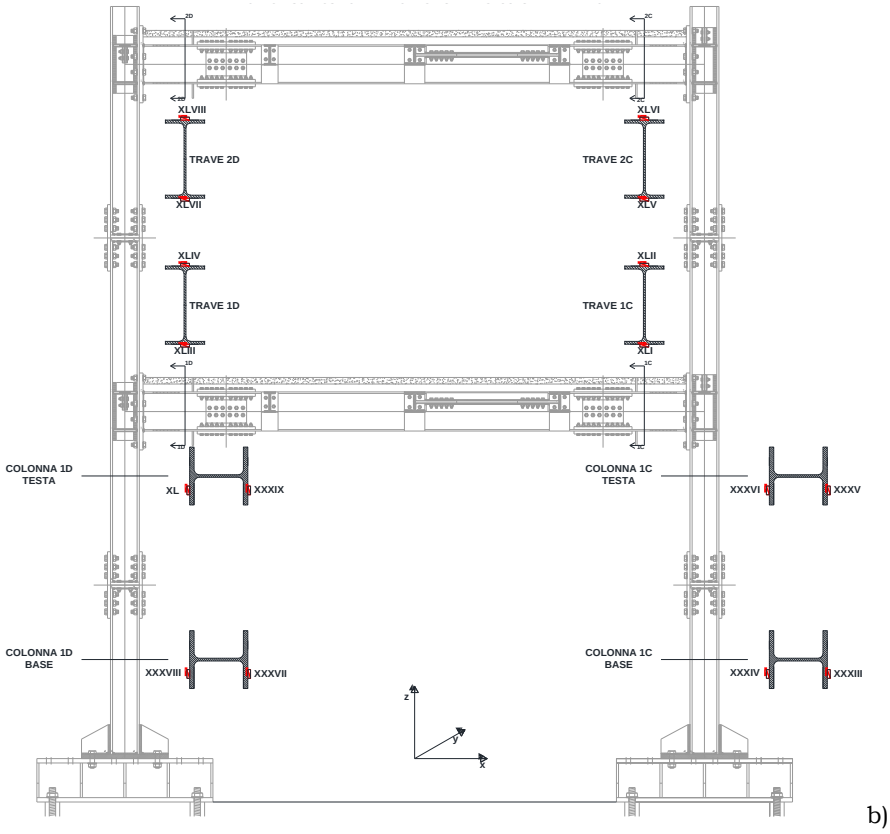

Fig. 5.180 – Stain gauges on frames

5.6.2. Pseudo-dynamic test

A pseudo-dynamic test has been performed using the Imperial Valley accelerogram and using a peak ground acceleration of *1.10g*.

On the basis of the preliminary tests in the elastic field conducted on the structure, the presence of an energy dissipation of a not negligible amount has been highlighted; therefore, for the test conducted in the

plastic field it has been decided to resort to a damping factor of 2%, as reported in Italian and European legislation.

As a result of this modification, by re-running the simulations with SeismoStruct, the non-compatibility of the scale factor adopted with the actuator capacities was highlighted and therefore it was decided to reduce the acceleration peak on the ground from $1.30g$ to $1.10\ g$. The negative consequence of this choice consists in the reduction of the foreseen rotations in correspondence of the connections from 30 $mrad$ to about $18 \div 20 mrad$.

Starting from these modifications, the test has been carried out, however, which has not reached its completion due to the plasticization of a tubular element designed to transfer the action of the first level actuator to the deck. This drawback has occurred since the actuator of the first level has applied an unexpected force, in the order of $1000kN$ because of problems of numerical convergence of the software Pseudo2 due to the onset of unexpected displacements at the base of both the structure and the frame contrast.

The test has been stopped at $8.00s$ of the accelerogam and a reinforcement in correspondence of the base and a direct connection between column bases and the steel braced frame had been needed before to restart the test.

The Fig. 5.182 and the Fig. 5.183 show the damage to the structural elements and the translations at the base of the structure and the contrast frame, which represent the causes.

Fig. 5.181 – Structural elements before damage

Fig. 5.182 – Structural elements after damage

Fig. 5.183 – Collapse of the slab

Fig. 5.184 – Displacement of the column base

Fig. 5.185 – Displacement of the steel braced

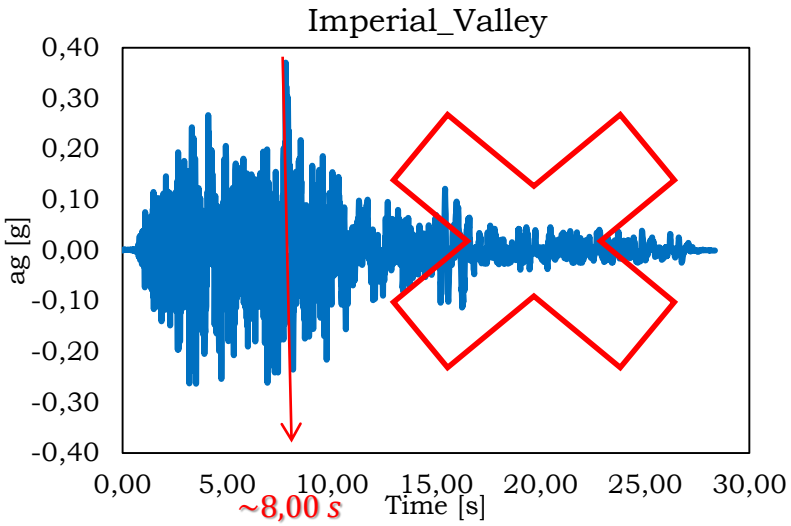

Fig. 5.186 – Interruption point of the accelerogram

5.6.3. Comparison between numerical analysis and experimental results

Regarding the results obtained during the incomplete test; it is possible to observe that, in terms of displacements, the results are quite in line with the forecasts, especially for the second bridge. Furthermore, it is possible to observe that the local maximum and minimum points occur with a good approximation to the same instants.

For the forces that the actuators apply to the rigid floor, it is possible to observe a greater dispersion in the comparison between simulation and prediction due not only, for example, to the load oscillation presented by the actuator placed at the first level, but to the integration and to the real response of the structure.

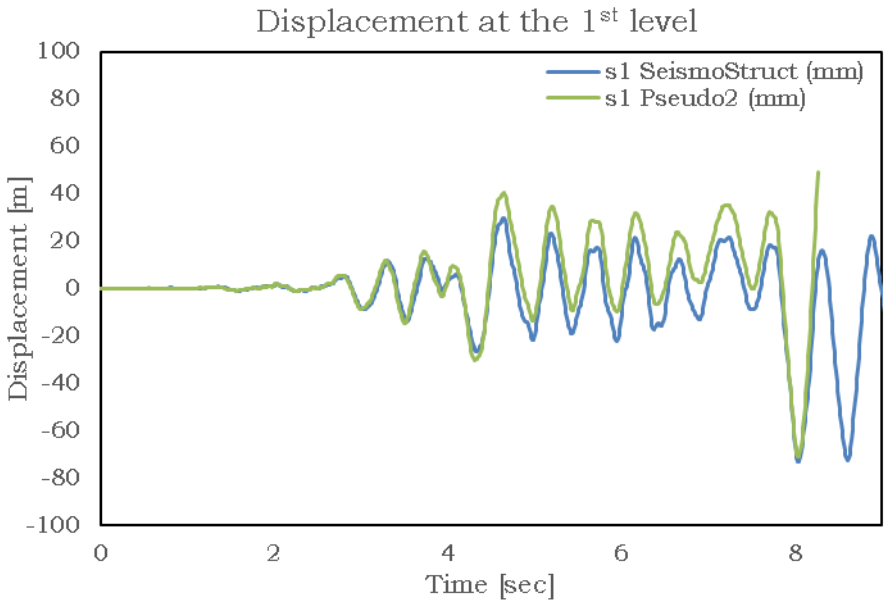

Fig. 5.187 – Displacement vs Time 1st level

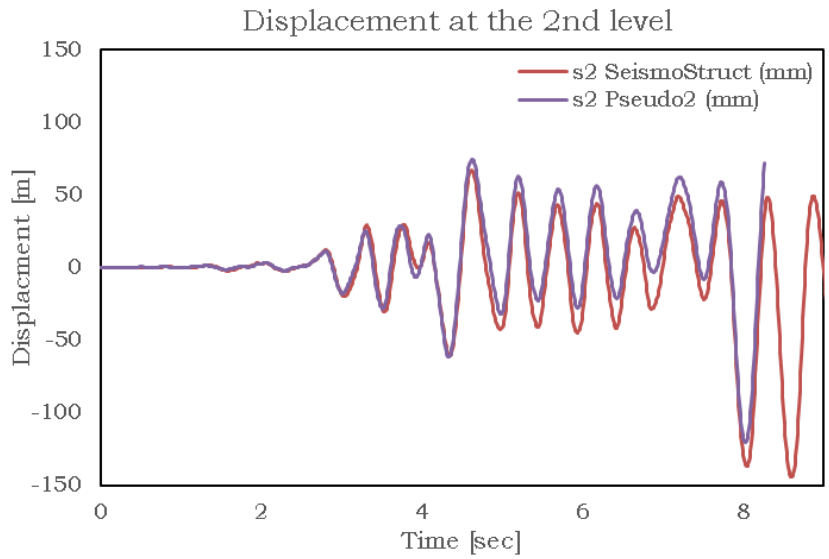

Fig. 5.188 – Displacement vs Time 2nd level

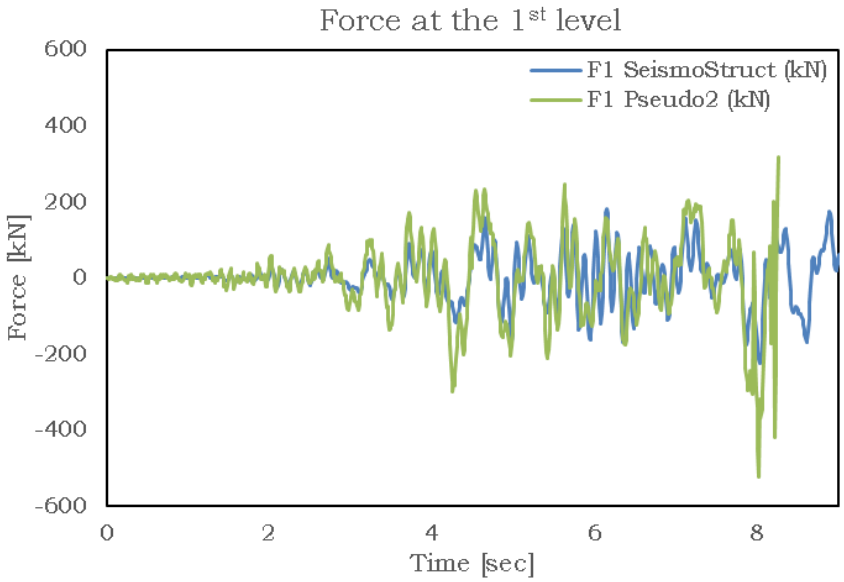

Fig. 5.189 – Force vs Time 1st level

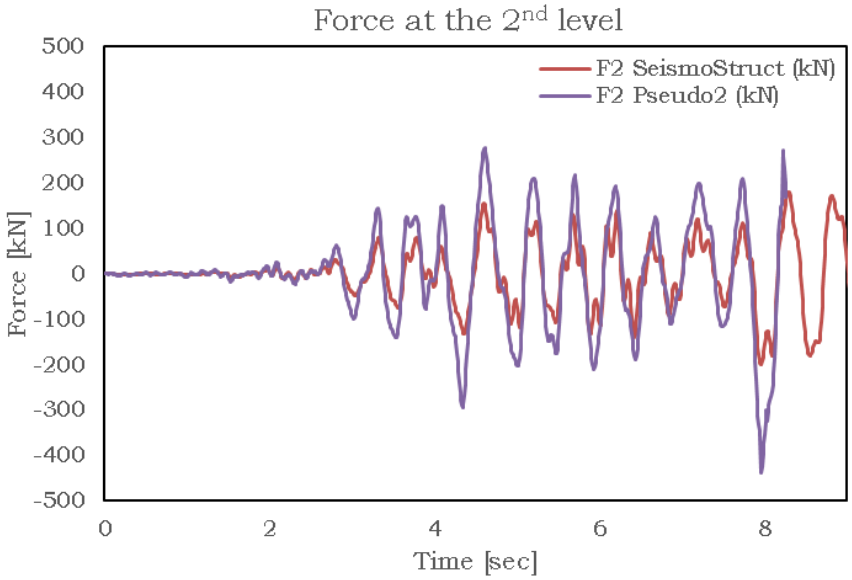

Fig. 5.190 – Force vs Time 2nd level

The forces at the second level are more stable and although it is possible to observe that the moments in which they are cancelled coincide in simulation and reality, there is a slight overestimation of the values through the analysis conducted with the SeismoStruct software.

In the following the recordings of the other monitored parameters are evaluated, in particular: curvatures, moments and rotations at the RBS connections.

For the evaluation of the rotations in the joints, potentiometric transducers connected to the endplates and to orthogonal plates to the flanges disposed at a certain distance from the narrowing towards the inside of the bays have been adopted.

It is expected that, due to the rotation of the connection, a transducer registers an elongation, while the other a shortening of the same order of magnitude, as shown in Fig. 5.191.

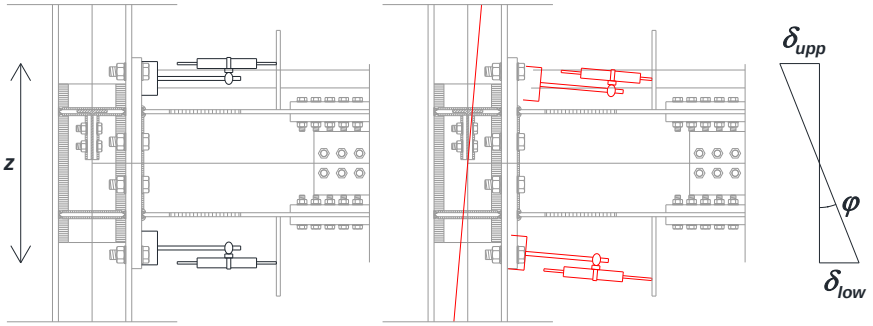

Fig. 5.191 – Transducers layout

These devices allow recording the relative displacements between the two connected elements:

$$\varphi = \frac{\delta_{sup} - \delta_{inf}}{z} \tag{5.152}$$

δ_{sup} represents the displacement recorded by the transducers arranged on the upper flanges.

δ_{inf} represents the displacement recorded by the transducers arranged on the lower flanges.

Rotations at first level columns ends have been assessed thanks to interstorey drift because no potentiometric transducers were applied to them:

$$\varphi = \frac{d_1}{h_{interstorey}} \tag{5.153}$$

d_1 represents floor displacement at level 1.

$h_{interstorey}$ is the interstorey height.

With a reasoning similar to the case of the definition of the rotations and considering that the distance between the strain gauges arranged on the flanges is equal to the height of the beam, it is possible to derive that:

$$\gamma = \frac{\varepsilon_{sup} - \varepsilon_{inf}}{h_{trave}} \tag{5.154}$$

ε_{sup} represents the deformation recorded by the strain-gauges arranged on the upper flanges.
ε_{inf} represents the deformation recorded by the strain-gauges arranged on the lower flanges.
h_{beam} represents the height of the beam.

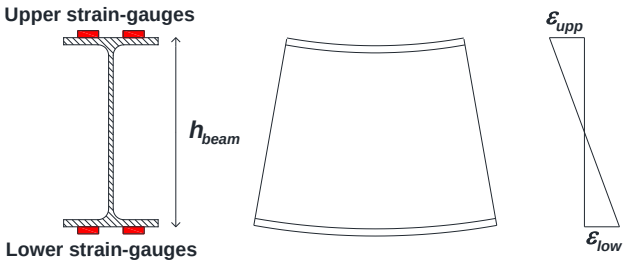

Fig. 5.192 – Curvature

Assuming the linearity of the moment-curvature bond is valid:

$$M = \chi EI \tag{5.155}$$

As strain-gauges have been installed at the base of the columns, it is possible to define the curvatures and therefore the corresponding moments in these sections.

Thanks to hysteretic curves, energy dissipated at beam and columns ends can be assessed. At step i of the accelerogram, dissipated energy is defined according to the following expression:

$$E_i = E_{i-1} + \frac{(M_i + M_{i-1})(\varphi_i - \varphi_{i-1})}{2} \frac{1}{n_{MRFs}} \quad (5.156)$$

E_i and E_{i-1} represent respectively energy dissipated at steps i and $i-1$.
M_i and M_{i-1} represent respectively the bending moment at steps i and $i-1$.
φ_i and φ_{i-1} represent respectively rotation at steps i and $i-1$.
n_{MRFs} represents the number of MRFs because in this case only data obtained by one MRF have been processed.

For each RBS connection of the most monitored frame, the results are reported in terms of moment-rotation curves and energy dissipated with the relative forecasts obtained with SeismoStruct.
In SeismoStruct the hysteretic curves have been evaluated directly at the link elements, having assumed that the rotations are concentrated only in those localized areas. It is possible to observe the marked differences in terms of hysteretic curves between simulation and reality both in terms of initial stiffness and dissipated energy: the simulation connections dissipate much more and starting from the first cycles, eventuality that does not occur in the real case, and this aspect is more marked for the connections placed at the second level which are less stressed than the others at the first.

In Table 5.70 main information about second test can be found out.

Table 5.70 – Pseudo-dynamic test RBS 1

Earthquake:			**Imperial Valley**
a_g/g =			*1.10*
Maximum base shear [kN]	***Pull***		*-664.48*
	Push		*454.96*
Peak first floor displacement [mm]	***Pull***		*-44.41*
	Push		*40.32*
Peak roof displacement [mm]	***Pull***		*-93.68*
	Push		*74.29*
Maximum interstorey drift [%]	***Pull***	***Level 1***	*-1.85*
		Level 2	*-2.05*
	Push	***Level 1***	*1.68*
		Level 2	*1.45*

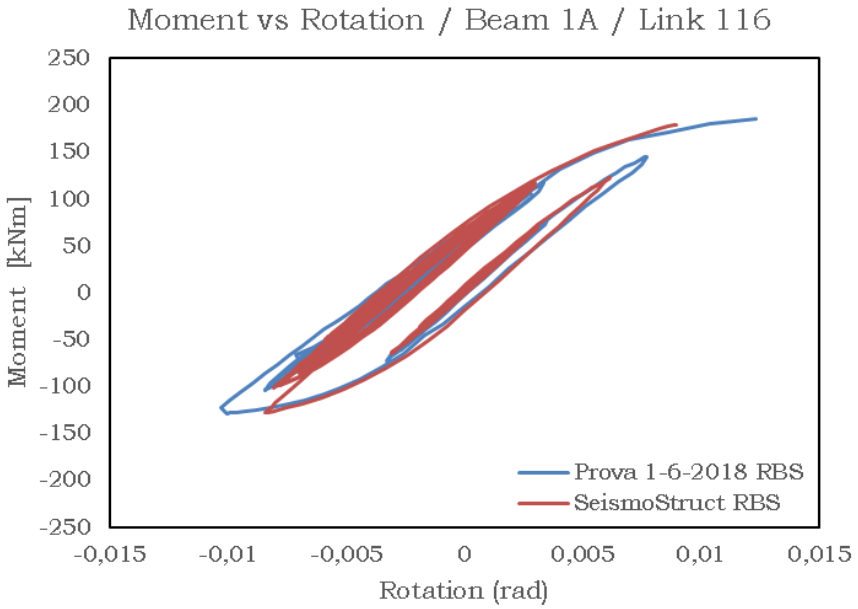

Fig. 5.193 – Moment vs rotation - Beam 1A - RBS 1

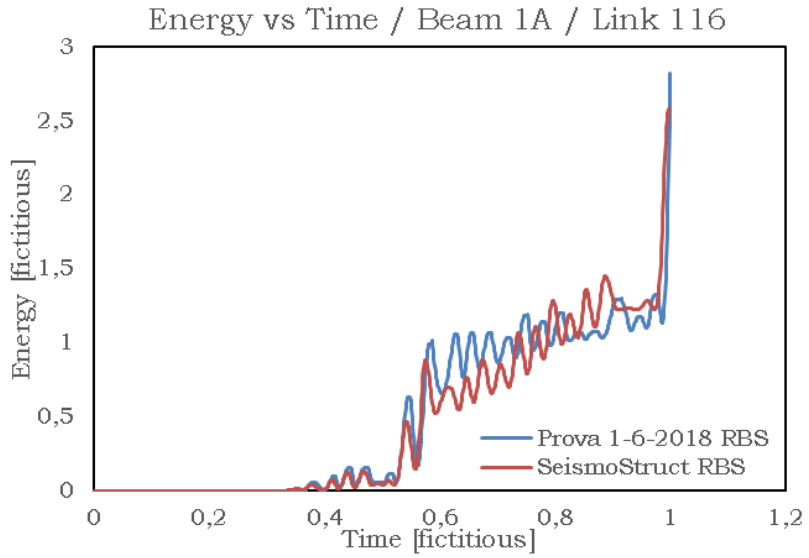

Fig. 5.194 – Energy vs time - Beam 1A – RBS

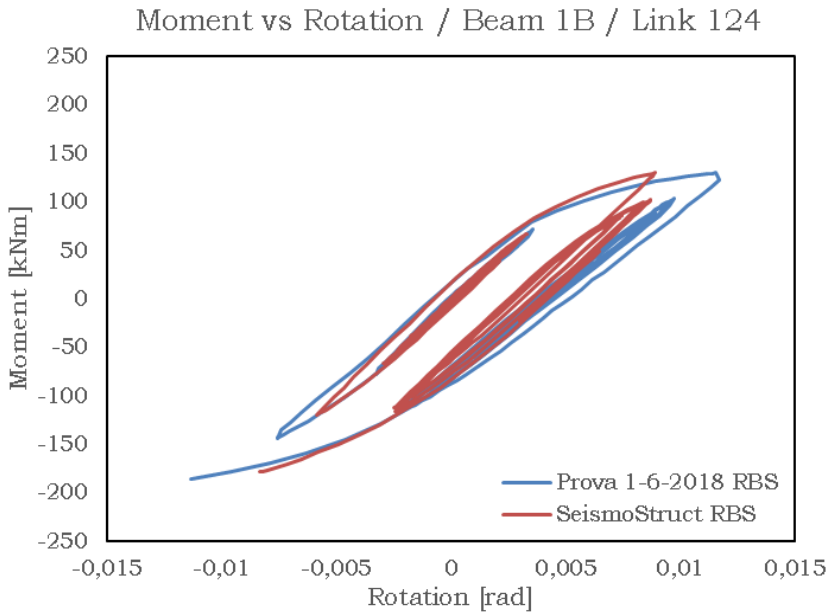

Fig. 5.195 – Moment vs rotation - Beam 1B - RBS 1

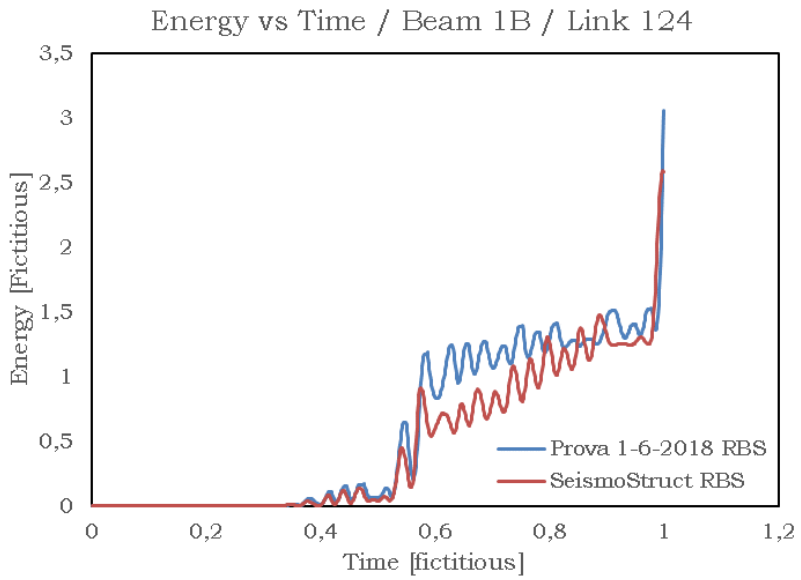

Fig. 5.196 – Energy vs time - Beam 1B- RBS

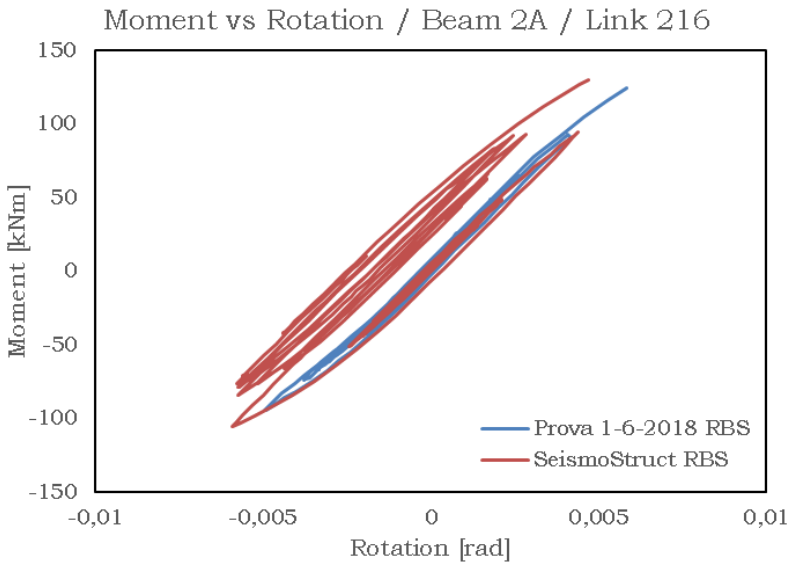

Fig. 5.197 – Moment vs rotation - Beam 2A - RBS 1

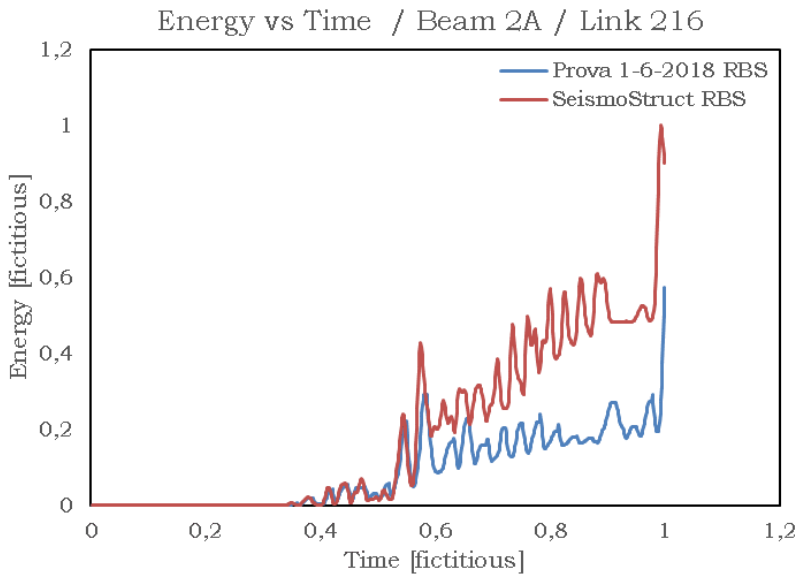

Fig. 5.198 – Energy vs time - Beam 2A- RBS

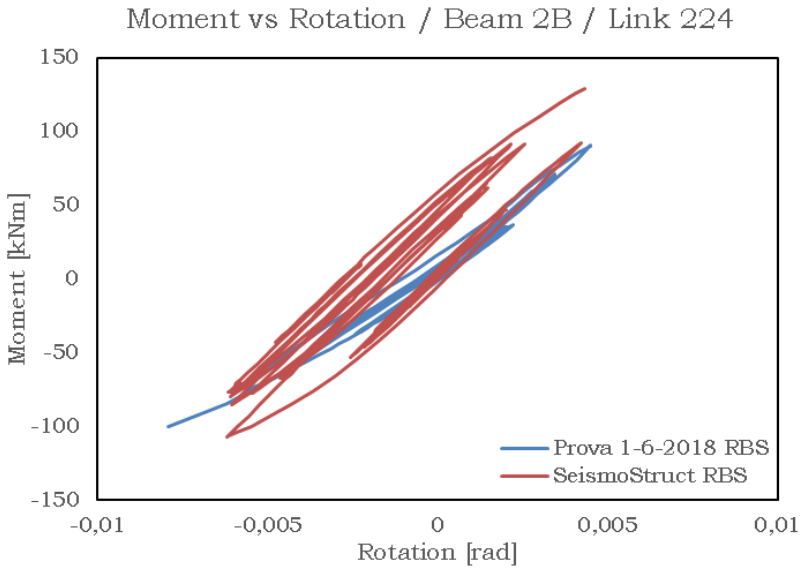

Fig. 5.199 – Moment vs rotation - Beam 2B - RBS 1

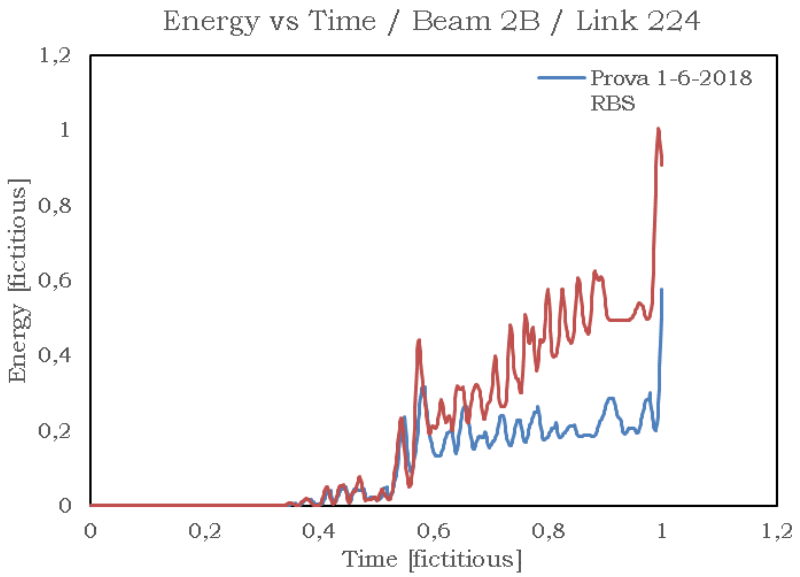

Fig. 5.200 – Energy vs time - Beam 2B – RBS

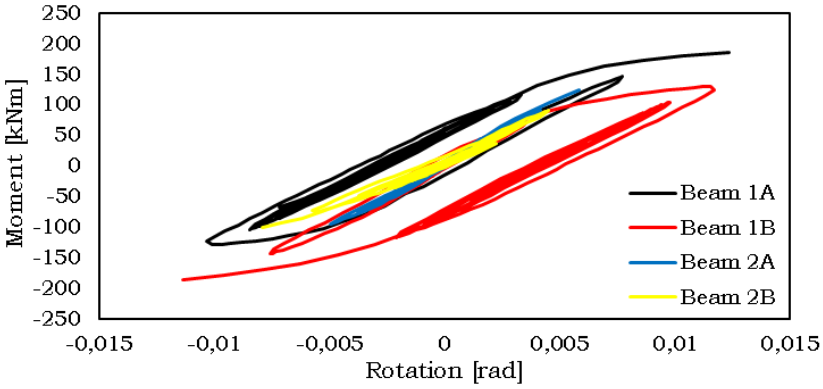

Fig. 5.201 – Beams hysteretic curves - RBS 1

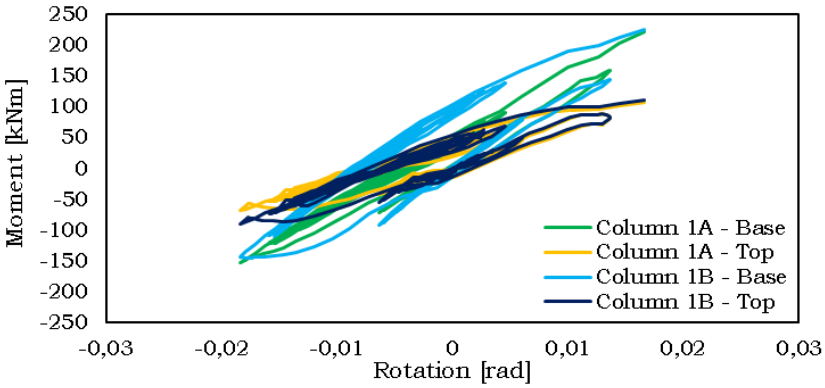

Fig. 5.202 – Columns hysteretic curves - RBS 1

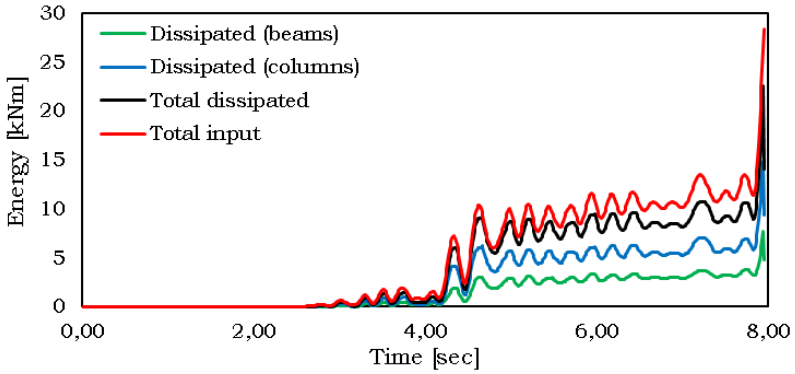

Fig. 5.203 – Overall dissipated energy - RBS 1

Main features observed in the first test can be highlighted also for the second one, which has been performed only after that the bases of the structure and the reaction wall have been connected by means of IPE300 profiles.

For this reason, only important differences among the two tests will be herein described.

This test has not been performed in 24h, but it has been interrupted in order to execute its different parts in three days. Only in processing data it was clear that this way of doing caused problems in the good performance of the test because floor displacements and hysteretic curves had to be corrected in order to take into account the elastic response of the structure at the end of each part of the test.
During the second test beams ends exhibit a noticeable excursion in plastic range compared to that one of the first test, so that for beams located at first level bending moments of about 200 kNm are achieved. Connections located at second level, instead, show a very low excursion in plastic range, achieving maximum bending moments of 150 kNm, and so compatible with yield moment adopted in the definition of plastic hinges in SeismoStruct model.
At columns bases maximum bending moments are about 360 kNm for column 1A and 270 kNm for column 1B and rotations of about 30 mrad; this fact highlights the plastic deformation of columns bases.
Columns energy dissipation is higher than beams one, as it happens for the first test.
Maximum base shear is equal to 751,33 kN and when it occurs maximum roof displacement (149,97 mm) is achieved too.

In Table 5.71 main information about second test can be found out.
Maximum interstorey drifts exceed the Eurocode 8 [1] upper limit, in this case, too. It is worth noticing that the energy curve related to the top of column 1B is not defined in a good manner probably because of problems of the equipment in acquiring data.

Table 5.71 – Pseudo-dynamic test RBS 2

Earthquake:			**Imperial Valley**
a_g/g =			*1.10*
Maximum base shear [kN]	***Pull***		*-751.33*
	Push		*667.09*
Peak first floor displacement [mm]	***Pull***		*-78.50*
	Push		*44.13*
Peak roof displacement [mm]	***Pull***		*-149.97*
	Push		*87.73*
Maximum interstorey drift [%]	***Pull***	***Level 1***	*-3.27*
		Level 2	*-2.98*
	Push	***Level 1***	*1.84*
		Level 2	*1.86*

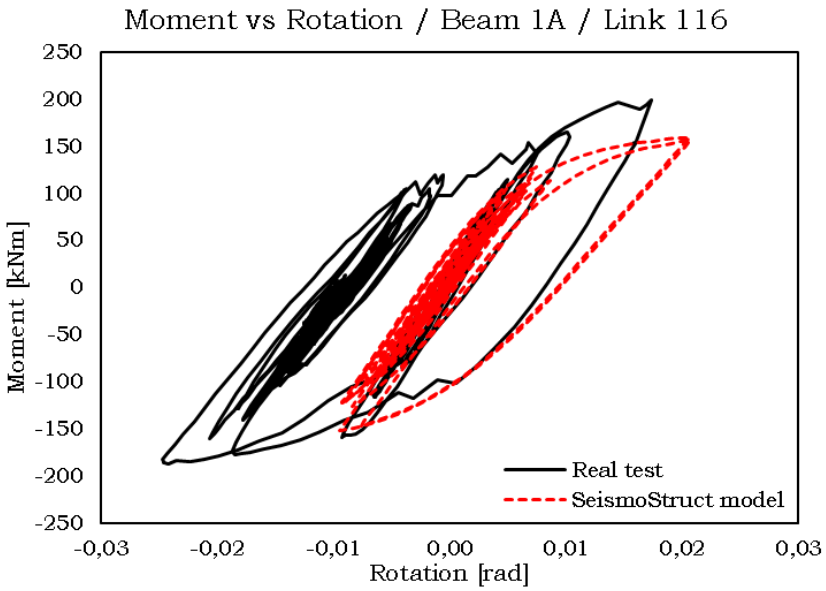

Fig. 5.204 – Moment vs rotation - Beam 1A - RBS 2

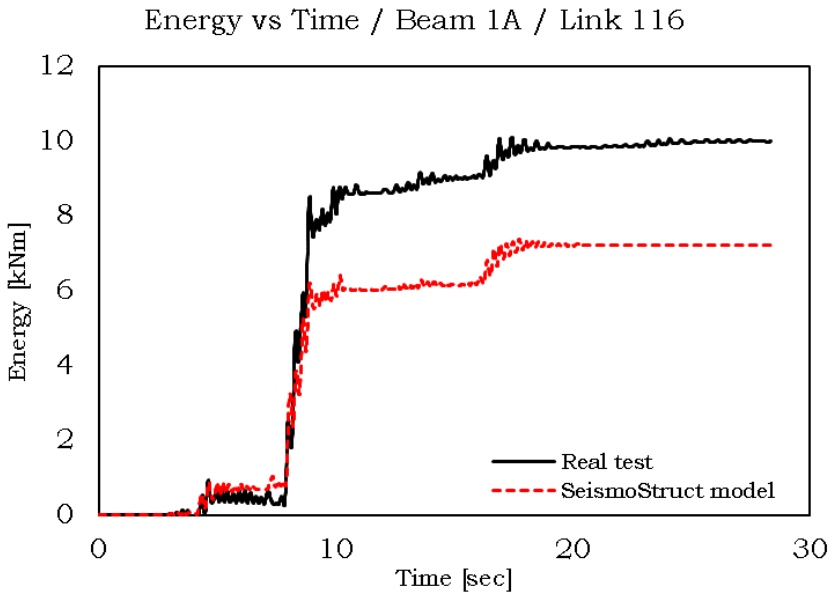

Fig. 5.205 – Energy vs time - Beam 1A - RBS 2

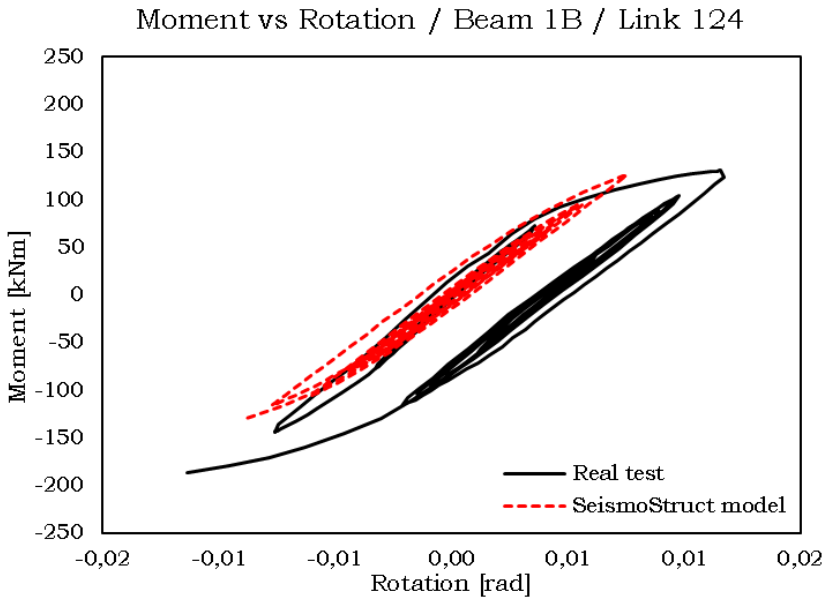

Fig. 5.206 – Moment vs rotation - Beam 1B - RBS 2

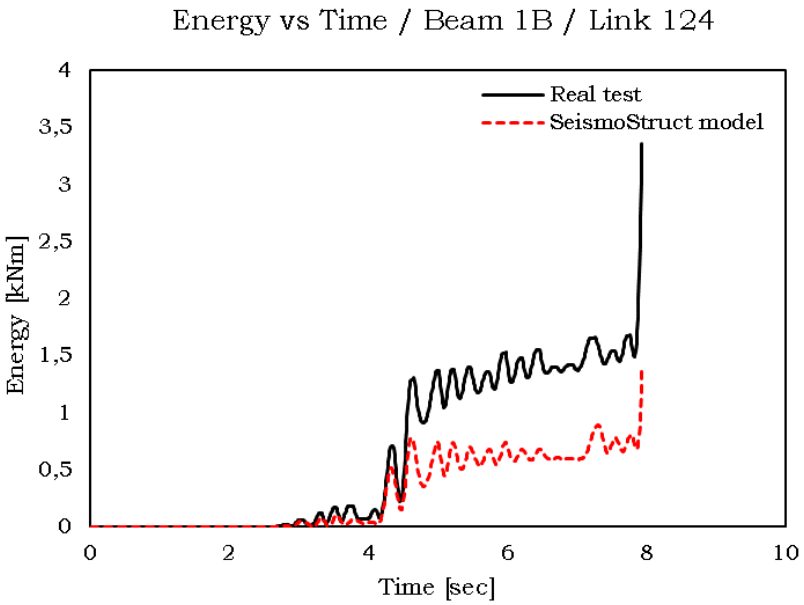

Fig. 5.207 – Energy vs time - Beam 1B - RBS 2

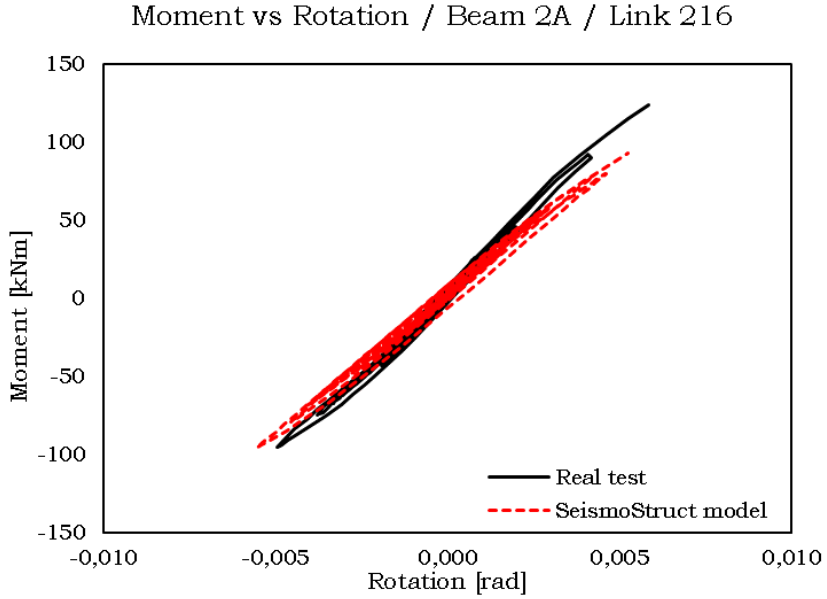

Fig. 5.208 – Moment vs rotation - Beam 2A - RBS 2

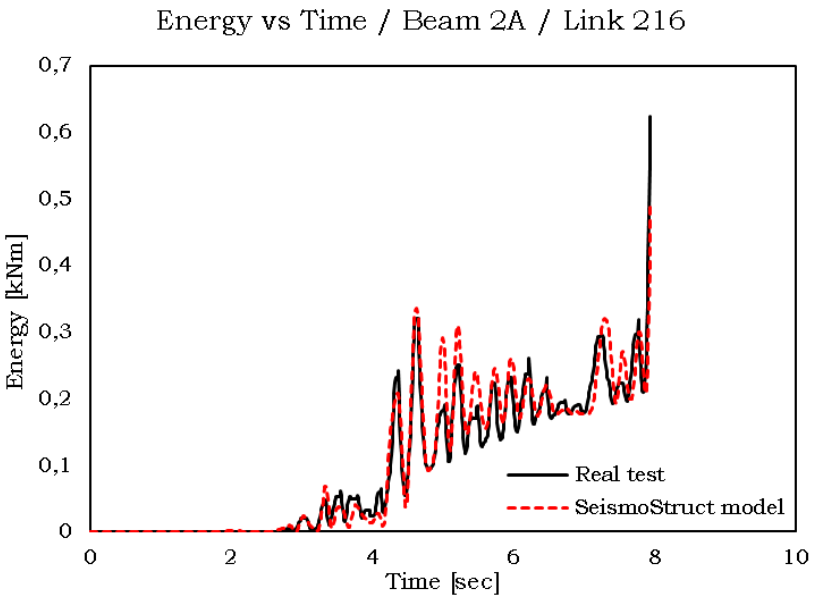

Fig. 5.209 – Energy vs time - Beam 2A - RBS 2

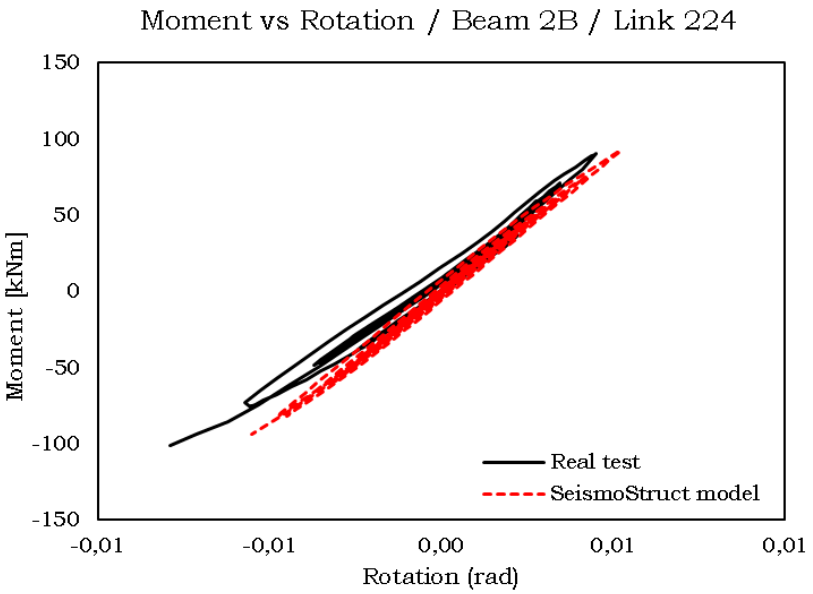

Fig. 5.210 – Moment vs rotation - Beam 2B - RBS 2

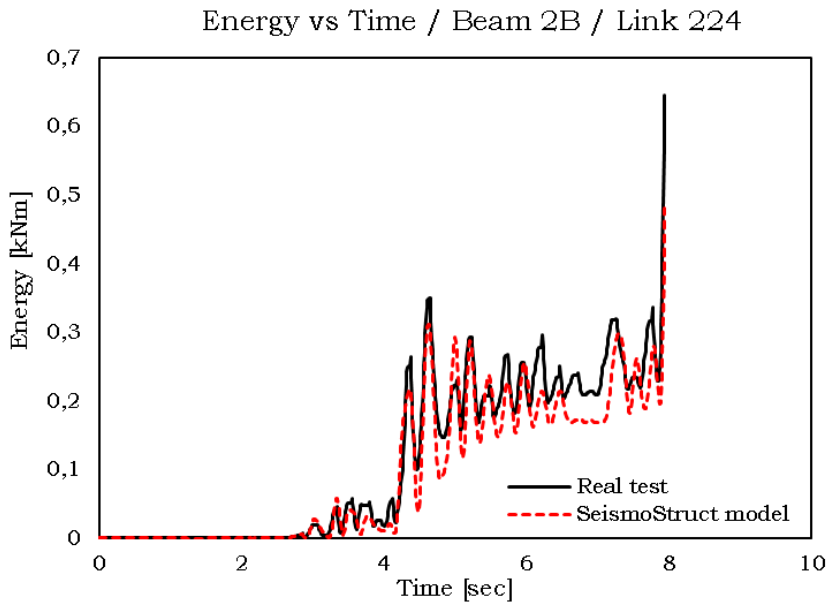

Fig. 5.211 – Energy vs time - Beam 2B - RBS 2

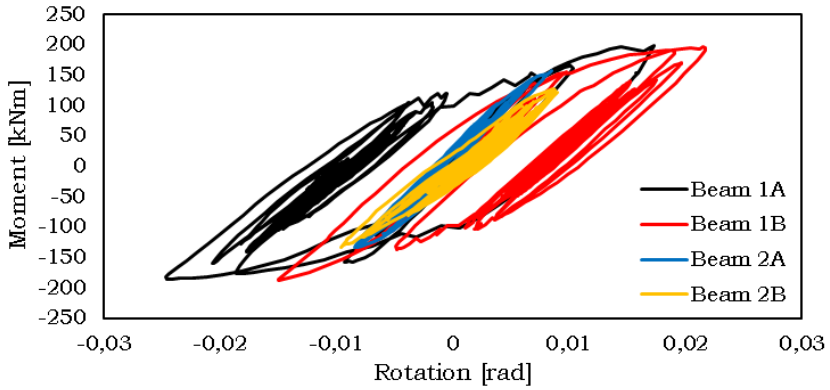

Fig. 5.212 – Beams hysteretic curves - RBS 2

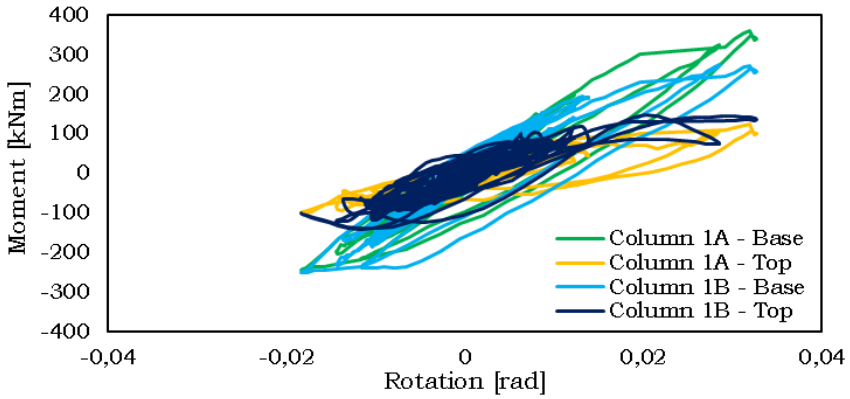

Fig. 5.213 – Columns hysteretic curves - RBS 2

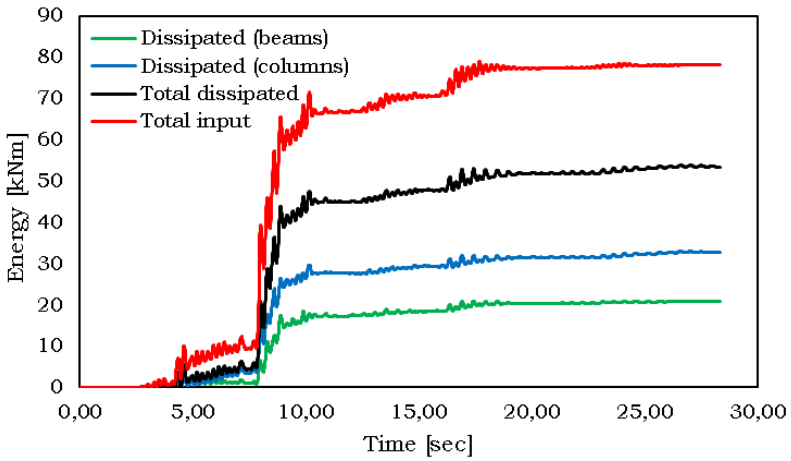

Fig. 5.214 – Overall dissipated energy - RBS 2

5.7. Pseudo-dynamic test on specimen equipped with FREEDAM connections

Before being able to carry out the test on the chassis equipped with FREEDAM connections it was necessary to carry out some work on the

structure. In particular, after the execution of the test on the frame equipped with RBS connections, which involved excursions in the plastic field of different structural elements, with not negligible deformations and visible to the naked eye, it has been necessary to replace in addition to the terminal part of the beams also the bases of the columns.

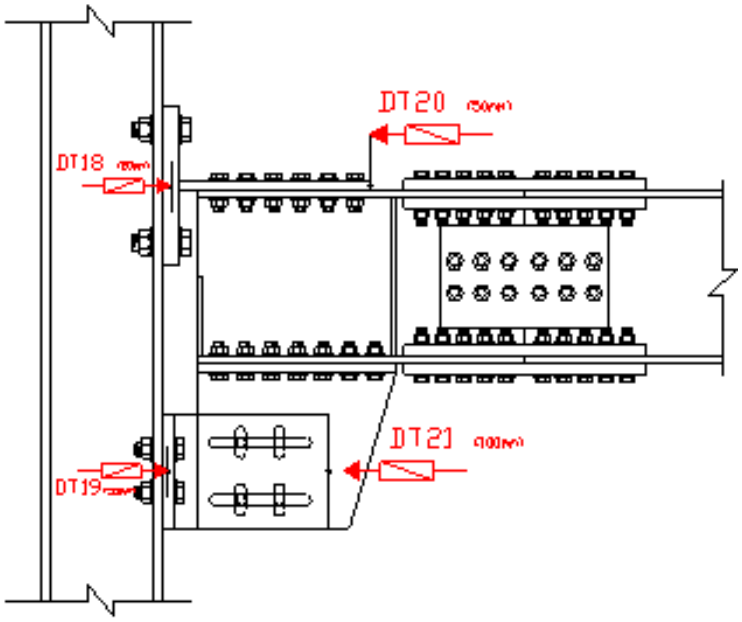

Fig. 5.215 – Position of the displacment trasducers - FREEDAM

Regarding the position of the sensors to monitor the frame during the test, there were no significant changes compared to the test carried out on the frame equipped with RBS connections, especially with reference to strain gauges. The main variation is due to the change in the position of the displacement transducers on the connection. The Fig. 5.215 shows the arrangement of the sensors for the new configuration.

For each FREEDAM connection of the most monitored frame, the results are reported in terms of moment-rotation curves and energy dissipated with the relative forecasts obtained with SeismoStruct.

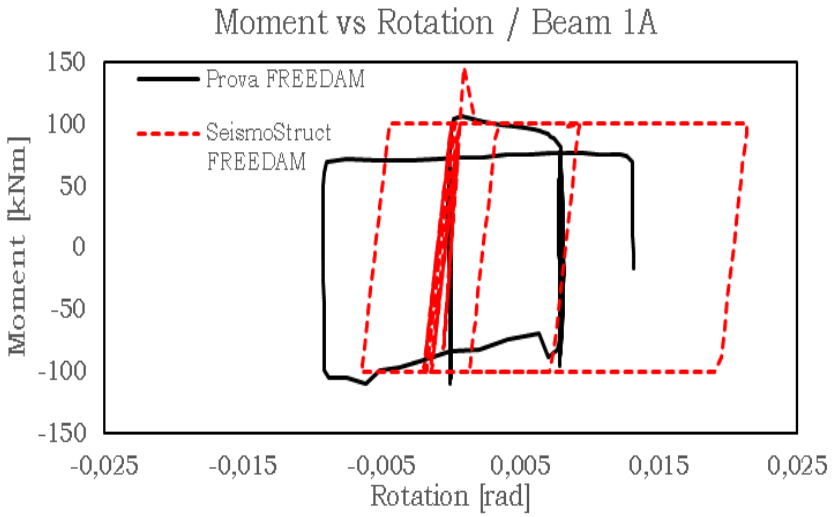

Fig. 5.216 – Moment vs rotation – Beam 1A- FREEDAM

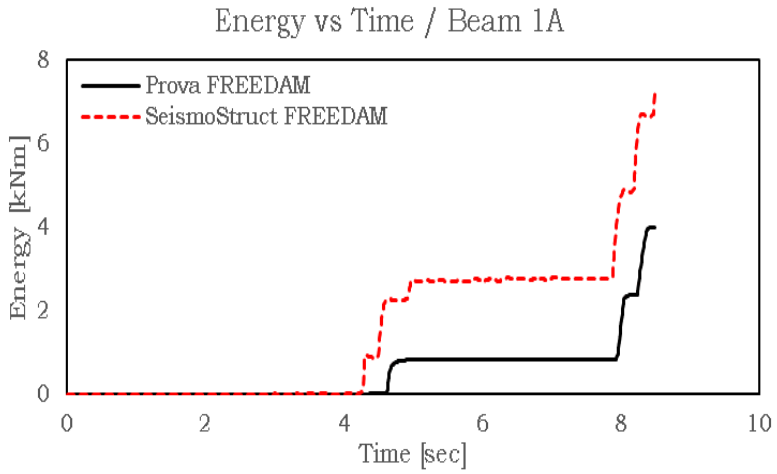

Fig.5.217 – Energy vs time – Bema 1A - FREEDAM

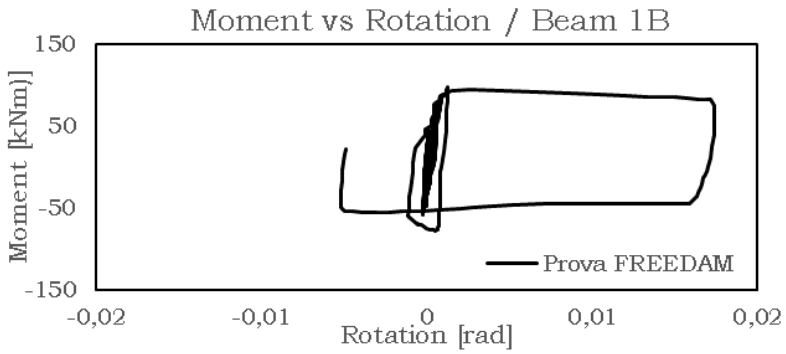

Fig. 5.218 – Moment vs rotation – Beam 1B – FREEDAM

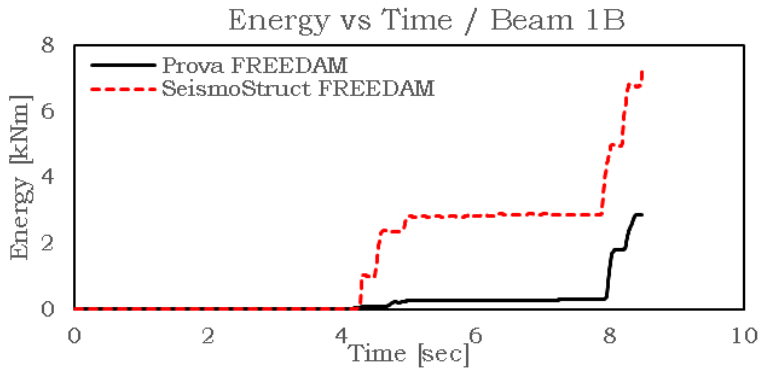

Fig. 5.219 – Energy vs time – Bema 1B - FREEDAM

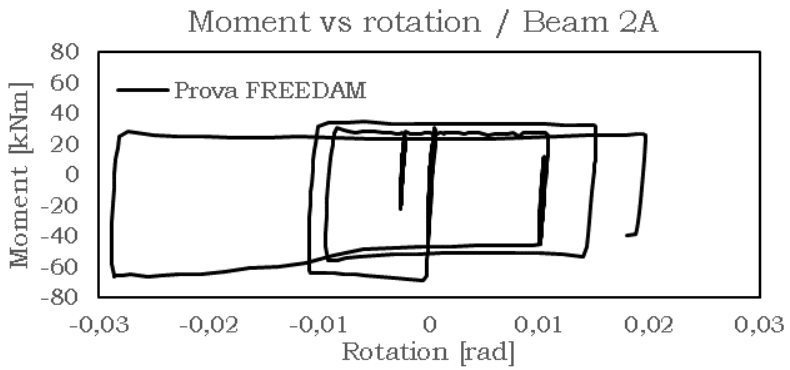

Fig. 5.220 – Moment vs rotation – Beam 2A – FREEDAM

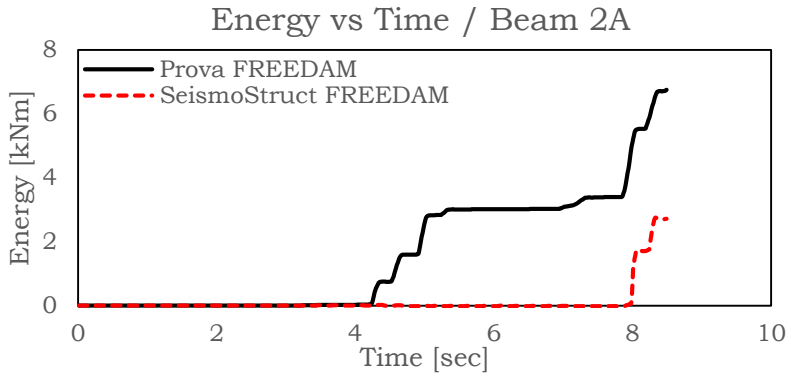

Fig. 5.221 – Energy vs time – Bema 2A - FREEDAM

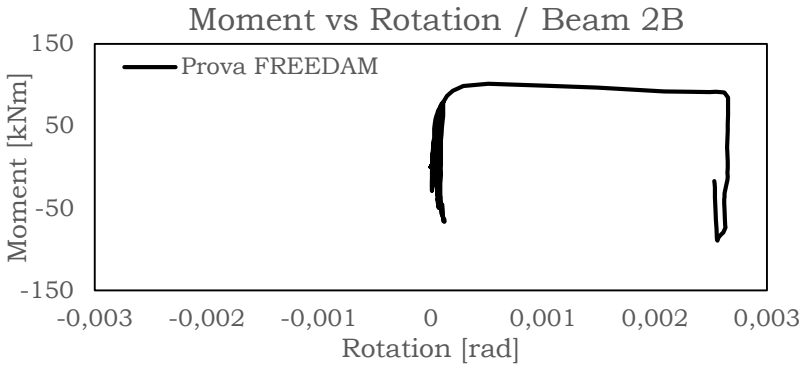

Fig. 5.222 – Moment vs rotation – Beam 2B – FREEDAM

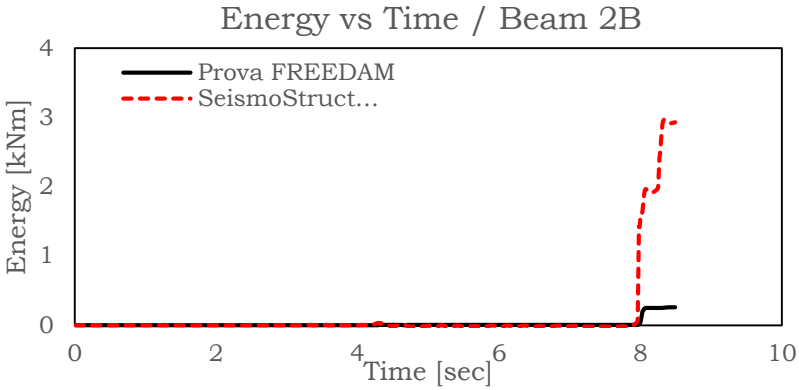

Fig. 5.223 – Energy vs time – Bema 2B - FREEDAM

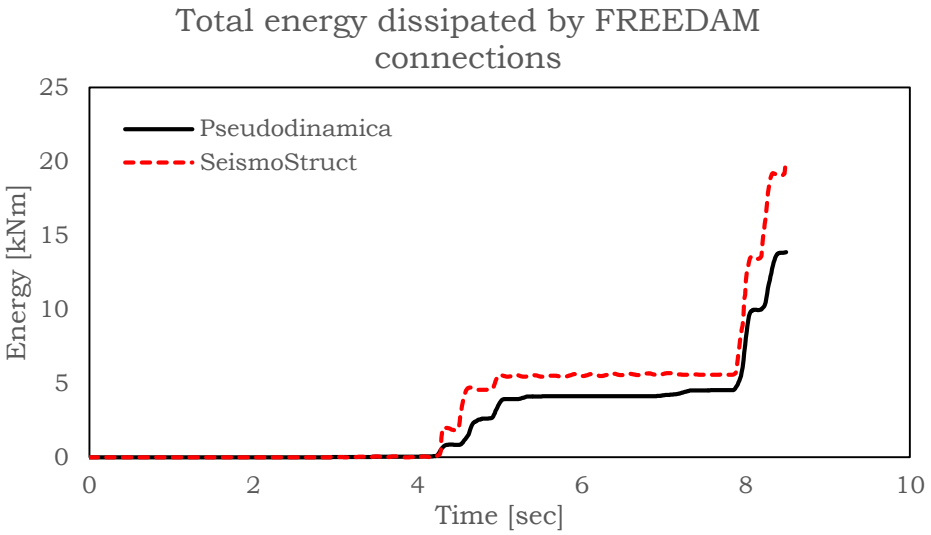

Fig. 5.224 – Total energy dissipated by FREEDAM connections

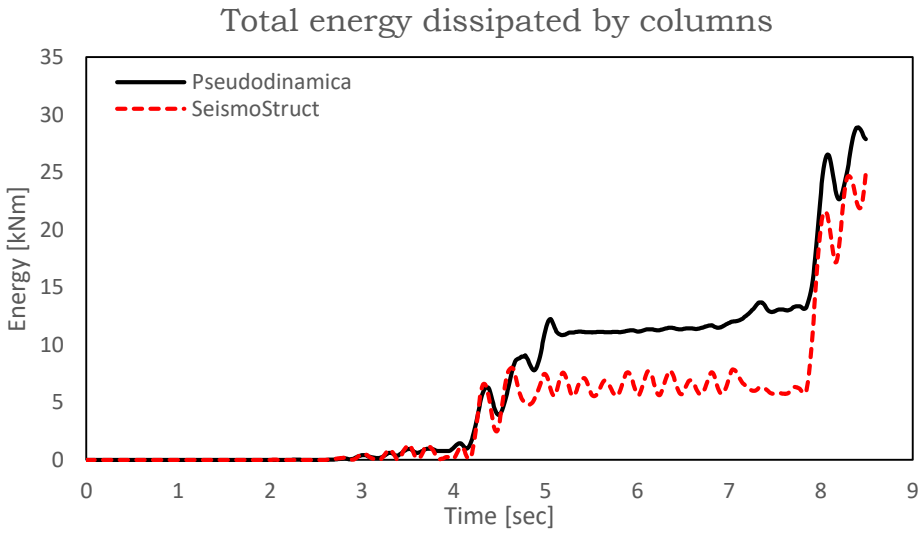

Fig. 5.225 – Total energy dissipated by FREEDAM connections

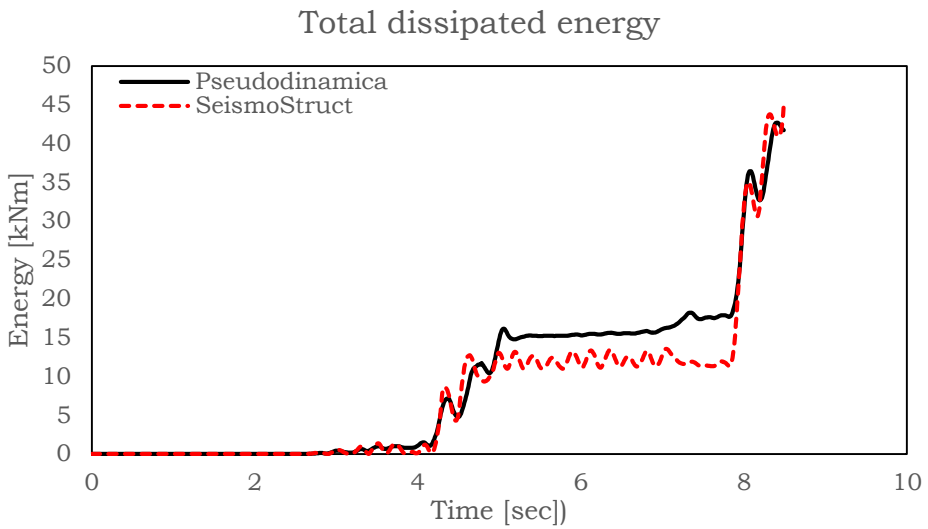

Fig. 5.226 – Total dissipated energy

5.8 References

1. EUROCODE 8, *Design of structures for earthquake – part 1: General rules, seismic actions and rules for buildings*, CEN, 2003.
2. F Iannone, M Latour, V Piluso, G Rizzano (2008) *Experimental analysis of bolted steel beam-tocolumn connections: component identification*. Journal of Earthquake Engineering 15
3. Montuori, R., Piluso, V., (2000): "*Plastic Design of Steel Frames with Dog-Bone Beam-to-Column Joints*", Third International Conference on Behaviour of Steel Structures in Seismic Areas, STESSA 200, 21-24 August, Montreal
4. Moore, K. S., Malley, J. O., and Engelhardt, M. D.: "*Design of Reduced Beam Section (RBS) Moment Frame Connections*", AISC Structural Steel Educational Council, Moraga, CA, 1999.

CHAPTER 6

Starting to a briefly overview of the traditional Moment Resisting Frames, this PhD thesis investigated an innovative typology of beam-to-column connection, namely FREEDAM connection, in order to demonstrate its ability to overcome the main drawbacks of the traditional strategies, in particular the capacity to withstand to seismic input without damage.

In the first part of the thesis several experimental tests on the dissipative joint component have been performed in order to evaluate the random friction material variability, the random variation of the bolts' tightening and the influence of the Belleville disc springs.

The tests on the friction materials at low and high velocities have demonstrated that the M4 material performs adequately for FREEDAM joints so that its use has been considered. Additionally, a statistical range of variation of the values of the friction coefficients to be used in design have been effectively evaluated. The experimental tests pointed out that, in order to reduce degradation of stick-slip, it is necessary to limit the preload to a maximum value of the 60% for all the analysed materials. Finally, the typology of bolted assembly does not seem influent on the friction damper behaviour. The use of disc springs helps to stabilize the bolts' force, but this stabilization does not influence significantly the hysteretic loops.

Another relevant issue investigated within this work is represented by the tightening procedure. In detail, the accuracy of the tightening procedures proposed by EN 1090-2 and the influence of time-related relaxation effect over the pre-load has been carried out. In the

experimental analysis, different bolt assemblies have been tested considering also the possibility to employ the standardised type of European disc springs.

Furthermore, the loss of preload phenomena has been analysed performing several short-term tests. The results of the tests have been used to estimate the loss during the lifetime of the connection, in such a way to take into account this issue during the design process of the connection.

Subsequently, the design procedure for FREEDAM joints have been detailed and applied in order to design the specimens tested under cyclic load conditions at the ISISE laboratory of the University of Coimbra (PT). In particular, the developed design procedure based on the application of the component method currently codified in Eurocode 3 properly integrated with the experimental information on the friction device behaviour seems to be accurate. In addition, the experimental analysis has evidenced that both the configuration with horizontal and vertical dampers are able to avoid, as wanted, damage in all the structural components, meeting therefore the design objectives and thus perform adequately in terms of energy dissipation capacity. Therefore, they can be considered as alternative configurations able to provide a sufficient hysteretic response.

The experimental campaign discussed in the last chapter of this thesis, performed at the STRENGTH laboratory of the University of Salerno, represents the final check of the effectiveness of the proposed connection. The reliability of innovative beam-to-column connections is confirmed by the results of the tests performed on two real structures

the first equipped with a traditional beam-to-column connection (RBS), the second one with FREEDAM connections.

In the first phase of the study only the structure equipped with RBS connections has been tested. An analytical model of the structure has been implemented in SeismoStruct software and it has been validated by experimental results because floor displacements and base shears have been forecasted in a very accurate way because scatters among analytical and experimental data are of about 10%.

Moment-rotation curves representative of hysteretic behaviour of connections have not been predicted in a good manner because maximum experimental rotations are lower while moments are higher than expectation even if such a kind of scatters are very low for tests performed without technical problems in acquiring data.

Nevertheless, it can be observed a good comparison in terms of energy dissipated by beams.

It has also been observed a higher damage in beams ends rather than in columns, as it was expected to be since the structure was conceived in order to exhibit a global type collapse mechanism.

It can be highlighted the good performance of pseudo-dynamic method in performing dynamic tests on real structures, even if, because of the lack of experience, some problems and drawbacks have been shown in this campaign.

The innovative beam-to-column connection typology has been accurately analysed by means of a pseudo dynamic tests on a real scale

MRFs equipped with this typology of connection. The results obtained demonstrate the ability of this system to present wide and stable hysteresis loops, managing to dissipate the seismic energy without damage in the structural elements.

Acknowledgment

Acknowledgment/Ringraziamenti

Al termine di questo lungo percorso di crescita, soprattutto umana, oltre che professionale, tale lavoro rappresenta l'occasione per ringraziare tutti coloro che, direttamente o indirettamente, hanno contribuito al raggiungimento di tale risultato.

In primis ringrazio il Prof. Gianvittorio Rizzano per avermi dato questa grande opportunità, per avermi indirizzato di volta in volta verso la cosa più giusta da fare, e per averlo fatto sempre con l'affetto e la cortesia che lo contraddistingue. E ancora ringrazio la Prof.ssa Aldina Santiago, per essere stata una guida autorevole e sempre disponibile durante la mia permanenza a Coimbra e non solo, ma soprattutto per il suo modo pacato e determinato col quale mi ha incoraggiato in ogni situazione.

Ringrazio inoltre il Prof. Vincenzo Piluso ed il Prof. Luis Simoes da Silva per avermi supportato durante tutte le attività di ricerca, lavorando al vostro fianco ho imparato cosa vuol dire l'amore incondizionato per la ricerca e quanto questo sia importante per il raggiungimento degli obiettivi prefissati.

Ringrazio i colleghi del gruppo dei "rizzaniani", l'ing. Massimo Latour e l'ing. Antonella Bianca Francavilla, un ringraziamento che va ben oltre il supporto nello svolgimento delle attività di ricerca, li ringrazio soprattutto per le risate, per le battute, per aver allietato anche i momenti più critici di questo percorso, grazie di cuore per aver reso questi anni trascorsi insieme davvero indimenticabili, senza di voi non sarei sopravvissuto a questa sfida.

Un ringraziamento va anche a tutti gli altri professori e colleghi coi quali abbiamo condiviso il percorso di questo lungo progetto di ricerca: il Prof. Jean Pierre Jaspart, il Prof. Jean François Demonceau e l'ing. Marina D'Antimo (Università di Liegi), il Prof. Raffaele Landolfo, il Prof. Mario D'Aniello e l'ing. Mariana Zimbru (Università di Napoli), il Prof. Rosario Montuori e l'ing. Elide

Nastri (Università di Salerno), l'ing. Maria Gabriellla Castellano e l'ing. Danilo de Fusco (FIP industriale), l'ing. Ana Francisca dos Santos (Università di Coimbra), l'ing. Igor Guerra e l'ing. Josè Silva (OFeliz metalomecanica), ing. Paolo Bocchi (Gruppo Salteco) .

Ringrazio l'ing. Antonio D'Imperio e l'ing. Riccardo Garella per il loro supporto allo svolgimento delle prove sperimentali presso il laboratorio dell'Università di Salerno, e allo stesso modo l'ing. Illidio dos Santos, l'ing. Claudio Martins, , i tecnici Tjago Cardoso, Miguel Queiroz , Luis Gaspar, Joao Vidal , Ruben Lopes, Jose Pais ed il mio tesista ing. Carlos Duraes per le prove svolte presso il laboratorio dell'Università di Coimbra.

Ringrazio inoltre il dott. Luigi Passeggiato e la sig.ra Raffaella Caldarelli per il loro supporto nel disbrigo delle attività amministrative connesse al progetto di ricerca e soprattutto per avermi seguito con pazienza nello svolgimento di ciascun adempimento, allo stesso modo ringrazio la sig.ra Manuela Rodrigues per avermi indirizzato sin dal mio primo giorno a Coimbra facendomi subito sentire come a casa .

Ringrazio i colleghi ed amici della "sala dottorandi" per aver reso sempre piacevole il lavoro soprattutto quando questo diventava pesante e stancante, pertanto ringrazio l'ing. Francesco Perri veterano della stanza, l'ing. Jamil kazna, l'ing. Roberta Muscati, l'ing. Marco Lamberti, l'ing. Agostina Orefice, l'ing. Elena De Chiara, l'ing. Corrado Chisari, l'ing. Giuseppe Ferrara, l'ing. Alessandro De Vita, l'ing. Simona Streppone, l'ing. Alessandro Pisapia.

Ringrazio i colleghi ed amici di Coimbra per aver reso piacevole la mia permanenza in Portogallo: l'ing. Helder David Craveiro, l'ing. Hugo Augusto, l'ing. Filip Ljubinkovic, l'ing. Rui Matos, l'ing. Damjan Cekerevac, l'ing. Mohammadreza Shahmohammadi, l'ing. Trayana Tankova, l'ing. Daniel Oliveira, l'ing. João Maximino, l'ing. Joel Cunha, l'ing. Jorge Teixeira , l'ing. José Araújo, l'ing. Yoshi Nieto, l'ing. Slobodanka Jovasevic.

Dopo aver ringraziato tutti coloro che hanno contribuito direttamente alla conclusione di questo percorso non posso non ringraziare chi, spesso da dietro le quinte, mi ha supportato comprendendo le mie assenze e incoraggiandomi durante tutte le fasi di questo lungo percorso.

Pertanto un sentito ringraziamento va ai miei genitori, ai quali mi rivolgo con gratitudine e riconoscenza per quanto hanno fatto per me e continuano a fare incondizionatamente.

Ringrazio mia sorella, per il poco tempo che le ho dedicato e per aver saputo gestire ogni problema in modo egregio durante i periodi che ho trascorso lontano da casa.

Ringrazio Nicola, per essere riuscito a darmi la sempre la carica positiva di cui avevo bisogno con le nostre scorribande notturne nei luoghi e agli orari più improbabili,.

Ringrazio Francesco, amico di vecchia anzi vecchissima data, per non esserci mai persi in quasi trent'anni.

Ringrazio Pasquale e Mina, coppia di amici strambi capaci di farmi ridere anche quando non pensavo esistesse qualcosa che potesse farmi passare il malumore del momento.

Ringrazio il dott. Francesco Donnarumma, col quale in questi anni sono sempre rimasto in contatto e che attraverso i suoi racconti ha saputo mostrarmi la mia città aldilà del degrado attuale trasmettermi l'amore incondizionato per le proprie radici storiche e culturali.

Ringrazio il maestro Raffaele Maisano e la sua famiglia, per avermi sempre ricordato che l'amicizia e la stima sono sentimenti senza tempo.

Ringrazio Fulvio e Mariassunta, Antonietta e Bartolo, Catello, Marina, per la loro amicizia vera e profonda che non ha mai risentito del tempo che passa.

Ringrazio gli amici del “gruppo del garage”, in particolare Nicola, Valentina, Maria F., Tonia, Elena, Carlo, Gianluca, Maria M., Anna, Laura, Marianna, Michela, Giuseppe, perché anche se distanti e ognuno perso nel proprio mondo, resteremo sempre un gruppo, così come ci ha insegnato Claudio.

Ringrazio l’amico Rito, col quale abbiamo condiviso il percorso del liceo e col quale persiste una profonda amicizia che ci vede legati anche a distanza.

Ringrazio la prof.ssa Fontana, esempio di cosa vuol dire amare veramente la cultura in tutte le sue sfaccettature, a lei va il mio sentito ringraziamento per avermi insegnato il metodo di studio, per avermi insegnato ad approfondire la conoscenza delle cose dubitando sempre della prima e più rassicurante soluzione.

Ringrazio gli amici Enrico e Vincenzo, perché con i loro racconti al Gabbiano hanno suscitato sempre la mia curiosità ed il mio interesse, a loro va tutta la mia stima.

In ultimo, ma non ultimo, preme ringraziare la persona che ha reso speciale ogni giorno della mia vita da quando ho avuto la fortuna di incrociare i suoi splendidi occhi neri, non posso non ringraziarla per la pazienza, il sacrificio, la dedizione con la quale ha abbracciato questo mio progetto, sostenendomi in ogni momento e contribuendo in modo determinante alraggiungimento di questo traguardo. A Patrizia, mia dolcissima promessa sposa, va il mio ringraziamento pieno d’@µ°®3.